Biological and Medical Physics, Biomedical Engineering

Xinjian Chen · Fei Shi · Haoyu Chen
Editors

Retinal Optical Coherence Tomography Image Analysis

Science Press Beijing

Springer

Biological and Medical Physics, Biomedical Engineering

BIOLOGICAL AND MEDICAL PHYSICS, BIOMEDICAL ENGINEERING

This series is intended to be comprehensive, covering a broad range of topics important to the study of the physical, chemical and biological sciences. Its goal is to provide scientists and engineers with textbooks, monographs, and reference works to address the growing need for information. The fields of biological and medical physics and biomedical engineering are broad, multidisciplinary and dynamic. They lie at the crossroads of frontier research in physics, biology, chemistry, and medicine.

Books in the series emphasize established and emergent areas of science including molecular, membrane, and mathematical biophysics; photosynthetic energy harvesting and conversion; information processing; physical principles of genetics; sensory communications; automata networks, neural networks, and cellular automata. Equally important is coverage of applied aspects of biological and medical physics and biomedical engineering such as molecular electronic components and devices, biosensors, medicine, imaging, physical principles of renewable energy production, advanced prostheses, and environmental control and engineering.

More information about this series at http://www.springer.com/series/3740

Xinjian Chen · Fei Shi · Haoyu Chen
Editors

Retinal Optical Coherence Tomography Image Analysis

Science Press
Beijing

Springer

Editors
Xinjian Chen
School of Electronic and Information Engineering
Soochow University
Suzhou, Jiangsu, China

Haoyu Chen
Joint Shantou International Eye Center
Shantou University and the Chinese University of Hong Kong
Shantou, Guangdong, China

Fei Shi
School of Electronic and Information Engineering
Soochow University
Suzhou, Jiangsu, China

ISSN 1618-7210 ISSN 2197-5647 (electronic)
Biological and Medical Physics, Biomedical Engineering
ISBN 978-981-13-1824-5 ISBN 978-981-13-1825-2 (eBook)
https://doi.org/10.1007/978-981-13-1825-2

Jointly published with Science Press
The print edition is not for sale in China. Customers from China please order the print book from: Science Press.

Library of Congress Control Number: 2018949879

This Springer imprint is published by the registered company Springer Nature Singapore Pte Ltd.
The registered company address is: 152 Beach Road, #21-01/04 Gateway East, Singapore 189721, Singapore

Foreword

Volumetric 3D optical coherence tomography (OCT) imaging of the eye has revolutionized diagnosis and management of patients with ophthalmic diseases. OCT was introduced in the 1980s with first biomedical OCT imaging applications appearing in the 1990s. The first broadly available ophthalmic OCT system—Zeiss Stratus—was introduced in 2002 and offered 2D "depth" imaging of the retina. As the technology developed, true 3D volumetric retinal scanners began to appear around 2008 with a number of manufacturers offering ophthalmic 3D-OCT imaging devices. Over the years, many variants of retinal OCT were introduced, starting with primarily 2D time-domain OCT technology capable of acquiring 400 axial scans (A-scans) per second, followed by spectral-domain OCT offering 50 times faster image acquisition with 27,000 A-scans/s, swept-source OCT (100,000 A-scans/s), Doppler OCT, adaptive-optics OCT, etc. Soon after, clinical utilization of the OCT for imaging the retinal layers and the optic nerve head became common and other ophthalmic applications emerged including OCT imaging of the choroid, optic disk, retinal vasculature, and other parts of the eye anatomy. OCT is increasingly used to image vascular flow, as well as eye function including anatomy-derived visual function. Consequently, OCT imaging is employed for diagnostic and treatment-guidance purposes in many diseases including age-related macular degeneration, diabetic macular edema, macular hole, papilledema, retinal vein occlusion, glaucoma, intraretinal tumors, etc.

Quantitative ophthalmic OCT image analysis has trailed the introduction of retinal OCT scanners with only a minimal delay. The experience with volumetric biomedical image analysis, which was developed in radiologic, cardiologic, and/or neuroscience applications over several decades, and the associated expertise of medical imaging researchers allowed rapid translation of this knowledge to ophthalmic OCT image analysis. The transition from primarily 2D retinal imaging using fundus photography, fluorescein angiography, and other 2D approaches that were mostly qualitative in clinical care to quantitative 3D analyses was arguably the fastest among all areas of clinical and translational medicine.

This book offers a timely overview of this very area of the ophthalmic imaging—OCT image acquisition, formation, quantitative OCT image analysis, and clinical applications. The book, edited by Xinjian Chen, Fei Shi, and Haoyu Chen, and entitled *Retinal Optical Coherence Tomography Image Analysis*, gives a comprehensive summary of the state of the art in 2018. The book is logically divided into 13 chapters, written by teams of international experts—medical imaging researchers, medical image analysis scholars, and clinically active research physicians. As a result, the book offers an excellent insight in translational applications of ophthalmic OCT imaging, starting with introductory aspects of imaging physics and covering many areas of analysis with a special focus on their relevance for retinal disease diagnosis, treatment, and outcome prediction.

The first chapter motivates the entire book and provides an introductory overview of clinical applications of OCT retinal imaging. The next group of chapters—Chaps. 2–4—give fundamentals of OCT imaging physics and OCT image acquisition, describe methods of obtaining high-quality OCT image data via denoising and enhancement, and provide a forward-looking synopsis of OCT image formation from sparse representations. The third and largest group of chapters—Chaps. 5–12—are devoted to quantitative OCT image analysis. It focuses on image segmentation, quantitative description of retinal morphology, diagnostic abilities of OCT for various ophthalmic diseases, and diagnostic utilization of retinal-layer-specific optical intensities. Separate chapters provide information about OCT-based analysis of the optic nerve head in glaucoma and methods for the analysis of the choroid. Three additional chapters deal with the difficult problems of retinal layer segmentation in the presence of morphology/topology-modifying diseases—fluid formation in the outer and inner retina in pigment epithelial detachment, quantification of the external limiting membrane integrity, and/or assessment of geographic atrophy and drusen. The entire family of detection and quantification of SEADs—symptomatic exudate-associated derangements—characteristically occurring in age-related macular degeneration, diabetic macular edema, and other retinal diseases is also covered. The last Chap. 13 outlines the predictive capabilities of OCT imaging for therapy guidance and outcome prediction from temporal OCT image sequences—while based on only a very small sample of patients, it provides a futuristic forward-looking peek in the envisioned capabilities of clinical OCT usage of longitudinal patient data.

The book is a welcome addition to the field of quantitative ophthalmic imaging. Its focus on and consistent treatment of volumetric retinal images from 3D retinal optical coherence tomography, its stress of translational aspects of these approaches, and the demonstrated advances obtained by direct shoulder-to-shoulder collaborations of medical imaging scholars, engineers, physicists, and physicians are an unquestionable strength of this interdisciplinary book. It will undoubtedly be well received by graduate and post-graduate students, ophthalmic imaging researchers, OCT imaging practitioners, and ophthalmic physicians alike.

Iowa City, USA

Milan Sonka, Ph.D.
The University of Iowa

Contents

Contributors

Zahra Amini Department of Bioelectrics & Biomedical Engineering, School of Advanced Technologies in Medicine, Medical Image & Signal Processing Research Center, Isfahan University of Medical Sciences, Isfahan, Iran

Delia Cabrera DeBuc Department of Ophthalmology, McKnight Vision Research Center, Bascom Palmer Eye Institute, University of Miami Miller School of Medicine, Miami, USA

Haoyu Chen Joint Shantou International Eye Center, Shantou University and the Chinese University of Hong Kong, Shantou, China

Qiang Chen School of Computer Science and Engineering, Nanjing University of Science and Technology, Nanjing, China

Xinjian Chen School of Electronics and Information Engineering, Soochow University, Suzhou, China; State Key Laboratory of Radiation Medicine and Protection, Soochow University, Suzhou, China

Jay Chhablani L V Prasad Eye Institute, Hyderabad, Telangana, India

Mattia Desana Image and Pattern Analysis Group (IPA), University of Heidelberg, Heidelberg, Germany

Luis de Sisternes Department of Radiology and Medicine (Biomedical Informatics Research) and Ophthalmology, Stanford University School of Medicine, Stanford, USA

Leyuan Fang College of Electrical and Information Engineering, Hunan University, Changsha, China

Enting Gao School of Electronics and Information Engineering, Soochow University, Suzhou, China

Soumya Jana Indian Institute of Technology, Hyderabad, Telangana, India

Raheleh Kafieh Department of Bioelectrics & Biomedical Engineering, School of Advanced Technologies in Medicine, Medical Image & Signal Processing Research Center, Isfahan University of Medical Sciences, Isfahan, Iran

Theodore Leng Byers Eye Institute at Stanford, Stanford University School of Medicine, Palo Alto, USA

Shutao Li College of Electrical and Information Engineering, Hunan University, Changsha, China

Danny Siu-Chun Ng Joint Shantou International Eye Center, Shantou University and the Chinese University of Hong Kong, Shantou, China

Sijie Niu School of Information Science and Engineering, University of Jinan, Jinan, China

Lingjiao Pan School of Electronics and Information Engineering, Soochow University, Suzhou, China

Hossein Rabbani Department of Bioelectrics & Biomedical Engineering, School of Advanced Technologies in Medicine, Medical Image & Signal Processing Research Center, Isfahan University of Medical Sciences, Isfahan, Iran

Fabian Rathke Image and Pattern Analysis Group (IPA), University of Heidelberg, Heidelberg, Germany

Ashutosh Richhariya L V Prasad Eye Institute, Hyderabad, Telangana, India

Daniel L. Rubin Department of Radiology and Medicine (Biomedical Informatics Research) and Ophthalmology, Stanford University School of Medicine, Stanford, USA

Christoph Schnörr Image and Pattern Analysis Group (IPA), University of Heidelberg, Heidelberg, Germany

Fei Shi School of Electronics and Information Engineering, Soochow University, Suzhou, China

Tingkun Shi Joint Shantou International Eye Center, Shantou University and the Chinese University of Hong Kong, Shantou, China

Gábor Márk Somfai Department of Ophthalmology, Semmelweis University, Budapest, Hungary; Retinology Unit, Pallas Kliniken Augenzentrum, Olten, Switzerland

Andrea Szigeti Department of Ophthalmology, Semmelweis University, Budapest, Hungary

Erika Tátrai Department of Ophthalmology, Semmelweis University, Budapest, Hungary

Jing Tian Department of Ophthalmology, McKnight Vision Research Center, Bascom Palmer Eye Institute, University of Miami Miller School of Medicine, Miami, USA

Boglárka Enikő Varga Department of Ophthalmology, Semmelweis University, Budapest, Hungary

Kiran Kumar Vupparaboina L V Prasad Eye Institute, Hyderabad, Telangana, India; Indian Institute of Technology, Hyderabad, Telangana, India

Bo Wang School of Electronics and Information Engineering, Soochow University, Suzhou, China

Menglin Wu School of Computer Science and Technology, Nanjing Tech University, Nanjing, China

Shuxia Zhu School of Electronics and Information Engineering, Soochow University, Suzhou, China

Weifang Zhu School of Electronics and Information Engineering, Soochow University, Suzhou, China

Chapter 1
Clinical Applications of Retinal Optical Coherence Tomography

Haoyu Chen, Tingkun Shi and Danny Siu-Chun Ng

The developments of medical imaging techniques and medical image analysis methods are always motivated by the needs arising from clinical applications. This chapter introduces anatomy of the eye and the retina, describes various types of eye diseases that can be visualized with OCT imaging, and therefore presents the must-know background knowledge for readers interested in retinal OCT image analysis.

1.1 Anatomy of the Eye and Retina

1.1.1 Simple Anatomy of the Eye

The eye is an organ that perceives light and visual information. There are five senses in human body, including vision, hearing, smell, touch and taste. More than 80% of information we received is obtained through vision perceived by the eyes.

The structure of the eye is like a ball, although it is not a perfect sphere. There are three layers of coats, enclosing three intraocular components: (1) The front of the eyeball is cornea, which is transparent and contribute to most of the refractive power of the eye; the posterior part of the outermost layer is sclera, which consists of fibrous tissue and protects the inner structures. (2) The middle layer of the eyeball is vascular tunic or uvea, which consists of iris, ciliary body and choroid. The center of iris is open and called pupil. The muscles inside the iris control the size of pupil and the amount of light getting into the retina. Ciliary body is responsible for the generation of aqueous humor and accommodation. The choroid is located just outside the retina and provides nutrition and oxygen for the outer part of retina. (3) The innermost

H. Chen (✉) · T. Shi · D. S.-C. Ng
Joint Shantou International Eye Center, Shantou
University and the Chinese University of Hong Kong, Shantou, China
e-mail: drchenhaoyu@gmail.com

X. Chen et al. (eds.), *Retinal Optical Coherence Tomography Image Analysis*,
Biological and Medical Physics, Biomedical Engineering,
https://doi.org/10.1007/978-981-13-1825-2_1

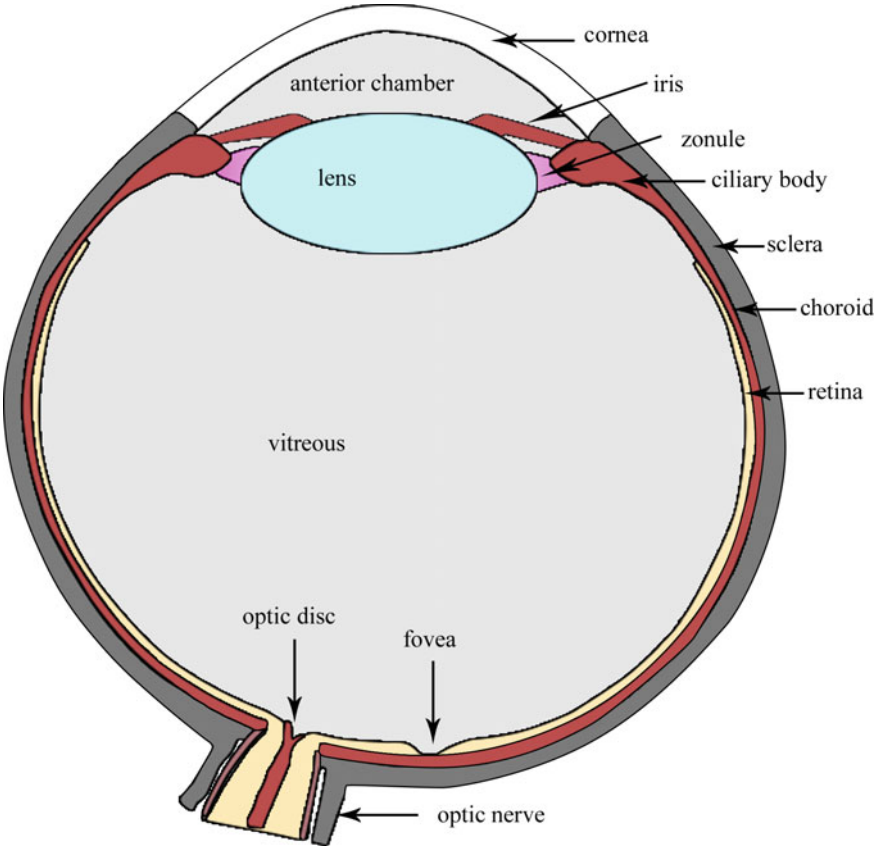

Fig. 1.1 Illustration of the anatomy of human eye

layer is retina, which is an extension of central nerve system and responsible for the transduction of visual signal into neural signal. The intraocular components include aqueous humor, lens and vitreous body. The lens is connected to ciliary body by the zonules. Aqueous humor and vitreous body locate in front and back of the lens (Fig. 1.1).

The eye is a very special organ. The optical media, including cornea, aqueous humor, lens and vitreous, are transparent. This character allows light getting into the innermost layer, retina, and also allows visualization of retinal structure using various instruments, including optical coherence tomography.

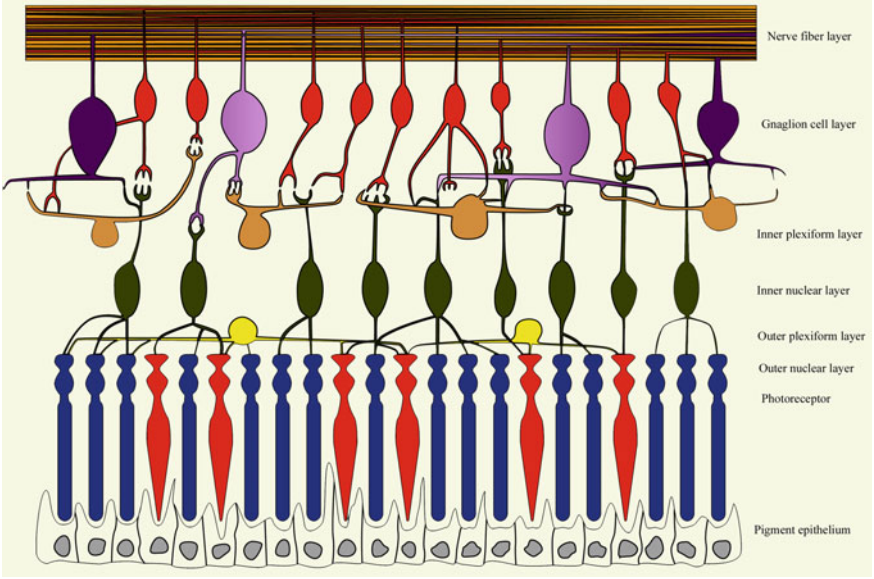

Fig. 1.2 Cross-sectional diagram showing the structure of human retina

1.1.2 Simple Histology of Retina

Retina is the most important structure of the eye. It is a neural tissue and transduces light into neural signal.

The histology of the retina consists of ten layers. From inner to outer, they are internal limiting membrane, retinal nerve fiber layer, retinal ganglion cell layer, inner plexiform layer, inner nuclear layer, outer plexiform layer, outer nuclear layer, external limiting membrane, photoreceptor inner and outer segment, retinal pigment epithelium. Retina is transparent except for the blood vessels and retinal pigment epithelium monolayer (Fig. 1.2). Transparency of retina allows light passing though and reaching the photoreceptors, where the photo-neural transduction occurs.

There are two blood supply systems to retina, retinal vascular system and choroidal vascular system. The retinal vascular system rises from optic disc, branches on the retinal nerve fiber layer, and forms three layers of capillary, located in the retinal ganglion cell layer, inner plexiform layer and outer plexiform layer. The retinal vascular system supplies the inner layers of retina. The outer retina is avascular, and oxygen and nutrition is supplied from the choroidal capillary through retinal pigment epithelium.

On fundus photography, the optic disc is an important landmark of the retina. It is about 1.5 mm diameter, with a cup at the center. It is located about 2.5 optic disc diameter nasal to the fovea, which is the center point of the macula. The fovea is special because it consists of abundant number of cone photoreceptors, which is

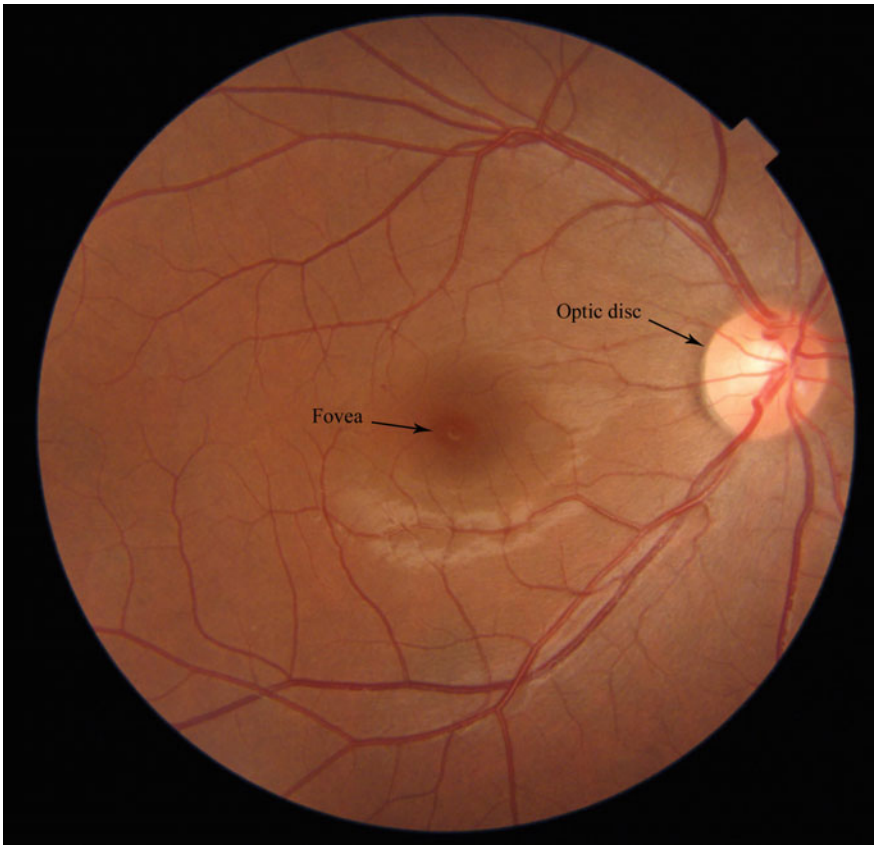

Fig. 1.3 Fundus photography of a normal human retina

responsible for fine vision and color vision. There is no inner retinal structure in fovea, hence, there is no blood vessel and allows light to reach the photoreceptors without any disturbance (Fig. 1.3).

1.1.3 Normal Macular OCT Image

OCT provides high resolution imaging for the cross-sectional structure of retina. The reflectivity of tissue is determined by the optical character of tissue itself. Vitreous has the lowest reflectivity in normal subjects. The highest reflective band at the inner retina is retinal nerve fiber layers, which is thickest at the parapapillary region and thinnest just temporal to the fovea. Generally, the nerve fiber layers have higher reflectivity compared with nuclear layers. OCT not only demonstrates the 10 layers of retina, but it is also able to visualize the detail structures of photoreceptor and choroid

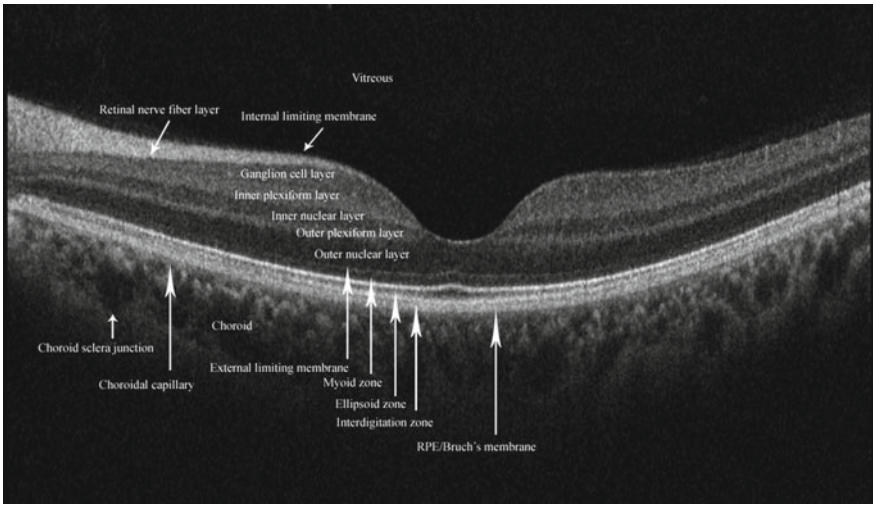

Fig. 1.4 Retinal layers on optical coherence tomography in normal subject

[1]. There are four hyper-reflective bands at outer retina: external limiting membrane, inner segment ellipsoid zone, interdigitation zone, and RPE/Bruch's complex. The choroidal-scleral interface can be identified and the thickness of choroid can be measured (Fig. 1.4).

1.2 Vitreomacular Interface Diseases

The vitreous body is a transparent structure which fills the space in front of the retina. In physiological condition, vitreous body provides mechanical support for retina. However, vitreous may degenerate with aging or under pathologic conditions. The disorders at vitreomacular interface cannot be well-recognized until recently due to the availability of OCT, which provides high resolution cross-sectional imaging for visualizing the vitreomacular interface.

There are several disorders at vitreomacular interface, including vitreomacular adhesion, vitreomacular traction, macular hole, epiretinal membrane. The disorders of vitreomacular interface can be seen in aging population, and also secondary to other diseases, such as high myopia, proliferative diabetic retinopathy, etc.

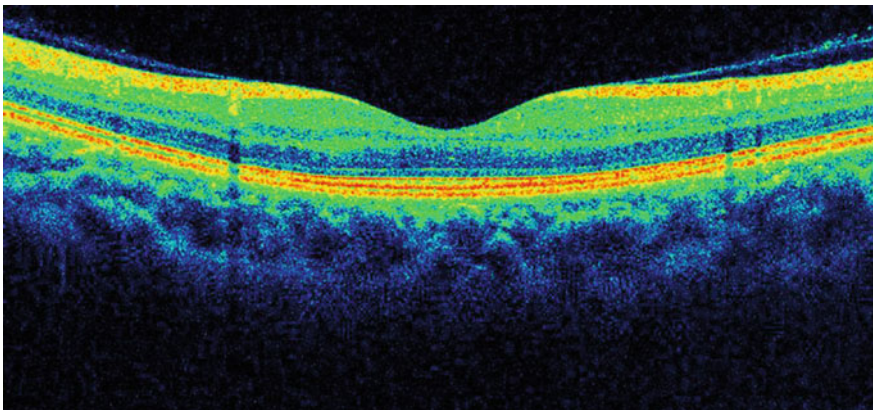

Fig. 1.5 Vitreomacular adhesion. There is separation of vitreous from retina at perifoveal region. Please note there is no morphological change of intraretinal structure

1.2.1 Vitreomacular Adhesion

Vitreomacular adhesion is defined as perifoveal vitreous detachment with the adhesion of vitreous at fovea, without changing the intraretinal structures [2]. Vitreomacular adhesion is a physiological status, because most eyes have complete vitreoretinal adhesion at birth, and develop to posterior vitreous detachment with aging. The vitreous is adhered to retina most tightly at fovea, optic disc and peripheral retina. The process of posterior vitreous detachment begins at perifoveal region. Vitreomacular adhesion can be further classified as focal ($\leq$1500 um) and broad (>1500 um) adhesions according to the size of adhesion (Fig. 1.5).

1.2.2 Vitreomacular Traction

Vitreomacular traction is defined as perifoveal vitreous detachment with the adhesion of vitreous at fovea which changes the intraretinal structures [2]. Traction at the fovea may result in contour changes at the inner surface, intraretinal pseudocyst and separation of retina from the RPE. These changes lead to metamorphopsia and vision decrease. Vitreomacular traction can also be classified as focal ($\leq$1500 um) and broad (>1500 um) adhesion according to the size of adhesion (Fig. 1.6).

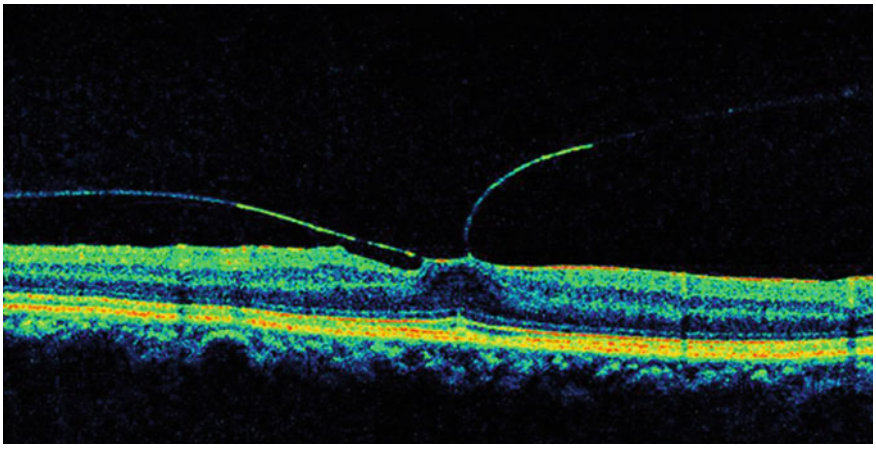

Fig. 1.6 OCT of focal vitreomacular traction shows the high reflectivity band incompletely detached from the retina and changes of the contour of the intraretinal structures due to the slightly elevated inner surface of fovea

1.2.3 Full Thickness Macular Hole (FTMH)

Macular hole was defined as interruption of full thickness retina tissue at fovea. The opening of retina involves all neural retinal layers, from internal limiting membrane to photoreceptor. On fundus photography, macular hole is usually round, with a circus of edema around the hole.

Macular hole is classified into 4 stages by Gass based on biomicroscopic examination: stage 1: impending macular hole; stage 2: small hole; stage 3: large hole; stage 4: full thickness macular hole with PVD [3]. Now, with OCT, the staging is redefined: stage 1 is now called vitreomacular traction; stage 2 is a small or medium macular hole with vitreomacular traction (Fig. 1.7); stage 3 is a medium or large macular hole with vitreomacular traction; stage 4 is a macular hole without vitreomacular traction (Fig. 1.8) [2].

OCT can help measuring the diameter of macular hole. The diameter is not consistent at different layers. It is most narrow in the middle. Therefore, usually two diameters are measured, the minimal diameter and the basal diameter. The diameter of macular hole usually ranges from 50–1000 μm. Furthermore, OCT demonstrates the detail morphological changes of macular hole. There are usually some intraretinal cysts around the hole.

OCT can also help differential diagnosis of macular hole. There are some cases with pseudo macular hole, which is actually caused by epiretinal membrane that elevated retina around fovea without interruption of neural retinal tissue (Figs. 1.9 and 1.10). There are also some cases with lamellar macular hole, with interruption of inner layers, but not the full thickness of retina.

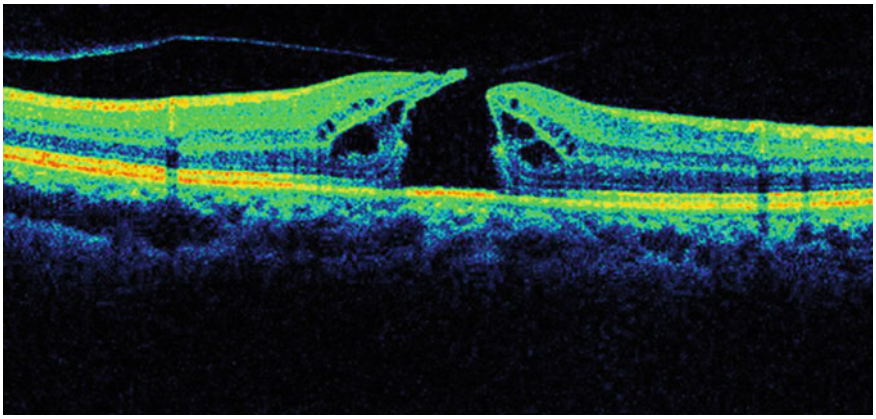

Fig. 1.7 Small full thickness macular hole with vitreomacular traction. The OCT image shows attachment of the vitreous to the lid of the hole and cystic changes

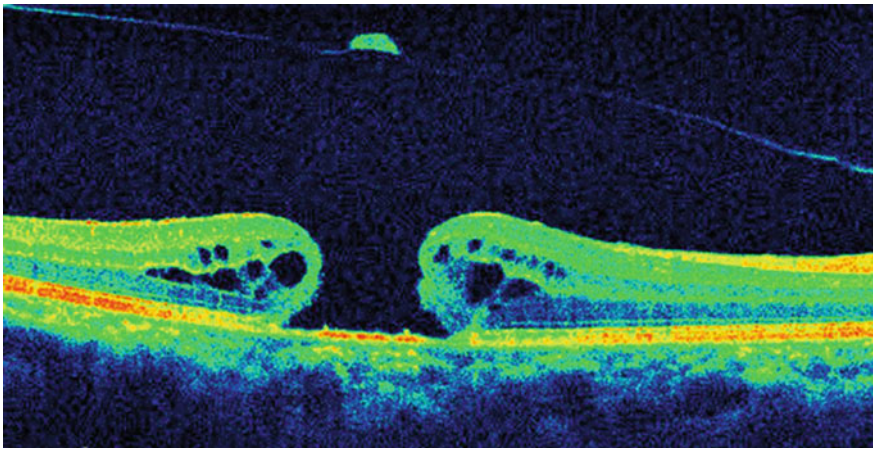

Fig. 1.8 Large full thickness macular hole without vitreomacular traction. The OCT image shows a full-thickness macular hole with intraretinal cystic spaces and an overlying operculum

OCT is also helpful in following up of macular hole after surgical repair. It shows that the inner layer of macular hole connects with each other first. Repairing of the outer retinal layers disruption takes a longer time which explains the prolonged visual disturbance after surgery. The morphology of repaired macular hole can be categorized into three patterns, U type (normal foveal contour), V type (steep foveal contour) and W type (foveal defect of neurosensory retina). This classification system correlates with visual recovery [4].

Fig. 1.9 Fundus photography demonstrates fibrocellular proliferation on macular region except fovea. It appears like a macular hole

1.2.4 Epiretinal Membrane

Epiretinal membrane (ERM) is due to proliferation of fibrocellular tissue on the inner surface of retina (Fig. 1.9). On OCT, it is characterized by medium to high reflective lines above neural retina. There are some adhesions of the epiretinal membrane to the inner surface of retina in multiple locations. Some adhesions may be wide and some may be focal. Sometimes in early stages of epiretinal membrane, the adhesion maybe very wide and the deadhesion area may not be identifiable. This is characterized by flattening of the retina inner surface (Fig. 1.10).

OCT is used not only for diagnosing epiretinal membrane, but also help planning for operation. From OCT images, the surgeon can identify the region where the distance between ERM and ILM is maximum which is the best location for initiation of membrane grasping to avoid damage of retinal tissue [5].

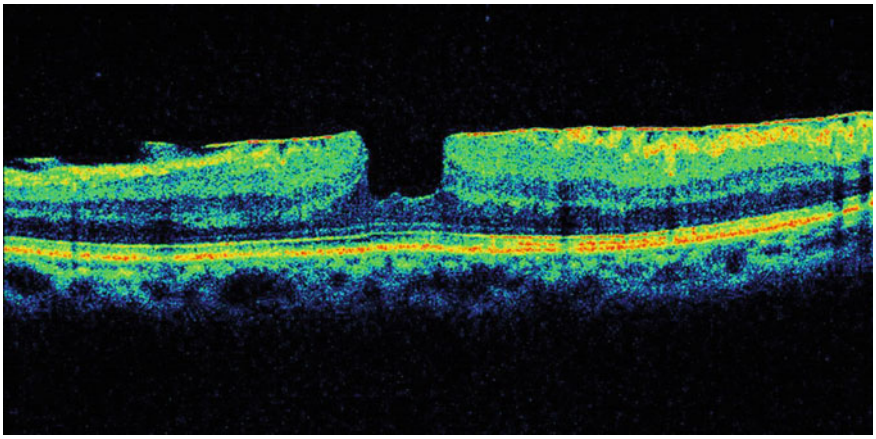

Fig. 1.10 OCT of the case in Fig. 1.9 shows high reflectivity anterior to the retina. Retinal inner surface is flattened and the retinal thickness is increased. There is no disruption of retina tissue and the fovea appear as a macular pseudohole

1.2.5 Myopic Traction Maculopathy

The pathogenesis of high myopia is axial elongation of the eyeball. The sclera remodels and elongates, however, the retina tissue and choroid do not elongate equivalently with the sclera, especially the internal limiting membrane and the retinal vessels [6].

The morphological characters of myopic traction maculopathy include the following:

1. Vitreous adhesion and traction at vitreomacular interface. The adhesions are not limited to the fovea, but also at other locations, especially large vessels.
2. Retinoschisis, which is the separation of retinal layers, caused by the traction force on the inner retinal surface.
3. Disruption of photoreceptor, which may manifest as "outer lamellar hole".
4. Localized retinal detachment at fovea, without full thickness macular hole (Fig. 1.11).
5. Full thickness macular hole with or without retinal detachment.

1.3 Glaucoma and Optic Neuropathy

Glaucoma is a group of ocular disorders characterized by progressive degeneration of optic nerve. OCT provides early diagnosis and monitoring of the disease progression [7]. Because retina is an extension of the central nervous system (CNS), many CNS diseases may manifest in the retina, where the optic nerve head is located.

There are several different commercially available OCT devices providing different scans and analyses modules. Generally, there are three important measurements

in retinal OCT for glaucoma and optic neuropathy, including parapapillary retinal nerve fiber layer thickness, retinal ganglion cells complex layer thickness, and morphology of optic nerve head.

1.3.1 Parapapillary Retinal Nerve Fiber Layer Thickness

Retinal nerve fibers are the axons of retinal ganglion cells which make up the retinal nerve fiber layer (RNFL) lying just below the internal limiting membrane. RNFL has high reflectivity and can be easily identified and segmented on OCT images. The nerve fibers exit the eyeball and connect to the brain via optic nerve. Therefore, RNFL thickness is the highest at the parapapillary regions. Typically, OCT provides a cube scan centered on the optic nerve head and produces a RNFL thickness map. The RNFL thickness at the 3.4 mm diameter circle is calculated at each pixel. The average thickness at each clock hour and quadrant are also calculated. The results have been compared to the distribution of normal database and displayed as false color scale. The symmetry of RNFL thickness has been calculated [8]. In early stage of glaucoma, the RNFL reduced mostly on the superotemporal and inferotemporal bundles, but the late stage, RNFL thinning involves the entire region (Fig. 1.12).

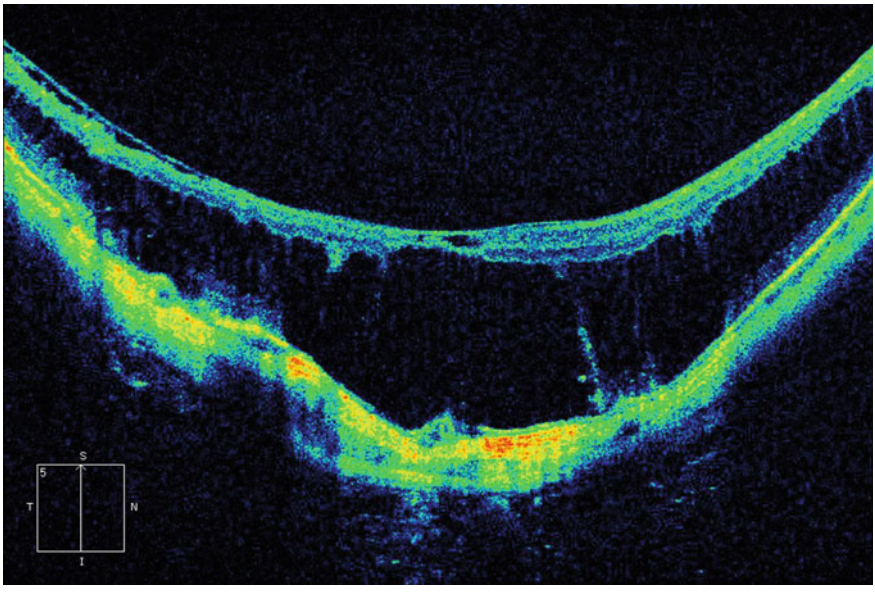

Fig. 1.11 OCT of a patient with high myopic maculopathy. There is vitreomacular interface traction, retinoschisis, disruption of photoreceptor

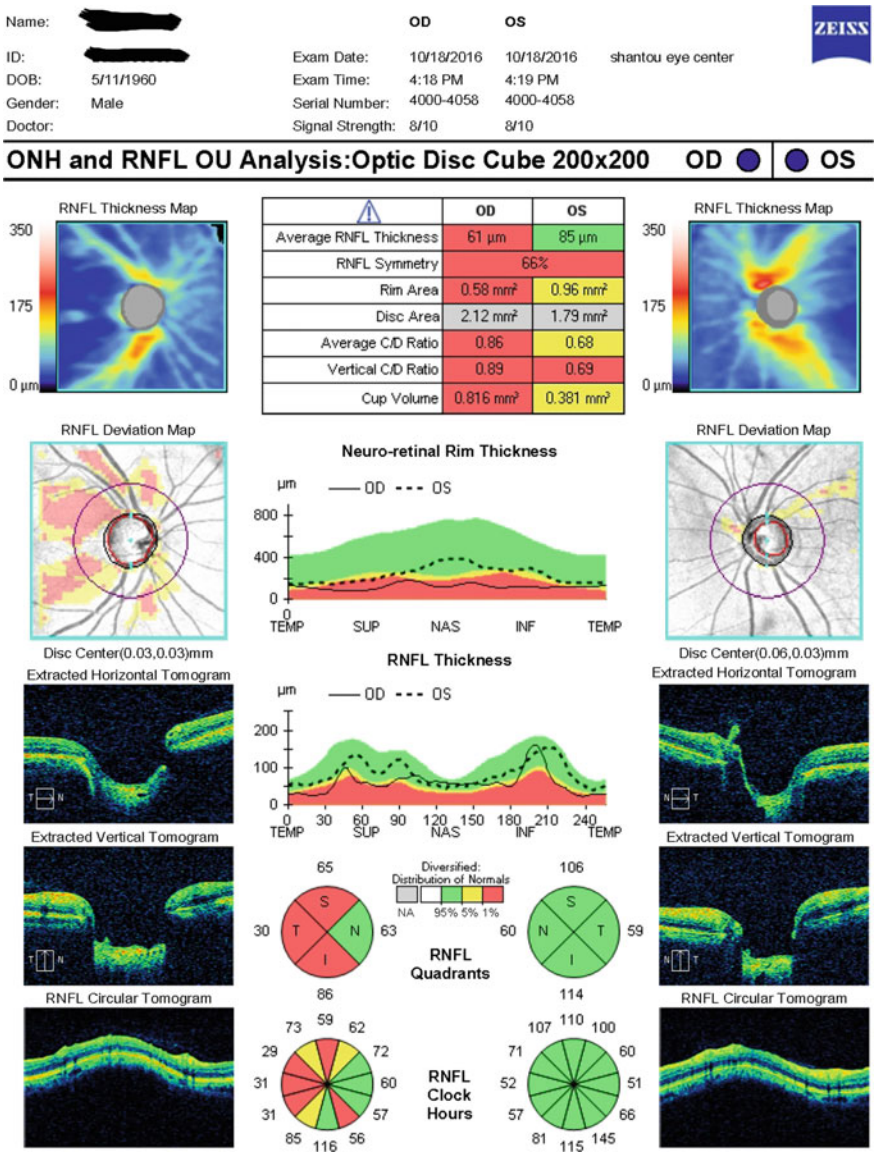

Fig. 1.12 Parapapillary retinal nerve fiber layer thickness and optic nerve head analysis of a case with glaucoma

1.3.2 Macular Ganglion Cell Thickness

The ganglion cell layer appears as a relatively hyporeflective layer between the RNFL and inner plexiform layer on OCT. It is the thickest at the macular region. However, it is difficult to segment ganglion cell layers based on reflectivity. Therefore, it was measured with other layer(s) together. In Zeiss Cirrus OCT, the Ganglion Cell Analysis consists of ganglion cell layer and inner plexiform layer. In Optovue OCT, the Ganglion cell complex include RNFL, GCL and IPL. Topcon OCT provides macular RNFL, GCL+IPL, and NFL+GCL+IPL thickness measurements. The scan region is divided into various sectors. The macular ganglion cell thickness map is displayed using similar color scale which are compared to normal database. In glaucoma patients, the ganglion cell thickness is reduced [9] (Fig. 1.13).

1.3.3 Optic Nerve Head Morphology

The morphology of optic nerve head is an important parameter for analyses of the amount of optic nerve damage using biomicroscope. In OCT, the borders of optic disc and optic cup can be automatically segmented in a similar way to the evaluations performed by ophthalmologists. The border of optic disc is defined as the termination of Bruch's membranes. The software can then calculate the disc area, cup area, rim area, average cup to disc ratio, vertical cup to disc ratio. These parameters are then compared to a normative database [10]. In patient with glaucoma, the optic cup/disc ratio is increased and the neuro-retinal rim thickness is reduced (Fig. 1.12).

1.4 Retinal Vascular Diseases

Retinal vascular diseases include retinal artery occlusion, retinal vein occlusion, retinal vasculitis, diabetic retinopathy, and others.

1.4.1 Retinal Artery Occlusion

Retinal artery occlusion is the sudden blockage of retinal blood supply. It can be further classified into central retinal artery occlusion and branch retinal artery occlusion. On fundus photography, retinal artery occlusion is characterized by whitening and opacity of retina, which is transparent in physiological condition. The fovea lacks inner retinal tissue and therefore, cannot be affected by the retinal artery occlusion. The fovea remains red but surrounded by the white opacity retina, which is known as "cherry red spot" (Fig. 1.14). On OCT, retinal thickness increases at acute stages

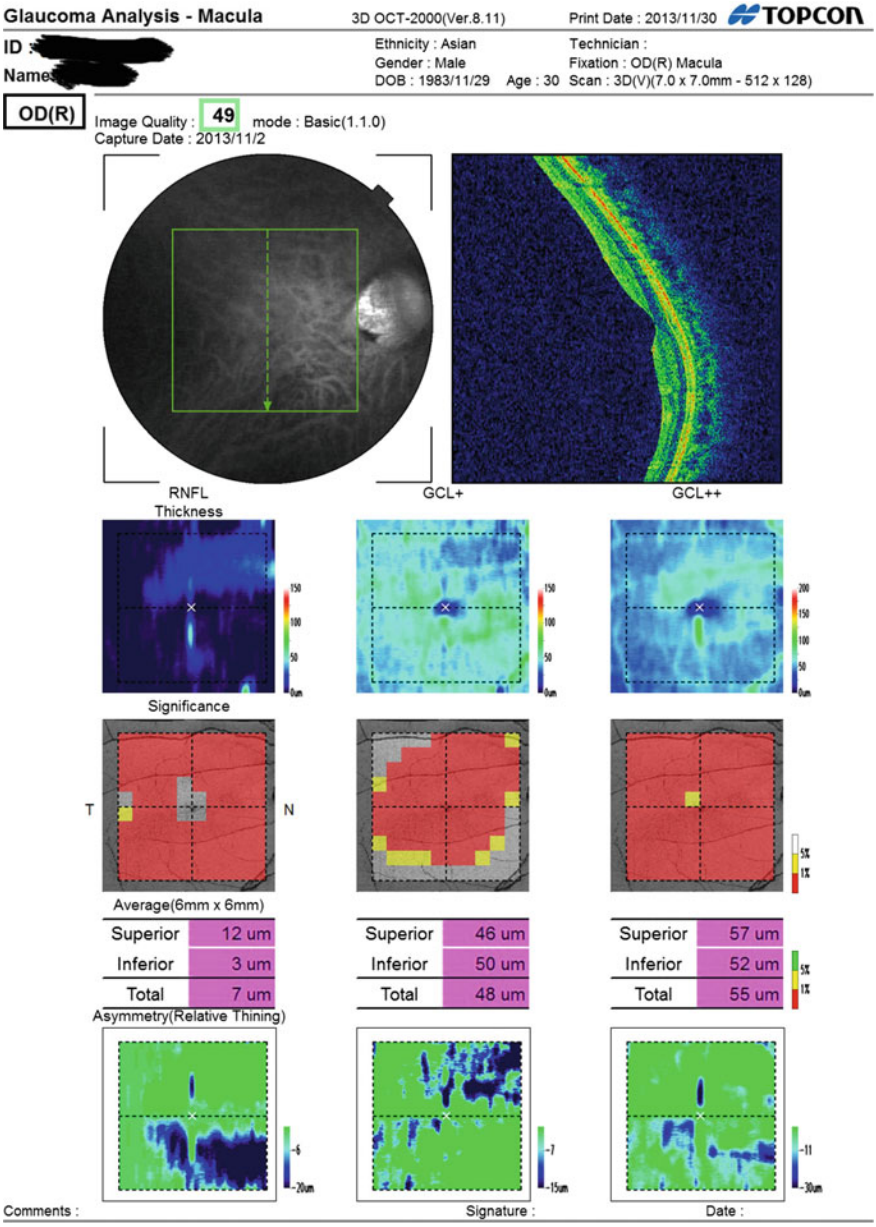

Fig. 1.13 Macular ganglion cell complex thickness analysis in a patient with primary open angle glaucoma

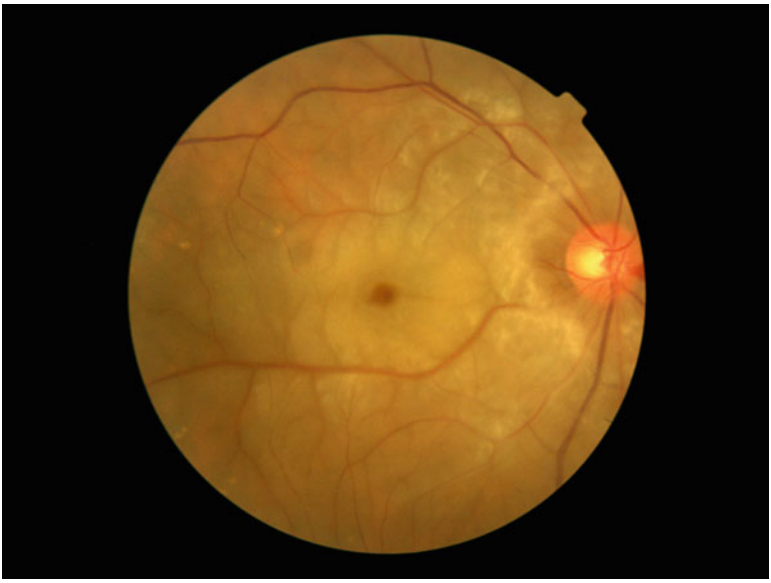

Fig. 1.14 Fundus photography of a CRAO case with a 'cherry-red spot' at the macula

and then reduces after regression of the whitening, mostly on the inner retinal layers [11]. Besides change of retinal thickness, the optical intensity of inner retinal layers increase, which suggest retinal ischemia, while the optical intensity of outer retinal layers decrease, which is caused by the shadowing effect of inner retinal layers (Fig. 1.15) [12]. Further study suggested that the optical intensity ratio of inner and outer layers is correlated with the visual outcome in patients with central retinal artery occlusion [13].

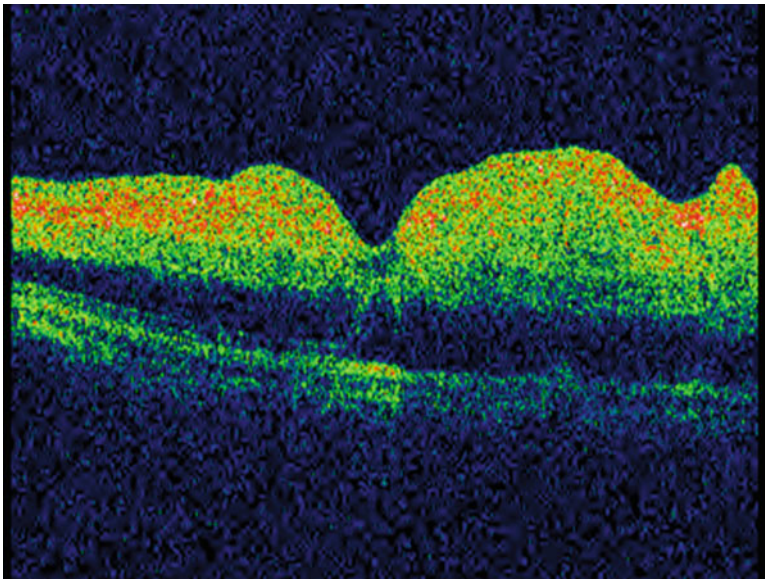

Fig. 1.15 OCT of the same eye as Fig. 1.14 shows diffuse retina thickening, high reflectivity at inner retina and reduced reflectivity at photoreceptor and RPE

1.4.2 Diabetic Retinopathy

Diabetic retinopathy is the most common cause of vision loss among people with diabetes and a leading cause of blindness among working-age adults. It is caused by damage to microvascular endothelial cells. The clinical manifestations of diabetic retinopathy include retinal hemorrhage, hard exudates, cotton wool spots and macular edema (Fig. 1.16).

On OCT, cotton wool spots are localized hyperreflectivity at retinal inner layers. Its appearance suggests retinal ischemia. Hard exudates are also hyperreflective spots, but located at deeper layers. They are caused by extracellular lipid which has leaked from abnormal retinal capillaries.

Macular edema is accumulation of fluid in macular region. Clinically, macular edema is defined as thickening of macular retina. On OCT, there are three types of macular edema, serous retinal detachment, intraretinal cysts and diffuse retinal thickening. Most macular edema are the combination of these characters (Fig. 1.17). Besides the cross-sectional morphology, OCT also provides quantitative measurement of retinal thickness at macula which is divided into 9 ETDRS regions (Fig. 1.18). The retinal thickness is useful for monitoring the progress of macular edema and its response to treatment [14].

1.4.3 Retinal Vein Occlusion

Retinal vein occlusion may involve either the central or branch retinal veins. The fundal manifestation of retinal vein occlusion also includes retinal hemorrhage, cotton wool spots, retinal hard exudates, macular edema. The OCT appearances are similar to those of diabetic retinopathy (Figs. 1.19 and 1.20).

1.5 Outer Retinal Degenerative Diseases

Outer retinal layers include outer nuclear layer, photoreceptor inner and outer segment, retinal pigment epithelium. Degeneration of outer retina can be caused by genetic mutation, or secondary to other factors, including traumatic impact, retinal detachment, inflammation, toxicity, or age related macular degeneration.

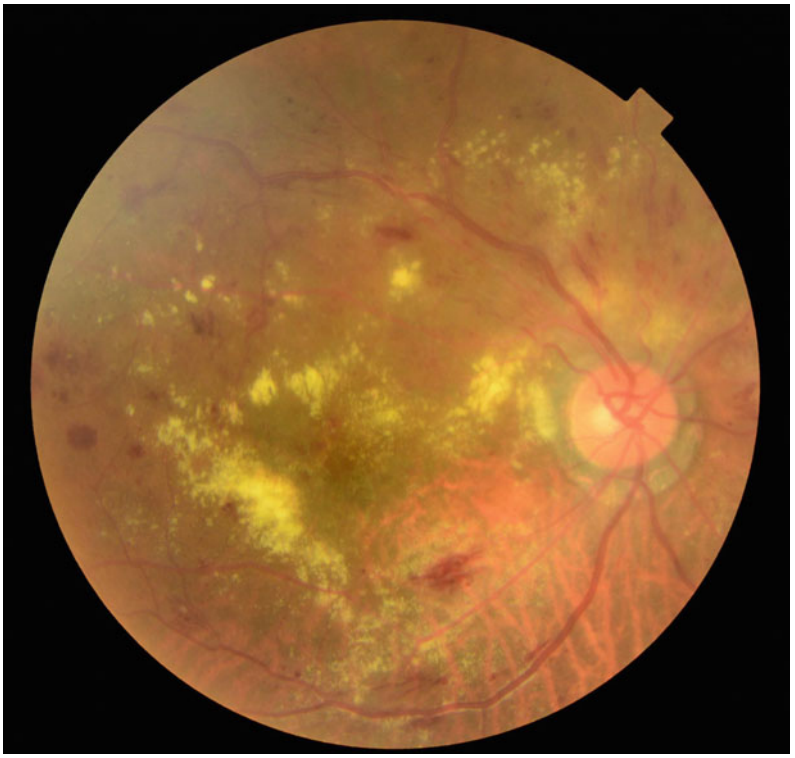

Fig. 1.16 Fundus photography of a patient with diabetic retinopathy showing extensive hard exudates around macular fovea and scattered dot hemorrhages

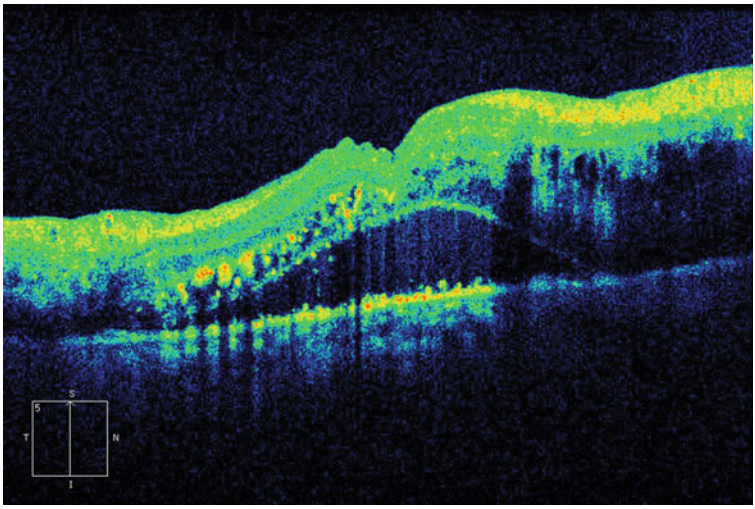

Fig. 1.17 OCT of the same eye as Fig. 1.16 shows high reflectivity spots at the intra neuroepithelial layer corresponding with extensive hard exudates, intraretinal cysts and serous retinal detachment

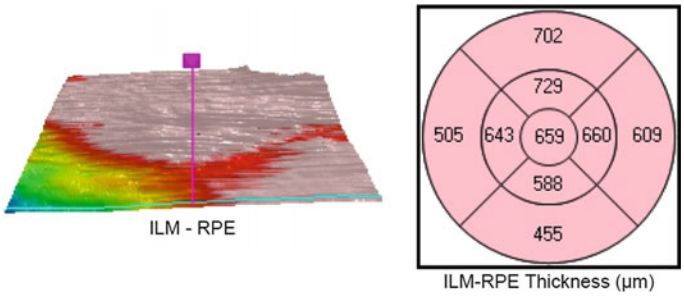

Fig. 1.18 Retinal thickness map (left) and the average retinal thickness at 9 ETDRS regions

Degeneration of photoreceptor is the major character of outer retinal diseases. Photoreceptor plays a critical role in vision. Therefore, degeneration of photoreceptor will lead to visual impairment. On OCT, disruption of photoreceptor inner segment ellipsoid zone is correlated with visual loss. Furthermore, retinal thickness would reduce, especially in outer retinal layers (Figs. 1.21 and 1.22) [15].

On fundoscopy, RPE changes are characterized by focal areas of mobilization of pigment (hypopigmentation and hyperpigmentation). On OCT, it appears as RPE deformation or thickening that may form irregularities which may progress to RPE atrophy in some cases. On OCT, in addition to the loss of RPE layer, the optical intensity of choroid would increase due to loss of shadowing effect of RPE (Figs. 1.21 and 1.22) [16].

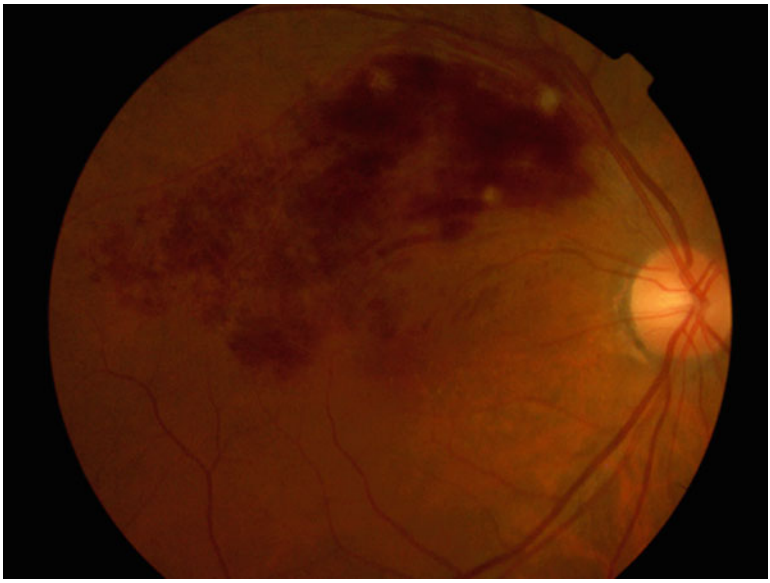

Fig. 1.19 Fundus photography of branch retinal vein occlusion shows flame-shaped and blot hemorrhages, cotton wool spots and venous tortuosity at superotemporal retina

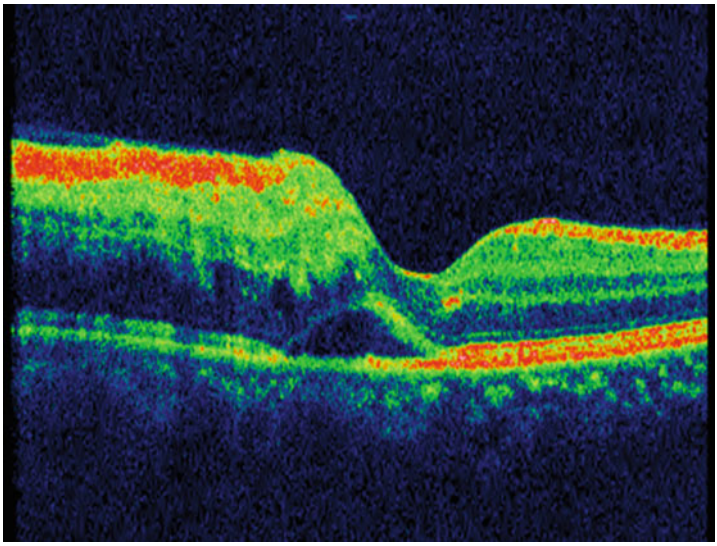

Fig. 1.20 OCT of the same eye as (Fig. 1.18) shows retinal thickening, inner retinal high reflectivity and serous retinal detachment at fovea

Drusen is degenerative nodular formations located in Bruch's membrane and beneath RPE. It consists of proteins, lipids, mucopolysaccharides, and other components. It is a landmark character of age-related maculopathy. On OCT, it is characterized by sub-RPE nodules with low or middle reflectivity (Figs. 1.21 and 1.22) [17].

1.6 Choroidal Neovascularization and Polypoidal Choroidal Vasculopathy

Choroidal neovascularization is the growth of new blood vessels from choroid vasculature through a break of the Bruch's membrane into sub-retinal or sub-RPE space. The etiology of choroidal neovascularization includes age related macular degeneration (AMD), high myopia, ocular inflammation and ocular trauma. Age related macular degeneration is a leading cause of irreversible blindness in elderly patients. It is usually located at macula and can cause central scotoma and severe visual loss. The choroidal neovascularization would lead to hemorrhage, exudation, and fibrosis. It can be further classified into type 1, type 2 and type 3. Type 1 neovascularization is also called occult. It refers to the neovascular tissue under RPE. Type 2 neovascularization refers to the neovascular tissues that break through RPE and grow into subretinal space. Type 3 neovascularization is also called retinal angiomatous proliferation and characterized by retinal-choroidal anastomosis [18].

On OCT, choroidal neovascularization is demonstrated as moderate to high reflective lesion located under or in front of RPE. It is usually accompanied by subretinal

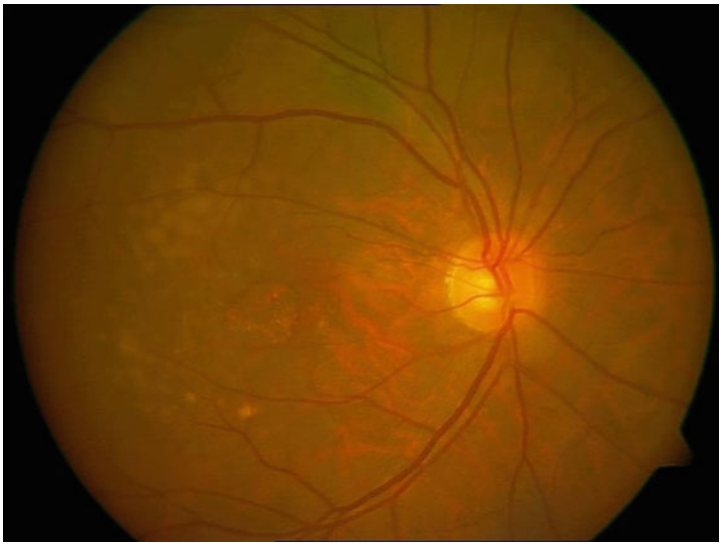

Fig. 1.21 Fundus photography shows geographic atrophy of retinal pigment epithelium at fovea and some soft drusen at perifoveal region

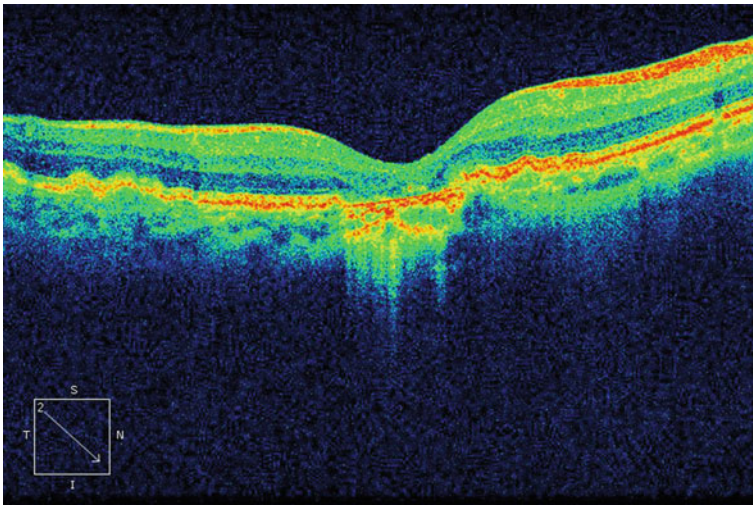

Fig. 1.22 OCT image shows defect of retinal pigment epithelium at fovea. Please note that the reflectivity of choroid increase because of reduced shadowing effect of RPE. Photoreceptor inner segment ellipsoid zone disruption and atrophy of outer nuclear layer can be found in the region of geographic atrophy. At temporal perifoveal region, RPE is elevated and there is mid-reflective material under RPE. These are drusen

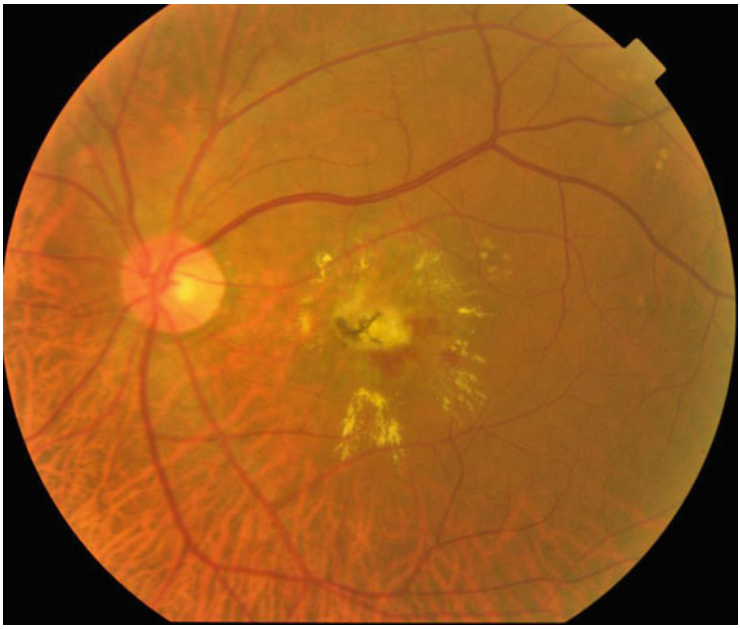

Fig. 1.23 An subretinal fibrovascular lesion in macula surrounded by some intraretinal hard exudate

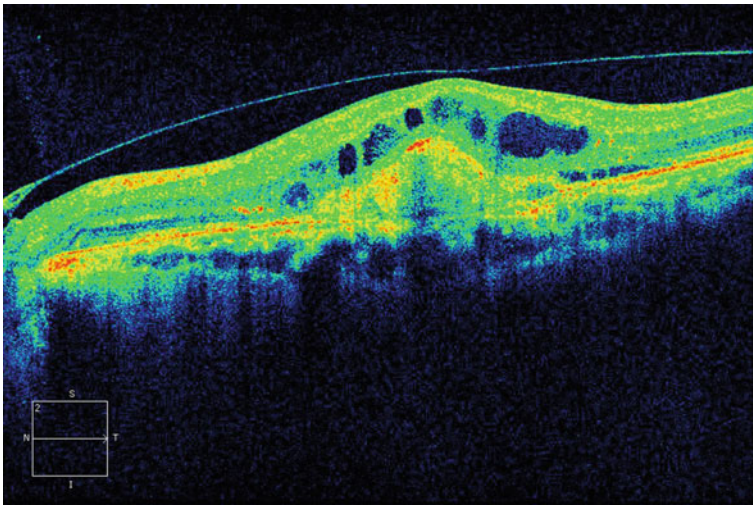

Fig. 1.24 OCT of the same eye as Fig. 1.23 showing a sub retina high reflectivity mass with subretinal and intraretinal fluid

Fig. 1.25 Serosanguineous retinal pigment epithelial detachment with associated subretinal hemorrhage

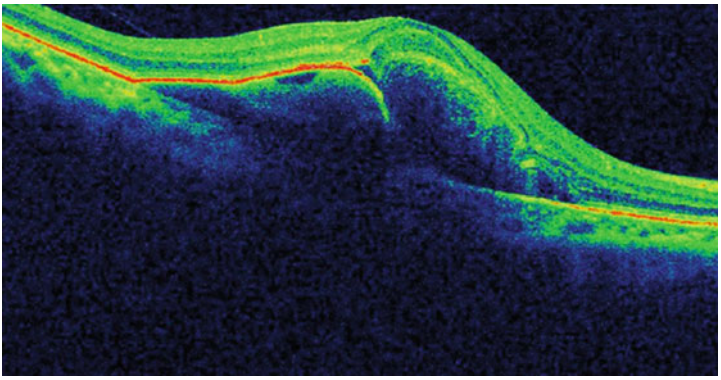

Fig. 1.26 OCT of the same eye as Fig. 1.25 showing sub-retinal hemorrhage and retina pigment epithelial detachment

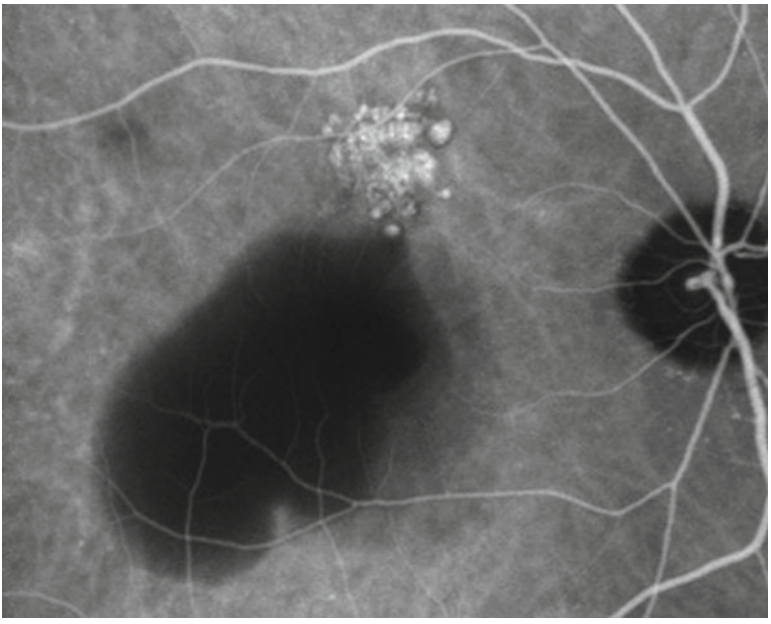

Fig. 1.27 The same eye as Fig. 1.25 on ICGA image showing hyperfluorescence due to polyps, branching vascular network and subretinal hemorrhage

or sub-RPE hemorrhage or fluid. In the late stage, choroidal neovascularization may progress to fibrosis and appear as hyperreflective lesion. The leaky neovascularization can cause intraretinal cysts which appear as non-reflective cysts in retina (Figs. 1.23 and 1.24). The thickness of macula can also be measured at the 9 ETDRS regions which are important parameters to monitor the prognosis of disease or response to therapy [18].

Polypoidal choroidal vasculopathy (PCV) is characterized by a branching vascular network from choroidal vasculature with polypoidal lesions under RPE. It is still controversial whether PCV is a subtype of AMD or a distinct disease. On OCT, pigment epithelium detachment, double-layer sign, and thumb-like polyps are more common in PCV eyes than in AMD eyes [19] (Figs. 1.25, 1.26 and 1.27).

References

1. G. Staurenghi, S. Sadda, U. Chakravarthy et al., Proposed lexicon for anatomic landmarks in normal posterior segment spectral-domain optical coherence tomography: the IN*OCT consensus. Ophthalmology **121**(8), 1572–1578 (2014)
2. J.S. Duker, P.K. Kaiser, S. Binder et al., The international vitreomacular traction study group classification of vitreomacular adhesion, traction, and macular hole. Ophthalmology **120**(12), 2611–2619 (2013)
3. J.D. Gass, Reappraisal of biomicroscopic classification of stages of development of a macular hole. Am. J. Ophthalmol. **119**(6), 752–759 (1995)
4. M. Imai, H. Iijima, T. Gotoh et al., Optical coherence tomography of successfully repaired idiopathic macular holes. Am. J. Ophthalmol. **128**(5), 621–627 (1999)
5. M. Pavlidis, L. Georgalas, N. Körber, Determination of a new parameter, elevated epiretinal membrane, by en face OCT as a prognostic factor for pars plana vitrectomy and safer epiretinal membrane peeling. J Ophthalmol. **2015**, 838646 (2015)
6. D.S.C. Ng, C.Y.L. Cheung, F.O. Luk, S. Mohamed, M.E. Brelen, J.C.S. Yam, C.W. Tsang, T.Y.Y. Lai, Advances of optical coherence tomography in myopia and pathologic myopia. Eye (Lond) **30**(7), 901–916 (2016)
7. C.K. Leung, Diagnosing glaucoma progression with optical coherence tomography. Curr. Opin. Ophthalmol. **25**(2), 104–111 (2014)
8. M.T. Leite, H.L. Rao, R.N. Weinreb, L.M. Zangwilla, C. Bowd, P.A. Sample, A. Tafreshi, F.A. Medeiros, Agreement among spectral-domain optical coherence tomography instruments for assessing retinal nerve fiber layer thickness. Am. J. Ophthalmol. **151**(1), 85–92 e1 (2011)
9. S.I. Balendra, E.M. Normando, P.A. Bloom, M.F. Cordeiro, Advances in retinal ganglion cell imaging. Eye (Lond) **29**(10), 1260–1269 (2015)
10. M. Michelessi, E. Lucenteforte, F. Oddone, M. Brazzelli, M. Parravano, S. Franchi, S.M. Ng, G. Virgili, Optic nerve head and fibre layer imaging for diagnosing glaucoma. Cochrane Database Syst. Rev. (11), CD008803 (2015)
11. M. Ritter, S. Sacu, G.G. Deák, K. Kircher, R.G. Sayegh, C. Pruente, U.M. Schmidt-Erfurth, In vivo identification of alteration of inner neurosensory layers in branch retinal artery occlusion. Br. J. Ophthalmol. **96**(2), 201–207 (2012)
12. H. Chen, X. Chen, Z. Qiu, D. Xiang, W. Chen, F. Shi, J. Zheng, W. Zhu, M. Sonka, Quantitative analysis of retinal layers' optical intensities on 3D optical coherence tomography for central retinal artery occlusion. Sci. Rep. **5**, 9269 (2015)
13. H. Chen, H. Xia, Z. Qiu, W. Chen, X. Chen, Correlation of optical intensity on optical coherence tomography and visual outcome in central retinal artery occlusion. Retina **36**(10), 1964–1970 (2016)

14. S. Ruia, S. Saxena, C.M. Gemmy Cheung, J.S. Gilhotra, T.Y. Lai, Spectral domain optical coherence tomography features and classification systems for diabetic macular edema: a review. Asia Pac. J. Ophthalmol. (Phila) **5**(5), 360–367 (2016)
15. H. Chen, Y. Lu, H. Huang, J. Zheng, P. Hou, W. Chen, Prediction of visual prognosis with spectral-domain optical coherence tomography in outer retinal atrophy secondary to closed globe trauma. Retina (2013)
16. F.G. Holz, E.C. Strauss, S. Schmitz-Valckenberg, M.V.L. Campagne, Geographic atrophy: clinical features and potential therapeutic approaches. Ophthalmology **121**(5), 1079–1091 (2014)
17. P.A. Keane, P.J. Patel, S. Liakopoulos, F.M. Heussen, S.R. Sadda, A. Tufail et al., Evaluation of age-related macular degeneration with optical coherence tomography. Surv. Ophthalmol. **57**(5), 389–414 (2012)
18. C.V. Regatieri, L. Branchini, J.S. Duker, The role of spectral-domain OCT in the diagnosis and management of neovascular age-related macular degeneration. Ophthalmic Surg. Lasers Imaging **42**(Suppl), S56–S66 (2011)
19. R. Liu, J. Li, Z. Li, S. Yu, Y. Yang, H. Yan, J. Zeng, S. Tang, X. Ding, Distinguishing polypoidal choroidal vasculopathy from typical neovascular age-related macular degeneration based on spectral domain optical coherence tomography. Retina **36**(4), 778–786 (2016)

Chapter 2
Fundamentals of Retinal Optical Coherence Tomography

Delia Cabrera DeBuc, Gábor Márk Somfai and Bo Wang

Understanding the underlying theory of medical imaging acquisition helps interpretation of the features manifested in the images and also gives guidance in developing medical image analysis methods. This chapter introduces the development and principles of retinal OCT imaging, and also explains the OCT features of multiple retinal structures.

2.1 Introduction

During the last few years, the retinal research field has undergone a dramatic change regarding diagnostic tools and therapies that have resulted in substantial benefits for patients suffering from retinal disease. Optical coherence tomography (OCT) has revolutionized the diagnosis and treatment of macular diseases which was enhanced by the widespread use of intravitreal anti-vascular endothelial growth factor (VEGF) agents for the treatment of neovascular age-related macular degeneration, branch and central vein occlusion and diabetic macular edema (DME). It is supposed that OCT is one of the most widely used ophthalmic decision-making technologies [1]. The recent introduction of OCT angiography (OCTA) and wide field imaging in

D. Cabrera DeBuc (✉)
Department of Ophthalmology, McKnight Vision Research Center, Bascom Palmer Eye Institute, University of Miami Miller School of Medicine, Miami, USA
e-mail: DCabrera2@med.miami.edu

G. M. Somfai
Retinology Unit, Pallas Kliniken Augenzentrum, Olten, Switzerland

G. M. Somfai
Department of Ophthalmology, Semmelweis University, Budapest, Hungary

B. Wang
School of Electronics and Information Engineering, Soochow University, Suzhou, China

X. Chen et al. (eds.), *Retinal Optical Coherence Tomography Image Analysis*,
Biological and Medical Physics, Biomedical Engineering,
https://doi.org/10.1007/978-981-13-1825-2_2

daily routine have resulted in some of the mean changes to the understanding and management of retinal diseases [2].

OCT uses retroreflected light to provide micron-resolution, cross-sectional scans of biological tissues [3–5]. The first micron-resolution OCT system for imaging the human retina in vivo was introduced in 1991 [3]. OCT is a compelling medical imaging technology in ophthalmology because it enables visualization of the cross-sectional structure of the retina and anterior eye with higher resolutions than any other non-invasive imaging modality [3]. The depth resolution of OCT is excellent, typically on the order of 0.01 mm or 0.4 thousandths of an inch. An OCT image represents a cross-sectional, micron-scale picture of the optical reflectance properties of the tissue [3]. This image can either be used to assess tissue features and pathologies qualitatively or to make quantitative measurements objectively.

2.2 Developments and Principles of Operation of Optical Coherence Tomography

OCT is an extension of optical coherence domain reflectometry to imaging in two or three dimensions [6]. This imaging technique generates a cross-sectional image by recording axial reflectance profiles while the transverse position of the optical beam on the sample is scanned. Thus, the longitudinal location of tissue structures is determined by measuring the time-of-flight delays of light backscattered from these structures. The optical delays are measured by low coherence interferometry. The light reflected from deeper layers has a longer propagation delay than light reflected from more superficial layers.

OCT can be used for retinal and anterior segment imaging. The OCT for ophthalmic examination is similar to a combination of a slit lamp for anterior segment imaging and a fundus camera for retinal imaging. The instrumentation includes a video display for operator viewing of the anterior segment or fundus while obtaining the OCT images and a simultaneous computer display of the tomograms. Images are stored via computer for the diagnostic record [7].

2.2.1 Time Domain OCT

Conventional or time domain OCT (TD-OCT) is based on the principle of low coherence interferometry: a powerful tool to "section" a transparent object. Low coherence means that the system employs a wide range of wavelengths. The most straightforward and currently the most common interferometer for OCT is a simple Michelson interferometer [8]. The scheme of a typical fiber optics TD-OCT system is shown in Fig. 2.1. A low-coherence source illuminates the interferometer. The light is split by a 50/50 fiber-coupler into a sample and a reference path. Light retroreflected from

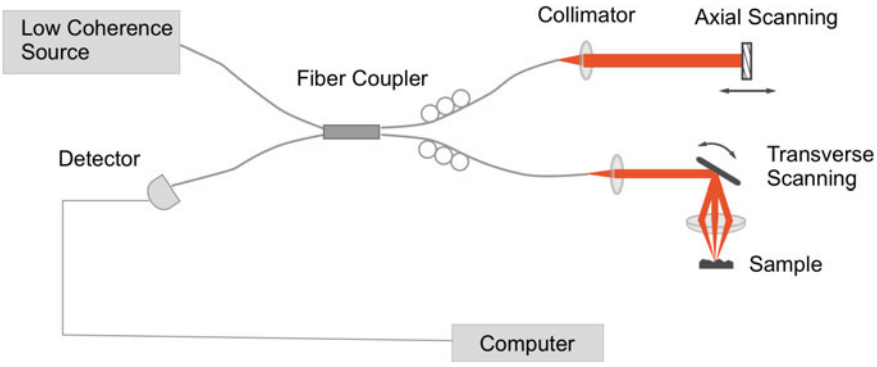

Fig. 2.1 Scheme of a typical fiber optics TD-OCT system

the reference and the sample is recombined at the fiber-coupler and half is collected by a photodetector in the detection arm of the interferometer. Also, the reference arm light is typically attenuated by orders of magnitude to improve the signal-to-noise ratio (SNR).

By rapidly varying the reference arm mirror and synchronously recording the magnitude of the resulting interference signal, a single axial profile or A-scan is obtained which is a graph of the optical reflectivity versus distance in the eye. A sequence of such A-scans is obtained by scanning the probe beam across the entire retina which forms a B-scan tomogram. As a result, a cross-sectional view of the structure, similar to a histology section is attained.

The axial resolution of an OCT image depends on the coherence length which is a fundamental property of the light source, whereas transverse resolution for OCT imaging is determined by focused spot size, as in microscopy. TD-OCT can achieve a translational resolution of about 8–10 μm, but the A-scan rate is only a few kHz which limits real-time 3D imaging application. For example, the motion of human eye often blurs the OCT images in the long imaging time duration.

2.2.2 Fourier Domain OCT

Fourier domain optical coherence tomography (FD-OCT) obtains the longitude information by measuring the reflective spectrum of the tissue. FD-OCT systems do not need mechanical time delay, and thus the A-scan rates are greatly improved. There are two mechanisms of FD-OCT systems: spectral-domain systems (SD-OCT) and swept-source systems (SS-OCT) [9, 10]. In the case of SD-OCT (Fig. 2.2), a broadband and continuous-wave low-coherence source is employed to illuminate the interferometer. The reference arm length is fixed, and the length of the reference arm and sample arm is approximately equal. The sample arm also contains a 2D lateral scanner and an objective lens. The detection arm includes a spectrometer, which consists

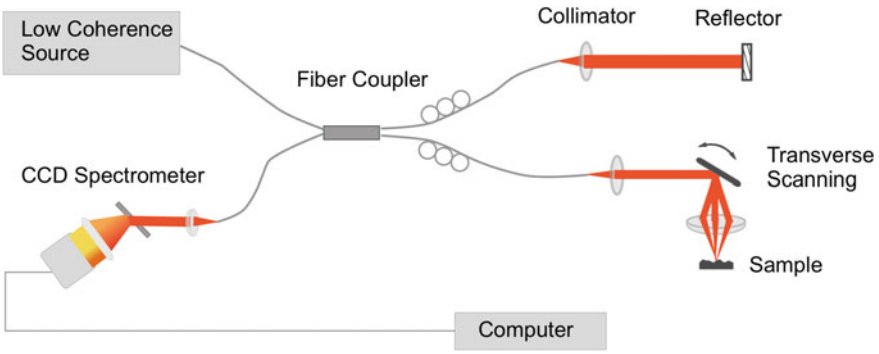

Fig. 2.2 Scheme of a FD-OCT system

of a dispersion grating and a linear detector, to measure the backscattering spectrum of the sample tissue. In the case of SS-OCT (Fig. 2.3), a swept-source laser is used to tune the broad bandwidth frequency quickly. The reference arm length is also fixed. A single point photodetector is employed in the detection arm to measure the magnitude of each component of the spectrum separately. SS-OCT systems can incorporate a balance detector design to suppress the impact of the laser heat fluctuation which can increase the sensitivity the sensitivity by approximately 10 dB. The A-scan longitude information can be retrieved by inverse Fourier transform of the spectrum data after interpolation processing which remaps the data linearly from wavelength space to wavenumber space. FD-OCT suffers from artifacts such as the direct current (DC), autocorrelation, and complex conjugate items which are caused by the inverse Fourier transform of real signals rather than complex signals. Methods such as phase shifting or quadrature projection phase correction are introduced to remove these artifacts [11–13]. The A-scan rate of SD-OCT depends on the data acquisition speed of the linear detector, while the A-scan rate of SS-OCT depends on the tuning speed of the swept-source. Both SD-OCT and SS-OCT systems can achieve a high A-scan rate.

Currently, the Swept-source OCT (SS-OCT) is able to obtain the highest imaging speed of any commercially available OCT devices with 100,000 A-scans obtained per second [14, 15]. The swept-soruce OCT technology enables high-resolution imaging with less artifacts due to the movement of the subject's eye. A significant advantage, compared to conventional OCT, is that it is possible to obtain clearer images in patients with cataracts and image deep structures such as the choroid and lamina cribrosa because the long wavelength of SS-OCT is less subject to light scattering by the retinal pigment epithelium (RPE). A further advantage of SS-OCT technology is that it does not suffer from a drop off in sensitivity with changing scan depth as conventional OCT. Therefore, the retina, vitreous, and deep ocular structures can be visualized in a single scan.

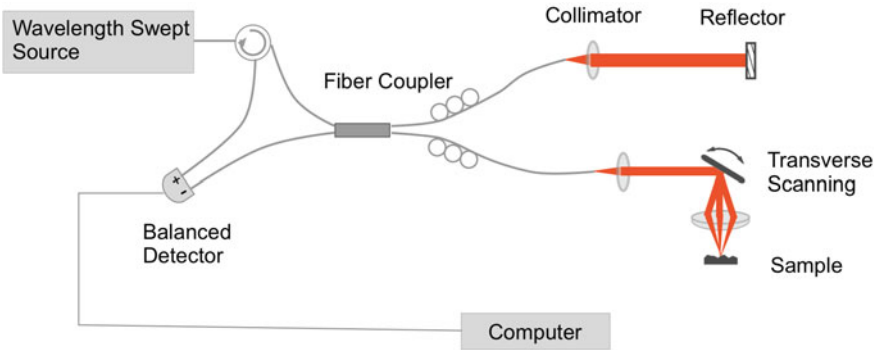

Fig. 2.3 Scheme of a SS-OCT system

2.2.3 Other Evolving OCT Technologies

Evolving OCT technologies are always under exploration and often ongoing to improve image resolution and further capabilities to generate better vessel contrast. For example, Doppler OCT imaging has demonstrated its clinical utility in detecting blood flow change in patients with various diseases as well as evaluating the three-dimensional architecture of neovascular complexes [16, 17]. Optical coherence angiography (OCA), one of the latest ophthalmic imaging developments, can be used to both quantitatively analyze blood flow and provide high-contrast images of the retinal vascular bed immediately and without the need for dye injection [18–20]. Recent studies have shown the potentialities of this modality to assess capillary dropout and confirm neovascularization in other retinal diseases [20–22]. Several studies reported to date have demonstrated that OCA applications in eye diseases may provide an alternative to more accurate diagnosis and management of these diseases by quantitatively assessing capillary dropout and retinal neovascularization [23].

Polarization Sensitive OCT (PS-OCT) exploits the information that is carried by polarized light to obtain additional evidence on the tissue [24]. Particularly, structures in the eye such as the retinal nerve fiber layer, retinal pigment epithelium, and the cornea change the light's polarization state. Consequently, a tissue-specific contrast in PS-OCT images is observed when using this technology due to polarization changing light-tissue interactions. Compared to conventional OCT, PS-OCT adds polarization contrast channel and provides quantitative measurements to the specific tissues. PS-OCT imaging systems adopt circular polarization light illumination in the sample arm and two orthogonal linear polarization state detectors in the detection arm to measure the full polarization state of the backscattering light from sample tissue. In the PS-OCT systems, more attention is needed to maintain the polarization of light precisely during the transmission which affects the measurement and reconstruction of polarization characteristics of tissues seriously.

Confocal scanning laser ophthalmoscopy (SLO) is integrated with OCT in most of commercial ophthalmology OCT systems. SLO utilizes two-dimensional scanning mirrors to scan a specific fundus area. This is same as the B-mode imaging in standard OCT. SLO and OCT share the same optical design in the sample arm and use a switchable reflector to guide backscattered light to a different detection arm. SLO, especially adaptive optics SLO (AOSLO) can provide better transverse resolution than OCT and needs no pupil dilation measurements [25]. SLO technology also enables accurate eye movement tracking which can guide and correct the scanning procedure of OCT. Fundus autofluorescence (FAF), a further SLO modality whose excitation light and detection light are in different wavelength regime are also introduced to integrate with OCT [26]. FAF images reflect density distribution of lipofuscin which is a biomarker of the retinal pigment epithelium. Also, adaptive optics OCT (AO-OCT) was introduced to compensate for aberrations to the imaging beam caused by the optics of the eye, which limits the transverse resolution in OCT [27]. In the sample arm of AO-OCT, a wavefront sensor measures the aberrations of light and then information is fed back to a wavefront corrector such as a deformable mirror which compensates the wavefront aberrations. It can improve the lateral resolution of retinal imagery near the diffraction limit. A combination of AO with PS-OCT has also been introduced by Cense et al. [28].

Full-field OCT (also called en-face OCT) is another way to achieve high lateral resolution retinal images [29, 30]. It employs full field illuminating and parallel detector to produce en-face imaging of tissues like a conventional microscope. Without the transverse scanning of sample light beam, the lateral resolution of en-face OCT is limited by the objective numerical aperture instead of scanning beam spot size. However, the lateral resolution can exceed 1 μ m with the use of objectives with high numerical aperture such as water-immersion objectives. The B-mode images of en-face OCT are continuous which benefits the visualization of small lesions due to the scanning direction parallels the anatomic fabric of retina.

OCT systems are still pursuing powerful imaging abilities to meet the requirements of medical diagnosis, especially the diagnosis of disease at the early stage when the structural images do not show obvious changes but the function of tissue becomes abnormal. The total oxygen metabolic rate is supposed to be a potential biomarker for early diagnosis of glaucoma, diabetic retinopathy and age-related macular degeneration [31]. A multi-modality OCT system combining the advantage of photoacoustic (PA) imaging and OCT is introduced to measure the oxygen metabolic rate where PA imaging could measure the oxygen saturation (SO_2) in the retinal and choroidal vasculature and Doppler OCT could obtain the blood flow velocity [32]. However, PA-OCT is currently limited to animal eye experiments due to the higher excitation laser energy which may cause unnecessary damage. Alternatively, visible light OCT (vis-OCT) is developed to obtain structural images, blood flow, oxygen saturation and oxygen metabolic rate of the human retina simultaneously with a single technique [33, 34]. The principle of vis-OCT is based on the absorption spectrum method which utilizes different absorption spectra of deoxygenated and oxygenated hemoglobin in the visible light regime.

Further developments of OCT technology may impact the diagnosis of eye diseases and improve the management of the significant clinical and public health problems associated to visual impairment. Finally, there is growing evidence to incorporate the OCT technology into clinical settings managing cerebrovascular and neruological diseases [35]. However, a low-cost approach solution must be reached to successfully introduce its application in telemedicine and population-based screening programs [36].

2.3 Interpretation of the Optical Coherence Tomography Image

The OCT signal from a tissue layer is a combination of its reflectivity and the absorption and scattering properties of the overlying tissue layers. Strong reflections occur at the boundaries between two materials of different refractive indices or may originate from a tissue that has a high scattering coefficient along with a disposition to scatter light in the perfectly backward direction [3, 26]. Thus, an OCT image is a map of the reflectivity of the sample. In most tissues, primary sources of reflection are collagen fiber bundles, cell walls, and cell nuclei. Dark areas (i.e. areas with low reflectivity) on the image represent homogeneous material with low reflectivities, such as air or clear fluids. The imaging light is attenuated in the sample which leads to an exponential decrease in the intensity of the image with depth. Blood attenuates the signal faster than collagenous tissues while fat and fluids attenuate the signal the least.

In OCT images, the signal strength is represented in false color or grey-scale. In the case of false color representation, high backscatter appears red-orange and low backscatter appears blue-black (see Fig. 2.4). Thus, tissues with different reflectivity are displayed in different colors. It is important to note that OCT image contrast arises from intrinsic differences in optical properties of tissues. Thus, coloring of different structures represent different optical properties in a false-color image, and it is not necessarily different tissue pathology (see Fig. 2.4). The exact relationship between the histology of the tissue and the OCT map is still under investigation. Usually, relative high layers correspond to areas of horizontal retinal elements such as the RNFL at the retinal surface or the deeper plexiform layers and finally the outermost single layer of RPE. Relative low reflectivity layers correspond to the nuclear layers and a single layer of photoreceptor inner and outer segments (see Figs. 2.4 and 1.4). Warm colors (red to white) represent areas of relatively high reflectivity, while cold colors (blue to black) represent areas of relatively low reflectivity. However, from a qualitative point of view, grey-scale OCT images are superior to the color-scale pictures, avoiding misleading interpretations of the OCT reflectivity.

A typical example of color coded OCT images of the human macular for normal and pathologic eyes is shown in Fig. 2.4. The OCT image shown in Fig. 2.4b is from a subject with DME. This image demonstrates thickening of the macula with

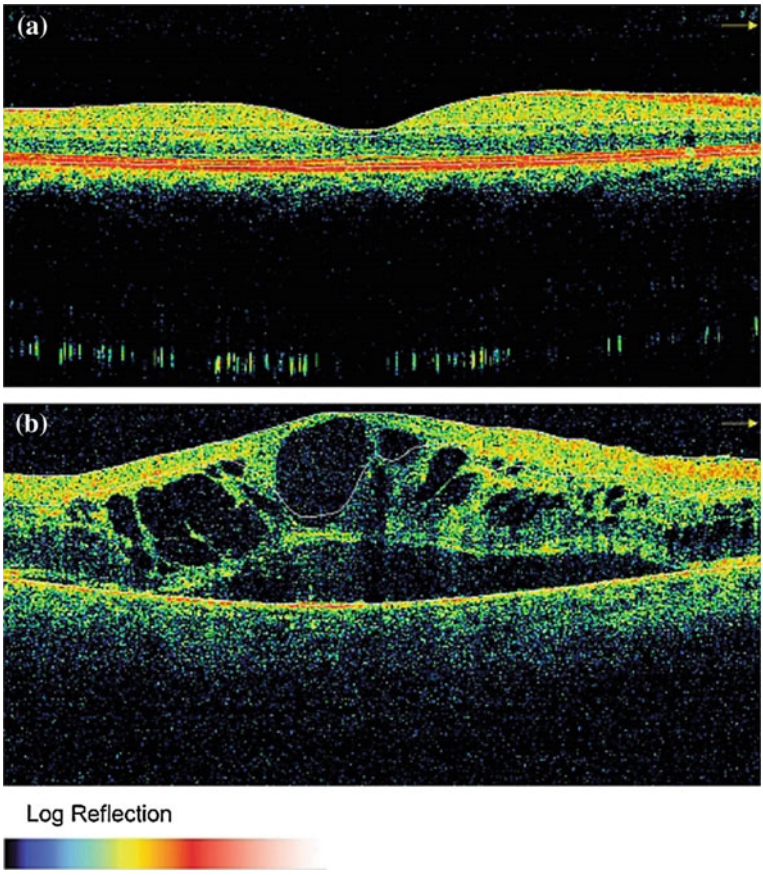

Fig. 2.4 OCT images of the retina for a healthy and pathologic human eye. **a** Image of the retina of a normal healthy subject. Note that the fovea has a characteristic depression with thinning of the retina corresponding to its normal anatomy. **b** OCT image from a subject with diabetic macular edema. Note the thickening of the macula with several sizeable hypo-reflective cystoid spaces in the central region. The OCT signal strength is represented in false color using the normally visible spectrum scale, and low backscatter appears blue-black

several large hyporeflective cystoid spaces in the fovea. When comparing the image of the pathologic subject with the one obtained in the normal healthy subject, the importance of quantifying the structural changes of retinal features and pathologies is more than evident.

In the retina, the vitreoretinal interface is demarcated by the reflections from the surface of the retina. The RPE and choriocapillaris layer (ChCap) is visualized as a highly reflective red layer and represents the posterior boundary of the retina. Below the choriocapillaris weakly scattered light returns from the choroid and sclera because of attenuation of the signal after passing through the neurosensory retina, RPE, and ChCap. The outer segments of the rods and cones appear as a dark layer

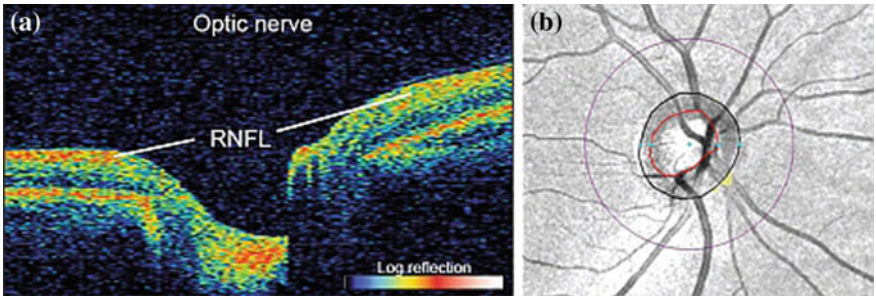

Fig. 2.5 OCT tomogram through the optic nerve (**a**) and corresponding video image (**b**). The retinal nerve fiber layer which emanates from the optic disc and decreases in thickness toward the macula can be clearly visualized. *Source* Savini et al. [37]

of minimal reflectivity anterior to the RPE and ChCap. The intermediate layers of the retina exhibit moderate backscattering (see Fig. 2.4). The fovea appears as a characteristic depression of the retina. The lateral displacement of the retina anterior to the photoreceptors is evident (see Fig. 2.4).

Retinal blood vessels are identified by their increased backscatter and by their blocking of the reflections from the RPE and ChCap (see Fig. 2.4). The larger choroidal vessels have minimally reflective dark lumens. Serial radial tomograms can be taken through the optic disc. These show the retinal thickness as it varies in the different planes. OCT imaging of the optic nerve head (ONH) clearly shows the cupping, as well as the ending of the choriocapillaris at the lamina (see Fig. 2.5) Circular tomograms around the optic nerve are very useful in documenting RNFL thickness and RNFL damage. These tomograms can be taken with different diameters while being centered on the optic nerve head. The circular tomogram is unwrapped and viewed as a section. Increased thickness at the superior and inferior margins of the ONH is evident and expected from the known retinal anatomy (see Fig. 2.5).

References

1. C.A. Puliafito, Optical coherence tomography: 20 years after. Ophthalmic Surg. Lasers Imaging **41**(Suppl 6), 5 (2010)
2. C.A. Puliafito, OCT angiography: the next era of OCT technology emerges. Ophthalmic Surg. Lasers Imaging Retina **45**(5), 360 (2014)
3. D. Huang, E.A. Swanson, C.P. Lin, J.S. Schuman, W.G. Stinson, W. Chang, M.R. Hee, T. Flotte, K. Gregory, C.A. Puliafito et al., Optical coherence tomography. Science **254**, 1178–1181 (1991)
4. J.A. Izatt, M.R. Hee, E.A. Swanson et al., Micrometer-scale resolution imaging of the anterior eye in vivo with optical coherence tomography. Arch. Ophthalmol. **112**, 1584–1589 (1994)
5. M.R. Hee, J.A. Izatt, E.A. Swanson, D. Huang, J.S. Schuman, C.P. Lin et al., Optical coherence tomography of the human retina. Arch. Ophthalmol. **113**, 325–332 (1995)

6. M.E. Brezinski, G.J. Tearney, B.E. Bouma, J.A. Izatt, M.R. Hee, E.A. Swanson, J.F. Southern, J.G. Fujimoto, Optical coherence tomography for optical biopsy: properties and demonstration of vascular pathology. Circulation **93**(6), 1206–1213 (1996)
7. C.A. Puliafito, M.R. Hee, J.S. Schuman, J.G. Fujimoto, *Optical Coherence Tomography of Ocular Diseases* (Slack Inc., Thorofare, NJ, 1996)
8. A.A. Michelson, E.W. Morley, Philos. Mag. S.5 **24**(151), 449–463 (1887)
9. R. Leitgeb, C.K. Hitzenberger, A.F. Fercher, Performance of fourier domain versus time domain optical coherence tomography. Opt. Express **11**(08), 889–894 (2003)
10. A. Yasin Alibhai, C. Or, A.J. Witkin, Swept source optical coherence tomography: a review. Curr. Ophthalmol. Rep. **6**(1), 7–16 (2018)
11. R.A. Leitgeb, C.K. Hitzenberger, A.F. Fercher, T. Bajraszewski, Phase-shifting algorithm to achieve high-speed long-depth-range probing by frequency-domain optical coherence tomography. Opt. Lett. **28**, 2201–2203 (2003)
12. J. Zhang, J.S. Nelson, Z.P. Chen, Removal of a mirror image and enhancement of the signal-to-noise ratio in Fourier-domain optical coherence tomography using an electro-optic phase modulator. Opt. Lett. **30**, 147–149 (2005)
13. M.V. Sarunic, B.E. Applegate, J.A. Izatt, Real-time quadrature projection complex conjugate resolved Fourier domain optical coherence tomography. Opt. Lett. **31**, 2426–2428 (2006)
14. M.A. Choma, M.V. Sarunic, C. Yang, J. Izatt, Sensitivity advantage of swept source and Fourier domain optical coherence tomography. Opt. Express **11**(18), 2183–2189 (2003)
15. J.F. de Boer, B. Cense, B.H. Park, M.C. Pierce, G.J. Tearney, B.E. Bouma, Improved signal-to-noise ratio in spectral-domain compared with time-domain optical coherence tomography. Opt. Lett. **28**, 2067–2069 (2003)
16. Z.P. Chen, T.E. Milner, S. Srinivas, X.J. Wang, A. Malekafzali, M.J.C. vanGemert, M.J.C. vanGemert, J.S. Nelson, Noninvasive imaging of in vivo blood flow velocity using optical Doppler tomography. Opt. Lett. **22**, 1119–1121 (1997)
17. J.A. Izatt, M.D. Kulkami, S. Yazdanfar, J.K. Barton, A.J. Welch, In vivo bidirectional color Doppler flow imaging of picoliter blood volumes using optical coherence tomograghy. Opt. Lett. **22**, 1439–1441 (1997)
18. S. Makita, Y. Hong, M. Yamanari, T. Yatagai, Y. Yasuno, Optical coherence angiography. Opt. Express **14**(17), 7821–7840 (2006)
19. R.K. Wang, S. Jackes, Z. Ma et al., Three dimensional optical angiography. Opt. Express **15**, 4083–4097 (2007)
20. Y. Huang, Q. Zhang, M.R. Thorell et al., Swept-source OCT angiography of the retinal vasculature using intensity differentiation-based optical microangiography algorithms. Ophthalmic Surg. Lasers Imaging Retina **45**(5), 382–389 (2014)
21. E. Moult, W. Choi, N.K. Waheed et al., Ultrahigh-speed swept-source OCT angiography in exudative AMD. Ophthalmic Surg. Lasers Imaging Retina **45**(6), 496–505 (2014)
22. M.R. Thorell, Q. Zhang, Y. Huang et al., Swept-source OCT angiography of macular telangiectasia type 2. Ophthalmic Surg. Lasers Imaging Retina **45**(5), 369–380 (2014)
23. A. Koustenis, A. Harris, J. Gross, I. Januleviciene, A. Shah, B. Siesky, Optical coherence tomography angiography: an overview of the technology and an assessment of applications for clinical research. Br. J. Ophthalmol. (2016)
24. M. Pircher, E. Goetzinger, R. Leitgeb, C.K. Hitzenberger, Transversal phase resolved polarization sensitive optical coherence tomography. Phys. Med. Biol. **49**, 1257–1263 (2004)
25. D. Merino, P. Loza-Alvarez, Adaptive optics scanning laser ophthalmoscope imaging: technology update. Clin. Ophthalmol. **10**, 743 (2016)
26. W.W. Lai, G.Y.O. Leung, C.W.S. Chan, I.Y.L. Yeung, D. Wong, Simultaneous spectral domain OCT and fundus autofluorescence imaging of the macula and microperimetric correspondence after successful repair of rhegmatogenous retinal detachment. Br. J. Ophthalmol. **94**(3), 311–318 (2010)
27. C.E. Bigelow, N.V. Iftimia, R.D. Ferguson, T.E. Ustun, B. Bloom, D.X. Hammer, Compact multimodal adaptive-optics spectral-domain optical coherence tomography instrument for retinal imaging. J. Opt. Soc. Am. A-Opt. Image Sci. Vis. **24**, 1327–1336 (2007)

28. B. Cense, W.H. Gao, J.M. Brown, S.M. Jones, R.S. Jonnal, M. Mujat, B.H. Park, J.F. de Boer, D.T. Miller, Retinal imaging with polarization-sensitive optical coherence tomography and adaptive optics. Opt. Express **17**, 21634–21651 (2009)
29. A. Dubois, L. Vabre, A.-C. Boccara, E. Beaurepaire, High-resolution full-field optical coherence tomography with a Linnik microscope. Appl. Opt. **41**(04), 805–812 (2002)
30. A. Dubois, K. Grieve, G. Moneron, R. Lecaque, L. Vabre, C. Boccara, Ultrahigh-resolution full-field optical coherence tomography. Appl. Opt. **43**(14), 2874–2883 (2004)
31. L. Li, K. Maslov, G. Ku, L.V. Wang, Three-dimensional combined photoacoustic and optical coherence microscopy for in vivo microcirculation studies. Opt. Express **17**(19), 16450–16455 (2009)
32. S. Jiao, M. Jiang, J. Hu, A. Fawzi, Q. Zhou, K.K. Shung, H.F. Zhang, Photoacoustic ophthalmoscopy for in vivo retinal imaging. Opt. Express **18**(4), 3967–3972 (2010)
33. J. Yi, Q. Wei, W. Liu, V. Backman, H.F. Zhang, Visible-light optical coherence tomography for retinal oximetry. Opt. Lett. **38**(11), 1796 (2013)
34. R.A. Linsenmeier, H.F. Zhang, Retinal oxygen: from animals to humans. Prog. Retinal Eye Res. **58**, 115–151 (2017)
35. D. Cabrera DeBuc, The role of retinal imaging and portable screening devices in tele-ophthalmology applications for diabetic retinopathy management. Curr. Diab. Rep. **16**(12), 132 (2016)
36. D. Cabrera DeBuc, G.M. Somfai, A. Koller, Retinal microvascular network alterations: potential biomarkers of cerebrovascular and neural diseases. Am. J. Physiol. Heart Circulatory Physiol. (2016). https://doi.org/10.1152/ajpheart.00201
37. G. Savini, M. Carbonelli, V. Parisi, P. Barboni, Repeatability of optic nerve head parameters measured by spectral-domain OCT in healthy eyes. Ophthalmic Surg. Lasers Imaging Retina **42**(3), 209–215 (2011)

Chapter 3
Speckle Noise Reduction and Enhancement for OCT Images

Zahra Amini, Raheleh Kafieh and Hossein Rabbani

The OCT imaging produces speckle noise due to multiple forward and backward scattered waves. The most important step of OCT preprocessing is noise reduction, which is helpful for more sophisticated processes like segmentation. Three OCT despeckling and enhancement methods are presented in this chapter, which are based on statistical modeling, data adaptive and non data adaptive transform based models, respectively.

3.1 OCT Background

Noninvasive methods for determination of anatomic information are of interest for many years. Some familiar methods are magnetic resonance imaging (MRI), computed tomography (CT scan) and ultrasound. Optical Coherence Tomography (OCT) is recently introduced to replace the ultrasound source with infrared light source and measure reflectance properties of tissue [1]. Each reflectance beam is called A-scan and a row of these beams make 2 dimensional B-scans. Series of such 2D images can be combined to produce a 3D volumetric measure of the anatomical area. Transparent anatomy of the retina to OCT energy source (light), makes this tissue a nice place to be scanned by this method. This transparency is easy to be understood since the light beam needs to pass through the whole retina to reach photoreceptors (on posterior surface) which have the responsibility of turning the light to electric signal of the brain. Figure 3.1 depicts the standard OCT scheme.

Z. Amini · R. Kafieh · H. Rabbani (✉)
Department of Bioelectrics & Biomedical Engineering, School of Advanced Technologies in Medicine, Medical Image & Signal Processing Research Center, Isfahan University of Medical Sciences, Isfahan, Iran
e-mail: hoss_rab@yahoo.com

X. Chen et al. (eds.), *Retinal Optical Coherence Tomography Image Analysis*,
Biological and Medical Physics, Biomedical Engineering,
https://doi.org/10.1007/978-981-13-1825-2_3

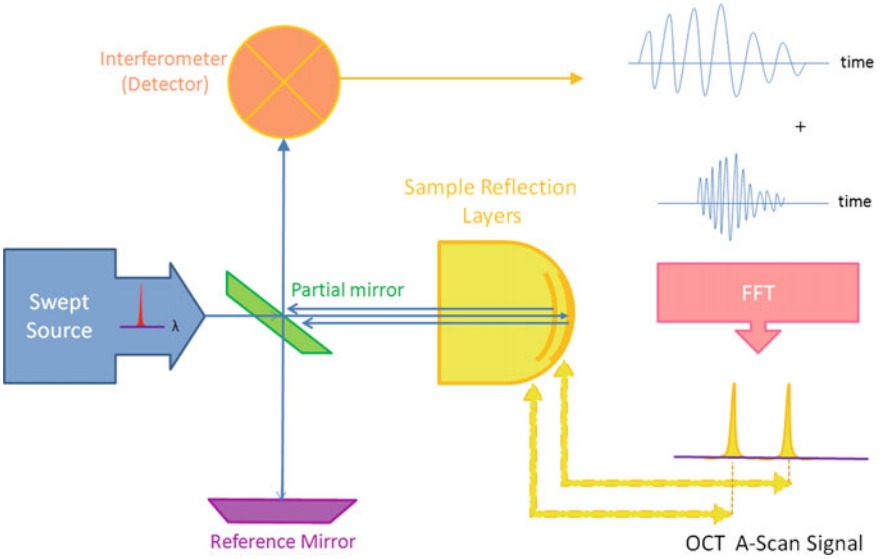

Fig. 3.1 Block-diagram of optical coherence tomography

In this chapter, we discuss the structural information of OCT with focus on its denoising. Several publications have addressed the theory and performance of OCT imaging, but very few works have principal information for applications like denoising.

Speckle noise is dominant in OCT and causes erroneous interpretation similar to ultrasound images. In time-domain techniques, axial movement of reference reflector would produce interferometric fringes and this movement was the main reason of low acquisition speed. In Fourier domain OCT, the fixed reference reflector leads to higher speeds up to several hundred thousand lines per second [2]. The resolution of Fourier domain OCT is also high in both axial and lateral directions.

Regarding the resolution of OCT images, a simple assumption is Gaussian profile sample arm beam in the region of the beam focus. This approach is a reasonable approximation and provides that spot size is proportional to the numerical aperture (NA) of the sample arm focusing optics, while depth of focus is proportional to NA^2. However, a more correct model is to treat the sample arm of an OCT system as a reflection-mode scanning confocal microscope. In such a case, lateral and axial resolutions are:

$$lateral\_resolution\ \delta_x = 0.37\frac{\lambda_0}{NA} \tag{3.1}$$

$$Axial\_resolution\ \delta_z = \frac{2\ \ln(2)}{\pi}\frac{\lambda_0^2}{\Delta\lambda} \tag{3.2}$$

where λ_0 is the center wavelength of the light source, numerical aperture of the objective is given by $NA = \sin(\alpha)$, α is half the angular optical aperture subtended by the objective [3].

Because of using coherent illuminations, speckle noise also affects OCT in both axial and lateral directions. Therefore, the effective resolution of OCT images, as the smallest detectable detail, is limited by this factor [4–9]. The speckle should not be treated as pure noise since it carries correlated information with noise [10].

3.1.1 Speckle

Speckle noise in OCT is because of multiple forward and backward scattered waves. Multiple forward scatter occurs because of the media between the source and the tissue to be measured. The media has a refractive index and corresponding forward scatter causes random delay both traveling to the sample and on the return trip. Multiple backscatter comes from material within the sample volume and material that is close by the volume that is the focus of the measurement [9]. Speckle noise must be accounted for either by filtering or using model based methods [11].

3.1.2 Speckle Properties

Interference of waves with random phases generates the speckle. Multiple forward and backward scattered wavelets have random phases since scattering objects in the sample have random depth distribution and refractive index in the sample is fluctuating [12].

First-order statistical properties of speckle can readily be quoted if amplitudes and phases of the individually scattered contributions are statistically independent, and identically distributed, have phases uniformly distributed over $(-\pi, \pi)$, and have waves that are perfectly polarized. Then we have 'fully developed' speckle [13] and the resultant phasor of the sample wave is a circular complex Gaussian random variable. The corresponding statistics of the sample intensity is negative exponential and the probability density function is [14]:

$$\mathrm{P}_{Is}(Is) = \begin{cases} \frac{1}{\langle I_s \rangle} \exp\left(-\frac{I_s}{\langle I_s \rangle}\right), & \text{if } I_s \geq 0 \\ 0, & \text{otherwise} \end{cases} \tag{3.3}$$

with moments $\langle I^n \rangle = n! \langle I \rangle^n$.

The contrast of a speckle pattern is defined as

$$C = \frac{\sigma_{I_s}}{\langle I_s \rangle} \tag{3.4}$$

Leading to the well known high speckle contrast $C = 1$ of fully developed polarized speckle; σ_{I_s} is the standard deviation of I_s.

Second order statistics of speckle is concerned with their temporal or spatial structure. A standard means to describe such properties are correlation functions. The characteristic depth extension of speckle in the OCT signal, e.g. can be estimated as correlation length of its intensity fluctuations. We assume statistically independent backscattered wavelets. In this case the intensity correlations can be obtained from the amplitude correlation $G(\tau)$ by [15]

$$\langle I(t)I(t+\tau\rangle = \langle I(t)\rangle^2[1+|G(\tau)|^2]. \tag{3.5}$$

Since the spectrum of light scattered back from the sample has approximately the same spectrum as the probe beam, the correlation length of its intensity fluctuations can be estimated by the corresponding coherence length I_c. In fact the real situation in OCT can be more complex: first, because of the reference beam we do not have fully developed speckle in OCT. Second, light backscattered at specularly reflecting interfaces does not generate speckle. Third, due to absorption, backscattered light can have a modified spectrum.

3.2 OCT Image Modeling

OCT images produce enormous amount of information of retina that interpretation of them with simple observation and common methods is generally impossible. So, some automatic systems for analyzing medical images are needed to decrease the amount of great information and help doctors for interpretation of them. In this regard, modeling of images can be known as a core of many processes. As soon as we determine a reliable model for OCT images, the rest of the processes may be explored more correctly.

It is understood that contrast enhancement and noise reduction algorithms for OCT images are also obtained based on the proposed model for image. In this base, Fig. 3.2 shows a classification of image modeling methods [16]. According to this classification, denoising methods such as other image processes may be studied in spatial domain or transform representations. The latter may also be subcategorized into parametric (non data adaptive) and non parametric (data adaptive) methods.

In data adaptive models basis functions of transform are directly defined by data. Algorithms such as Principle Component Analysis (PCA) [17], Independent Component Analysis (ICA) [18–20] and Dictionary Learning (DL) [21] lie in the data adaptive subgroup. In the other branch, we have some models in the frequency domain such as Fourier and Discrete Cosine transform (DCT) and some others involve different X-lets. These X-lets themselves can be subdivided into some groups based on their definition's space. A summarized table about various atomic representation methods and their parameters is given in Table 3.1 [16, 22]. Based on Fig. 3.2, scale-translation transforms like wavelets take place in the first group of these X-lets [23]. In the second group frequency is also added to the scale and translation parameters; some

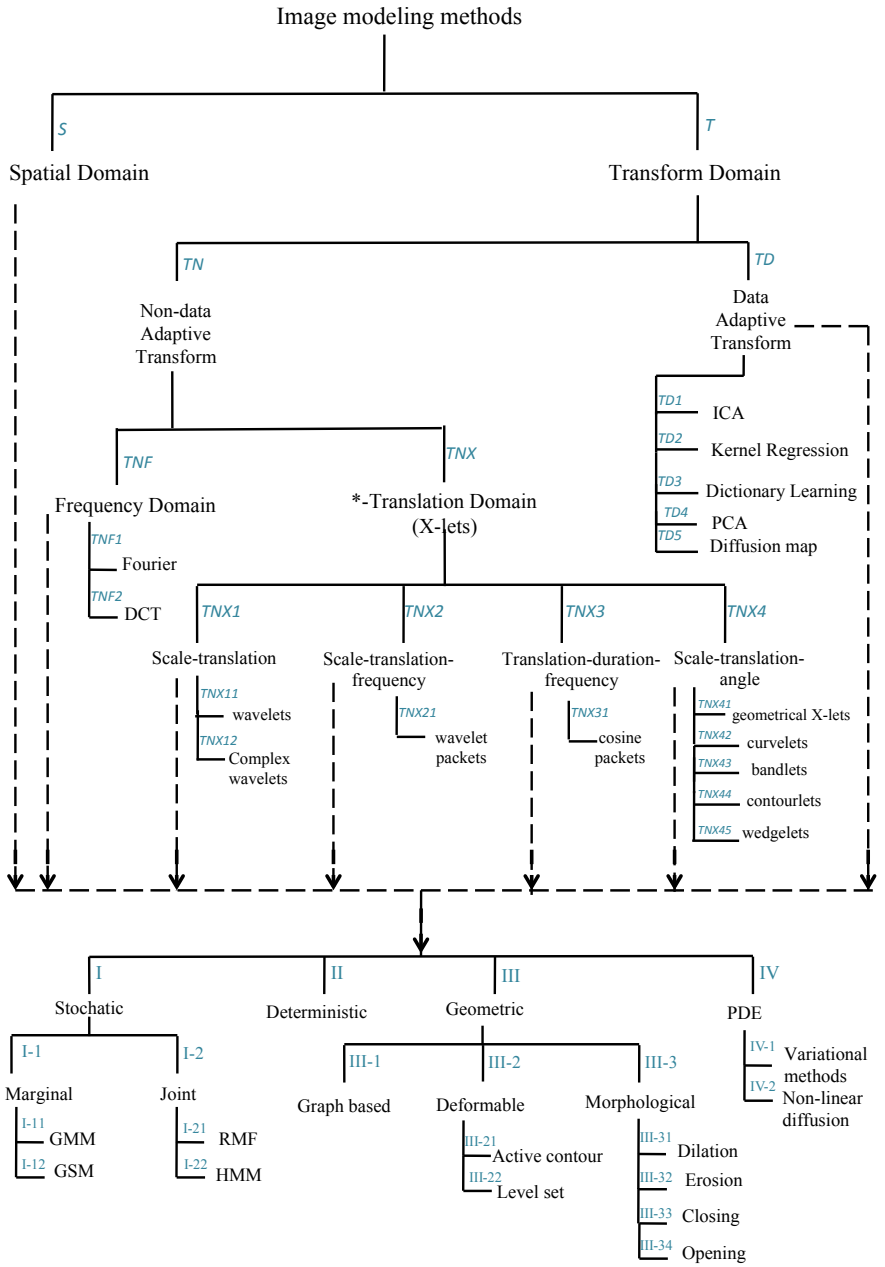

Fig. 3.2 A classification of various modeling methods [16]

transforms like wavelet packets are placed in this group. Three parameters included translation, duration and frequency are saved and studied in the third group models like cosine packet transform. Finally, X-lets that involve scale, translation and angle (or rotation) such as Curvelet, Contourlet, Wedgelet and Bandlet lie to the last group.

Besides, both of the spatial and transform models can be used as a deterministic, stochastic, partial differential equation (PDE) based [24–26] or geometric models [24, 27–29]. For example, using a deterministic model an image can be proposed as a matrix while in statistical model image is proposed as a random field. In this base for denoising problem average operator is obtained using first model while in the context of second model denoising is converted to an estimation problem.

It is noteworthy that these models aren't entirely distinct from each other and in some cases they may have overlap. Combinations of these models results in new image modeling frameworks such as using energy flow model [30] which is a PDE-based model in sparse domain [31] or Likewise combination of statistical model and transform-based model [32]. Similarly the theory of multi-resolution representation can be added on top of graph-based methods for using diffusion wavelet for image modeling [33].

In particular about OCT images, the denoising methods have been categorized to denoising methods before producing magnitude of OCT interference signal which usually are hardware based methods, and denoising methods after producing magnitude of the OCT signal. Table 3.2 shows a review of proposed denoising methods for OCT data [22].

Because of our limitation in access to hardware of devices and also to have an investigation from modeling point of view, we focus more on the second group denoising methods. Based on our classification in Fig. 3.2, these denoising methods can be work in the spatial or transform domain. Some spatial models for decreasing noise in OCT images are traditional methods such as low pass filters, linear smoothing, mean, median and wiener filters and using two one dimensional filters. However, some advanced methods like non linear anisotropic filter [34, 35], directional filtering [36, 37], complex diffusion [38], support vector machine (SVM) approach [39] and adaptive vector-valued kernel function [40] are used in this domain. In the transform based group, some data adaptive methods like PCA [41] and some non-data adaptive models which are based on wavelets [42] [43], Curvelets [44], dual tree Complex Wavelet [45–47], and wavelet diffusion [48] have been used for denoising.

Until now, the best results have been reported for the sparse data-driven methods [22], they improved the result of denoising by combination of DL and wavelet thresholding.

In Table 3.3, various methods which used in OCT denoising are summarized and also define that each of these methods lie on which group of image modeling classification (based on Fig. 3.2). For example, "T-TD3" shows using DL model in transform domain and "T-TNX11" indicates using wavelet.

Based on specific characteristics of OCT images and provided results of different models mentioned in Table 3.3, it can be concluded that two more appropriate models in denoising tasks on OCT images are statistical models and transform models. The next sections are devoted to these two dominant models and the transform models

Table 3.1 Summary of transform models discussed above [16, 22]

		Transform name	Dimension	Parameters	Introduced in	References
Non-data adaptive transforms	Single scale	Fourier transform	1D/2D/3D	Frequency	1948	Campbell and Foster [72]
		Cosine transform (DCT)	1D/2D/3D	Frequency	1974	Ahmed et al. [73]
	Multi-scale	Separable wavelet transform	1D/2D/3D	Scale-translation	1988	Daubechies [23]
		Wavelet packet transform	1D/2D/3D	Scale-translation- frequency	1992	Coifman [74]
		Geometrical X-lets (wedgelet)	2D	Scale-translation- angle	1997	Donoho [75]
		Complex wavelet transform	2D/3D	Scale-translation	1998	Kingsbury [76]
		Geometrical X-lets (curvelet)	2D/3D	Scale-translation- angle	2000	Candès and Donoho [77]
		Geometrical X-lets (bandlet)	2D	Scale-translation- angle	2004	Pennec and Mallat [78]
		Geometrical X-lets (contourlet)	2D	Scale-translation- angle	2005	Do and Vetterli [79]
		Geometrical X-lets (circlet)	2D	Scale-translation- angle	2011	Chauris [80]
		Geometrical X-lets (Surfacelet)	3D	Scale-translation- angle	2005	Lu and Do [81]
Data-adaptive transforms	Single scale	Principal component analysis (PCA)	1D/2D/3D	Eigen vectors	1986	Jolliffe [17]
		Independent component analysis (ICA)	1D/2D/3D	Eigen vectors	1994	Comon [82]
	Multi-scale	Conventional method of optimal directions (MOD)	1D/2D/3D	Duration-translation	1999	Engan and Aase [83]
		Conventional K-SVD	1D/2D/3D	Duration-translation	2006	Aharon [56]
		Complex wavelet based K-SVD	1D/2D/3D	Scale-translation- angle	2015	Kafieh et al. [22]

Table 3.2 Available denoising methods in OCT images [22]

Denoising method			
Complex domain methods (hardware methods)	Modification in optical setup		Alternation in incident angle of the laser beam [5, 84–86]
			Alternation in the recording angle of the back reflected light [87]
			Alternation in the frequency of the laser beam [88]
	Adjustment in imaged subject itself		Weighted averaging schemes [89]
			Registration of multiple frames by cross correlation [90, 91]
			Eye tracking systems [92]
Magnitude domain methods	Spatial domain	Traditional methods	Low-pass filtering [93]
			2D linear smoothing [1]
			Median filter [94–100]
			Adaptive wiener filter [71]
			Mean filter [71, 101, 102]
			Two 1D filters [103]
		Advanced methods	I-divergence regularization approach [104]
			Non-linear anisotropic filter [27, 34, 35, 62]
			Complex diffusion [26, 38]
			Directional filtering [36, 37]
			Adaptive vector-valued kernel function [40]
			SVM approach [39]
			Bayesian estimations [105]
	Transform domain	Non-Parametric methods	Sparsity-based denoising [54, 106]
			Robust principal component analysis [41]
		Parametric methods	Wavelet–based methods [42, 43, 51, 62, 63, 107]
			Dual tree complex wavelet transformation [43, 45–47, 69, 108]
			Curvelet transform
			Circular symmetric Laplacian mixture model in wavelet diffusion [44, 65]
None [109–114]			

Table 3.3 Summary of different processing on OCT images and their related models based on Fig. 3.2 [16]

Method	Application	Modeling approach	Researchers
Low-pass filtering	Denoising	S-II	Hee [93]
2D linear smoothing	Denoising	S-II	Huang [1]
Median filter	Denoising	S-II	Koozekanani [95], Rogowska [96], Shahidi [97], Boyer [98], Srinivasan [99], Lee et al. [100], George[115], Herzog [116]
Adaptive wiener filter	Denoising	S-I	Ozcan [71]
Mean filter	Denoising	S-II	Ozcan [71], Ishikawa [101], Mayer [102]
Two 1D filters	Denoising	S-II	Baroni [103]
Non-linear anisotropic filter	Denoising	S-IV-2	Garvin[27], Cabrera Fernández [34], Gregori [35], Puvanathasan [62]
Complex diffusion	Denoising	S-IV-2	Bernardes [38], Salinas [26]
Directional filtering	Denoising	S-II	Bagci [37], Rogowska [36]
Adaptive vector-valued kernel function	Denoising	T-TD	Mishra [40]
SVM approach	Denoising	S-II	Fuller [39]
Bayesian estimations	Denoising	S-I	Wong [105]
Sparsity-based denoising	Denoising	T-TD3	Fang [54]
Sparsity-based denoising	Denoising	T-TD3/TNX11	Fang [106]
Robust principal component analysis	Denoising	T-TNX	Luan [41]
Complex wavelet/ksvd	Denoising	T-TD3/TNX12	Kafieh [22]
Wavelet –based methods	Denoising	T-TNX11	Gupta [42], Mayer [43], Pizurica [51], Adler [63], Zlokolica [64], Quellec [107]
Dual tree complex wavelet transformation	Denoising	T-TNX12	Mayer [43], Chitchian [45], Kajic [46, 47], Rabbani [69], Forouzanfar [108]
Curvelet transform	Denoising	T-TNX42	Jian [67], Jian [44]
Circular symmetric Laplacian mixture model in wavelet diffusion	Denoising	T-TNX11/T-I-1	Kafieh, R. [48]

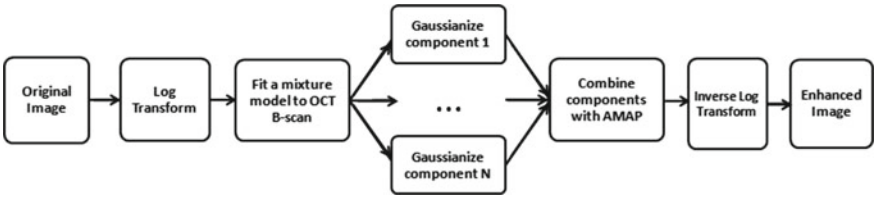

Fig. 3.3 The block diagram of the proposed method [49]

in subcategories of data adaptive and non data adaptive will be more elaborated by providing details of sample methods and corresponding results.

3.3 Statistical Model for OCT Contrast Enhancement

3.3.1 Method

In [49] we presented a new statistical model for OCT images and used it for contrast enhancement of these images. This model is based on a nonlinear Gaussianization transform and tries to convert the probability distribution function (pdf) of each OCT intra-retinal layer to a Gaussian distribution.

As mentioned before, OCT images suffer from speckle noise as a multiplicative noise and using a logarithm operator can approximately convert this noise to additive Gaussian noise [32, 50]. Hence, OCT data is firstly transformed to the logarithmic domain and the proposed method which includes three main blocks is implemented in logarithmic space. Finally, the exponential operator is applied to the enhanced data. Figure 3.3 shows the block diagram of the proposed method whereas in the first block after logarithm transform, we try to find a suitable well-fitted mixture model and its parameters for the OCT image. Because of layered structure of the retina and also monotonically decaying behavior of the OCT intensities in each layer [10], a Normal-Laplace mixture model is chosen as a suitable prior distribution for OCT images. Now each component of this mixture model is gaussianized with specific mean and variance, so that each enhanced component can be obtained in the second block. These components are combined with each other in the third block to construct the entire enhanced image. Indeed, in this block all of the gaussianized components are combined by the Averaged Maximum A Posterior (AMAP) method.

The pseudo code of the proposed algorithm for contrast enhancement is summarized as follows:

1. *Transform image to the logarithmic domain by logarithm operator*
2. *Fit a Normal-Laplace mixture model to the data using Expectation-Maximization (EM) algorithm*

2.1. *Initialization: Choose initial values for* $a_i^0, \mu_i^0, \sigma_i^0$*; where* a_i *is the coefficient of ith component's pdf and* μ_i *and* σ_i *are the pdf parameters of i*th *component*,
2.2. *E-step: Compute responsibility factors as a* $N \times 1$ *auxiliary variable that for each observed data represents the likelihood that the observed data is produced by component i.*
2.3. *M-step: Update parameters* $a_i^k, \mu_i^k, \sigma_i^k$ *using likelihood function maximization*
2.4. *Iteration: Substitute the updated parameters in the previous step to calculate pdf for each component* $(f_i(y))$
2.5. *Continue until the parameters satisfy convergence conditions*

3. *Calculate the CDF of each Normal-Laplace component using final values of* μ_i, σ_i *and* σ_n
4. *Gaussianize each Normal-Laplace component using proposed Gaussianization Transform*
5. *Use AMAP method to obtain a weighted summation of enhanced components*
6. *Apply exponential operator to find the contrast enhanced image.*

3.3.2 Results

To analyze the proposed model for OCT contrast enhancement, two datasets from different OCT imaging systems, Topcon 3D OCT-1000 and Cirrus HD-OCT (Carl Zeiss Meditec, Dublin, CA), are used and three evaluation measures are applied. The first two measures are Contrast to Noise Ratio (CNR), and Edge Preservation (EP) and are computed based on methods described in [51]. In addition, another measure Evaluation Measure of Enhancement (EME) which is introduced by Agaian et al. [52] is used as a new measure for evaluating contrast enhancement. The proposed method is compared with the Contrast-Limited Adaptive Histogram Equalization (CLAHE) method and Agaian's method for contrast enhancement (transform histogram shaping) [52]. All of these three methods are tested on both datasets. Both the visual and numerical results illustrate the superiority of the proposed method. Figure 3.4 displays an example of the proposed method in comparison to other methods. Furthermore, Table 3.4 shows the results averaged over all 130 Topcon B-scans and the averaged result over 60 Zeiss B-scans is displayed in Table 3.5.

This improvement in contrast enhancement in compare to other methods stems from considering a specific pdf for the OCT data and then converting it to a proportionate Gaussian distribution, thus providing the possibility of enhancement for these images. These computations are useful for pre-processing retinal OCT images to make them more suitable for visualization or further automated processing like alignment or segmentation tasks. Hence, using this model as a preprocessing step improves intra-retinal layer segmentation results and demonstrates the efficacy of this model.

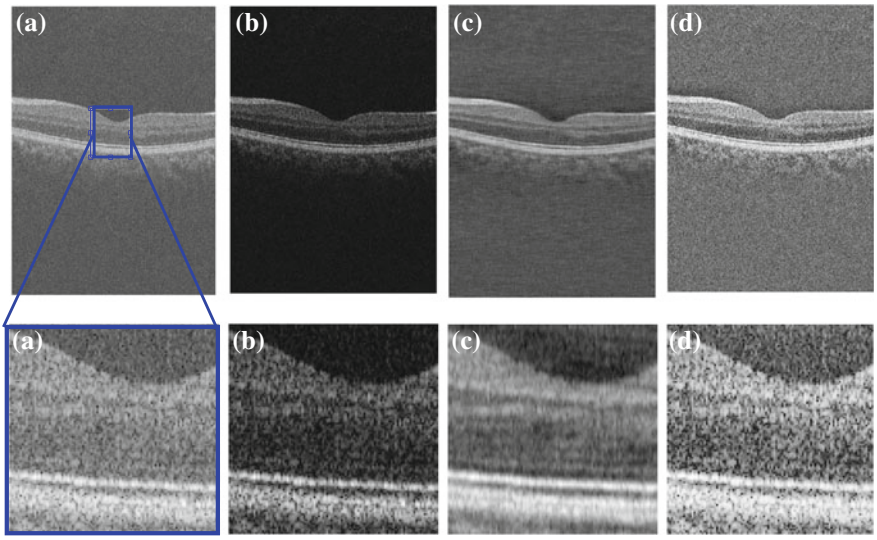

Fig. 3.4 Contrast enhancement results in a sample Topcon image. **a** original image, **b** proposed method, **c** transform histogram shaping method, **d** CLAHE method. The second row shows an enlargement of the specified region of first row images [49]

Table 3.4 Evaluation measure results; averaged over 130 OCT B-scans from the Topcon device [49]

Method	Measure		
	CNR	EP	EME
Original	5.4880	1.0000	2.3250
Proposed method	13.4171	0.9037	5.4956
Transform hist. shaping	11.6249	0.8875	1.3270
CLAHE	4.5240	0.9626	4.0596

Table 3.5 Evaluation measure results; averaged over 60 OCT B-scans from the Zeiss device [49]

Method	Measure		
	CNR	EP	EME
Original	6.0480	1.0000	13.8075
Proposed method	14.7005	0.9235	15.9087
Transform hist. shaping	12.4268	0.8930	0.4188
CLAHE	5.6013	0.9990	9.4917

3.4 Data Adaptive—Transform Models for OCT Denoising

As mentioned in Sect. 3.2, in non-parametric (data adaptive) methods, the basis is extracted regarding each dataset and there is no parameter to be selected. Single scale and multi scale non-parametric models may be subcategorized for more detail. Single scale models include PCA, ICA, diffusion maps and dictionary learning methods. Diffusion wavelets and complex wavelet transform along with dictionary learning are instances for multi scale models [22].

Nonparametric representations are relatively new in OCT denoising [43, 53, 54], but they have specific properties which makes them appropriate for this task. They are acquired from the data (better fit to OCT data), applicable on higher dimensional data (adaptable to 3D OCT data), and able to provide multi scale representation (to match different anatomical properties of OCT).

One sample denoising method on OCT, with focus on nonparametric models is elaborated below [16]. The method incorporates dictionary learning to improve the performance of available wavelet-thresholding. To do so, dictionaries are learned from the data instead of applying ready-to–use basis functions. Furthermore, conventional start dictionary (discrete cosine transform) is replaced by dual tree complex wavelet to take advantage of its shift invariant properties. Three dimensional versions of the method are also introduced to be applied on 3D volumes of OCT.

3.4.1 Conventional Dictionary Learning

Dictionary learning in denoising of OCT was first proposed in [54, 55] by learning a sparse dictionary from a selected number of higher signal-to-noise ratio (SNR) B-scans and using such dictionaries for denoising of low-SNR B-scans. The main problem in this work was need for high-SNR slices which are not accessible in most of available datasets.

In this section, K-SVD algorithm [56] is applied on OCT data. For construction of sparse land, each data (x) can be represented over a redundant dictionary matrix $D \in \Re^{n \times k}$(with $k > n$):

$$\hat{\alpha} = \arg\ \min_{\alpha} \|D\alpha - x\|_2^2 \quad \text{subject to } \|\alpha\|_0 < t \tag{3.6}$$

for a defined value of t. Having a noisy version of x named y, the maximum a posteriori (MAP) estimator for denoising the data is built by solving:

$$\hat{\alpha} = \arg\ \min_{\alpha} \|D\alpha - y\|_2^2 + \mu\|\alpha\|_0 \tag{3.7}$$

In K-SVD, the algorithm iterates in two stages to solve the above equation [56, 57] and the dictionary D can be learned on patches extracted from the image. In the first stage, D is supposed to be unknown, and similar to [56]:

$$\left\{\hat{D}, \hat{\alpha}_{ij}, \hat{X}\right\} = \arg\min_{\hat{D},\alpha_{ij},X} \lambda \|X - Y\|_2^2 + \Sigma_{ij}\mu_{ij}\left\|\alpha_{ij}\right\|_0 + \Sigma_{ij}\left\|D\alpha_{ij} - R_{ij}X\right\|_2^2 \tag{3.8}$$

In this expression, the first term is the log-likelihood global force to guaranty the proximity between the noisy version Y, and its denoised (and unknown) version X [57]. The second and the third terms represent the data prior and assure that in the denoised version, every patch (x_{ij}) has a sparse representation. α_{ij} is expected to be the representation of each patch (x_{ij}) on dictionary D (according to the third term). Every patch is shown by $x_{ij} = R_{ij}X$ by size of $\sqrt{n} \times \sqrt{n}$ where R_{ij} is a $n \times N$ matrix for an $\sqrt{N} \times \sqrt{N}$ image, that extracts the (ij) blocks.

In the second stage, D and X are assumed to be fixed, and the representation using a sparse coding stage by orthonormal matching pursuit (OMP) [58] is computed. Having the representations in hand, the dictionary can be updated using K-SVD approach [56]. This method is called 2D conventional dictionary learning (2D CDL) in next sections for comparison of performance.

3.4.2 Dual Tree Complex Wavelet Transform

The original method in [56] uses redundant DCT as start dictionary, but due to a highly non-convex functional for penalty minimized in (3.8) is, local minimum solutions should be devised to be eliminated. A dual tree complex wavelet transform (CWT) [59] is then proposed instead of redundant DCT to improve the results of conventional algorithms [16].

CWT is nearly shift invariant and directionally selective in two and higher dimensions because of a redundancy factor of 2^d for d-dimensional signals (lower than the undecimated Discrete wavelet transform (DWT)). The multidimensional (M-D) dual-tree CWT is non-separable but is based on a computationally efficient, separable filter bank (FB) [60].

A complex-valued scaling function and complex-valued wavelet are required in CWT [59]:

$$\psi_c(t) = \psi_h(t) + j\psi_g(t) \tag{3.9}$$

where $\psi_h(t)$ is real and even and $j\psi_g(t)$ is imaginary and odd. In order to have an analytic signal, supported only on one-half of the frequency axis, $\psi_h(t)$ and $\psi_g(t)$ should form a Hilber transform pair.

The oriented complex 2D dual-tree wavelet transform is four-times expansive, but it has the benefits of being oriented, approximately analytic, and full shift-invariant. A 2D wavelet transform that is both oriented and complex (approximately analytic) can also be easily developed by taking complex part of $\psi(x, y) = \psi(x)\psi(y)$ where $\psi(x)$ is a complex (approximately analytic) wavelet given by $\psi(x) = \psi h(x) + j\psi g(x)$.

Similar to 2D approach, 3D DWT suffers from more serious checkerboard artifact. It is shown in [61] that 3D dual-tree wavelet transforms is a good candidate for processing medical volume data and video sequences.

3.4.3 *Dictionary Learning with Wise Selection of Start Dictionary*

This method is called 2D/3D complex wavelet-based dictionary learning (2D-CWDL and 3D-CWDL) [16]. The CWT cannot be used in its algebraic form since in dictionary learning approaches an explicit dictionary is needed to be multiplied by the data. The matrix representation can be calculated for this purpose.

Suppose that the usual 2D separable Discrete Wavelet Transform (DWT) implemented using the filters $\{h_0(n), h_1(n)\}$ can be represented by the square matrix F_{hh}. If x is a real image, the real and imaginary parts of the oriented complex 2D dual-tree wavelet transform can be represented by W_{r2D} and W_{i2D}, respectively [60], where I is an identity matrix.

$$W_{r2D} = \frac{1}{2}\begin{bmatrix} I & -I \\ I & I \end{bmatrix}\begin{bmatrix} F_{hh} \\ F_{gg} \end{bmatrix} x. \tag{3.10}$$

$$W_{i2D} = \frac{1}{2}\begin{bmatrix} I & I \\ I & -I \end{bmatrix}\begin{bmatrix} F_{gh} \\ F_{hg} \end{bmatrix} x. \tag{3.11}$$

Therefore, the complex coefficients can be calculated by:

$$F_{C2D} = \frac{1}{4}\begin{bmatrix} I & -I & I & I \\ I & I & I & -I \\ I & I & -I & I \\ I & -I & -I & -I \end{bmatrix}\begin{bmatrix} F_{hh} \\ F_{gg} \\ i.F_{gh} \\ i.F_{hg} \end{bmatrix} \tag{3.12}$$

This dictionary can now be used as start dictionary in dictionary learing of 2D-CWDL.

Similarly, one may use 3D dual-tree wavelet transform as start dictionary of 3D-CWDL. It can be shown that real and imaginary parts of the oriented complex 3D dual-tree wavelet transform can be represented by W_{r3D} and W_{i3D}:

$$W_{r3D} = \frac{1}{4}\begin{bmatrix} I & -I & -I & -I \\ I & -I & I & I \\ I & I & -I & I \\ I & I & I & -I \end{bmatrix}\begin{bmatrix} F_{hhh} \\ F_{ggh} \\ F_{ghg} \\ F_{hgg} \end{bmatrix}. \tag{3.13}$$

$$W_{i3D} = \frac{1}{4}\begin{bmatrix} I & -I & I & I \\ -I & I & I & I \\ I & I & I & -I \\ -I & -I & I & -I \end{bmatrix}\begin{bmatrix} F_{hgh} \\ F_{ggg} \\ F_{ghh} \\ F_{hhg} \end{bmatrix}. \tag{3.14}$$

The complex coefficients can be calculated in 3D as start dictionaries of 3D-CWDL by:

$$F_{C2D} = \frac{1}{16}\begin{bmatrix} I & -I & -I & -I & I & -I & I & I \\ I & -I & I & I & I & I & I & -I \\ I & I & -I & I & -I & I & I & I \\ I & I & I & -I & -I & -I & I & -I \\ I & I & I & -I & I & I & -I & I \\ I & I & -I & I & I & -I & -I & -I \\ I & -I & I & I & -I & -I & -I & I \\ I & -I & -I & -I & -I & I & -I & -I \end{bmatrix}\begin{bmatrix} F_{hhh} \\ F_{ggh} \\ F_{ghg} \\ F_{hgg} \\ i.F_{hgh} \\ i.F_{ggg} \\ i.F_{ghh} \\ i.F_{hhg} \end{bmatrix} \tag{3.15}$$

3.4.4 Results

Datasets from two different OCT imaging systems are utilized [16] which includes Topcon 3D OCT-1000, and Cirrus Zeiss Meditec. Each set is consisted of six randomly selected 3D OCTs. Subjects in Topcon dataset are diagnosed to have Retinal pigment epithelial detachment (PED), and the ones in Zeiss dataset are diagnosed to have symptomatic exudates associated derangement (SEAD). OCT data for Topcon dataset is obtained from Feiz eye hospital, Isfahan, Iran; and Zeiss dataset is provided by Retinal Image Analysis Laboratory of Iowa [45]. The performance of 11 different speckle reduction methods are compared [16] (described in Table 3.6).

The value of the measurements for each denoising method on 144 randomly selected slices is summarized in [16] and results for 72 randomly selected slices acquired from Topcon OCT imaging is provided in Table 3.7. Some samples of datasets are also depicted after application of denoising methods in Fig. 3.5. As it can be seen in Table 3.7, the performance of the proposed method in 3D R/I CWDL are considerably better than other methods in CNR and Equivalent Number of Look (ENL). Performance of all of the studied methods are similar in EP and 2D SDWT had the highest Texture preservation (TP) which is obtained because of the least difference appeared in the resulted image which cannot be considered as a positive point. TP is low for 3D CCWT which shows unwanted flattening of this method.

Table 3.6 List of speckle reduction methods, evaluated in [16]

Category	Name	Short name
Dictionary learning	2D conventional dictionary learning	2D CDL
	2D/3D double sparse dictionary learning	2D/3D DSDL
	Real part of 2D/3D dictionary learning with start dictionary of dual tree complex wavelet	2D/3D RCWDL
	Imaginary part of 2D/3D Dictionary learning with start dictionary of dual tree complex wavelet	2D/3D ICWDL
Wavelet transform	2D separable discrete wavelet transform	2D SDWT
	Real part of 2D dual tree Complex wavelet transform	2D RCWT
	Complex 2D dual tree Complex wavelet transform	2D CCWT
	Complex 3D dual tree Complex wavelet transform	3D CCWT

3.5 Non Data Adaptive—Transform Models for OCT Denoising

The non data adaptive models are the most common models in sparse domain. For OCT despeckling, since wavelet domain techniques (as a well known non data adaptive transform model) incorporate the speckle statistics in the despeckling process usually better results comparing to spatial domain methods could be achieved. Such techniques apply wavelet transform [42, 44, 45, 62–65] directly on data or on log-transformed data (i.e., non-homomorphic/ homomorphic methods). As elaborated in [69], in wavelet domain, noise is converted to additive noise [51] and an appropriate shrinkage function can be used for speckle noise reduction in wavelet domain (Fig. 3.6).

It is clear from Fig. 3.6 that the kind of transform and shrinkage function play the main roles in denoising process. As explained in Sect. 3.4.2, dual-tree complex wavelet transform has several properties such as shift invariance and directional selectivity which makes it superior comparing to many other sparse transforms. Specially in high dimensional data analysis, some of these properties such as directional selectivity (and good compactness of energy and sparsity in each subband) makes it of more interest. For OCT data which is a 3D capturing of data from the eye, it is better to use a 3D transform instead of slide-by-slide applying of 2D transforms (it results in a better sparsity which is one of the main properties of sparse transforms). So, 3D dual-tree complex wavelet transform is chosen as a 3D transform. In this base,

Table 3.7 The value of the proposed measurements for each denoising method in datasets from Topcon device [16]

	Original	2D CDL	2D DSDL	3D DSDL	2D RCWDL	3D RCWDL	2D ICWDL	3D ICWDL	2D SDWT	2D RCWT	2D CCWT	3D CCWT
CNR	3.09 ± 1.35	24.24 ± 10.63	28.09 ± 10.19	78.83 ± 33.20	24.25 ± 10.61	88.91 ± 32.00	24.26 ± 10.63	86.91 ± 31.49	14.66 ± 6.60	26.51 ± 11.55	34.67 ± 15.28	55.06 ± 23.47
EP	1 ± 0	0.88 ± 0.01	0.86 ± 0.01	0.86 ± 0.01	0.88 ± 0.01	0.86 ± 0.01	0.88 ± 0.01	0.87 ± 0.01	0.90 ± 0.01	0.87 ± 0.01	0.85 ± 0.01	0.81 ± 0.01
TP	1 ± 0	0.18 ± 0.03	0.17 ± 0.04	0.19 ± 0.05	0.18 ± 0.04	0.14 ± 0.03	0.18 ± 0.04	0.13 ± 0.03	0.23 ± 0.03	0.13 ± 0.02	0.09 ± 0.02	0.06 ± 0.02
ENL	28.69 ± 0.49	2045.08 ± 367.62	2183.56 ± 423.96	19,059.32 ± 9852.14	2047.14 ± 364.41	22,231.73 ± 354.43	2047.43 ± 364.63	22,196.73 ± 354.55	671.47 ± 44.49	2316.04 ± 430.29	4434.58 ± 1270.34	8653.17 ± 3846.45
Evaluation time (s)	–	24.87 ± 1.35	3.43 ± 0.10	11.3 ± 0.97	5.15 ± 0.11	9.41 ± 1.07	5.14 ± 0.63	9.52 ± 1.06	0.12 ± 0.01	0.19 ± 0.02	0.54 ± 0.01	0.96 ± 0.01

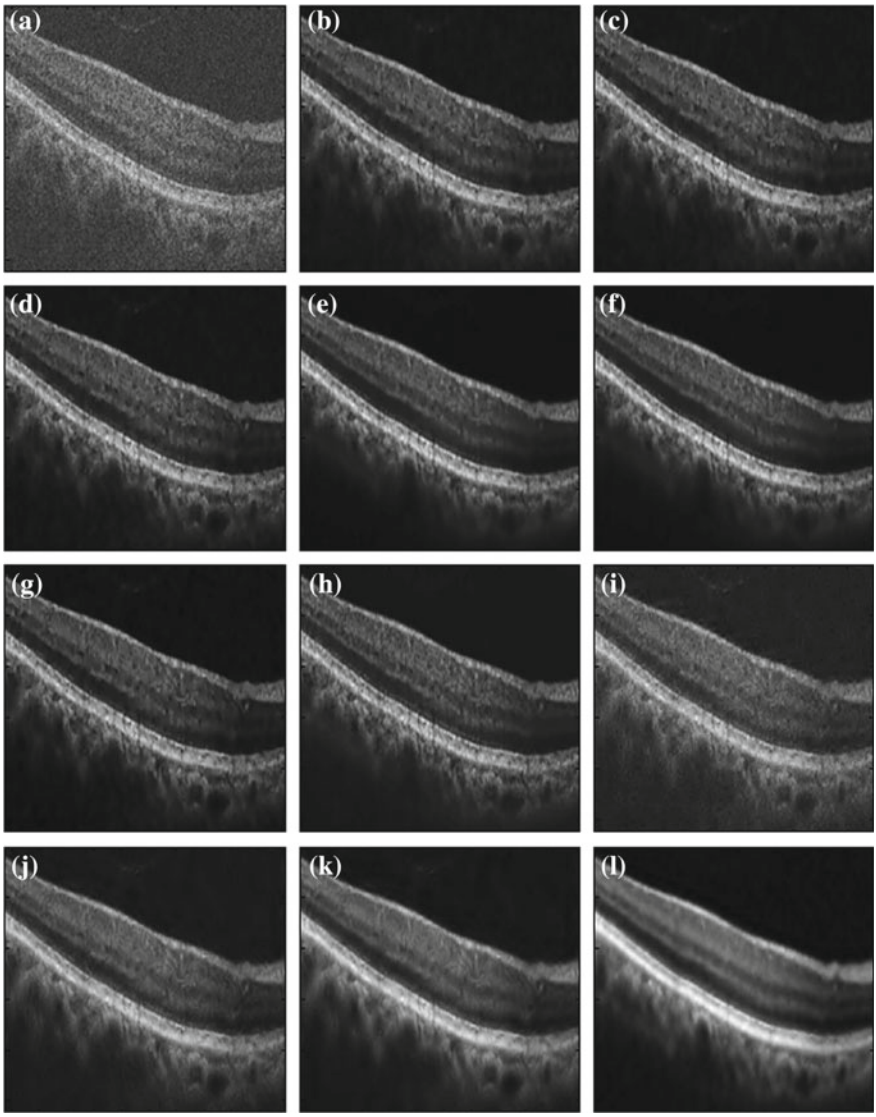

Fig. 3.5 Denoising results in a sample Topcon image. **a** Original noisy image, **b** 2D CDL, **c** 2D ICWDL, **d** 2D RCWDL, **e** 3D ICWDL, **f** 3D RCWDL, **g** 2D DSDL, **h** 3D DSDL, **i** 2D SDWT, **j** 2D RCWT, **k** 2D CCWT, **l** 3D CCWT [16]

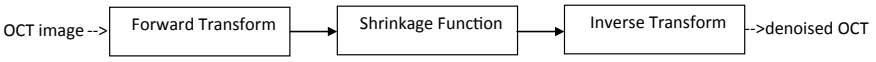

Fig. 3.6 The block diagram of non data adaptive transform based OCT denoising

when we use hommomorphic method in 3D dual-tree complex wavelet domain, the forward transform in Fig. 3.6 would be log transform+forward 3D dual-tree complex wavelet transform.

Another important factor in transform-based denoising process is finding an appropriate shrinkage function. Using sparse transforms facilitate statistical modeling of data due to attractive properties of data in sparse domains. For example, in wavelet domain the marginal pdfs of natural signals have leptokurtic distribution and although adjacent coefficients within/between subband(s) are uncorrelated but they are not independent. Case we can propose the following model for OCT data in 3D dual-tree complex wavelet domain:

$$\begin{aligned} p_{\bar{w}(k)}(\bar{w}(k)) &= a(k)p_1(\bar{w}(k)) + (1-a(k))p_2(\bar{w}(k)) \\ &= \frac{a(k)\mathrm{e}^{-\frac{w_1^2(k)}{2\sigma_{11}^2(k)}-\frac{w_2^2(k)}{2\sigma_{12}^2(k)}}}{2\pi\sigma_{11}(k)\sigma_{12}(k)} + \frac{(1-a(k))\mathrm{e}^{-\frac{w_1^2(k)}{2\sigma_{21}^2(k)}-\frac{w_2^2(k)}{2\sigma_{22}^2(k)}}}{2\pi\sigma_{21}(k)\sigma_{22}(k)} \end{aligned} \tag{3.16}$$

For kth wavelet coefficient, $\bar{w}(k) = (w_1(k), w_2(k))$ where $w_2(k)$ represent the parent of $w_1(k)$ at the spatial position k (at the next coarser scale), and $a(k) \in [0, 1]$, $\sigma_{11}(k)$, $\sigma_{12}(k)$, $\sigma_{21}(k)$, $\sigma_{22}(k)$ are the parameters of mixture model which will be estimated using EM algorithm.

The proposed model of "mixture of bivariate Gaussian pdfs with local parameters" is bivariate mixture and local which is able to simultaneously capture the persistence, sparsity and clustering properties of wavelet coefficients.

The correlation index of this bivariate pdf represents is zero:

$$\begin{aligned} E(w_1(k)w_2(k)) &= \iint w_1(k)w_2(k)p_{\bar{w}(k)}(\bar{w}(k))\mathrm{d}\bar{w}(k) \\ &= (1-a(k)) \iint w_1(k)w_2(k)p_2(\bar{w}(k))\mathrm{d}w_1(k)\mathrm{d}w_2(k) \\ &\quad + a(k) \iint w_1(k)w_2(k)p_1(\bar{w}(k))\mathrm{d}w_1(k)\mathrm{d}w_2(k) = 0 \end{aligned} \tag{3.17}$$

The marginal pdf of $w_1(k)$ and $w_2(k)$ would be univariate Gaussian mixture pdfs with local parameters [68]:

$$\begin{aligned} p_{w_1(k)}(w_1(k)) &= \int_{-\infty}^{\infty} p_{\bar{w}(k)}(\bar{w}(k))\mathrm{d}w_2(k) \\ &= a(k)\frac{\exp\left(-\frac{w_1^2(k)}{2\sigma_{11}^2(k)}\right)}{\sigma_{11}(k)\sqrt{2\pi}} + (1-a(k))\frac{\exp\left(-\frac{w_1^2(k)}{2\sigma_{21}^2(k)}\right)}{\sigma_{21}(k)\sqrt{2\pi}} \end{aligned} \tag{3.18}$$

$$p_{w_2(k)}(w_2(k)) = \int_{-\infty}^{\infty} p_{\bar{w}(k)}(\bar{w}(k))\mathrm{d}w_1(k)$$
$$= a(k)\frac{\exp\left(-\frac{w_2^2(k)}{2\sigma_{21}^2(k)}\right)}{\sigma_{21}(k)\sqrt{2\pi}} + (1-a(k))\frac{\exp\left(-\frac{w_2^2(k)}{2\sigma_{22}^2(k)}\right)}{\sigma_{22}(k)\sqrt{2\pi}} \tag{3.19}$$

It is clear that

$$p_{\bar{w}(k)}(\bar{w}(k)) \neq p_{w_1(k)}(w_1(k))p_{w_2(k)}(w_2(k)) \tag{3.20}$$

which means $w_1(k)$, $w_2(k)$ are not independent.

3.5.1 Denoising by Minimum Mean Square Error (MMSE) Estimator

As a common model the following multiplicative model is proposed for speckle noise in 3D OCT data:

$$x(i) = s(i)g(i) \tag{3.21}$$

where i indicates the ith voxel of 3D OCT data.

Applying log transformation in homomorphic methods we would have:

$$W(\log x(i)) = W(\log s(i)) + W(\log g(i)) \tag{3.22}$$

where W represents 3D RCWT.

This equation can be written as:

$$y(k) = w(k) + n(k) \tag{3.23}$$

where $w(k)$ and $y(k)$ shows respectively the kth noise-free and noisy 3D RCWT coefficients, and $n(k)$ represents the noise in the 3D RCWT domain.

In contrast, in non-homomorphic techniques the wavelet transform is directly applied on speckled data which results in an unbiased estimation of the data. So, we would have:

$$W(x(i)) = W(s(i)g(i)) = W(s(i) + s(i)(g(i)-1)) = W(s(i)) + W(s(i)(g(i)-1)) \tag{3.24}$$

which can be written as:

$$y(k) = w(k) + n(k) \tag{3.25}$$

where w(k) and y(k) shows respectively the kth noise-free and noisy 3D RCWT coefficients, and n(k) represents the noise in the 3D RCWT domain. Considering an independent unit-mean random process for g, we would have E[W(s(g − 1))] = 0 and since E[W(s)W(s(g − 1))] = 0, w(k) and n(k) would be zero-mean uncorrelated random variables.

So, we can use the following bivariate model in 3D RCWT domain for both homomorphic and non-homomorphic approaches:

$$\bar{y}(k) = \bar{w}(k) + \bar{n}(k) \tag{3.26}$$

where $\bar{w}(k) = (w(k), w_p(k))$, $\bar{y}(k) = (y(k), y_p(k))$, $\bar{n}(k) = (n(k), n_p(k))$ and $w_p(k)$, $y_p(k)$, and $n_p(k)$ show the parent coefficients of w(k), y(k), and n(k) respectively. Here, we test both Additive white Gaussian noise (AWGN) and two-sided Rayleigh model for noise in wavelet domain [66–68]:

$$p_{\bar{n}}(\bar{n}(k)) = \frac{1}{2\pi\sigma_n^2} \exp\left(-\frac{n_1^2(k) + n_2^2(k)}{2\sigma_n^2}\right) \tag{3.27}$$

$$p_{\bar{n}}(\bar{n}(k)) = \frac{|n_1(k)n_2(k)|}{4\alpha^4} \exp\left(-\frac{n_1^2(k) + n_2^2(k)}{2\alpha^2}\right) \tag{3.28}$$

where $\sigma_n^2 = 2\alpha^2$ is the noise variance.

Using MMSE estimator for the estimation of $\bar{w}(k)$ from $\bar{y}(k) = \bar{w}(k) + \bar{n}(k)$, the optimal solution would be the posterior mean:

$$\hat{w}(k) = \frac{\iint w(k) p_{\bar{n}}(\bar{y}(k) - \bar{w}(k)) p_{\bar{w}(k)}(\bar{w}(k)) \mathrm{d}\bar{w}(k)}{\iint p_{\bar{n}}(\bar{y}(k) - \bar{w}(k)) p_{\bar{w}(k)}(\bar{w}(k)) \mathrm{d}\bar{w}(k)} \tag{3.29}$$

which for a mixture model of $p_{\bar{w}(k)}(\bar{w}(k)) = a(k)p_1(\bar{w}(k)) + (1 - a(k))p_2(\bar{w}(k))$ would be:

$$\begin{aligned}
\hat{w}(k) &= \frac{\iint w(k) p_{\bar{n}}(\bar{y}(k) - \bar{w}(k))[a(k)p_1(\bar{w}(k)) + (1 - a(k))p_2(\bar{w}(k))]\mathrm{d}\bar{w}(k)}{\iint p_{\bar{n}}(\bar{y}(k) - \bar{w}(k))[a(k)p_1(\bar{w}(k)) + (1 - a(k))p_2(\bar{w}(k))]\mathrm{d}\bar{w}(k)} \\
&= \frac{a(k) \iint w(k) p_{\bar{n}}(\bar{y}(k) - \bar{w}(k)) p_1(\bar{w}(k)) \mathrm{d}\bar{w}(k)}{a(k)g_1(\bar{y}(k)) + (1 - a(k))g_2(\bar{y}(k))} \\
&\quad + \frac{(1 - a(k)) \iint w(k) p_{\bar{n}}(\bar{y}(k) - \bar{w}(k)) p_2(\bar{w}(k)) \mathrm{d}\bar{w}(k)}{a(k)g_1(\bar{y}(k)) + (1 - a(k))g_2(\bar{y}(k))}
\end{aligned} \tag{3.30}$$

where

$$g_i(\bar{y}(k)) = \iint p_{\bar{n}}(\bar{y}(k) - \bar{w}(k)) p_i(\bar{w}(k)) \mathrm{d}\bar{w}(k), \quad i = 1, 2 \tag{3.31}$$

By substituting "mixture of bivariate Gaussian pdfs with local parameters" as the prior distribution of 3D RCWT coefficients, i.e., $p_{\bar{w}(k)}(\bar{w}(k))$ for AWGN we would have:

$$g_i(\bar{y}(k)) = \frac{\exp\left(-\frac{1}{2}\left(\frac{y^2(k)}{\sigma_n^2+\sigma_{i1}^2(k)} + \frac{y_p^2(k)}{\sigma_n^2+\sigma_{i2}^2(k)}\right)\right)}{2\pi\sqrt{(\sigma_n^2+\sigma_{i1}^2(k))(\sigma_n^2+\sigma_{i2}^2(k))}}, \quad i = 1, 2 \tag{3.32}$$

Similarly, after some simplifications for two-sided Rayleigh noise $g_i(\bar{y}(k))$ would be:

$$\begin{aligned} g_i(\bar{y}(k)) = & \frac{\exp\left(-\frac{y^2(k)}{2\sigma_{i1}^2(k)} - \frac{y_p^2(k)}{2\sigma_{i2}^2(k)}\right)}{8\pi(1+\frac{\sigma_{i1}^2(k)}{\alpha^2})(1+\frac{\sigma_{i2}^2(k)}{\alpha^2})\sigma_{i1}(k)\sigma_{i2}(k)} \\ & \times (2 + z_i(k)\sqrt{\pi}erfcx(-z_i(k)) \\ & - z_i(k)\sqrt{\pi}erfcx(z_i(k)))(2 + z_{ip}(k)\sqrt{\pi}erfcx(-z_{ip}(k)) \\ & - z_{ip}(k)\sqrt{\pi}erfcx(z_{ip}(k))), \\ i = & 1, 2 \end{aligned} \tag{3.33}$$

where

$$z_i(k) = \frac{y(k)}{\sigma_{i1}^2(k)}\sqrt{\frac{1}{\frac{2}{\alpha^2} + \frac{2}{\sigma_{i1}^2(k)}}}, \quad i = 1, 2 \tag{3.34}$$

$$z_{ip}(k) = \frac{y_p(k)}{\sigma_{i2}^2(k)}\sqrt{\frac{1}{\frac{2}{\alpha^2} + \frac{2}{\sigma_{i2}^2(k)}}}, \quad i = 1, 2 \tag{3.35}$$

The numerators of (3.30) can be obtained as MMSE estimate of a single component model [69]. So, for AWGN, the shrinkage function (3.30), which is called *BiGaussMixShrinkL*, can be written as:

$$\hat{w}(k) = \frac{\frac{\sigma_{11}^2(k)}{\sigma_{11}^2(k)+\sigma_n^2} + R(\bar{y}(k))\frac{\sigma_{21}^2(k)}{\sigma_{21}^2(k)+\sigma_n^2}}{1 + R(\bar{y}(k))} y(k) \tag{3.36}$$

where

$$R(\bar{y}(k)) = \frac{(1-a(k))\frac{\exp\left(-\frac{1}{2}\left(\frac{y^2(k)}{\sigma_n^2+\sigma_{21}^2(k)} + \frac{y_p^2(k)}{\sigma_n^2+\sigma_{22}^2(k)}\right)\right)}{\sqrt{(\sigma_n^2+\sigma_{21}^2(k))(\sigma_n^2+\sigma_{22}^2(k))}}}{a(k)\frac{\exp\left(-\frac{1}{2}\left(\frac{y^2(k)}{\sigma_n^2+\sigma_{11}^2(k)} + \frac{y_p^2(k)}{\sigma_n^2+\sigma_{12}^2(k)}\right)\right)}{\sqrt{(\sigma_n^2+\sigma_{11}^2(k))(\sigma_n^2+\sigma_{12}^2(k))}}} \tag{3.37}$$

Similarly, for two-sided Rayleigh noise, the shrinkage function (3.30), which is called *BiGaussRayMixShrinkL*, can be written as:

$$\hat{w}(k) = \frac{1}{1+R(\bar{y}(k))} \frac{2z_1(k)\sqrt{2}\left(2-\frac{\sigma_{11}^2(k)}{\alpha^2}\right)+\sqrt{\frac{\pi}{2}}\left(1-\frac{\sigma_{11}^2(k)z_1^2(k)}{\alpha^2}\right)(erfcx(z_1(k))-erfcx(-z_1(k)))}{\sqrt{\frac{1}{\alpha^2}+\frac{1}{\sigma_{11}^2(k)}}(2+z_1(k)\sqrt{\pi}erfcx(-z_1(k))-z_1(k)\sqrt{\pi}erfcx(z_1(k)))}$$
$$+ \frac{R(\bar{y}(k))}{1+R(\bar{y}(k))} \frac{2z_2(k)\sqrt{2}\left(2-\frac{\sigma_{21}^2(k)}{\alpha^2}\right)+\sqrt{\frac{\pi}{2}}\left(1-\frac{\sigma_{21}^2(k)z_2^2(k)}{\alpha^2}\right)(erfcx(z_2(k))-erfcx(-z_2(k)))}{\sqrt{\frac{1}{\alpha^2}+\frac{1}{\sigma_{21}^2(k)}}(2+z_2(k)\sqrt{\pi}erfcx(-z_2(k))-z_2(k)\sqrt{\pi}erfcx(z_2(k)))} \tag{3.38}$$

where

$$R(\bar{y}(k)) = \frac{1-a(k)}{a(k)} \frac{\left(1+\frac{\sigma_{11}^2(k)}{\alpha^2}\right)\left(1+\frac{\sigma_{12}^2(k)}{\alpha^2}\right)\sigma_{11}(k)\sigma_{12}(k)}{\left(1+\frac{\sigma_{21}^2(k)}{\alpha^2}\right)\left(1+\frac{\sigma_{22}^2(k)}{\alpha^2}\right)\sigma_{2i1}(k)\sigma_{22}(k)} \frac{\exp\left(-\frac{y^2(k)}{2\sigma_{21}^2(k)}-\frac{y_p^2(k)}{2\sigma_{22}^2(k)}\right)}{\exp\left(-\frac{y^2(k)}{2\sigma_{11}^2(k)}-\frac{y_p^2(k)}{2\sigma_{12}^2(k)}\right)}$$
$$\times \frac{(2+z_2(k)\sqrt{\pi}erfcx(-z_2(k))-z_2(k)\sqrt{\pi}erfcx(z_2(k)))(2+z_{2p}(k)\sqrt{\pi}erfcx(-z_{2p}(k))}{(2+z_1(k)\sqrt{\pi}erfcx(-z_1(k))-z_1(k)\sqrt{\pi}erfcx(z_1(k)))(2+z_{1p}(k)\sqrt{\pi}erfcx(-z_{1p}(k))}$$
$$\frac{-z_{2p}(k)\sqrt{\pi}erfcx(z_{2p}(k))}{-z_{1p}(k)\sqrt{\pi}erfcx(z_{1p}(k))} \tag{3.39}$$

Figure 3.7 shows shrinkage functions BiGaussMixShrink and BiGaussRayMixShrink with sample constant parameters.

To apply BiGaussMixShrink and BiGaussRayMixShrink shrinkage functions on 3D RCWT data, we should estimate the parameters $\sigma_{ij}(k)$ for $i,j=1,2$ and $a(k)$ (that are for noise-free data) from noisy observation. For this reason, the following local EM algorithm is employed:

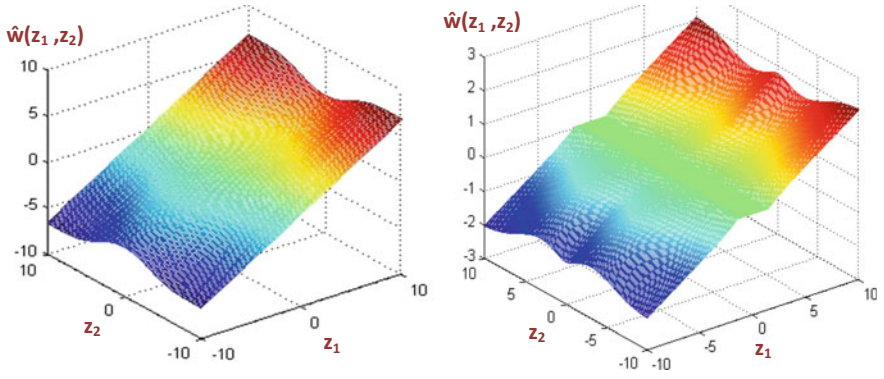

Fig. 3.7 Shrinkage functions produced from BiGaussMixShrink (left image) and BiGaussRayMixShrink (right image) for sample parameters

Table 3.8 Outline of the proposed OCT despeckling algorithm

Step 1:	3D Complex Wavelet Transformation of Noisy OCT to Find $\bar{y}(k)$ and σ_n.
Step 2:	Estimation of the Prior (Finding Mixture Model Parameters in Each Subband).
2.1.3. Initialization for $a(k)$ and $\sigma_{11}(k)$,$\sigma_{12}(k)$, $\sigma_{21}(k)$, $\sigma_{22}(k)$. *2.2. Using (3.40) to find $r_1(k)$, $r_2(k)$.* *2.3. Using (3.41) to update $a(k)$ by substituting $r_1(k)$, $r_2(k)$ from step 2.2.* *2.4. Updating the parameters of prior, $\sigma_{11}(k)$, $\sigma_{12}(k)$, $\sigma_{21}(k)$, $\sigma_{22}(k)$, using (3.42) and (3.43).* *2.5. Finding $g_i(\bar{y}(k))$ from (3.32) for AWGN and (3.33) for two-sided Rayleigh noise using updated value in step 2.3.* *2.6. Iteration step 2.2 to 2.4 until parameter convergence.*	
Step 3:	Substituting the Final Parameters in Step 2 in Shrinkage Function (3.36) for AWGN (after obtaining $R(\bar{y}(k))$ using (3.37)) and Shrinkage Function (3.38) for two-sided Rayleigh noise (after obtaining $R(\bar{y}(k))$ using (3.39)).
Step 4:	Inverse 3D Complex Wavelet Transformation.

E step:

$$r_1(k) \leftarrow \frac{a(k)g_1(\bar{y}(k))}{a(k)g_1(\bar{y}(k)) + (1-a(k))g_2(\bar{y}(k))}, \quad r_2(k) \leftarrow 1 - r_1(k) \tag{3.40}$$

M-step:

$$a(k) \leftarrow \frac{1}{M} \sum_{j \in \mathrm{N}(K)} r_1(j), \tag{3.41}$$

$$\sigma_{1m}^2(k) \leftarrow \frac{\sum_{j \in \mathrm{N}(K)} r_i(j) y^2(k)}{\sum_{j \in \mathrm{N}(K)} r_i(j)} - \sigma_n^2, \quad m = 1, 2 \tag{3.42}$$

$$\sigma_{2m}^2(k) \leftarrow \frac{\sum_{j \in \mathrm{N}(K)} r_i(j) y_p^2(k)}{\sum_{j \in \mathrm{N}(K)} r_i(j)} - \sigma_n^2, \quad m = 1, 2 \tag{3.43}$$

where M shows the number of samples in window $\mathrm{N}(k)$, which is centered at $\bar{y}(k)$ and σ_n is estimated by $\sigma_n = median\{|\ noisy\ wavelet\ coefficients\ in\ finest\ scale\ |\}/0.6745$ [69].

The final OCT despeckling algorithm is concluded in Table 3.8.

As discussed in the literature [69, 70], instead of proposing isotropic window $\mathrm{N}(k)$, using anisotropic window would result in better modeling and denoising results. In this base local polynomial approximation- intersection of confidence intervals (LPA-ICI) method [70] can be employed to obtain the anisotropic window around each pixel (Fig. 3.8) and this method can be extended to 3D space (Fig. 3.9).

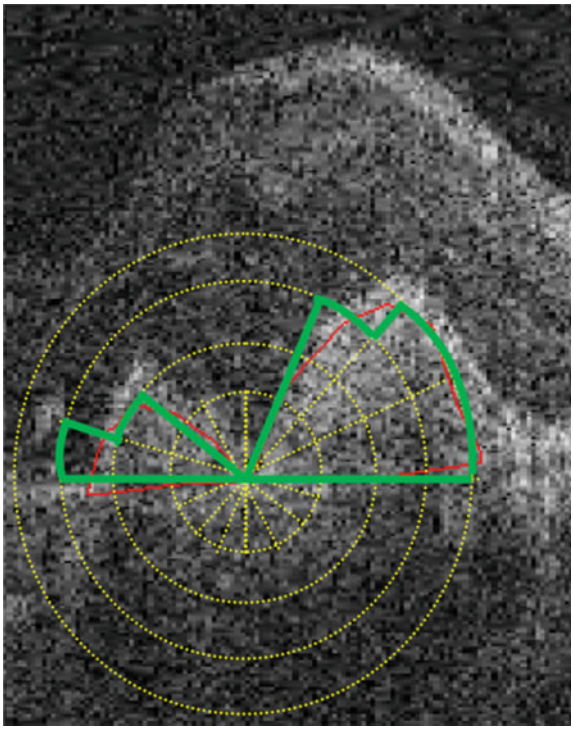

Fig. 3.8 The red line illustrates the manually depicted SEAD by an ophthalmologist. The yellow circles illustrates the isotropic windows with various radiuses. The green line shows the obtained anisotropic based on LPA-ICI rule

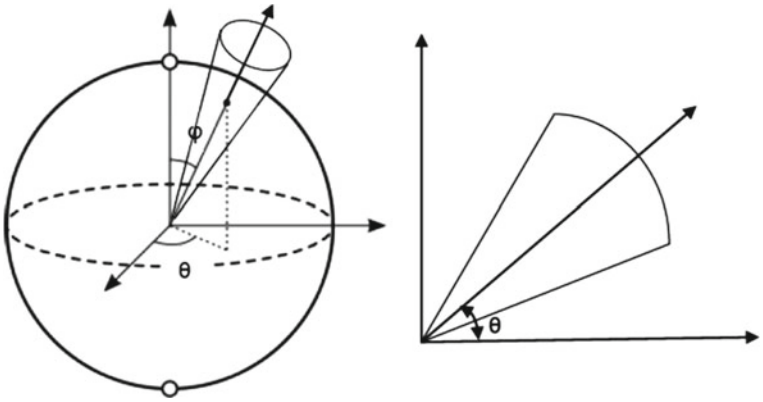

Fig. 3.9 Comparison between a circular sector for direction θ in 2D case (right image) with a conical body produced for direction (θ, φ) in 3D case (left image) [72]

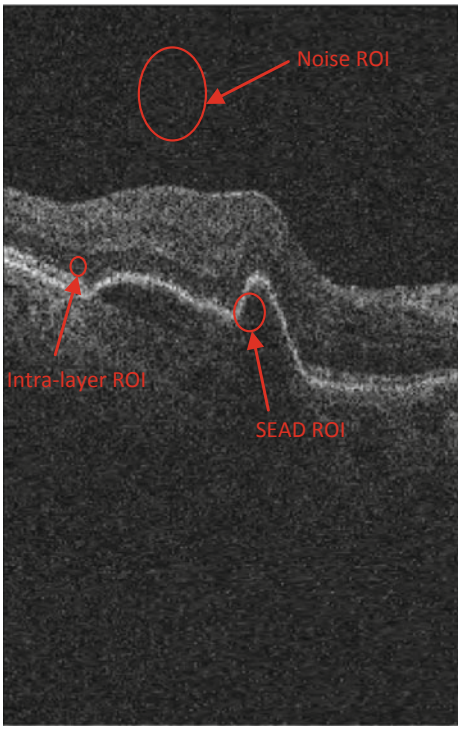

Fig. 3.10 A sample B-scan and proposed ROIs. MSNR and CNR reported in Table 3.9

3.5.2 Results

The proposed despeckling algorithm in Table 3.8 was applied on 20 3D OCT datasets in the presence of wet AMD pathology (SEAD) and MSNR and CNR were measured. The Region of Interest (ROI) region was defined within the SEAD as shown in Fig. 3.10.

Table 3.9 shows MSNR and CNR of selected ROIs. In addition CNR curves for 156 selected ROIs in Fig. 3.11 show the SNR improvements of various versions of proposed method. It can be concluded that non-homomorphic *BiGaussMixShrinkL* method outperforms other methods.

Another way for evaluation of proposed despeckling algorithm is investigation of the performance of intralayer segmentation algorithms before and after applying our despeckling algorithm. Figure 3.12 illustrates this comparison for the segmented layers of a $650 \times 512 \times 128$ Topcon 3D OCT-1000 imaging system by applying the proposed method in [74]. It is observed that although the first layer and layers under inner/outer segment junction cannot be detected before despecking, they are detectable truly after despeckling by our algorithm.

Table 3.9 The results of MSNR and CNR using several ROIs such as shown in Fig. 3.10

Methods					
Local (L) Non-Local (NL)	Homomorphic (H) Non-Homomorphic (NH)	Gaussian Noise (G) Two-sided Rayleigh Noise (R)	$MSNR_{ROI1}$	$MSNR_{ROI2}$	CNR
L	H	G	7.00	15.76	8.76
NL	H	G	7.56	17.03	9.47
L	NH	G	12.27	27.76	13.49
NL	NH	G	10.77	22.73	11.95
L	H	R	5.89	13.11	7.22
NL	H	R	8.63	19.59	10.95
L	NH	R	10.75	22.55	11.81
NL	NH	R	10.88	23.05	12.17
Original image			2.56	5.30	2.74

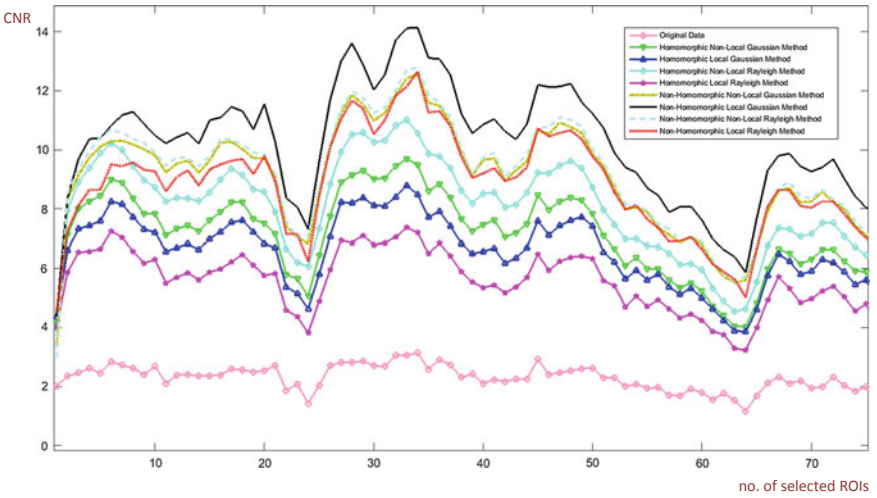

Fig. 3.11 A comparison between CNR curves for 156 selected ROIs from OCT dataset

3.6 Conclusion

In this chapter we discussed about several methods of OCT despeckling and enhancement in the modeling point of view. Considering statistical and transform based modeling, three algorithms were introduced based on (1) statistical gaussinization of each OCT intraretinal layer, (2) 3D data-adaptive sparse modeling of OCT, and (3) statistical modeling of OCT in 3D non-data-adaptive sparse domain. Incorporating the structural information of OCT data (geometric modeling) on top of the advantages

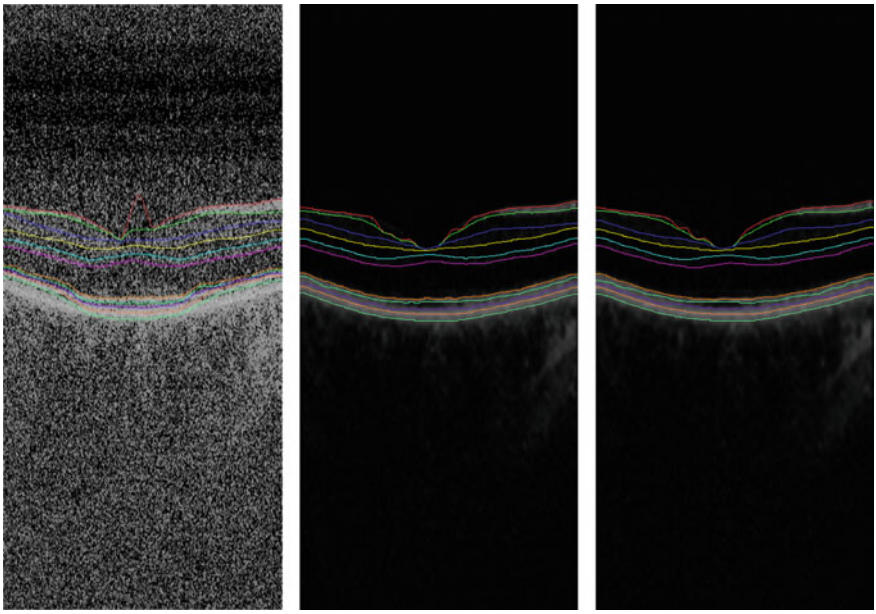

Fig. 3.12 A comparison between the segmented layers of a $650 \times 512 \times 128$ Topcon 3D OCT-1000 imaging system using proposed method in [74]. From left to right: original image, denised image by nonlocal homomorphic *BiGaussRayMixShrinkL* method, and local homomorphic *BiGaussRayMixShrinkL* method

of statistical and transform-based models can result in an optimum solution for OCT enhancements as the current model usually are not able to satisfy all requirements of clinicians. Some methods are able to preserve the edges while corrupt the important intra-retinal texture vs. the others which cannot keep the layers' information while they aim to keep the texture and attenuate the noise. It seems that finding an optimum combination of mentioned image models for modeling layers, intra-retinal textures and edges/textures of abnormalities in OCT images will guide us toward the state-of-the-art OCT enhancement technique.

References

1. D. Huang, E.A. Swanson, C.P. Lin, J.S. Schuman, W.G. Stinson, W. Chang et al., Optical coherence tomography. Science **254**, 1178 (1991). (New York, NY)
2. B. Potsaid, I. Gorczynska, V.J. Srinivasan, Y. Chen, J. Jiang, A. Cable et al., Ultrahigh speed spectral/Fourier domain OCT ophthalmic imaging at 70,000 to 312,500 axial scans per second. Opt. Express **16**, 15149–15169 (2008)
3. J. Izatt, M. Choma, Theory of optical coherence tomography, in *Optical Coherence Tomography* (Springer, Berlin, 2008), pp. 47–72

4. M. Szkulmowski, I. Gorczynska, D. Szlag, M. Sylwestrzak, A. Kowalczyk, M. Wojtkowski, Efficient reduction of speckle noise in optical coherence tomography. Opt. Express **20**, 1337–1359 (2012)
5. M. Bashkansky, J. Reintjes, Statistics and reduction of speckle in optical coherence tomography. Opt. Lett. **25**, 545–547 (2000)
6. D.D. Duncan, S.J. Kirkpatrick, R.K. Wang, Statistics of local speckle contrast. JOSA A **25**, 9–15 (2008)
7. J.W. Goodman, Some fundamental properties of speckle. JOSA **66**, 1145–1150 (1976)
8. B. Karamata, K. Hassler, M. Laubscher, T. Lasser, Speckle statistics in optical coherence tomography. JOSA A **22**, 593–596 (2005)
9. J.M. Schmitt, S. Xiang, K.M. Yung, Speckle in optical coherence tomography. J. Biomed. Opt. **4**, 95–105 (1999)
10. N.M. Grzywacz, J. De Juan, C. Ferrone, D. Giannini, D. Huang, G. Koch et al., Statistics of optical coherence tomography data from human retina. IEEE Trans. Med. Imaging **29**, 1224–1237 (2010)
11. D.H. Ross, Finding Bands in Optical Coherence Tomography Images using Curve and Function Fitting (The University of Alabama at Birmingham, 2014)
12. A.F. Fercher, W. Drexler, C.K. Hitzenberger, T. Lasser, Optical coherence tomography-principles and applications. Rep. Prog. Phys. **66**, 239 (2003)
13. N. George, C. Christensen, J. Bennett, B. Guenther, Speckle noise in displays. JOSA **66**, 1282–1290 (1976)
14. J.W. Goodman, Some effects of target-induced scintillation on optical radar performance. Proc. IEEE **53**, 1688–1700 (1965)
15. R. Loudon, *The Quantum Theory of Light* (OUP, Oxford, 2000)
16. Z. Amini, H. Rabbani, Classification of medical image modeling methods: a review. Curr. Med. Imaging Rev. **12**, 130–148 (2016)
17. I. Jolliffe, *Principal Component Analysis* (Wiley Online Library, New York, 2002)
18. A. Jung, An introduction to a new data analysis tool: Independent component analysis, in *Proceedings of Workshop GK" Nonlinearity"-Regensburg* (2001)
19. A. Hyvärinen, E. Oja, Independent component analysis: algorithms and applications. Neural Networks **13**, 411–430 (2000)
20. M.P. Arakeri, G.R.M. Reddy, A comparative performance evaluation of independent component analysis in medical image denoising, in *2011 International Conference on Recent Trends in Information Technology (ICRTIT)* (2011), pp. 770–774
21. I. Tosic, P. Frossard, Dictionary learning. Sig. Process. Mag. IEEE **28**, 27–38 (2011)
22. R. Kafieh, H. Rabbani, I. Selesnik, Three dimensional data-driven multi scale atomic representation of optical coherence tomography. IEEE Trans. Med. Imaging **34**, 1042–1062 (2015)
23. I. Daubechies, *Ten Lectures on Wavelets*, vol. 61 (SIAM, Philadelphia, PA, 1992)
24. T.F. Chan, J.J. Shen, *Image Processing and Analysis: Variational, PDE, Wavelet, and Stochastic Methods* (SIAM, Philadelphia, PA, 2005)
25. M. Jain, S. Sharma, R.M. Sairam, Effect of blur and noise on image denoising based on PDE, in *International Journal of Advanced Computer Research* (*IJACR*), vol. 3(1) Issue-8 March-2013 (2013)
26. H.M. Salinas, D.C. Fernandez, Comparison of PDE-based nonlinear diffusion approaches for image enhancement and denoising in optical coherence tomography. IEEE Trans. Med. Imaging **26**, 761–771 (2007)
27. M.K. Garvin, M.D. Abràmoff, R. Kardon, S.R. Russell, X. Wu, M. Sonka, Intraretinal layer segmentation of macular optical coherence tomography images using optimal 3-D graph search. IEEE Trans. Med. Imaging **27**, 1495–1505 (2008)
28. L.D. Cohen, I. Cohen, Finite-element methods for active contour models and balloons for 2-D and 3-D images. IEEE Trans. Pattern Anal. Mach. Intell. **15**, 1131–1147 (1993)
29. Y. Yu, S. Zhang, K. Li, D. Metaxas, L. Axel, Deformable models with sparsity constraints for cardiac motion analysis. Med. Image Anal. **18**, 927–937 (2014)

30. G. Peyré, *Advanced Signal, Image and Surface Processing* (University Paris-Dauphine, Ceremade, 2010)
31. S.J. Wright, R.D. Nowak, M.A. Figueiredo, Sparse reconstruction by separable approximation. IEEE Trans. Signal Process. **57**, 2479–2493 (2009)
32. H. Rabbani, R. Nezafat, S. Gazor, Wavelet-domain medical image denoising using bivariate Laplacian mixture model. IEEE Trans. Biomed. Eng. **56**, 2826–2837 (2009)
33. R.R. Coifman, M. Maggioni, Diffusion wavelets. Appl. Comput. Harmonic Anal. **21**, 53–94 (2006)
34. D. Cabrera Fernández, N. Villate, C. Puliafito, P. Rosenfeld, Comparing total macular volume changes measured by optical coherence tomography with retinal lesion volume estimated by active contours. Invest. Ophtalmol. Vis. Sci. **45**, 3072 (2004)
35. G. Gregori, R. Knighton, A robust algorithm for retinal thickness measurements using optical coherence tomography (Stratus OCT). Invest. Ophtalmol. Vis. Sci. **45**, 3007 (2004)
36. J. Rogowska, M.E. Brezinski, Evaluation of the adaptive speckle suppression filter for coronary optical coherence tomography imaging. IEEE Trans. Med. Imaging **19**, 1261–1266 (2000)
37. A.M. Bagci, M. Shahidi, R. Ansari, M. Blair, N.P. Blair, R. Zelkha, Thickness profiles of retinal layers by optical coherence tomography image segmentation. Am. J. Ophthalmol. **146**, 679–687 (2008). (e1)
38. R. Bernardes, C. Maduro, P. Serranho, A. Araújo, S. Barbeiro, J. Cunha-Vaz, Improved adaptive complex diffusion despeckling filter. Opt. Express **18**, 24048–24059 (2010)
39. A.R. Fuller, R.J. Zawadzki, S. Choi, D.F. Wiley, J.S. Werner, B. Hamann, Segmentation of three-dimensional retinal image data. IEEE Trans. Visual Comput. Graphics **13**, 1719–1726 (2007)
40. A. Mishra, A. Wong, K. Bizheva, D.A. Clausi, Intra-retinal layer segmentation in optical coherence tomography images. Opt. Express **17**, 23719–23728 (2009)
41. F. Luan, Y. Wu, Application of RPCA in optical coherence tomography for speckle noise reduction. Laser Phys. Lett. **10**, 035603 (2013)
42. V. Gupta, C.C. Chan, C.-L. Poh, T.H. Chow, T.C. Meng, N.B. Koon, Computerized automation of wavelet based denoising method to reduce speckle noise in OCT images, in *International Conference on Information Technology and Applications in Biomedicine, ITAB* (2008), pp. 120–123
43. M.A. Mayer, A. Borsdorf, M. Wagner, J. Hornegger, C.Y. Mardin, R.P. Tornow, Wavelet denoising of multiframe optical coherence tomography data. Biomed. Opt. Express **3**, 572–589 (2012)
44. Z. Jian, Z. Yu, L. Yu, B. Rao, Z. Chen, B.J. Tromberg, Speckle attenuation in optical coherence tomography by curvelet shrinkage. Opt. Lett. **34**, 1516–1518 (2009)
45. S. Chitchian, M.A. Fiddy, N.M. Fried, Denoising during optical coherence tomography of the prostate nerves via wavelet shrinkage using dual-tree complex wavelet transform. J. Biomed. Opt.cs **14**, 014031–014031-6 (2009)
46. V. Kajić, M. Esmaeelpour, B. Považay, D. Marshall, P.L. Rosin, W. Drexler, Automated choroidal segmentation of 1060 nm OCT in healthy and pathologic eyes using a statistical model. Biomed. Opt. Express **3**, 86–103 (2012)
47. V. Kajić, B. Považay, B. Hermann, B. Hofer, D. Marshall, P.L. Rosin et al., Robust segmentation of intraretinal layers in the normal human fovea using a novel statistical model based on texture and shape analysis. Opt. Express **18**, 14730–14744 (2010)
48. R. Kafieh, H. Rabbani, M.D. Abramoff, M. Sonka, Curvature correction of retinal OCTs using graph-based geometry detection. Phys. Med. Biol. **58**, 2925 (2013)
49. Z. Amini, H. Rabbani, Statistical modeling of retinal optical coherence tomography. IEEE Trans. Med. Imaging **35**, 1544–1554 (2016)
50. A. Achim, A. Bezerianos, P. Tsakalides, Novel Bayesian multiscale method for speckle removal in medical ultrasound images. IEEE Trans. Med. Imaging **20**, 772–783 (2001)
51. A. Pizurica, L. Jovanov, B. Huysmans, V. Zlokolica, P. De Keyser, F. Dhaenens et al., Multiresolution denoising for optical coherence tomography: a review and evaluation. Curr. Med. Imaging Rev. **4**, 270–284 (2008)

52. S.S. Agaian, B. Silver, K.A. Panetta, Transform coefficient histogram-based image enhancement algorithms using contrast entropy. IEEE Trans. Image Process. **16**, 741–758 (2007)
53. J. Zhou, A.L. Cunha, M.N. Do, Nonsubsampled contourlet transform: construction and application in enhancement, in *IEEE International Conference on Image Processing 2005* (2005), pp. I-469–72
54. L. Fang, S. Li, Q. Nie, J.A. Izatt, C.A. Toth, S. Farsiu, Sparsity based denoising of spectral domain optical coherence tomography images. Biomed. Opt. Express **3**, 927–942 (2012)
55. P. Chatterjee, P. Milanfar, Clustering-based denoising with locally learned dictionaries. IEEE Trans. Image Process. **18**, 1438–1451 (2009)
56. M. Aharon, M. Elad, A. Bruckstein, k -SVD: an algorithm for designing overcomplete dictionaries for sparse representation. IEEE Trans. Sig. Process. **54**, 4311–4322 (2006)
57. M. Elad, M. Aharon, Image denoising via sparse and redundant representations over learned dictionaries. IEEE Trans. Image Process. **15**, 3736–3745 (2006)
58. Y.C. Pati, R. Rezaiifar, P.S. Krishnaprasad, Orthogonal matching pursuit: recursive function approximation with applications to wavelet decomposition, in *1993 Conference Record of the Twenty-Seventh Asilomar Conference on Signals, Systems and Computers,* vol.1 (1993), pp. 40–44
59. N. Kingsbury, Complex wavelets for shift invariant analysis and filtering of signals. Appl. Comput. Harmonic Anal. **10**, 234–253 (2001)
60. I.W. Selesnick, R.G. Baraniuk, N.C. Kingsbury, The dual-tree complex wavelet transform. Sig. Process. Mag. IEEE **22**, 123–151 (2005)
61. I.W. Selesnick, K.Y. Li, Video denoising using 2D and 3D dual-tree complex wavelet transforms. Wavelets Appl. Sign. Image Process. X **5207**, 607–618 (2003)
62. P. Puvanathasan, K. Bizheva, Interval type-II fuzzy anisotropic diffusion algorithm for speckle noise reduction in optical coherence tomography images. Opt. Express **17**, 733–746 (2009)
63. D.C. Adler, T.H. Ko, J.G. Fujimoto, Speckle reduction in optical coherence tomography images by use of a spatially adaptive wavelet filter. Opt. Lett. **29**, 2878–2880 (2004)
64. V. Zlokolica, L. Jovanov, A. Pizurica, P. De Keyser, F. Dhaenens, W. Philips, Wavelet-based denoising for 3D OCT images, in *Proceedings of SPIE* (2007), p. 66960P
65. Z. Jian, L. Yu, B. Rao, B.J. Tromberg, Z. Chen, Three-dimensional speckle suppression in optical coherence tomography based on the curvelet transform. Opt. Express **18**, 1024–1032 (2010)
66. S. Gupta, R.C. Chauhan, S.C. Saxena, Robust non-homomorphic approach for speckle reduction in medical ultrasound images. Med. Biol. Eng. Compu. **43**(2), 189–195 (2005)
67. S. Gupta, L. Kaur, R.C. Chauhan, S.C. Saxena, A versatile technique for visual enhancement of medical ultrasound images. Digit. Signal Proc. **17**(3), 542–560 (2007)
68. S. Yan, J. Yuan, M. Liu, C. Hou, Speckle noise reduction of ultrasound images based on an undecimated wavelet packet transform domain nonhomomorphic filtering, in *Proceedings of the 2nd International Conference on Biomedical Engineering and Informatics* (October 2009), pp. 1–5
69. H. Rabbani, M. Sonka, M.D. Abramoff, Optical coherence tomography noise reduction using anisotropic local bivariate gaussian mixture prior in 3-D complex wavelet domain. Int. J. Biomed. Imaging **2013**, Article ID 417491, 23 p (2013)
70. V. Katkovnik, K. Egiazarian, J. Astola, Adaptive window size image de-noising based on intersection of confidence intervals (ICI) rule. J. Math. Imaging Vis. **16**(3), 223–235 (2002)
71. A. Ozcan, A. Bilenca, A.E. Desjardins, B.E. Bouma, G.J. Tearney, Speckle reduction in optical coherence tomography images using digital filtering. JOSA A **24**, 1901–1910 (2007)
72. G.A. Campbell, R.M. Foster, *Fourier Integrals for Practical Applications* (Bell telephone laboratories, New York, 1948)
73. N. Ahmed, T. Natarajan, K.R. Rao, Discrete cosine transform. IEEE Trans. Comput. **100**, 90–93 (1974)
74. R.R. Coifman, M.V. Wickerhauser, Entropy-based algorithms for best basis selection. IEEE Trans. Inf. Theory **38**, 713–718 (1992)
75. D.L. Donoho, Wedgelets: nearly minimax estimation of edges. Ann. Stat. **27**, 859–897 (1999)

76. N.G. Kingsbury, The dual-tree complex wavelet transform: a new technique for shift invariance and directional filters, in *Proceedings 8th IEEE DSP Workshop,* Utah (1998), p. 86
77. E. Candes, L. Demanet, D. Donoho, L. Ying, Fast discrete curvelet transforms. Multiscale Model. Simul. **5**, 861–899 (2006)
78. E. Le Pennec, S. Mallat, Bandelet image approximation and compression. Multiscale Model. Simul. **4**, 992–1039 (2005)
79. M.N. Do, M. Vetterli, The contourlet transform: an efficient directional multiresolution image representation. IEEE Trans. Image Process. **14**, 2091–2106 (2005)
80. H. Chauris, I. Karoui, P. Garreau, H. Wackernagel, P. Craneguy, L. Bertino, The circlet transform: a robust tool for detecting features with circular shapes. Comput. Geosci. **37**, 331–342 (2011)
81. Y. Lu, M.N. Do, 3-D directional filter banks and surfacelets, in *SPIE Optics & Photonics* (2005), p. 59141Q
82. P. Comon, Independent component analysis, a new concept? Sig. Process. **36**, 287–314 (1994)
83. K. Engan, S.O. Aase, J. Husoy, Frame based signal compression using method of optimal directions (MOD), in *IEEE International Symposium on Circuits and Systems* (1999), pp. 1–4
84. N. Iftimia, B.E. Bouma, G.J. Tearney, Speckle reduction in optical coherence tomography by "path length encoded" angular compounding. J. Biomed. Opt. **8**, 260–263 (2003)
85. L. Ramrath, G. Moreno, H. Mueller, T. Bonin, G. Huettmann, A. Schweikard, Towards multi-directional OCT for speckle noise reduction, in *Medical Image Computing and Computer-Assisted Intervention–MICCAI 2008* (Springer, Berlin, 2008), pp. 815–823
86. M. Hughes, M. Spring, A. Podoleanu, Speckle noise reduction in optical coherence tomography of paint layers. Appl. Opt. **49**, 99–107 (2010)
87. A. Desjardins, B. Vakoc, G. Tearney, B. Bouma, Speckle reduction in OCT using massively-parallel detection and frequency-domain ranging. Opt. Express **14**, 4736–4745 (2006)
88. M. Pircher, E. Go, R. Leitgeb, A.F. Fercher, C.K. Hitzenberger, Speckle reduction in optical coherence tomography by frequency compounding. J. Biomed. Opt. **8**, 565–569 (2003)
89. B. Sander, M. Larsen, L. Thrane, J. Hougaard, T. Jørgensen, Enhanced optical coherence tomography imaging by multiple scan averaging. Br. J. Ophthalmol. **89**, 207–212 (2005)
90. E. Götzinger, M. Pircher, C.K. Hitzenberger, High speed spectral domain polarization sensitive optical coherence tomography of the human retina. Opt. Express **13**, 10217–10229 (2005)
91. T.M. Jørgensen, J. Thomadsen, U. Christensen, W. Soliman, B. Sander, Enhancing the signal-to-noise ratio in ophthalmic optical coherence tomography by image registration—method and clinical examples. J. Biomed. Opt. **12**, 041208–041210 (2007)
92. R.D. Ferguson, D.X. Hammer, L.A. Paunescu, S. Beaton, J.S. Schuman, Tracking optical coherence tomography. Opt. Lett. **29**, 2139–2141 (2004)
93. M.R. Hee, J.A. Izatt, E.A. Swanson, D. Huang, J.S. Schuman, C.P. Lin et al., Optical coherence tomography of the human retina. Arch. Ophthalmol. **113**, 325–332 (1995)
94. A. George, J. Dillenseger, A. Weber, A. Pechereau, Optical coherence tomography image processing. Investigat. Ophthalmol. Vis. Sci. **41**, 165–173 (2000)
95. D. Koozekanani, K. Boyer, C. Roberts, Retinal thickness measurements from optical coherence tomography using a Markov boundary model. IEEE Trans. Med. Imaging **20**, 900–916 (2001)
96. J. Rogowska, M.E. Brezinski, Image processing techniques for noise removal, enhancement and segmentation of cartilage OCT images. Phys. Med. Biol. **47**, 641 (2002)
97. M. Shahidi, Z. Wang, R. Zelkha, Quantitative thickness measurement of retinal layers imaged by optical coherence tomography. Am. J. Ophthalmol. **139**, 1056–1061 (2005)
98. K.L. Boyer, A. Herzog, C. Roberts, Automatic recovery of the optic nervehead geometry in optical coherence tomography. IEEE Trans. Med. Imaging **25**, 553–570 (2006)
99. V.J. Srinivasan, B.K. Monson, M. Wojtkowski, R.A. Bilonick, I. Gorczynska, R. Chen et al., Characterization of outer retinal morphology with high-speed, ultrahigh-resolution optical coherence tomography. Invest. Ophthalmol. Vis. Sci. **49**, 1571–1579 (2008)

100. K. Lee, M.D. Abràmoff, M. Niemeijer, M.K. Garvin, M. Sonka, 3-D segmentation of retinal blood vessels in spectral-domain OCT volumes of the optic nerve head, *Presented at the Proceedings of SPIE Medical Imaging: Biomedical Applications in Molecular, Structural, and Functional Imaging* (2010)
101. H. Ishikawa, D.M. Stein, G. Wollstein, S. Beaton, J.G. Fujimoto, J.S. Schuman, Macular segmentation with optical coherence tomography. Invest. Ophthalmol. Vis. Sci. **46**, 2012–2017 (2005)
102. M. Mayer, R. Tornow, R. Bock, J. Hornegger, F. Kruse, Automatic nerve fiber layer segmentation and geometry correction on spectral domain OCT images using fuzzy C-means clustering. Invest. Ophthalmol. Vis. Sci. **49**, pp. E-Abstract 1880 (2008)
103. M. Baroni, P. Fortunato, A. La Torre, Towards quantitative analysis of retinal features in optical coherence tomography. Med. Eng. Phys. **29**, 432–441 (2007)
104. D.L. Marks, T.S. Ralston, S.A. Boppart, Speckle reduction by I-divergence regularization in optical coherence tomography. JOSA A **22**, 2366–2371 (2005)
105. A. Wong, A. Mishra, K. Bizheva, D.A. Clausi, General Bayesian estimation for speckle noise reduction in optical coherence tomography retinal imagery. Opt. Express **18**, 8338–8352 (2010)
106. F. Leyuan, L. Shutao, R.P. McNabb, N. Qing, A.N. Kuo, C.A. Toth et al., Fast acquisition and reconstruction of optical coherence tomography images via sparse representation. IEEE Trans. Med. Imaging **32**, 2034–2049 (2013)
107. G. Quellec, K. Lee, M. Dolejsi, M.K. Garvin, M.D. Abràmoff, M. Sonka, Three-dimensional analysis of retinal layer texture: identification of fluid-filled regions in SD-OCT of the macula. IEEE Trans. Med. Imaging **29**, 1321–1330 (2010)
108. M. Forouzanfar, H. Moghaddam, A directional multiscale approach for speckle reduction in optical coherence tomography images, in *IEEE International Conference on Electrical Engineering, ICEE'07,* Lahore (2007), pp. 1–6
109. M.D. Abràmoff, K. Lee, M. Niemeijer, W.L. Alward, E.C. Greenlee, M.K. Garvin et al., Automated segmentation of the cup and rim from spectral domain OCT of the optic nerve head. Invest. Ophthalmol. Vis. Sci. **50**, 5778–5784 (2009)
110. A. Yazdanpanah, G. Hamarneh, B. Smith, M. Sarunic, Intra-retinal layer segmentation in optical coherence tomography using an active contour approach, in *Medical Image Computing and Computer-Assisted Intervention–MICCAI 2009* (Springer, Berlin, 2009), pp. 649–656
111. Q. Yang, C.A. Reisman, Z. Wang, Y. Fukuma, M. Hangai, N. Yoshimura et al., Automated layer segmentation of macular OCT images using dual-scale gradient information. Opt. Express **18**, 21293 (2010)
112. R. Kafieh, H. Rabbani, M.D. Abramoff, M. Sonka, Intra-retinal layer segmentation of 3D optical coherence tomography using coarse grained diffusion map. Med. Image Anal. (2013)
113. H. Bogunovic, M. Sonka, Y. Kwon, P. Kemp, M. Abramoff, X. Wu, Multi-surface and multi-field co-segmentation of 3-D retinal optical coherence tomography. IEEE Trans. Med. Imaging **99**, 247–253 (2014)
114. F. Rathke, S. Schmidt, C. Schnörr, Probabilistic intra-retinal layer segmentation in 3-D OCT images using global shape regularization. Med. Image Anal. **18**, 781–794 (2014)
115. D.J. George A, A. Weber, A. Pechereau, Optical coherence tomography image processing. Investigat. Ophthalmol. Vis. Sci. **41**, 165–173 (2000)
116. A. Herzog, K.L. Boyer, C. Roberts, Robust extraction of the optic nerve head in optical coherence tomography, in *Computer Vision and Mathematical Methods in Medical and Biomedical Image Analysis* (Springer, Berlin, 2004), pp. 395–407

Chapter 4
Reconstruction of Retinal OCT Images with Sparse Representation

Leyuan Fang and Shutao Li

In addition to the speckle noise introduced in the acquisition process, clinical-used OCT images often have high resolution and thus create a heavy burden for storage and transmission. To alleviate these problems, this chapter introduces several sparse representation based reconstruction methods for denoising, interpolation and compression, which enhance the quality of the OCT images and efficiently manage such large of amounts of data.

4.1 Introduction

Optical coherence tomography (OCT) is a non-invasive, cross-sectional imaging modality which has been widely applied for diverse medical applications, especially for diagnostic ophthalmology [1]. In clinical diagnosis, the ophthalmologists often require high resolution and high signal-to-noise-ratio (SNR) OCT images. However, due to the highly controlled imaging environment (e.g., limited light intensities), the acquired OCT images are seriously interfered by heavy noise [2–4]. In addition, to accelerate the acquisition process, relatively low spatial sampling rates are often used in capturing clinical OCT images [5]. Both the heavy noise and low spatial sampling rates negatively affect the analysis of the OCT image, necessitating the utilization of effective denoising and interpolation techniques. Furthermore, storage and transmission of the high resolution and high SNR OCT images consumes a vast amount of memory and communication bandwidth, which exceeds the limits of current clinical data archiving systems, and creates a heavy burden for remote consultation and diagnosis. Therefore, development of efficient image compression technique is often required to process such large amounts of data.

L. Fang · S. Li (✉)
College of Electrical and Information Engineering, Hunan University, Changsha, China
e-mail: shutao_li@hnu.edu.cn

X. Chen et al. (eds.), *Retinal Optical Coherence Tomography Image Analysis*,
Biological and Medical Physics, Biomedical Engineering,
https://doi.org/10.1007/978-981-13-1825-2_4

Denoising, interpolation and compression are well-known reconstruction problems in the image processing field [6]. During the past decades, various models have been proposed to reconstruct high quality OCT images for many applications [3, 4, 7–14]. Classical reconstruction methods often design a smoothness priori based model (e.g., anisotropic filtering, Tikhonov filtering [15], and total variation [7]), and reconstruct the image in spatial domain. Some recent approaches transform the input image into another domain (e.g., using the discrete cosine transform (DCT) [16], wavelet transformation [17], and curvelet transformation [18]). Although the transform based methods can provide a better reconstruction performance compared with the spatial domain methods, the transform based methods (e.g. DCT and wavelet) are often built on a fixed mathematical model and may have limited adaptability [19] for representing structures in ocular OCT volumes.

Recently, motivated by the sparse coding mechanism of mammalian vision system [20], the sparse representation theory has been demonstrated to be a very powerful tool for numerous image processing applications [2, 5, 21–24]. The sparse representation can decompose the input image as a linear combination of basis functions (also called as the atoms) selected from the dictionary. The dictionary atoms can be trained from a number of sampled images similar to the input image [25], and so can be more adaptive for representing the input image. Several very recent works have also applied the sparse representation to OCT image reconstruction problems [2, 5, 9, 11–13, 26, 27]. Unlike the 2-D natural image, the 3-D OCT image has more complex spatial-temporal structures. For example, the 3-D OCT image has many types and scales of pathology structures (e.g., different layers and drusen) in the spatial domain, while still has high correlations in the temporal domain. Therefore, according to the special structures of 3-D OCT image, this chapter will introduce three sparse representation models and apply them to the OCT image denoising, interpolation and compression.

The rest of this chapter is organized as follows. Section 4.2 briefly reviews the traditional sparse reconstruction model and how to utilize it for the reconstruction problems. Considering the OCT image structures, we introduce three our proposed sparsity based methods and apply them for the OCT image denoising, interpolation and compression problems in Sect. 4.3. Section 4.4 concludes this chapter.

4.2 Sparse Representation for Image Reconstruction

Given an input 2-D image of size $N \times M$, most sparse representation methods first divide this image into Υ overlapping (for image denoising and interpolation [28, 29]) or non-overlapping (for image compression [30–32]) patches $\mathbf{X}_i \in \mathbb{R}^{n \times m}$, $i = 1, 2 \ldots, \Upsilon$, $n < N$ and $m < M$. Here, i represents a particular patch corresponding to the lateral and axial position of its center in a 2D image. The vector form of each patch $\mathbf{X}_i$ is represented as $\mathbf{x}_i \in \mathbb{R}^{q \times 1} (q = n \times m)$, obtained by lexicographic ordering. The sparse representation can represent the input patch $\mathbf{x}_i$ as a linear combination of a few atoms selected from a dictionary ($\mathbf{D} \in \mathbb{R}^{q \times z}$, $q < z$), as follows

$$\mathbf{x}_i = \mathbf{D}\boldsymbol{\alpha}_i \tag{4.1}$$

where the $\boldsymbol{\alpha}_i \in \mathbb{R}^{z\times 1}$ is the sparse coefficient vector for the patch $\mathbf{x}_i$ and the dictionary $\mathbf{D}$ consists of z atoms $\{\mathbf{d}_j\}_{j=1}^{z}$.

For a denoising problem, the sparse model assumes that the clean OCT image patch can be well decomposed on a few atoms selected from the dictionary, whereas the noise cannot be represented by the dictionary. Therefore, the sparsity based denoising model can be formulated as follows [28]

$$\hat{\boldsymbol{\alpha}}_i = \arg\min_{\boldsymbol{\alpha}_i} \|\boldsymbol{\alpha}_i\|_0 \text{ subject to} \|\mathbf{x}_i - \mathbf{D}\boldsymbol{\alpha}_i\|_2^2 \leq \varepsilon, \tag{4.2}$$

where $\|\boldsymbol{\alpha}_i\|_0$ is the ℓ_0-norm counting the number of non-zero coefficients in $\boldsymbol{\alpha}_i$ and $\varepsilon = q(C\sigma)$ is the error tolerance. C is a constant, and σ is the standard deviation of noise in the input patch $\mathbf{x}_i$, which can be estimated by the approach in [33]. The problem (4.2) can be rewritten by considering the sparsity level constraint,

$$\hat{\boldsymbol{\alpha}}_i = \arg\min_{\boldsymbol{\alpha}_i} \|\mathbf{x}_i - \mathbf{D}\boldsymbol{\alpha}_i\|_2^2 \text{ subject to } \|\boldsymbol{\alpha}_i\|_0 \leq T, \tag{4.3}$$

where T is the sparsity level, representing the maximum number of non-zero coefficients in $\boldsymbol{\alpha}_i$. In both (4.2) and (4.3), two fundamental problems need to be addressed: (1) design the dictionary $\mathbf{D}$ to best represent the patch $\mathbf{x}_i$ and (2) obtain the sparse coefficient $\boldsymbol{\alpha}_i$. For the first problem, machine learning based methods (e.g., K-SVD [25] and recursive least squares dictionary learning algorithm [32]) are popularly utilized to learn the dictionary $\mathbf{D}$ from a large number of training samples similar to the test image. For the second problem, the greedy pursuit (e.g., orthogonal matching pursuit (OMP) [34]) can be used to obtain an approximate solution. After obtaining the dictionary $\mathbf{D}$ and sparse coefficient $\hat{\boldsymbol{\alpha}}_i$ of each patch, we can use $\mathbf{D}\hat{\boldsymbol{\alpha}}_i$ to reconstruct the related patch and all the reconstructed patches are returned to their original positions to generate the denoised image.

For the interpolation problem, we first denote an original high resolution image as $\mathbf{Y}_H \in \mathbb{R}^{N\times M}$, the decimation operator as $\mathbf{S}$, and the corresponding low resolution image as $\mathbf{Y}_L = \mathbf{S}\mathbf{Y}_H \in \mathbb{R}^{(N/S)\times(M/S)}$. Given the observed low resolution image $\mathbf{Y}_L$, the objective of the image interpolation is to obtain the estimated high resolution $\hat{\mathbf{Y}}_H$, such that $\hat{\mathbf{Y}}_H \approx \mathbf{Y}_H$. In [29], Yang et al., extended the above sparse model to interpolation problem by jointly learning two dictionaries $\mathbf{D}_L$ and $\mathbf{D}_H$ in the low resolution feature space χ_L and high resolution feature space χ_H. This method assumes that the sparse coefficient of low resolution image patch $\mathbf{x}_L \in \chi_L$ on $\mathbf{D}_L$ is the same as that of the high resolution image patch $\mathbf{x}_H \in \chi_H$ with respect to $\mathbf{D}_H$. Therefore, given the observed $\mathbf{x}_L$, we can seek its sparse coefficient and reconstruct the high resolution image patch $\hat{\mathbf{x}}_H$ as well as the corresponding image $\hat{\mathbf{Y}}_H$ with $\mathbf{D}_H$.

For the compression problem, we firstly subtract the mean of each image patch $\mathbf{X}_i$ and denote the patch as $\mathbf{X}_i^s$. Then, we solve the (4.2) or (4.3) to obtain the sparse coefficient $\boldsymbol{\alpha}_i^s$ of each image patch $\mathbf{X}_i^s$. The obtained $\boldsymbol{\alpha}_i^s$ is very sparse which means that only a very small number of non-zero coefficients exist in $\boldsymbol{\alpha}_i^s$. Then, the com-

pression of patch $\mathbf{x}_i$ can be achieved by storing the positions and values of non-zero coefficients in $\boldsymbol{\alpha}_i^s$ and the mean value of $\mathbf{x}_i$.

4.3 Sparsity Based Methods for the OCT Image Reconstruction

4.3.1 Multiscale Sparsity Based Tomographic Denoising (MSBTD)

4.3.1.1 Multiscale Structural Dictionary

As described in Sect. 4.2, a fundamental problem for the sparsity based denoising model is the selection of the dictionary $\mathbf{D}$. The popular sparsity based denoising algorithms usually use the noisy image itself to train the dictionary (denoted as $\mathbf{D}^{Noise}$) [28]. Though these kinds of methods can provide promising results for natural images, the high level of noise in OCT images will negatively interfere with the training process, degrade the quality of the trained dictionary, and subsequently lead to a suboptimal denoising result. An ideal approach is to train the dictionary from the noiseless image. Since in practice, such an ideal OCT image is not available, we create a less noisy image $\mathbf{Y}^{Ave}$, obtained from registering and averaging a sequence of (e.g., T) repeated B-scans from a unique position (see Fig. 4.1). Compared with the $\mathbf{D}^{Noise}$, the dictionary trained on this averaged image, $\mathbf{D}^{Ave}$, is less affected by noise.

To compare the above two dictionary training strategy, we use the popular K-SVD training algorithm [25] and the proposed MSBTD algorithm described in the following subsection for the dictionary training. Figure 4.2 shows examples of the dictionaries trained by the K-SVD algorithm on a low-SNR B-scan (see Fig. 4.3a) and MSBTD algorithm on an averaged high-SNR image (see Fig. 4.3b, c), respectively. As can be observed, compared with the $\mathbf{D}^{Ave}$, the $\mathbf{D}^{Noise}$ is more affected by noise in the OCT image. Therefore, unlike the work in [28], the proposed MSBTD algorithm denoises each low-SNR image utilizing a dictionary learned from a nearby (or even distant) averaged image. This learning strategy can reduce the noise disturbance in the dictionary learning process, and thus is expected to enhance the denoising result, without significantly increasing the image acquisition time.

On the other hand, the popular learning algorithms (e.g., K-SVD [28] and its variants [19]) often learn a universal dictionary $\mathbf{D}$ on a large number of training patches. Such a universal dictionary might be neither optimal nor efficient to represent different kinds of structures in the retinal OCT images. Therefore, the proposed MSBTD algorithm learns a set of subdictionaries $\left\{\mathbf{D}_k^{Str} \in \mathbb{R}^{Q\times Q}\right\}$, $k = 1, 2, \ldots, \mathrm{K}$, each best fit a particular structure [35, 36]. This is achieved by first clustering the training patches into K structural clusters using the k-means approach. The centroid of each cluster ($\mathbf{c}_k \in \mathbb{R}^Q$) will be used in a later dictionary selection step. Then, the

principle component analysis (PCA) algorithm is utilized to train a subdictionary from each of the K clusters.

To effectively exploit the properties of different structures and textures on ocular OCT images (e.g. each retinal layer has a different thickness and various kinds of pathology), different scales information should be considered in the dictionary training process. To achieve this, a multiscale strategy is incorporated into the above structural learning process. Specifically, the training image is first zoomed in and out via upsampling and downsampling processes. Then, the original and these magnified images are divided into same sized patches. In this way, although the patch size is fixed, patches from different magnified scales can be considered as variable sized patches from a particular scale. Next, the structural learning process is applied on the patches from the same scale (s) to create the multiscale structural dictionary, which is the concatenation of the subdictionaries ($\left\{\mathbf{D}_{k,s}^{Mstr}\right\}$, $s = 1, 2, \ldots, \mathrm{S}$) from all scales. A schematic representation of the multiscale structural dictionary learning process is illustrated in Fig. 4.3. The upsampling and downsampling processes are implemented by the bilinear interpolation.

4.3.1.2 Nonlocal Denoising Process

This subsection introduces how to utilize the learned dictionary for denoising OCT images. For each patch $\mathbf{x}_i$, we find an appropriate subdictionary $\mathbf{D}_i^A$ from the learned

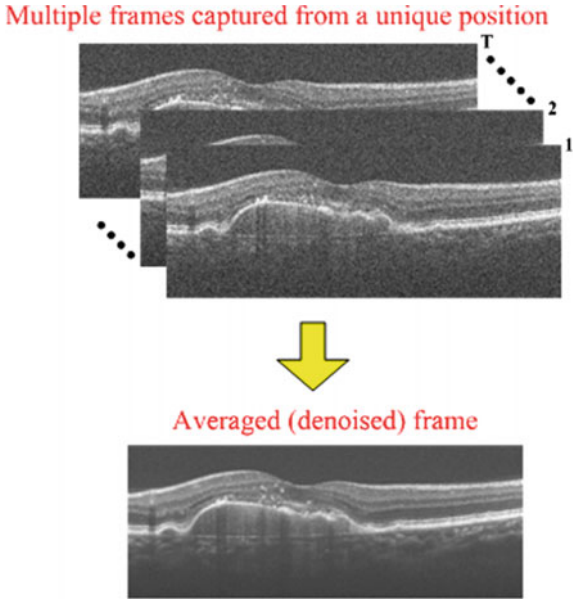

Fig. 4.1 Creation of a less noisy (averaged) frame by an average operation on the multiple frames captured form a unique position

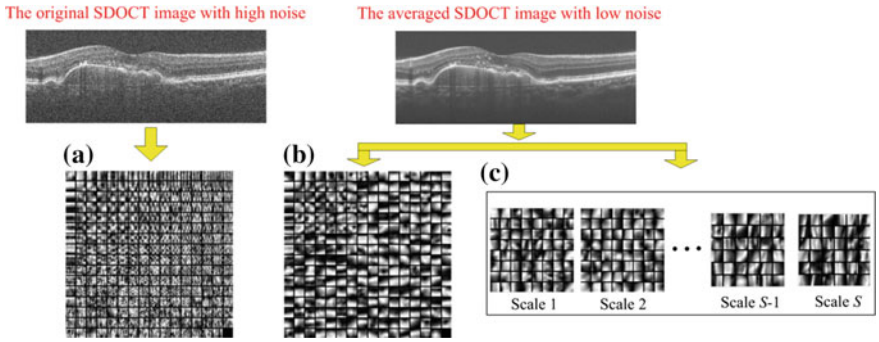

Fig. 4.2 Dictionaries trained on **a** the original low-SNR OCT image by the K-SVD algorithm, **b** averaged high-SNR image by the K-SVD algorithm, and **c** averaged high-SNR image by the proposed MSBTD training algorithm (due to the limited space, only the first atom of each learned subdictionary is shown)

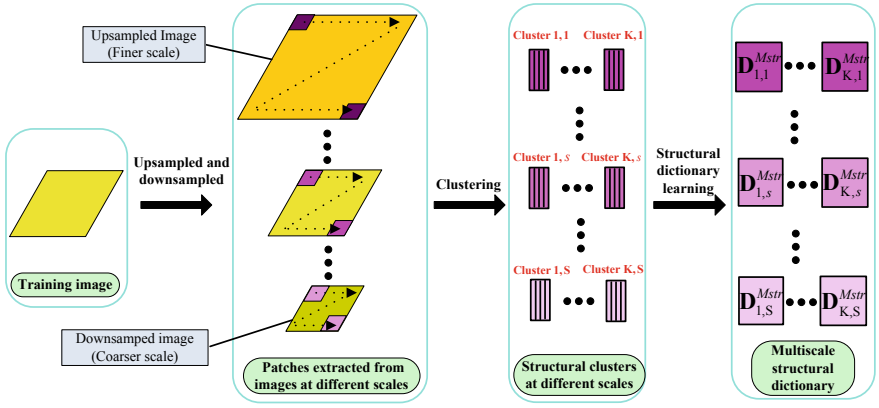

Fig. 4.3 Algorithmic flowchart of multiscale structural dictionary learning process

multiscale structural dictionary to sparsely represent the patch, which achieves denoising of that patch. The denoising steps are detailed as follows.

To seek the best subdictionary among the learned subdictionaries for each noisy patch, the representative features of the patch $\mathbf{x}_i$ is compared with each subdictionary. To represent each subdictionary, we use the centroid atom ($\mathbf{c}_{k,s} \in \mathbb{R}^{(w \cdot z) \times 1}$) of the corresponding k-means cluster (noted in the above Section) [36]. For the representative feature of each patch, its high-frequency component (denoted by $\mathbf{x}_i^{Hf}$) is used. We find the best fitted subdictionary $\mathbf{D}_i^A$ for the patch $\mathbf{x}_i$ based on the normalized correlation [21] between $\mathbf{c}_{k,s}$ and $\mathbf{x}_i^{Hf}$:

$$A = (k_i, s_i) = \arg\max_{k,s} \left| \left\langle \mathbf{c}_{k,s}, \mathbf{x}_i^{Hf} \right\rangle \right|. \tag{4.4}$$

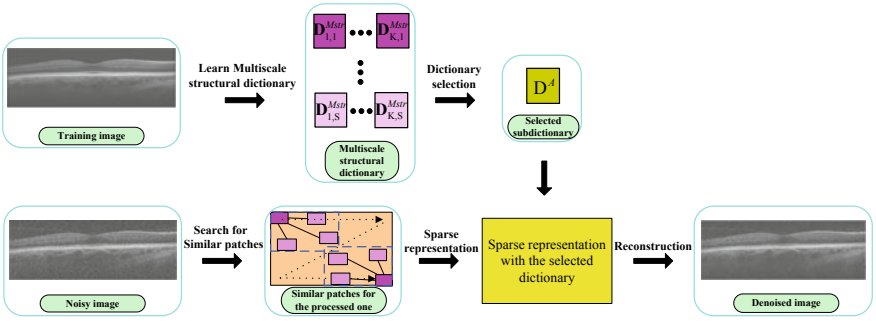

Fig. 4.4 The outline of the MSBTD algorithm

After finding the best representative subdictionary, as in work [37], we define the objective function for the sparse representation of the noisy patch as follows:

$$(\hat{\boldsymbol{\alpha}}_i, \hat{\boldsymbol{\beta}}_i) = \arg\min_{\boldsymbol{\alpha}_i, \boldsymbol{\beta}_i} \left\{ \left\| \mathbf{x}_i - \mathbf{D}_i^A \boldsymbol{\alpha}_i \right\|_2^2 + \lambda_1 \|\boldsymbol{\alpha}_i\|_0 + \lambda_2 \left\| \boldsymbol{\alpha}_i - \boldsymbol{\beta}_i \right\|_0 \right\}, \tag{4.5}$$

where λ_1 and λ_2 are scalar Lagrange multipliers and $\boldsymbol{\alpha}_i$ is a sparse coefficient of the patch $\mathbf{x}_i$. $\boldsymbol{\beta}_i$ represents the sparse coefficient of a noiseless patch. The term $\|\boldsymbol{\alpha}_i\|_0$ can utilize the sparsity in a local patch, while the term $\left\|\boldsymbol{\alpha}_i - \boldsymbol{\beta}_i\right\|_0$ (via $\boldsymbol{\beta}_i$) attempts to exploit the non-local similarities in the images [38]. Since there is no noiseless patch available, we adopt the average patch as the noiseless patch. The average patch is computed by the average of J patches with the highest similarity to the processed patch $\mathbf{x}_i$ searched within a window. The problem (4.5) can be solved by an iterative reweighted algorithm [37]. After obtaining the sparse coefficient $\hat{\boldsymbol{\alpha}}_i$, we can compute the related denoised patch and the reconstructed image with the dictionary $\mathbf{D}_i^A$. The outline of the whole denoising process is illustrated in Fig. 4.4.

4.3.1.3 Experimental Results

To verify the effectiveness of the proposed MSBTD method, its performance is compared with that of four denoising approaches: Tikhonov [15], New SURE [39], K-SVD [28], and BM3D [40]. In these experiments, the parameters of the proposed MSBTD method are empirically selected and kept unchanged. Since most structures in the SDOCT image lie on the horizontal direction, the patch and the search window sizes are selected to be rectangle of size 3×20 and 40×60 pixels, respectively. The number J of similar patches in each searching window is set to 20, while the cluster number K is set to 70 in the k-means clustering. Before the multiscale learning process, the original image is upsampled two times, each by a factor 1.25 and downsampled three times, each by a factor of 1.5625 to create the training images of six scales. The parameters of the iterative reweighted algorithm for solving the problem (4.5) are set to the default values in [37]. The parameters of the Tikhonov method [15] are tuned to achieve its best results, while the parameters of the New

SURE, K-SVD, and BM3D methods are chosen to the default values as in [28, 39, 40].

All the methods are tested on datasets from 17 eyes from 17 subjects with and without non-neovascular age-related macular degeneration (AMD) enrolled in the A2A SDOCT study. Ten datasets are selected from normal subjects while the remaining datasets are from AMD subjects. All the datasets are acquired using the SDOCT imaging systems from Bioptigen, Inc. (Research Triangle Park, NC). For each patient, two kinds of SDOCT scans were acquired. (1) A square (~6.6 $\times$ 6.6 mm) volume scan with 1000 A-scans and 100 B-scans, including the fovea. (2) An azimuthally repeated scan with 1000 A-Scans and 40 B-Scans targeted at the fovea. Each A-scan is cropped to achieve B-Scans of size 280 $\times$ 1000, which only includes the informative areas (excluding the smooth dark areas deep below the choroid or in the vitreous). For the repeated 40 B-scans, the ImageJ (software; National Institutes of Health, Bethesda, Maryland, USA) StackReg Registration plug-in [41] is firstly used for the registration and then the registered B-scans are averaged to create the corresponding noiseless B-scan.

The mean-to-standard-deviation ratio (MSR) [42], contrast-to-noise ratio (CNR) [43], and peak signal-to-noise-ratio (PSNR) are adopted as the quantitative metrics to evaluate the performance of different denoising methods. The MSR and CNR are computed as,

$$\mathrm{MSR} = \frac{\mu_f}{\sigma_f}, \tag{4.6}$$

$$\mathrm{CNR} = \frac{|\mu_f - \mu_b|}{\sqrt{0.5(\sigma_f^2 + \sigma_b^2)}}, \tag{4.7}$$

where μ_b and σ_b are the mean and the standard deviation of the background region (e.g. red box #1 in Fig. 4.5), while μ_f and σ_f are the mean and the standard deviation of the foreground regions (e.g. red box #2–6 in Fig. 4.5). The PSNR is global metric, which is computed as,

$$\mathrm{PSNR} = 20 \cdot \log_{10}\left(\frac{\mathrm{Max}_{\mathbf{R}}}{\sqrt{\frac{1}{H}\sum_{h=1}^{H}\left(\mathbf{R}_h - \hat{\mathbf{R}}_h\right)^2}}\right), \tag{4.8}$$

where $\mathbf{R}_h$ is the hth pixel in the reference noiseless image $\mathbf{R}$, $\hat{\mathbf{R}}_h$ represents the hth pixel of the denoised image $\hat{\mathbf{R}}$, H is the total number of pixels, and $\mathrm{Max}_{\mathbf{R}}$ is the maximum intensity value of $\mathbf{R}$. Since there is no ideal "noiseless" image available, the averaged foveal image is used as a noiseless approximation to the corresponding foveal B-scan from the noisy volumetric scan.

Figure 4.5 shows two raw SDOCT retinal images (from a normal and an AMD subject) and their visually denoised results obtained from various denoising methods. Since the boundaries between retinal layers contain important pathologic information

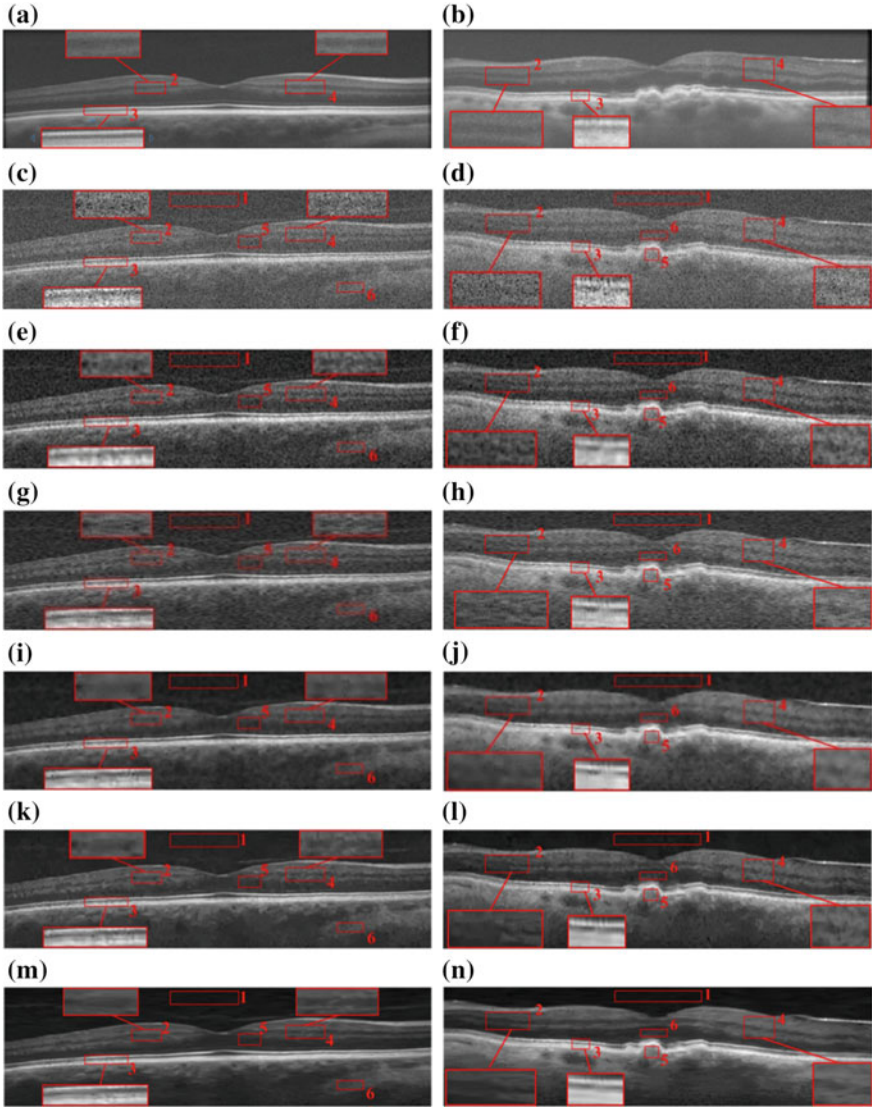

Fig. 4.5 Denoising results for two test SDOCT retinal images using the Tikhonov [15], New SURE [39], K-SVD [28], BM3D [40] and the proposed MSBTD method. The left and right columns show the foveal images from a normal subject and an AMD patient, respectively. **a**, **b** The averaged (high-SNR) images for the multiscale structural dictionary training. **c**, **d** Low-SNR noisy foveal images from the volumetric scans. **e**, **f** Denoising results using the Tikhonov method. **g**, **h** Denoising results using the New SURE method. **i**, **j** Denoising results using the K-SVD method. **k**, **l** Denoising results using the BM3D method. **m**, **n** Denoising results using the MSBTD method

Table 4.1 Mean and standard deviation of the MSR and CNR results for seventeen SDOCT retinal images using the Tikhonov [15], New SURE [39], K-SVD [28], BM3D [40] and the proposed MSBTD method

	Original	Tikhonov [15]	New SURE [39]	K-SVD [28]	BM3D [40]	MSBTD
Mean (CNR)	1.27	3.13	2.49	4.11	3.89	**4.76**
Standard deviation (CNR)	0.43	0.94	0.60	1.23	1.05	1.54
Mean (MSR)	3.20	7.62	6.74	11.22	11.52	**14.76**
Standard deviation (MSR)	0.46	0.95	1.69	2.77	2.42	4.75

The best results in the table are labeled in bold

Table 4.2 Mean and standard deviation of the PSNR (dB) for seventeen SDOCT foveal images obtained from the Tikhonov [15], New SURE [39], K-SVD [28], BM3D [40], and the proposed MSBTD method

	Tikhonov [15]	New SURE [39]	K-SVD [28]	BM3D [40]	MSBTD
Mean (PSNR)	23.67	23.46	26.13	26.04	**26.46**
Standard deviation (PSNR)	0.96	1.40	1.70	1.65	1.72

The best result the table is labeled in bold

[44], three boundary regions (boxes #2, 3, 4) in these images are marked with red rectangle and magnified. As can be seen, the Tikhonov and New SURE methods show limited noise suppression for the test images. Though the K-SVD method can better remove the noise, it introduces over-smoothing, thus leading to significant loss of image details. The BM3D method can achieve improved noise suppression and limit the over-smoothing problem to some extent, but creating obvious artifacts. By contrast, application of the proposed MSBTD method results in noticeably improved noise suppression, while preserving details compared to other methods. Especially, note in the layer boundary preservation in the area magnified by the red boxes (e.g. #2 and #4).

To quantitatively compare these methods, the MSR and CNR are computed on six regions of interest (similar to the red boxes #1–6 in Fig. 4.5) from 17 test images of different (randomly selected) subjects. For each image, the averaged the MSR and CNR values for the five foreground regions (e.g. red box #2–6 in Fig. 4.5) is computed. We report the mean and standard deviation of these averaged MSR and CNR results across all the test images in Table 4.1.

Next, we compared the PSNR of all the test methods on the seventeen subjects. The mean and standard deviation of the PSNR results are reported in Table 4.2. Similar

to the case of MSR and CNR in Table 4.1, we observe that the MSBTD method also delivers the best results in the PSNR. Furthermore, we note that although the PSNR of the K-SVD is close to that of the MSBTD method, two clinical experts preferred the visual outcome of the MSBTD method, as illustrated in Fig. 4.6.

4.3.2 Sparsity Based Simultaneous Denoising and Interpolation (SBSDI)

As described in the Sect. 4.2, Yang et al., introduced a sparsity based interpolation method for the nature images [29]. However, unlike the natural images, the real obtained low resolution OCT image is interfered by very high levels of noise. In this subsection, we introduce a novel SBSDI method, which can simultaneously denoise and interpolate OCT images.

4.3.2.1 Low-Resolution-Low-SNR and High-Resolution-High-SNR Dictionary Pair and Mapping Training

Inspired by the machine learning based approaches [29, 45, 46], the objective of the proposed SBSDI method is to obtain the relationship between two feature spaces: low-resolution-low-SNR (LL) space $\chi_{L,L}$ and ideal high-resolution-high-SNR (HH) space $\chi_{H,H}$ from a large number of training samples. After the relationship is obtained, we can reconstruct the ideal HH image $\mathbf{Y}_{H,H} \in \chi_{H,H}$ using the observed LL image $\mathbf{Y}_{L,L} \in \chi_{L,L}$.

Dictionary and Mapping Training

To create HH images as the ideal training datasets, we first adopt a customized scanning pattern to acquire a number of repeated densely sampled B-scans from nearly the same position. Then, we register and average all these images to obtain the ideal HH image [47]. In the densely acquired B-scans, we randomly select a single noisy yet still high resolution frame and downsample this noisy frame to create the related LL image. The process for generating the HH and LL training images is illustrated in Fig. 4.7.

We link the LL and HH spaces by establishing a relationship between their related dictionary atoms and sparse coefficients. Instead of enforcing the equality restriction on the sparse coefficients [29], we require the dictionaries (denoted as $\mathbf{D}_{L,L}$ and $\mathbf{D}_{H,H}$) for the two feature spaces to be strictly matched. That is, the selected dictionary atoms for reconstructing the LL image strictly correspond to the counterpart atoms for recovering the HH image. To meet this, we can directly extract a large number of spatially matched LL and HH patches from training image pairs (Fig. 4.8). However, sparse coding over the dictionary with large number of samples will create very high computational cost. To achieve a more compact representation, we can train the dictionary pair on a large number of extracted training patches

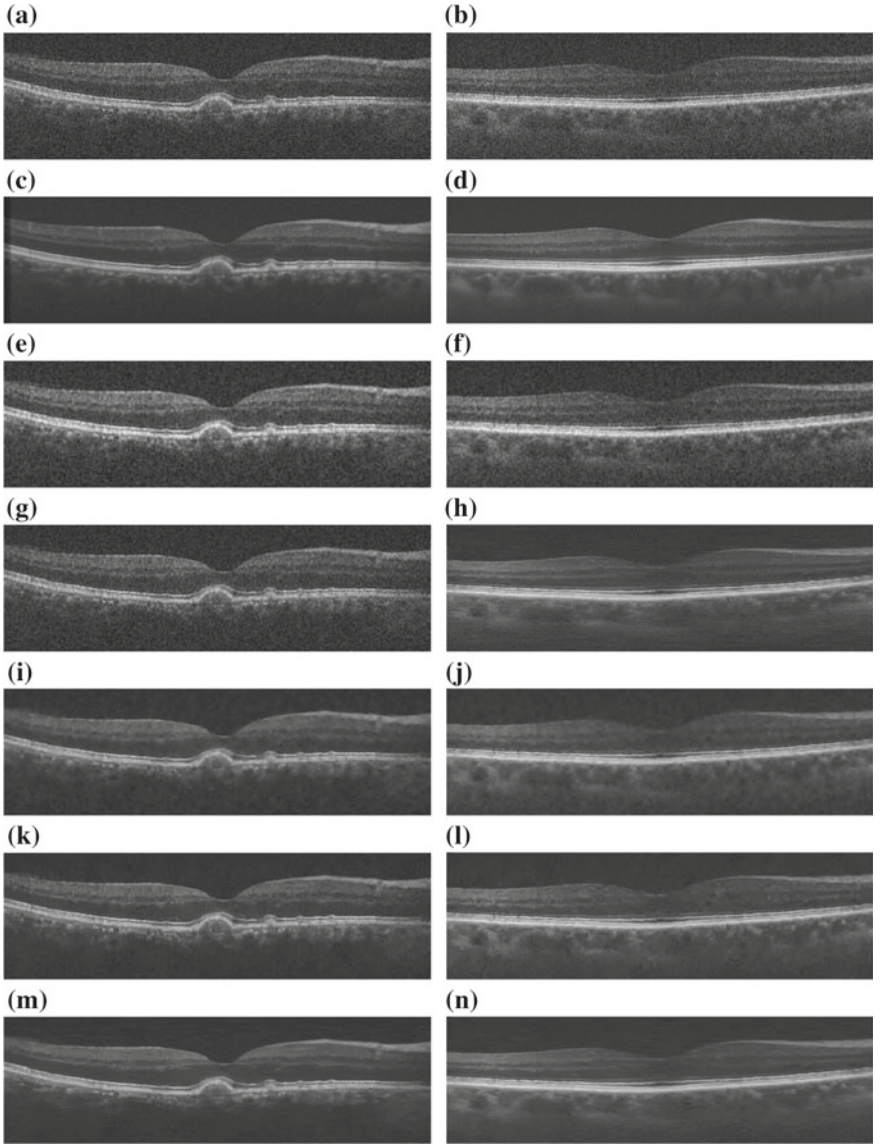

Fig. 4.6 Visual comparison of denoising results from the Tikhonov [15], New SURE [39], K-SVD [28], BM3D [40] and the proposed MSBTD method on two SDOCT test images. **a**, **b** Test SDOCT images. **c**, **d** Averaged images. **e**, **f** Denoising results using the Tikhonov method (Left: PSNR = 22.67, Right: PSNR = 24.01). **g**, **h** Denoising results using the New SURE method (Left: PSNR = 25.39, Right: PSNR = 25.35). **i**, **j** Denoising results using the K-SVD method (Left: PSNR = 27.98, Right: PSNR = 25.81). **k**, **l** Denoising results using the BM3D method (Left: PSNR = 27.72, Right: PSNR = 25.69). **m**, **n** Denoising results using the MSBTD method (Left: PSNR = 28.19, Right: PSNR = 26.06)

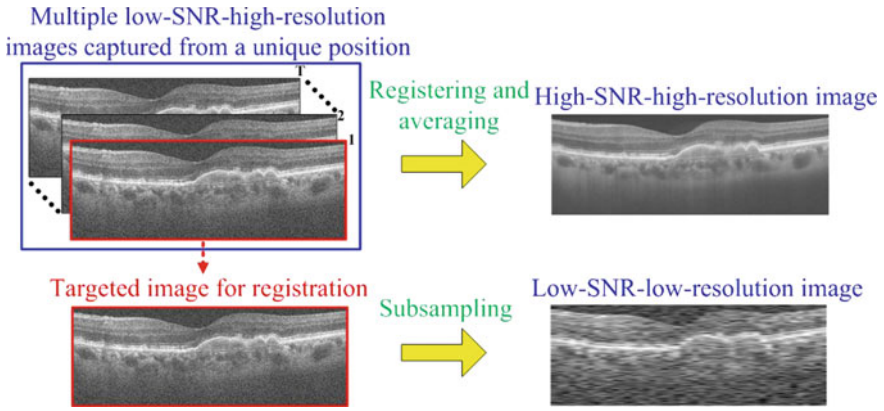

Fig. 4.7 Process for generating the HH and LL training images

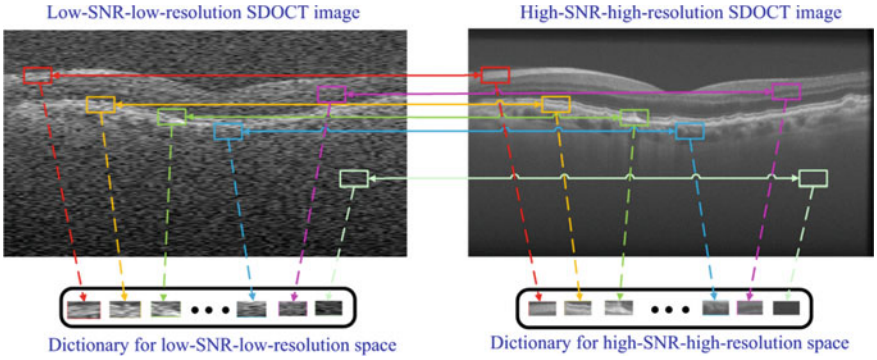

Fig. 4.8 Selection of patches from the LL and HH images to construct their corresponding dictionaries

[25]. Then, we make the learned dictionary pair matched. In the dictionary learning stage, the positions of the nonzero sparse coefficients determine the selected training patches to update the atom [25]. Therefore, if the positions of non-zero coefficients in $\left\{\boldsymbol{\alpha}_{L,L}^{i}\right\}_{i=1}^{Z}$ are the same as that in $\left\{\boldsymbol{\alpha}_{H,H}^{i}\right\}_{i=1}^{Z}$, the dictionary atoms in $\mathbf{D}_{L,L}$ and $\mathbf{D}_{H,H}$ will be updated with the spatially matched patch pairs [25] and thus $\mathbf{D}_{L,L}$ will still match with $\mathbf{D}_{H,H}$ in the learning process. Based on this, we modify the original OMP algorithm [34], and propose a coupled OMP (COMP) algorithm to pursuit the position matched coefficients $\left\{\boldsymbol{\alpha}_{H,H}^{i}\right\}_{i=1}^{Z}$ and $\left\{\boldsymbol{\alpha}_{L,L}^{i}\right\}_{i=1}^{Z}$. Since $\mathbf{D}_{H,H}$ is unknown in the image reconstruction phase, during the atom selection process, positions of the selected atoms in $\mathbf{D}_{H,H}$ should be the same as that of the chosen atoms in $\mathbf{D}_{L,L}$. To achieve this, we first employ the original OMP algorithm to seek the coefficient $\boldsymbol{\alpha}_{L,L}^{i}$ of $\mathbf{x}_{L,L}^{i}$ and preserve the index set of the selected atoms $\mathbf{G}$. Then, we compute $\boldsymbol{\alpha}_{H,H}^{i}$ with the atoms set $\mathbf{G}$

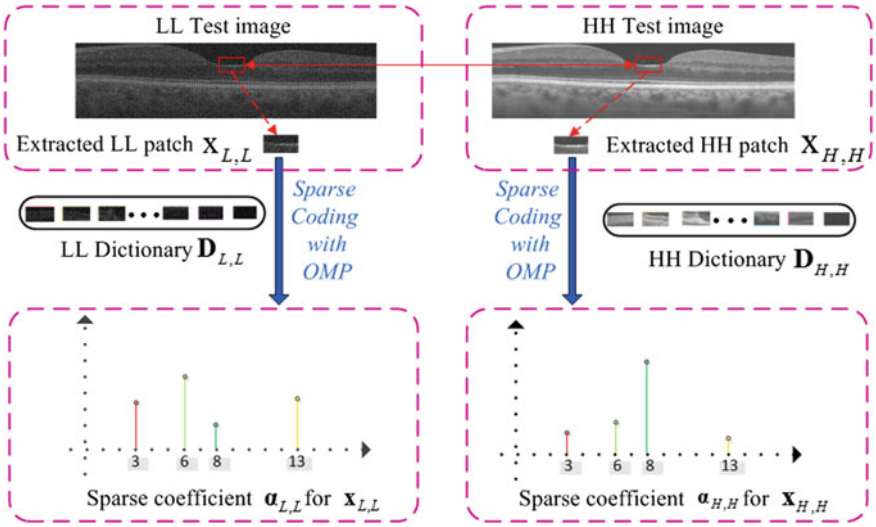

Fig. 4.9 Sparse coefficients $\boldsymbol{\alpha}_{L,L}$ and $\boldsymbol{\alpha}_{H,H}$ obtained by the decomposition of LL patch $\mathbf{x}_{L,L}$ and HH patch $\mathbf{x}_{H,H}$ over dictionaries $\mathbf{D}_{L,L}$ and $\mathbf{D}_{H,H}$ with the OMP algorithm

$$\boldsymbol{\alpha}^i_{H,H} = \left(\mathbf{D}^T_{\mathbf{G}}\mathbf{D}_{\mathbf{G}}\right)^{-1}\mathbf{D}^T_{\mathbf{G}}\mathbf{x}^i_{H,H}. \tag{4.9}$$

After the $\left\{\boldsymbol{\alpha}^i_{L,L}\right\}_{i=1}^{Z}$ and $\left\{\boldsymbol{\alpha}^i_{H,H}\right\}_{i=1}^{Z}$ are obtained, we learn the dictionary pair $\mathbf{D}_{L,L}$ and $\mathbf{D}_{H,H}$ with the quadratically constrained quadratic programming (QCQP) [48] algorithm.

After the above dictionary training step, the positions of the non-zero coefficients in both $\boldsymbol{\alpha}^i_{L,L}$ and $\boldsymbol{\alpha}^i_{H,H}$ are the same. However, the non-zero values in $\boldsymbol{\alpha}^i_{L,L}$ and $\boldsymbol{\alpha}^i_{H,H}$ might be different, as illustrated in Fig. 4.9. Therefore, we find a mapping function ($\mathbf{M}$) which relates sparse coefficients in the LL space to the sparse coefficients in the HH space:

$$\boldsymbol{\alpha}^i_{H,H} = \mathbf{M}^i_{L,L}. \tag{4.10}$$

As in [49], we train this mapping matrix using the sparse coefficients $\left\{\boldsymbol{\alpha}^i_{H,H}\right\}_{i=1}^{Z}$ and $\left\{\boldsymbol{\alpha}^i_{L,L}\right\}_{i=1}^{Z}$ from the dictionary learning stage,

$$\hat{\mathbf{M}} = \arg\min_{\mathbf{M}} \left\| \left\{\boldsymbol{\alpha}^i_{H,H}\right\}_{i=1}^{Z} - \mathbf{M}\left\{\boldsymbol{\alpha}^i_{L,L}\right\}_{i=1}^{Z} \right\|_F^2 + \beta\|\mathbf{M}\|_F^2, \tag{4.11}$$

where β is a regularization parameter to balance the terms in the objective function. Since (4.11) is a ridge regression problem, it can be solved as,

$$\mathbf{M} = \left(\left\{\boldsymbol{\alpha}_{H,H}^{i}\right\}_{i=1}^{Z}\right)\left(\left\{\boldsymbol{\alpha}_{L,L}^{i}\right\}_{i=1}^{Z}\right)^{T}\left(\left(\left\{\boldsymbol{\alpha}_{L,L}^{i}\right\}_{i=1}^{Z}\right)\left(\left\{\boldsymbol{\alpha}_{L,L}^{i}\right\}_{i=1}^{Z}\right)^{T} + \beta \cdot \mathbf{I}\right)^{-1}, \quad (4.12)$$

where $\mathbf{I}$ is an identity matrix.

We incorporate the structural clustering strategy into the dictionary pair and mapping training process. Specifically, we first adopt the K-means approach to cluster the training patches $\left\{\mathbf{x}_{L,L}^{i}\right\}_{i=1}^{R}$ and $\left\{\mathbf{x}_{H,H}^{i}\right\}_{i=1}^{R}$ into $(f+v)$ structural clusters. Then, in each cluster $s = 1, \ldots, (f+v)$, we learn one pair of compact LL and HH dictionaries $\mathbf{D}_{L,L}^{s}$, and $\mathbf{D}_{H,H}^{s}$ as well as the corresponding mapping function $\mathbf{M}^{s}$ with the above learning method. In addition, one centroid atom $\mathbf{c}_s$ can be computed to represent each cluster.

4.3.2.2 Image Reconstruction

In the image reconstruction stage, for each test LL patch $\mathbf{x}_{L,L}^{i}$, we first seek the best sub-dictionary ($\mathbf{D}_{L,L}^{A}$ and $\mathbf{D}_{H,H}^{A}$) and mapping transform ($\mathbf{M}^{A}$) based on the Euclidian distance between $\mathbf{x}_{L,L}^{i}$ and $\mathbf{c}_s$,

$$A = s_i = \arg\min_{s} \left\|\mathbf{c}_s - \mathbf{x}_{L,L}^{i}\right\|_2^2. \quad (4.13)$$

After the best sub-dictionary is found, we use the learned dictionary $\mathbf{D}_{L,L}^{A}$ to seek the sparse coefficients $\boldsymbol{\alpha}_{L,L}^{i}$ of the observed LL patches ($\mathbf{x}_{L,L}^{i}$) from

$$\hat{\boldsymbol{\alpha}}_{L,L}^{i} = \arg\min_{\boldsymbol{\alpha}_{L,L}^{i}} \left\|\boldsymbol{\alpha}_{L,L}^{i} - \mathbf{D}_{L,L}^{A}\boldsymbol{\alpha}_{L,L}\right\|_2 + \lambda\left\|\boldsymbol{\alpha}_{L,L}^{i}\right\|_0. \quad (4.14)$$

Then, we reconstruct the latent HH patch as $\mathbf{D}_{H,H}^{A}\mathbf{M}^{A}\hat{\boldsymbol{\alpha}}_{L,L}^{i}$. In this way, we can directly reconstruct the single 2-D images. Furthermore, since OCT is a 3-D image, its information from nearby slices should also be used to enhance the denoising performance. Therefore, we further propose to utilize the information of nearby slices in the reconstruction process with a joint operation. The basic assumption of the joint operation is that similar patches from nearby slices can be well decomposed on the same atoms of the selected dictionary, but with different coefficient values. The current processed patch is denoted as $\mathbf{x}_{L,L}^{i}$ while the patches from its nearby slices are denoted as $\left\{\mathbf{x}_{L,L}^{i+w}\right\}_{w=-W}^{W}$. Simultaneous decomposition of the patches $\left\{\mathbf{x}_{L,L}^{i+w}\right\}_{w=-W}^{W}$ with the joint assumption equals to the problem,

$$\begin{aligned}\left\{\hat{\boldsymbol{\alpha}}_{L,L}^{i+w}\right\}_{w=-W}^{W} &= \min_{\left\{\boldsymbol{\alpha}_{L,L}^{i+w}\right\}_{w=-W}^{W}} \sum_{w=-W}^{W} \left\|\mathbf{x}_{L,L}^{i+w} - \mathbf{D}_{L,L}^{A}\boldsymbol{\alpha}_{L,L}^{i+w}\right\|_2 \text{ subject to } \left\|\boldsymbol{\alpha}_{L,L}^{i+w}\right\|_0 \\ &\leq T, w = -W, \ldots, W, \end{aligned} \quad (4.15)$$

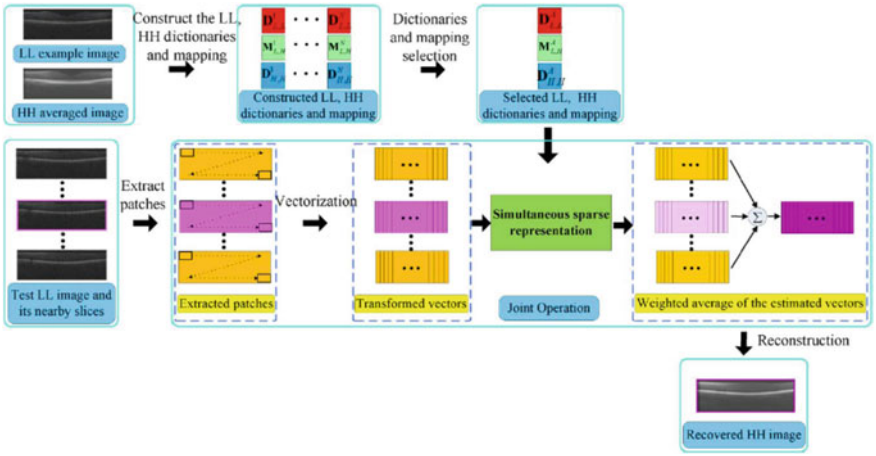

Fig. 4.10 Outline of the SBSDI framework

where T is the maximum number of nonzero coefficients in $\boldsymbol{\alpha}_{L,L}^{i+w}$, and the position of the nonzero coefficients in $\left\{\hat{\boldsymbol{\alpha}}_{L,L}^{i+w}\right\}_{w=-W}^{W}$ are the same while coefficient values become different. The SOMP algorithm [50] can be employed to efficiently solve the above problem. Then, the joint operation can reconstruct the current HH patch as: $\hat{\mathbf{x}}_{H,H}^{i} = \sum_{w=-W}^{W} b_i^w \hat{\mathbf{x}}_{H,H}^{i+w}$, where $\hat{\mathbf{x}}_{H,H}^{i+w} = \mathbf{D}_{H,H}^{A}\mathbf{M}_i^A\hat{\boldsymbol{\alpha}}_{L,L}^{i+w}$ is the estimated patch and b_i^w is the weight, computed by

$$b_i^w = \exp\left(-\left\|\mathbf{x}_{L,L}^{i+w} - \mathbf{x}_{L,L}^{i}\right\|_2^2 / h\right)/Norm. \tag{4.16}$$

$Norm$ is a normalization factor and h is a predetermined scalar. Finally, we return the estimated patches to their original positions to reconstruct the OCT image. The outline of the SBSDI framework is illustrated in Fig. 4.10.

4.3.2.3 Experimental Results

The proposed SBSDI method was tested on two kinds of retinal OCT images: (1) synthetic images created from high resolution images that were then subsampled and (2) real test images consisting of images captured at a low sampling rate. For test synthetic images, we subsampled the previously acquired high-resolution images with both random and regular patterns, thus reducing the number of A-scans in each B-scan. For real test datasets, we directly acquired low-resolution images with a regularly sampled pattern. Both the human and mouse retinal images were used in these experiments. All these studies followed the tenants of the Declaration of Helsinki.

We first tested a compressive sampling method [51] on both randomly and regularly subsampled synthetic datasets to examine the random sampling scheme advocated in [12, 13]. As can be observed in Fig. 4.11, random sampling had insignificant benefits over the conventional regularly sampling scheme for our application. Therefore, we apply the regular sampling for both the synthetic and real experimental datasets. In these experiments, we compared our proposed SBSDI method with four competing approaches: Tikhonov [15], Bicubic, BM3D [40] +Bicubic and ScSR [29]. The BM3D+Bicubic method is a combination of the state-of-the-art denoising algorithm BM3D with the bicubic interpolation approach. The ScSR method utilizes the joint dictionary learning operation to train the LL and HH dictionaries from the related LL and HH training patches, without considering the correlations from 3D nearby slices.

In these experiments, the parameters of the proposed method were empirically selected and kept unchanged for all images in both synthetic and real experimental datasets. Since most of the similar structures in SDOCT images lay along the horizontal direction, the patch size was chosen to be 4×8 and 4×16 pixel wide rectangles for 50 and 75% data missing, respectively. As the patch size becomes bigger, our algorithm will remove the noise more efficiently, but may result in stronger smoothing and the loss of image detail. We set the number of nearby slices for the joint operation to 4 (2 slices above and 2 slices below the current processed image, respectively). Slices that are far distant from the target B-scan being processed have not been added since they often have different image content. In the clustering stage, the cluster number f in the detailed group and v in the smooth group were set to 70 and 20, respectively. As the detailed group has more complex structures than the smooth group, the f number of the detailed group is larger than that of the smooth group. From each cluster, 500 vectors were selected to construct the initial structural sub-dictionary. The sparsity level T for both COMP and SOMP algorithms were set to 3. We select the iteration number J in the dictionary learning process to 10, which almost reaches convergence in our learning problem. We select the parameters β in (11) and h in (16) to 0.001, 12, and 80, respectively.

For the synthetic datasets, the low-SNR-high-resolution datasets previously utilized in the Sect. 4.3.2.3 were also used here. As described in Sect. 4.3.2.3, these datasets were acquired from 28 eyes of 28 subjects with and without non-neovascular age-related macular degeneration (AMD). For each patient, we acquired two sets of SDOCT scans. The first scan was a volume containing the retinal fovea with 1000 A-scans per B-scan and 100 B-scans per volume. The second scan was centered at the fovea with 1000 A-scans per B-scan and 40 azimuthally repeated B-Scans. We selected the central foveal B-scan within the first volume and further subsampled this scan with both random and regular patterns, to create simulated LL test images (e.g. Fig. 4.11a, c). The set of azimuthally repeated B-scans was registered using the StackReg image registration plug-in [41] for ImageJ to construct the HH averaged image (e.g. Fig. 4.11j). In the 28 datasets, 18 LL and HH pairs from 18 different datasets were randomly selected to test the performance of the proposed method, while the remaining 10 LL and HH pairs were used to train the dictionaries and the mapping functions. The constructed dictionaries and mapping functions were also

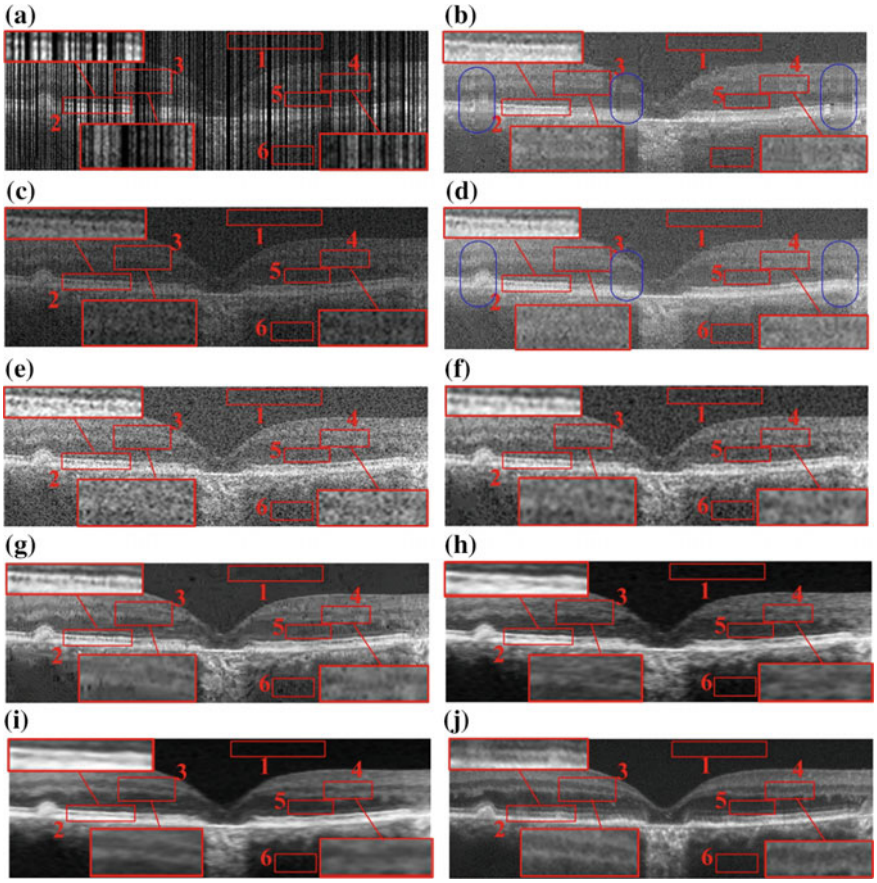

Fig. 4.11 Two types of sampling patterns and their reconstruction results by CS-recovery, Bicubic, Tikhonov, BM3D+Bicubic, ScSR, and our SBSDI method. **a** Randomly sampled image with 50% data missing. **b** Image (**a**) reconstructed by CS-recovery (PSNR = 19.46). **c** Regularly sampled image with 50% data missing. **d** Image (**c**) reconstructed by CS-recovery (PSNR = 19.01). **e** Image (**c**) reconstructed by Bicubic (PSNR = 17.77). **f** Image (**c**) reconstructed by Tikhonov [15] (PSNR = 22.23). **g** Image (**c**) reconstructed by BM3D+Bicubic (PSNR = 23.26). **h** Image (**c**) reconstructed by ScSR (PSNR = 22.11). **i** Image (**c**) reconstructed by SBSDI (PSNR = **24.56**). **j** Registered and averaged image which was acquired 80 times slower than the image in (**i**)

used for the following real experimental datasets. For the real experimental datasets, we utilized the Bioptigen SDOCT imagers to directly acquire full and subsampled volumes from 13 human subjects with a regularly sampled pattern in clinic. That is, for each subject, we scanned a square volume centered at the retinal fovea with 500 A-scans per B-scan and 100 B-scans per volume.

Figure 4.11a–d and Fig. 4.12a–d show qualitative comparisons of regularly and randomly sampled foveal images (with 50 and 75% of the original data discarded) and their reconstructed versions obtained from the CS-recovery method [52]. As can be observed, the CS-recovery results from the random sampling scheme (Figs. 4.11b

and 4.12b) have more areas exhibiting striped blurring (e.g. blue ellipse areas) than their regularly sampled counterparts (Figs. 4.11d and 4.12d). Based on this, we tested the Tikhonov [15], Bicubic, BM3D [40] +Bicubic and the proposed SBSDI method on regularly sampled images (Fig. 4.11c). For better visual comparison, we mark and magnify three boundary areas (boxes #2, 3, 4) in these images. Results from the Tikhonov, Bicubic, and ScSR methods appeared noisy with indistinct boundaries for many meaningful anatomical structures. Although the BM3D [53] +Bicubic technique delivers improved noise suppression, it introduces splotchy/blocky (cartoonish) artifacts. By contrast, application of our SBSDI method that exploits the 3D information resulted in noticeably improved noise suppression while preserving details compared to other methods. Especially in the regions marked by red boxes #3, 4, the SBSDI result even shows clearer layers compared with the densely sampled averaged image (Figs. 4.11j and 4.12j).

4.3.3 3D Adaptive Sparse Representation Based Compression (3D-ASRC)

As described in Sect. 4.2, the traditional compression method is only designed for the 2-D image. In common clinical scanning protocols, neighboring OCT slices have very similar content in many regions, as can be observed in Fig. 4.13b. On the other hand, those same nearby slices can also exhibit localized differences (see the areas labeled with the red rectangles in Fig. 4.13b). Therefore, the 3D-ASRC algorithm was proposed for the compression of 3D OCT images, which can utilize the high correlations while still considering the differences of nearby slices. The proposed 3D-ASRC method is composed of three main parts: (a) 3D adaptive sparse representation; (b) 3D adaptive encoding; (c) decoding and reconstruction, which will be described in the following subsections. The outline of the proposed 3D-ASRC algorithm is illustrated in Fig. 4.14.

4.3.3.1 3D Adaptive Sparse Representation

The volume of OCT B-scans are divided into several groups, each with T nearby slices according to the similarities among them [54] and each slice in an OCT volume is partitioned into many non-overlapping patches with the mean of each patch is subtracted from them. Meanwhile, we define nearby patches as a set of patches centered around the patch $\mathbf{x}_i^1$ from slices in the same group as $\left\{\mathbf{x}_i^t\right\}_{t=1}^T$, where t denotes a particular B-scan in that group. The i in $\left\{\mathbf{x}_i^t\right\}_{t=1}^T$ indexes the i-th nearby patch of the similar group. By rewriting Eq. (4.2), the sparse coefficient vectors $\left\{\boldsymbol{\alpha}_i^t\right\}_{t=1}^T$ of the nearby patches $\left\{\mathbf{x}_i^t\right\}_{t=1}^T$ can be obtained by optimizing:

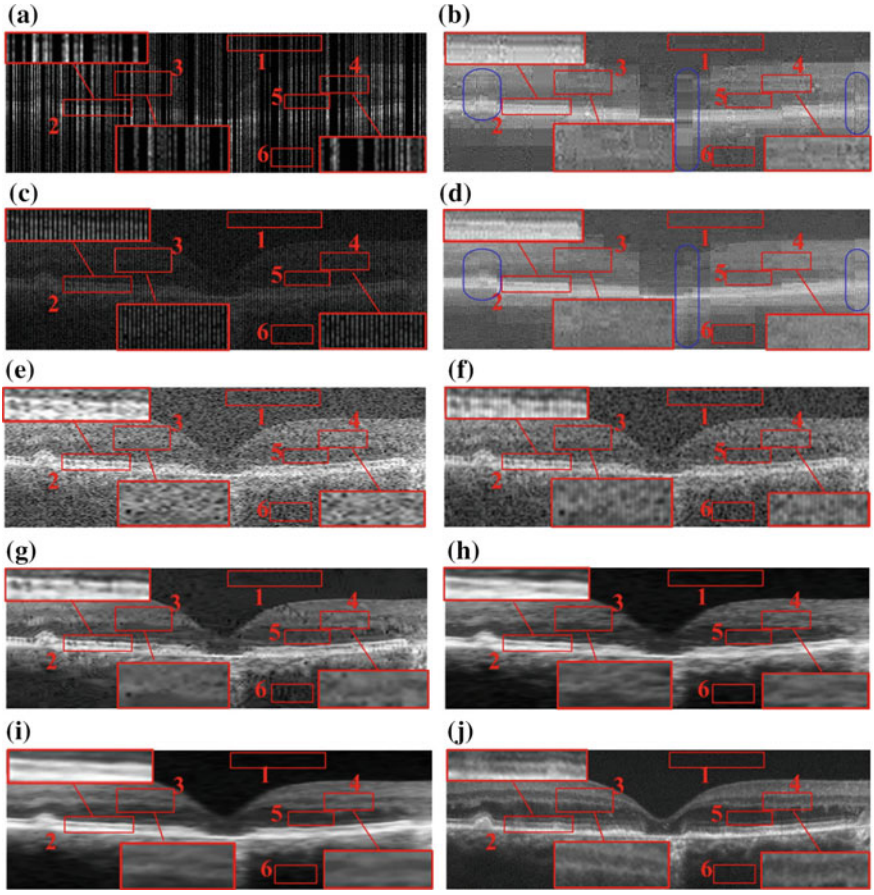

Fig. 4.12 Two types of sampling patterns and their reconstruction results by CS-recovery [51], Bicubic, Tikhonov [15], BM3D [40] + Bicubic, ScSR [29], 2D-SBSDI-nomap, 2D-SBSDI, and our SBSDI method. **a** Randomly sampled image with 75% data missing. **b** Image (**a**) reconstructed by CS-recovery [51] (PSNR = 20.83). **c** Regularly sampled image with 75% data missing. **d** Image (**c**) reconstructed by CS-recovery [51] (PSNR = 20.67). **e** Image (**c**) reconstructed by Bicubic (PSNR = 17.75). **f** Image (**c**) reconstructed by Tikhonov [15] (PSNR = 22.68). **g** Image (**c**) reconstructed by BM3D [40] + Bicubic (PSNR = 23.28). **h** Image (**c**) reconstructed by ScSR (PSNR = 23.09). **i** Image (**c**) reconstructed by SBSDI (PSNR = 24.58). **j** Registered and averaged image which was acquired 160 times slower than the image in (**g**, **h**, **i**)

$$\left\{\hat{\boldsymbol{\alpha}}_i^t\right\}_{t=1}^T = \arg\min_{\boldsymbol{\alpha}_i^t} \sum_{t=1}^T \left\|\boldsymbol{\alpha}_i^t\right\|_0 \text{ subject to } \sum_{t\in\{1,\ldots,T\}} \left\|\mathbf{x}_i^t - \mathbf{D}\boldsymbol{\alpha}_i^t\right\|_2^2 \le \varepsilon \tag{4.17}$$

To solve (4.17), there are two problems: dictionary construction and nearby patches sparse decomposition. Therefore, we proposed an offline structural dictionary learning strategy and an online 3D adaptive sparse decomposition algorithm to obtain the sparse coefficients vectors $\left\{\hat{\boldsymbol{\alpha}}_i^t\right\}_{t=1}^T$, as described in the following.

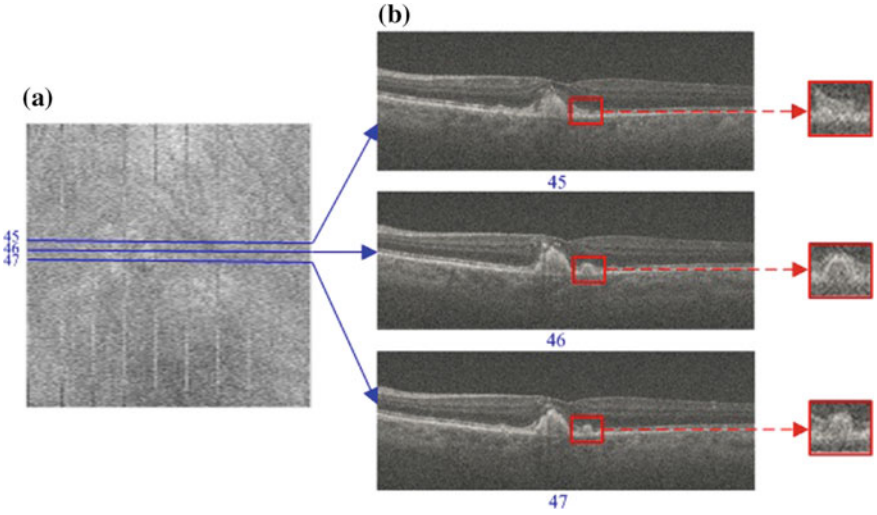

Fig. 4.13 Clinical OCT scan patterns sample the field-of-view, to avoid missing small abnormalities, and thus result in highly correlated neighboring B-scans. **a** Summed-voxel projection [55] *en face* SDOCT image of a non-neovascular age-related macular degeneration (AMD) patient from the Age-Related Eye Disease Study 2 (AREDS2) Ancillary SDOCT (A2A SDOCT) [52]. **b** Three B-scans acquired from adjacent positions. The red rectangular regions are zoomed into show the differences between these neighboring scans

Structural Dictionary Construction

We learn the appropriate overcomplete dictionary of basis functions from a set of high-quality training data. The high-quality training data is obtained by capturing, registering, and averaging repeated low-SNR B-scans from spatially very close positions [56]. In addition, typical clinical OCT images may contain many complex structures (e.g. retinal OCT scans show different layers and pathologies such as cysts [54]) and thus one universal dictionary $\mathbf{D}$ might not be optimal for representing these varied structures. Therefore, following our previous works in [5, 26], we learn H sets of structural sub-dictionaries $\left\{\mathbf{D}_h^{\text{structural}} \in \mathbb{R}^{q\times n}\right\}, h = 1, \ldots, H$, each designed to represent one specific type of structure. This is achieved by first adopting the k-means approach to divide the training patches into H clusters. For each cluster h, one sub-dictionary $\mathbf{D}_{\hat{h}_i^t}^{\text{structural}}$ is learned by the K-SVD algorithm [25] and one centroid $\mathbf{c}_h \in \mathrm{R}^q$ patch is also obtained by the k-means approach.

3D Adaptive Sparse Decomposition

Firstly, we search for the structural sub-dictionary that is most suitable to represent each test patch ($\mathbf{x}_i^t$). We use the Euclidian distance between the patch and the sub-dictionary centroid $\mathbf{c}_h$ for selecting the appropriate sub-dictionary $\mathbf{D}_{\hat{h}_i^t}^{\text{structural}}$:

$$\hat{h}_i^t = \arg\min_{h_i^t} \left\|\mathbf{c}_h - \mathbf{x}_i^t\right\|_2^2, t = 1, \ldots, T, \text{ and } h = 1, \ldots, H. \tag{4.18}$$

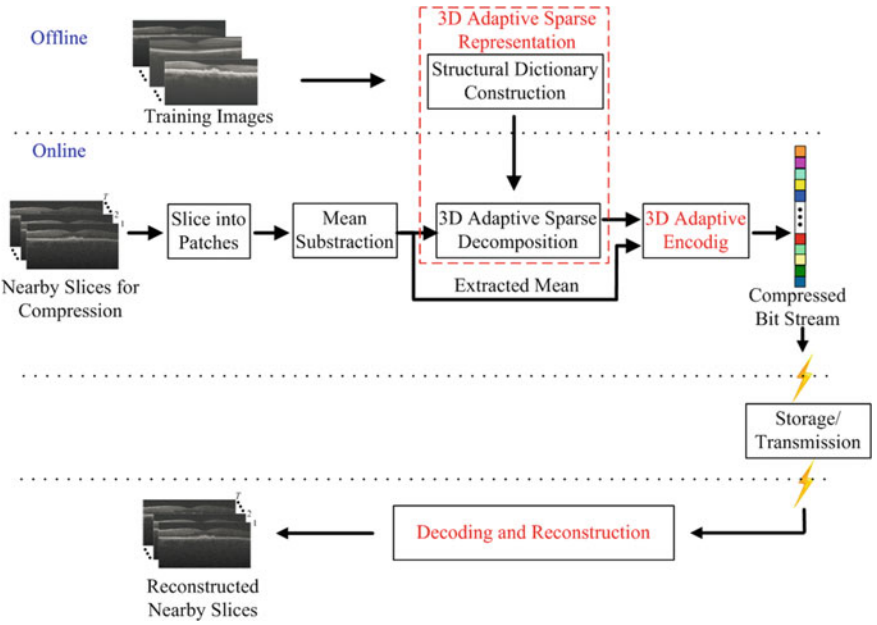

Fig. 4.14 Outline of the proposed 3D-ASRC algorithm

Then, we find the set of sparse coefficients corresponding to such sub-dictionaries to best represent a set of nearby patches $\left\{\mathbf{x}_i^t\right\}_{t=1}^T$. We utilize index $\left\{\hat{h}_i^t\right\}_{t=1}^T$ to define two classes of nearby patches: "*similar*" and "*different*" since the nearby slices have most similar areas and still have large localized differences (see the areas labeled with the red rectangles in Fig. 4.13b). In a similar set of patches ($\left\{\mathbf{x}_{\text{sim},i}^t\right\}_{t=1}^T$), all patches correspond to the same sub-dictionary, while in a different set of patches $\left\{\mathbf{x}_{\text{dif},i}^t\right\}_{t=1}^T$, each patch may correspond to different sub-dictionaries.

The "similar" nearby patches are highly compressible as they can be jointly represented by the same atoms from the commonly selected sub-dictionary $\mathbf{D}_{\hat{h}_i^{com}}^{\text{structural}}$. This is achieved by incorporating the row-sparsity constraint [50] on the sparse coefficients matrix $\mathbf{A}_{\text{sim},i} = \left[\boldsymbol{\alpha}_{\text{sim},i}^1, \ldots, \boldsymbol{\alpha}_{\text{sim},i}^T\right]$:

$$\hat{\mathbf{A}}_{\text{sim},i} = \arg\min_{\hat{\mathbf{A}}_{\text{sim},i}} \left\|\mathbf{A}_{\text{sim},i}\right\|_{\text{row},0} \text{ subject to } \sum_{t\in\{1,\ldots,T\}} \left\|\mathbf{x}_{\text{sim},i}^t - \mathbf{D}_{\hat{h}_i^{com}}^{\text{structural}} \boldsymbol{\alpha}_{\text{sim},i}^t\right\|_2^2 \leq \varepsilon, \tag{4.19}$$

where $\|\cdot\|_{\text{row},0}$ stands for the joint sparse norm [50, 57, 58], which is used to select a small number of most representative non-zero rows in $\mathbf{A}_{\text{sim},i}$. We utilize simultaneous OMP (SOMP) [50] to solve this problem. In $\hat{\mathbf{A}}_{\text{sim},i}$, while the values of the nonzero coefficients in different sparse vectors $\boldsymbol{\alpha}_{\text{sim},i}^1, \ldots, \boldsymbol{\alpha}_{\text{sim},i}^T$ might be different,

their positions are the same, a property which we will exploit in the next subsection for enhanced compression.

A simple trick that can help us further reduce the total number of nonzero coefficients needed to represent a similar set of patches is to estimate the variance of the sparse vectors $\left\{\hat{\boldsymbol{\alpha}}_{sim,i}^{t}\right\}_{t=1}^{T}$. If the variance of the sparse vectors in a set is below a threshold, we denote this set as "very similar" and then fuse the corresponding sparse vectors into one vector $\boldsymbol{\alpha}_{vs,i}$. Otherwise, we denote them as "not very similar" $\left\{\boldsymbol{\alpha}_{nvs,i}^{t}\right\}_{t=1}^{T}$ and keep all the coefficients:

$$\begin{cases} \boldsymbol{\alpha}_{vs,i} = \text{mean}\left\{\boldsymbol{\alpha}_{\text{sim},i}^{t}\right\}_{t=1}^{T}, \text{if variance}\left(\left\{\boldsymbol{\alpha}_{\text{sim},i}^{t}\right\}_{t=1}^{T}\right) \leq b \times \varepsilon \\ \left\{\boldsymbol{\alpha}_{nvs,i}^{t}\right\}_{t=1}^{T} = \left\{\boldsymbol{\alpha}_{\text{sim},i}^{t}\right\}_{t=1}^{T}, \text{if variance}\left(\left\{\boldsymbol{\alpha}_{\text{sim},i}^{t}\right\}_{t=1}^{T}\right) > b \times \varepsilon \end{cases}, \tag{4.20}$$

where b is a constant and the mean is the operation to compute the mean of the $\left\{\boldsymbol{\alpha}_{\text{vs},i}^{t}\right\}_{t=1}^{T}$.

The "different" nearby patches $\left\{\mathbf{x}_{\text{dif},i}^{t}\right\}_{t=1}^{T}$ are independently decomposed on the sub-dictionaries $\mathbf{D}_{\hat{h}_i^t}^{\text{structral}}$ that can best fit each of them, which amounts to the problem:

$$\left\{\hat{\boldsymbol{\alpha}}_{\text{dif},i}^{t}\right\}_{t=1}^{T} = \arg\min_{\boldsymbol{\alpha}_{\text{dif}}^{t}} \sum_{t=1}^{T} \left\|\boldsymbol{\alpha}_{\text{dif},i}^{t}\right\|_0 \text{ subject to } \sum_{t\in\{1,\ldots,T\}} \left\|\mathbf{x}_{\text{dif},i}^{t} - \mathbf{D}_{\hat{h}_i^t}^{\text{structural}} \boldsymbol{\alpha}_{\text{dif},i}^{t}\right\|_2^2 \leq \varepsilon. \tag{4.21}$$

We solve this problem by applying the OMP algorithm [34] separately on each patch. Note that the positions and values of the nonzero coefficients in $\left\{\hat{\boldsymbol{\alpha}}_{dif,i}^{t}\right\}_{t=1}^{T}$ might be varied for reflecting the differences among the nearby patches $\left\{\mathbf{x}_{\text{dif},i}^{t}\right\}_{t=1}^{T}$. The proposed 3D sparse representation algorithm is summarized in Fig. 4.15.

4.3.3.2 3D Adaptive Encoding, Decoding and Image Reconstruction

To encode the positions and values of the nonzero coefficients representing a set of nearby patches, we first quantize the sparse vectors using a uniform quantizer [32]. Then, we utilize an adaptive strategy to preserve the positions and values of the nonzero coefficients as follows:

For the "very similar" nearby patches, both the positions and values of the nonzero coefficients are the same and these sparse vectors are already fused into one vector $\boldsymbol{\alpha}_{vs,i}$. Thus, only one sequence is required to store the position information and one sequence is used to preserve the value information, as shown in Fig. 4.16a.

For the "not very similar" nearby patches, the positions of the nonzero coefficients in $\left\{\boldsymbol{\alpha}_{nvs,i}^{t}\right\}_{t=1}^{T}$ are the same while their values are different. Thus, only one sequence is needed to store the position information while another T sequences are employed to preserve the value information, as shown in Fig. 4.16b. For the "different" nearby

3D Adaptive Sparse Representation

Input: Offline: $\mathbf{x}_1,...,\mathbf{x}_U$ training patches extracted from the less noisy training images;

Online: $\mathbf{x}_i^1,...,\mathbf{x}_i^T$ nearby patches extracted from the position i of the nearby slices.

A) Offline Structural Dictionary Construction:

1: Cluster the training patches $\mathbf{x}_1,...,\mathbf{x}_U$ into H groups using the k-means approach.

2: For each cluster, compute one centroid $\mathbf{c}_h$ and learn one structural sub-dictionary $\mathbf{D}_h^{\text{structural}}$.

B) Online 3D Adaptive Sparse Decomposition:

1: Select the fitted sub-dictionaries $\mathbf{D}_{\hat{h}_i}^{\text{structural}}$ for the nearby patches $\mathbf{x}_i^1,...,\mathbf{x}_i^T$ in Eq. (4-18).

2: Based on the selected sub-dictionaries, divide the nearby patches into two groups: Similar and Different.

3: If nearby patches are similar, obtain their sparse vectors $\left\{\hat{\boldsymbol{\alpha}}_{\text{sim},i}^t\right\}_{t=1}^T$ by jointly decomposing nearby patches on the same atoms from the commonly selected sub-dictionary in Eq. (4-19).

4: Further divide the sparse vectors $\left\{\hat{\boldsymbol{\alpha}}_{\text{sim},i}^t\right\}_{t=1}^T$ into two groups: very similar $\boldsymbol{\alpha}_{\text{vs},i}$ and not very similar $\left\{\hat{\boldsymbol{\alpha}}_{\text{nvs},i}^t\right\}_{t=1}^T$ in Eq. (4-20).

5: If nearby patches are different, obtain their sparse vectors $\left\{\hat{\boldsymbol{\alpha}}_{\text{dif},i}^t\right\}_{t=1}^T$ by separately decomposing nearby patches on different sub-dictionaries in Eq. (4-21).

Output: $\left\{\hat{\boldsymbol{\alpha}}_{\text{dif},i}^t\right\}_{t=1}^T$ if the nearby patches are different; $\left\{\hat{\boldsymbol{\alpha}}_{\text{nvs},i}^t\right\}_{t=1}^T$ if the nearby slices are not very similar; $\boldsymbol{\alpha}_{\text{vs},i}$ if the nearby patches are very similar.

Fig. 4.15 3D adaptive sparse representation algorithm

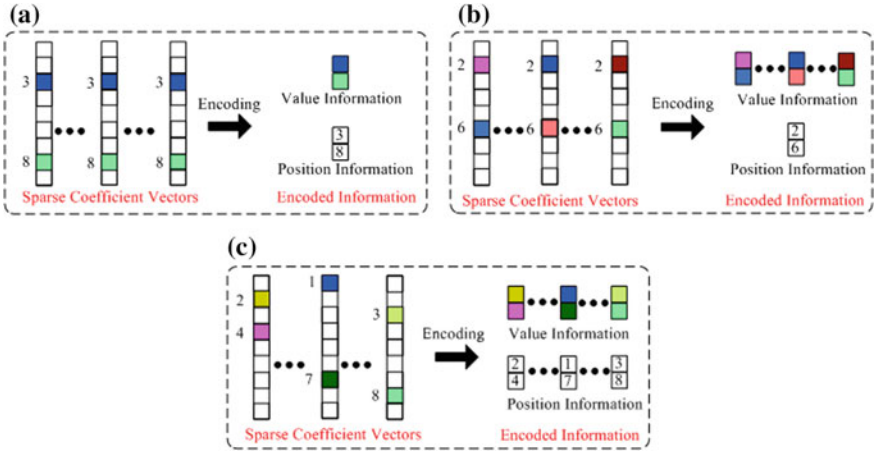

Fig. 4.16 3D adaptive encoding for the three classes of the nearby sparse vectors **a** Very similar; **b** Not very similar; **c** Different. Note that the color blocks in the sparse vectors denote the nonzero coefficients. Different colors represent different values

patches the positions and values of the nonzero coefficients in $\left\{\hat{\boldsymbol{\alpha}}_{dif,i}^{t}\right\}_{t=1}^{T}$ are different. Thus, the position information is preserved using T different sequences, while the value information is stored with other T different sequences, as shown in Fig. 4.16c. We label the three classes ("Very similar", "Not very similar", and "Different") of nearby slices as 0, 1, and 2, respectively. These class types are stored in one sequence. In addition, the means $\left\{m_i^t\right\}_{t=1}^{T}$ of nearby patches $\left\{\mathbf{x}_i^t\right\}_{t=1}^{T}$ are quantized and stored into T different sequences. Furthermore, indexes $\left\{h_i^t\right\}_{t=1}^{T}$ of the selected sub-dictionaries for nearby patches are stored with another T sequences. Finally, we apply Huffman coding [59] on the above sequences to create one bit stream. At the decoding site, given the compressed bit stream, we first extract the mean $\left\{m_i^t\right\}_{t=1}^{T}$, sparse vectors $\left\{\boldsymbol{\alpha}_i^t\right\}_{t=1}^{T}$, and indexes $\left\{h_i^t\right\}_{t=1}^{T}$ of the selected sub-dictionaries for each set of nearby patches. Then, a set of nearby patches $\left\{\mathbf{x}_i^t\right\}_{t=1}^{T}$ are reconstructed by,

$$\mathbf{x}_i^t = \mathbf{D}_{h_i^t}^{\text{structural}} \boldsymbol{\alpha}_i^t + m_i^t, t = 1, \ldots, T. \tag{4.22}$$

Subsequently, each patch $\hat{\mathbf{x}}_i^{t_s}$ (where t_s denotes a specific patch) is further enhanced by weighted averaging of the nearby patches: $\hat{\mathbf{x}}_i^{t_s} = \sum_{t=1}^{T} w_i^{t,t_s} \hat{\mathbf{x}}_i^t$, where w_i^{t,t_s} [5] is estimated as:

$$w_i^{t,t_s} = \frac{\exp\left(-\left\|\hat{\mathbf{x}}_i^t - \hat{\mathbf{x}}_i^{t_s}\right\|_2^2 / h\right)}{\text{Norm}}. \tag{4.23}$$

In (4.13), Norm is defined as $\sum_{t=1}^{T} \exp\left(-\left\|\hat{\mathbf{x}}_i^t - \hat{\mathbf{x}}_i^{t_s}\right\|_2^2 / h\right)$ and h is a predefined scalar. Finally, we recover each B-scan by combining its reconstructed patches in a raster-scan order.

4.3.3.3 Experimental Results

To validate the effectiveness of the proposed 3D-ASRC algorithm, we compared its performance with those of four well-known compression approaches: JPEG 2000, MPEG-4, SPIHT [60], K-SVD [30], and three variants of the proposed algorithm: SRC-Dif, 2D-ASRC, 3D-ASRC-WA. For the SRC-Dif method, we utilize the "different-patch" based sparse representation and encoding scheme for compression. For the 2D-ASRC method, we denoted a number of spatial nearby patches within one slice as the nearby patches. For the 3D-ASRC-WAmethod, we do not use the 3D weighted averaging technique for the final reconstruction, compared to the 3D-ASRC method.

In our experiments, we first used volumetric scans of human retinas from 26 different subjects with and without non-neovascular AMD, imaged by an 840-nm wavelength SDOCT system from Bioptigen, Inc. (Durham, NC, USA) with an axial

resolution of ~4.5 μm per pixel in tissue. In addition, we also performed our experiments on a mouse dataset acquired by a different SDOCT system, (Bioptigen Envisu R2200), with ~2 μm axial resolution in tissue.

Based on our experiments on training data, we empirically selected the parameters for the proposed 3D-ASRC algorithm. We chose the patch size in each slice to be a rectangle of size 6×12 pixels (height × width). The number of nearby slices T was set to 5 (corresponding to ~300 μ azimuthal distance). In retinal imaging, slices from farther distances may have significant differences and thus adding them might actually reduce compression efficiency. In the dictionary training stage, the value of cluster H was chosen to be 10. In each cluster, the size of the trained dictionary was set to 72×500. The parameter b in (4.20) was set to 0.001. For the test datasets in our experiments, the mean and standard deviation of parameter C for the compression ratios = [10, 15, 20, 25, 30, 35, 40] were [1.00, 1.07, 1.12, 1.15, 1.17, 1.19, 1.21], and [0.053, 0.054, 0.052, 0.055, 0.055, 0.057, 0.059], respectively. The parameters for the JPEG 2000 and MPEG-4 were set to the default values in the Matlab [43] and QuickTime Player Pro 7.0 software [61], respectively. For the K-SVD algorithm, the patch size was set to 6×12 and the trained dictionary was of size 72×500. For the 2D-ASRC method, the number of spatial nearby patches was selected to 9 and the other parameters were set to the same values as in our 3D-ASRC method. We adopted the peak signal-to-noise-ratio (PSNR) and feature similarity index measure (FSIM) [62] to evaluate the performances of the compression methods.

We tested the JPEG 2000, MPEG-4, SPIHT [60], K-SVD [30], SRC-Dif, 2D-ASRC, 3D-ASRC-WA, and 3D-ASRC methods on seven different compression ratios ranging from 10 to 40. The corresponding quantitative comparisons (PSNR and FSIM) of all the test methods at different compression ratios are reported in Table 4.3. As can be seen in Table 4.2, the proposed 3D-ASRC method consistently delivered better PSNR and FSIM results than the other methods. Figures 4.17 show qualitative comparisons of reconstructed results from the tested methods using the compression ratio of 10. Since boundaries between retinal layers and drusen contain meaningful anatomic and pathologic information [44], we magnified one boundary area and one dursen area in each figure. As can be observed in Fig. 4.17, results from JPEG 2000, K-SVD, and MPEG-4 methods appear very noisy with indistinct boundaries for many important structural details (see the zoomed boundary areas of both the dataset 1 and 2). The SPIHT method greatly suppresses noise, but increases blur and introduces visible artifacts (see the zoomed drusen and boundary areas in Fig. 4.17). Compared to the above methods, the proposed SRC-Dif, 2D-ASRC, 3D-ASRC-WA methods deliver comparatively better structural details, but still show some noise artifacts. By contrast, the proposed 3D-ASRC method achieves noticeably improved noise suppression, and preserves meaningful anatomical structures.

Table 4.3 Mean of the PSNR (left) and FSIM (right) for 16 foveal images from 16 different subjects reconstructed by JPEG 2000, MPEG-4, SPIHT [60], K-SVD [30], SRC-DIF, 2D-ASRC, 3D-ASRC-WA, and 3D-ASRC under different compression ratios

Method	Compression ratio						
	10	15	20	25	30	35	40
JPEG 2000	19.67/0.65	20.33/0.67	20.70/0.69	21.34/0.70	21.92/0.70	22.41/0.71	22.78/0.71
MPEG-4	20.42/0.72	22.44/0.78	22.63/0.79	22.71/0.79	22.76/0.79	23.21/0.78	23.22/0.79
SPIHT	25.56/0.80	26.17/0.82	26.50/0.82	26.68/0.82	26.79/0.82	26.86/0.82	26.89/0.82
K-SVD	20.74/0.68	22.51/0.70	22.51/0.72	23.06/0.74	23.56/0.75	23.94/0.75	24.28/0.76
SRC-Dif	26.98/0.85	27.26/0.86	27.45/**0.87**	27.54/**0.87**	27.56/**0.87**	27.58/0.86	27.55/0.86
2D-ASRC	26.14/0.81	26.51/0.82	26.73/0.82	26.85/0.83	26.89/0.83	26.91/0.83	26.99/0.83
3D-ASRC-WA	26.31/0.82	26.70/0.83	26.97/0.84	27.11/0.85	27.23/0.85	27.29/0.85	27.33/0.85
3D-ASRC	**27.60/0.88**	**27.65/0.87**	**27.68/0.87**	**27.71/0.87**	**27.75/0.87**	**27.75/0.87**	**27.74/0.87**

The best results in this table are labeled in bold

4.4 Conclusions

In this chapter, we presented three adaptive sparse representation methods for the denoising, interpolation, and compression of OCT images. Specifically, for the denoising problem, we proposed a multiscale sparsity based method called MSBTD, which can well represent the multiscale information of the pathology structures and learn high quality dictionaries from the nearby high SNR B-scan. For the interpolation problem, we proposed an efficient sparsity based image reconstruction framework called SBSDI that achieve a simultaneous interpolation and denoising of the clinical SDOCT images via a pair of semi-coupled dictionaries. For the compression problem, we introduced a 3D adaptive sparse compression called 3D-ASRC, which can simultaneously represent the nearby slices of the SDOCT images via a 3D adaptive sparse representation algorithm. Such a 3D adaptive algorithm exploits similarities among nearby slices, yet is sensitive in preserving their differences. Experiments on real acquired clinical OCT images demonstrate the superiority of the proposed three sparsity based reconstruction methods over several state-of-the-art reconstruction methods.

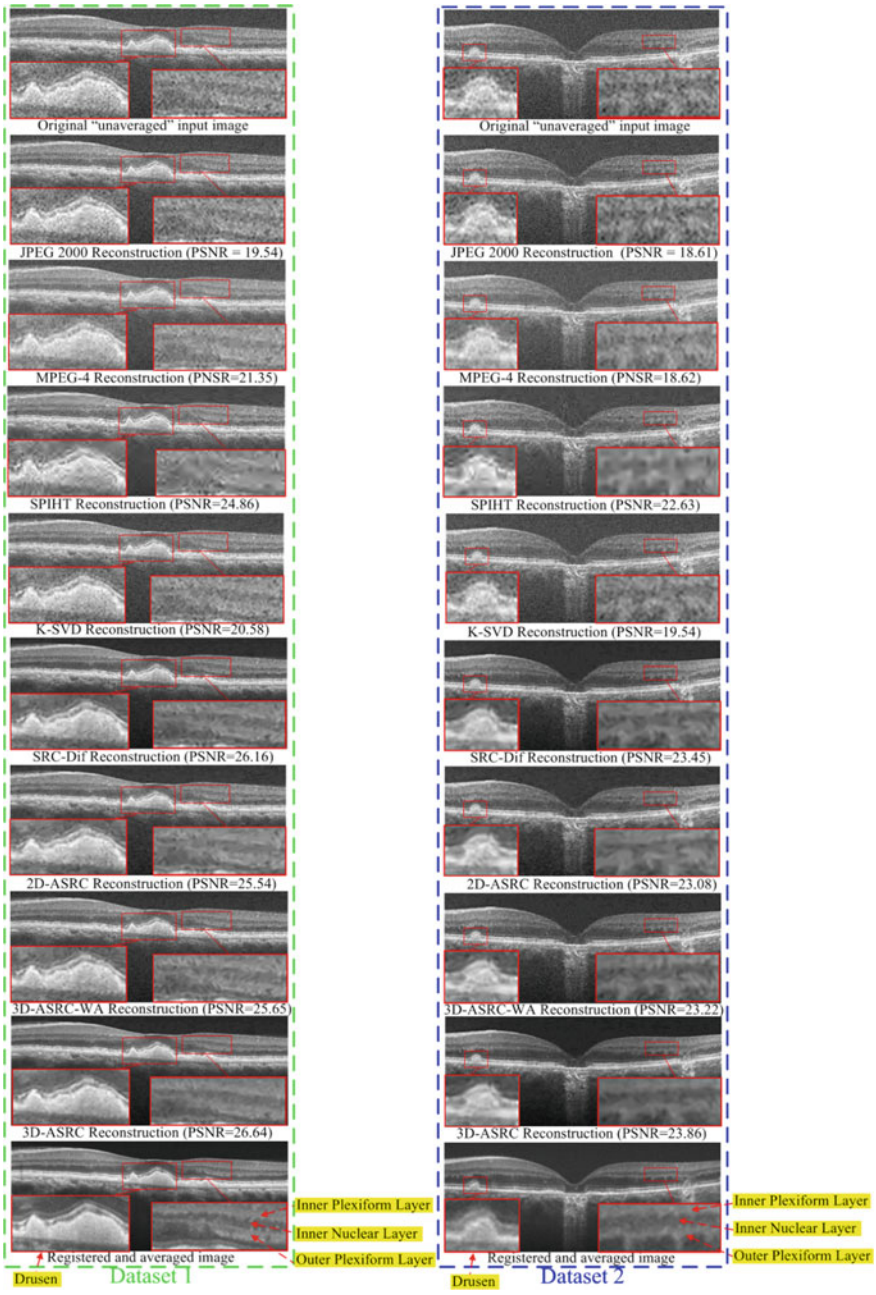

Fig. 4.17 Reconstructed results using the JPEG 2000, MPEG-4, SPIHT [60], K-SVD [30], SRC-Dif, 2D-ASRC, 3D-ASRC-WA and 3D-ASRC with compression ratio = 10 on two human retinal datasets

References

1. W. Drexler, U. Morgner, R.K. Ghanta, F.X. Kärtner, J.S. Schuman, J.G. Fujimoto, Ultrahigh-resolution ophthalmic optical coherence tomography. Nat. Med. **7**, 502–507 (2001)
2. L. Fang, S. Li, Q. Nie, J.A. Izatt, C.A. Toth, S. Farsiu, Sparsity based denoising of spectral domain optical coherence tomography images. Biomed. Opt. Express **3**, 927–942 (2012)
3. H.M. Salinas, D.C. Fernández, Comparison of PDE-based nonlinear diffusion approaches for image enhancement and denoising in optical coherence tomography. IEEE Trans. Med. Imag. **26**, 761–771 (2007)
4. A. Wong, A. Mishra, K. Bizheva, D.A. Clausi, General Bayesian estimation for speckle noise reduction in optical coherence tomography retinal imagery. Opt. Exp. **18**, 8338–8352 (2010)
5. L. Fang, S. Li, R. McNabb, Q. Nie, A. Kuo, C. Toth et al., Fast acquisition and reconstruction of optical coherence tomography images via sparse representation. IEEE Trans. Med. Imag. **32**, 2034–2049 (2013)
6. P. Milanfar, A tour of modern image filtering: new insights and methods, both practical and theoretical. IEEE Signal Process. Mag. **30**, 106–128 (2013)
7. A. Ozcan, A. Bilenca, A.E. Desjardins, B.E. Bouma, G.J. Tearney, Speckle reduction in optical coherence tomography images using digital filtering. J. Opt. Soc. Am. **24**, 1901–1910 (2007)
8. A. Boroomand, A. Wong, E. Li, D.S. Cho, B. Ni, K. Bizheva, Multi-penalty conditional random field approach to super-resolved reconstruction of optical coherence tomography images. Biomed. Opt. Exp. **4**, 2032–2050 (2013)
9. X. Liu, J.U. Kang, Compressive SD-OCT: the application of compressed sensing in spectral domain optical coherence tomography. Opt. Exp. **18**, 22010–22019 (2010)
10. D. Xu, N. Vaswani, Y. Huang, J.U. Kang, Modified compressive sensing optical coherence tomography with noise reduction. Opt. Lett. **37**, 4209–4211 (2012)
11. D. Xu, Y. Huang, J.U. Kang, Real-time compressive sensing spectral domain optical coherence tomography. Opt. Lett. **39**, 76–79 (2014)
12. E. Lebed, P.J. Mackenzie, M.V. Sarunic, F.M. Beg, Rapid volumetric OCT image acquisition using compressive sampling. Opt. Exp. **18**, 21003–21012 (2010)
13. A.B. Wu, E. Lebed, M.V. Sarunic, M.F. Beg, Quantitative evaluation of transform domains for compressive sampling-based recovery of sparsely sampled volumetric OCT images. IEEE Trans. Biomed. Eng. **60**, 470–478 (2013)
14. K.L. Lurie, R. Angst, A.K. Ellerbee, Automated mosaicing of feature-poor optical coherence tomography volumes with an integrated white light imaging system. IEEE Trans. Biomed. Eng. **61**, 2141–2153 (2014)
15. G.T. Chong, S. Farsiu, S.F. Freedman, N. Sarin, A.F. Koreishi, J.A. Izatt et al., Abnormal foveal morphology in ocular albinism imaged with spectral-domain optical coherence tomography. Arch. Ophthalmol. **127**, 37–44 (2009)
16. G.K. Wallace, The JPEG still picture compression standard. ACM Commun. **34**, 30–44 (1991)
17. H. Rabbani, R. Nezafat, S. Gazor, Wavelet-domain medical image denoising using bivariate laplacian mixture model. IEEE Trans. Biomed. Eng. **56**, 2826 (2009)
18. Z. Jian, L. Yu, B. Rao, B.J. Tromberg, Z. Chen, Three-dimensional speckle suppression in optical coherence tomography based on the curvelet transform. Opt. Exp. **18**, 1024–1032 (2010)
19. R. Rubinstein, A.M. Bruckstein, M. Elad, Dictionaries for sparse representation modeling. Proc. IEEE **98**, 1045–1057 (2010)
20. B.A. Olshausen, D.J. Field, Emergence of simple-cell receptive field properties by learning a sparse code for natural images. Nature **381**, 607–609 (1996)
21. S. Li, L. Fang, H. Yin, An efficient dictionary learning algorithm and its application to 3-D medical image denoising. IEEE Trans. Biomed. Eng. **59**, 417–427 (2012)
22. A. Wong, A. Mishra, P. Fieguth, D.A. Clausi, Sparse reconstruction of breast mri using homotopic minimization in a regional sparsified domain. IEEE Trans. Biomed. Eng. **60**, 743–752 (2013)
23. S. Li, H. Yin, L. Fang, Group-sparse representation with dictionary learning for medical image denoising and fusion. IEEE Trans. Biomed. Eng. **59**, 3450–3459 (2012)

24. S. Chen, H. Liu, Z. Hu, H. Zhang, P. Shi, Y. Chen, Simultaneous reconstruction and segmentation of dynamic pet via low-rank and sparse matrix decomposition. IEEE Trans. Biomed. Eng. **62**, 1784–1795 (2015)
25. M. Aharon, M. Elad, A.M. Bruckstein, The K-SVD: an algorithm for designing of overcomplete dictionaries for sparse representation. IEEE Trans. Signal Process. **54**, 4311–4322 (2006)
26. L. Fang, S. Li, X. Kang, J.A. Izatt, S. Farsiu, 3-D Adaptive sparsity based image compression with applications to optical coherence tomography. IEEE Trans. Med. Imag. **34**, 1306–1320 (2015)
27. R. Kafieh, H. Rabbani, I. Selesnick, Three dimensional data-driven multi scale atomic representation of optical coherence tomography. IEEE Trans. Med. Imag. **34**, 1042–1062 (2015)
28. M. Elad, M. Aharon, Image denoising via sparse and redundant representations over learned dictionaries. IEEE Trans. Image Process. **15**, 3736–3745 (2006)
29. J. Yang, J. Wright, T.S. Huang, Y. Ma, Image super-resolution via sparse representation. IEEE Trans. Image Process. **19**, 2861–2873 (2010)
30. O. Bryt, M. Elad, Compression of facial images using the K-SVD algorithm. J. Vis. Commun. Image Represent. **19**, 270–282 (2008)
31. J. Zepeda, C. Guillemot, E. Kijak, Image compression using sparse representations and the iteration-tuned and aligned dictionary. IEEE J. Sel. Topics Signal Process. **5**, 1061–1073 (2011)
32. K. Skretting, K. Engan, Image compression using learned dictionaries by RLS-DLA and compared with K-SVD. in *Proceedings of IEEE International Conference on Acoustics Speech Signal Processing*, pp. 1517–1520 (2011)
33. A. Foi, Noise estimation and removal in MR imaging. in *Proceeding of IEEE International Symposium Biomedical Imaging* (2011), pp. 1809–1814
34. S.G. Mallat, Z. Zhang, Matching pursuits with time-frequency dictionaries. IEEE Trans. Signal Process. **41**, 3397–3415 (1993)
35. P. Chatterjee, P. Milanfar, Clustering-based denoising with locally learned dictionaries. IEEE Trans. Image Process. **18**, 1438–1451 (2009)
36. W. Dong, L. Zhang, G. Shi, X. Wu, Image deblurring and super-resolution by adaptive sparse domain selection and adaptive regularization. IEEE Trans. Image Process. **20**, 1838–1857 (2011)
37. W. Dong, L. Zhang, G. Shi, Centralized sparse representation for image restoration. in *IEEE International Conference on Computer Vision*, pp. 1259–1266 (2011)
38. J. Mairal, F. Bach, J. Ponce, G. Sapiro, A. Zisserman, Non-local sparse models for image restoration. in *Proceedings of IEEE International Conference on Computer Vision*, pp. 2272–2279 (2009)
39. F. Luisier, T. Blu, M. Unser, A new SURE approach to image denoising: Interscale orthonormal wavelet thresholding. IEEE Trans. Image Process. **16**, 1057–7149 (2007)
40. K. Dabov, A. Foi, V. Katkovnik, K. Egiazarian, Image denoising by sparse 3-D transform-domain collaborative filtering. IEEE Trans. Image Process. **16**, 2080–2095 (2007)
41. P. Thévenaz, U.E. Ruttimann, M. Unser, A pyramid approach to subpixel registration based on intensity. IEEE Trans. Image Process. **7**, 27–41 (1998)
42. G. Cincotti, G. Loi, M. Pappalardo, Frequency decomposition and compounding of ultrasound medical images with wavelets packets. IEEE Trans. Med. Imag. **20**, 764–771 (2001)
43. P. Bao, L. Zhang, Noise reduction for magnetic resonance images via adaptive multiscale products thresholding. IEEE Trans. Med. Imag. **22**, 1089–1099 (2003)
44. S.J. Chiu, X.T. Li, P. Nicholas, C.A. Toth, J.A. Izatt, S. Farsiu, Automatic segmentation of seven retinal layers in SDOCT images congruent with expert manual segmentation. Opt. Express **18**, 19413–19428 (2010)
45. R. Zeyde, M. Elad, M. Protter, On single image scale-up using sparse-representations. in *Curves Surfaces*, pp. 711–730 (2012)
46. K.S. Ni, T.Q. Nguyen, Image superresolution using support vector regression. IEEE Trans. Image Process. **16**, 1596–1610 (2007)
47. A.W. Scott, S. Farsiu, L.B. Enyedi, D.K. Wallace, C.A. Toth, Imaging the infant retina with a hand-held spectral-domain optical coherence tomography device. Am. J. Ophthalmol. **147**, 364–373 (2009)

48. J. Yang, Z. Wang, Z. Lin, S. Cohen, T. Huang, Coupled dictionary training for image super-resolution. IEEE Trans. Image Process. **21**, 3467–3478 (2012)
49. S. Wang, L. Zhang, Y. Liang, Q. Pan, Semi-coupled dictionary learning with applications to image super-resolution and photo-sketch synthesis. in *Proceedings of IEEE International Conference on Computer Vision Pattern Recognition*, pp. 2216–2223 (2012)
50. J.A. Tropp, A.C. Gilbert, M.J. Strauss, Algorithms for simultaneous sparse approximation. Part I: greedy pursuit. Signal Process. **86**, 572–588 (2006)
51. E. Candes, J. Romberg, Sparsity and incoherence in compressive sampling. Inverse Prob. **23**, 969–985 (2007)
52. S. Farsiu, S.J. Chiu, R.V. O'Connell, F.A. Folgar, E. Yuan, J.A. Izatt et al., Quantitative classification of eyes with and without intermediate age-related aacular degeneration using optical coherence tomography. Ophthalmology **121**, 162–172 (2014)
53. C. Guillemot, F. Pereira, L. Torres, T. Ebrahimi, R. Leonardi, J. Ostermann, Distributed monoview and multiview video coding. IEEE Signal Process. Mag. **24**, 67–76 (2007)
54. J.Y. Lee, S.J. Chiu, P. Srinivasan, J.A. Izatt, C.A. Toth, S. Farsiu et al., Fully automatic software for quantification of retinal thickness and volume in eyes with diabetic macular edema from images acquired by cirrus and spectralis spectral domain optical coherence tomography machines. Invest. Ophthalmol. Vis. Sci. **54**, 7595–7602 (2013)
55. S. Jiao, R. Knighton, X. Huang, G. Gregori, C. Puliafito, Simultaneous acquisition of sectional and fundus ophthalmic images with spectral-domain optical coherence tomography. Opt. Express **13**, 444–452 (2005)
56. A. Cameron, D. Lui, A. Boroomand, J. Glaister, A. Wong, K. Bizheva, Stochastic speckle noise compensation in optical coherence tomography using non-stationary spline-based speckle noise modelling. Biomed. Opt. Exp. **4**, 1769–1785 (2013)
57. Y. Chen, N.M. Nasrabadi, T.D. Tran, Hyperspectral image classification using dictionary-based sparse representation. IEEE Trans. Geosci. Remote Sens. **49**, 3973–3985 (2011)
58. L. Fang, S. Li, X. Kang, J.A. Benediktsson, Spectral-spatial hyperspectral image classification via multiscale adaptive sparse representation. IEEE Trans. Geosci. Remote Sens. **52**, 7738–7749 (2014)
59. K. Skretting, J.H. Husøy, S.O. Aase, Improved Huffman coding using recursive splitting. in *Proceedings of Norwegian Signal Processing, NORSIG*, pp. 92–95 (1999)
60. A. Said, W.A. Pearlman, A new fast and efficient image codec based on set partitioning in hierarchical trees. IEEE Trans. Circuits Syst. Video Technol. **6**, 243–250 (1996)
61. Software was downloaded at: http://www.apple.com/quicktime/extending/
62. L. Zhang, L. Zhang, X. Mou, D. Zhang, FSIM: a feature similarity index for image quality assessment. IEEE Trans. Image Process. **20**, 2378–2386 (2011)

Chapter 5
Segmentation of OCT Scans Using Probabilistic Graphical Models

Fabian Rathke, Mattia Desana and Christoph Schnörr

The most prominent structure in retinal OCT images is the intra-retinal layers. Therefore layer segmentation is one of the most studied problems in OCT image processing. In this chapter, a probabilistic approach for retinal layer segmentation is presented. It exploits texture and shape information based on a graphical model. The approach can be extended to a locally adaptive graphical model that additionally discriminates between healthy and pathologically deformed scan structure.

5.1 Introduction

Since its introduction in 1991 [1], optical coherence tomography (OCT) has become a standard tool in clinical ophthalmology [2]. The introduction of spectral-domain OCT [3] dramatically increased the resolution as well as the imaging speed and enabled the acquisition of 3-D volumes composed of hundreds of 2-D scans. Since the manual segmentation of retina scans is tedious and time-consuming, automated segmentation methods become evermore important given the growing amount of gathered data.

Related Work. Various segmentation approaches have been published. All have in common that they utilize texture information, based on the spatial variation of the intensity functions and its gradient. In order to obtain accurate and stable segmentations and to reduce the sensitive to texture artifacts, some form of regularization is applied. We focus on the methods used for regularization in related work and to which degree shape prior knowledge is utilized.

Many approaches solely impose smoothness on segmented retina boundaries, without any shape prior information. References [4–7] find column-wise maxima of the appearance terms and then apply outlier detection along with interpolation to account for erroneous segmentations. Chiu et al. [8] construct a graph for each boundary with weights determined by gradient information and find the shortest path using dynamic programming. Starting with easy to detect boundaries, the segmenta-

F. Rathke (✉) · M. Desana · C. Schnörr
Image and Pattern Analysis Group (IPA), University of Heidelberg, Heidelberg, Germany
e-mail: fabian.rathke@iwr.uni-heidelberg.de

X. Chen et al. (eds.), *Retinal Optical Coherence Tomography Image Analysis*,
Biological and Medical Physics, Biomedical Engineering,
https://doi.org/10.1007/978-981-13-1825-2_5

tion of subsequent boundaries is guided by restricting their search region. They also demonstrated the applicability of their approach to the segmentation of pathological scans [9, 10]. Tian et al. [11, 12], which use an adaptation of [8], published two OCT benchmark datasets which we will use for performance evaluation along with their results as baselines. Finally, Duan et al. [13] proposed a similar approach, with the exception that the shortest path is found in the continuous domain.

Another set of approaches, including [14–17], build an undirected graphical model that includes more than one boundary. Here shape regularization is imposed on the pairwise interaction of *adjacent* boundaries, constraining their relative positions. This form of shape prior information is encoded into the model either as hard constraints [14] or as probabilistic soft constraints [15, 16]. Inference is performed via graph cuts. Due to computational limitations, only local shape information is used and not all boundaries are inferred at the same time.

Finally, Kajiè et al. [18] apply the popular active appearance approach for matching statistical models of appearance and shape to a given OCT scan. Although non-local shape modeling is within the scope of their approach, only landmarks at sparsely sampled boundary positions are used, and only a maximum likelihood point estimate is inferred, rather than employing a global probabilistic shape model as does our approach.

Contribution. We present a probabilistic approach to the segmentation of OCT retina scans (See Fig. 5.1 for the segmented retina layers). We utilize a *global* shape prior that takes into account both short and long-term dependencies between retina layers, which has not be explored in related work so far. All boundaries are detected at the same time, which makes obsolete additional processing steps required in other work, like detection of the fovea, flattening of the retina, or denoising. Since imposing global shape information is not justified when dealing with *pathological* deformations, we outline ongoing work that demonstrates how the model can be adapted to such cases.

Organization. We introduce in Sect. 5.2 our graphical model and explain how inference is done by evaluating the posterior distribution of segmentations. A thorough evaluation on five different datasets, composed of healthy data and mild pathologies, follows in Sect. 5.3. We highlight benefits of inference based on a full probability distribution. In Sect. 5.4, we discuss an extension of our approach that also handles severe pathological deformations. We conclude and point out further directions of research in Sect. 5.5.

5.2 A Probabilistic Graphical Model for Retina Segmentation

5.2.1 The Graphical Model

Mathematically, an OCT scan is a matrix $y \in \mathbb{R}^{N \times M}$ of N rows and M columns, containing gray values $y_{i,j}$ in the range $[0, 1] = \{x \in \mathbb{R} \mid 0 \leq x \leq 1\}$. A segmentation

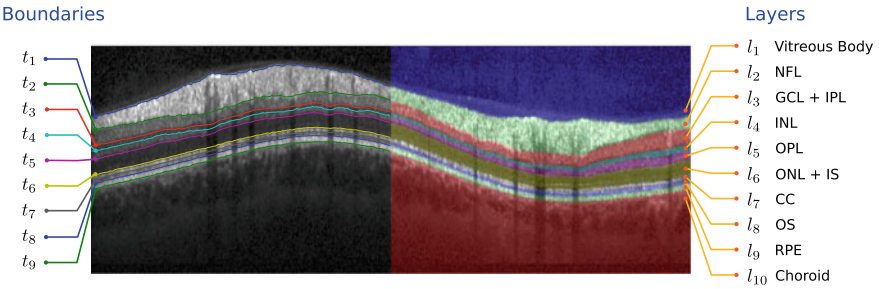

Fig. 5.1 The retinal layers segmented by our approach and their corresponding anatomical names: Nerve fiber layer (NFL), ganglion cell layer and inner plexiform layer (GCL + IPL), inner nuclear layer (INL), outer plexiform layer (OPL), outer nuclear layer and inner segment (ONL + IS), connecting cilia (CC), outer segment (OS), retinal pigment epithelium (RPE)

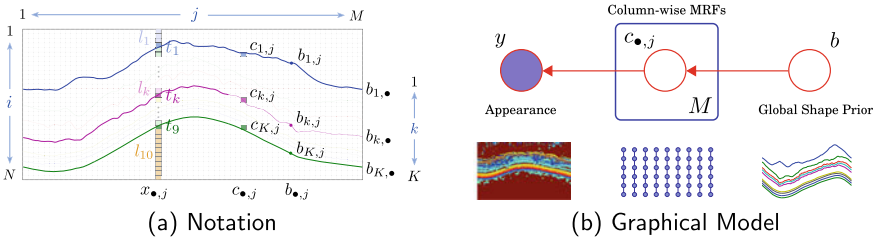

Fig. 5.2 **a** Important variables used throughout this section. Note the difference between real valued boundary position $b_{k,j}$ and its discretized counterpart $c_{k,j}$. **b** The different components of our graphical model

of y with K retina boundaries (corresponding to $K+1$ layers) is given by the matrix $b \in \mathbb{R}^{K \times M}$, where each entry $b_{k,j}$ has the range $[1, N]$. While b is continuous, graphical models typically are discrete, since they exist in the pixel-domain of y. We thus introduce $c \in \mathbb{N}^{K \times M}$, the discretized version of b, with entries $c_{k,j} \in \{1, \ldots, N\}$.

The ansatz for our probabilistic graphical model is given by

$$p(y, c, b) = p(y|c)p(c|b)p(b), \tag{5.1}$$

where the factors are

$p(y\|c)$	appearance, data likelihood term,
$p(c\|b)$	Markov Random Field regularizer, determined by the shape prior and
$p(b)$	global shape prior.

In what follows we will detail each component, thereby completing the definition of our graphical model. Figure 5.2b depicts the components of this model.

Notation. Figure 5.2a illustrates our notation: Subindices $j = \{1, \ldots, M\}$ and $i = \{1, \ldots, N\}$ denote image columns and rows and $k \in \{1, \ldots, K\}$ denotes boundaries 1 to K, e.g. $b_{k,j} \in \mathbb{R}$ is the position of the kth boundary in column j. We use $\bullet$ to

include all possibilities for k, i, j: For example $b_{\bullet,j} \in \mathbb{R}^K$ are all boundary positions in column j. When possible, we will drop $\bullet$ and write b_j to denote $b_{\bullet,j}$. Finally, $b_{\setminus j}$ denotes all entries of b except those for column j.

Appearance $p(y|c)$. Given a segmentation c, we can assign class labels $x_{i,j} \in \mathcal{X}$ to each pixel from

$$\mathcal{X} = \{\mathcal{X}_l, \mathcal{X}_t\}, \qquad \mathcal{X}_l = \{l_1, \ldots, l_{K+1}\}, \quad \mathcal{X}_t = \{t_1, \ldots, t_K\},$$

where labels in $\mathcal{X}_l$ indicate affiliation of pixel $y_{i,j}$ to retina layers 1 to $K+1$ ($K = 10$ in this work) and labels in $\mathcal{X}_t$ to boundaries between them, c.f. Fig. 5.1. To obtain a mapping $c \mapsto x = x(c)$ consistent with physiology, we require c to satisfy the ordering constraint

$$1 \leq c_{1,j} < c_{2,j} < \cdots < c_{K,j} \leq N, \quad \forall j = 1, \ldots, M. \tag{5.2}$$

We will use a patch-based model. Since OCT scans display a large variability in brightness and contrast, each patch is normalized by subtracting its mean and projected onto a low-dimensional subspace using PCA. We define the probability of pixel $y_{i,j}$ belonging to the class $x_{i,j}$ as

$$p(y_{i,j}|x_{i,j}(c)) = \mathcal{N}(\tilde{y}_{i,j}; \mu_{x_{i,j}}, \Sigma_{x_{i,j}}), \tag{5.3}$$

where $\tilde{y}_{i,j}$ is the low-dimensional projection of the patch around pixel $y_{i,j}$. Note that in this definition, $p(y_{i,j}|x_{i,j}(c))$ does not integrate to 1 over the range of $y_{i,j}$. This is taken care of, when we introduce discriminative appearance terms in the next section. The class-conditional moments μ_x, Σ_x for all $x \in \mathcal{X}$ are learned offline. Regularized estimates for Σ_x are obtained by utilizing the graphical lasso approach [19], imposing sparsity on Σ_x^{-1}.

We define pixels $y_{i,j}$ to be conditionally independent given c. Furthermore, in Rathke et al. [20] it was shown that the model performs best when restricted to terms belonging to transition classes t_k. Thus $p(y|c)$ factorizes into

$$p(y|c) = \prod_{j=1}^{M} \prod_{i:x_{i,j} \in \mathcal{X}_l} p(y_{i,j}|x_{i,j}(c))^0 \prod_{i:x_{i,j} \in \mathcal{X}_t} p(y_{i,j}|x_{i,j}(c)), \tag{5.4}$$

where we do not take into account pixel with labels $\mathcal{X}^l = \{l_1, \ldots, l_{10}\}$.

Shape Prior $p(b)$. We use a shape model to represent typical shape variations, due to both biological variability as well as to the image formation process. We model b as random vector with Gaussian distribution

$$p(b) = \mathcal{N}(b; \mu, \Sigma), \tag{5.5}$$

where parameters μ and Σ again are learned offline. We regularize the estimation of Σ by probabilistic PCA [21], which assumes a linear Gaussian model for b:

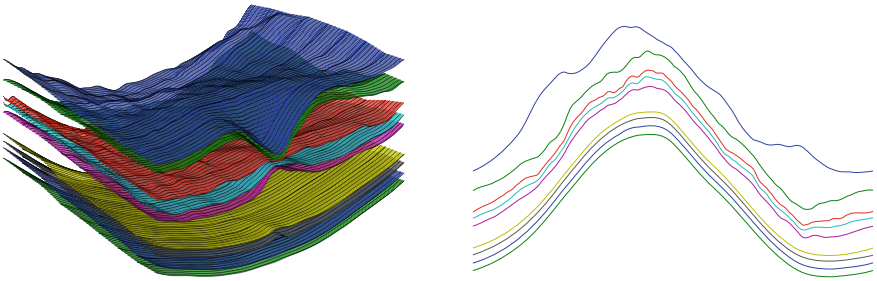

Fig. 5.3 Samples drawn from the the shape prior distribution $p(b)$ trained on volumes (left) and circular scans (right). Only one half of the volume is shown

$$b = Ws + \mu + \epsilon, \quad s \sim \mathcal{N}(0, I), \quad \epsilon \sim \mathcal{N}(0, \sigma^2 I). \tag{5.6}$$

The matrix $W \in \mathbb{R}^{K \cdot M \times q}$ maps the low-dimensional vector $s \in \mathbb{R}^q$ onto b. Each column of W denotes a certain shape variation that gets added to the mean shape μ. Given n training segmentations $X \in \mathrm{R}^{n \times M \cdot K}$, W is obtained by the first m eigenvectors of $\mathrm{cov}(X)$ weighted by the corresponding eigenvectors, and μ simply is $\overline{X}$. Figure 5.3 depicts samples drawn from two different $p(b)$, modeling fovea-centered 3-D volumes (left panel, with the fovea clearly visible) and circular scans (right panel).

A very useful feature of this representation of b is the fact, that both the covariance matrix as well as its inverse can be decomposed into a low-rank representation based on W, reducing complexity as well as memory requirements of many operations related to Σ and Σ^{-1}.

Shape-Induced Regularizers $p(c|b)$. Shape b and appearance y are combined via a Markov random field over the discrete variable c. It is composed of independent column-wise chain models, enabling parallel inference:

$$p(c|b) = \prod_{j=1}^{M} p(c_{\bullet,j}|b), \qquad p(c_{\bullet,j}|b) = p(c_{1,j}|b) \prod_{k=2}^{K} p(c_{k,j}|c_{k-1,j}, b). \tag{5.7}$$

The conditional distributions in (5.7) are specified in terms of b:

$$p(c_{1,j} = n|b) = \int_{n-\frac{1}{2}}^{n+\frac{1}{2}} p(b_{1,j} = \tau|b_{\setminus j})d\tau, \tag{5.8a}$$

$$p(c_{k,j} = n|c_{k-1,j} = m, b) = \int_{n-\frac{1}{2}}^{n+\frac{1}{2}} \int_{m-\frac{1}{2}}^{m+\frac{1}{2}} p(b_{k,j} = \tau|b_{\setminus j})p(b_{k,j} = \tau|b_{k-1,j} = \nu)d\tau d\nu. \tag{5.8b}$$

As a result the communication *across* image columns is induced not by the structure of the Markov random field but by the definition of its marginal distributions, conditioning on $b_{\setminus j}$. While the definition (5.8) does not take the ordering constraint (5.2) into account, this is done during inference (Section "Second Summand log $P(c|b)$ of $J(q_b, q_c)$" in Appendix).

2-D versus 3-D. Our description so far considered OCT scans of dimension two. Nevertheless, our approach is equally applicable to 3-D volumes. We use the very same notation, since adding additional B-Scans will only increase the number of image columns M. Similarly, the connectivity of the graphical model $p(y, c, b)$ can be transferred one-to-one.

5.2.2 Variational Inference

We wish to infer the posterior distribution

$$p(b, c|y) = \frac{p(y|c)p(c|b)p(b)}{p(y)}. \tag{5.9}$$

Since we lack a closed form solution and the problem at hand is high-dimensional, it is intractable. As a consequence we resort to an approximative scheme based on *variational inference*: Approximate the posterior by a tractable distribution $q(b, c)$ and minimize its distance to $p(b, c|y)$. We choose the factorized approximating distribution

$$q(b, c) = q_b(b)q_c(c). \tag{5.10}$$

This merely decouples the continuous shape prior Markov random field, but otherwise both components will be represented exactly, see the definition of q_b and q_c below. Similarity between q and p is measured by the Kullback-Leibler distance

$$\begin{aligned} \mathrm{KL}\left(q(b, c) \,\|\, p(b, c|y)\right) &= \int_b \sum_c q(b, c) \log \frac{q(b, c)}{p(b, c|y)} db \\ &= -\int_b \sum_c q(b, c) \Big(\log \left(p(y|c)p(c|b)p(b)\right) - \log p(y) - \log q(b, c) \Big) db\,. \end{aligned} \tag{5.11}$$

We use the marginal likelihood $\log p(y)$ to introduce *discriminative* appearance terms into the model, using

$$\log \frac{p(y|c)}{p(y)} = \log \frac{p(y|c)p(c)}{p(y)} - \log p(c) = \log p(c|y) - \log p(c).$$

where we used Bayes theorem [22, Eq. (A.3)] to equate $\frac{p(y|c)p(c)}{p(y)}$ with $p(c|y)$. Since $p(b)$ already contains prior knowledge about the shape of boundary positions, we assume an uninformative prior for c. Hence dropping $p(c)$ and taking into account the factorization of q, (5.11) results in the objective function

$$J(q_b, q_c) = -\int_b \sum_c q_b(b) q_c(c) \log\Big(p(c|y)\, p(c|b)\, p(b)\Big) db - H[q_b] - H[q_c], \tag{5.12}$$

where $H[q_b]$ and $H[q_c]$ are the entropies of q_b and q_c.

Definitions of q_c and q_b. For q_c we adopt the structure of $p(c|b)$, that is, written in a slightly different but equivalent form

$$q_c(c) = \prod_{j=1}^{M} q_c(c_{1,j}) \prod_{k=2}^{K} \frac{q_c(c_{k,j}, c_{k-1,j})}{q_c(c_{k-1,j})}. \tag{5.13}$$

For q_b we adopt the Gaussian model of b

$$q_b(b) = \mathcal{N}(b; \bar{\mu}, \bar{\Sigma}), \tag{5.14}$$

where the bar-notation distinguishes the parameters of q_b from those of $p(b)$.

Explicit Form of $J(q_b, q_c)$. Direct optimization of the objective (5.12) requires to sum over all combinations of c and integrating over b, and therefore is intractable as well. In order to obtain a tractable formulation, we have make use of the independence assumption $q(c, b) = q_b(b) q_c(c)$ (5.10) and rewrite $J(q_b, q_c)$ accordingly. The resulting expression derived in Section "Derivation of the Objective (5.15)" in Appendix reads

$$\begin{aligned} \min_{q_c, \bar{\mu}, \bar{\Sigma}} \; & -\sum_{j=1}^{M} \Big((q_{c;1,j})^T \theta_{1,j} + \sum_{k=2}^{K} \langle q_{c;k\wedge k-1,j}, \Theta_{k,j} \rangle + (q_{c;K,j})^T \theta_{K,j} \Big) - H[q_c] \\ & + \frac{1}{2} \langle K, \bar{\Sigma} + \bar{\mu}\bar{\mu}^T - 2\bar{\mu}\mu^T \rangle - \frac{1}{2} \log\det \bar{\Sigma} + C \end{aligned} \tag{5.15}$$

subject to normalization and marginalization constraint for q_c [23, p. 78]. The term $\log\det \bar{\Sigma}$ automatically enforces positive definiteness of $\bar{\Sigma}$, necessary for a valid Gaussian density q_b. Here terms $q_{c;k,j}$ and $q_{c;k\wedge k-1,j}$ denotes vectors containing all elements of distributions $q_c(c_{k,j})$ and $q_c(c_{k-1,j}, c_{k,j})$.

Broadly speaking, terms in the first row correspond to the optimization of q_c, and are derived in Sections "First Summand $\log P(c|y)$ of $J(q_b, q_c)$", "Second Summand $\log P(c|b)$ of $J(q_b, q_c)$" and "Entropy Terms $H[q_b]$ and $H[q_c]$" in Appendix, while terms in the second row correspond to the the optimization of q_b and are derived in Sections "Third Summand $\log P(b)$ of $J(q_b, q_c)$" and "Entropy Terms $H[q_b]$ and $H[q_c]$" in Appendix.

Optimization. We minimize (5.15) with respect to the parameters of q_b and the discrete distributions $q_{c;k,j}$ and $q_{c;k\wedge k-1,j}$. Since the factorization (5.10) decouples q_c and q_b, these optimizations can be carried out independently. Recall that q_c has a tree-structure in each image column, thus can be optimized using the sum-product algorithm, e.g. [24, Chap. 8.4.4]. The optimization with respect to $\bar{\mu}$ and $\overline{\Sigma}$ is given in closed form. Details about the optimization of q_b can be found in Section "Optimization with Respect to q_b" in Appendix. Both subproblems are *strictly* convex, thus by alternatingly optimizing with respect to q_b and q_c, the functional $J(q_b, q_c)$, being bounded from below over the feasible set of variables, is guaranteed to converge to some local minimum.

To initialize the optimization, we set q_b to a uniform distribution. Afterwards we initialize q_b given q_c and iteratively optimize until convergence.

5.3 Results

5.3.1 Segmentation Performance

5.3.1.1 Datasets

We will evaluate our approach on five datasets, two of which contain 2-D circular scans and the other three consist of 3-D volumes, c.f. Table 5.1. Besides in-house datasets, we also measure performance on two publicly available datasets, both published by Tian et al. [11, 12].

Both 2-D datasets consist of circular scans measured around the optical nerve head with a diameter of 12°, corresponding to approximately 3.4 mm, with 768 A-scans of depth resolution 3.87 µm/pixel and 496 pixel. While the first dataset consists of healthy scans, the second one contains eyes with glaucoma in different stages: A medical expert provided ground truth for the boundary separating NFL and GCL, crucial for Glaucoma, as well as a grading for the pathological scans: *pre-perimetric* glaucoma (PPG), meaning the eye is exhibiting structural symptoms of the disease but the visual field and sight are not impaired yet, as well as *early*, *moderate* and *advanced* primary open-angle glaucoma (PGE, PGM and PGA). Ground truth for the remaining eight boundaries was produced by the first author.

Table 5.1 Datasets used for performance evaluation

Type	Source	Subjects	# Surfaces	# Labeled B-Scans	Pathology
2-D	In-house	80	9	1	–
	In-house	55	9	1	Glaucoma
3-D	In-house	35	9	17	–
	Tian et al. [11]	10	6	10	–
	Tian et al. [12]	10	5	5	Mild RP

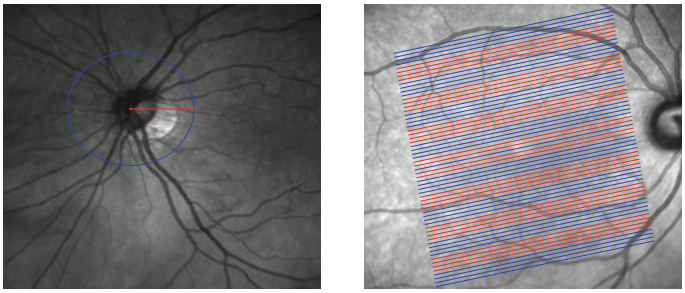

(a) 2-D circular scan (b) 3-D volume

Fig. 5.4 Fundus images that depict **a** the trajectory and radius of a 2-D circular scan centered around the optic nerve head and **b** the area covered by a 3-D volume consisting of 61 fovea-centered B-Scans. Alternating coloring illustrates the partitioning into 17 different regions. For each region a separate model is trained

The 3-D datasets consist of *fovea-centered* volumes. Our in-house dataset contains 35 subjects and each volume is composed of 61 B-Scans with 768×496 pixel. To exclude the nerve head, our model covers a smaller area of 500×496 pixel, corresponding to approximately 5.7×7.3 mm. Ground truth was obtained as follows: Each volume was divided into 17 regions, and a B-scan randomly drawn from each region was labeled. Figure 5.4b depicts the location of all 61 B-Scans and their partition into regions indicated by color. Both datasets of Tian et al. consist of 10 volumes each, with 10 and 5 B-Scans labeled. The ground truth provided is a subset of the surfaces labeled by us. The second dataset consists of subjects with mild non-proliferative diabetic retinopathy, an early stage of the disease with only small deformations, which our approach can handle easily.

5.3.1.2 Model Parameters

Table 5.2 summarizes the model parameters and the values they were set to for all experiments. For the appearance models we set α_{glasso} to 0.01, a parameter of the glasso approach [19] that controls the sparseness of $\Sigma^{-1}_{x_{i,j}}$. A patch-size of 15×15 and the projection onto the first $q_{\text{pca}} = 20$ eigenvectors resulted in smooth segmentation boundaries. Similar, we used $q_{\text{ppca}} = 20$ eigenvectors to build the shape prior model, after examining the eigenvalue spectrum of the empirical covariance matrix S.

Table 5.2 Set of model parameter values used throughout all experiments

Parameters	Appearance			Shape	Inference
	α_{glasso}	q_{pca}	Patch-Size	q_{ppca}	Variance of $p(b_{k,j}\|b_{\setminus j})$
Value	0.01	20	15×15	20	10

An important parameter during the inference is the variance of $p(b_{k,j}|b_{\setminus j})$, which balances the influence of appearance and shape. Artificially increasing this parameter results in broader normal distributions (that is wider stripes in Fig. 5.12b), which makes q_c less dependent of $\bar{\mu}$ during inference, and q_b less sensitive to q_c when estimating $\bar{\mu}$.

5.3.1.3 Error Measures and Test Framework

For each boundary as well as the entire scan we computed the unsigned distance in µm (1 px= 3.87 µm) between estimates $\hat{c}_{k,j} = \mathbb{E}_{q_c}[c_{k,j}]$ and manual segmentations $s_{k,j} \in \mathbb{R}$, that is

$$E^k_{\text{unsgn}} = \frac{1}{M}\sum_{j=1}^{M} |\hat{c}_{k,j} - s_{k,j}|, \qquad E_{\text{unsgn}} = \frac{1}{K}\sum_{k=1}^{K} E^k_{\text{unsgn}}\,.$$

For volumes we additionally averaged over all B-Scans in the volume.

Results were obtained via cross-validation: After splitting each data set into a number of subsets, each subset in turn is used as a test set, while the remaining subsets are used for training: We used 10-fold cross-validation for the healthy circular scans and leave-one-out cross-validation for our 3-D dataset, to maximize the number of training examples in each split. For the glaucoma dataset we trained a model on all healthy circular scans and similar for the Tian et al. datasets we used all our volumes for training, without any cross-validation.

5.3.1.4 Performance Evaluation

Results for all datasets are summarized in Table 5.3. Datasets are reported in the same order as in Table 5.1.

2-D. In general, boundaries 1 and 6–9 turned out to be easier to segment than boundaries 2–5. While boundary 1 has an easily detectable texture, boundaries 6–9 with their regular shape particularly profit from the shape regularization. Boundaries 2-5 on the other hand pose a harder challenge with their high variability of texture and shape. Figure 5.5a depicts an example segmentation.

For the pathological scans segmentation performance decreased with the progression of the disease. However, the average error for the first three classes was still smaller than or equal to one pixel. The decline in performance had several reasons: Since glaucoma is known to cause a thinning of the nerve fiber layer (NFL), the shape prior trained on healthy scans encounters difficulties adapting to very abnormal shapes. Furthermore, we observed a reduced scan quality for glaucomatous scans, also reported by others (e.g. [6, 7]). In the most advanced stage of the disease the NFL can vanish at some locations. Since this anomaly is not part of the training data, the model failed in these regions. We discuss possible modifications to overcome this problem in Sect. 5.4. The right panel in Fig. 5.5 shows an example of a PGA-type scan and its segmentation.

Table 5.3 Unsigned error for all datasets (c.f. Table 5.1) in μm (1px = 3.87 µm). Boundary numbers 1–9 correspond to Fig. 5.1. Results for other approaches are marked by a citation. Duan et al. [13] only provide the average result and detailed results for two boundaries

Dataset	Type	Avg.	1	2	3	4	5	6	7	8	9
2-D	Healthy	**2.92**	2.06	4.68	3.67	3.31	3.30	2.10	2.34	2.81	2.01
2-D	PPG	**3.64**	2.66	6.66	4.57	4.43	4.34	2.67	2.59	2.82	2.06
	PGE	**3.97**	3.76	5.65	5.37	5.78	4.40	2.76	2.95	3.40	1.63
	PGM	**4.00**	4.51	6.74	5.49	5.44	4.15	2.88	2.21	2.94	1.64
	PGA	**5.62**	6.53	9.95	8.80	8.30	5.05	2.99	2.42	4.19	2.36
3-D	Healthy	**2.46**	1.36	3.32	3.17	3.23	3.27	1.61	1.86	2.27	2.07
3-D	Healthy	3.17	2.93	**3.24**	**3.63**	3.92	4.00	1.65	–	**3.43**	**2.61**
		3.87 [11]	**2.67**	4.34	3.73	**3.89**	5.18	2.10	–	6.23	2.83
		3.10 [13]	–	–	–	–	**3.55**	**1.57**	–	–	–
3-D	Mild RP	**4.08**	4.39	**4.15**	3.84	–	**4.65**	–	–	–	**3.37**
		4.48 [12]	**3.70**	4.49	3.84	–	5.75	–	–	–	4.63

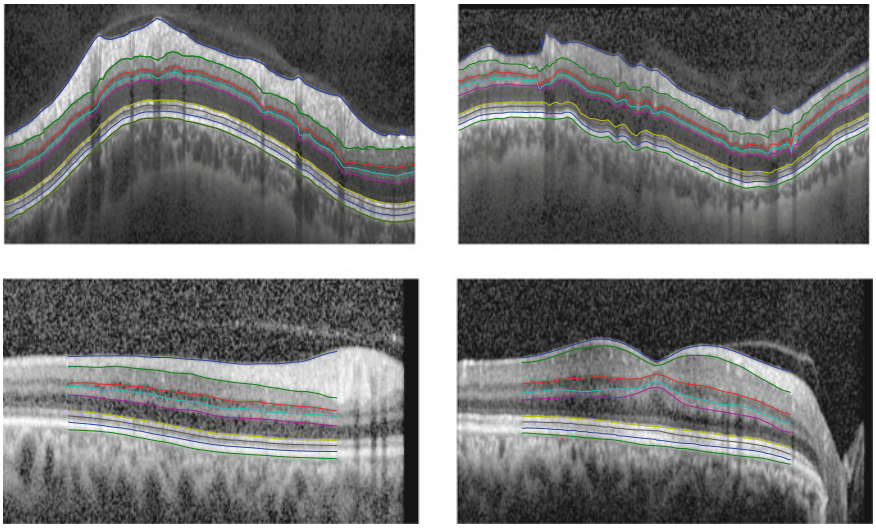

Fig. 5.5 Top panel: (Left) Segmentation of a healthy 2-D circular scan and (right) an advanced glaucomatous circular scan. Bottom panel: Two B-Scans of subject 6 from the dataset with mild diabetic retinopathy [12]

3-D. In contrast to 2-D scans, the labeling of OCT volumes is very time consuming, hence our dataset only consisted of 35 samples. Thus we were left with less data points to train a shape model of much higher dimension. Consequently, we observed a reduced ability of $p(b)$ respectively $q_b(b)$ to generalize well to unseen scans. We tackled this problem by suppressing the connectivity between different B-scans inside the volume, which corresponds to a block-diagonal covariance matrix Σ, where each block is obtained separately using PPCA. This significantly reduced the amount of parameters that had to be determined, and improved accuracy significantly.

We tested our approach on our in-house dataset as well as the two datasets published by Tian et al. For the latter two we had to deal with the problem, that no position inside the volume was given for the B-Scans. Since this information in necessary to pick the correct shape prior, we used the following approach: We run the model for *each* region 1–17 (see Fig. 5.4b for the distribution of regions) and then picked the region (a) with the lowest error (supervised) and (b) with the highest model likelihood (unsupervised). This gave an upper and lower bound on the true error, and we averaged over these two to obtain the final result.

In Table 5.3 we also report results from Tian et al., which we could outperform in both datasets, as well as those of Duan et al. [13] for the first Tian dataset, which are very good as well. Unfortunately, they only provided specific results for two boundaries besides the average error, so its difficult to fully grasp their strong and weak points. For all 3-D datasets results are worst for the retinopathy dataset due to its pathological nature. Still, the segmentation of our approach is fairly accurate, with an average error of around 1 pixel.

5.3.2 Pathology Detection

5.3.2.1 Model Likelihoods

A key property of our model is the *inference of full probability distributions over segmentations* q_c and q_b, instead of only modes thereof. Figure 5.6 shows boxblots of four terms (b–e) of the objective function $J(q_b, q_c)$ and compares them to the unsigned error (a), broken down for the healthy scans as well as the different stages of glaucoma. Singleton entropy (b) and mutual information (c) are the two summands of the negative entropy of q_c, see (5.33). The data (d) and shape (e) terms represent the first two summands of $J(q_b, q_c)$ (5.12), presented in details in the Sections "First Summand log $P(c|y)$ of $J(q_b, q_c)$" and "Second Summand log $P(c|b)$ of $J(q_b, q_c)$" in Appendix.

The shape term, which measures how much the data-driven distribution q_c differs from the shape-driven expectation $\mathbb{E}_{q_b}[\log p(c|b)]$, is highly discriminative between healthy and pathological scans. The data term on the other hand measures how well the appearance terms fit the actual segmentation and correlates well with the unsigned error.

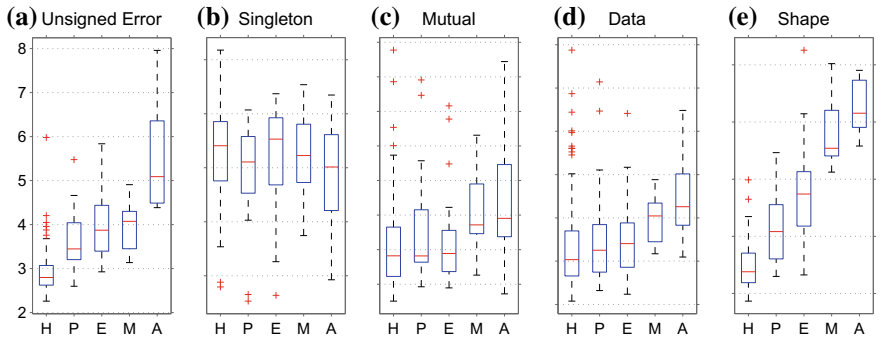

Fig. 5.6 Different terms (**b**–**e**) of the objective function $J(q_b, q_c)$ and the unsigned error (**a**) for healthy (**H**) as well as glaucomatous scans (**P**PG, PG**E**, PG**M** and PG**A**). While "Shape" is very discriminative for glaucomatous scans, "Mutual" and "Data" correlate well with the unsigned error

5.3.2.2 Abnormality Detection

Glaucoma detection. A state-of-the-art method for the clinical diagnosis of glaucoma is based on NFL thickness, averaged for example over the whole scan or one of its four quadrants (superior, inferior, temporal and nasal) [25, 26]. We will compare this methodology to an approach based on the shape term presented in the previous section. Estimates of the NFL thickness were obtained from the Spectralis device software, version 5.6. Using the setup of Bowd et al. [25], we investigated specificities of 70 and 90% as well as the area under the curve (AUC) of the receiver operating characteristic (ROC).[1] In all cases, our shape-based discriminator performed at least as good as the best thickness-based one. Especially for pre-perimetric scans, which feature only subtle structural changes, our approach improves diagnostic accuracies significantly: Fig. 5.7a provides ROC curves of the two *overall* best performing NFL measures and our shape-based measure for this class.

Global Quality. We obtained a *global* quality measure, by combining the mutual information and the shape term. Given the values for all scans, we re-weighted both terms into the ranges [0, 1] and took their sum. Thereby we could establish a quality index that had a very good correlation of 0.82 with the unsigned segmentation error. See Fig. 5.7b for a plot of all quality index/error pairs and a linear fit thereof. The estimate of this fit and the true segmentation error differs on average by only 0.51 μm. This shows that the model is able to additionally deliver the quality of its segmentation.

Local Quality. Finally, we determined a way to distinguish *locally* between regions of high and low model confidence. This could for example point out regions where a manual (or potentially automatic) correction is necessary. To this end we examined

[1] The AUC can be interpreted as the probability, that a random pathological scan gets assigned a higher score than a random healthy scan.

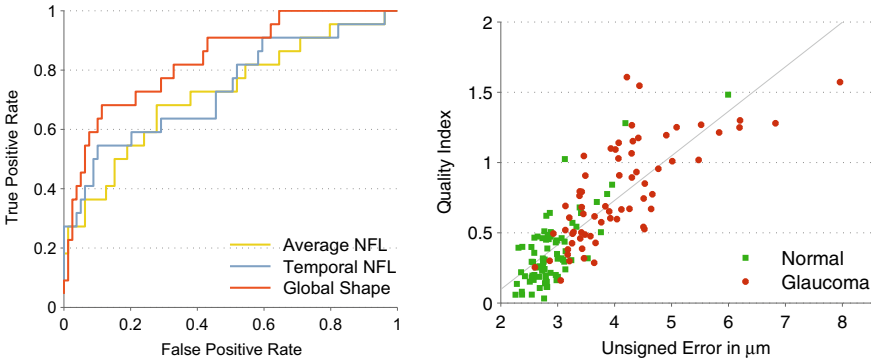

Fig. 5.7 Left: ROC curves for the two overall best performing NFL-based classifiers and our shape prior based approach for the earliest stage of glaucoma. Right: High correlation of our quality estimation index, obtained by comparing terms (c) and (e) from Fig. 5.6 to the actual unsigned error Fig. 5.6a. We see a large correlation between both measures

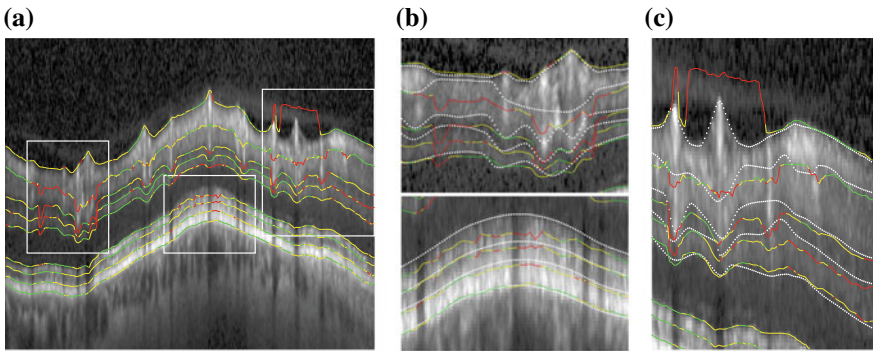

Fig. 5.8 **a** An advanced primary open-angle glaucoma scan and the segmentation thereof ($E_{\text{unsgn}} = 6.81\,\mu\text{m}$), augmented by the local quality estimates of the model, with red representing highest uncertainty. **b** and **c** Close-ups of the three areas, the model is (correctly) most uncertain about. White dotted lines represent ground truth

the correlation of the data terms with the unsigned error. We calculated its mean for instances with segmentation errors smaller than 0.5 and bigger than 2 pixels. This yielded three ranges of confidence in the quality of the segmentation. For each image we fine-tuned these ranges by dividing by max(Quality Index(CurrentImage), 1).

Figure 5.8a shows a PGA-type scan with annotated segmentation, whose error is 6.83 µm. The advanced thinning of the NFL and the partly blurred appearance caused the segmentation to fail in some parts of the scan. Close-ups (b) and (c) show that the model correctly identified those erroneously segmented regions. The average errors of the three categories are 4.67, 5.43 and 18.36 µm respectively.

5.3.2.3 Pathology Classification

Srinivasan et al. [27] published a dataset of 45 volumetric scans, composed of 15 healthy scans, and 15 scans affected by diabetic macular edema (DME) and age-related macular degeneration (AMD) respectively. Since deformations for these pathologies can become very large, our model cannot adapt to them. Figure 5.9 displays segmentations of typical representatives for each class with overlaid confidence estimates (green not shown explicitly). The red and yellow areas exhibit characteristic patterns for both pathologies, which we can use to train a classifier.

For each volume we segmented all B-Scans, calculated the confidence values and averaged them over regions 1–17 (Fig. 5.4b). In this way we obtained a feature vector of fixed size, while the number of B-Scans varied between 31 and 97 throughout the dataset. Using PCA, we then found more compact representations and finally concatenated all low-dimensional vectors of one volume. Having obtained a feature vector for each volume, we then removed one example from each class and used the remaining volumes to train a random forest and predicted the classes for the leave-out set of 3 scans. We repeated this procedure for the whole dataset.

Our results are given in Table 5.4 together with the results of three published classification approaches, which rely on different feature descriptors from computer vision. While our approach classifies one volume wrong, [27, 28] make two mistakes. And while Wang et al. [29] also only make one mistake, they prefilter the AMD and

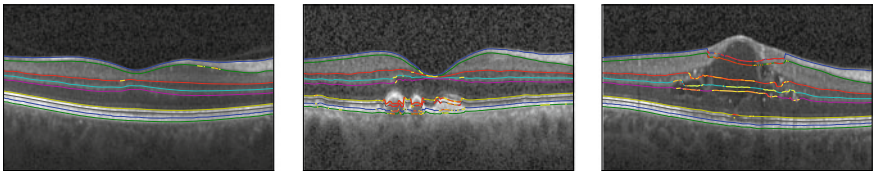

Fig. 5.9 Segmentations of a healthy and two pathological scans. While the segmentation fails in pathological areas, the model detects those failures (yellow, orange and red markings). These patterns can be used to train a classifier for the detection of AMD and DME

Table 5.4 Classification results of various approaches for the dataset of Srinivasan et al. [27]. Our approach only makes one mistake, classifying one DME volume as AMD, outperforming or performing on par with actual classification approaches

	Normal	AMD	DME	Method[a]
Our approach	15/15	15/15	14/15	Model likelihoods + RF
Lemaitre et al. [28]	13/15	–	15/15	LBP-Features + RF
Srinivasan et al. [27]	13/15	15/15	15/15	HOG-Features + SVM
Wang et al. [29]	14/15	15/15	15/15	LCP-Features + SVM

[a] *LBP* linear binary patterns, *HOG* histogram of oriented gradients, *LCP* linear configuration pattern, *SVM* support vector machine, *RF* random forest

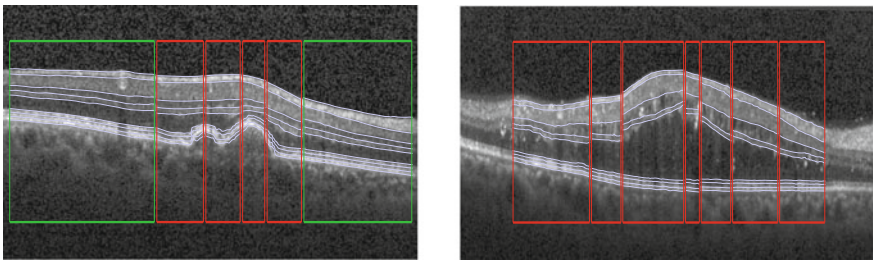

(a) AMD (b) DME

Fig. 5.10 Preliminary results for our proposed model extension using SPNs, demonstrating the potential of the approach. Red windows indicate a modified shape prior model $\theta^{\text{ill}_i}_{a,b}$ (c.f. (5.16))

DME datasets from all B-Scans without deformations, a step that requires human interaction.

5.4 Segmenting Pathological Scans

In this section we propose an extension of our probabilistic model in order to take also into account retina images with pathologies, characterized by strong local deformations of the normal retina structure. While using the prior probability distribution that was learned from healthy data (Sect. 5.2.1) helps in segmenting healthy OCT scans, it can be detrimental for scans including pathological structure, since it makes segmentation more robust against noise but on the other hand less adaptable to irregularities caused by pathologies. This problem can be addressed by augmenting the shape prior by a set of *local* priors, which can be selected in a *globally optimal* way using the principle of maximum-likelihood and dynamic programming. Figure 5.10 shows two preliminary results.

Setup. We assume that models of pathological structure are translation invariant, local and approximately independent. This assumption is appropriate for actual retinal scans, since pathologies result in local deformations and appear at multiple horizontal positions of the image. Independence and locality allow to factorize the full distribution $p(y, b, c)$ into local distributions. Translation invariance implies that the same modification can be applied at every horizontal position in the scan.

Recall that the shape prior W in Eq. (5.6) represents typical shape variations of healthy retina layers. In order to extend the graphical model to local pathological deformations, we define a set of I translation-invariant pathology-specific modes $\{W^{ill_1}, W^{ill_2}, ..., W^{\text{ill}_I}\}$ and obtain a model of local deformations by adding these translation-invariant modes to W. The modified prior in the horizontal region $[a, b]$ between columns a and b, and with pathological model W^{ill_i}, is determined by

$$\theta^{\text{ill}_i}_{a,b} := \left(W_{a,b}\ W^{\text{ill}_i}_{1,b-a}\right), \qquad \theta^{\text{healthy}}_{a,b} := W_{a,b}, \qquad i \in \{1, \ldots, I\}. \tag{5.16}$$

Here subscripts a, b indicate the truncation of W to entries of columns between a and b. Truncating the modes in W corresponds to taking the marginal Gaussian model over the corresponding area. Also, note that the subscript $1, b-a$ indicates the translation invariance of our pathological shape modifications.

Now, let $L_{a,b}(\theta^l_{a,b})$ be the log-probability of the retina segmentation for region $[a, b]$ for some $l \in \{\text{healthy}, \text{ill}_1, \text{ill}_2, \ldots, \text{ill}_I\}$:

$$L_{a,b}(\theta^l_{a,b}) := \log q\left(c_{a,b}, b_{a,b} | \theta^l_{a,b}\right). \tag{5.17}$$

Here we made explicit the dependency on $\theta^l_{a,b}$ of q. Furthermore, let $X = \{x_1, x_2, ..., x_K, M\}$ denote the partition of the M columns into $K+1$ regions, and let $\theta = \{\theta^{l_1}_{1,x_1}, \theta^{l_2}_{x_1,x_2}, \ldots, \theta^{l_K}_{x_K,M}\}$ denote a corresponding set of modified shape priors. Then, exploiting the independence property, the log-probability for the full scan can be written as sum of local terms:

$$L_{1,M}(\theta, X, K) = L_{1,x_1}(\theta^{l_1}_{1,x_2}) + L_{x_1,x_2}(\theta^{l_2}_{x_1,x_2}) + \ldots + L_{x_K,M}(\theta^{l_K}_{x_K,M}). \tag{5.18}$$

Maximum Likelihood. The objective is to find the optimal combination of regions and corresponding priors θ:

$$\max_K \max_X \max_\theta \; L_{1,M}(\theta, X, K). \tag{5.19}$$

The global optimum of this combinatorial problem can be found with *dynamic programming*. To this end, let $L^*_{a,b}$ denote the optimal selection of X and θ in region $[a, b]$ which satisfies the recursion (cf. Fig. 5.11)

$$L^*_{a,b} = \max\left(\max_{x\in(a,b)}\left(L^*_{a,x} + L^*_{x,b}\right), \max_{l_i\in\{\text{healthy},\text{ill}_1,\text{ill}_2,\ldots,\text{ill}_I\}} L_{a,b}(\theta^{l_i}_{a,b})\right). \tag{5.20}$$

This equation expresses $L^*_{a,b}$ as the maximum between the best single model over area $[a, b]$ and the optimal factorization in two adjacent areas $L^*_{a,x}$ and $L^*_{x,b}$. To compute

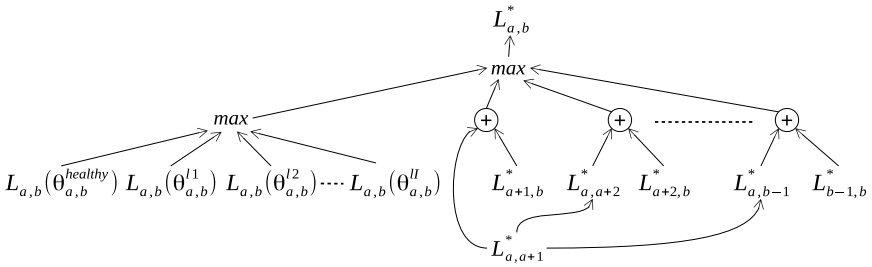

Fig. 5.11 Graphical representation of Eq. (5.20). The quantity $L^*_{a,a+1}$ is efficiently reused in several computations. This structure implements a Sum-Product Network, as discussed in Sect. 5.5.2

$L^*_{a,b}$ for regions of width $w = b - a$, we need quantities $L^*_{a,x}$, $L^*_{x,b}$ for all regions of smaller width. Given these, the complexity is dominated by $\mathcal{O}(I)$ evaluations of the base model to determine the rightmost maximum in (5.19).

This leads to an iterative algorithm: for increasing $w \in \{w_{min}, 2w_{min}, \ldots, M\}$, compute $L^*_{a,b}$ for all regions of that width. Finally, $L^*_{1,M}$ is the optimal selection of θ, X, K over the whole image. The total number of base model evaluations is $\mathcal{O}(I\ (M/w_{min})^2)$, which is tractable for sufficiently large w_{min}.

5.5 Discussion

5.5.1 Conclusion

We presented a probabilistic approach for the segmentation of retina layers in OCT scans. The approach entails to infer a full posterior distribution $p(b, c|y)$ that we evaluate using a variational method. This turned out to be beneficial in several ways: Since the inference scheme comprises efficient subproblems, segmenting one B-Scan only requires about 2 s. Furthermore, the quality of the computed segmentation can be assessed and further used for pathology detection. The segmentation performance was very good for five datasets, even in the presence of mild pathologies.

5.5.2 Prospective Work

While our major focus has been on healthy data and mild pathologies so far, we outlined in Sect. 5.4 ongoing work about an adaption of our model to more severe pathological deformations. We conclude this section by briefly discussing two major aspects of corresponding ongoing and future work.

Interpretation as Sum-Product Network. The algorithm of Sect. 5.4 has an interpretation as maximum a posteriori (MAP) inference in a probabilistic architecture called Sum-Product Network (SPN), introduced in [30]. This connection may support future extensions and applications of our model.

Let X be a set of continuous variables. A SPN $S(X)$ is a directed acyclic graph with sums and products as internal nodes and probability distributions $\{L_k(X_k)\}$ as leaves, where $X_k \subseteq X$. In SPNs, product nodes represent factorizations and sum nodes represent mixtures of the distributions rooted in children nodes, thus creating a hierarchical mixture model. Inference has linear costs in the number of edges, and it is performed by first evaluating the leaf distributions and then evaluating the internal nodes from the leaves to the root. MAP inference is similarly performed after replacing the sum operator by the max mapping.

Our algorithm can be directly interpreted as MAP inference on a SPN performed in logarithmic space, by substituting the sums with products in Eq. (5.18)

(since $\ln \prod(\cdot) = \sum \ln(\cdot)$) and leaving the max nodes unchanged (since $\ln \max(\cdot) = \max \ln(\cdot)$). This allows us to treat our model as a fully fledged tractable probabilistic model. In particular, the posterior probability of a leaf node $L_k \in S$ is given by $L_k(X_k)\frac{\partial S(X)}{\partial L_k}$, where $L_k(X_k)$ denotes the value of L_k for evidence X_k, and $\frac{\partial S(X)}{\partial L_k}$ denotes the derivative of the SPN value $S(X)$ with respect to leaf node L_k, which can be computed in time that is linear in the number of SPN edges [30]. In our case, leaf models constitute the retina segmentation model, and consequently *posterior marginals* for these models can be computed efficiently, to assign a probability to each choice of segmentation and priors. This property can be used to evaluate the confidence of a segmentation and to suggest explicitly alternative segmentations weighted by the respective probability - an aspect to be explored in our future work.

Learning Local Pathological Priors. There are various ways, how pathology specific modes can be obtain. Given a sufficient amount of labeled data, they can be learning in a *supervised* fashion. In the *semi-supervised* case, one can hand-design pathological modes according to the known properties of the pathology, as was done in our preliminary experiments. For example, pathological modes for the circular-shaped fluid deposits in AMD are very similar to sinusoidal functions.

Finally, it is also possible to learn priors in a completely *unsupervised* way by defining a parametric shape model, e.g. a spline, perform a grid-search over parameter configurations and select those splines that yielded the best fits in terms of the likelihood of the segmentations. While computationally expensive, this can be performed offline, with only the best k splines used in the final model.

Acknowledgements Support of the German Science Foundation, grant GRK 1653, is gratefully acknowledged.

Appendix

Derivation of the Objective (5.15)

In this section we will perform the derivations that are needed to rewrite the objective $J(q_b, q_c)$ in (5.12) into the final optimization problem (5.15).

First Summand $\log P(c|y)$ of $J(q_b, q_c)$

The term $p(c|y)$ does not depend on b, so q_b integrates out. Moreover, using the structure of q_c and $p(c|y)$, we have

$$-\int_b \sum_c q_b(b) q_c(c) \log p(c|y) = -\sum_{j=1}^{M} \sum_{c_{\bullet,j}} q_c(c_{\bullet,j}) \sum_{i=1}^{N} \log p(x_{i,j}(c_{\bullet,j})|y_{i,j}), \tag{5.21}$$

where the second sum takes into account all combinations of boundary assignments for $c_{\bullet,j}$. Since we only use terms for labels in $\mathcal{X}^t$ and each label depends only on one $c_{k,j}$, we can further simplify (5.21) into

$$-\sum_{j=1}^{M}\sum_{k=1}^{K} q_c(c_{k,j}) \log p(x_{c_{k,j},j} = t_k | y_{c_{k,j},j}) = -\sum_{j=1}^{M}\sum_{k=1}^{K} q_{c;k,j}^T \psi_{k,j}, \tag{5.22}$$

where $\psi_{k,j} \in \mathbb{R}^N$ contains all log-probabilities for boundary t_k in column j. Here $q_{c;k,j} \in \mathbb{R}^N$ denotes the full discrete probability for all image rows (c.f. (5.13)). If we would also consider appearance terms belonging to layers l_k, the derivation would be similar as for the term $p(c|b)$ in the next section.

Second Summand $\log P(c|b)$ of $J(q_b, q_c)$

We consider the expectation of $p(c|b)$:

$$-\int_b \sum_c q(b,c) \log p(c|b) = -\mathbb{E}_{q_c}\Big[\mathbb{E}_{q_b}[\log p(c|b)]\Big]. \tag{5.23}$$

We begin by giving expressions for the conditional densities of $p(b)$ defined in (5.8). Using the standard form for conditional normal distributions (e.g. [22, Eq. (A.6)]), the moments of $p(b_j|b_{\setminus j})$ are

$$\begin{aligned} p(b_j|b_{\setminus j}) &= \mathcal{N}(b_j; \mu_{j|\setminus j}, \Sigma_{j|\setminus j}), \\ \mu_{j|\setminus j} = \mu_j - \Sigma_{j|\setminus j} K_{j,\setminus j}(b_{\setminus j} - \mu_{\setminus j}), &\qquad \Sigma_{j|\setminus j} = (K_{jj})^{-1}. \end{aligned} \tag{5.24}$$

The marginal density $p(b_{k,j}|b_{\setminus j})$ is obtained by restricting the moments of (5.24) to k. The moments of $p(b_{k,j}|b_{k-1,j})$ are defined in the same way.

Expectation with respect to q_b. We note that terms $p(b_j|b_{\setminus j})$ depend on $b_{\setminus j}$ via $(\mu_{j|\setminus j})_k$. It suffices to adopt the most crude numerical integration formula (integrand = step function) to make this dependency explicit: $\int_{a-1/2}^{a+1/2} f(x)dx \approx f(a)$. Applying the logarithm, we obtain a representation that is convenient for the evaluation of $\int_b \cdots q_b db$. For (5.8a) we have:

$$\begin{aligned} \mathbb{E}_{q_b}[\log p(c_{1,j} = n|b)] &= \mathbb{E}_{q_b}[\log p(b_{1,j} = n|b)] \\ &= C - \frac{1}{2(\Sigma_{j|\setminus j})_{1,1}}\Big(n^2 - 2n\mathbb{E}_{q_b}\left[(\mu_{j|\setminus j})_1\right] + \mathbb{E}_{q_b}\left[\left((\mu_{j|\setminus j})_1\right)^2\right]\Big). \end{aligned} \tag{5.25}$$

Replacing $(\mu_{j|\setminus j})_1$ with its definition (5.24) and abbreviating the kth row of $\Sigma_{j|\setminus j} K_{j,\setminus j} \in \mathbb{R}^{K\times K\cdot(M-1)}$ by the column vector λ_k^j yields

$$= C - \frac{1}{2(\Sigma_{j|\setminus j})_{1,1}} \left(2(n - \mu_{1,j})(\lambda_1^j)^T \mathbb{E}_{q_b}[b_{\setminus j}] + (\lambda_1^j)^T \left(\mathbb{E}_{q_b}[b_{\setminus j} b_{\setminus j}^T] - 2\mu_{\setminus j} \mathbb{E}_{q_b}[b_{\setminus j}]\right) \lambda_1^j\right),$$

where the moments of $b_{\setminus j}$ with respect to q_b are

$$\mathbb{E}_{q_b}[b_{\setminus j}] = \bar{\mu}_{\setminus j}, \qquad \mathbb{E}_{q_b}[b_{\setminus j} b_{\setminus j}^T] = \overline{\Sigma}_{\setminus j,\setminus j} + \bar{\mu}_{\setminus j} \bar{\mu}_{\setminus j}^T . \tag{5.26}$$

Terms in (5.8b)

$$\begin{aligned} &\mathbb{E}_{q_b}[\log p(c_{k,j} = n | c_{k-1,j} = m, b)] \\ &\quad = \mathbb{E}_{q_b}[\log(p(b_{k,j} = n | b_{\setminus j}) p(b_{k,j} = n | b_{k-1,j} = m))], \end{aligned} \tag{5.27}$$

are products of two Gaussians. The dependency on $b_{\setminus j}$ is again due to $p(b_{k,j} = n | b_{\setminus j})$. The product of two Gaussians is again Gaussian, e.g. [22, Eq. (A.7)], and evaluating (5.27) in the same manner as above yields a similar result as for (5.25). We define matrices $\Omega_{k,j}$ and vectors $\omega_{1,j}$ by

$$\begin{aligned} (\Omega_{k,j})_{m,n} &= \mathbb{E}_{q_b}[\log p(c_{k,j} = n | c_{k-1,j} = m, b)], \\ (\omega_{1,j})_n &= \mathbb{E}_{q_b}[\log p(c_{1,j} = n | b)], \end{aligned} \tag{5.28}$$

for $k = 2, \ldots, K$, $j = 1, \ldots, M$ and $1 \leq m \leq n \leq N$. To enforce ordering constraints (5.2), we set all entries of $\Omega_{k,j}$ for $m > n$ to zero. Figure 5.12 illustrates how the transition matrix $\Omega_{k,j}$ (right panel) is composed of the two components $\mathbb{E}_{q_b}[\log p(b_{k,j} | b_{k-1,j})]$ (left panel) and $\mathbb{E}_{q_b}[\log p(b_{k,j} | b_{\setminus j})]$ (middle panel). While the first term provides local information about the distance of two neighboring boundaries in one column, the latter provides global information about the expected position of $b_{k,j}$ taking into account $\mathbb{E}_{q_b}[b_{\setminus j}]$, the expected boundary positions at all other image columns given q_b.

Expectation with respect to q_c. The Markov random field factorizes over columns. Furthermore, each term in $p(c|b)$ depends on at most two $c_{k,j}$. We thus have

Fig. 5.12 Illustration of a transition matrix $\Omega_{k,j}$ (**c**) and the local (**a**) and global (**b**) shape information it is composed of

$$
\begin{aligned}
-\int_b \sum_c q(b,c)\log p(c|b) &= -\sum_{j=1}^{M}\sum_{c_{\bullet,j}} q_c(c_{\bullet,j})\mathbb{E}_{q_b}[\log p(c_{\bullet,j}|b)] \\
&= -\sum_{j=1}^{M}\sum_{c_{1,j}=1}^{N} q_c(c_{1,j})\mathbb{E}_{q_b}[\log p(c_{1,j})|b)] \\
&\quad + \sum_{k=2}^{K}\sum_{c_{k,j}=1}^{N}\sum_{c_{k-1,j}=1}^{N} q_c(c_{k,j},c_{k-1,j})\mathbb{E}_{q_b}[\log p(c_{k,j}|c_{k-1,j},b])
\end{aligned}
\tag{5.29}
$$

Finally, using the notation introduced in (5.28), we can rewrite (5.29) in vectorized form as

$$
-\sum_{j=1}^{M}\left((q_{c;1,j})^T\omega_{1,j} + \sum_{k=2}^{K}\langle q_{c;k\wedge k-1,j}, \Omega_{k,j}\rangle\right). \tag{5.30}
$$

Third Summand $\log P(b)$ of $J(q_b, q_c)$

We use the relation

$$
a^T Ba = \mathrm{tr}(aa^T B) = \langle aa^T, B\rangle,
$$

valid for symmetric matrices, where $\langle\cdot,\cdot\rangle$ denotes here the inner product over matrices. Making use of (5.26), we obtain

$$
-\int_b q_b(b)\log p(b)db = C + \frac{1}{2}\langle\Sigma^{-1}, \overline{\Sigma} + \bar{\mu}\bar{\mu}^T - 2\bar{\mu}\mu^T + \mu\mu^T\rangle. \tag{5.31}
$$

Entropy Terms $H[q_b]$ and $H[q_c]$

Finally, we make explicit the entropies of q_b and q_c. For the normal distribution q_b we have that

$$
-H[q_b] = \int_b q_b(b)\log q_b(b)db = C - \frac{1}{2}\log|\overline{\Sigma}|, \tag{5.32}
$$

see for example [22, Eq. (A.20)]. For the negative entropy of q_c, making use of the structure of q_c, we have

$$
\begin{aligned}
-H[q_c] = \sum_{j=1}^{M}\Bigg(&\sum_{k=1}^{K}\sum_{c_{k,j}} q_c(c_{k,j})\log q_c(c_{k,j}) \\
&+ \sum_{k=2}^{K}\sum_{c_{k-1,j}}\sum_{c_{k,j}} q_c(c_{k,j},c_{k-1,j})\log\frac{q_c(c_{k,j},c_{k-1,j})}{q_c(c_{k-1,j})q_c(c_{k,j})}\Bigg).
\end{aligned}
$$

Optimization with Respect to q_b

The previous section derived the terms of the objective function $J(q_b, q_c)$. We now turn to the problem of optimizing $J(q_b, q_c)$ with respect to $\bar{\mu}$ and $\overline{\Sigma}$, the parameters of q_b. Recall that in (5.28) we defined vectors $\omega_{1,j}$ and matrices $\Omega_{k,j}$ whose entries were all depend on $\bar{\mu}$ and $\overline{\Sigma}$. More dependencies are due to the expectation of $p(b)$ with respect to q_b (5.31) and the entropy of q_b (5.32). Inspecting all these terms, we see that $\bar{\mu}$ and $\overline{\Sigma}$ are independent from each other, so we can optimize them separately.

Optimization With Respect to $\overline{\Sigma}$. Optimizing (5.15) with respect to $\overline{\Sigma}$ yields

$$\min_{\overline{\Sigma}} -\frac{1}{2}\log|\overline{\Sigma}| + \frac{1}{2}\langle K + \tilde{P}, \overline{\Sigma}\rangle, \tag{5.33}$$

which has the closed-form solution: $\overline{\Sigma} = (K + \tilde{P})^{-1}$. The newly introduced matrix $\tilde{P}$ contains the dependencies of terms $\omega_{1,j}$ and $\Omega_{k,j}$ on $\overline{\Sigma}$ as detailed next.

Derivation of $\tilde{P}$. Only considering terms in the nth entry of $(\omega_{1,j})$ that depend on $\overline{\Sigma}$, we obtain

$$(\omega_{1,j})_n(\overline{\Sigma}) = -\frac{1}{2(E_{j|\setminus j})_{1,1}}(\lambda_1^j)^T\,\overline{\Sigma}_{\setminus j,\setminus j}\lambda_1^j,$$

and accordingly for $(\Omega_{k,j})_{m,n}(\overline{\Sigma})$. We defined λ_k^j in Sect. A.1.2 as the kth row of $\Sigma_{j|\setminus j}K_{j,\setminus j}$, hence as a column vector of length $K\cdot(M-1)$. We introduce the extended version $\tilde{\lambda}_k^j$ of length KM, padded with zero entries such that

$$(\tilde{\lambda}_k^j)^T\,\overline{\Sigma}\,\tilde{\lambda}_k^j = (\lambda_k^j)^T\,\overline{\Sigma}_{\setminus j,\setminus j}\lambda_k^j. \tag{5.34}$$

Note that entries of $(\Omega_{k,j})(\overline{\Sigma})$ and $(\omega_{1,j})(\overline{\Sigma})$ are independent of m and n and therefore independent of q_c. Thus

$$(q_{c;1,j})^T\omega_{1,j}(\overline{\Sigma}) = 1\cdot\omega_{1,j}(\overline{\Sigma}), \qquad \langle q_{c;k\wedge k-1,j}, \Omega_{k,j}(\overline{\Sigma})\rangle = 1\cdot\Omega_{k,j}(\overline{\Sigma}).$$

Using $b^TBb = \langle bb^T, B\rangle$, we obtain for (5.30)

$$\begin{aligned}
&-\sum_{j=1}^{M}\Big((q_{c;1,j})^T\omega_{1,j}(\overline{\Sigma}) + \sum_{k=2}^{K}\big\langle q_{c;k\wedge k-1,j}, \Omega_{k,j}(\overline{\Sigma})\big\rangle\Big)\\
&\quad= \frac{1}{2}\sum_{j=1}^{M}\sum_{k=1}^{K}\left\langle\frac{1}{(E_{j|\setminus j})_{k,k}}\tilde{\lambda}_k^j(\tilde{\lambda}_k^j)^T, \overline{\Sigma}\right\rangle\\
&\quad= \frac{1}{2}\langle\tilde{P}, \overline{\Sigma}\rangle.
\end{aligned}$$

Since $\tilde{P}$ is independent of q_c and depends only on the sufficient statistics of $p(b)$, we do not have to update it while optimizing $J(q_b, q_c)$. Furthermore, since it is composed of linear combinations of submatrices of K, it can be expressed solely in terms of W and $\sigma^2 I$.

Optimization With Respect to $\bar{\mu}$. Optimizing (5.15) with respect to $\bar{\mu}$ yields

$$\min_{\bar{\mu}} \frac{1}{2}\langle K + \tilde{P}, \bar{\mu}(\bar{\mu} - 2\mu)^T \rangle + \tilde{p}^T \bar{\mu}, \tag{5.35}$$

with the solution $\bar{\mu} = \mu - (K + \tilde{P})^{-1}\tilde{p}$. Again $\tilde{p}$ captures the dependencies of $\omega_{1,j}$ and $\Omega_{k,j}$, this time on $\bar{\mu}$, and is derived below. $\tilde{P}$ is the same as above. To minimize (5.35), we use conjugate gradient descent which enables us to calculate $\bar{\mu}$ using $(K + \tilde{P})$ instead of $(K + \tilde{P})^{-1}$.

Derivation of $\tilde{p}$. Only considering terms in $\omega_{1,j}$ depending on $\bar{\mu}$, we obtain

$$(\omega_{1,j})_n(\bar{\mu}) = -\frac{1}{2(E_{j|\setminus j})_{1,1}}\left(2(n - \mu_{1,j})\lambda_1^j \bar{\mu}_{\setminus j} + \lambda_1^j(\bar{\mu}_{\setminus j}\bar{\mu}_{\setminus j}^T - 2\mu_{\setminus j}\bar{\mu}_{\setminus j}^T)(\lambda_1^j)^T\right)$$

and accordingly for $(\Omega_{k,j})_{m,n}(\bar{\mu})$. The first term is dependent on n and thus on q_c, whereas the remaining terms are again independent and q_c marginalizes out as above. Using again $(\tilde{\lambda}_1^j)^T$ as the extended version of λ_1^j (see (5.34)) we obtain

$$\begin{aligned}
&-\sum_{j=1}^{M}\left((q_{c;1,j})^T\omega_{1,j}(\bar{\mu}) + \sum_{k=2}^{K}\left\langle (q_{c;k\wedge k-1,j})^T, \Omega_{k,j}(\bar{\mu})\right\rangle\right) \\
&\quad= \frac{1}{2}\sum_{j=1}^{M}\sum_{k=1}^{K}\frac{1}{(E_{j|\setminus j})_{k,k}}\left(2\left(\mathbb{E}_{q_c}[c_{k,j}] - \mu_{k,j}\right)(\tilde{\lambda}_k^j)^T\bar{\mu} + \langle \tilde{\lambda}_k^j(\tilde{\lambda}_k^j)^T, \bar{\mu}(\bar{\mu} - 2\mu)^T\rangle\right) \\
&\quad= \frac{1}{2}\sum_{j=1}^{M}\sum_{k=1}^{K} 2\tilde{p}_{k,j}^T\bar{\mu} + \langle \tilde{P}_{k,j}, \bar{\mu}(\bar{\mu} - 2\mu)^T\rangle \\
&\quad= \tilde{p}^T\bar{\mu} + \frac{1}{2}\left\langle \tilde{P}, \bar{\mu}(\bar{\mu} - 2\mu)^T\right\rangle.
\end{aligned}$$

Since $\tilde{p}$ is dependent on q_c, it is updated at every iteration.

References

1. D. Huang, E.A. Swanson, C.P. Lin, J.S. Schuman, W.G. Stinson, W. Chang, M.R. Hee, T. Flotte, K. Gregory, C.A. Puliafito et al., Optical coherence tomography. Science **254**(5035), 1178–1181 (1991)
2. J. Schuman, C. Puliafito, J. Fujimoto, *Optical Coherence Tomography of Ocular Diseases* (Slack Incorporated, Thorofare, 2004)

3. M. Wojtkowski, R. Leitgeb, A. Kowalczyk, T. Bajraszewski, A.F. Fercher, In vivo human retinal imaging by Fourier domain optical coherence tomography. J. Biomed. Opt. **7**(3), 457–463 (2002)
4. C. Ahlers, C. Simader, W. Geitzenauer, G. Stock, P. Stetson, S. Dastmalchi, U. Schmidt-Erfurth, Automatic segmentation in three-dimensional analysis of fibrovascular pigmentepithelial detachment using high-definition optical coherence tomography. Brit. J. Ophthalmol. **92**(2), 197–203 (2008)
5. D.C. Fernández, H.M. Salinas, C.A. Puliafito, Automated detection of retinal layer structures on optical coherence tomography images. Opt. Express **13**(25), 10200–10216 (2005)
6. H. Ishikawa, D.M. Stein, G. Wollstein, S. Beaton, J.G. Fujimoto, J.S. Schuman, Macular segmentation with optical coherence tomography. Invest. Ophthalmol. Vis. Sci. **46**(6), 2012–2017 (2005)
7. M.A. Mayer, J. Hornegger, C.Y. Mardin, R.P. Tornow, Retinal nerve fiber layer segmentation on FD-OCT scans of normal subjects and glaucoma patients. Biomed. Opt. Express **1**(5), 1358–1383 (2010)
8. S.J. Chiu, X.T. Li, P. Nicholas, C.A. Toth, J.A. Izatt, S. Farsiu, Automatic segmentation of seven retinal layers in SDOCT images congruent with expert manual segmentation. Opt. Express **18**(18), 19413–19428 (2010)
9. S.J. Chiu, J.A. Izatt, R.V. O'Connell, K.P. Winter, C.A. Toth, S. Farsiu, Validated automatic segmentation of AMD pathology including drusen and geographic atrophy in SD-OCT images. Invest. Ophthalmol. Vis. Sci. **53**(1), 53 (2012)
10. S.J. Chiu, M.J. Allingham, P.S. Mettu, S.W. Cousins, J.A. Izatt, S. Farsiu, Kernel regression based segmentation of optical coherence tomography images with diabetic macular edema. Biomed. Opt. Express **6**(4), 1172–1194 (2015)
11. J. Tian, B. Varga, G.M. Somfai, W.H. Lee, W.E. Smiddy, D. Cabrera DeBuc, Real-time automatic segmentation of optical coherence tomography volume data of the macular region. PLOS ONE **10**(8), 1–20 (2015)
12. J. Tian, B. Varga, E. Tatrai, P. Fanni, G.M. Somfai, W.E. Smiddy, D.C. Debuc, Performance evaluation of automated segmentation software on optical coherence tomography volume data. J. Biophotonics **9**(5), 478–489 (2016)
13. Duan, J., Tench, C., Gottlob, I., Proudlock, F., Bai, L.: Automated segmentation of retinal layers from optical coherent tomography images using geodesic distance. arXiv preprint arXiv:1609.02214 (2016)
14. M.K. Garvin, M.D. Abrámoff, X. Wu, S.R. Russell, T.L. Burns, M. Sonka, Automated 3-D intraretinal layer segmentation of macular spectral-domain optical coherence tomography images. IEEE Trans. Med. Imaging **28**(9), 1436–1447 (2009)
15. Q. Song, J. Bai, M. Garvin, M. Sonka, J. Buatti, X. Wu et al., Optimal multiple surface segmentation with shape and context priors. IEEE Trans. Med. Imaging **32**(2), 376–386 (2013)
16. P. Dufour, L. Ceklic, H. Abdillahi, S. Schroder, S. De Dzanet, U. Wolf-Schnurrbusch, J. Kowal, Graph-based multi-surface segmentation of OCT data using trained hard and soft constraints. IEEE Trans. Med. Imaging **32**(3), 531–543 (2013)
17. A. Lang, A. Carass, M. Hauser, E.S. Sotirchos, P.A. Calabresi, H.S. Ying, J.L. Prince, Retinal layer segmentation of macular OCT images using boundary classification. Biomed. Opt. Express **4**(7), 1133–1152 (2013)
18. V. Kajić, B. Povazay, B. Hermann, B. Hofer, D. Marshall, P.L. Rosin, W. Drexler, Robust segmentation of intraretinal layers in the normal human fovea using a novel statistical model based on texture and shape analysis. Opt. Express **18**(14), 14730–14744 (2010)
19. J. Friedman, T. Hastie, R. Tibshirani, Sparse inverse covariance estimation with the graphical lasso. Biostatistics **9**(3), 432–441 (2008)
20. F. Rathke, S. Schmidt, C. Schnörr, Probabilistic intra-retinal layer segmentation in 3-D OCT images using global shape regularization. Med. Image Anal. **18**(5), 781–794 (2014)
21. M.E. Tipping, C.M. Bishop, Probabilistic principal component analysis. J. R. Stat. Soc. **61**(3), 611–622 (1999)

22. Rasmussen, C.E., Williams, C.K.I.: *Gaussian Processes for Machine Learning* (MIT Press, 2006)
23. M.J. Wainwright, M.I. Jordan, Graphical models, exponential families, and variational inference. Found. Trends Mach. Learn. **1**(1–2), 1–305 (2008)
24. C.M. Bishop, *Pattern Recognition and Machine Learning* (Springer, New York, 2006)
25. C. Bowd, L.M. Zangwill, C.C. Berry, E.Z. Blumenthal, C. Vasile, C. Sanchez-Galeana, C.F. Bosworth, P.A. Sample, R.N. Weinreb, Detecting early glaucoma by assessment of retinal nerve fiber layer thickness and visual function. Invest. Ophthalmol. Vis. Sci. **42**(9), 1993–2003 (2001)
26. M.T. Leite, H.L. Rao, L.M. Zangwill, R.N. Weinreb, F.A. Medeiros, Comparison of the diagnostic accuracies of the Spectralis, Cirrus, and RTVue optical coherence tomography devices in glaucoma. Ophthalmology **118**(7), 1334–1339 (2011)
27. P.P. Srinivasan, L.A. Kim, P.S. Mettu, S.W. Cousins, G.M. Comer, J.A. Izatt, S. Farsiu, Fully automated detection of diabetic macular edema and dry age-related macular degeneration from optical coherence tomography images. Biomed. Opt. Express **5**(10), 3568–3577 (2014)
28. G. Lemaître, M. Rastgoo, J. Massich, S. Sankar, F. Mériaudeau, D. Sidibé, Classification of SD-OCT volumes with LBP: application to DME detection, in *OMIA* (2015)
29. Y. Wang, Y. Zhang, Z. Yao, R. Zhao, F. Zhou, Machine learning based detection of age-related macular degeneration (AMD) and diabetic macular edema (DME) from optical coherence tomography (OCT) images. Biomed. Opt. Express **7**(12), 4928–4940 (2016)
30. H. Poon, P. Domingos, Sum-product networks: a new deep architecture, in *UAI* (2011), pp. 337–346

Chapter 6
Diagnostic Capability of Optical Coherence Tomography Based Quantitative Analysis for Various Eye Diseases and Additional Factors Affecting Morphological Measurements

Delia Cabrera DeBuc, Jing Tian, Andrea Szigeti, Erika Tátrai, Boglárka Enikő Varga and Gábor Márk Somfai

Successful retinal layer segmentation allows quantitative studies of the retinal structures based on OCT images, which mainly refer to the layer thickness measurements and morphology analyses. The aim of this chapter is to summarize the diagnostic capability of OCT based quantitative analysis for various eye diseases and additional factors affecting morphological measurements.

6.1 Introduction

OCT provides a non-invasive, high-speed and high-resolution approach to visualize the cross-sectional or even three-dimensional tissue structures in vivo. OCT has added significant contributions to many fields of clinical research since its invention in 1991 and since then it has possibly become the most commonly used ophthalmic decision-making technology [1–4]. The diagnostic capabilities of OCT have renovated the ophthalmology practice and provided demonstrable clinical benefits. Widespread clinical adoption of this technology has resulted in ophthalmic OCT images obtained each second by the medical community, anywhere in the world. This success has

D. Cabrera DeBuc (✉) · J. Tian
Department of Ophthalmology, McKnight Vision Research Center, Bascom Palmer Eye Institute, University of Miami Miller School of Medicine, Miami, USA
e-mail: dcabrera2@med.miami.edu

A. Szigeti · E. Tátrai · B. E. Varga · G. M. Somfai
Department of Ophthalmology, Semmelweis University, Budapest, Hungary

G. M. Somfai
Retinology Unit, Pallas Kliniken Augenzentrum, Olten, Switzerland

X. Chen et al. (eds.), *Retinal Optical Coherence Tomography Image Analysis*, Biological and Medical Physics, Biomedical Engineering,
https://doi.org/10.1007/978-981-13-1825-2_6

been accomplished throughout teamwork of clinicians, researchers and industry that significantly contributed to facilitating clinical solutions into a medical device.

During the last decade, OCT technology has advanced drastically in terms of speed, resolution and sensitivity and has become a key diagnostic tool in the areas of retinal and optic nerve pathologies [5]. Recent advancements in OCT imaging allow the visualization of retinal structures in a few seconds with an axial resolution of ~2 microns. The upgrade of both scanning speed and resolution has significantly increased the potential of OCT to visualize more detailed retinal structures, and thus has further enhanced its capability of providing qualitative assessment of tissue features and pathologies or objective quantitative measurements.

The qualitative assessment of the OCT image involves mostly the description of the structural changes of the retina from the vitreo-retinal interface down to the choroid. In this chapter, we are not aiming to describe these morphological features as they would involve almost the entire spectrum of retinal pathologies. However, it is important to emphasize the common language intended to be used for the description of retinal structure that has been the source of substantial debate ever since OCT imaging has been introduced in the clinical practice. Recently, the International Nomenclature for Optical Coherence Tomography (IN·OCT) Panel has developed its recommendations for the usage of common language in OCT nomenclature (see [6].

The quantitative assessment of retinal OCT images refers mostly to the thickness measurements on OCT images. These thickness measurements can help the clinician in the decision-making process in various pathologies, for example, in DME. The Diabetic Retinopathy Clinical Research Network (DRCR.net) has made substantial work in defining the nomenclature and landmarks to be used for OCT diagnostics, the most important of these being the central subfield mean thickness of the macula [7–10]. However, quantitative measurements can also be made for various retinal features, like the area of retinal atrophy and drusen volume in dry age-related macular degeneration, the thickness of the macular ganglion cell complex (GCC), retinal nerve fiber layer (RNFL) and the opening of the Bruch's Membrane in the optic nerve head (ONH) in glaucoma diagnostics [11–14]. Recently, the thickness measurement of the choroid has become possible and offers an exciting insight into retinal pathophysiology [15]. Finally, the optical and textural properties of the OCT scans can be quantitatively described, although this latter has not yet been used in the daily diagnostic routine [16, 17].

An exciting field in OCT diagnostics is the segmentation of the retinal layers seen on the B-scans. Our group has been among the first in the field to describe OCT image segmentation [18] and applied it clinically to both time- and frequency-domain OCT imaging data. The assessment of retinal microstructure can help to better understand the cross-talk between the various cell types and cellular layers of the retina in health and disease and it may provide a window to the central nervous system. In glaucoma, the macular ganglion cell complex (GCC, comprising the macular RNFL, Ganglion cell layer (GCL) and inner plexiform layer (IPL)) seems to be a very sensitive marker for diagnostics and monitoring of disease progression [19].

It has been shown that there is a loss of the GCC in both type 1 and 2 diabetes before clinically detectable retinopathy would occur that is most possibly attributable to retinal diabetic neurodegeneration [20–22]. We could also show that in the case of cataract surgery the photoreceptors seem to be mostly involved in the subtle thickening of the retina, an effect that can be potentially avoided using femtosecond-laser assisted surgical procedures [23].

There are multiple, promising results with OCT segmentation in multiple sclerosis (MS), Alzheimer's disease, Parkinson's, vascular dementia, etc. where the thickness of the RNFL (cpRNFL) and the macular GCL may provide a surrogate marker for pathological processes in the central nervous system [16, 24–32]. Recently, it has been shown that circumpapillary RNFL measurements may even predict the risk of disability worsening in MS [33].

OCT image segmentation has also been shown to be useful in heredodegenerative diseases, for example in retinitis pigmentosa, Stargardt's disease, and other macular dystrophies. In the case of retinitis pigmentosa we could show that inner retinal layers can still be preserved when there is already observable damage in the outer layers of the macula.

In this chapter, the diagnostic capability of OCT based quantitative analysis for various eye diseases and additional factors affecting morphological measurements are outlined based on a review of the literature and specific related studies published to date from our group. We have organized the chapter as follows. The quantitative measurements of retinal pathology based on the OCT image along with image quality, artifacts and error issues is presented in Sect. 6.2. Section 6.3 provides the necessary clinical background about the specific retinal diseases that will be outlined in this chapter to show the diagnostic capabilities of OCT technology as well as additional factors affecting OCT measurements. Section 6.4 offers some concluding remarks.

6.2 OCT-Based Retinal Morphological Measurements

6.2.1 Quantitative Measurements of Retinal Morphology

OCT can aid in identifying, monitoring and quantitatively assessing various posterior segment conditions including macular edema, age-related macular degeneration, full and partial-thickness macular hole, epiretinal membrane, intaretinal exudate, idiopathic central serous chorioretinopathy, RPE detachment, detachment of the neurosensory retina, macular lesions associated with ONH pits or glaucoma and numerous other conditions.

As a matter of fact, OCT can demonstrate the presence of edema where it is not seen on biomicroscopy or angiographically. A very important feature of the OCT system is that it provides information on the retinal structures. For example, the location of fluid accumulation in relation to the different retinal layers may be determined and the response to treatment without the need to perform invasive

studies such as fluorescein angiography may be objectively monitored. At the same time, it may be possible to explain why some patients respond to treatment while others do not. OCT has significant potential both as a diagnostic tool and particularly to objectively monitor subtle retinal changes induced by therapeutic interventions. Thus, OCT may become a valuable tool in determining the minimum maintenance dose of a certain drug in the treatment of retinal diseases, and may demonstrate retinal changes that explain the recovery in some patients without angiographically demonstrable improvement and lack of recovery in others.

In the clinical routine, measurement of retinal thickness by the OCT software depends on the identification of the boundaries of the various cellular layers of the retina. Once the various layers can be identified and correlated with the histological structure of the retina, it may seem relevant to measure not only the entire thickness of the retina, but the thickness of the various cellular layers. Moreover, measuring the reflectance of the various retinal layers on OCT images may also be of interest. Drexler et al. have shown in in vitro and in vivo studies that physiological processes of the retina lead to optical density changes that can be observed by a special M-mode OCT imaging, known as optophysiology [34, 35]. Thus, it also seems rational that quantitative analysis of reflectance changes may provide clinically relevant information in retinal pathophysiology [16].

6.2.2 Quality, Artifacts, and Errors in Optical Coherence Tomography Images

Several investigators have demonstrated a relatively high reproducibility of OCT measurements [7, 8, 36–42]. However, quantitative retinal thickness data generated by OCT could be prone to error as a result of image artifacts, operator errors, decentration errors resulting from poor fixation, and failure of accurate retinal boundary detection by the commercial and custom-built software algorithms. Therefore, the correct image acquisition along with the accurate and reproducible quantification of retinal features by OCT is crucial for evaluating disease progression and response to therapy. Usually, image analysis quality largely depends upon the quality of the acquired signal itself. Thus, controlling and assessing the OCT image quality is of high importance to obtain the best quantitative and qualitative assessment of retinal morphology. At present, the commercial software of some OCT systems (e.g. Cirrus OCT) provides a quality score, identified as the signal strength (SS) but the clinical advantage of this parameter is not really known. The quality score is based on the total amount of the retinal signal received by the OCT system. We note that the SS score should not be used as an image quality score since it is basically a SS score. Stein et al. found that SS outperformed signal-to-noise ratio (SNR) in terms of poor image discrimination [42]. SNR is a standard parameter used to objectively evaluate the quality of acquired images. Stein et al. suggested that SS possibly provides insight into how operators subjectively assess OCT images, and stated that SS is a

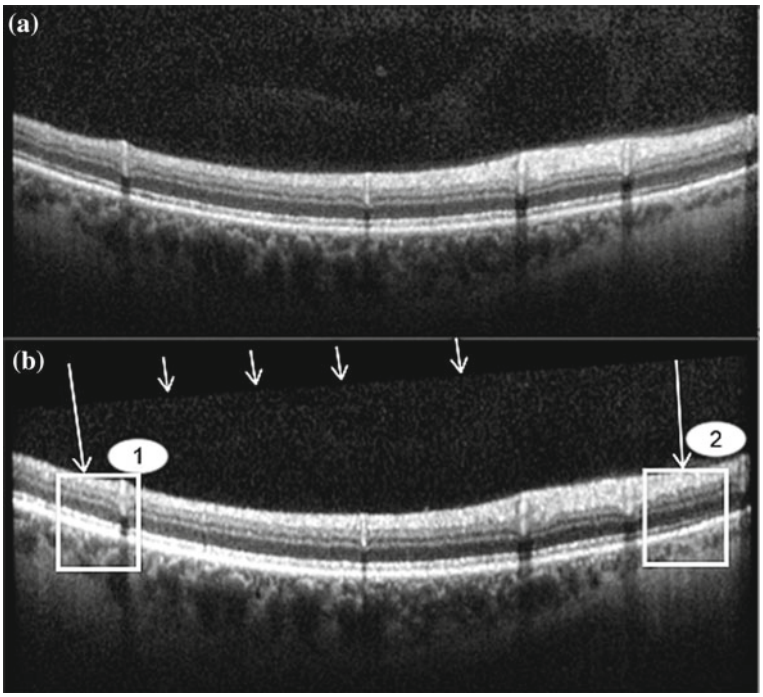

Fig. 6.1 Inter-B-scan (Heidelberg Engineering, Heidelberg, Germany) and inter-volume reflectance variation due to the tilted incident beam. **a** The B-scan from a baseline visit. **b** The B-scan of the repeated OCT volume scan. The incident angle could be visualized from the image border formed from the speckle noise on (**b**). The intensities on the left and right side of the retina (region 1 and 2) were different due to the difference of path length drawn as indicated with the long arrows. The incident angle generates the intra B-scan variations on region 1 and 2 inter-volume variation between volume (**a**) and (**b**)

combination of image quality (SNR) and uniformity of SS within a scan [43]. However, additional detail about SS interpretation is not available from the manufacturer because of its proprietary nature.

On the other hand, certain types of retinal pathology have a propensity to generate poorer quality images and it is difficult to determine whether these pathological images are of poor quality, or if these are the best possible quality images that can be acquired in an eye with advanced retinal damage. While scanning patients in our clinic, we have observed several different types of scan artifacts. Some of these artifacts have been observed previously, and have been also analyzed in a systematic manner [40, 44, 45]. In general, six types of scan artifacts have been identified and classified in two different categories: (I) artifacts caused by limitations in the built-in algorithm identifying the retinal boundaries, such as (1) misidentification of the inner retina, (2) misidentification of the outer retina, and (3) artifacts caused by a degraded scan image; (II) artifacts derived from poor scan acquisition related to operator error:

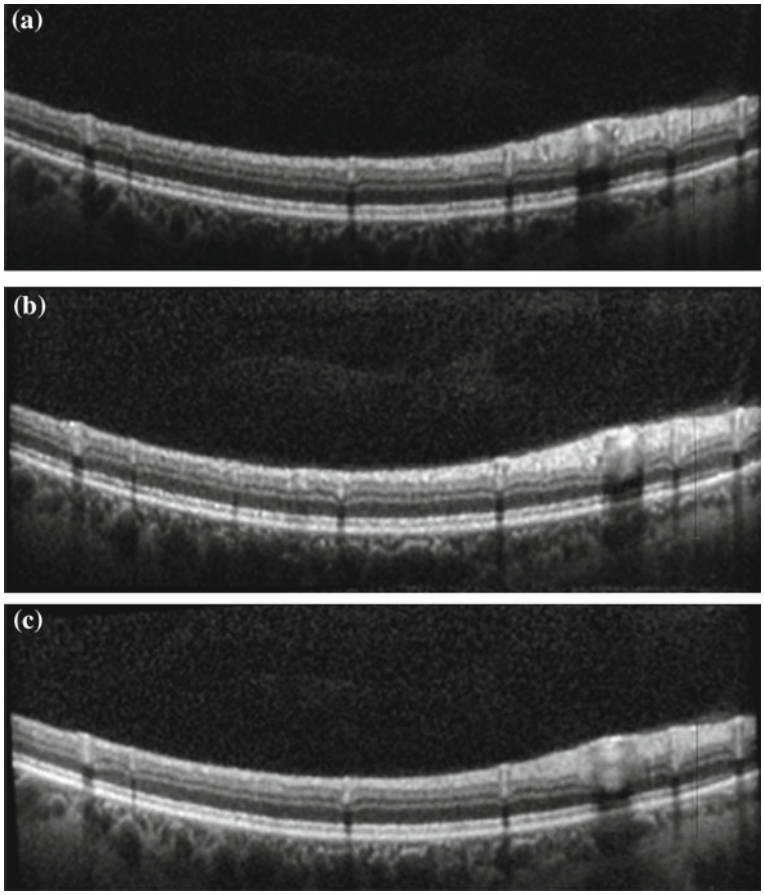

Fig. 6.2 Inter-B-scan (Heidelberg Engineering, Heidelberg, Germany) and inter-volume reflectance variation due to difference in image quality **a** B-scan of a OCT volume on superior quadrants with Q = 29. **b** the adjacent B-scan of image (**a**) in the same volume with Q = 25. **c** B-scan of repeated volume on the same location as image (**a**) with Q = 23. The image quality difference caused drastic change in reflectance between adjacent scans and repeated volumes

(4) "off center" artifacts that occurred when the foveal center is misidentified; (5) "cut edge" artifacts, that occurred when the edge of the scan is truncated improperly; (6) "out of register" artifacts, defined as a scan that is shifted superiorly such that the inner retina is truncated [45]. Changes in internal reflectivity due to error related artifact procedures in a normal healthy subject obtained with Spectralis OCT (Heidelberg Engineering, Heidelberg, Germany) are shown in Figs. 6.1, 6.2 and 6.3. The Spectralis SD-OCT system advises quality score (Q) values $\geq$15 on a scale of 0 to 40.

Finally, it is worth to mention that the retinal thickness values provided by the commercial OCT mapping software should be carefully reappraised. For example, due to the operator pitfall's errors, it may be possible that the OCT custom built-

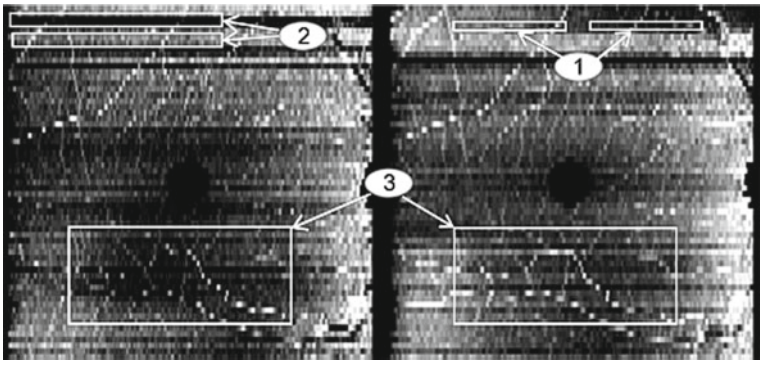

Fig. 6.3 Imaging artifacts in enface map of ganglion cell layer and inner plexiform layer complex in volumetric OCT data (Heidelberg Engineering, Heidelberg, Germany). Left and right images are the enface maps of ganglion cell layer and inner plexiform layer complex from two repeated macular OCT volumes ($496 \times 768 \times 61$ voxels) of right eye of a healthy patient acquired by Spectralis SD-OCT. Regions highlighted with white rectangles illustrated (1) intra-B-scan reflectance variations (2) inter-B-scan reflectance variation and (3) inter-volume reflectance variation

in algorithms fail to locate properly the inner and outer boundaries of the various cellular layers of the retina. The estimated locations could be sensitive to relative differences in reflectance between the outer and deeper retinal structures. Thus, even scans of normal eyes could have boundary misidentification artifacts under operator errors.

6.2.3 Effect of Axial Length on Thickness

The measurement of the axial length (AL) of the eye and the thickness of the ocular wall is obtained using ultrasound which is a standard diagnostic method in ophthalmology [46]. The first paper describing the measurement of the ocular coat dimensions using ultrasound and the correlation between the thickness of the ocular wall and AL was published in 1984 [47]. Eight years later, Németh et al. showed that the volume of the ocular coats is nearly constant in healthy eyes; furthermore, their results confirmed that the thickness of the ocular wall correlates negatively with the AL of the eye [48]. On the other hand, in eyes with uveitis, hypotonia or exophthalmus, the thickness and volume of the ocular wall were increased, as a result of the edema, while in eyes with glaucoma both the thickness and volume of the ocular wall were decreased, probably as a consequence of the destruction of the ganglion cells [48]. Previous studies suggested that there is a correlation between retinal thickness and AL, age, OCT image quality, gender or race in healthy eyes [49–55]. This study evaluated the effect of AL on the thickness of the total retina and the thickness of the intraretinal layers in healthy eyes using OCT image segmentation.

Szigeti et al. evaluated the correlation between AL and the thickness of intraretinal layers in the macula. Their results showed that in the macular area the thickness of the retina and all intraretinal layers, except for the RNFL, GCC and the RPE, correlated with AL with an increasing trend towards the outer layers in the peripheral ring which suggests that the outer layers are elongating or "stretching" with increasing eyeball length [56] (see Table 6.1). Since the OCT examination was carried out in the macula in a limited, 6 mm diameter wide retinal area, they did not have the opportunity to measure the total volume of the retinal layers involving the entire retina to the ora serrata and thus they were not able to get comparable results to those published by Németh et al. using ultrasound [48].

Conflicting results were reported in previous studies about the correlation between AL and thickness of the intraretinal layers. Cheung et al. measured the thickness of the circumpapillary RNFL and other characteristic parameters of the optic disc (like the area of the ONH, the area of the rim area, the area of the excavation and the cup/disc ratio) using spectral domain OCT (SD-OCT) [57]. They found that AL was significantly and strongly correlated with each examined parameter. Mwanza et al. examined the effect of AL on the thickness of the GCL+IPL complex in the macula, also using SD-OCT [58]. Their results indicated that the thickness of the GCL+IPL complex decreased significantly by the increase in AL. On the contrary, Ooto et al. did not find the same trend as the above authors for the correlation between AL and the thickness of any of the intraretinal layers using automatic segmentation and intraretinal layer thickness measurement on SD-OCT images [53]. It is worth to note that mild and high myopic eyes were excluded from the study by Ooto et al., while these were included in the study by Cheung et al. and Mwanza et al. [53, 57, 58]. Therefore, the explanation for the different results could at least in part be that the standard deviation of the AL of the examined eyes was very low in the study of Ooto et al., hence the significant deviations which are observable in the case of shorter or longer eyes did not affect their results.

Szigeti et al. results showed that the weighted mean thickness of the nuclear layers (GCL+IPL, INL and ONL) correlated with AL after adjustment for age, sex and image quality, the correlation getting stronger towards the outer layers. Compared to the above-mentioned studies, in Szigeti et al. study the AL of the eyes was relatively in a wide range which could also contribute to their results [56].

According to two previous studies using OCT, the total thickness of the central, 1 mm diameter wide area of the macula (the central subfield) and total macular volume also correlate with AL, although with relatively low coefficients of correlation ($r = -0.222$ and $r = 0.308$, respectively) [59, 60]. Szigeti et al. results were in line with these findings as the correlation between total retinal thickness (a derivative of total macular volume) and AL was somewhat higher ($r = -0.378$) compared to the above-mentioned studies [56].

It remains unknown whether thinning in axial myopia occurs equally in all retinal layers. Abbott et al. studied the changes in retinal thickness (in total and across layers) in a mammalian animal model (tree shrews, *Tupaia belangeri*) of high axial myopia using OCT and histological sections from the same retinal tissue. Analysis of retinal layers revealed that the IPL, INL, and OPL are showing the most thinning

Table 6.1 Results of thickness (μm) measurements of intraretinal layers of our study subjects. The results are organized by study regions, in the central area, pericentral and peripheral rings (*source* Szigeti et al. [56])

Macular layer	Mean ± SD (μm)	Unadjusted correlation		Partial correlation	
		r	p	r	p
RNFL					
Whole	36.38 ± 2.48	0.167	0.232	0.169	0.241
pericentral ring	23.88 ± 2.47	0.238	0.086	0.222	0.121
peripheral ring	41.49 ± 2.99	0.137	0.329	0.138	0.338
GCL+IPL					
Whole	70.42 ± 5.62	−0.310	**0.024**	−0.328	**0.020**
pericentral ring	94.79 ± 6.47	0.036	0.796	0.015	0.919
peripheral ring	65.85 ± 6.12	−0.387	**0.004**	−0.402	**0.004**
GCC					
Whole	106.80 ± 7.08	−0.188	0.178	−0.199	0.166
pericentral ring	118.66 ± 7.65	0.108	0.443	0.086	0.552
peripheral ring	107.34 ± 7.76	−0.253	0.068	−0.262	0.066
INL					
Whole	33.92 ± 1.94	−0.319	**0.020**	−0.321	**0.023**
pericentral ring	38.49 ± 2.52	0.087	0.534	0.121	0.402
peripheral ring	33.81 ± 2.14	−0.418	**0.002**	−0.429	**0.002**
OPL					
Whole	32.36 ± 1.53	−0.290	**0.035**	−0.277	0.051
pericentral ring	37.99 ± 2.37	0.009	0.948	0.004	0.980
peripheral ring	31.90 ± 1.57	−0.369	**0.007**	−0.360	**0.010**
ONL					
Whole	81.44 ± 5.68	−0.318	**0.005**	−0.399	**0.004**
Fovea	118.43 ± 9.69	−0.150	0.282	−0.119	0.409
pericentral ring	90.53 ± 7.95	−0.310	**0.022**	−0.330	**0.019**
peripheral ring	77.51 ± 5.33	−0.426	**0.001**	−0.448	**0.001**

(continued)

Table 6.1 (continued)

Macular layer	Mean ± SD (μm)	Unadjusted correlation		Partial correlation	
		r	p	r	p
RPE					
Whole	12.20 ± 1.49	0.130	0.925	0.063	0.665
Fovea	14.56 ± 1.65	−0.234	0.092	−0.212	0.140
pericentral ring	11.90 ± 1.93	−0.242	0.081	−0.214	0.135
peripheral ring	12.17 ± 1.48	0.058	0.680	0.140	0.333
Total retina					
Whole	292.23 ± 12.49	−0.383	**0.005**	−0.378	**0.007**
Fovea	237.13 ± 19.55	0.108	0.442	0.148	0.304
pericentral ring	321.82 ± 13.39	−0.112	0.424	−0.114	0.431
peripheral ring	285.55 ± 13.09	−0.456	**0.001**	−0.450	**0.001**
cpRNFL	102.88 ± 7.73	−0.198	0.204	−0.171	0.290

SD standard deviation, *RNFL* retinal nerve fiber layer, *GCL+IPL* ganglion cell and inner plexiform layer complex, *INL* inner nuclear layer, *OPL* outer plexiform layer, *ONL* outer plexiform layer, *RPE* retinal pigment epithelium, *cpRNFL* circumpapillary retinal nerve fiber layer. The p values in bold represent statistically significant differences with $p \ll 0.05$. The results in bold letters indicate the significant correlations obtained between AL with thickness of macular layers, with both unadjusted data and data after adjusting for age, signal strength value and sex

[61]. From the biomechanics point of view, thinning of intermediate thinner layers in myopic eyes could be explained by stiffness conditions of the tissue exposed to mechanical stress with traction and shear forces acting at its innermost surface [62].

A real cell density measurements (cells/mm^2) showed all neuronal cell types (photoreceptors, bipolar/horizontal cells, amacrine cells and ganglion cells) were involved in retinal thinning [61]. Szigeti et al. results are in accordance with the above; however, they also observed changes of the ONL suggesting the additional involvement of the photoreceptors, as well. These changes in the outer retina may be mediated by fluid forces (e.g. active flows), such as the RPE active pump flux that creates a pressure-driven fluid flow between the choroidal space and the subretinal space [63].

Wolsley et al. showed retinal thinning measured by OCT in human myopes compared to emmetropes along a line from 16° superior temporal to the fovea to 16° inferior nasal. The thinning appeared to slowly increase from 4° to 16° nasally and temporally, but regional differences were not analyzed in detail. Their possible explanation is the retinal laminar thickness change due to the shearing between retinal cell layers and cone packing [64]. The fact that the retinal thinning was more pronounced in the peripheral retinal layers correlates with our results that the correlations between

AL and thickness of the retinal layers are stronger in the outer regions, perhaps due to the lower shear resistance of the thinner peripheral retina [65, 66].

The introduction of the latest SD-OCT devices led not only to a dramatic increase in mapping speed and some increase in axial resolution, but the examination of the choroid became also possible. In the past years, promising results have been obtained by the manual segmentation and measurement of choroidal thickness on OCT images. Li et al. and Sogawa et al. demonstrated strong negative correlation between AL and choroidal thickness measured in the subfoveal area of young and healthy eyes ($r = -0.624$ and $r = -0.735$, respectively) [67, 68]. Unfortunately, it is not possible to obtain choroidal thickness from TD-OCT images due to the poor penetration and thus low resolution beneath the RPE, which is one of the shortcomings of this study.

As the growth of the eyeball is stipulated to continue until the age of 20 years [69], it is important to note that a longitudinal study spanning from adolescence to early adulthood would be necessary to evaluate the effect of AL on the thickness of intraretinal layers of the macula under and above the age of 20 years. Szigeti et al. hypothesized that as the eyeball stops to grow the nuclear layers follow the shape of an elongated globe and get thinner by lateral stretching, while the other layers are not capable of this stretching [56]. It should, however, be taken into consideration with such a study that longer AL decreases the magnification of fundus imaging, making transverse dimensions appear smaller on the OCT scan, in inverse proportion to AL [52]. Based on the Szigeti et al. study it is suggested that the effect of AL should be taken into consideration when using OCT image segmentation techniques in future clinical studies involving [56].

6.3 Capability of Optical Coherence Tomography Based Quantitative Analysis for Various Eye Diseases

The diagnostic capabilities of OCT have renovated the ophthalmology practice and provided demonstrable clinical benefits. Widespread clinical adoption of this technology has resulted in ophthalmic OCT images obtained each second by the medical community, anywhere in the world. During the last decade, the upgrade of scanning speed, resolution, and sensitivity has significantly increased the potential of OCT to visualize more detailed retinal structures. However, the amount of data to be analyzed has also increased significantly. Automatic analysis algorithms or software are therefore essential to the clinical applications because the huge amount of volumetric data is no longer possible to be analyzed by visual identification or manual labeling. As the retina is a multi-layered tissue, it is important to segment the various layers or surfaces to fully explore the retinal structure and function. The development of OCT segmentation software has progressed extensively during the last decade. It was originally a proprietary software solution of individual manufacturers of OCT but it has become a generic software solution of various research groups that have developed algorithms to automatically detect retinal surfaces [18, 70–83]. A review

of the early methods can be found in [84]. What follows is by no means an in-depth review of diseases, methods and technological advancements in the diagnosis of the retinal diseases outlined; rather, it is intended to provide a short review of our research findings about OCT diagnostic capabilities for various retinal disorders using quantitative analyses.

6.3.1 Diabetic Retinopathy

Diabetic retinopathy (DR) is a leading cause of adult vision loss world-wide that offers a significant diagnostic challenge. DR has sporadic visual or ophthalmic warnings until visual loss develops [85]. It is now obvious that satisfactory screening protocols can identify diabetic retinopathy at an earlier stage, when preventive steps can be taken in time. Therefore, the effective management and prevention of eye complications in diabetes requires the development of novel functional and structural techniques, therapeutic strategies as well as methods for immediate quantitative results, and interpretation of clinical data. The current diabetic eye healthcare strategies only aim at a model of care for treating DR based on diagnosis rather than an opportunity for preventative eye care and health promotion. Ophthalmoscopy, fundus photography, and fluorescein angiography are the standard tools to diagnose DR and DME [86, 87]. However, a wide range of possible solutions, such as advanced imaging devices like OCTs, eyewear innovations, groundbreaking eye care treatment, functional tests, vision training, and mobile applications are demonstrating new ways to promote better eye health and improve the general well-being of individuals with diabetes.

Particularly, in DR assessments, OCT has been used to measure volume and total thickness of the retina along with structural changes of the various cellular layers of the retina with the aid of segmentation algorithms [84, 88]. In addition to reveal the presence of exudate, photoreceptor atrophy, and haemorrhage; OCT facilitates the visualization of fluid regions. The role of OCT in the assessment and management of diabetic eye complications has become significant in understanding the vitreoretinal relationships and the internal architecture of the retina in diabetes [88–93]. OCT has improved DR and mostly DME management by enabling the direct evaluation of retinal thickness and the quantitative follow-up of retinal thickness changes that may greatly influence therapeutic decisions.

Several studies support the concept that early DR includes a neurodegenerative component [90–104]. In 2009, thinning of the total retina in T1D patients with mild non-proliferative diabetic retinopathy (MDR) relative to normal controls was found to be a result of selective thinning of intraretinal layers [105]. This study team also published results that demonstrated loss of visual function in the macula and related thinning of the GCL in the pericentral area of the macula of diabetic individuals [21, 94].

Another study comparing eyes with MDR to diabetic eyes with no DR, found a reduced RNFL thickness in the pericentral and peripheral macular regions, and

reduced thickness of the GCL+IPL in the pericentral region of the macula [20]. While Vujosevic et al. [97] and van Dijk et al. [21, 22] only found early alterations in the inner retina in diabetics without DR or with initial DR; Cabrera DeBuc et al. study suggested that the outer segment of the photoreceptor layer may be vulnerable in both type 1 diabetic individuals both with and without early DR [96]. The results by Cabrera DeBuc et al. might also indicate that an early sign of vascular alteration development could be detected by investigating the changes in optical properties and thickness of the OPL. However, further investigation is required to find whether outer retinal changes might be associated with long-term inner retinal pathology [96]. Akshikar et al. [98] has also reported significant thinning of the outer retinal segment in the ETDRS (Early Treatment Diabetic Retinopathy Study) regions when investigating macular thickness differences in age-matched subjects using Spectralis SD-OCT. Inconsistent results are present across different studies and indicate that caution should be taken when preparing future studies involving diabetic subjects and OCT imaging [21, 90, 91, 99–103].

Doppler OCT imaging has also demonstrated its clinical utility in detecting blood flow change in patients with DR as well as evaluating the three-dimensional architecture of neovascular complexes in proliferative DR (PDR) [104]. OCTA, one of the latest ophthalmic imaging developments, can be used to both quantitatively analyze blood flow and provide high-contrast images of the retinal vascular bed immediately and without the need for dye injection [106–109]. Recent studies have shown the potentialities of this modality to assess capillary dropout and confirm neovascularization in other retinal diseases [110–112]. Although not too many studies have been reported to date, OCTA applications in diabetes eye complications may provide an alternative to more accurate diagnosis and management of DR and DME by quantitatively assessing capillary dropout and retinal neovascularization [113].

Further developments of OCT technology may impact DR diagnosis and improve the management of this major clinical and public health problem. However, a low-cost approach solution must be reached to successfully introduce its application in population-based screening programs.

6.3.2 Multiple Sclerosis

Multiple sclerosis (MS) is a chronic inflammatory disorder that affects the central nervous system. The disease is characterized by demyelination that leads to axonal dysfunction and neuronal loss [114]. Unmyelinated neuronal axons offer a good possibility to examine axonal loss as the thickness of the myelin sheath does not affect the nerve thickness results. The innermost layer of the retina is the RNFL being comprised of the axons of the retinal ganglion cells which get myelin sheath only after leaving the eye through the lamina cribrosa. Therefore, the thickness measurement of the RNFL might be a good marker of the axonal damage in MS patients.

The loss of retinal nerve fibers around the optic disc (cpRNFL) has been found in the eyes of MS patients both with and without optic neuritis (ON) in the history [28, 112–119]. However, recent studies have shown that also macular thickness and volume are decreased in the eyes of patients with MS [27, 28, 115, 120, 121], presumably caused by the thinning of the GCL and IPL [33, 119, 121–123]. Objective markers might be necessary not only for the diagnosis but also the follow-up of neuronal damage in MS, which could help to determine the effect of any possible therapeutic interventions in the future as well. Most of the published studies on MS using OCT technology have assessed axonal damage by analyzing retinal thickness measurements. However, optical properties and texture measures of the retinal tissue are also attractive parameters to consider in the overall evaluations. In what follows we review the studies that considered both structural and optical properties measurements.

6.3.2.1 Thickness Measurements

Tatrai et al. [13] evaluated the usefulness of macular OCT image segmentation in patients with MS to determine the structural changes of the retina of MS patients. Particularly, OCT examination was performed in thirty-nine patients with MS and in thirty-three healthy subjects. In this study, the parameter which could discriminate best the eyes of healthy subjects from the eyes of MS patients was also determined. Their results showed that the thickness of the macular GCC had the highest sensitivity and specificity to detect axonal loss independent of ON, outperforming the cpRNFL thickness data provided by the analysis software of the commercially available Stratus OCT device. A strong correlation with disease severity measured by the Expanded Disability Status Scale (EDSS) score was also obtained in the case of the GCC thickness which implies that this parameter might also be useful in the estimation of disease progression as a surrogate marker. This study has also shown that ON is followed by a targeted loss of ganglion cells in the macula which can also be objectively assessed by quantitative analysis of OCT macular images.

Several studies have reported the atrophy of the RNFL around the optic disc in patients with MS with and even without ON in medical history [28, 112–119]. Tatrai et al. [13] findings confirmed that the mean overall cpRNFL thickness and the cpRNFL thickness in each quadrant is significantly lower in the eyes of MS patients with a history of ON compared to the non-ON-affected eyes and also in comparison with healthy eyes except for the nasal quadrant (see Fig. 6.4.). However, their results showed that in the non-affected eyes of MS patients the cpRNFL thickness is decreased only in the temporal quadrant compared to healthy eyes. Furthermore, the most pronounced reduction in the thickness of cpRNFL (27 and 17% in the ON-affected and non-affected eyes, respectively) was also observed in the temporal quadrant. These findings agree with previous OCT studies confirming that the fibers of the papillomacular bundle are the most susceptible to damage in ON [117, 124]. One important aspect of this fact, as it has been widely reported in glaucomatous damage, is that the evaluation of the sectoral thickness values could provide the pos-

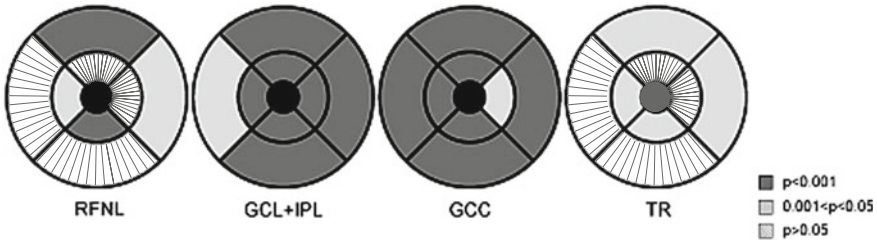

Fig. 6.4 Regional differences between the non-affected eyes of MS patients and healthy eyes. The colors show the extent of thinning based on the p-values of the thickness comparisons. We note the central subfield (R1: black color) was excluded from the analysis for the layers which are not present in the foveal area. Abbreviations: GCC, ganglion cell complex; GCL+IPL, ganglion cell layer and inner plexiform layer complex; RNFL, retinal nerve fiber layer; TR, total retina

sibility to discriminate the RNFL atrophy caused by glaucomatous damage and other disorders affecting the optic nerve, such as MS [28].

Because of neuronal loss, not only the thickness of the cpRNFL is decreased but also the macula was found to be thinner in the eyes of MS patients in previous reports [27, 28, 115, 120, 121]. Histopathological studies had qualitatively shown the atrophy of the inner retina in the eyes of MS patients, while atrophy of the ONL was not detected [125, 126]. However, no quantitative measurements were performed because of technical difficulties, e.g. the partial post-mortem detachment occurring in the retina in many of the eyes. Lately, some studies evaluating a low number of patients and using OCT technology showed that the thickness of the inner retinal layers is decreased in the eyes of MS patients [119, 121–123]. However, the reliability of the methodologies used in these studies is not known. Burkholder et al. analyzed a large sample consisting of 530 subjects with relapsing remitting MS, assessing the volume of the total retina in the inner and outer ETDRS rings (also referred to as pericentral and peripheral macular rings). Their results showed the thinning of the inner and outer retinal ETDRS rings in the eyes of MS patients; however, the local morphological changes of the observed thinning could not be identified as they did not use any segmentation methodology. The OCT image segmentation methodology used in our study allowed the quantification of local retinal changes in patients with MS in vivo. Our results confirmed that the atrophy of the RNFL, GCL+IPL and consequently the GCC is present in the macula of patients with MS even in eyes without ON in previous history. Furthermore, Tatrai et al. [13] demonstrated that the outer layers of the retina are not involved in this process. Although it was not an inclusion criterion, all patients had only one episode of ON in the history; therefore, the observed changes were not biased by the number of ON episodes. The thinning of the retina was most pronounced in the inner inferior, inner temporal, outer superior and outer nasal regions (see Fig. 6.4). The average cpRNFL thickness showed the strongest correlation with the thickness of the GCL+IPL and GCC in the macula while a weaker correlation was observed with the thickness of the total retina.

Previously, the mean overall cpRNFL thickness was found to correlate significantly with functional parameters such as EDSS score and contrast sensitivity [127–129]. However, the thickness of the GCL+IPL in the macula as reported by Tatrai et al. [13] was found to correlate better with these functional parameters, which might thus be a better marker of axonal damage [130]. Tatrai et al. [13] results showed good correlation between the EDSS score and the mean overall cpRNFL thickness and the thickness of the GCL+IPL and the GCC in the macula. However, the ROC (Receiver operating characteristic) analysis revealed that the value most capable of determining the presence of neuronal damage was the weighted mean thickness of the GCC having an AUC (Area under curve) value of 0.892 with a cutoff value of 104 μm having the highest sensitivity and specificity. The thickness of the RNFL and GCL+IPL separately showed lower AUCs than the GCC which could be explained with the better reproducibility of the GCC due to the high contrast between the IPL and INL layers. Although Tatrai et al. results showed that the weighted mean GCC thickness may provide a sensitive tool for the assessment of axonal degeneration, care should be taken when interpreting its value as numerous neurodegenerative disorders, such as glaucoma [19, 131–134]. Alzheimer's disease [29, 30] or Parkinson's disease [24–26] may also lead to ganglion cell death. The use of regional values could help the differential diagnosis between various forms of neurodegeneration, as glaucoma could presumably lead to an infero-superior pattern of GCC loss in the macula, while according to Tatrai et al. [13] results MS is rather leading to a horizontal loss of the GCC most probably due to the loss of the papillo-macular nerve bundle. However, further research is warranted to justify the above hypothesis.

Tatrai et al. [13] results imply that mainly the ganglion cells are affected in MS and changes can be already present in eyes without previous history of ON which could be the result of axonal loss due to the disease process of MS or mild ON events not accompanied by pain. Using OCT image segmentation, Tatrai et al. could also show in vivo that the neuronal damage affects the ganglion cells and not the outer retina, while episodes of ON are resulting in a further pronounced loss of the retinal ganglion cells. Furthermore, their measurements obtained with a custom-built software were shown to be more sensitive compared to standard measurements extracted by the Stratus OCT device (e.g. cpRNFL, total macular volume) and showed a stronger correlation with physical disability measured by the EDSS. This implies the potential clinical usefulness of the quantification of the macular GCC thickness by OCT image segmentation, which could also facilitate the cost-effective follow-up of neuronal damage due to MS.

6.3.2.2 Optical Properties Measurements

Although thickness differences may discern regions with signs of retinal disease from normal regions, differences in texture descriptors of normal and abnormal retinal tissue may also provide additional information of disease development. In fact, the appropriateness of texture to classify tissues in OCT images has been shown in previous studies [135]. By analyzing the spatial arrangement of color or intensities

in an image or selected region of interest (ROI), the image irregularities can be measured. Consequently, texture features, such as contrast and fractal dimension could be analyzed for the macula and each intraretinal layer. The fractal dimension (FD) of a profile or surface is a roughness measure regarded as a local property of the system with higher values indicating rougher surface [136]. There are different methods to determine the FD. The typical conventional approach used to calculate the FD of an image is the box-counting method but the power spectrum method is demonstrated to be more robust [137, 138].

The most common parameter investigated during the OCT examination is retinal thickness. Reflectance is the direct measurement from which thickness is calculated in OCT systems. The human retina is an almost transparent tissue that only reflects about 1% of the incident light [139]. Retinal tissue is characterized by many small random fluctuations in refractive index caused by the ultrastructure of the tissue [140]. Therefore, incident light on tissue is deflected or scattered off this structure. Therefore, differences in optical properties of normal and abnormal retinal tissue may also provide additional information of disease development in pathological eyes allowing OCT technology to be used for quantitative analysis of tissue optical properties [43, 141, 142]. Accordingly, Bizheva et al. have shown previously that optical properties of the retina may change due to their metabolic activity. They were using OCT for this purpose and named the method optophysiology [34]. Huang et al. have shown the early changes of reflectance of the RNFL in a rat model of glaucoma preceding the pathological changes in the retina [52]. Gao et al. shown previously that diabetes not only causes thinning of the inner retinal layers, but also reduces the amplitude of the back-reflected signal from these layers [142]. Consequently, diagnostic predictors based on reflectance changes may be of interest in MS as well where pathological processes of the inner retina have been well described previously.

Varga et al. assessed the differences in texture descriptors and optical properties of retinal tissue layers in 38 patients with MS and 24 healthy subjects [16]. Patient group was divided based on the medical history, whether they previously had had ON episode or not. Optical parameters such as contrast, FD, layer index and total reflectance were measured. They found significant difference in contrast in the RNFL, GCL+IPL, GCC, INL and OPL when comparing MS with ON to the other groups. Higher fractal dimension values were observed in GCL+IPL and INL layers when comparing healthy and MS with ON groups. A significant difference was found in layer index in the RNFL, GCL+IPL and GCC layers in all comparisons. A significant difference was observed in total reflectance in the RNFL, GCL+IPL and GCC layers between the three examination groups. Overall, this study found that texture and optical properties of the retinal tissue undergo pronounced changes in MS even without ON. These results draw attention to the structural and optical changes in the macular area in MS even without ON supporting the previous view of ongoing neurodegeneration also present in the retina [31, 32, 120, 143]. The inner retinal changes appear to be related to central nervous system changes, e.g. intracranial or brain substructure volume reduction (i.e. brain atrophy) [31, 144, 145]. Therefore, OCT may provide a possibility to better understand the neurobiological changes in neurodegenerative diseases such as MS and may help to develop both diagnostic

and prognostic biomarkers that can predict clinical progress. In addition, the authors reported that the outer retina showed no significant differences between the groups which was in contrast with Somfai et al. earlier report showing significant FD changes in diabetic patients where, similarly, neurodegeneration was a proposed mechanism in the background of the observed changes [17]. This could point to the fact of a different disease mechanism at the level of the photoreceptors.

The observed differences in optical properties in Varga et al. study can be related both to circulation or inflammatory alterations of the inner retina. There is only little evidence about the changes in microcirculation of the retina in MS. A recent study by Wang et al. using OCT angiography showed significantly reduced flow index around the ONH in eyes after ON compared to healthy controls but no differences were shown in the parafoveal circulation [146]. Although this may suggest that our observations were most possibly not influenced by alterations in macular microcirculation, recent results also using hemodynamic information have revealed retinal impaired microcirculation in the macular region [147–150]. Therefore, further investigation is needed to better characterize the structure-function relationship in MS. On the other hand, inflammation may presumably be present also in the retina, possibly supported by the "inside-out" theory of MS, namely the migration of autoreactive T cells across the blood-brain barrier from the systemic circulation leading to inflammation [146]. The blood-retina barrier is very like the blood-brain barrier and indeed, the histological study by Green et al. described inflammatory cellular infiltrates surrounding retinal veins in the connective tissue of the RNFL and GCL in 29% of the relapsing remitting and secondary MS eyes [125]. It should be noted, however, that the observed inflammation was more localized (i.e. not in all vessels or the entire retina) than the neurodegeneration observed which makes the direct correlation with our observed trends questionable in terms of revealing inflammatory alterations present or not in our study data. However, considering that the inner capillary network lies in the GCL and the outer capillary network runs from the IPL to the OPL through the INL, the significant differences observed between the study groups when analyzing reflectance and texture descriptors of the RNFL and GCL+IPL complex should be further explored in a larger study and correlated to microvasculature measurements (e.g. blood flow velocity and perfusion) using advanced optical imaging technologies [146, 151, 152]. Investigating these two capillary networks in relation to structural, optical and functional measures may provide a much better insight to determine the role of the retinal microcirculation (i.e. capillaries, arterioles and venules) in the increased risk of progression of MS in the presence of vascular comorbidities [153].

Although optical properties of the retinal tissue are not standardized measures for detecting pathological changes of the retina, in contrast to thickness measurements, reflectance-based measures are direct measures obtained from OCT images. Therefore, it is expected that these additional properties along with thickness information could facilitate a better diagnosis of retinal diseases.

6.3.3 Amblyopia

Amblyopia remains an important cause of low visual acuity, affecting 2–6% of the general population [154–157]. Unilateral amblyopia is defined as reduced best-corrected visual acuity (BCVA) secondary to an abnormal visual experience during the critical period of visual development. Classic causes include strabismus, anisometropia, form deprivation or a combination of these factors [158].

The neural sites that are influenced by visual deprivation are still under investigation. Nevertheless, it has been reported by several studies in humans [159, 160] and also in animal species [160–164] that visual deprivation has an effect on the cell growth in the lateral geniculate body that receives input from the amblyopic eye and on the shift in the dominance pattern in the visual cortex [165], Banko et al. revealed that latencies of the event-related potential components increased and were more variable in the amblyopic eye compared to the fellow eye, although the initial neural site of the visual deficit in this condition is still under investigation [166].

Evidences for direct retinal changes in amblyopic eyes are still inconclusive and controversial [167–169], although electroretinograms elicited by patterned stimuli in humans with various types of amblyopia were found to be significantly reduced [170, 171]. Studies using OCT imaging of the retina have produced discordant results, some investigators have found an increased circumpapillary RNFL(cpRNFL) [172–174] or/and macular thickness [172, 174–178] in amblyopic eyes, whereas others have found no significant differences between amblyopic and healthy eyes [179–184].

Amblyopia occurs during the period when the neuronal network between the retina and the cerebral cortex is developing and maturing. The neural sites that are influenced by visual deprivation are still under investigation. However, some animal studies demonstrated abnormal findings in retinal microstructures, including degeneration of retinal ganglion cells [158, 185], decreased nucleolar volume and cytoplasmic cross-sectional area of retinal ganglion cells [168], an increased number of amacrine synapses in the IPL [186, 187], a reduction in the number of bipolar synapses in the IPL [186], thinning of the IPL [168, 188], and a decrease in the density of Müller fibres [188].

Evidence for direct retinal changes in amblyopic eyes remain inconclusive and controversial. Yen et al. hypothesized that amblyopia may affect the postnatal maturation of the retina, including the postnatal reduction of retinal ganglion cells, which would lead to a measurable increase in the thickness of the RNFL in amblyopic eyes [173]. If this indeed occur, it is likely that the arrest of normal postnatal changes would result not only in increased RNFL thickness but also would affect the normal maturation of the macula, including movement of Henle's fibers away from the foveola and a decrease in foveal cone diameter, and would result in increased foveal thickness [173]. According to this assumption and the above-mentioned animal studies we could reasonably hypothesize that some anatomic rearrangement could be present in the retina.

A small number of previous studies that aimed the assessment of retinal structural changes in amblyopia has been reported. Enoch were the first of many authors to sug-

gest a specific cause for an organic anomaly affecting the retina in amblyopia [189]. More recently, using a third-generation nerve fiber analyzer (GDx, Laser Diagnostic Technologies, San Diego, CA), Colen et al. measured RNFL thickness in strabismic amblyopia and reported no significant difference between amblyopic and sound eyes [190]. In 2005, Altintas et al. carried out OCT examination on 14 unilateral strabismic amblyopic patients and no difference was seen in macular and cpRNFL thickness or macular volume [179]. Kee et al. enrolled 26 unilateral amblyopic children (6 strabismic, 15 anisometropic, 5 combined amblyopes), and found no difference in cpRNFL in any of examined 4 quadrants (superior, inferior, nasal, temporal) and foveal thickness between neither the amblyopic eye and fellow eye, nor between values of these amblyopic patients and 42 normal control children using TD-OCT [181]. However, they found statistically significant difference in mean thickness values of the fovea and the RNFL of the amblyopic eyes of the children with anisometropic amblyopia (n = 15) and strabismic amblyopia (n = 6) (146.5 vs. 173.1 μm $p = 0.046$, cpRNFL 112.9 vs. 92.8 μm $p = 0.034$). They did not measure the AL, and in the anisometropic group 10 of 15 children were myop.

Repka et al. completed studies in 2006 and 2009 evaluating 17 patients aged 5–28 years and subsequently 37 amblyopic children and found no difference in cpRNFL thickness between amblyopic and sound eyes using TD-OCT [182, 183]. Similarly, in 2011, Walker et al. investigated 30 adults (mean age: 56 years) with amblyopia (using Cirrus HD-OCT) and found no statistically significant difference in RNFL thickness of any circumpapillary quadrants and macular thickness in any anatomical location [184].

In 2004, Yen et al. used 2nd generation OCT to measure cpRNFL in 38 patients (mean age 26.4, range 6–75 years) with unilateral amblyopia (strabismic and refractive amblyopia) and found no significant difference between strabismic amblyopic and normal eyes [173]. However, the cpRNFL was significantly thicker in eyes with refractive amblyopia compared with the fellow eye and the differences were significant in the multivariate regression analysis as well with adjustment for AL, spherical equivalent(SE), age and sex [173]. Yoon et al. had similar findings in a study of 31 hyperopic anisometropic children regarding cpRNFL thickness (115.2 vs. 109.6 μm, $p = 0.019$) but found no difference in mean macular retinal thickness (252.5 vs. 249.7 μm) [174]. They did not measure the AL.

In the Sydney Childhood Eye Study, Huynh et al. tested 48 unilateral amblyopes (17 strabismic, 19 hyperopic anisometropia) and reported that amblyopic eyes had slightly greater foveal minimum thickness than the normal fellow eye (by 5.0 μm) and the right eyes of non-amblyopic children (by 10 μm) [177]. This difference was more pronounced in 6-year old children (6.9 μm) than 12–year old children (4.2 μm) [177]. The IOD in foveal minimum thickness was greater in children who did not receive any treatment for unilateral amblyopia [177]. Foveal minimum thickness remained significantly greater in amblyopic than non-amblyopic eyes, after adjusting for amblyopia severity and Interocular difference (IOD) in AL ($p = 0.01$). In their study the inner macular ring was significantly thinner in amblyopic children, and there were no significant differences in outer macular ring thicknesses, central and total macular volume or in cpRNFL [177].

In 2011, Alotaibi et al. evaluated 93 unilateral amblyopic eyes (36 strabismic, 33 anisometropic, 24 combined) and found significantly thicker RNFL (259.3 vs. 255.6 μm, $p < 0.0001$) in the overall amblyopic group, and no significant difference in macular and foveal thickness [172]. There was slightly higher macular and foveal thickness only in the anisometropic amblyopic group (macular thickness: 256.76 vs. 246.61 μm $p = 0.050$; foveal thickness: 187.12 vs. 177.61 μm $p = 0.039$). However, they did not measure the AL either [172].

In the studies by Dickmann et al. a significant difference between the amblyopic and the fellow eye was found in mean macular thickness only in the strabismic amblyopic group, and there was no difference for the refractive amblyopic group, similarly to the cpRNFL in any of the amblyopic groups [175, 176]. Alotaibi and Dickmann suggested based on their findings that amblyopia of different etiologies is associated with the loss of different neural cells [172, 175, 176]. Later, in 2012, Dickmann evaluated 15 strabismic (esotropic) and 15 anisometropic amblyopic patients, and found no intereye differences in cpRNFL, macular thickness and foveal volume in neither group using SD-OCT [180].

In 2011, Pang et al. investigated 31 myopic children with unilateral amblyopia [178]. The refractive error in spherical equivalent in the amblyopic eyes was -10.79 ± 3.40 diopters and in the normal fellow eyes was -1.67 ± 2.90 D. The mean magnitude of anisometropia was 9.12 ± 3.53 D, ranging from 3.63 to 17.50 D. They found a statistically significant difference in macular thickness between amblyopic and fellow eyes, with amblyopic eyes having greater foveal thickness but reduced inner and outer macular thickness [178]. No statistically significant differences were identified in the macular thicknesses between subgroups (purely myopic anisometropia n = 24, combined mechanism amblyopia n = 7). IOD in AL (measured AL with A-scan ultrasound biometry) showed a moderate correlation with the nasal, superior and temporal outer macular thickness [178].

To the best of our knowledge, there are three recent studies that employed some form of OCT image segmentation in amblyopia so far. Al-Haddad et al. used one single horizontal SD-OCT scan for the manual segmentation of six layers of the central 1000 μm diameter area and found an increase in the INL and a decrease in the ONL in the temporal area in amblyopic eyes compared to the fellow eyes, while the mean foveal thickness was increased in amblyopic eyes (228.56 ± 20.2 vs. 221.7 ± 15.3 μm) [191]. Tugcu et al. used the built-in analysis option of the RTVue OCT platform to measure the thickness of the GCC and found an increase in strabismic amblyopia (99.29 vs. 103.08 μm, $p = 0.019$, amblyopic vs. nonamblopic eye) while there was no such difference for the anisometropic or combined subgroups [171]. Park et al. enrolled 20 unilateral amblyopic children (16 strabismus, 2 anisoastigmatism, 2 unilateral ptosis) with a mean age of 9.0 ± 4.03 (4–19 years) and examined horizontal and vertical SD-OCT scans through the fovea [182]. Thickness values were measured at the foveal centre and in 500 and 1500 μm distance from the foveal centre in all 4 quadrants (superior, inferior, nasal, temporal). The thickness of each retinal layer (GCL+IPL, INL, OPL, ONL, IS, OS, RPE) was measured manually using the callipers provided with the SD-OCT instrument. They found significantly decreased thickness in the thickness of the GCL+IPL at all four nasal and temporal

macular locations and at the outer superior and inferior locations. The ONL was thinner at the inner and outer temporal locations and thicker at the inner and outer superior and inner nasal locations. The NFL and OPL were thicker in the amblyopic eyes than in the fellow eyes in some areas and thinner in other areas [182]. It should be noted that none of these studies corrected their results for either age or AL.

Szigeti et al. [192] used OCT image segmentation methodology involving the entire macular area, extracting seven retinal layers. They found that subtle changes may be present in the retina in unilateral amblyopia. As there was evidence showing the confounding effect of AL and age they used state-of-the-art statistical methodology to keep these variables under control. As most of the similar previous studies in the field were using basic comparisons, they also performed such analyses. Interestingly, the basic pairwise comparisons indicated significant changes in the GCC r in the pericentral region and in the OPL layer calculated for the total macula and measured in the peripheral region. However, after applying rigorous statistical methodology to account for the effects of AL and age, these differences disappeared, while a significant difference was revealed for the central (foveal) ONL. This implies that the photoreceptors and not the ganglion cells could be affected by amblyopia, this being the opposite of what was earlier speculated.

Previous studies reported that there was a correlation between retinal thickness and AL, age, or even race in healthy eyes [51, 59, 60, 193, 194] and that AL may influence the thickness of the intraretinal layers in the macula [13]. Song et al. found that AL correlated negatively with average outer macular thickness, overall average macular thickness and macular volume [59].

In unilateral amblyopia, Szigeti et al. found significant difference in AL between amblyopic and fellow eyes (not only in the anisometropic subgroup), and multiple regression showed a statistically significant correlation between IOD in the thickness of most retinal layers and IOD in AL [192]. For this reason, the effect of AL must be taken into consideration in statistical analyses to obtain reliable results, just as we did in our study. In contrast, most of the previous studies about amblyopic retinal OCT measurements were not considering this potential effect of AL, which could influence their results. A summary of these studies, also mentioned above, can be found in Table 6.2.

In support of Szigeti et al. results, there is early evidence showing that photoreceptors may be affected in amblyopia. First, Enoch suggested that photoreceptor orientation is abnormal in amblyopic eyes using the Stiles-Crawford function [189], while others did not found indication of retinal dysfunction at the level of the cone photoreceptors in amblyopic eyes. Later, three groups described electro-oculographic abnormalities in amblyopic patients, with their results providing evidence for a retinal abnormality in amblyopia [195–197]. These results were also suggestive of the RPE being involved in the process. Indeed, the RPE plays an important role in maintaining visual pigment density and perhaps also in the maintenance of photoreceptor orientation.

Leone et al. reviewed the literature on measuring macular thickness in amblyopes and proposed that increased macular thickness found by several studies may be due to inadvertent measurement of a parafoveal eccentric point in amblyopia [198]. To

Table 6.2 Summary of previous studies employing optical coherence tomography of the retina in patients with amblyopia (*source* Szigeti et al. [192])

Study (first author, year)	Study size (n)	Age (years)	Type of amblyopia	OCT type	AL data	cpRNFL	Macular parameters (amblyopic vs. fellow eyes)
Yen et al. [173]	38	26.4 ± 18.3	Mixed (S, A)	TD-OCT(2)	A-scan	Increased	Not studied
	18	25.4 ± 18.6	A			Increased	Not studied
	20	27.4 ± 18.6	S			No difference	Not studied
Yoon et al. [174]	31	7.7 (5–12)	Hyperopic A	TD-OCT(3)	ND	Increased	Not studied
Altintas et al. [179]	14	10.4 (5–18)	S	TD-OCT(3)	ND	No difference	No difference
Kee et al. [181]	26	8 (4–12)	Mixed (S, A, AS)	TD-OCT(3)	ND	No difference	No difference
Repka et al. [182]	17	11.2 (5–30)	Mixed (S, A, AS)	TD-OCT(3)	ND	No difference	Not studied
Huynh et al. [177]	48	6 and 12 year-children	Mixed	TD-OCT(3)	Optical	No difference	Increased FMT
Repka et al. [183]	37	9.2 (7–12)	Mixed (S, A, AS)	TD-OCT(3)	ND	No difference	Not studied
Dickmann et al. [176]	20	14.8 (5–47)	S (esotropia)	TD-OCT(3)	ND	No difference	Increased MT and FV
	20	15.6 (6–56)	A		ND	No difference	No difference
Walker et al. [184]	30	56 (33–82)	Mixed (S, A, AS)	SD-OCT	ND	No difference	No difference
Pang et al. [178]	31	9.6 (5–18)	Mixed (myopic A, AS)	TD-OCT(3)	A-scan	Not studied	No difference
AL-Haddad et al. [204]	45	20 ± 12	Mixed (S, A)	SD-OCT	ND	No difference	No difference

(continued)

Table 6.2 (continued)

Study (first author, year)	Study size (n)	Age (years)	Type of amblyopia	OCT type	AL data	cpRNFL	Macular parameters (amblyopic vs. fellow eyes)
Park et al. [174]	20	9.0 (4–19)	Mixed (S, A, ptosis)	SD-OCT	ND	Not studied	No difference in mean FT and MT, but difference in retinal microstructure (e.g. decrease in the GCL+IPL layer)
Dickmann et al. [175]	15	19.7 (13–30)	S (esotropia)	TD-OCT(3)	ND	No difference	Increased MT and FV
	15	19.8 (10–38)	A		ND	No difference	No difference
Alotaibi et al. [172]	93	8.7 (5–12)	Mixed (S, A, AS)	OCT	ND	Increased	No difference
	36		S			Increased	No difference
	33		A			Increased	Increased MT and FV
	24		AS			Increased	No difference
Dickmann et al. [180]	30	11.5 (5–23)	Mixed (S, A)	SD-OCT	ND	No difference	No difference
AL-Haddad et al. [204]	45	20.6 ± 13.4	Mixed (S, A)	SD-OCT	ND	Not studied	Increased mean FT

ND no data, *FT* foveal thickness, *FV* foveolar volume, *MT* macular thickness, *FMT* foveal minimum thickness; type of amblyopia: *A* anisometropic amblyopia, *S* strabismic amblyopia, *AS* combined amblyopia patients with strabismus and anisometropia; *TD-OCT (2)* second generation time-domain OCT, *TD-OCT (3)* third generation time-domain OCT, *SD-OCT* spectral domain OCT

address this issue, central fixation was confirmed in each subject in our study by ensuring the location of the foveal depression at the center of the macular scan. Furthermore, interocular mean differences of macular thickness in non-amblyopic patients have been investigated and were minimal, even if degrees of asymmetry existed in considered individual patients. In addition, Szigeti et al. concluded that patient age and AL should be taken into consideration in segmentation studies in amblyopia [192]. Using their methodology they could observe subtle changes in amblyopic eyes affecting the ONL of the fovea suggesting the possible involvement of the photoreceptors. However, further studies are warranted to support this hypothesis.

6.4 Concluding Remarks

In conclusion, we consider that macular OCT image segmentation showing in vivo structural changes of retinal tissue will yield a better insight into macular pathology and therefore should play an important role in the future of the diagnosis and follow-up of neurological diseases affecting the optic nerve, such as MS which influences a continuously increasing number of patients worldwide. Furthermore, it seems that texture and optical properties of the retina derived from OCT images may provide a useful additional tool in the hands of clinicians for the assessment of neurodegeneration and neuronal loss-related changes occurring in MS and other neurodegenerative diseases. This may help the better differentiation of eyes with pathology and more precise targeting of potential therapeutic interventions and could also be useful in the follow-up of patients. In both types of diabetes there are early changes observable in the retina of both the structure and its optical properties that may shed light on the pathological processes preceding the occurrence of manifest retinopathy.

It is important to point out that retinal thickness measured by SD-OCT is different from that measured by TD-OCT because the delineation of the outer boundary of the retina differs in the two instruments as most SD-OCT instruments include the outer segment–RPE–Bruch's membrane–choriocapillaris complex in the measurements. This needs to be kept in mind when making therapeutic decisions based on thickness data, like, for example, in diabetes. It is well known that segmentation errors are less frequent with SD-OCT that can be attributed to the greater acquisition speed and better resolution of SD-OCT devices. Partly for this reason, the custom-built software used in our studies facilitates the manual correction of segmentation errors by the operators reducing the number of erroneous thickness calculations due to artifacts. It is known that there is a high agreement and intraclass repeatability of macular thickness in eyes with pathologies obtained by three OCT devices (Stratus TD-OCT and two SD-OCTs, Spectralis and Cirrus OCT) even though each OCT device has a unique method of defining algorithms and cannot be used interchangeably [199].

When performing OCT image segmentation studies involving adults it is suggested to take the effect of AL into consideration; additionally, it will be useful to verify our observations in young subjects [56, 192].

The development of automated segmentation software is essential in exploiting the diagnostic capability of OCT. The clinical segmentation reality of common pathologies could vary across retinal regions and diseases. Therefore, the segmentation accuracy of the retinal structure is critical for the proper assessment of retinal pathology and current treatment practice. However, the optimal automated segmentation software for OCT volume data remains to be established. While the need for unbiased performance evaluation of automated segmentation algorithms is obvious, there does not exist a suitable dataset with ground truth that reflects the realities of everyday retinal features observed in clinical settings (e.g. pathologic cases which contain discontinues surfaces and additional abnormalities disrupting the retinal structure). In addition to the lack of a common ground truth in OCT imaging, minor information of the retinal tissue from the OCT volume data is commonly revealed besides the thickness of retinal layers [96, 200–202]. Recent advances in OCT technology are adding the capability to extract information on blood flow and perfusion status of the retinal tissue as well as on changes in the polarization state of the probing light beam when interacting with the retinal tissue [203]. Therefore, it is expected that a more complete characterization of the retinal tissue could potentiate the diagnostic capability of the OCT technology. This chapter has introduced and discussed several important issues surrounding the diagnostic capabilities of the OCT technology and different factors should be considered when both obtaining and analyzing the OCT images. In summary, the use of OCT technology in clinical settings is of great value, but reliable data analysis and proper diagnosis of the various retinal diseases requires careful considerations when using OCT devices. There is no doubt that further improvements are warrantee as the technology evolves to help advance the judgment and decision making processes of OCT developments and clinical applications.

References

1. D. Huang, E.A. Swanson, C.P. Lin, J.S. Schuman, W.G. Stinson, W. Chang, M.R. Hee, T. Flotte, K. Gregory, C.A. Puliafito et al., Optical coherence tomography. Science **254**, 1178–1181 (1991)
2. A.M. Zysk, F.T. Nguyen, A.L. Oldenburg, D.L. Marks et al., Optical coherence tomography: a review of clinical development from bench to bedside. J. Biomed. Opt. **12**(5), 051403 (2007)
3. R. Hamdan, R.G. Gonzalez, S. Ghostine, C. Caussin, Optical coherence tomography: From physical principles to clinical applications. Arch. Cardiovasc. Dis. **105**(10), 529–534 (2012)
4. C.A. Puliafito, Optical coherence tomography: 20 years after. Ophthalmic Surg. Lasers Imaging **41**(Suppl(6)), 5 (2010)
5. J.S. Schuman, C.A. Puliafito, J.G. Fujimoto, S.D. Jay, *Optical Coherence Tomography of Ocular Diseases*, 3rd edn. (Slack Inc., Thorofare, 2004)
6. G. Staurenghi, S. Sadda, U. Chakravarthy, R.F. Spaide, Proposed lexicon for anatomic landmarks in normal posterior segment spectral-domain optical coherence tomography. The INOCT consensus. Ophthalmology **121**, 1572–1578 (2014)
7. D.J. Browning, Interobserver variability in optical coherence tomography for macular edema. Am. J. Ophthalmol. **137**, 1116–1117 (2004)

8. D.J. Browning, C.M. Fraser, Intraobserver variability in optical coherence tomography. Am. J. Ophthalmol. **138**, 477–479 (2004)
9. A. Polito, M. Del Borrello, M. Isola, N. Zemella, F. Bandello, Repeatability and reproducibility of fast macular thickness mapping with stratus optical coherence tomography. Arch. Ophthalmol. **123**, 1330–1337 (2005)
10. M.G. Krzystolik, S.F. Strauber, L.P. Aiello, R.W. Beck, B.B. Berger, N.M. Bressler, D.J. Browning, R.B. Chambers, R.P. Danis, M.D. Davis, A.R. Glassman, V.H. Gonzalez, P.B. Greenberg, J.G. Gross, J.E. Kim, C. Kollman, Diabetic Retinopathy Clinical Research Network. Reproducibility of macular thickness and volume using Zeiss optical coherence tomography in patients with diabetic macular edema. Ophthalmology **114**, 1520–1525 (2007)
11. P.F. Stetson, Z. Yehoshua, C.A. Garcia Filho, R. Portella Nunes, G. Gregori, P.J. Rosenfeld, OCT minimum intensity as a predictor of geographic atrophy enlargement. Invest. Ophthalmol. Vis. Sci. **55**(2), 792–800 (2014). https://doi.org/10.1167/iovs.13-13199
12. N.S. Abdelfattah, H. Zhang, D.S. Boyer, P.J. Rosenfeld, W.J. Feuer, G. Gregori, S.R. Sadda, Drusen volume as a predictor of disease progression in patients with late age-related macular degeneration in the fellow eye. Invest. Ophthalmol. Vis. Sci. **57**(4), 1839–1846 (2016). https://doi.org/10.1167/iovs.15-18572
13. E. Tatrai, M. Simo, A. Iljicsov, J. Nemeth, D. Cabrera Debuc, G.M. Somfai, In vivo evaluation of retinal neurodegeneration in patients with multiple sclerosis. PLoS ONE **7**(1), e30922 (2012). https://doi.org/10.1371/journal.pone.0030922
14. B.C. Chauhan, V.M. Danthurebandara, G.P. Sharpe, S. Demirel, C.A. Girkin, C.Y. Mardin, A.F. Scheuerle, C.F. Burgoyne, Bruch's membrane opening minimum rim width and retinal nerve fiber layer thickness in a normal white population: a multicenter study. Ophthalmology **122**(9), 1786–1794 (2015). https://doi.org/10.1016/j.ophtha.2015.06.001
15. H. Laviers, H. Zambarakji, Enhanced depth imaging-OCT of the choroid: a review of the current literature. Graefes Arch. Clin. Exp. Ophthalmol. **252**(12), 1871–1883 (2014). https://doi.org/10.1007/s00417-014-2840-y. Epub 4 Nov 2014
16. B.E. Varga, W. Gao, K.L. Laurik, E. Tátrai, M. Simó, G.M. Somfai, D. Cabrera DeBuc, Investigating tissue optical properties and texture descriptors of the retina in patients with multiple sclerosis. PLoS One 30; **10**(11), e0143711 (2015). https://doi.org/10.1371/journal.pone.0143711. eCollection 2015
17. G.M. Somfai, E. Tátrai, L. Laurik, B.E. Varga, V. Ölvedy, W.E. Smiddy, R. Tchitnga, A. Somogyi, D. Cabrera DeBuc, Fractal-based analysis of optical coherence tomography data to quantify retinal tissue damage. BMC Bioinform. **15**, 295 (2014)
18. D. Cabrera Fernández, H. Salinas, C.A. Puliafito, Automated detection of retinal layer structures on optical coherence tomography images. Opt. Express **13**(25), 10200–10216 (2005)
19. N.R. Kim, S. Hong, J.H. Kim, S.S. Rho, G.J. Seong et al., Comparison of macular ganglion cell complex thickness by Fourier-domain OCT in normal tension glaucoma and primary open-angle glaucoma. J. Glaucoma **22**(2), 133–139 (2013)
20. D. Cabrera DeBuc, G.M. Somfai, Early detection of retinal thickness changes in diabetes using Optical Coherence Tomography. Med. Sci. Monit. **16**, MT15–MT21 (2010)
21. H.W. van Dijk, F.D. Verbraak, P.H. Kok et al., Decreased retinal ganglion cell layer thickness in patients with type 1 diabetes. Invest. Ophthalmol. Vis. Sci. **51**, 3660–3665 (2010)
22. H.W. van Dijk, F.D. Verbraak, P.H.B. Kok et al., Early neurodegeneration in the retina of type 2 diabetic patients. Invest. Ophthalmol. Vis. Sci. **53**, 2715–2719 (2012)
23. Z.Z. Nagy, M. Ecsedy, I. Kovács, Á. Takács, E. Tátrai, G.M. Somfai, D. Cabrera, DeBuc, Macular morphology assessed by optical coherence tomography image segmentation after femtosecond laser-assisted and standard cataract surgery. J. Cataract Refract. Surg. **38**(6), 941–946 (2012). https://doi.org/10.1016/j.jcrs.2012.02.031.d
24. O. Altintas, P. Iseri, B. Ozkan, Y. Caglar, Correlation between retinal morphological and functional findings and clinical severity in Parkinson's disease. Doc. Ophthalmol. **116**, 137–146 (2008)
25. M.E. Hajee, W.F. March, D.R. Lazzaro, A.H. Wolintz, E.M. Shrier et al., Inner retinal layer thinning in Parkinson disease. Arch. Ophthalmol. **127**, 737–741 (2009)

26. R. Inzelberg, J.A. Ramirez, P. Nisipeanu, A. Ophir, Retinal nerve fiber layer thinning in Parkinson disease. Vis. Res. **44**, 2793–2797 (2004)
27. C. Almarcegui, I. Dolz, V. Pueyo, E. Garcia, F.J. Fernandez et al., Correlation between functional and structural assessments of the optic nerve and retina in multiple sclerosis patients. Neurophysiol. Clin. **40**, 129–135 (2010)
28. M. Bock, A.U. Brandt, J. Dorr, H. Kraft, N. Weinges-Evers et al., Patterns of retinal nerve fiber layer loss in multiple sclerosis patients with or without optic neuritis and glaucoma patients. Clin. Neurol. Neurosurg. **112**, 647–652 (2010)
29. C. Paquet, M. Boissonnot, F. Roger, P. Dighiero, R. Gil et al., Abnormal retinal thickness in patients with mild cognitive impairment and Alzheimer's disease. Neurosci. Lett. **420**, 97–99 (2007)
30. V. Parisi, R. Restuccia, F. Fattapposta, C. Mina, M.G. Bucci et al., Morphological and functional retinal impairment in Alzheimer's disease patients. Clin. Neurophysiol. **112**, 1860–1867 (2001)
31. S. Saidha, E.S. Sotirchos, J. Oh, S.B. Syc, M.A. Seigo, N. Shiee et al., Relationships between retinal axonal and neuronal measures and global central nervous system pathology in multiple sclerosis. JAMA Neurol. **70**(1), 34–43 (2013)
32. E. Tatrai, A. Szigeti, J. Nemeth, D. Cabrera DeBuc, G.M. Somfai, The effect of axial length on the thickness of the intraretinal layers in the macula. ARVO Meeting Abstracts **53**, 4102 (2012)
33. E.H. Martinez-Lapiscina, S. Arnow, J.A. Wilson et al., Retinal thickness measured with optical coherence tomography and risk of disability worsening in multiple sclerosis: a cohort study. Lancet Neurol. (2016). https://doi.org/10.1016/s1474-4422(16)00068-5. Epub 18 Mar 2016
34. K. Bizheva, R. Pflug, B. Hermann, B. Povazay, H. Sattmann, P. Qiu et al., Optophysiology: depth-resolved probing of retinal physiology with functional ultrahigh-resolution optical coherence tomography. Proc. Natl. Acad. Sci. U.S.A. **103**(13), 5066–5071 (2006). https://doi.org/10.1073/pnas.0506997103. PubMed PMID: 16551749; PubMed Central PMCID: PMC1405907
35. B. Hermann, B. Považay, A. Unterhuber, M. Lessel, H. Sattmann et al., Optophysiology of the human retina with functional ultrahigh resolution optical coherence tomography. IOVS **47**, 1672 (2006)
36. J.S. Hardin, G. Taibbi, S.C. Nelson, D. Chao, G. Vizzeri, Factors affecting Cirrus-HD OCT optic disc scan quality: a review with case examples. J. Ophthalmol. **2015**, 746150 (2015). https://doi.org/10.1155/2015/746150. Epub 2015 Aug 13
37. E.Z. Blumenthal, J.M. Williams, R.N. Weinreb, C.A. Girkin, C.C. Berry, L.M. Zangwill, Reproducibility of nerve fiber layer thickness measurements by use of optical coherence tomography. Ophthalmology **107**, 2278–2282 (2002)
38. P. Carpineto, M. Ciancaglini, E. Zuppardi, G. Falconio, E. Doronzo, L. Mastropasqua, Reliability of nerve fiber layer thickness measurements using optical coherence tomography in normal and glaucomatous eyes. Ophthalmology **110**, 190–195 (2003)
39. P. Massin, E. Vicaut, B. Haouchine, A. Erginay, M. Paques, A. Gaudric, Reproducibility of retinal mapping using optical coherence tomography. Arch. Ophthalmol. **119**, 1135–1142 (2001)
40. G.C. Hoffmeyer, MacPac: a systematic protocol for OCT scanning of macular pathology. J. Ophthal. Photograph **25**, 64–70 (2003)
41. L.A. Paunescu, J.S. Schuman, L.L. Price, P.C. Stark et al., Reproducibility of nerve fiber thickness, macular thickness, and optic nerve head measurements using StratusOCT. Invest. Ophthalmol. Vis. Sci. **45**, 1716–1724 (2004)
42. J.S. Schuman, T. Pedut-Kloizman, E. Hertzmark, Reproducibility of nerve fiber layer thickness measurements using optical coherence tomography. Ophthalmology **103**, 1889–1898 (1996)
43. D.M. Stein, H. Ishikawa, R. Hariprasad, G. Wollstein, R.J. Noecker, J.G. Fujimoto et al., A new quality assessment parameter for optical coherence tomography. Br. J. Ophthalmol. **90**(2), 186–190 (2006). https://doi.org/10.1136/bjo.2004.059824. PubMed PMID: 16424531; PubMed Central PMCID: PMC1860175

44. G.J. Jaffe, J. Caprioli, Optical coherence tomography to detect and manage retinal disease and glaucoma. Am. J. Ophthalmol. **137**, 156–169 (2004)
45. R. Ray, S.S. Stinnett, G.J. Jaffe, Evaluation of image artifact produced by OCT of retinal pathology. Am. J. Ophthalmol. **139**, 18–29 (2005)
46. R.H. Silverman, High-resolution ultrasound imaging of the eye—a review. Clin. Exp. Ophthalmol. **37**, 54–67 (2009)
47. R. Guthoff, R.W. Berger, J. Draeger, Measurements of ocular coat dimensions by means of combined A- and B-scan ultrasonography. Ophthalmic Res. **16**, 289–291 (1984)
48. J. Németh, Z. Horóczi, Changes in the ocular dimensions after trabeculectomy. Int. Ophthalmol. **16**(4–5), 355 (1992)
49. N. Demirkaya, H.W. van Dijk, S.M. van Schuppen, M.D. Abramoff, M.K. Garvin, M. Sonka et al., Effect of age on individual retinal layer thickness in normal eyes as measured with spectral-domain optical coherence tomography. Invest. Ophthalmol. Vis. Sci. **54**, 4934–4940 (2013)
50. J. Huang, X. Liu, Z. Wu, S. Sadda, Image quality affects macular and retinal nerve fiber layer thickness measurements on fourier-domain optical coherence tomography. Ophthalmic Surg. Lasers Imaging **42**, 216–221 (2011)
51. P.J. Kelty, J.F. Payne, R.H. Trivedi, J. Kelty, E.M. Bowie, B.M. Burger, Macular thickness assessment in healthy eyes based on ethnicity using Stratus OCT optical coherence tomography. Invest. Ophthalmol. Vis. Sci. **49**, 2668–2672 (2008)
52. X.R. Huang, Y. Zhou, R.W. Knighton, W. Kong, W.J. Feuer, Wavelength-dependent change of retinal nerve fiber layer reflectance in glaucomatous retinas. Invest. Ophthalmol. Vis. Sci. **53**(9), 5869–58676 (2012). Epub 2012/07/28. https://doi.org/10.1167/iovs.12-10001. PubMed PMID: 22836775; PubMed Central PMCID: PMCPMC3428115
53. S. Ooto, M. Hangai, A. Tomidokoro, H. Saito, M. Araie, T. Otani et al., Effects of age, sex, and axial length on the three-dimensional profile of normal macular layer structures. Invest. Ophthalmol. Vis. Sci. **52**, 8769–8779 (2011)
54. H.L. Rao, A.U. Kumar, J.G. Babu, A. Kumar, S. Senthil, C.S. Garudadri, Predictors of normal optic nerve head, retinal nerve fiber layer, and macular parameters measured by spectral domain optical coherence tomography. Invest. Ophthalmol. Vis. Sci. **52**, 1103–1110 (2011)
55. C. Samarawickrama, A. Pai, S.C. Huynh, G. Burlutsky, T.Y. Wong, P. Mitchell, Influence of OCT signal strength on macular, optic nerve head, and retinal nerve fiber layer parameters. Invest. Ophthalmol. Vis. Sci. **51**, 4471–4475 (2010)
56. A. Szigeti, E. Tátrai, B.E. Varga, A. Szamosi, D. Cabrera DeBuc, Z.Z. Nagy, J. Németh, G.M. Somfai, The effect of axial length on the thickness of intraretinal layers of the macula. PLoS ONE **10**(11), e0142383 (2015). https://doi.org/10.1371/journal.pone.0142383
57. C.Y. Cheung, D. Chen, T.Y. Wong, Y.C. Tham, R. Wu, Y. Zheng et al., Determinants of quantitative optic nerve measurements using spectral domain optical coherence tomography in a population-based sample of non-glaucomatous subjects. Invest. Ophthalmol. Vis. Sci. **52**, 9629–9635 (2011)
58. J.C. Mwanza, M.K. Durbin, D.L. Budenz, C.A. Girkin, C.K. Leung, J.M. Liebmann et al., Profile and predictors of normal ganglion cell-inner plexiform layer thickness measured with frequency-domain optical coherence tomography. Invest. Ophthalmol. Vis. Sci. **52**, 7872–7879 (2011)
59. W.K. Song, S.C. Lee, E.S. Lee, C.Y. Kim, S.S. Kim, Macular thickness variations with sex, age, and axial length in healthy subjects: a spectral domain-optical coherence tomography study. Invest. Ophthalmol. Vis. Sci. **51**, 3913–3918 (2010)
60. A.C. Wong, C.W. Chan, S.P. Hui, Relationship of gender, body mass index, and axial length with central retinal thickness using optical coherence tomography. Eye (Lond.) **19**, 292–297 (2005)
61. C.J. Abbott, U. Grünert, M.J. Pianta, N.A. McBrien, Retinal thinning in tree shrews with induced high myopia: optical coherence tomography and histological assessment. Vis. Res. **51**(3), 376–385 (2011)

62. K. Franze, M. Francke, K. Guenter, A.F. Christ, N. Koerber, A. Reichenbach, J. Guck, Spatial mapping of the mechanical properties of the living retina using scanning force microscopy. Soft Matter **7**, 3147–3154 (2011)
63. T. Chou, M. Siegel, The mechanics of retinal detachment. Phys. Biol. **9**, 046001 (2012). http://faculty.biomath.ucla.edu/tchou/pdffiles/blister16.pdf
64. C.J. Wolsley, K.J. Saunders, G. Silvestri, R.S. Anderson, Investigation of changes in the myopic retina using multifocal electroretinograms, optical coherence tomography and peripheral resolution acuity. Vis. Res. **48**(14), 1554–1561 (2008). https://doi.org/10.1016/j.visres.2008.04.013
65. M.I. Abdalla, M. Hamdi, Applanation ocular tension in myopia and emmetropia. Br. J. Opthalmol. **54**, 122–125 (1970)
66. T.T. Andreassen, Biomechanical properties of keratoconus and normal corneas. Exp. Eye Res. **31**, 435–441 (1980)
67. X.Q. Li, M. Larsen, I.C. Munch, Subfoveal choroidal thickness in relation to sex and axial length in 93 Danish university students. Invest. Ophthalmol. Vis. Sci. **52**, 8438–8441 (2011)
68. K. Sogawa, T. Nagaoka, A. Takahashi, I. Tanano, T. Tani, A. Ishibazawa et al., Relationship between choroidal thickness and choroidal circulation in healthy young subjects. Am. J. Opthalmol. **153**, 1129–1132 e1121 (2012)
69. H.C. Fledelius, A.S. Christensen, C. Fledelius, Juvenile eye growth, when completed? An evaluation based on IOL-Master axial length data, cross-sectional and longitudinal. Acta Ophthalmol. **92**, 259–264 (2014)
70. D. Koozekanani, K. Boyer, C. Roberts, Retinal thickness measurements from optical coherence tomography using a Markov boundary model. IEEE Trans. Med. Imaging **20**(9), 900–916 (2001)
71. T. Fabritius, S. Makita, M. Miura, R. Myllylä, Y. Yasuno, Automated segmentation of the macula by optical coherence tomography. Opt. Express **17**(18), 15659–15669 (2009)
72. M. Shahidi, Z. Wang, R. Zelkha, Quantitative thickness measurement of retinal layers imaged by optical coherence tomography. Am. J. Ophthalmol. **139**(6), 1056–1061 (2005)
73. H. Ishikawa, D.M. Stein, G. Wollstein, S. Beaton, J.G. Fujimoto, J.S. Schuman, Macular segmentation with optical coherence tomography. Invest. Ophthalmol. Vis. Sci. **46**(6), 2012–2017 (2005)
74. G. Gregori, R.W. Knighton, A robust algorithm for retinal thickness measurements using optical coherence tomography (Stratus OCT). Invest. Ophthalmol. Vis. Sci. **45**(13), p3007 (2004)
75. M.D. Abràmoff, M.K. Garvin, M. Sonka, Retinal imaging and image. IEEE Trans. Med. Imaging **1**(3), 169–208 (2010)
76. S.J. Chiu, X.T. Li, P. Nicholas, C.A. Toth, J.A. Izatt, S. Farsiu, Automatic segmentation of seven retinal layers in SDOCT images congruent with expert manual segmentation. Opt. Express **18**, 19413–19428 (2010)
77. M.K. Garvin, M.D. Abràmoff, X. Wu, S.R. Russell, T.L. Burns, M. Sonka, Automated 3-D intraretinal layer segmentation of macular spectral-domain optical coherence tomography images. IEEE Trans. Med. Imaging **28**(9), 1436–1447 (2009)
78. A. Lang, A. Carass, M. Hauser, E.S. Sotirchos, P. Calabresi, H.S. Ying, J.L. Prince, Retinal layer segmentation of macular OCT images using boundary classification. Biomed. Opt. Express **4**(7), 1133–1152 (2013)
79. P.A. Dufour, L. Ceklic, H. Abdillahi, S. Schroder et al., Graph-based multi-surface segmentation of OCT data using trained hard and soft constraints. IEEE Trans. Med. Imaging **32**(3), 531–543 (2013)
80. A. Yazdanpanah, G. Hamarneh, B.R. Smith, M.V. Sarunic, Segmentation of intra-retinal layers from optical coherence tomography images using an active contour approach. IEEE Trans. Med. Imaging **30**(2), 484–496 (2011)
81. V. Kajić, B. Povazay, B. Hermann, B. Hofer, D. Marshall et al., Robust segmentation of intraretinal layers in the normal human fovea using a novel statistical model based on texture and shape analysis. Opt. Express **18**(14), 14730–14744 (2010)

82. Q. Chen, T. Leng, L. Zheng, L. Kutzscher, J. Ma et al., Automated drusen segmentation and quantification in SD-OCT images. Med. Image Anal. **17**(8), 1058–1072 (2013)
83. M.A. Mayer, J. Hornegger, C.Y. Mardin, R.P. Tornow, Retinal nerve fiber layer segmentation on FD-OCT scans of normal subjects and glaucoma patients. Biomed. Opt. Express **1**(5), 1358–1383 (2010)
84. D. Cabrera DeBuc, A review of algorithms for segmentation of retinal image data using optical coherence tomography, in *Image Segmentation*, ed. by P.-G. Ho, InTech (2011). Available from: http://www.intechopen.com/books/image-segmentation/a-review-of-algorithms-for-segmentation-of-retinal-image-data-using-optical-coherence-tomography
85. American Diabetes Association, Diabetic retinopathy. Diabetes Care **25**, S90–S93 (2005)
86. Diabetes Information Clearinghouse. Diabetes, heart disease, and stroke (2005) NIH Publication No.06-5094
87. J. Cunha-Vaz, J.R. Faria de Abreu, A.J. Campos, Early breakdown of the blood-retinal barrier in diabetes. Br. J. Ophthalmol. **59**, 649–656 (1975)
88. P.E. Stanga, A.C. Bird, Optical coherence tomography (OCT): principles of operation, technology, indications in vitreoretinal imaging and interpretation of results. Int. Ophthalmol. **23**, 191–197 (2001)
89. U.H. Schaudig, C. Glaefke, F. Scholz et al., Optical coherence tomography for retinal thickness measurement in diabetic patients without clinically significant macular edema. Ophthalmic Surg. Lasers **31**, 182–186 (2000)
90. T. Oshitari, K. Hanawa, E. Adachi-Usami, Changes of macular and RNFL thicknesses measured by Stratus OCT in patients with early stage diabetes. Eye (Lond.) **23**, 884–889 (2009)
91. B. Asefzadeh, B.M. Fisch, C.E. Parenteau et al., Macular thickness and systemic markers for diabetes in individuals with no or mild diabetic retinopathy. Clin. Exp. Ophthalmol. **36**, 455–463 (2008)
92. W. Goebel, T. Kretzchmar-Gross, Retinal thickness in diabetic retinopathy: a study using optical coherence tomography (OCT). Retina **22**, 759–767 (2002)
93. N.M. Bressler, A.R. Edwards, A.N. Antoszyk et al., Retinal thickness on Stratus optical coherence tomography in people with diabetes and minimal or no diabetic retinopathy. Am. J. Ophthalmol. **145**, 894–901 (2008)
94. H.W. van Dijk, F.D. Verbraak, M. Stehouwer et al., Association of visual function and ganglion cell layer thickness in patients with diabetes mellitus type 1 and no or minimal diabetic retinopathy. Vis. Res. **28**, 244–248 (2011)
95. D. Cabrera DeBuc, H.M. Salinas, S. Ranganathan, E. Tatrai, W. Gao et al., Improving image segmentation performance and quantitative analysis via a computer-aided grading methodology for optical coherence tomography retinal image analysis. J. Biomed. Opt. **15**, 046015 (2010)
96. D. Cabrera DeBuc, E. Tatrai, L. Laurik et al., Identifying local structural and optical derangement in the neural retina of individuals with type 1 diabetes. J. Clin. Exp. Ophthalmol. **4**, 289 (2013). https://doi.org/10.4172/2155-9570.1000289
97. S. Vujosevic, E. Midena, Retinal layers changes in human preclinical and early clinical diabetic retinopathy support early retinal neuronal and müller cells alterations. J. Diabetes Res. Article ID 905058 (2013). https://doi.org/10.1155/2013/905058
98. R. Akshikar, M. Richardson, R. Crosby-Nwaobi et al., Retinal neuronal changes in people with diabetes. Invest. Ophthalmol. Vis. Sci. **53**, 2852 (2012)
99. C. Biallosterski, M.E. van Velthoven, R.P. Michels et al., Decreased optical coherence tomography measured pericentral retinal thickness in patients with diabetes mellitus type 1 with minimal diabetic retinopathy. Br. J. Ophthalmol. **91**, 1135–1138 (2007)
100. D.J. Browning, C.M. Fraser, S. Clark, The relationship of macular thickness to clinically graded diabetic retinopathy severity in eyes without clinically detected diabetic macular edema. Ophthalmology **115**, 533–539 (2008)
101. I. Pires, R.C. Bernardes, C.L. Lobo et al., Retinal thickness in 25 eyes with mild nonproliferative retinopathy in patients with type 2 diabetes mellitus: comparison of measurements obtained by retinal thickness analysis and optical coherence tomography. Arch. Ophthalmol. **120**, 1301–1306 (2002)

102. J.M. Lopes de Faria, H. Russ, V.P. Costa, Retinal nerve fibre layer loss in patients with type 1 diabetes mellitus without retinopathy. Br. J. Ophthalmol. **86**, 725–728 (2002)
103. A. Verma, P.K. Rani, R. Raman et al., Is neuronal dysfunction an early sign of diabetic retinopathy? Microperimetry and spectral domain optical coherence tomography (SD-OCT) study in individuals with diabetes, but no diabetic retinopathy. Eye (Lond.) **23**, 1824–1830 (2009)
104. Y. Wang, A. Fawzi, O. Tan et al., Retinal blood flow detection in diabetic patients by Doppler Fourier domain optical coherence tomography. Opt. Express **17**, 4061–4073 (2009)
105. H.W. van Dijk, P.H. Kok, M. Garvin et al., Selective loss of inner retinal layer thickness in type 1 diabetic patients with minimal diabetic retinopathy. Invest. Ophthalmol. Vis. Sci. **50**, 3404–3409 (2009)
106. S. Makita, Y. Hong, M. Yamanari, T. Yatagai, Y. Yasuno, Optical coherence angiography. Opt. Express **14**(17), 7821–7840 (2006)
107. R.K. Wang, S. Jackes, Z. Ma et al., Three dimensional optical angiography. Opt. Express **15**, 4083–4097 (2007)
108. Y. Yasuno, Y. Hong, S. Makita et al., In vivo high-contrast imaging of deep posterior eye by 1-mm swept source optical coherence tomography and scattering optical coherence angiography. Opt. Express **15**, 6121–6139 (2007)
109. Y. Jia, O. Tan, J. Tokayer et al., Split-spectrum amplitude-decorrelation angiography with optical coherence tomography. Opt. Express **20**, 4710–4725 (2012)
110. E. Moult, W. Choi, N.K. Waheed et al., Ultrahigh-speed swept-source OCT angiography in exudative AMD. Ophthalmic Surg. Lasers Imaging Retina **45**(6), 496–505 (2014)
111. M.R. Thorell, Q. Zhang, Y. Huang et al., Swept-source OCT angiography of macular telangiectasia type 2. Ophthalmic Surg. Lasers Imaging Retina **45**(5), 369–380 (2014)
112. Y. Huang, Q. Zhang, M.R. Thorell et al., Swept-source OCT angiography of the retinal vasculature using intensity differentiation-based optical microangiography algorithms. Ophthalmic Surg. Lasers Imaging Retina **45**(5), 382–389 (2014)
113. T.S. Hwang, Y. Jia, S.S. Gao, S.T. Bailey, A.K. Lauer, C.J. Flaxel, D.J. Wilson, D. Huang, Optical coherence tomography angiography features of diabetic retinopathy. Retina **35**(11), 2371–2376 (2015). https://doi.org/10.1097/iae.0000000000000716
114. E. Silber, M.K. Sharief, Axonal degeneration in the pathogenesis of multiple sclerosis. J. Neurol. Sci. **170**, 11–18 (1999)
115. C. Fjeldstad, M. Bemben, G. Pardo, Reduced retinal nerve fiber layer and macular thickness in patients with multiple sclerosis with no history of optic neuritis identified by the use of spectral domain high-definition optical coherence tomography. J. Clin. Neurosci. **18**, 1469–1472 (2011)
116. V. Parisi, G. Manni, M. Spadaro, G. Colacino, R. Restuccia et al., Correlation between morphological and functional retinal impairment in multiple sclerosis patients. Invest. Ophthalmol. Vis. Sci. **40**, 2520–2527 (1999)
117. V. Pueyo, J. Martin, J. Fernandez, C. Almarcegui, J. Ara et al., Axonal loss in the retinal nerve fiber layer in patients with multiple sclerosis. Multiple Scler. **14**, 609–614 (2008)
118. J. Sepulcre, M. Murie-Fernandez, A. Salinas-Alaman, A. Garcia-Layana, B. Bejarano et al., Diagnostic accuracy of retinal abnormalities in predicting disease activity in MS. Neurology **68**, 1488–1494 (2007)
119. H. Tegetmeyer, E. Kühn, Quantitative analysis of changes in macular layers following optic neuritis. Neuro-Ophthalmology **35**, 101–107 (2011)
120. B.M. Burkholder, B. Osborne, M.J. Loguidice, E. Bisker, T.C. Frohman et al., Macular volume determined by optical coherence tomography as a measure of neuronal loss in multiple sclerosis. Arch. Neurol. **66**, 1366–1372 (2009)
121. S. Saidha, S.B. Syc, M.K. Durbin, C. Eckstein, J.D. Oakley et al., Visual dysfunction in multiple sclerosis correlates better with optical coherence tomography derived estimates of macular ganglion cell layer thickness than peripapillary retinal nerve fiber layer thickness. Multiple Scler. **17**(12), 1449–14463 (2011)

122. E.C. Davies, K.M. Galetta, D.J. Sackel, L.S. Talman, E.M. Frohman et al., Retinal ganglion cell layer volumetric assessment by spectral-domain optical coherence tomography in multiple sclerosis: application of a high-precision manual estimation technique. J. Neuroophthalmol. **31**, 260–264 (2011)
123. S.B. Syc, S. Saidha, S.D. Newsome, J.N. Ratchford, M. Levy et al., Optical coherence tomography segmentation reveals ganglion cell layer pathology after optic neuritis. Brain **135**, 521–533 (2012). https://doi.org/10.1093/brain/awr264
124. A. Klistorner, H. Arvind, T. Nguyen, R. Garrick, M. Paine et al., Multifocal VEP and OCT in optic neuritis: a topographical study of the structure-function relationship. Doc. Ophthalmol. **118**, 129–137 (2009)
125. A.J. Green, S. McQuaid, S.L. Hauser, I.V. Allen, R. Lyness, Ocular pathology in multiple sclerosis: retinal atrophy and inflammation irrespective of disease duration. Brain **133**, 1591–1601 (2010)
126. J.B. Kerrison, T. Flynn, W.R. Green, Retinal pathologic changes in multiple sclerosis. Retina **14**, 445–451 (1994)
127. F. Costello, W. Hodge, Y.I. Pan, E. Eggenberger, M.S. Freedman, Using retinal architecture to help characterize multiple sclerosis patients. Can. J. Ophthalmol. **45**, 520–526 (2010)
128. J.B. Fisher, D.A. Jacobs, C.E. Markowitz, S.L. Galetta, N.J. Volpe et al., Relation of visual function to retinal nerve fiber layer thickness in multiple sclerosis. Ophthalmology **113**, 324–332 (2006)
129. A.P. Henderson, S.A. Trip, P.G. Schlottmann, D.R. Altmann, D.F. Garway-Heath et al., An investigation of the retinal nerve fibre layer in progressive multiple sclerosis using optical coherence tomography. Brain **131**, 277–287 (2008)
130. S. Saidha, S.B. Syc, M.A. Ibrahim, C. Eckstein, C.V. Warner et al., Primary retinal pathology in multiple sclerosis as detected by optical coherence tomography. Brain **134**, 518–533 (2011)
131. A. Garas, P. Vargha, G. Hollo, Diagnostic accuracy of nerve fibre layer, macular thickness and optic disc measurements made with the RTVue-100 optical coherence tomograph to detect glaucoma. Eye (Lond.) **25**, 57–65 (2011)
132. N.R. Kim, E.S. Lee, G.J. Seong, J.H. Kim, H.G. An et al., Structure-function relationship and diagnostic value of macular ganglion cell complex measurement using Fourier-domain OCT in glaucoma. Invest. Ophthalmol. Vis. Sci. **51**, 4646–4651 (2010)
133. A. Schulze, J. Lamparter, N. Pfeiffer, F. Berisha, I. Schmidtmann et al., Diagnostic ability of retinal ganglion cell complex, retinal nerve fiber layer, and optic nerve head measurements by Fourier-domain optical coherence tomography. Graefes Arch. Clin. Exp. Ophthalmol. **249**, 1039–1045 (2011)
134. O. Tan, V. Chopra, A.T. Lu, J.S. Schuman, H. Ishikawa et al., Detection of macular ganglion cell loss in glaucoma by Fourier-domain optical coherence tomography. Ophthalmology **116**(2305–2314), e2301–e2302 (2009)
135. K.W. Gossage, T.S. Tkaczyk, J.J. Rodriguez, J.K. Barton, Texture analysis of optical coherence tomography images: feasibility for tissue classification. J. Biomed. Opt. **8**(3), 570–575 (2003). https://doi.org/10.1117/1.1577575. PubMed PMID: 12880366
136. T. Gneiting, M. Schlather, Stochastic models that separate fractal dimension and the Hurst effect. SIAM Rev. **46**(2), 269–282 (2004). https://doi.org/10.1137/s0036144501394387
137. N. Sarkar, B.B. Chaudhuri, An efficient approach to estimate fractal dimension of textural images. Pattern Recogn. **25**(9), 1035–1041 (1992). https://doi.org/10.1016/0031-3203(92)90066-R
138. M. Hasegawa, J. Liu, K. Okuda, M. Nunobiki, Calculation of the fractal dimensions of machined surface profiles. Wear **192**(1), 40–45 (1996)
139. Y. Huang, Optical coherence tomography (OCT) in hereditary retinal degeneration: layer-by-layer analysis in normal and diseased retinas. Ph.D. dissertation, University of Pennsylvania, 1999
140. V.D. Svet, About holographic (interferometric) approach to the primary visual perception (2013)

141. M. Hammer, D. Schweitzer, E. Thamm, A. Kolb, Optical properties of ocular fundus tissues determined by optical coherence tomography. Opt. Commun. **186**(1–3), 149–153 (2000). https://doi.org/10.1016/S0030-4018(00)01054-3
142. W. Gao, E. Tatrai, G.M. Somfai, D. Cabrera DeBuc, Assessing the performance of optical properties determination of intraretinal layers in healthy normal and type 1 diabetic eyes using optical coherence tomography. Invest. Ophthalmol. Vis. Sci. **52**(6), 3689 (2011)
143. L.J. Balcer, D.H. Miller, S.C. Reingold, J.A. Cohen, Vision and vision-related outcome measures in multiple sclerosis. Brain J. Neurol. **138**, 11–27 (2015)
144. E. Gordon-Lipkin, B. Chodkowski, D.S. Reich, S.A. Smith, M. Pulicken, L.J. Balcer et al., Retinal nerve fiber layer is associated with brain atrophy in multiple sclerosis. Neurology **69**(16), 1603–1609 (2007)
145. E. Grazioli, R. Zivadinov, B. Weinstock-Guttman, N. Lincoff, M. Baier, J.R. Wong et al., Retinal nerve fiber layer thickness is associated with brain MRI outcomes in multiple sclerosis. J. Neurol. Sci. **268**(1–2), 12–17 (2008)
146. X. Wang, Y. Jia, R. Spain, B. Potsaid, J.J. Liu, B. Baumann et al., Optical coherence tomography angiography of optic nerve head and parafovea in multiple sclerosis. Br. J. Ophthalmol. **98**(10), 1368–1373 (2014). https://doi.org/10.1136/bjophthalmol-2013-304547. PubMed PMID: 24831719
147. F. Zipp, O. Aktas, The brain as a target of inflammation: common pathways link inflammatory and neurodegenerative diseases. Trends Neurosci. **29**(9), 518–527 (2006). https://doi.org/10.1016/j.tins.2006.07.006. PubMed PMID: 16879881
148. H. Jiang, D. Cabrera DeBuc, S. Delgado, A. Tao, B. Lam, J. Wang, Quantification of macular blood flow volume and microvascular network in multiple sclerosis (MS) (P2.264). Neurology **82**(10 Supplement), P2.264 (2014)
149. H. Jiang, S. Delgado, J. Yuan, W. Yan, D. Cabrera DeBuc, B. Lam et al., Impairment of the retinal nerve fiber integrity and blood flow velocity in multiple sclerosis (P5.224). Neurology **84**(14 Supplement), P5.224 (2015)
150. H. Jiang, Y. Ye, D. Cabrera DeBuc, M. Shen, B.L. Lam, L. Ge et al., Spectral oximetry measured with ultra-high resolution optical coherence tomography in multiple sclerosis, in *38th Annual North American Neuro-Ophthalmology Society (NANOS) Meeting*, 11–16 February, San Antonio, TX (2012) (poster presentation)
151. B.R. White, M.C. Pierce, N. Nassif, B. Cense, B.H. Park, G.J. Tearney et al., In vivo dynamic human retinal blood flow imaging using ultra-high-speed spectral domain optical Doppler tomography. Opt. Express **11**(25), 3490–3497 (2003). https://doi.org/10.1364/oe.11.003490. PubMed PMID: WOS:000187324900021
152. P.K. Stys, G.W. Zamponi, J. van Minnen, J.J. Geurts, Will the real multiple sclerosis please stand up? Nat. Rev. Neurosci. **13**(7), 507–514 (2012). https://doi.org/10.1038/nrn3275. PubMed PMID: 22714021
153. B. Braaf, K.A. Vermeer, K.V. Vienola, J.F. de Boer, Angiography of the retina and the choroid with phase-resolved OCT using interval-optimized backstitched B-scans. Opt. Express **20**(18), 20516–20534 (2012). https://doi.org/10.1364/oe.20.020516. PubMed PMID: WOS:000308414800087
154. T.D. France, Evidence-based guidelines for amblyogenic risk factors. Am. Orthopt. J. **56**, 7–14 (2006)
155. P.A. Graham, Epidemiology of strabismus. Br. J. Ophthalmol. **58**, 224–231 (1974)
156. L. Kiorpes, S.P. McKee, Neural mechanisms underlying amblyopia. Curr. Opin. Neurobiol. **9**, 480–486 (1999)
157. G. Roper-Hall, Current concepts of amblyopia: a neuro-ophthalmology perspective. Am. Orthopt. J. **57**, 2–11 (2007)
158. G.K. Noorden, Mechanisms of amblyopia. Adv. Ophthalmol. **34**, 93–115 (1977)
159. G.K. Noorden, M.L. Crawford, The lateral geniculate nucleus in human strabismic amblyopia. Invest. Ophthalmol. Vis. Sci. **33**, 2729–2732 (1992)
160. G.K. Noorden, M.L. Crawford, R.A. Levacy, The lateral geniculate nucleus in human anisometropic amblyopia. Invest. Ophthalmol. Vis. Sci. **24**, 788–790 (1983)

161. M.P. Headon, T.P. Powell, Cellular changes in the lateral geniculate nucleus of infant monkeys after suture of the eyelids. J. Anat. **116**, 135–145 (1973)
162. S.M. Sherman, J.R. Wilson, Behavioral and morphological evidence for binocular competition in the postnatal development of the dog's visual system. J. Comp. Neurol. **161**, 183–195 (1975)
163. G.K. Noorden, Histological studies of the visual system in monkeys with experimental amblyopia. Invest. Ophthalmol. **12**, 727–738 (1973)
164. T.N. Wiesel, D.H. Hubel, Effects of visual deprivation on morphology and physiology of cells in the cats lateral geniculate body. J. Neurophysiol. **26**, 978–993 (1963)
165. E.C. Campos, C. Schiavi, P. Benedetti, R. Bolzani, V. Porciatti, Effect of citicoline on visual acuity in amblyopia: preliminary results. Graefes Arch. Clin. Exp. Ophthalmol. **233**, 307–312 (1995)
166. E.M. Banko, J. Kortvelyes, J. Nemeth, B. Weiss, Z. Vidnyanszky, Amblyopic deficits in the timing and strength of visual cortical responses to faces. Cortex **49**, 1013–1024 (2013)
167. K.L. Chow, Failure to demonstrate changes in the visual system of monkeys kept in darkness or in colored lights. J. Comp. Neurol. **102**, 597–606 (1955)
168. E. Rasch, H. Swift, A.H. Riesen, K.L. Chow, Altered structure and composition of retinal cells in dark-reared mammals. Exp. Cell Res. **25**, 348–363 (1961)
169. C.P. Wendell-Smith, Effect of light deprivation on the postnatal development of the optic nerve. Nature **204**, 707 (1964)
170. G.B. Arden, S.L. Wooding, Pattern ERG in amblyopia. Invest. Ophthalmol. Vis. Sci. **26**, 88–96 (1985)
171. B. Tugcu, B. Araz-Ersan, M. Kilic, E.T. Erdogan, U. Yigit et al., The morpho-functional evaluation of retina in amblyopia. Curr. Eye Res. **38**, 802–809 (2013)
172. A.G. Alotaibi, B. Al Enazi, Unilateral amblyopia: optical coherence tomography findings. Saudi J. Ophthalmol. **25**, 405–409 (2011)
173. M.Y. Yen, C.Y. Cheng, A.G. Wang, Retinal nerve fiber layer thickness in unilateral amblyopia. Invest. Ophthalmol. Vis. Sci. **45**, 2224–2230 (2004)
174. S.W. Yoon, W.H. Park, S.H. Baek, S.M. Kong, Thicknesses of macular retinal layer and peripapillary retinal nerve fiber layer in patients with hyperopic anisometropic amblyopia. Korean J. Ophthalmol. **19**, 62–67 (2005)
175. A. Dickmann, S. Petroni, V. Perrotta, A. Salerni, R. Parrilla et al., A morpho-functional study of amblyopic eyes with the use of optical coherence tomography and microperimetry. J. AAPOS **15**, 338–341 (2011)
176. A. Dickmann, S. Petroni, A. Salerni, R. Dell'Omo, E. Balestrazzi, Unilateral amblyopia: an optical coherence tomography study. J. AAPOS **13**, 148–150 (2009)
177. S.C. Huynh, C. Samarawickrama, X.Y. Wang, E. Rochtchina, T.Y. Wong et al., Macular and nerve fiber layer thickness in amblyopia: the Sydney Childhood Eye Study. Ophthalmology **116**, 1604–1609 (2009)
178. Y. Pang, G.W. Goodfellow, C. Allison, S. Block, K.A. Frantz, A prospective study of macular thickness in amblyopic children with unilateral high myopia. Invest. Ophthalmol. Vis. Sci. **52**, 2444–2449 (2011)
179. O. Altintas, N. Yuksel, B. Ozkan, Y. Caglar, Thickness of the retinal nerve fiber layer, macular thickness, and macular volume in patients with strabismic amblyopia. J. Pediatr. Ophthalmol. Strabismus **42**, 216–221 (2005)
180. A. Dickmann, S. Petroni, V. Perrotta, R. Parrilla, S. Aliberti et al., Measurement of retinal nerve fiber layer thickness, macular thickness, and foveal volume in amblyopic eyes using spectral-domain optical coherence tomography. J. AAPOS **16**, 86–88 (2012)
181. S.Y. Kee, S.Y. Lee, Y.C. Lee, Thicknesses of the fovea and retinal nerve fiber layer in amblyopic and normal eyes in children. Korean J. Ophthalmol. **20**, 177–181 (2006)
182. M.X. Repka, N. Goldenberg-Cohen, A.R. Edwards, Retinal nerve fiber layer thickness in amblyopic eyes. Am. J. Ophthalmol. **142**, 247–251 (2006)

183. M.X. Repka, R.T. Kraker, S.M. Tamkins, D.W. Suh, N.A. Sala et al., Retinal nerve fiber layer thickness in amblyopic eyes. Am. J. Ophthalmol. **148**, 143–147 (2009)
184. R.A. Walker, S. Rubab, A.R. Voll, V. Erraguntla, P.H. Murphy, Macular and peripapillary retinal nerve fibre layer thickness in adults with amblyopia. Can. J. Ophthalmol. **46**, 425–427 (2011)
185. K.L. Chow, A.H. Riesen, F.W. Newell, Degeneration of retinal ganglion cells in infant chimpanzees reared in darkness. J. Comp. Neurol. **107**, 27–42 (1957)
186. E. Fifkova, Effect of visual deprivation and light on synapses of the inner plexiform layer. Exp. Neurol. **35**, 458–469 (1972)
187. L. Sosula, P.H. Glow, Increase in number of synapses in the inner plexiform layer of light deprived rat retinae: quantitative electron microscopy. J. Comp. Neurol. **141**, 427–451 (1971)
188. L. Weiskrantz, Sensory deprivation and the cat's optic nervous system. Nature **181**, 1047–1050 (1958)
189. J.M. Enoch, Receptor amblyopia. Am. J. Ophthalmol. **48**(3), 262–274 (1959)
190. T.P. Colen, J.T. de Faber, H.G. Lemij, Retinal nerve fiber layer thickness in human strabismic amblyopia. Binocular Vis. Strabismus Q. **15**, 141–146 (2000)
191. C.E. Al-Haddad, G.M. El Mollayess, Z.R. Mahfoud, D.F. Jaafar, Z.F. Bashshur, Macular ultrastructural features in amblyopia using high-definition optical coherence tomography. Br. J. Ophthalmol. **97**, 318–322 (2013)
192. A. Szigeti, E. Tátrai, A. Szamosi, P. Vargha, Z.Z. Nagy, J. Németh, D. Cabrera DeBuc, G.M. Somfai, A morphological study of retinal changes in unilateral amblyopia using optical coherence tomography image segmentation. PLoS One 6;**9**(2), e88363 (2014)
193. B. Alamouti, J. Funk, Retinal thickness decreases with age: an OCT study. Br. J. Ophthalmol. **87**, 899–901 (2003)
194. A.H. Kashani, I.E. Zimmer-Galler, S.M. Shah, L. Dustin, D.V. Do et al., Retinal thickness analysis by race, gender, and age using Stratus OCT. Am. J. Ophthalmol. **149**(496–502), e491 (2010)
195. H.E. Bedell, Central and peripheral retinal photoreceptor orientation in amblyopic eyes as assessed by the psychophysical Stiles-Crawford function. Invest. Ophthalmol. Vis. Sci. **19**, 49–59 (1980)
196. P.J. Delint, C. Weissenbruch, T.T. Berendschot, D.V. Norren, Photoreceptor function in unilateral amblyopia. Vis. Res. **38**, 613–617 (1998)
197. C. Williams, D. Papakostopoulos, Electro-oculographic abnormalities in amblyopia. Br. J. Ophthalmol. **79**, 218–224 (1995)
198. J. Leone, K. Koklanis, Z. Georgievski, R. Wilkinson, Macular and retinal nerve fibre layer thickness in strabismus and anisometropic amblyopia. Binocular Vis. Strabismus Q. **23**, 227–234 (2008)
199. E. Hatef, A. Khwaja, Z. Rentiya, M. Ibrahim, M. Shulman et al., Comparison of time domain and spectral domain optical coherence tomography in measurement of macular thickness in macular edema secondary to diabetic retinopathy and retinal vein occlusion. J. Ophthalmol. **2012**, 354783 (2012)
200. Z. Hu, M. Nittala, S. Sadda, Comparison and normalization of retinal reflectivity profiles between spectral-domain optical coherence tomography devices. Invest. Ophthalmol. Vis. Sci. **54**(15), 5492 (2013)
201. H. Chen, X. Chen, Z. Qiu, D. Xiang, W. Chen, F. Shi, J. Zheng, W. Zhu, M. Sonka, Quantitative analysis of retinal layers' optical intensities on 3D optical coherence tomography for central retinal artery occlusion. Sci. Rep. **5**, 9269 (2015)
202. K.A. Vermeer, J. van der Schoot, H.G. Lemij, J.F. de Boer, RPE-normalized RNFL attenuation coefficient maps derived from volumetric OCT imaging for glaucoma assessment. Invest. Ophthalmol. Vis. Sci. **53**(10), 6102–6108 (2012)

203. T.E. de Carlo, A. Romano, N.K. Waheed, J.S. Duker, A review of optical coherence tomography angiography (OCTA). Int. J. Retin. Vitr. **1**(1), 5 (2015)
204. C.E. Al-Haddad, G.M. Mollayess, C.G. Cherfan, D.F. Jaafar, Z.F. Bashshur, Retinal nerve fibre layer and macular thickness in amblyopia as measured by spectral-domain optical coherence tomography. Br. J. Ophthalmol. **95**, 1696–1699 (2011)

Chapter 7
Quantitative Analysis of Retinal Layers' Optical Intensities Based on Optical Coherence Tomography

Enting Gao, Fei Shi, Haoyu Chen and Xinjian Chen

In addition to the morphologic parameters of retinal structures, OCT images also provide the signal/reflection intensity information, which is however much less studied. This chapter introduces several studies on the quantitative analysis of the retinal layers' optical intensity, both for normal subjects and for patients with central retinal artery occlusion.

7.1 Introduction

Optical coherence tomography (OCT) is an in vivo, non-invasive imaging technology providing cross-sectional images of the retina structure [1]. It has significantly improved our understanding in eye physiology and in pathogenesis of ocular diseases. It also greatly helped the clinicians in diagnosis and management of retinal diseases [2]. OCT not only allows observation of the morphology of normal or disordered retinal tissue, but also provides quantitative measurement. Currently, most commercial OCT machines provide automatic measurements of the peripapillary retinal nerve fiber layer (RNFL) thickness and total macular retinal thickness. Advanced imaging

E. Gao · F. Shi · X. Chen
School of Electronics and Information Engineering, Soochow University, Suzhou, China

X. Chen (✉)
State Key Laboratory of Radiation Medicine and Protection, Soochow University, Suzhou, China
e-mail: xjchen@suda.edu.cn

H. Chen
Joint Shantou International Eye Center, Shantou University, Chinese University of Hong Kong, Shantou, China

X. Chen et al. (eds.), *Retinal Optical Coherence Tomography Image Analysis*, Biological and Medical Physics, Biomedical Engineering,
https://doi.org/10.1007/978-981-13-1825-2_7

analysis further provides the measurement of optic head [3], macular ganglion cells complex [4], choroidal thickness [5], etc.

However, OCT is not only valuable in providing morphological indices, but also offers quantitative measurements of local optical intensities (also called optical density or reflectivity) of the underlying normal and/or pathological tissues. It has been qualitatively observed that OCT optical intensity can provide clues for distinguishing pathological changes, for example, the optical intensity of inner retina increased in retinal artery occlusion [6]. In age-related macular degeneration, the optical intensity increased with development and regression of choroidal neovascularization [7]. In glaucoma patients, the optical intensity of the retinal nerve fiber layer (RNFL) has been shown to be lower than that in normal subjects, and decreases with increasing disease severity [8, 9]. Compared to normal vitreous, exudation lesions show higher reflectivity, whereas degeneration changes have lower optical intensity [10]. Similarly, optical intensity of pigment epithelial detachment can be used to differentiate serous, fibrovascular and drusenoid types [11]. In addition, reflectivity of the cystoid space varies with fluorescein pooling intensity, suggesting that blood—retinal barrier disruption can lead to content changes in diabetic macular edema [12]. Moreover, loss of reflectivity in the photoreceptor ellipsoid region has been reported to occur early and can be detected from the first clinical presentation in patients with idiopathic perifoveal telangiectasia [13]. These results suggested that the optical intensities of intraretinal or subretinal spaces can be used as biomarkers and provide clues to the pathogenesis of retinal diseases.

However, quantitative assessment of OCT optical intensity was much less reported, compared to the dimension analysis. In 2000, Pons et al. [8] reported that the internal reflectivity of RNFL was lower in patients with glaucoma compared to control. It was confirmed in spectral domain OCT recently [14, 15]. A study by Giani et al. [16], using OCT, shows that quantitative analysis of choroidal neovascularization (CNV) reflectivity can differentiate leaky CNV from that without leakage, providing additional information regarding the fluorescein angiography leakage status.

There are also lack of the information of normal range and physiological variation of retinal optical intensities. Since application of newly developed parameters depends on an understanding of normal conditions, it is critical to establish a normative database of specific criteria. To our knowledge, few studies have been carried out on retinal optical intensity distribution in normal subjects. The effect of determinants such as sex, age, race, optic disc area, axial length and refractive error [17–19] which affect retinal thickness measurements on optical intensity remained unknown.

In this chapter, we will introduce a few studies on the OCT optical intensity of retinal layers based on a validated automatic computer algorithm [20–23]. In the first study [24], the optical intensities in all retinal layers on spectral domain OCT was measured, and the variations and relationships among retinal layers' optical intensities in normal subjects were investigated. In the second study [25], the retinal optical intensity distribution of normal subjects was investigated in each retinal layer and nine macular sectors based on areas defined in the Early Treatment Diabetic Retinopathy Study (ETDRS) [26]. To collect reference data on the determinants,

they also evaluated the effects of age, sex, height, weight, refractive status, axial length, image quality, optic disc area and rim/disc area ratio on optical intensity. In the third study [27], the optical intensity of each retinal layer in central retinal artery occlusion (CRAO) was quantitatively investigated and compared with the same measurements obtained from normal controls.

7.2 Automatic Layer Segmentation in OCT Images

The segmentation of retinal layers in OCT scans has been an important work since we want to establish the distribution and variations of the intensity in the retinal layers. Eleven surfaces were automatically segmented using a validated 3D graph search approach [20–23]. The workflow included preprocessing and layer segmentation. The preprocessing part was a denoising step. OCT data speckle noise was first reduced by a curvature anisotropic diffusion filter. Retinal boundaries were later automatically detected by finding an optimal closed set in a vertex-weighted graph. The RNFL, ganglion cell layer (GCL), inner plexiform layer (IPL), inner nuclear layer (INL), outer plexiform layer (OPL), outer nuclear layer (ONL), photoreceptor layer and retinal pigment epithelium (RPE) were identified (Fig. 7.2). Every B-scan image was visually inspected by an ophthalmologist (B.C.) and excluded if any misidentification of boundaries between retinal layers occurred. Choroid was defined as the region within 25 pixels below the RPE (Fig. 7.1).

7.3 The Optical Intensity of Retinal Layers of Normal Subjects

7.3.1 Data Acquisition

Forty normal subjects were included in the first study. Spectral domain OCT scanning was obtained using the Topcon 3D OCT-1000 (Topcon Corporation, Tokyo, Japan). 6×6 mm macular-centered OCT volumes were obtained, which consisted of 64 B scans. Axial and transverse resolution was 6 and 20 μm respectively. A fundus photograph was obtained at the same time. The image was $512 \times 64 \times 480$ voxels, with each voxel corresponding to $11.72 \times 93.75 \times 3.50\,\mu m^3$. The image quality index was given by the OCT software and ranged from 0 to 100. Raw data were exported with intensity ranged from 0 to 65,535. Intensity was expressed in arbitrary units (AU).

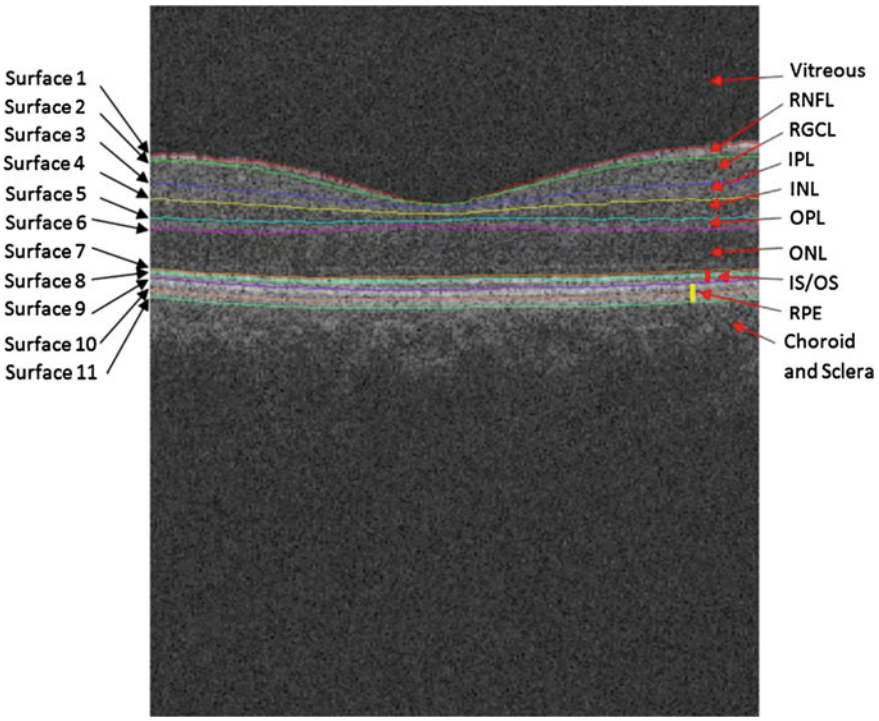

Fig. 7.1 Segmented surfaces and regions on macular spectral domain optical coherence tomography

7.3.2 Statistical Analysis

For each layer, and for each subject, the mean and standard deviation of optical intensities were calculated. The optical intensities of each layer were compared between male and female by Student's independent *t*-test. The correlations between the mean intensities of each two layers, and between each layer's intensity and age/imaging quality were analyzed with Pearson's correlation. Correlation coefficient *r* was calculated. The adjusted variance with image quality index as normalizing parameter and was calculated as $variance \times (1 - r^2_{with\_imaga\_quality})$. Adjusted coefficient of variation was calculated as adjusted standard deviation over the mean.

Table 7.1 Mean and standard deviation of optical intensities in different layers

	Mean	SD	Variance	r^2 (%)	Adjusted variance	Adjusted SD	Adjusted coefficient of variation
Vitreous	13,963.50	105	11,032	27.90	7955	89.2	0.0064
Retinal nerve fiber layer	28,516.50	1491.2	2,223,605	55.90	980,035	990	0.0347
Retinal ganglion cells	22,821.30	1301.4	1,693,558	75.50	415,076	644.3	0.0282
Inner plexiform layer	22,351.70	1329.1	1,766,570	81.80	322,371	567.8	0.0254
Inner nuclear layer	19,092.10	1047.9	1,098,045	89.90	110,480	332.4	0.0174
Outer plexiform layer	20,095.20	1225.2	1,501,154	89.20	162,590	403.2	0.0201
Outer nuclear layer	17,005.00	782.7	612,695	94.70	32,542	180.4	0.0106
Photoreceptor	28,615.40	1669.9	2,788,601	62.70	1,041,087	1020.3	0.0357
Retinal pigment epithelium	30,780.20	1489.6	2,218,907	64.30	791,861	889.9	0.0289
Choroid	19,791.60	964.5	930,165	58.40	386,699	621.9	0.0314
All areas	15,863.30	292.3	85,435	87.60	10,630	103.1	0.0065

7.3.3 Results of Quantitative Analysis of Retinal Layer Optical Intensities of Normal Subjects

The mean, standard deviation and adjusted standard deviation of different layers' optical intensities were listed in Table 7.1 and showed in Fig. 7.2.

As shown in Fig. 7.3, the correlation among the optical intensities of intraretinal layers were moderate to good, with r ranged from 0.524 to 0.988, all $p < 0.001$. Among them, the correlation between optical intensities of GCL, IPL, INL, OPL were very strong, with $r > 0.934$, all $p < 10^{-18}$. On the contrary, the correlation of intensities of vitreous with all intraretinal layers were only mild to moderate, with r ranged from 0.363 to 0.541 (all $p < 0.03$), except the low correlation with photoreceptor ($r = 0.251$, $p = 0.119$). The choroid layer's intensity had moderate correlation with intraretinal layers, with r ranging from 0.418 to 0.725 (all $p < 0.01$).

Totally 23 male and 17 female subjects were included in the study. The mean age were 37.9 ± 14.9 years old. No statistically difference of the optical intensities were found in any layers between male and female (all $p > 0.05$). The mean

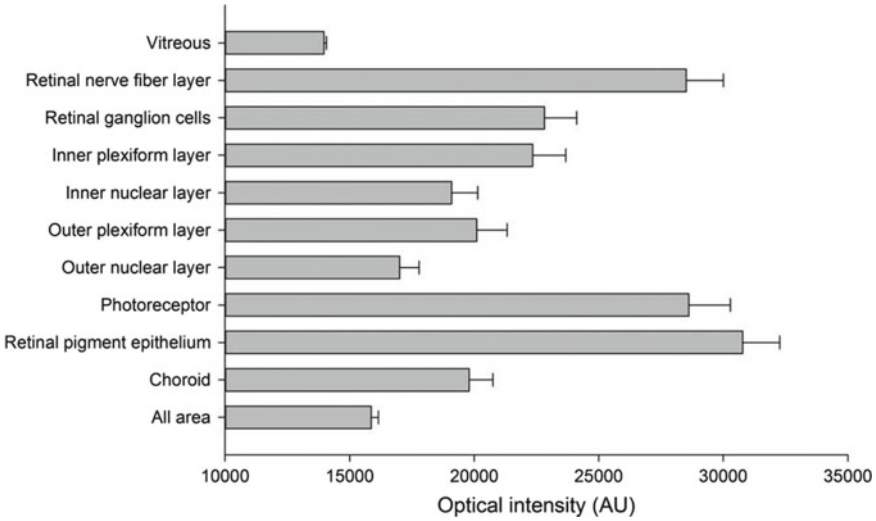

Fig. 7.2 The mean and standard deviation of optical intensities of each layers

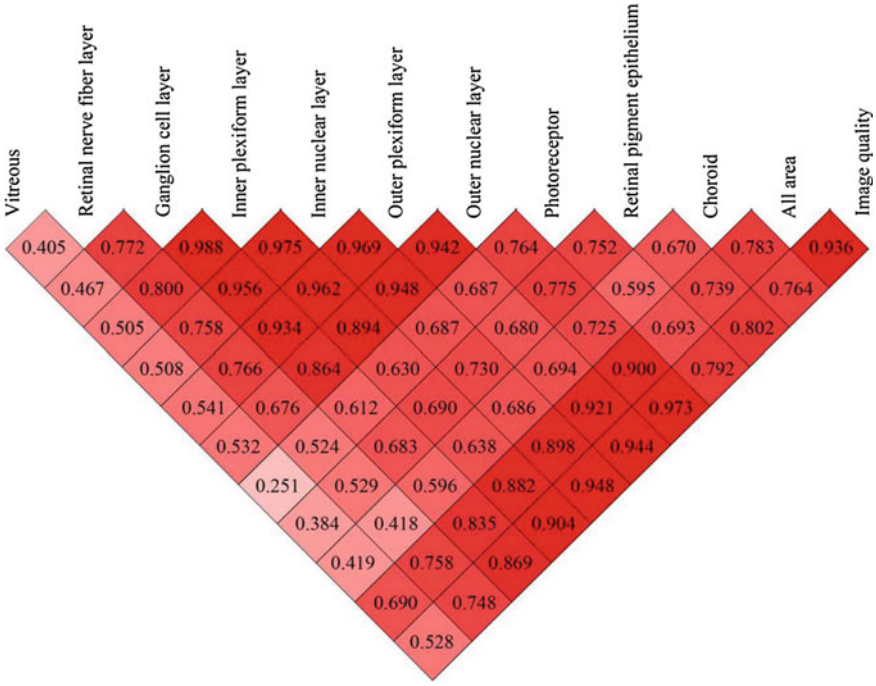

Fig. 7.3 Correlation coefficient matrix of optical intensities among all layers and image quality

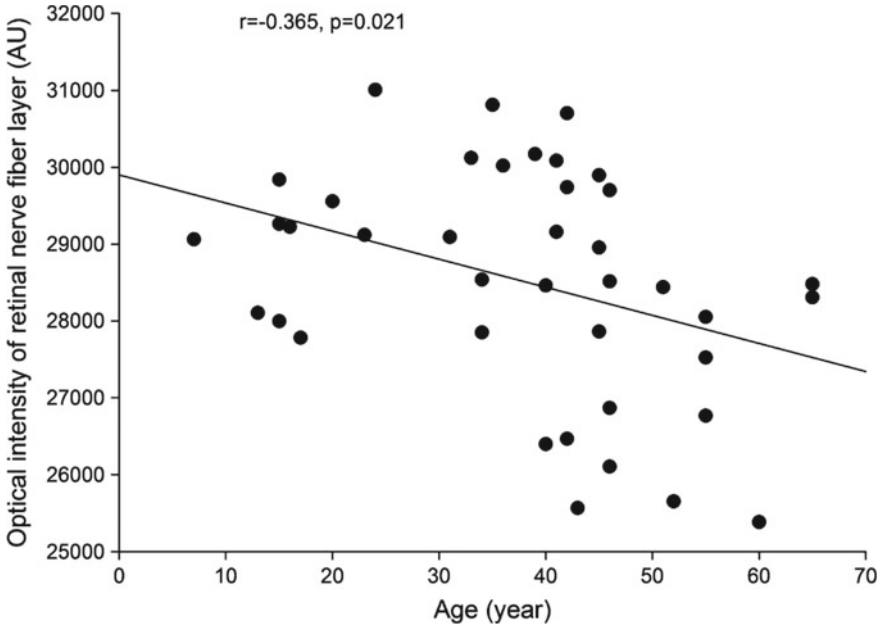

Fig. 7.4 Correlation of optical intensity in retinal nerve fiber layer with age

image quality index were 51.8 ± 8.3. The image quality index had strong correlation with optical intensities of retinal layers (r between 0.748 and 0.973, $p < 10^{-8}$), but moderate correlation with vitreous intensity ($r = 0.528, p = 0.0005$). Age was not correlated with optical intensities in any layers except RNFL, which has $r = -0.365$, $p = 0.021$ (Fig. 7.4). The correlation remained significant after adjust of image quality ($b = -24.2$, $p = 0.025$).

7.3.4 Discussion

This analysis is based on 3D data and investigated all retinal layers, therefore provided complete profile of the scanned area. Furthermore, this study is fully automatic, which eliminated inter-observer variation. Although the study used the data from Topcon 3D-OCT 1000, the algorithm can be applied to SD-OCT images from any manufacturer.

It is found in the study that the optical intensities in different layers correlated with each other. They were also strongly correlated with image quality, which represented signal strength in Topcon 3D-OCT 1000. Therefore, the study confirmed that optical intensity was affected by the signal strength.

From the conclusion above, it is necessary to normalize the intensity with signal strength. Various methods have been used in the literature [10, 12, 16] and different layer intensities have been used as reference. This study found that in normal subjects, the optical intensity in GCL, IPL, INL, OPL and ONL were highly correlated with each other and image quality, their r^2 with image quality is more than 80%. Based on these results, we recommend GCL, IPL, INL, OPL or ONL as references for normalization. In addition, as the image quality index and the optical intensity of all areas both had good correlation with optical intensities of intraretinal layers, they can also be the reference for normalization.

A week negative correlation was found between RNFL with age ($r = -0.365$, $p = 0.021$), even after adjust of image quality, which did not apply to other layers. It is a new finding. It is well recognized that the RNFL thickness was reduced in glaucoma patients [28] and aged subjects [29]. The optical intensity of RNFL was also reported lower in patients with glaucoma compared to control or ocular hypertension [8, 14]. Hence, further investigations are desired to clarify the role RNFL optical intensity in diagnosis of glaucoma.

7.4 Distribution and Determinants of the Optical Intensity of Retinal Layers of Normal Subjects

The automatic segmentation approach was also used to determine the distribution of optical intensity of each layer and regions specified by the Early Treatment of Diabetic Retinopathy Study (ETDRS) in 231 eyes from 231 healthy subjects ranging in age from 18 to 80 years old [26]. Forty-four eyes were randomly chosen to be scanned by two operators for reproducibility analysis. Univariate and multivariate analysis were performed between retinal optical intensity and sex, age, height, weight, spherical equivalent (SE), axial length, image quality, disc area and rim/disc area ratio (R/D area ratio).

7.4.1 Data Acquisition and Image Processing

All subjects received scans by experienced operators with Topcon 3D OCT-2000 (Topcon, Tokyo, Japan, software version: 8.11.003.04) without pupil dilatation. Three-dimensional image data were acquired using the scan mode of 3D macular (512×128) centered at the fovea and covering a 6×6 mm^2 area. Scanning was performed with the measurement beam perpendicular to the retina (light entered the eyes across the central position of the pupil). Forty-four eyes were randomly chosen to be scanned by the two operators on the same day for reproducibility analysis. The axial resolution was 5–6 μm and transverse resolution was 20 μm. Images, of a quality of 45 or higher, were included. Parameters, such as disc area and rim/disc

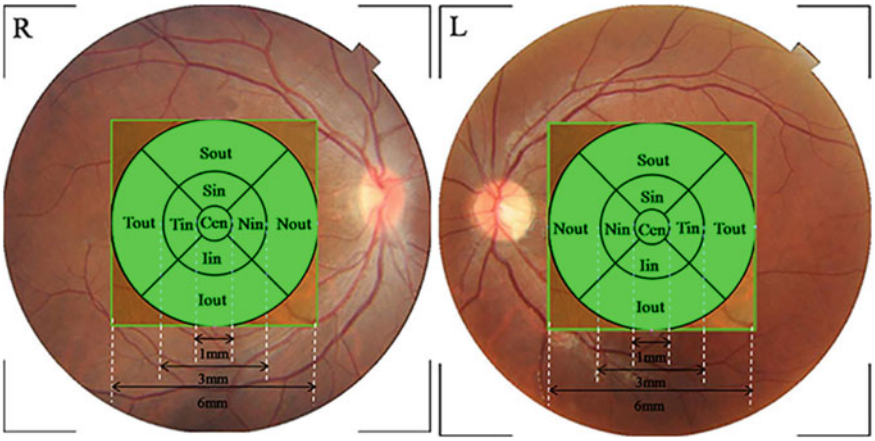

Fig. 7.5 Early treatment diabetic retinopathy study (ETDRS) chart of the right (R) and left (L) eyes. The ETDRS plot is centered at the fovea. It includes three circles with diameters of 1, 3 and 6 mm. The area is further divided into four quadrants: superior, inferior, nasal and temporal. Cen, central subfield; Sin, Superior inner ring; Nin, Nasal inner ring; Iin, Inferior inner ring; Tin, Temporal inner ring; Sout, Superior outer ring; Nout, Nasal outer ring; Iout, Inferior outer ring; Tout, Temporal outer ring

area ratio, were obtained through the 3D disc (512 × 128) scan. Reference plane for optic disc parameters analysis was set at 120 μm above the RPE according to the default setting.

As in the previous section, the OCT images were segmented using the automatic method to obtain the retina layers. In addition, we identified the lowest location of surface 1, built an ETDRS chart (Fig. 7.5) centered at this point and measured the optical intensities of every voxel in each layer and each ETDRS sector.

7.4.2 Statistical Analysis

Statistical analysis was performed with commercial statistical software (IBM SPSS Statistics v.17 for Windows; SPSS Inc. Chicago, IL). To evaluate interoperator differences, the intraclass correlation coefficient (ICC) was used. The mean and standard deviation (SD) of optical intensity for each retinal layer were calculated in the six age groups. Independent samples t-test and Pearson's correlation were used to evaluate the effect of sex, age, height, weight, spherical equivalent, axial length, image quality, disc area and rim/disc area ratio on optical intensity. Factors significant at $p < 0.05$ were included in the stepwise multiple regression analysis. Sigmaplot (version 12.5, Systat Inc.) was employed to draw contour plots. A $p < 0.05$ was considered statistically significant.

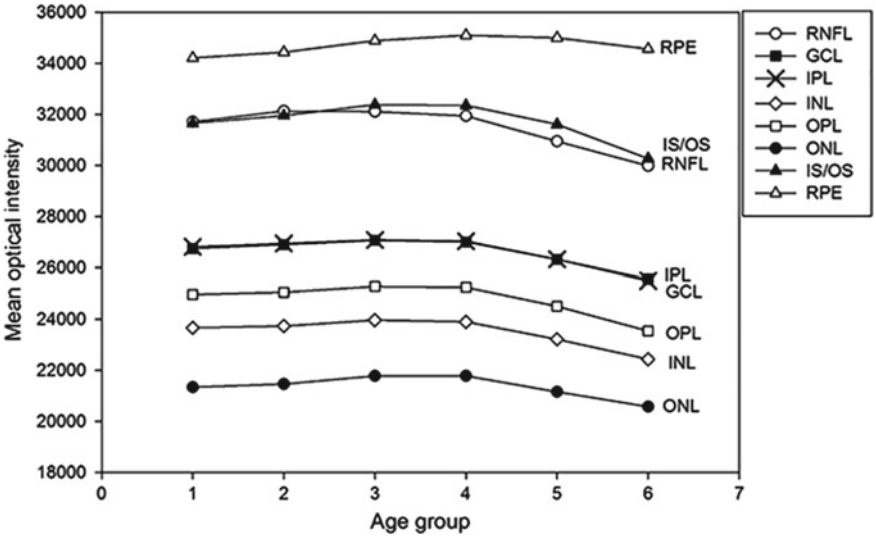

Fig. 7.6 Mean optical intensity of retinal layers in different age groups. Groups 1–6 represent the agegroups (age 20–29, 30–39, 40–49, 50–59, 70+). Mean optical intensity of different retinal layers are shown in correspondinglegends. Mean optical intensity was highest in RPE layer, followed by photoreceptor layer, RNFL, IPL, GCL, OPL, INL and ONL. Optical intensity was stable prior to 50 years of age, and then decreased in most retinallayers (RNFL to photoreceptor layer)

7.4.3 Retinal Optical Intensity Measurement

The reproducibility of retinal optical intensity analysis is high. For measurements over the entire scan area and each retinal layer, ICCs ranged from 0.815 to 0.941.

Table 7.2 shows the mean and SD of the macular retinal optical intensity of each age group. Mean optical intensity was highest in RPE layer, photoreceptor layer and RNFL, followed by IPL and GCL, and lowest in ONL (Fig. 7.6). Optical intensity from RNFL to photoreceptor layer decreased with age after 50 years old (r ranged from -0.440 to -0.158, all $p < 0.01$, Spearman's test). For RPE layer, the optical intensity increased with older age groups ($r = 0.318$, $p < 0.01$, Spearman's test).

Mean optical intensity for all subjects by ETDRS region is shown in Table 7.3. Optical intensity maps (Fig. 7.7) show specific distribution patterns. In the central area, the optical intensity of RNFL, GCL, IPL, INL, OPL and photoreceptor layer were at a lower level while that of RPE was at its highest. There was a circinate area with higher intensity at the parafoveal region in ONL. In RNFL and GCL, mean optical intensity of the nasal sectors was greater than the temporal sectors, while ONL, photoreceptor layer and RPE showed the opposite distribution ($p < 0.05$, paired t-test).

Table 7.2 Macular retinal optical intensity of different age groups

Age (y)	20–29	30–39	40–49	50–59	60–69	70+	Total
RNFL	31,716.53 ± 1002.41	32,130.35 ± 536.43	32,112.86 ± 771.76	31,945.08 ± 806.99	30,949.73 ± 787.94	29,987.39 ± 1033.03	31,558.68 ± 1097.91
GCL	26,745.71 ± 671.09	26,904.80 ± 569.90	27,065.58 ± 778.21	27,009.75 ± 805.48	26,323.79 ± 929.56	25,561.10 ± 838.19	26,653.71 ± 896.17
IPL	26,822.60 ± 670.00	26,949.93 ± 569.32	27,087.39 ± 767.53	27,040.68 ± 754.32	26,327.70 ± 918.01	25,492.97 ± 823.89	26,677.85 ± 903.37
INL	23,667.89 ± 644.00	23,734.76 ± 561.02	23,969.33 ± 752.29	23,898.58 ± 733.82	23,215.58 ± 939.54	22,439.48 ± 810.12	23,538.66 ± 875.85
OPL	24,961.40 ± 678.86	25,052.67 ± 600.28	25,284.47 ± 768.46	25,247.65 ± 721.44	24,506.97 ± 979.62	23,542.35 ± 814.52	24,824.14 ± 933.38
ONL	21,340.80 ± 572.63	21,464.02 ± 536.60	21,784.25 ± 691.05	21,781.30 ± 656.26	21,155.73 ± 835.27	20,576.29 ± 955.45	21,381.69 ± 794.03
PR	31,660.07 ± 1404.50	31,955.85 ± 1359.32	32,386.75 ± 1617.76	32,353.75 ± 1055.47	31,614.73 ± 1009.89	30,272.35 ± 1194.85	31,759.63 ± 1444.96

Table 7.3 Macular optical intensity in ETDRS regions

Retinal layers	Cen	Inner ring			
		Sin	Nin	Lin	Tin
RNFL	24,102.52 ± 1251	30,843.87 ± 1384	29,839.42 ± 1422	30,687.22 ± 1322	29,005.43 ± 1545
RGCL	25,053.23 ± 1124	26,148.73 ± 1131	25,942.91 ± 1061	25,876.91 ± 1091	25,798.12 ± 1064
IPL	25,903.58 ± 1137	26,641.79 ± 1126	26,615.80 ± 1064	26,336.48 ± 1096	26,583.51 ± 1055
INL	24,052.05 ± 1133	23,625.45 ± 1076	23,624.06 ± 1012	23,300.45 ± 1047	23,619.90 ± 1006
OPL	24,023.62 ± 1217	25,261.45 ± 1120	25,256.25 ± 1038	24,893.74 ± 1094	25,194.93 ± 1093
ONL	21,486.65 ± 975	21,807.71 ± 1015	21,652.77 ± 961	21,569.35 ± 1013	21,617.72 ± 971
PR	31,574.06 ± 1734	32,899.26 ± 1859	32,778.81 ± 2176	32,590.06 ± 2165	33,227.47 ± 1839
RPE	36,030.78 ± 1070	35,443.49 ± 1003	35,489.23 ± 1103	35,060.54 ± 1218	35,672.81 ± 983
Retinal layers	Outer ring				Whole ETDRS
	Sout	Nout	Iout	Tout	
RNFL	32,285.48 ± 1480	32,742.87 ± 1521	31,618.63 ± 1231	29,972.42 ± 1564	31,558.68 ± 1098
RGCL	27,122.16 ± 1257	26,911.89 ± 1121	26,825.53 ± 1040	26,494.2 ± 1156	26,653.71 ± 896
IPL	26,852.89 ± 1275	26,799.34 ± 1111	26,397.12 ± 1032	26,788.47 ± 1141	26,677.85 ± 903
INL	23,603.41 ± 1178	23,563.84 ± 1039	23,141.81 ± 963	23,692.28 ± 1064	23,538.66 ± 876
OPL	24,926.75 ± 1242	25,050.16 ± 1084	24,343.63 ± 1057	25,121.60 ± 1125	24,824.14 ± 933
ONL	21,377.63 ± 1029	21,406.76 ± 944	20,987.83 ± 882	21,605.05 ± 943	21,381.69 ± 794
PR	31,920.69 ± 1905	31,902.14 ± 2123	31,221.00 ± 1843	32,614.52 ± 1723	31,759.63 ± 1445
RPE	34,686.48 ± 1048	34,707.6 ± 1102	33,936.19 ± 1058	35,206.9 ± 900	34,677.20 ± 696

7.4.4 Determinants of Retinal Optical Intensity

Differences between men and women in mean optical intensity were not significant (all $p < 0.05$, independent-samples t-test). The results of Pearson correlation analysis between optical intensity and age, height, weight, spherical equivalent, axial length, image quality, disc area and rim/disc area ratio. Image quality was significantly correlated with all retinal layer optical intensities, with the correlation coefficient r ranging from 0.503 to 0.851 (all $p < 0.01$). Age was negatively correlated with optical intensity from RNFL to photoreceptor layer ($-0.517 < r < -0.242$, $p < 0.01$), but positively correlated with that in RPE ($r = 0.287$, $p < 0.01$). Axial length was also negatively correlated with optical intensity from OPL to RPE. Spherical equivalent was positively correlated with only ONL and RPE optical intensity. The relationship of disc area and optical intensity in most layers was weak but significant in RPE layer. No statistically significant relationships were found between retinal optical intensity and height, weight and rim/disc area ratio.

The results of stepwise multiple linear regression analysis was calculated. Factors significant at $p < 0.05$ with any retinal layer optical intensity from the univariate analysis were included. Significant determinants of optical intensity for most retinal layers were age and image quality. The effect of image quality was more pronounced in the optical intensity of ONL ($\beta = 0.851$), followed by INL, OPL and IPL, and was

less pronounced in photoreceptor layer. The negative correlation between age and optical intensity from RNFL to OPL, except for ONL and photoreceptor layer, as well as the positive correlation between age and RPE optical intensity, remained after adjustment of other factors, such as image quality. The strongest association with age was the optical intensity of RPE layer (had the highest standardized β values = 0.456). No correlation was found, after adjustment, between retinal optical intensity and sex, height, weight, SE, axial length, disc area and rim/disc area ratio.

7.4.5 Discussion

In this study, by analyzing three-dimensional OCT data with our automatic software, the retinal optical intensity of adults in different age groups was described, and the effects of various factors on this parameter was explored. The interoperator reproducibility of optical intensity measurement in healthy eyes was good. Mean optical intensity was highest in RPE layer, photoreceptor layer and RNFL, and lowest in ONL. Optical intensity was low in the central area of RNFL, GCL, IPL, INL, OPL and photoreceptor layers, and high in the center of RPE layer. In RNFL and GCL, mean optical intensity of the nasal sectors was greater than in the temporal sectors, whereas the ONL, photoreceptor layer and RPE had the opposite distribution. The results also demonstrated that retinal optical intensity of most retinal layers increased with image quality, and decreased with age. There was no relationship between retinal optical intensity and sex, height, weight, SE, axial length, disc area or rim/disc area ratio.

7.5 The Optical Intensity Distribution in Central Retinal Artery Occlusion (CRAO)

7.5.1 Central Retinal Artery Occlusion

Central retinal artery occlusion (CRAO) is an ocular emergency that can lead to severe ischemia of the retina and cause a sudden loss of vision [30]. In the acute phase, whitish opacification of the retina is present at the posterior pole except fovea, which does not have inner retinal layers. The opacification typically resolves spontaneously within a month [31]. On fundus fluorescein angiography, delay of arteriovenous transit time and retinal artery filling time is usually observed [32]. However, fluorescein angiography is invasive, and subject to severe complications, including a possibility of allergic shock. Furthermore, fluorescein angiography provides only limited information about the severity of retinal damage [33].

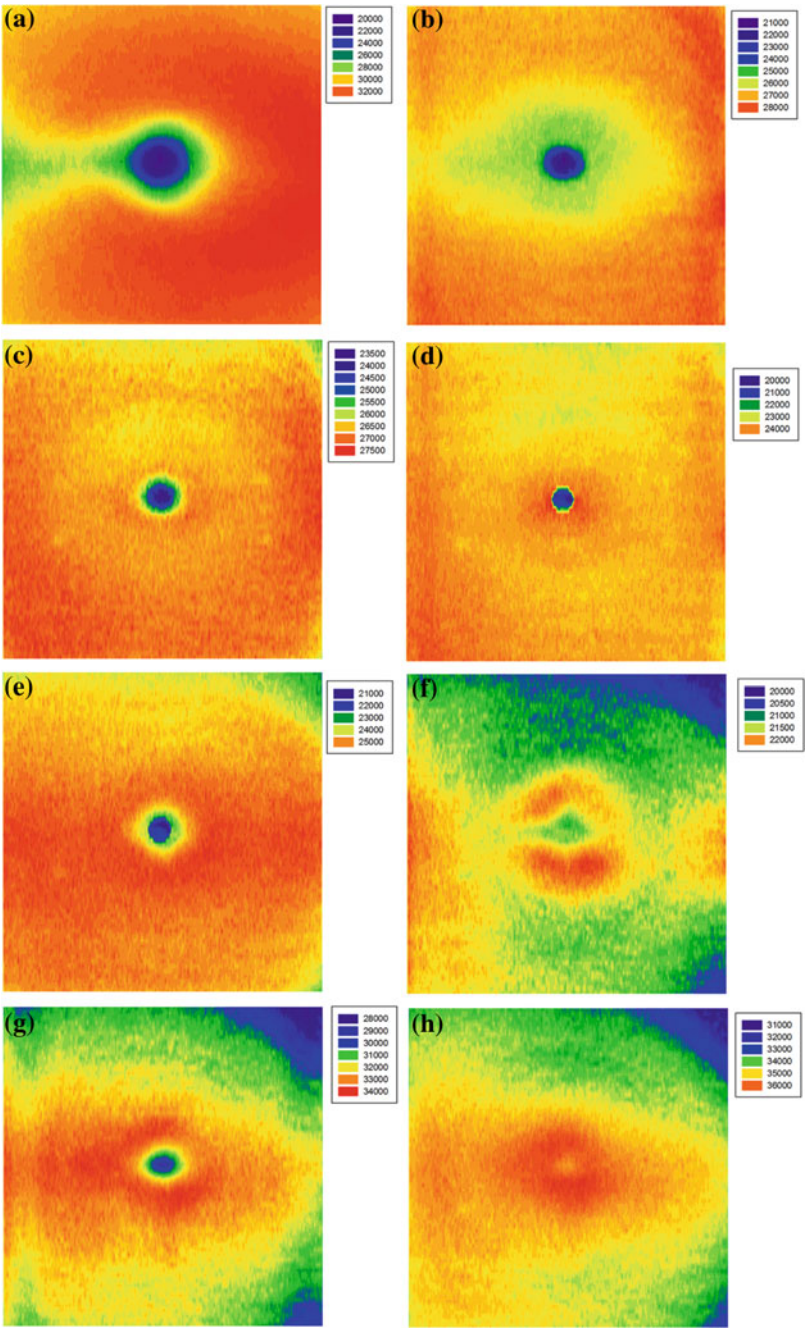

Fig. 7.7 Mean optical intensity distribution of retinal layers. Color spectra to the right of each image show the optical intensity range of each layer. The right side of each image represents the nasal quadrant, the left side represents the temporal quadrant. The retinal layer is stated in the upper left of images. **a** RNFL, **b** GCL, **c** IPL, **d** INL, **e** OPL, **f** ONL, **g** photoreceptor, and **h** RPE

In 2006, it was first reported that the retinal thickness was increased in the acute phase of CRAO, and was subsequently reduced at follow-up of several months. However, the observed extent of retinal edema did not correlate with the visual prognosis [34]. Later, with the introduction of spectral domain OCT with higher resolution, it was found that the thickness of inner retina decreased in chronic phase of CRAO but there was no similar change in the outer retina [35]. Recently, it was reported that in the acute phase of branch retinal artery occlusion (BRAO), the thicknesses were markedly increased in the inner layers including the retinal nerve fiber layer (RNFL)/ganglion cell layer (GCL), inner plexiform layer (IPL) and inner nuclear layer (INL)/outer plexiform layer (OPL), and mildly increased in the outer nuclear layer (ONL). In the chronic phase, reduction of thickness was noted with an observed loss of differentiation between the IPL and INL/OPL. In contrast, no thickness change of the photoreceptor/retinal pigment epithelium (RPE) layer was observed in either the acute or chronic phase [36].

Besides change of the retinal thickness, it was also observed that the reflectivity increased in the inner retina and correspondingly decreased in the outer retina in the acute phase of CRAO. In the chronic phase, the increased reflectivity of the inner retinal layers were reduced and the decreased reflectivity in the outer retina layer recovered [37, 38]. However, the observed reflectivity changes have not been assessed quantitatively in any of the previous studies.

7.5.2 Subjects and Data Acquisition

In this study [27], forty eyes of 40 patients diagnosed as CRAO who received 3D-OCT examination within one week of onset were included. Since most CRAO patients are elderly, we included 33 eyes of 33 subjects aged >=65 years old without any retinal disorder or high myopia were included as controls. All the study subjects received comprehensive ophthalmic examinations including fundus photography and spectral domain 3D-OCT examination.

Spectral domain OCT examination was performed using Topcon 3D OCT-1000 (Topcon Corporation, Tokyo, Japan). Macula was scanned using standard 6×6 mm protocol, in which 3D acquisition consisted of 64 B-scan slices. Fundus photographs were obtained from each subject at the same time. The OCT image size was $512 \times 64 \times 480$ voxel. Image quality index was provided by the on-board OCT software. The raw images were exported from the OCT scanner for analysis.

7.5.3 Image Analysis

The same automatic segmentation method was used to obtain the retinal layers from the OCT image volumes. The following layers were obtained between the surfaces, vitreous, NFL, GCL, IPL, INL, OPL, ONL + Henle's fiber layer (HFL), photoreceptor

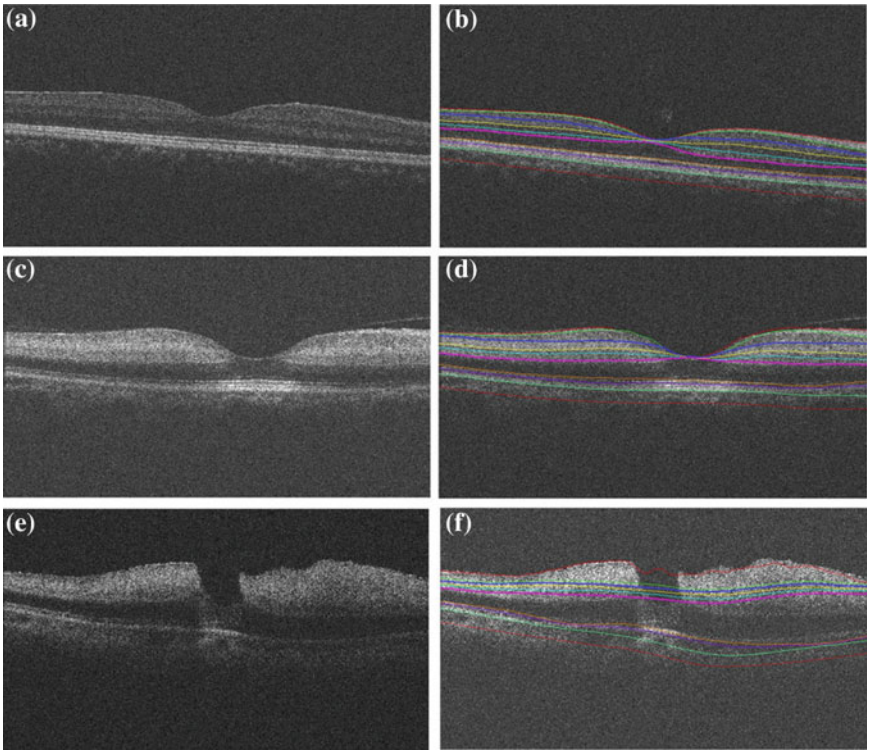

Fig. 7.8 Segmented surfaces and regions on macular spectral domain optical coherence tomography. **a**, **b**: control subjects; **c**, **d**: central retinal artery occlusion patients with correctly segmented retinal layers; **e**, **f**: central retinal artery occlusion patients with substantially increased brightness of the inner retina and related insufficient separation of inner retinal layers on OCT, causing layer segmentation errors—an example is shown. **a**, **c**, **e**: original OCT images; **b**, **d**, **f**: segmentation results

and RPE. The surface between the choroid and the sclera is difficult to identify for Topcon 3D-1000 images, therefore the region, 25 pixels (about 125 mm) wide, immediately under the RPE was used to represent the choroid.

As the method was original designed for normal retina, no segmentation error was observed in any of the 33 control subjects, and correct 3D OCT segmentation was achieved in 29 of 40 CRAO patients. The 29 images were included in further analysis. The segmentation of the OCT images of the remaining 11 CRAO cases was not good due to insufficient quality of OCT image data. These cases were not included in further analysis. In these cases, the optical intensity was very high at each layer of inner retina and the overall brightness (saturation) of image intensities made finding interfaces between layers impossible. Figure 7.8 shows examples of OCT image segmentation.

7.5.4 Results

Due to the difficulty to enroll exactly age-matched normal controls, the CRAO subjects were slightly older compared to the control group (77.0 ± 5.7 vs 71.9 ± 4.5 years old, $p < 0.001$). There was no statistically significant difference of gender distribution or perceived quality of included images between the CRAO and control groups. No statistically significant correlation was found between the optical intensities of retinal layers and the disease duration from the onset to the image acquisition (all $p > 0.05$).

The mean and standard deviation of optical intensities and optical intensity ratios in each layer are shown in Table 7.4. Results of multilinear regression after adjusting for optical intensity of the entire region and age are given in Table 7.4 and Fig. 7.9. There was no statistically significant difference of optical intensities between the CRAO and control subjects in the vitreous and RNFL (standardized beta = 0.160 and 0.050 respectively, both $p > 0.5$). Optical intensities in GCL, IPL, INL and OPL were higher in CRAO compared to controls (standardized beta = 0.657, 0.702, 0.777 and 0.694, respectively, all $p < 0.001$). Optical intensity at ONL+HFL was not different between the CRAO and control groups (standardized beta = 0.047, $p > 0.5$). Optical intensities at the photoreceptor, RPE, and choroidal layers were lower in the CRAO cases compared to controls (standardized beta = −0.412, −0.611 and −0.559, all $p < 0.001$). Discriminant analysis found that the optical intensity of INL was most strongly associated with the CRAO disease status (Wilks' Lambda = 0.641).

7.5.5 Discussion

The optical intensities in each segmented retinal layer detected from 3D-OCT for CRAO patients and normal controls have been quantitatively investigated in this study. The results showed that the optical intensities of vitreous, RNFL and ONL were not different between CRAO and controls. The optical intensities of layers in the inner retina, from GCL to OPL, were higher in CRAO than in controls, with the most prominent increase identified at the INL. While the optical intensities from the photoreceptor to choroidal layers were lower in CRAO patients than in controls, the photoreceptor layer exhibited the most pronounced OCT image intensity decrease.

Table 7.4 Comparison of optical intensity in each layers between central retinal artery occlusion and control adjusting for age and the optical intensity of the entire scanned regions

	Optical intensity		Optical intensity ratio		Unstandardized beta	Standardized beta	P
	Control	CRAO	Control	CRAO			
Vitreous	13,893.9 ± 96.5	13,953.9 ± 164.6	0.89 ± 0.01	0.88 ± 0.02	4.2	0.16	0.901
Retinal nerve fiber layer	26,598.5 ± 1598.1	28,232.6 ± 2120	1.69 ± 0.09	1.77 ± 0.11	202.6	0.05	0.584
Retinal ganglion cell layer	21,567.8 ± 1301.4	26,219.3 ± 1980.1	1.37 ± 0.06	1.64 ± 0.11	3709.4	0.657	<0.001
Inner plexiform layer	21,052.8 ± 1211.5	26,559.5 ± 1915.7	1.34 ± 0.06	1.66 ± 0.1	4441	0.702	<0.001
Inner nuclear layer	18,235.6 ± 857.9	23,899.1 ± 1758.6	1.16 ± 0.04	1.5 ± 0.09	4863.3	0.777	<0.001
Outer plexiform layer	18,791.6 ± 1084.7	23,389.7 ± 1660.4	1.15 ± 0.03	1.4 ± 0.1	3708.8	0.694	<0.001
Outer nuclear layer + Henle's fiber layer	16,380.9 ± 657.5	16,757.9 ± 1002.9	1.04 ± 0.03	1.05 ± 0.05	80.3	0.047	0.664
Photoreceptor	25,458.3 ± 1893.3	22,885.4 ± 3406.9	1.62 ± 0.11	1.44 ± 0.21	−22,440.8	−20.412	0.001
Retinal pigment epithelium	30,454.5 ± 1375.2	26,160.6 ± 3998	1.94 ± 0.07	1.64 ± 0.25	−24,376.7	−20.611	<0.001
Choroid	20,638.7 ± 1130.9	19,224.1 ± 1753.5	1.32 ± 0.06	1.21 ± 0.1	−21,787.7	−20.559	<0.001
Entire region	15,688.0 ± 252.7	15,943.2 ± 333.4	NA	NA	NA	NA	NA

NA: not applicable; CRAO: central retinal artery occlusion

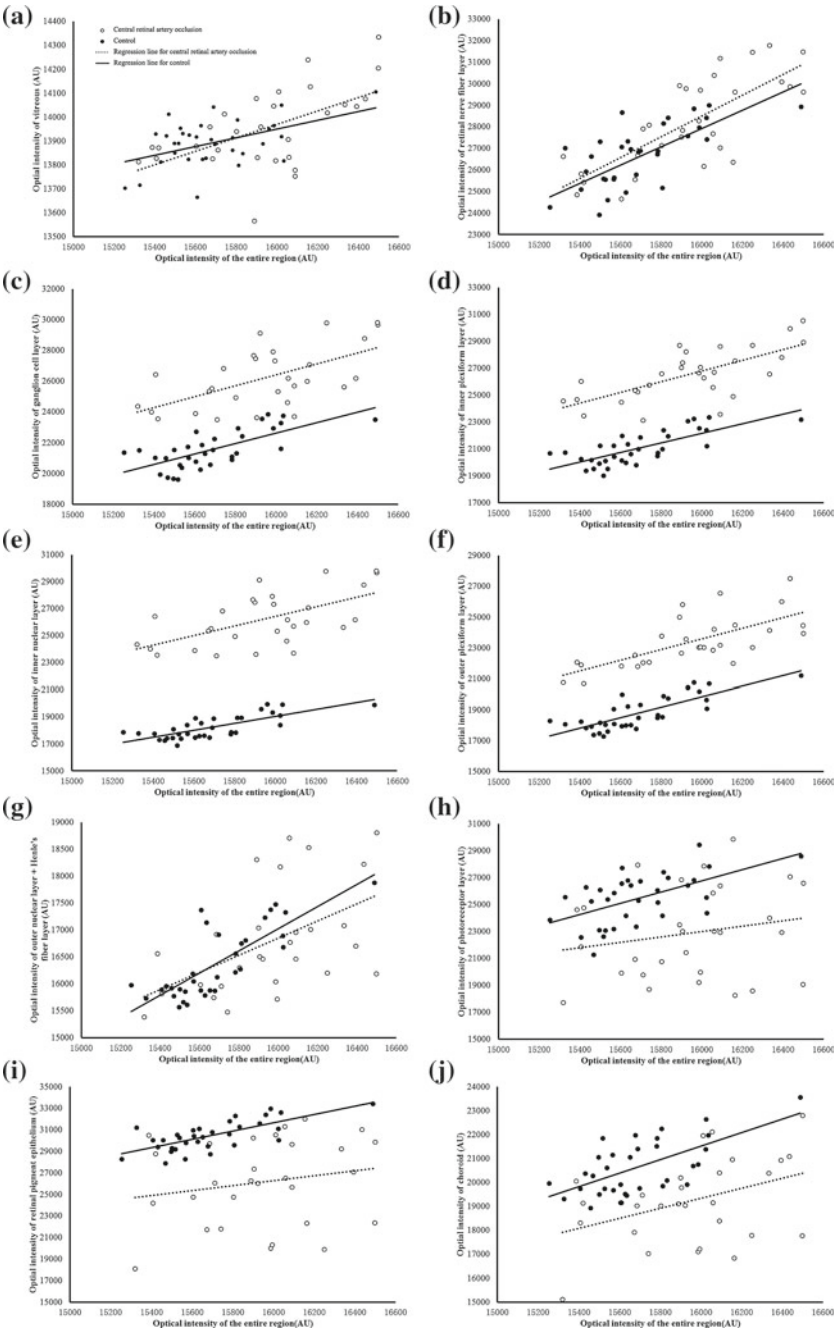

Fig. 7.9 Regression of optical intensities in each layer with intensities of the entire retinal region in retinal artery occlusion patients and controls. Circles represent patients with central retinal artery occlusion, black dots represent control subjects

It is well known that there are two sources of blood supply to the neurosensory retina; the central retinal artery and the choroidal blood vessels, which supply the inner and outer retina, respectively. There are two layers of capillary networks originating from the branches of the central retinal artery. The inner capillary network lies within the GCL. The outer capillary network runs from the IPL to the OPL through the INL [39]. The results showed that the optical intensities increased from the GCL to the OPL in CRAO patients. This finding shows a local correspondence of image intensity increases with layers supplied by the central retinal artery. On histology of a CRAO mouse model, pyknotic nuclei, vacuolated spaces, and degenerative changes were noted in the GCL and INL [40]. In this study, the maximum increases of optical intensity or optical intensity ratio were detected in the INL. Furthermore, discriminant analysis found that the optical intensity of INL is the best indicator of CRAO. Recently, it was reported that deep capillary ischemia frequently manifests itself by increased optical intensities in the middle retinal layers, especially the INL [41]. There is a large number of metabolically active cells in the INL and the INL is surrounded by a deep capillary network branched from the central retinal artery system and is therefore subject to ischemia.

Most impressively, the optical intensity of RNFL was not different between the CRAO and control groups. The blood supply of RNFL is also provided from the central retinal artery system. In a pathological study of human autopsy eyes with CRAO, severe edema of the RNFL was frequently noted [42]. It is conceivable that edema of RNFL does not affect its OCT optical intensity. The exact cellular and molecular mechanism of change of optical intensity in CRAO remains unknown and deserves further investigation. The ONL, photoreceptor, RPE and choroidal layers are not supplied by the retinal artery and its branches. Animal and human autopsy studies previously showed that the outer retina does not change in CRAO [40, 42]. Our results found that the optical intensities in the outer retina from the photoreceptor layer to the choroid were reduced in the acute CRAO phase, especially in the photoreceptor and RPE layers. However, the optical intensities of the photoreceptor and RPE layers are still high at the foveal region, where no layered inner retinal structure is present (Fig. 7.9c–f.) On ophthalmoscopic examination, the whitish opacification of the CRAO retina is caused by reduced transparence of the inner retina, and the cherry red spot at the fovea is due to a relative transparency of the fovea devoid of the inner retina layer tissue [43]. This evidence suggests that the reduction of optical intensities in outer layers may be associated with a shadowing effect caused by increased optical density in the inner retina as observed on CRAO patients.

In conclusion, the OCT optical intensity of inner retina increases in patients with CRAO compared to normal controls, possibly due to layer-specific ischemia, while the optical intensities of the outer retina and the choroid decrease, possibly due to a shadowing effect associated with the inner retinal density increases.

7.6 Summary

This chapter describes studies of optical intensity, a new index of retina conditions based on OCT images. These studies used a validated automatic segmentation method to quantify the optical intensities in each retinal layer on 3D OCT for normal and CRAO subjects. With the advantage of this method, changes of optical intensity in each layer can be quantified and objectively analyzed. The statistical distribution and location distribution of optical intensity, and its correlation with demographic and other ocular characteristics can be studied. The optical intensity of CRAO patients can be compared with normal controls. Intriguing results were obtained by these studies. The change of optical intensity for each retinal layer will be further studied for other types of ocular diseases, and it is expected that this index can be used for in vivo studies of OCT-derived disease severity.

References

1. V.J. Srinivasan, D.C. Adler, Y. Chen, I. Gorczynska, R. Huber, J.S. Duker, J.S. Schuman, J.G. Fujimoto, Ultrahigh-speed optical coherence tomography for three-dimensional and en face imaging of the retina and optic nerve head. Invest. Ophthalmol. Vis. Sci. **49**(11), 5103–5110 (2008)
2. W. Geitzenauer, C.K. Hitzenberger, U.M. Schmidt-Erfurth, Retinal optical coherence tomography: past, present and future perspectives. Br. J. Ophthalmol. **95**(2), 171–177 (2011)
3. B. Yang, C. Ye, M. Yu, S. Liu, D.S. Lam, C.K. Leung, Optic disc imaging with spectral-domain optical coherence tomography: variability and agreement study with Heidelberg retinal tomograph. Ophthalmology **119**(9), 1852–1857 (2012)
4. M.S. Sung, B.W. Kang, H.G. Kim, H. Heo, S.W. Park, Clinical validity of macular ganglion cell complex by spectral domain-optical coherence tomography in advanced glaucoma. J. Glaucoma. (2012)
5. L. Zhang, K. Lee, M. Niemeijer, R.F. Mullins, M. Sonka, M.D. Abràmoff, Automated segmentation of the choroid from clinical SD-OCT. Invest. Ophthalmol. Vis. Sci. **53** (2012)
6. H. Ozdemir, S. Karacorlu, M. Karacorlu, Optical coherence tomography findings in central retinal artery occlusion. Retina **26**(1), 110–112 (2006)
7. T. Fukuchi, K. Takahashi, H. Ida, K. Sho, M. Matsumura, Staging of idiopathic choroidal neovascularization by optical coherence tomography. Graefes Arch. Clin. Exp. Ophthalmol. **239**(6), 424–429 (2001)
8. M.E. Pons, H. Ishikawa, R. Gürsesozden, J.M. Liebmann, H.L. Dou, R. Ritch, Assessment of retinal nerve fiber layer internal reflectivity in eyes with and without glaucoma using optical coherence tomography. Arch. Ophthalmol. **118**(8), 1044–1047 (2000)
9. J. Van der Schoot, K.A. Vermeer, J.F. de Boer, H.G. Lemij, The effect of glaucoma on the optical attenuation coefficient of the retinal nerve fiber layer in spectral domain optical coherence tomography images. Invest. Ophthalmol. Vis. Sci. **53**(4), 2424–2430 (2012)
10. D. Barthelmes, F.K. Sutter, M.C. Gillies, Differential optical densities of intraretinal spaces. Invest. Ophthalmol. Vis. Sci. **49**(8), 3529–3534 (2008)
11. S.Y. Lee, P.F. Stetson, H. Ruiz-Garcia, F.M. Heussen, S.R. Sadda, Automated characterization of pigment epithelial detachment by optical coherence tomography. Invest. Ophthalmol. Vis. Sci. **53**(53), 164–170 (2012)
12. T. Horii, T. Murakami, K. Nishijima, T. Akagi, A. Uji, N. Arakawa, Y. Muraoka, N. Yoshimura, Relationship between fluorescein pooling and optical coherence tomographic reflectivity of cystoid spaces in diabetic macular edema. Ophthalmology **119**(5), 1047–1055 (2012)

13. D. Barthelmes, M.C. Gillies, F.K. Sutter, Quantitative OCT analysis of idiopathic perifoveal telangiectasia. Invest. Ophthalmol. Vis. Sci. **49**(5), 2156–2162 (2008)
14. J. Van der Schoot, K.A. Vermeer, J.F. de Boer, H.G. Lemij, The effect of glaucoma on the optical attenuation coefficient of the retinal nerve fiber layer in spectral domain optical coherence tomography images. Invest. Ophthalmol. Vis. Sci. **53**(4), 2424–30 (2012)
15. K.A. Vermeer, J. van der Schoot, H.G. Lemij, J.F. de Boer, RPE-normalized RNFL attenuation coefficient maps derived from volumetric OCT imaging for glaucoma assessment. Invest. Ophthalmol. Vis. Sci. **53**(10), 6102–6108 (2012)
16. A. Giani, D.D. Esmaili, C. Luiselli, M. Cigada, P. Salvetti, J.W. Miller, G. Staurenghi, Displayed reflectivity of choroidal neovascular membranes by optical coherence tomography correlates with presence of leakage by fluorescein angiography. Retina **31**(5), 942–948 (2011)
17. S. Ooto, M. Hangai, A. Tomidokoro, H. Saito, M. Araie, T. Otani, S. Kishi, K. Matsushita, N. Maeda, M. Shirakashi, H. Abe, S. Ohkubo, K. Sugiyama, A. Iwase, N. Yoshimura, Effects of age, sex, and axial length on the three-dimensional profile of normal macular layer structures. Invest. Ophthalmol. Vis. Sci. **52**(12), 8769–8779 (2011)
18. C.Y. Cheung, D. Chen, T.Y. Wong, Y.C. Tham, R. Wu, Y. Zheng, C.Y. Cheng, S.M. Saw, M. Baskaran, C.K. Leung, T. Aung, Determinants of quantitative optic nerve measurements using spectral domain optical coherence tomography in a population-based sample of non-glaucomatous subjects. Invest. Ophthalmol. Vis. Sci. **52**(13), 9629–9635 (2011)
19. T. Alasil, K. Wang, P.A. Keane, H. Lee, N. Baniasadi, J.F. de Boer, T.C. Chen, Analysis of normal retinal nerve fiber layer thickness by age, sex, and race using spectral domain optical coherence tomography. J. Glaucoma **22**(7), 532–541 (2013)
20. M.D. Abràmoff, M.K. Garvin, M. Sonka, Retinal imaging and image analysis. IEEE Trans. Med. Imaging **3**, 169–208 (2010)
21. M.K. Garvin, M.D. Abràmoff, X. Wu et al., Automated 3-D intraretinal layer segmentation of macular spectral-domain optical coherence tomography images. IEEE Trans. Med. Imaging **28**(9), 1436–1447 (2009)
22. X. Chen, M. Niemeijer, L. Zhang, K. Lee, M.D. Abramoff, M. Sonka, 3D segmentation of fluid-associated abnormalities in retinal OCT: probability constrained graph-search–graph-cut. Med. Imaging IEEE Trans. **31**(8), 1521–1531 (2012)
23. F. Shi, X. Chen, H. Zhao, W. Zhu, D. Xiang, E. Gao, M. Sonka, H. Chen, Automated 3-D retinal layer segmentation of macular optical coherence tomography images with serous pigment epithelial detachments. IEEE Trans. Med. Imaging **34**(2), 441–452 (2015)
24. X. Chen, P. Hou, C. Jin, W. Zhu, X. Luo, F. Shi, M. Sonka, H. Chen, Quantitative analysis of retinal layer optical intensities on three-dimensional optical coherence tomography. Invest. Ophthalmol. Vis. Sci. **54**(10), 6846 (2013)
25. B. Chen, E. Gao, H. Chen, J. Yang, F. Shi, C. Zheng, W. Zhu, D. Xiang, X. Chen, M. Zhang, Profile and determinants of retinal optical intensity in normal eyes with spectral domain optical coherence tomography. Plos One **11**(2) (2016)
26. Retinopathy/Pathology D. Photocoagulation for diabetic macular edema. Early treatment diabetic retinopathy study report number 1. Early Treatment Diabetic Retinopathy Study research group. Arch. Ophthalmol. **103**(12), 1796–806 (1985)
27. H. Chen, X. Chen, Z. Qiu, D. Xiang, W. Chen, F. Shi, J. Zheng, W. Zhu, M. Sonka, Quantitative analysis of retinal layers' optical intensities on 3D optical coherence tomography for central retinal artery occlusion. Sci. Rep. **5**(10), 6846–6851 (2015)
28. C.K. Leung, C.Y. Cheung, R.N. Weinreb, Q. Qiu, S. Liu, H. Li, G. Xu, N. Fan, L. Huang, C.P. Pang, D.S. Lam, Retinal nerve fiber layer imaging with spectral-domain optical coherence tomography: a variability and diagnostic performance study. Ophthalmology **116**(7), 1257–1263, 63 e1-2 (2009)
29. C.K. Leung, M. Yu, R.N. Weinreb, C. Ye, S. Liu, Retinal nerve fiber layer imaging with spectral-domain optical coherence tomography: a prospective analysis of age-related loss. Ophthalmology **119**(4), 731–737 (2012)
30. S. Cugati, D.D. Varma, C.S. Chen, A.W. Lee, Treatment options for central retinal artery occlusion. Current Treat. Options Neurol. **15**(1), 63–77 (2013)

31. N.G. Ghazi, E.P. Tilton, B. Patel, R.M. Knape, S.A. Newman, Comparison of macular optical coherence tomography findings between postacute retinal artery occlusion and nonacute optic neuropathy. Retina **30**(4), 578–585 (2010)
32. R. Mathew, E. Papavasileiou, S. Sivaprasad, Autofluorescence and high-definition optical coherence tomography of retinal artery occlusions. Clin. Ophthalmol. **4**(1), 1159–1163 (2009)
33. C.K. Leung, C.C. Tham, S. Mohammed, E.Y. Li, K.S. Leung, W.M. Chan, D.S. Lam, In vivo measurements of macular and nerve fibre layer thickness in retinal arterial occlusion. Eye **21**(12), 1464–1468 (2007). (London, England)
34. D. Schmidt, T. Kube, N. Feltgen, Central retinal artery occlusion: findings in optical coherence tomography and functional correlations. Eur. J. Med. Res. **11**(6), 250–252 (2006)
35. K. Shinoda, K. Yamada, C.S. Matsumoto, K. Kimoto, K. Nakatsuka, Changes in retinal thickness are correlated with alterations of electroretinogram in eyes with central retinal artery occlusion. Graefe's Arch. Clin. Exp. Ophthalmol. **246**(7), 949–954 (2008)
36. M. Ritter, S. Sacu, G.G. Deák, K. Kircher, R.G. Sayegh, C. Pruente, U.M. Schmidt-Erfurth, In vivo identification of alteration of inner neurosensory layers in branch retinal artery occlusion. Br. J. Ophthalmol. **96**(2), 201–207 (2012)
37. S.M. Falkenberry, M.S. Ip, B.A. Blodi, J.B. Gunther, Optical coherence tomography findings in central retinal artery occlusion. Ophthalmic Surg. Lasers Imaging Official J. Int. Soc. Imaging Eye **37**(6), 502–505 (2006)
38. H. Ozdemir, M. Karacorlu, S.A. Karacorlu, F. Senturk, Localized foveal detachment in a patient with central retinal artery occlusion with cilioretinal sparing. Eur. J. Ophthalmol. **22**(3), 492–494 (2012)
39. H. Kolb, Simple Anatomy of the Retina (2013) http://webvision.med.utah.edu/book/part-i-foundations/simple-anatomy-of-the-retina/. Date of access: 21 Jan 2015
40. N. Goldenberg-Cohen, S. Dadon, B.-C.R. Avraham, M. Kramer, M. Hasanreisoglu, I. Eldar, D. Weinberger, I. Bahar, Molecular and histological changes following central retinal artery occlusion in a mouse model ☆. Exp. Eye Res. **87**(4), 327–333 (2008)
41. S. Yu, F. Wang, C.E. Pang, L.A. Yannuzzi, K.B. Freund, Multimodal imaging findings in retinal deep capillary ischemia. Retina **34**(4), 636–646 (2014)
42. L.E. Zimmerman, Embolism of central retinal artery; secondary to myocardial infarction with mural thrombosis. Arch. Ophthalmol. **73**, 822–826 (1965)
43. J.C. Suvarna, S.A. Hajela, Cherry-red spot. J. Postgrad. Med. **54**(1), 54–57 (2008)

Chapter 8
Segmentation of Optic Disc and Cup-to-Disc Ratio Quantification Based on OCT Scans

Menglin Wu, Theodore Leng, Luis de Sisternes, Daniel L. Rubin and Qiang Chen

With optical nerve head centered OCT imaging, this special region can be visualized in 3-D, enabling detailed quantification of its structure. In this chapter, an automated algorithm is presented for optic disc segmentation in 3-D spectral domain optical coherence tomography, based on which the cup-to-disc ratio an important indicator of early glaucoma can be calculated.

8.1 Introduction

Glaucoma is a chronic neurodegenerative disease of the optic nerve, which demonstrates classic structural characteristics including cupping of the optic nerve head, focal and diffuse retinal rim loss, and nerve fiber layer defects [1]. There is a need to identify early internal structural changes in glaucoma. The cup-to-disc (C/D) ratio is an important indicator for evaluating the glaucomatous changes of the optic nerve head (ONH) [2]. To quantify the ratio, specialists commonly perform planimetry

M. Wu
School of Computer Science and Technology,
Nanjing Tech University, Nanjing, China

T. Leng
Byers Eye Institute at Stanford, Stanford University School of Medicine,
Palo Alto, USA

L. de Sisternes · D. L. Rubin
Department of Radiology and Medicine (Biomedical Informatics Research)
and Ophthalmology, Stanford University School of Medicine, Stanford, USA

Q. Chen (✉)
School of Computer Science and Engineering, Nanjing University of Science
and Technology, Nanjing, China
e-mail: chen2qiang@njust.edu.cn

X. Chen et al. (eds.), *Retinal Optical Coherence Tomography Image Analysis*,
Biological and Medical Physics, Biomedical Engineering,
https://doi.org/10.1007/978-981-13-1825-2_8

in 2-D color fundus photographs. However, manual planimetry has been proven time-consuming and is wrought with interobserver variability [3, 4]. With the introduction of spectral-domain optical coherence tomography (SD-OCT), which is a high-resolution cross-section and noncontact imaging technology, it is possible to image the ONH in a 3-D manner, enabling a more detailed quantification of its structure and possible changes [5].

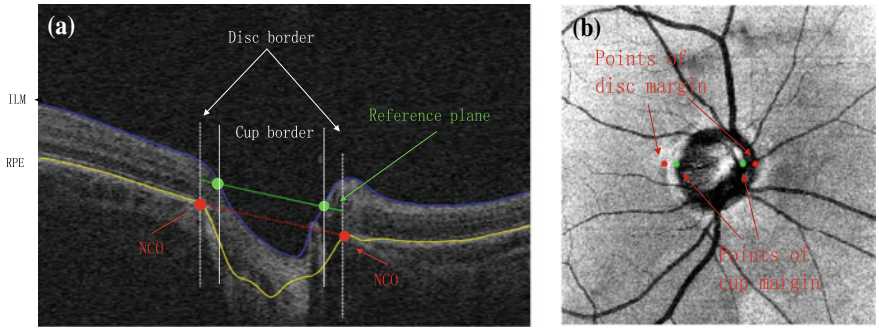

Fig. 8.1 **a** Central B-scan (number 100 of 200) of an example SD-OCT volume. The two NCO points at the end of the RPE (indicated by the yellow outline as automatically segmented by 3-D graph search algorithm) are denoted by red dots. The green line indicates the reference plane and its intersections with inner limiting membrane (ILM, indicated by the blue outline as automatically segmented by 3-D graph search algorithm) are cup boundary points denoted by green circle markers. **b** The projection fundus image of the same volume. The red and green dots are the points of optic disc and cup margin, respectively, which correspond to the columns of NCO and cup borders in (**a**)

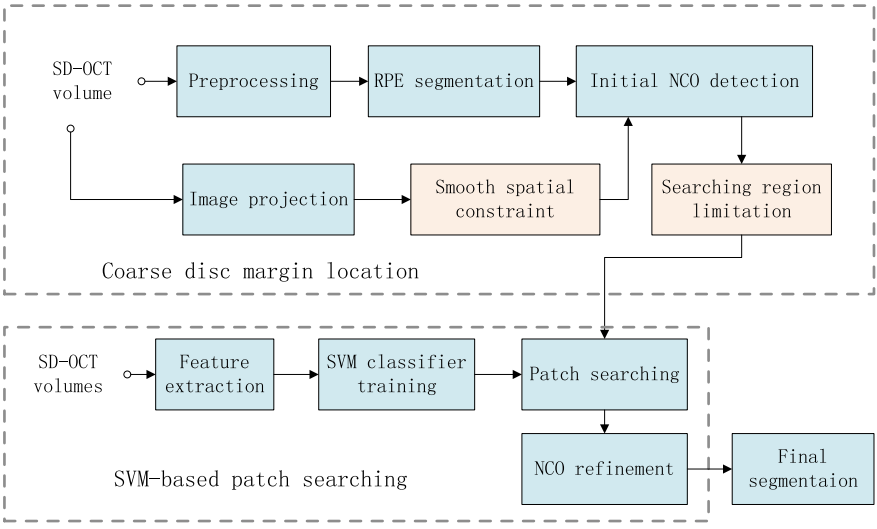

Fig. 8.2 Flowchart of the proposed algorithm

In [1, 6], Strouthidis et al. pointed out that neural canal opening (NCO) is an objective anatomic landmark consistent with SD-OCT optic disc margin anatomy. Furthermore, Hu et al. found out that the NCO can serve as longitudinally stable reference plane and it is not likely to change with glaucomatous progression [7]. As shown in Fig. 8.1a, NCO is defined as the termination of the retinal pigment epithelium (RPE) layer. A parallel line of 150 μm above the connecting line of the two NCO points indicates the standard reference plane [8, 9]. The circular ring between two intersections of the ONH surface and the reference plane are defined as the cup border. Although there has been some debate about the determination of the reference plane [10–12], we adopted this classic definition. In Fig. 8.2b, the red and the green dots are the points of disc and cup margin in projection fundus image, corresponding to the columns of the NCO and the cup borders, respectively. Therefore, the disc margin can be constituted by the NCO in SD-OCT images.

8.2 Optic Disc Segmentation

In order to quantify the *C*/*D* ratio, many automatic methods have segmented the optic disc and cup in color fundus photographs. For example, Aquino et al. proposed a template-based method to detect optic disc boundary, using circular Hough transform for boundary approximation [13]. Yu et al. also presented a hybrid level-set approach for optic disc segmentation based on the deformable model, which combined region and local gradient information [14]. In [15], a superpixel classification based algorithm was applied to determine the optic disc by contrast enhanced histogram and center surround statistics. Furthermore, comparisons of the active contour models for glaucoma screening were performed in [16].

Recently, there have been several studies for glaucoma detection in SD-OCT images [17–23]. Antony et al. presented an automated intraretinal layer segmentation algorithm to calculate the thickness of the retinal nerve fiber layer in normal and glaucoma scans [17]. To detect glaucoma structural damage at an early stage, Xu et al. generated a 2-D feature map from a SD-OCT volume by grouping super pixels and utilized a boosting algorithm to classify glaucoma cases [18]. Another category of approaches is based on optic disc segmentation. Work by Hu et al. [19] transformed the SD-OCT slices to planar projection images, and used graph search algorithm to detect the two boundaries of optic disc and cup simultaneously. In [20, 21], Lee et al. proposed a multi-scale 3-D graph search algorithm to segment retinal surfaces for OCT scan flattening, and then classified each voxel column (A-scan) using k-NN classifier according to the features obtained from the projection image and the retinal surfaces. By observing that the optic disc bounded by RPE has a different structural appearance from the area with the disc, Fu et al. applied low-rank reconstruction to detect the boundary of optic disc [22]. Based on this work, Miri et al. proposed a multi-modal pixel classification method to segment the optic disc, combining stereo fundus and SD-OCT volumes [23]. However, these previous methods required the assistance of color fundus photographs. Additionally, A-scan-based classification

may suffer from morphological diversity of the ONH and lose important 3-D global information.

In this chapter, we introduce an automated optic disc segmentation and C/D ratio quantification method based on neural canal opening (NCO) detection in the optic nerve head [24]. Unlike the methods that directly segment the optic disc in projection image or using classifier to determine which A-scan belongs to the cup or rim, our approach attempts to extract the NCO from SD-OCT scans for the delineation of the disc margin. The proposed approach utilizes a two-stage strategy. The first step is to locate the coarse disc margin by the segmentation of the retinal pigment epithelium (RPE) layer and the smooth constraint of consecutive B-scans. In the second step, we develop a support vector machine (SVM)-based patch search method to find the most likely patch centered at the NCO and refine the segmentation result. Using the NCO and reference plane, the cup border can be evaluated. Finally, the C/D ratio is calculated by the cup diameter dividing the disc diameter. To the best of our knowledge, our approach is the first to automatically segment the optic disc by a NCO detection-based patching search method. The two-stage strategy combines the global and local information for optic disc segmentation. When determining the coarse disc margin location, we utilize the structural characteristics of ONH for initial NCO detection, while in the patch searching procedure, the visual content similarity near the NCO is applied for the final segmentation.

8.2.1 Overview of the Method

Figure 8.2 shows the flowchart of the proposed algorithm, which comprises two main stages: the coarse disc margin location and the SVM-based patch search. In the first stage, each B-scan in the volume is denoised and rescaled during preprocessing. Then, a 3-D graph search algorithm is applied to automatically segment the RPE layer [21]. Based on the segmentation result, we determined the initial NCO position by the maximum curvature of the detected RPE boundary and the smooth spatial constraint of the consecutive B-scans. In the second stage, we select image patches from SD-OCT volumes, and utilize a probabilistic SVM classifier for training after feature extraction of the patches. Then, the searching procedure is generated at the region restricted by the initial NCO location. The patch of maximum probability, centered at NCO, is regarded as the final NCO position. After the two steps, the cup border can be calculated by the location of the NCO and the ILM boundary, and the C/D ratio can be quantified.

8.2.2 Coarse Disc Margin Location

The purpose of this step is to limit NCO region for the subsequent patch search procedure. This step involves image preprocessing, RPE segmentation and initial NCO detection.

8.2.2.1 Preprocessing

Since coherent optical beams have low temporal coherence and high spatial coherence, SD-OCT images contain speckle noise [25]. Speckle size may vary in the axial and lateral dimensions, which is mainly determined by source bandwidth and numerical aperture. In addition, shot noise is also present in SD-OCT images, which can be adequately described by the additive white Gaussian noise (AWGN) process [26]. To facilitate the segmentation of RPE and ILM layer, we pre-processed the images by bilateral filtering denoising [27, 28], which has proven adequate for edge preservation.

For added effectiveness in the NCO detection, we also resampled the SD-OCT images in x-axis direction. Specifically, each B-scan in the volume was rescaled from 200×1024 to 600×400 in the axial and x-axis direction, respectively. An example of a B-scan after denoising and rescaling is shown in Fig. 8.3b.

8.2.2.2 RPE Layer Segmentation

The 3-D graph search-based segmentation algorithm has proven to be effective for detecting multiple intraretinal surfaces [29–31]. With some appropriate feasibility constraints, the surface segmentation problem can be directly converted to a minimum closed set finding problem in a geometric graph and solved in a low-order polynomial time. We applied the multi-scale 3-D graph search approach introduced in [14] to segment the outer boundary of the RPE for subsequent NCO detection. As shown in Fig. 8.3c, the green and yellow curves indicate the segmented ILM and RPE boundaries, respectively.

8.2.2.3 Initial NCO Detection

From the RPE curve fitting in Fig. 8.3c, we observed that the visible parts of the RPE follow an approximately linear curvature, and change dramatically at the termination of the RPE. Therefore, we selected points with maximum curvature as the NCO. However, there are several morphological characteristics that should be noticed: (1) The NCO points are restricted in a certain region by the imaging position and prior anatomical knowledge. The NCO always localizes near the center of the image, as the images are taken aimed to be centered at the optic disc, and it is also noticeable

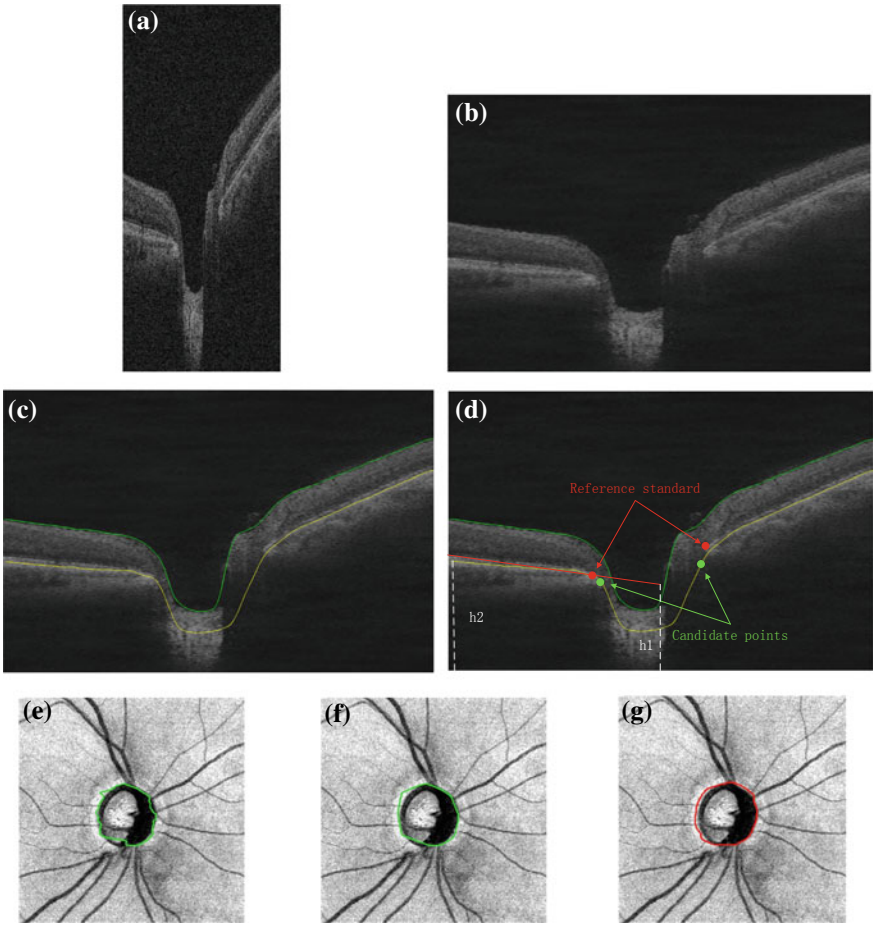

Fig. 8.3 Procedures of coarse margin location. **a** Original B-san. **b** Denoised and rescaled image. **c** Layer segmentation result. **d** Initial NCO detection. **e** Projection image with initial NCO detection. **f** Convex hull fitting after initial NCO detection result. **g** Expert-defined reference standard

that the axial depth of the NCO locations do not vary substantially from the average height of the visible parts of RPE. (2) The position of the NCO locations should not appreciably change in consecutive B-scans. In this paper we refer to this as a spatial correlation smoothness constraint. Based on these constraints, we firstly calculated the positions of NCO candidates as:

$$p_0 = \left\{ (x, y) | \underset{(x,y)\in \mathrm{RPE}}{\arg\max}\, C(x, y), x \in \left[\tfrac{1}{4}w, \tfrac{3}{4}w\right], y \in [h_1, h_2] \right\} \tag{8.1}$$

where p_0 denotes the NCO candidate in the RPE boundary and $C(x, y)$ represents the curvature of the given point. We used the location constraint to ensure p_0 in an appropriate region. w denotes the width of the image so that the lateral position x is limited at the center part of the image. We also restricted the height of the NCO between h_1 and h_2, which are two adaptive parameters. Taking the left NCO point as an example, we fitted a straight line to the left-side flat part of the RPE boundary, indicated as $g(x)$ (shown in red in Fig. 8.3d), and assigned $h_1 = \min(g(x_1), g(x_2))$ and $h_2 = \max(g(x_1), g(x_2))$, where x_1 and x_2 are assumed as the start and the end x-coordinate of the fitting line, fixed to 0–300 in this paper. The equivalent operation was also conducted for the right NCO point and the right-side part of the RPE boundary. An example of the initial NCO detection is shown in Fig. 8.3d.

In the projection fundus image, we firstly defined a scope of disc margin in x-axis direction as $[x_l - 10, x_r + 10]$, where x_l and x_r are the average x-coordinate of the left and right NCO candidates in B-scans 95#–105#, respectively, considering the distance between the left and right NCO is largest in central B-scans, and filtered the individual outliers beyond this scope. Then, we defined a disc margin smoothing procedure by the spatial correlation smoothness constraint as:

$$p_i = \begin{cases} (x, y_i) & if \sum_{p_j \in N(p_i)} ||x - x_j||/n \leq k \\ \left(\sum_{p_j \in N(p_i)} x_j/n, y_i \right) & \text{else} \end{cases} \tag{8.2}$$

where p_i indicates the point of the disc margin in projection image corresponding to the column of p_0, and y_i is the serial number of the B-scan. The $N(p)$ denotes the disc margin points in former 2 and latter 2 consecutive B-scans of the current B-scan defined as a neighborhood and $n = 4$ represents the neighborhood size, while the constant k is set to 5. The x-coordinate locations of the initially selected points are smoothed by considering the selected locations in neighboring B-scans, in order to restrict the NCO locations in the consecutive B-scans to not change more than a threshold amount.

Figure 8.3e shows the NCO detection result in the projection fundus image. The green curve indicates the coarse disc margin by mapping NCO points from each B-scan to the projection image. For preserving the shape of the optic head, we refined the disc margin using a convex hull fitting operation, as shown in Fig. 8.3f. A manual expert-defined reference standard is shown in Fig. 8.3g for comparison.

Although the result indicates that the coarse disc margin is close to the reference standard, its determination still depends on the precision of the RPE segmentation. The points with maximum curvature may not be the optimal location for the NCO when the segmentation result is poor. Therefore, we developed a SVM-based patch searching method to refine the NCO detection in a following step.

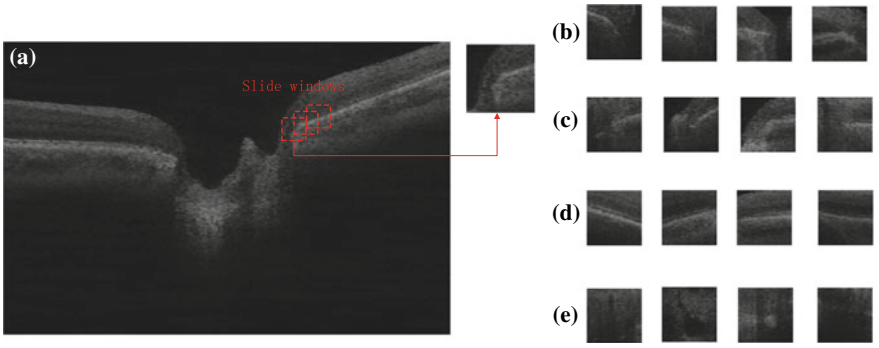

Fig. 8.4 SVM-based patch searching. **a** Patch searching using slide windows denoted by red dotted boxes. **b–e** four classes of the image samples

8.2.3 SVM-Based Patch Searching

Because the initial NCO detection is influenced by the RPE segmentation, we developed a patch searching method to refine the optic disc segmentation. The purpose of this method is to find the most likely patch whose center represents the NCO. We utilized a SVM classifier [32] to select the patches with maximum probability of belonging to classes defined as those centered at the left or right NCO (Figs. 8.4b, c, obtained from slide windows near the initial NCO location (Fig. 8.4a).

8.2.3.1 Sample Selection

For SVM classifier training, we selected 1600 image samples from 20 SD-OCT volumes as training set, which were divided into four classes: (1) patches centered at the left NCO (Fig. 8.4b); (2) patches centered at the right NCO (Fig. 8.4c); (3) patches including the RPE layer (Fig. 8.4d); (4) patches of background among two NCO points (Fig. 8.4e). The size of each patch was set to be 81×81 to ensure that it is discriminative and robust for classification. All the patches were selected near the true NCO or NCO candidates calculated in Sect. 8.2.2.3.

8.2.3.2 Feature Extraction

We extracted two kinds of texture features for patch description: local binary pattern (LBP), histogram of gradient (HOG). The LBP and HOG features were then combined to form a complete feature set.

The LBP is a simple and efficient textural operator which labels the pixels of an image by thresholding the neighborhood of each pixel with the value of the center pixel and generates the result as a binary number [33, 34]. It can be viewed as a

unifying approach to the traditionally divergent statistical and structural models of texture analysis. In this paper, we applied a typical circle LBP operator introduced in [34] for computational efficiency, where the number of neighborhood and the radius are 8 and 2, respectively. Therefore, we obtained a 59 dimensional feature vector of LBP for each image sample.

The HOG descriptor counts the occurrences of gradient orientation in localized portions of an image [35, 36]. It considers that the local object appearance and shape within an image can be described by the distribution of intensity gradients or edge directions. Because of its discriminative power and computational simplicity, HOG has become a popular approach in various applications. An 81 dimensional HOG feature vector was calculated for each image sample here.

We used a serial fusion strategy to combine LBP and HOG features. By a serial linear combination, the two types of the feature vectors are fused into a discriminating vector for classification. Hence the dimension of the fusion feature is 140.

8.2.3.3 Patch Searching

After SVM training, we determined a searching range and calculated the probability of each patch within the range belonging to class 1 or 2. We assumed that the true NCO is near the NCO candidate selected in the initial detection step, so we limited the search range in the x-direction to $[x_0 - 30, x_0 + 30]$ pixels, where x_0 denotes the x-coordinate of the NCO candidate. To reduce the influence of RPE segmentation error, we allowed a height offset of $[-5, 10]$ pixels from the detected RPE boundary. We also defined an interval between two slide windows of 5 pixels.

Considering $\{I_1, I_2, \ldots I_n\} \in R^m$ as the feature vectors obtained from the patches, the probability that a patch I_j belong to class k is determined by the prediction of SVM as p_{jk}. The maximum of p_{j1} (or p_{j2}) indicates that I_j is the most likely patch centered at left (or right) NCO.

For achieving more precise segmentation results, we finely imposed a set of constrains and refinements in the optimal patch selection. Firstly, we assumed that the calculated NCO should be close enough to the initial NCO candidates. If the distance between these two points is more than 35 pixels, we select the top 5 patches with maximum probability of belonging to class 1 or 2, and refined NCO location as the center of the patch closest to the NCO candidate. Secondly, according to the spatial correlation smoothness constraint of the consecutive B-scans, we adjusted the position of NCO by Eq. (8.2).

8.3 Evaluation of Optic Disc Segmentation and C/D Ratio Quantification

8.3.1 Evaluation of Optic Disc Segmentation

To evaluate the performance of the proposed algorithm, we compared our segmentation results with a previously proposed A-scan classification-based segmentation method and a manual segmentation on the 42 SD-OCT test volumes. Segmentation methods based on A-scan classification have been previously proposed in [20, 21, 23] and aim to label each A-scan (corresponding to one pixel in the projection image) in B-scan images as cup, rim or background using k-NN classifier. We extracted a 15 dimensional feature vector from each A-scan as described in [21] to train the k-NN classifier. The manual segmentations were generated by two experienced experts who manually marked the NCO for each B-scan and calculated the cup border by the reference plane to segment optic disc and cup in projection images. The reference standard was obtained based on the two readers' consensus results in projection images.

We utilized unsigned border error (UBE) and Dice similarity coefficient (DSC) to estimate the accuracy of the tested segmentation algorithms [20, 21]. The UBE indicates the average closest distances between all boundary points from segmentation regions of an algorithm and reference standard, while the DSC denotes the spatial overlap between those two regions. Considering S and R as the regions outlined by a segmentation algorithms and a reference standard, respectively, the UBE and DSC were calculated as:

$$\mathrm{UBE} = \left(\sum \mathrm{Dist}_{\min}(S - R, S) + \sum \mathrm{Dist}_{\min}(R - S, R)\right)/\mathrm{Num}(S + R) \quad (8.3)$$

$$\mathrm{DSC}(S, R) = 2(S \cap R)/(S + R) \quad (8.4)$$

where the $\mathrm{Dist}_{\min}(r, s)$ denotes the minimum Euclidean distance between one pixel in region r and all the pixels in region s, and $\mathrm{Num}(a)$ is the number of pixels in region a.

Tables 8.1 and 8.2 report the UBE and DSC of the disc and cup segmentations using the algorithm presented here and different feature sets (LBP, HOG, and fusion of both of them). It is observed that the performance using the fusion of LBP and HOG features is slightly better than LBP and HOG, which indicates that the fusion features are more discriminative for our segmentation algorithm. Therefore, we selected the fusion features for subsequent evaluation.

As a qualitative evaluation, Fig. 8.5 displays the NCO detection by our algorithms in B-scan images and the comparisons of ONH segmentation by different algorithms in projection images. It was apparent that our patch searching-based method achieved a more accurate disc and cup segmentation than the coarse disc margin location method (introduced in Sect. 8.2.2.3) and A-scan classification-based seg-

mentation. The optic disc margin segmented by coarse disc margin location seems consistently larger than by the manual segmentation since it applies convex hull fitting to preserve the largest margin for the patch searching procedure. The disc and cup margins segmented by the patch searching-based method are smoother than by the A-scan classification-based segmentation because it considers the spatial correlation smoothness constraint, rather than by directly classifying each A-scan independently. Tables 8.3 and 8.4 show the UBE and DSC of the different evaluated algorithms comparing with the reference standard from the 42 SD-OCT test volumes.

To evaluate the efficiency of optic disc segmentation, we recorded the average computational time of our algorithm with different features and compared this with that from the A-scan classification-based segmentation algorithm, shown in Table 8.5. We determined that the run time of patch searching is mainly determined by feature extraction. Although fusion feature is more discriminating for our algorithm, it required more time to perform segmentation. The computation cost of an A-scan classification-based segmentation is high because the k-NN classifier cannot use a pre-training model and needs to calculate the distance of each query instance to all training samples.

8.3.2 *Evaluation of* C/D *Ratio Quantification*

C/*D* ratio is an important ONH parameter for early glaucoma detection. There are several definitions of the *C*/*D* ratio, such as area *C*/*D* ratio, horizontal *C*/*D* ratio, vertical *C*/*D* ratio [37] and linear *C*/*D* ratio [4]. In this paper, we used area *C*/*D* ratio, defined as:

$$\text{ratio}_{c,d} = S_{\text{cup}}/S_{\text{disc}} \tag{8.5}$$

Table 8.1 Unsigned border error for LBP, HOG and fusion feature (Mean ± SD)

	LBP	HOG	Fusion
Disc (pixel)	2.771 ± 1.571	2.225 ± 1.418	2.216 ± 1.406
Disc (mm)	0.084 ± 0.047	0.067 ± 0.043	0.067 ± 0.042
Cup (pixel)	1.509 ± 0.886	1.242 ± 0.893	1.164 ± 0.869
Cup (mm)	0.045 ± 0.027	0.037 ± 0.027	0.035 ± 0.026

Table 8.2 Dice similarity coefficient for LBP, HOG and fusion feature (Mean ± SD)

	LBP	HOG	Fusion
Disc	0.910 ± 0.035	0.918 ± 0.034	0.919 ± 0.034
Cup	0.908 ± 0.127	0.925 ± 0.115	0.928 ± 0.116

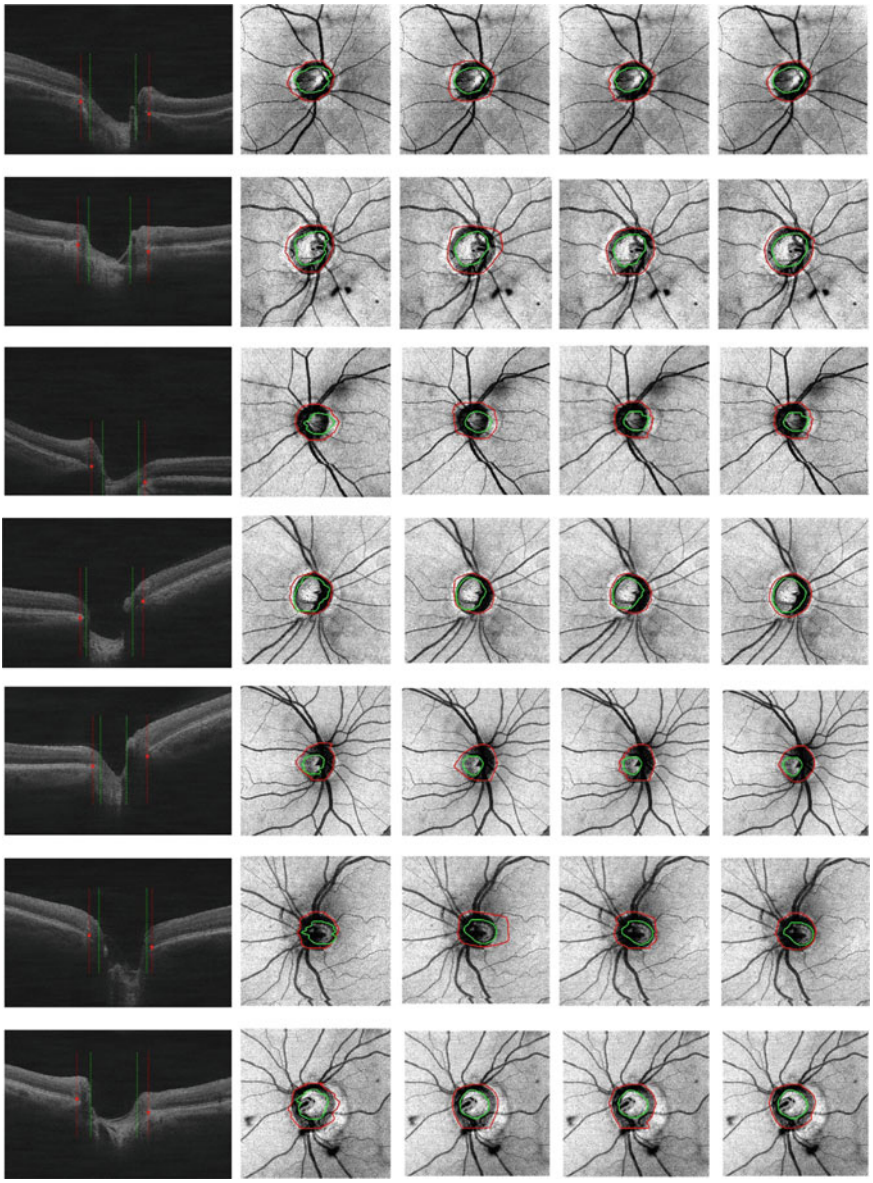

Fig. 8.5 Visualization of the ONH segmentation produced by our algorithms from 7 randomly selected eyes, compared with A-scan classification-based method and the reference standard. From left to right: NCO detection in central B-scan (number 100 of 200) of the SD-OCT volume (the red dots denote the NCO points, the red lines indicate the disc border and the green line indicate the cup border), A-scan classification-based segmentation, coarse optic disc and cup margin location, patch searching-based segmentation and reference standard. The red and green curves denote the disc and cup margin, respectively

Table 8.3 Unsigned border error for different segmentation algorithms (Mean ± SD)

	A-scan Classification	Coarse margin location	Patch searching
Disc (pixel)	3.245 ± 1.531	3.971 ± 1.870	2.216 ± 1.406
Disc (mm)	0.098 ± 0.046	0.120 ± 0.056	0.067 ± 0.042
Cup (pixel)	2.338 ± 0.993	1.140 ± 0.763	1.164 ± 0.869
Cup (mm)	0.070 ± 0.030	0.034 ± 0.023	0.035 ± 0.026

Table 8.4 Dice similarity coefficient for different segmentation algorithms (Mean ± SD)

	A-scan Classification	Coarse margin location	Patch searching
Disc	0.905 ± 0.035	0.868 ± 0.057	0.919 ± 0.034
Cup	0.917 ± 0.113	0.925 ± 0.125	0.928 ± 0.116

Table 8.5 Computational time comparison

	LBP	HOG	Fusion	A-scan classification
Time (s)	86.68	12.57	103.04	109.62

Table 8.6 Error of *C*/*D* evaluation by different algorithms (Mean ± SD)

	A-scan Classification	Coarse margin location	Patch searching
Evaluation error	0.060 ± 0.044	0.073 ± 0.036	0.045 ± 0.033

where S_{disc} is the area of optic disc and S_{cup} is the area of cup, both defined in a projection image. Area *C*/*D* ratios were calculated by the proposed algorithm, A-scan classification-based segmentation and the reference standard are shown in Fig. 8.6a, and the error of C/D ratio evaluation (defined as the difference between *C*/*D* ratios calculated by algorithms and the collected manual segmentation) is shown in Fig. 8.6b. The mean and standard deviation of the error are also summarized in Table 8.6. The results indicate that the evaluation error of the patch searching-based segmentation is lower than those of the other two segmentation algorithms for automated C/D ratio calculation. The coarse margin location causes the highest error because it fails to obtain the precise disc margin. Our algorithm proposed here achieved the best performance in C/D ratio quantification.

8.4 Conclusion

In this chapter, a patch search-based optic disc segmentation algorithm has been introduced for quantifying the C/D ratio in SD-OCT volumes. Compared with traditional

methods, our algorithm has several advantages: (1) A two-stage strategy combines the global and local information for optic disc segmentation. In coarse disc margin location, we consider the structural characteristics of ONH for initial NCO detection. In the patch searching procedure, we seek to find the most likely patch centered at the NCO near NCO candidates. (2) Unlike A-scan classification-based segmentation methods that directly classify every column in B-scan images as disc (rim or background), our algorithm only searches in a restricted region, increasing efficiency. Furthermore, the SVM classifier spends less computational time than a k-NN classifier because it can use pre-training model data, further boosting efficiency. (3) As shown in Fig. 8.5, the segmentation results of the proposed algorithm have smoother

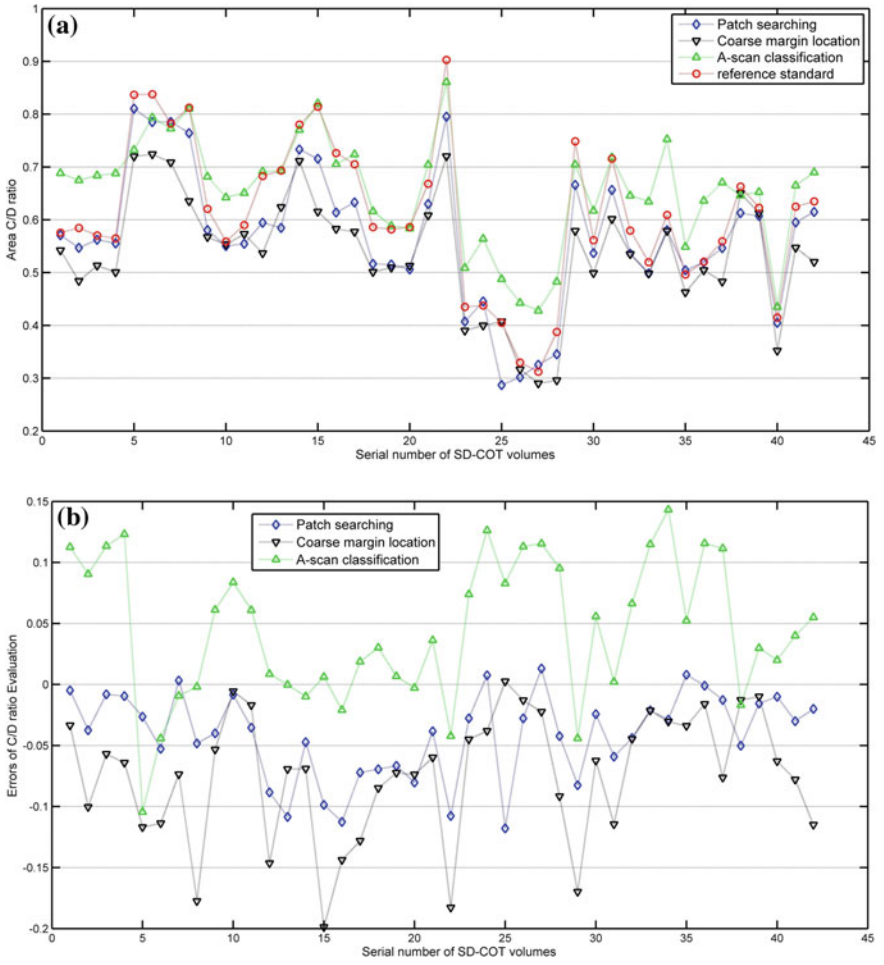

Fig. 8.6 Comparisons of C/D ratio quantification by different algorithms. **a** Area C/D ratio quantification. **b** Error of C/D ratio evaluation

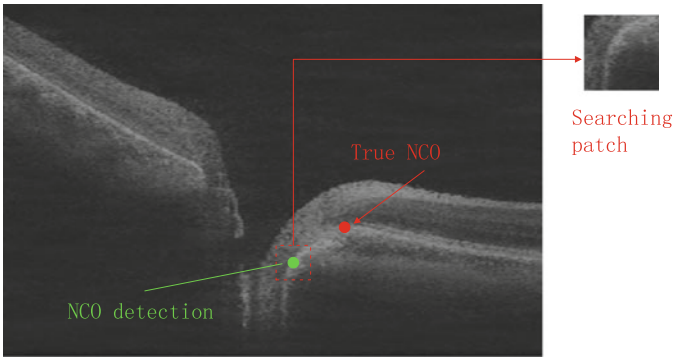

Fig. 8.7 An example of inaccurate NCO detection

margins than those of other methods. This is due to the fact that our method imposes spatial correlation smoothness constraints to finely tune the final segmented result.

Although the experimental results demonstrate that the proposed algorithm can achieve high segmentation accuracy and be an efficient clinical tool for quantifying the *C*/*D* ratio, there are several limitations: (1) The computation cost principally depends on feature extraction. In Table 8.5, it is observed that the time cost of our algorithm with the fusion feature does not yet meet the needs of real-time segmentation. Therefore, efficient feature extraction is required. (2) The results produced by our method could present inaccuracies in severely tilted images. Figure 8.7 shows an example of inaccurate NCO detection. The patch has a maximum probability of class 2 in the searching procedure, but the detected NCO is far away from the true NCO since the similarity of visual content may not fully reflect anatomical characteristics.

In future research, we plan to improve our algorithm in two ways. Feature selection will be refined to increase the computational efficiency and NCO detection will be improved by incorporating anatomical structures to improve the segmentation accuracy.

References

1. N.G. Strouthidis, H. Yang, B. Fortune, J.C. Downs, C.F. Burgoyne, Detection of optic nerve head neural canal opening within histomorphometric and spectral domain optical coherence tomography data sets. Invest. Ophth. Vis. Sci. **50**(1), 214–223 (2009)
2. J.S. Schuman, G. Wollstein, T. Farra, E. Hertzmark, A. Aydin, J.G. Fujimoto, L.A. Paunescu, Comparison of optic nerve head measurements obtained by optical coherence tomography and confocal scanning laser ophthalmoscopy. Am. J. Ophthalmol. **135**(4), 504–512 (2003)
3. Y.H. Kwon, M. Adix, M.B. Zimmerman, S. Piette, E.C. Greenlee, W.L. Alward, M.D. Abràmoff, Variance owing to observer, repeat imaging, and fundus camera type on cup-to-disc ratio estimates by stereo planimetry. J. Glaucoma **18**(4), 305–310 (2009)

4. M.D. Abràmoff, K. Lee, M. Niemeijer, W.L. Alward, E.C. Greenlee, M.K. Garvin, Y.H. Kwon, Automated segmentation of the cup and rim from spectral domain OCT of the optic nerve head. Invest. Ophth. Vis. Sci. **50**(12), 5778–5784 (2009)
5. J. Xu, H. Ishikawa, G. Wollstein, R.A. Bilonick, L. Kagemann, J.E. Craig, J.S. Schuman, Automated volumetric evaluation of stereoscopic disc photography. Opt. Expr. **18**(11), 11347–11359 (2010)
6. N.G. Strouthidis, H. Yang, J.F. Reynaud, J. Grimm, S.K. Gardiner, B. Fortune, C.F. Burgoyne, Comparison of clinical and spectral domain optical coherence tomography optic disc margin anatomy. Invest. Ophth. Vis. Sci. **50**(10), 4709–4718 (2009)
7. Z. Hu, M.D. Abramoff, Y.H. Kwon, K. Lee, M.K. Garvin, Automated segmentation of neural canal opening and optic cup in 3D spectral optical coherence tomography volumes of the optic nerve head. Invest. Ophth. Vis. Sci. **51**(11), 5708–5717 (2010)
8. F.A. Medeiros, L.M. Zangwill, C. Bowd, R.M. Vessani, R. Susanna, R.N. Weinreb, Evaluation of retinal nerve fiber layer, optic nerve head, and macular thickness measurements for glaucoma detection using optical coherence tomography. Am. J. Ophthalmol. **139**(1), 44–55 (2005)
9. A. Manassakorn, K. Nouri-Mahdavi, J. Caprioli, Comparison of retinal nerve fiber layer thickness and optic disk algorithms with optical coherence tomography to detect glaucoma. Am. J. Ophthalmol. **141**(1), 105–115 (2006)
10. T.C. Chen, Spectral domain optical coherence tomography in glaucoma: qualitative and quantitative analysis of the optic nerve head and retinal nerve fiber layer (an AOS thesis). Trans. Am. Ophthalmol. Soc. **107**, 254–281 (2009)
11. B.C. Chauhan, C.F. Burgoyne, From clinical examination of the optic disc to clinical assessment of the optic nerve head: a paradigm change. Am. J. Ophthalmol. **156**(2), 218–227 (2013)
12. P. Hrynchak, N. Hutchings, D. Jones, T. Simpson, A comparison of cup-to-disc ratio measurement in normal subjects using optical coherence tomography image analysis of the optic nerve head and stereo fundus biomicroscopy. Ophthal. Physl. Opt. **24**(6), 543–550 (2004)
13. A. Aquino, M.E. Gegúndez-Arias, D. Marín, Detecting the optic disc boundary in digital fundus images using morphological, edge detection, and feature extraction techniques. IEEE T. Med. Imaging **29**(11), 1860–1869 (2010)
14. H. Yu, E.S. Barriga, C. Agurto, S. Echegaray, M.S. Pattichis, W. Bauman, P. Soliz, Fast localization and segmentation of optic disk in retinal images using directional matched filtering and level sets. IEEE T. Inf. Technol. B. **16**(4), 644–657 (2012)
15. J. Cheng, J. Liu, Y. Xu, F. Yin, D.W.K. Wong, N.M. Tan, T.Y. Wong, Superpixel classification based optic disc and optic cup segmentation for glaucoma screening. IEEE T. Med. Imaging **32**(6), 1019–1032 (2013)
16. C. Muramatsu, T. Nakagawa, A. Sawada, Y. Hatanaka, T. Hara, T. Yamamoto, H. Fujita, Automated segmentation of optic disc region on retinal fundus photographs: comparison of contour modeling and pixel classification methods. Comput. Meth. Prog. Bio. **101**(1), 23–32 (2011)
17. B.J. Antony, M.D. Abràmoff, K. Lee, P. Sonkova, P. Gupta, Y. Kwon, M.K. Garvin, Automated 3D segmentation of intraretinal layers from optic nerve head optical coherence tomography images. In: Proceedings of SPIE Medical Imaging 76260U (2010)
18. J. Xu, H. Ishikawa, G. Wollstein, J.S. Schuman, 3D optical coherence tomography super pixel with machine classifier analysis for glaucoma detection. In: Proceedings of IEEE conference on Engineering in Medicine and Biology Society, pp. 3395–3398. IEEE, Piscataway (2011)
19. Z. Hu, M. Niemeijer, K. Lee, M.D. Abramoff, M. Sonka, M. K. Garvin, Automated segmentation of the optic disc margin in 3-D optical coherence tomography images using a graph-theoretic approach. In: Proceedings of SPIE Medical Imaging 72620U (2009)
20. K. Lee, M. Niemeijer, M.K. Garvin, Y.H. Kwon, M. Sonka, M.D. Abràmoff, 3-D segmentation of the rim and cup in spectral-domain optical coherence tomography volumes of the optic nerve head. In: Proceedings of SPIE Medical Imaging 72622D (2009)
21. K. Lee, M. Niemeijer, M.K. Garvin, Y.H. Kwon, M. Sonka, M.D. Abràmoff, Segmentation of the optic disc in 3-D OCT scans of the optic nerve head. IEEE T. Med. Imaging **29**(1), 159–168 (2010)

22. H. Fu, D. Xu, S. Lin, D. Wong, J. Liu, Automatic optic disc detection in OCT slices via low-rank reconstruction. IEEE T. Bio. Eng. **62**(4), 1151–1158 (2015)
23. M.S. Miri, K. Lee, M. Niemeijer, M.D. Abràmoff, Y.H. Kwon, M.K. Garvin, Multimodal segmentation of optic disc and cup from stereo fundus and SD-OCT images. In: Proceedings of SPIE Medical Imaging 86690O (2013)
24. M. Wu, T. Leng, L. de Sisternes, D.L. Rubin, Q. Chen, Automated segmentation of optic disc in SD-OCT images and cup-to-disc ratios quantification by patch searching-based neural canal opening detection. Opt. Expr. **23**(24), 31216–31229 (2015)
25. Q. Chen, T. Leng, L. Zheng, L. Kutzscher, J. Ma, L. de Sisternes, D.L. Rubin, Automated drusen segmentation and quantification in SD-OCT images. Med. Image Anal. **17**(8), 1058–1072 (2013)
26. M. Gargesha, M.W. Jenkins, A.M. Rollins, D.L. Wilson, Denoising and 4D visualization of OCT images. Opt. Expr. **16**(16), 12313–12333 (2008)
27. C. Tomasi, R. Manduchi, Bilateral filtering for gray and color images. In: Proceedings of IEEE Conference on Computer Vision, pp. 839–846. IEEE, Piscataway (1998)
28. Q. Chen, W. Fan, S. Niu, J. Shi, H. Shen, S. Yuan, Automated choroid segmentation based on gradual intensity distance in HD-OCT images. Opt. Expr. **23**(7), 8974–8994 (2015)
29. K. Li, X. Wu, D.Z. Chen, M. Sonka, Optimal surface segmentation in volumetric images—a graph-theoretic approach. IEEE T. Pattern Anal. **28**(1), 119–134 (2006)
30. M.K. Garvin, M.D. Abràmoff, X. Wu, S.R. Russell, T.L. Burns, M. Sonka, Automated 3-D intraretinal layer segmentation of macular spectral-domain optical coherence tomography images. IEEE T. Med. Imaging **28**(9), 1436–1447 (2009)
31. X. Chen, J.K. Udupa, U. Bagci, Y. Zhuge, J. Yao, Medical image segmentation by combining graph cuts and oriented active appearance models. IEEE T. Image Process. **21**(4), 2035–2046 (2012)
32. C. Cortes, V. Vapnik, Support-vector networks. Mach. Learn. **20**(3), 273–297 (1995)
33. T. Ojala, M. Pietikäinen, T. Mäenpää, Multiresolution gray-scale and rotation invariant texture classification with local binary patterns. IEEE T. Pattern Anal. **24**(7), 971–987 (2002)
34. T. Ojala, M. Pietikäinen, T. Mäenpää, A generalized Local Binary Pattern operator for multiresolution gray scale and rotation invariant texture classification. In: Proceedings of International Conference on Advances in Pattern Recognition, pp. 397–406. IEEE, Piscataway (2001)
35. N. Dalal, B. Triggs, Histograms of oriented gradients for human detection. In: proceedings of IEEE Conference on Computer Vision and Pattern Recognition, pp. 886–893. IEEE, Piscataway (2005)
36. J. Zhang, K. Huang, Y. Yu, T. Tan, Boosted local structured hog-lbp for object localization. In: proceedings of IEEE Conference on Computer Vision and Pattern Recognition, pp. 1393–1400. IEEE, Piscataway (2011)
37. G.J. Jaffe, J. Caprioli, Optical coherence tomography to detect and manage retinal disease and glaucoma. Am. J. Ophthalmol. **137**(1), 156–169 (2004)

Chapter 9
Choroidal OCT Analytics

Kiran Kumar Vupparaboina, Ashutosh Richhariya, Jay Chhablani and Soumya Jana

The advance in OCT imaging techniques allow visualization of the deeper structures of the eye, including the choroid, the structural change of which is associated with various diseases. In this chapter, methodologies are presented for automatic quantification of choroidal measurements such as thickness, volume and stromal-luminal ratio, which are indicators crucial in disease diagnosis and treatment response monitoring.

9.1 Introduction

The choroid layer, sandwiched between the retinal pigment epithelium (RPE) and the sclera, has complex vasculature, performs critical physiological functions [1–5], and assumes crucial role in diagnosing various disease conditions. Such diseases include age-related macular degeneration (AMD), central serous chorioretinopathy (CSC), Vogt-Koyanagi-Harada syndrome, and choroiditis [6–10]. The advent of OCT has lead to improved visualization of the choroid, and hence improved diagnosis [11]. Among various OCT technologies, the spectral domain OCT (SD-OCT) is perhaps the most ubiquitous [12]. Typical SD-OCT images are shown in Fig. 9.1. The left portion of each image, called *en-face*, depicts the infrared face-on view of retina, while the dashed line on it indicates the vertical location of the OCT plane. The right part depicts an OCT scan, consisting of retina (layered), including RPE (bright), choroid (granular), and sclera (smooth), from top to bottom (from inner to outer layer, physiologically), as labeled in the last image [13]. Usually, OCT is performed at various (e.g., 97) vertical locations, and the ophthalmologist browses through OCT

K. K. Vupparaboina (✉) · A. Richhariya · J. Chhablani
L V Prasad Eye Institute, Hyderabad, Telangana 500034, India
e-mail: kiran1559@gmail.com

K. K. Vupparaboina · S. Jana
Indian Institute of Technology, Hyderabad, Telangana 502285, India

X. Chen et al. (eds.), *Retinal Optical Coherence Tomography Image Analysis*,
Biological and Medical Physics, Biomedical Engineering,
https://doi.org/10.1007/978-981-13-1825-2_9

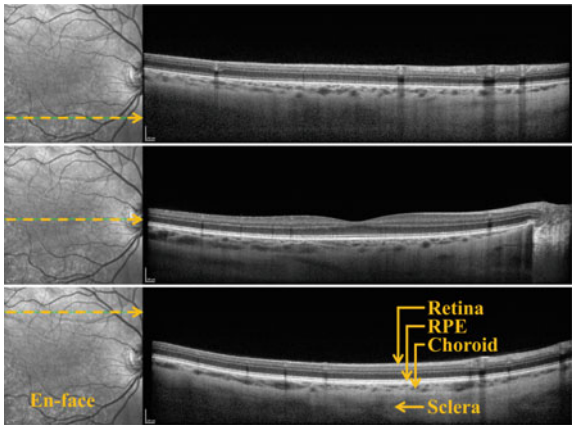

Fig. 9.1 Three sample images of a set of 97 SD-OCT images of the posterior segment of the eye (courtesy Dr. William R Freeman, University of California, San Diego, La Jolla, CA). A typical OCT image contains en-face on the left portion, and retina, RPE (outermost part of retina), choroid and sclera on the right portion

images, paying attention to the choroid region to assess its condition. Further, to perform accurate diagnosis and monitoring of treatment response, ophthalmologists envision to seek various parameters of interest such as choroidal thickness distribution and volume, and stromal-luminal ratio.

Accordingly, this chapter focus on choroidal analytics with a aim to (i) facilitating clinicians with automated tools for quantifying various parameters of interest, and (ii) providing next generation screening/visualization tool for performing better/stress-free diagnosis. In particular, we discuss automated quantification of (i) thickness and volume, as well as (ii) stromal-luminal ratio pertaining to the choroid.

The rest of the chapter is organized as follows. In Sect. 9.2, automated quantification of choroid thickness and volume is discussed. Subsequently, automated quantification of choroidal stromal-luminal ratio is discussed in Sect. 9.3. Finally. we conclude in Sect. 9.4 with a summary.

9.2 Automated Segmentation and High-Level Analytics

In managing choroidal diseases, high-level OCT analytics of choroid assumed significant role. In particular, gross indicators such as choroidal thickness distribution has been widely examined in understanding effect of various diseases on choroid and in turn on visual acuity [14]. Recently, choroid volume has also been investigated and has shown improved understanding of diseases [15]. In this backdrop, this section primarily focuses on quantification of such gross indicators. However, quantification of finer details of the choroid facilitate much better understanding of diseases associated with choroid [16], which will be discussed in Sect. 9.3.

9.2.1 Problem Setup and Solution Approaches

Choroidal thickness distribution estimated from OCT images emerged as an important metric in disease management [14]. Consequently, estimation accuracy has assumed a vital role in ensuring accurate diagnostic outcome [17]. Choroidal thickness measurements have in turn been used to obtain choroidal volume. So far, such thickness measurements have been performed by experts by manually delineating the choroid inner and outer boundaries and then taking the difference. Such manual analysis of OCT scans is time consuming, laborious as well as susceptible to fatigue-induced error. Manual estimation of choroidal volume is rarely performed in view of the inordinate time and effort involved. Against this backdrop, automated segmentation of choroid layer could be crucial in reducing professional effort and time per subject, potentially allowing more subjects to obtain specialized medical attention. Further, choroidal volume now being routinely used in addition to the usual choroidal thickness. Automation would also avoid human error induced by fatigue and tedium. Accordingly, we propose a novel automated algorithm for choroid segmentation and related thickness and volume measurements.

Since the last few years, automation of choroid segmentation have been attracting considerable attention. In view of the eye physiology (Fig. 9.1), choroid segmentation consists of two tasks: detecting (i) choroid inner boundary (CIB) and (ii) choroid outer boundary (COB). Of these, the first task is relatively well posed because the RPE, defining the CIB, is significantly brighter than adjacent layers. Indeed, the gradient-based approach in various flavors has proven accurate not only in detecting CIB [18, 19], but also in the related problem of detecting boundaries between successive retinal layers with well-defined brightness transition [20, 21]. Accordingly, we shall also adopt a gradient-based approach for CIB detection. In contrast, the task of detecting the COB poses considerable challenge. This happens because the COB is essentially a notional divide between the choroidal granularity and the scleral uniformity, which is not defined by marked variation in brightness, and often open to subjective interpretation. Even so, gradient-based deterministic methods have been suggested for COB detection [22, 23]. However, statistical methods appear more suitable to handle the inherent uncertainties involved. Accordingly, machine learning [24, 25] as well as gradient-based probabilistic methods [19] have been attempted. Yet, aforementioned attempts does not directly exploit the structural transition from granularity to uniformity across the COB. Against this backdrop, SSIM-based method has been proposed to quantify the structural dissimilarity between choroid and sclera using the yardstick of structural similarity (SSIM) index to find an initial estimate of the COB, followed by Hessian analysis to remove the discontinuities in the initial estimate [26]. However, the resulting boundary, although adequately separates the choroidal vessels from scleral uniformity, generally is not smooth and deviates substantially from smooth boundaries manually drawn by experts [27]. With a view to obtaining close match with the latter, tensor voting is employed to achieve the desired smoothing. From a clinical perspective, even accurate estimate of choroidal thickness on its own could sometimes be inadequate in assessing choroidal involvement in chorioretinal

diseases. To see this, suppose specific scans are taken at selected foveal locations. Then the thickness measure would clearly be inadequate in representing the overall choroidal distribution. In contrast, volumetric analysis of the choroid would be better suited to assess the disease course and response to treatment [17]. Against this backdrop, SSIM-based method also automated choroidal volume measurement [26].

Turning to performance comparison among algorithms reported, it poses considerable challenge due to various factors. In several cases standard datasets and ground truth results did not exist. Specifically, algorithms, considered the state of the art, were tested on disparate datasets, making comparison among those algorithms difficult. Further, as manual measurements are also subjective in nature, those also should not be used as reference. Against this backdrop, SSIM-based method proposed to use the variability in manual measurements as the reference, and the compare against that the variability between mean manual and algorithmic performances [26]. Further, thorough statistical analysis is carried out comparing algorithmic results with observer repeatability. Importantly, quotient measures are defined to facilitate comparison among algorithms tested on different datasets vis-à-vis manual methods. In view of above observations, the rest of the section focuses on detailed description of the SSIM-based methodology for automated quantification of choroidal thickness and volume.

9.2.2 Materials and Methods

Primarily this algorithm attempts to automatically detect choroid inner boundary (CIB) and choroid outer boundary (COB), which are manually drawn by an expert in Fig. 9.2. We begin by describing the experimental datasets and the proposed methodology.

9.2.2.1 Experimental Datasets

OCT scans considered are performed by a single retina specialist, using Heidelberg Retina Angiograph (HRA - Spectralis, Heidelberg Engineering, Dossenheim, Germany). The Spectralis OCT device provides up to 40,000 A scans/s with a depth resolution of 7 μm in tissue and a transverse resolution of 14 μm using a superluminescence diode with a mean wavelength of 870 nm. Raster imaging consisting of

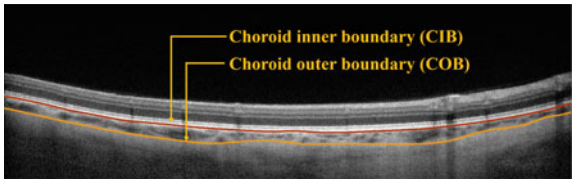

Fig. 9.2 Choroid inner boundary and choroid outer boundary, labeled manually

97 high-resolution B scans was performed with each eye, centered on the fovea. An internal fixation light was used to center the scanning area on the fovea. Each scan was 9.0 mm in length and spaced 30 μm apart from each other. Single OCT images consisting of 512 A lines were acquired in 0.78 ms. The scans were obtained for analysis after 25 frames, and averaged using built-in automatic averaging software (TruTrack; Heidelberg Engineering, Heidelberg, Germany) to obtain a high quality choroidal image. In this work, experimental evaluation is performed on B-scans taken from three healthy adult subjects, from whom one eye randomly chosen per subject and 97 B-scans are taken per eye. The first two datasets has image resolution 351 × 770 and the third dataset has 496 × 1536 (covering larger area). Manual segmentation is performed twice by same expert on each scan to study the observer repeatability. In particular, ImageJ software is used to perform manual segmentation [28]. The average of two such manual segmentations is taken as the reference.

9.2.2.2 Methodology

As depicted in Fig. 9.3, the SSIM-based methodology consists of various steps: (i) denoising, (ii) localization of choriod and (iii) choroid outer boundary (COB) detection.

9.2.2.2.1 Denoising: Generally, OCT images are noisy (Fig. 9.4a), and appropriate denoising improves algorithmic accuracy. Accordingly, for denoising, the block-matching and 3D filtering (BM3D) algorithm, which is generally accepted as the state of the art, is adopted [29]. This algorithm is based on an enhanced sparse representation in transform-domain, where enhancement of the sparsity is achieved by grouping similar 2D image blocks into 3D data arrays called "groups", followed by performing collaborative filtering on them. As groups exhibit high correlation, a decorrelating transform attenuates noise. Finally, denoised images are obtained by applying the inverse transform (Fig. 9.4b).

9.2.2.2.2 Localization of Choroid: Next RPE inner boundary is located. This further helps us locate the RPE outer boundary, which defines the CIB, and specify a region of interest (ROI) between CIB and sclera which is expected to contain the COB.

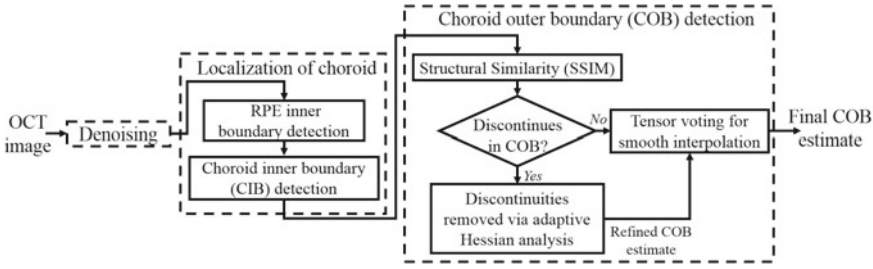

Fig. 9.3 Schematic of SSIM-based methodology

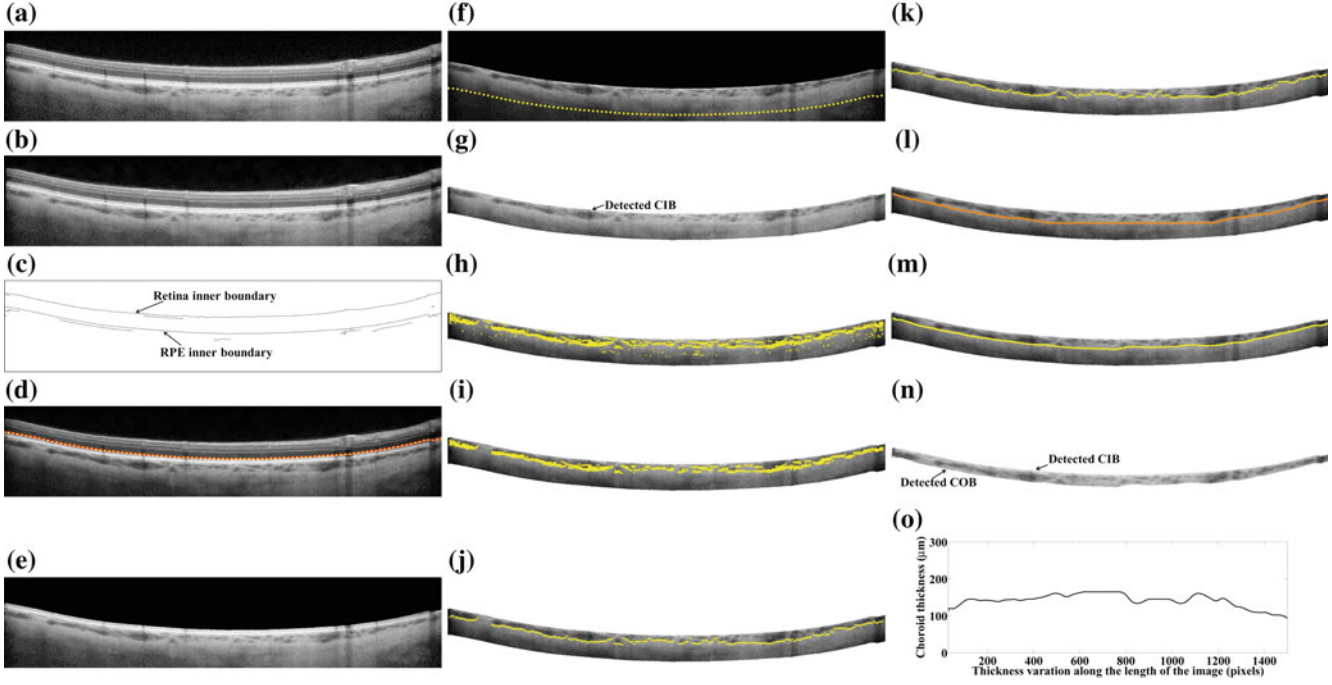

Fig. 9.4 Choroid inner and outer boundary segmentation: **a** the 95-th OCT scan from the third dataset; **b** denoised OCT scan; **c** output of Canny edge detection; **d** detected RPE inner boundary mapped onto original slice; **e** and **f** respective images after peeling off retinal layers inside RPE, and RPE. Lower boundary of region of interest (ROI) is marked in (**f**); **g** extracted ROI; **h** Pixels with SSIM index below threshold; **i** outcome of connected components algorithm; **j** outermost pixels in (**i**), initial estimate of COB based on SSIM (**k**) Refined COB estimate using adaptive Hessian analysis; **l** manually drawn COB; **m** final COB after interpolation using tensor voting; **n** segmented choroid; and **o** choroid thickness variation

A. RPE inner boundary detection: Noting the higher brightness of the RPE compared to that of the adjacent layers, an initial edge map is obtained using the gradient-based Canny edge operator [30]. However, also notice in Fig. 9.4a that sharp change in brightness occurs not only at the RPE inner boundary, but at the retinal inner boundary as well. Accordingly, the edge operator principally detects both the above boundaries alongside some secondary edges (Fig. 9.4c). Of these, the outer one of the principal edges is taken as the RPE inner boundary and removed its discontinuities using the dilation operator (Fig. 9.4d) [30].
B. Choroid inner boundary (CIB) detection: Now the various retinal layers inside RPE inner boundary are peeled off (Fig. 9.4e). The RPE outer boundary, which also defines the CIB, occurs at a more or less uniform distance from the RPE inner boundary, and is then detected based on gradient-based bright-to-dim transition. subsequently, the RPE layer is also peeled off (Fig. 9.4f). At this point, detection of the COB is remained. To this end, a region of interest (ROI) of sufficient thickness outside the CIB is selected such that the ROI would contain the COB (Fig. 9.4g).

9.2.2.2.3 Choroid Outer Boundary (COB) Detection: The steps employed for COB detection are outlined in the flowchart of Fig. 9.3.

A. Initial COB estimate based on SSIM: Observe in Fig. 9.4a that the sclera (uniform) and the choroid (granular) have dissimilar structure. Accordingly, such dissimilarity is exploited by taking a small window from sclera as a template, and calculate the structural similarity (SSIM) index between the template and the neighborhood (of the same size as the template) of every pixel throughout the ROI. Here SSIM between two windows A and B of equal dimensions is given by [31]

$$\mathrm{SSIM}(A, B) = \frac{(2\mu_A\mu_B + c_1)(2\sigma_{AB} + c_2)}{(2\mu_A^2\mu_B^2 + c_1)(\sigma_A^2 + \sigma_B^2 + c_2)}, \tag{9.1}$$

where μ_A and μ_B denote the respective means, and σ_A^2 and σ_B^2 the respective variances of windows A and B, whereas σ_{AB} denotes their covariance. Further, c_1 and c_2 are small constants, chosen to stabilize the expression. As the template is chosen from the sclera, we expect scleral pixels to have higher and choroidal pixels to have lower SSIM indices. Indeed the lowest SSIM values are observed in the transition region between sclera and the choroid, i.e., near the COB. More accurately, pixels with SSIM index below a suitable threshold are mostly concentrated on the choroid side of the COB, and generally isolated on the scleral side (Fig. 9.4h). Such scleral pixels are removed using the connected components algorithm (Fig. 9.4i) [30]. Finally, the lower boundary of the remaining sub-threshold pixels is taken as an initial estimate of the COB (Fig. 9.4j), which however is generally discontinuous.

B. Refinement via eigenvalue analysis of the Hessian matrix: To remove such discontinuities, an adaptive Hessian analysis method is adopted [32, 33]. In particular, first whether a pixel belongs to a blood vessel (present only in the choroid) or not is found. To this end, we estimate the Hessian matrix H at every pixel based on its neighborhood, compute the eigenvalues λ_1 and λ_2 of H, and verify whether λ_1 is small and λ_2 is large, which has been shown to correspond to dark tubular structures such as choroidal blood vessels [34]. To complicate matters, the intensities across the length of the scan was not uniform, and hence a unique threshold pair on the eigenvalues may not suffice in detecting choroid vessel cross-sections accurately. Accordingly, to improve accuracy, thresholds on λ_1 and λ_2 are picked in an adaptive manner, and add the outer boundary of newly detected choroid vessels to our initial COB estimate, thereby removing undesirable discontinuities (Fig. 9.4k).

C. Smooth interpolation using tensor voting: The refined COB estimate appears to divide the choroidal granularity and the scleral uniformity adequately, albeit in jagged manner. In contrast, manual delineation of the COB by an expert is generally smooth (Fig. 9.4l). To achieve similar smoothness in our automated COB estimate, tensor voting is adopted [35, 36]. Directly applying tensor voting on the refined COB estimate may lead to omission of some choroid vessels, because final boundary may pass through the choroid layer cutting some of the blood vessels. Therefore, post preprocessing is performed on the refined COB estimate, which involves discarding boundary pixels that are close to local minima. This is done by dividing each scan into three windows along the length and fixing a local threshold based on mean thickness value of the corresponding window. Further, threshold is chosen slightly greater than the local mean. Before proceeding further, we describe in brief the tensor voting technique, which propagates information using tokens, conveying various objects' orientation preferences (i.e., votes) to their neighbors. When such votes are tallied, objects belonging to the same structure tend to join together. The influence of a vote decays away from the object, and the saliency decay function (DF) is generally taken as Gaussian:

$$DF(s, k, \sigma) = e^{\left(\frac{s^2+ck^2}{\sigma^2}\right)}, \tag{9.2}$$

where s denotes arc length, and k curvature, while c controls the degree of decay with curvature, and σ the scale of voting, which in turn determines the effective neighborhood size [36]. Now, in order to achieve the desired smoothing of the post-processed COB, tensor voting is applied in two stages. First, a relatively large σ is applied with a view to finding a mean interpolated COB. Finally, a smaller σ is used to smoothen small left-over transients. This results in our final estimation of the COB (Fig. 9.4m). Subsequently, the choroid between the estimated CIB and the estimated COB is segmented (Fig. 9.4n), and hence obtain the thickness distribution (Fig. 9.4o).

9.2.3 *Results and Statistical Analysis*

Following the aforementioned steps, the CIB and the COB estimates in each OCT B-scan of the three datasets at hand are obtained. In Fig. 9.5, results for six B-scans per dataset as representative are depicted. For visual comparison, manual COB delineations performed by experts are also depicted alongside. Next a quantitative assessment of the proposed automated algorithm in terms of estimation accuracy of the resulting choroidal thickness distribution and volume is presented.

9.2.3.1 Choroidal Thickness

First estimation of choroidal thickness distribution is considered, and then the estimation accuracy is quantified.

9.2.3.1.1 Thickness Distribution: Choroidal thickness distribution obtained using the proposed method is presented for each dataset in Fig. 9.6c, while the corresponding distribution obtained using the manual reference, taken as the average of the two manual segmentations, is presented in Fig. 9.6b. For positional reference, corresponding en-face images are depicted in Fig. 9.6a. Further, the estimation error, measured by the difference (D) between the automated and the manual reference thickness estimates, is presented in Fig. 9.6d, while the corresponding absolute error/difference (AD) is presented in Fig. 9.6e. The absolute error appears to be tolerable, while a tendency to underestimate thickness is noticed. Ideally, one desires automated algorithms to perform as well as the manual approach. Next, a thorough statistical

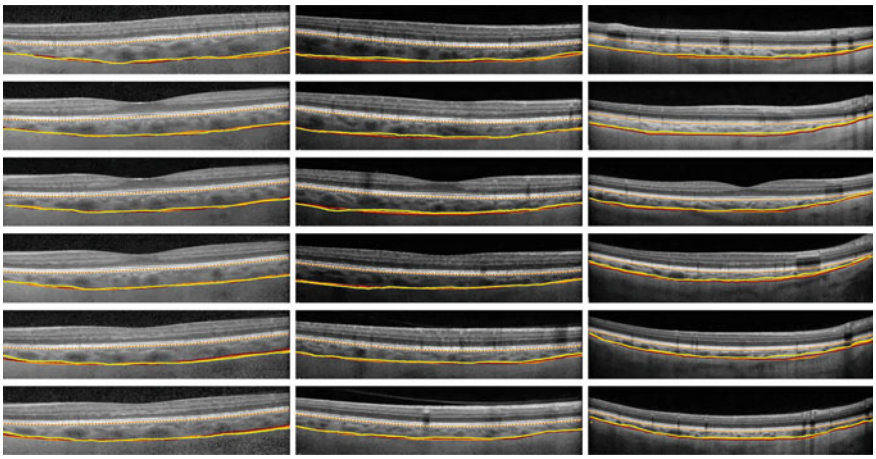

Fig. 9.5 Left: 6 B-scan images from 97 scan dataset—1; Middle:—6 B-scan images from 97 scan dataset–2; Right:—6 B-scan images from 97 scan dataset—3 with labeled manual (orange, maroon) and SSIM-based automated (yellow) segmentation

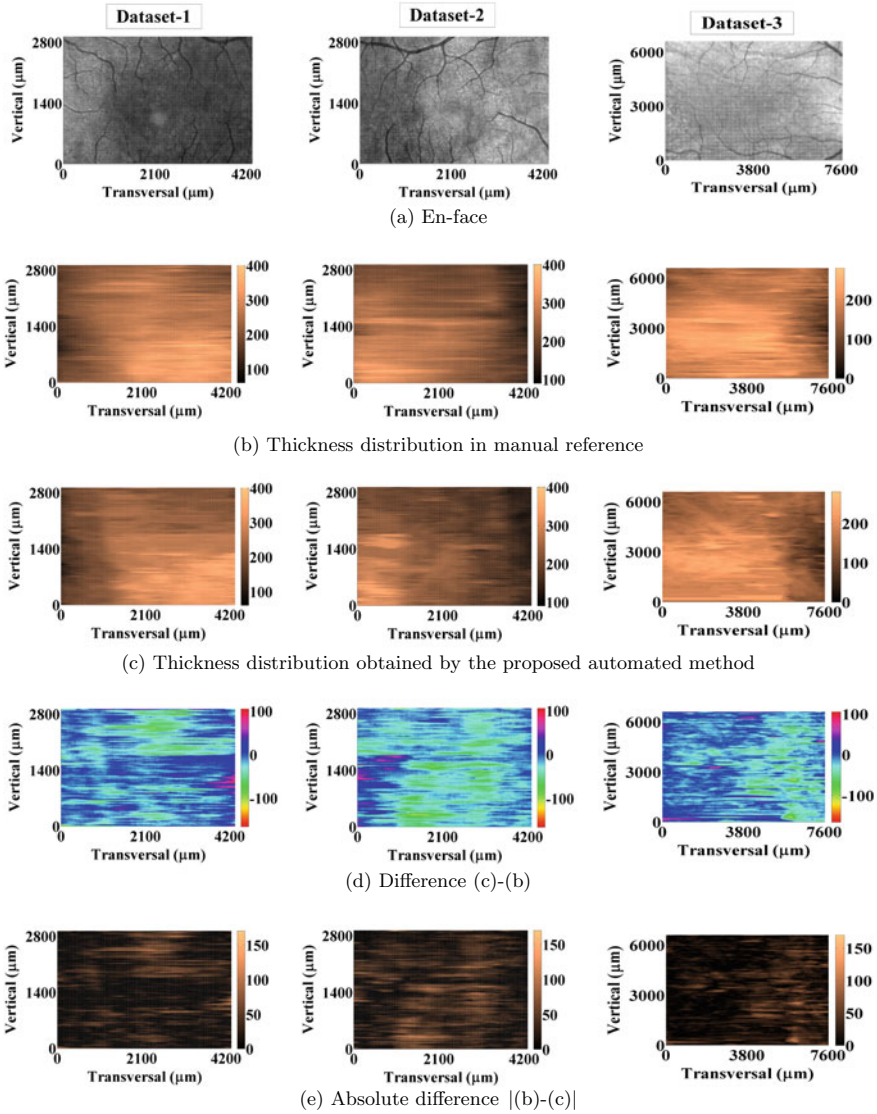

Fig. 9.6 Thickness distribution comparison for the three datasets

analysis is presented to quantitatively establish closeness to such ideal goal as well as comparative advantage over reported algorithms.

9.2.3.1.2 Statistical Performance Measures: For a collection $\{z_k\}_{k=1}^{N}$ of samples of quantity z, its mean Mz, standard deviation (SD) SDz, and coefficient of variation (CV) CVz are defined by

$$\mathrm{M}z = \frac{1}{N}\sum_{k=1}^{N} z_k, \qquad \mathrm{SD}z = \sqrt{\frac{1}{N}\sum_{k=1}^{N}(z_k - \mathrm{M}z)^2}, \qquad \mathrm{CV}z = \frac{\mathrm{SD}z}{\mathrm{M}z}, \tag{9.3}$$

which respectively measure the central tendency, the dispersion, and the standardized dispersion. In particular, the estimation accuracy of choroidal thickness distribution is quantified in terms of four quantities—namely, difference (D), absolute difference (AD), correlation coefficient (CC) and Dice coefficient (DC). Accordingly, we define specific measures, such as MAD, MCC, SDDC, CVCC, CVDC (replacing z by the suitable specific quantity). Here note that the standardized dispersion measure CVz is meaningful only if z is nonnegative. Accordingly, since difference (D) is signed, CVD is not meaningful and not reported. Further, statistical measures are computed for results obtained not only by the proposed algorithm (superscripted '*auto*') but by manual methods (superscripted '*ref*') as well. In particular, the average of the two manual segmentations is taken as reference in such computations. To ensure fair comparison, the results are reported vis-à-vis observer repeatability, i.e., the consistency of performing manual segmentations multiple times by same observer.

A. Difference and Absolute difference: Suppose x_i and y_i denote the thickness values at the i-th ($i = 1, \ldots, N$) column (A-scan index) in two measurements. Then the difference (D) and the absolute difference (AD) between those measurements at the i-th column are respectively given by

$$\mathrm{D}_i = (x_i - y_i), \qquad \mathrm{AD}_i = |x_i - y_i|. \tag{9.4}$$

For each scan, corresponding mean difference (MD) and mean absolute difference (MAD) are obtained based on (9.3). For the 291 B-scans from the three datasets, the proposed algorithm achieves MD between $-52.98\,\mu$m and $13.75\,\mu$m with an average of $-16.63\,\mu$m and standard deviation (SDD) of $19.79\,\mu$m, while the MD between the two manual segmentations varies between $-30.67\,\mu$m and $20.18\,\mu$m with an average of $-5.65\,\mu$m and SDD of $14.53\,\mu$m. Figure 9.7 provides further dataset-wise details. Difference plots for the three datasets are furnished in Fig. 9.6. Inspecting those values, there appears to be a slight negative bias in the proposed method vis-à-vis the reference manual method, indicating room for further improvement. However, the standard deviations appear to be desirably close.

Proceeding further, the sign of the error is ignored and turned to obtain the absolute difference (AD) measure. The MAD between the estimated thickness and the reference thickness for our 291 B-scans, are plotted in Fig. 9.8a. To facilitate comparison, MAD between two manual segmentations, measuring observer repeatability, are also presented. The proposed automated algorithm achieves MAD between 5.63 and $52.98\,\mu$m with an average of $21.88\,\mu$m and standard deviation (SDAD) of $17.43\,\mu$m, while the MAD between manual segmentations varies between 5.55 and $38.71\,\mu$m with an average of $13.74\,\mu$m and SDAD of $11.67\,\mu$m.

Evaluation criteria	Method	Parameter	Unit	Dataset-1	Dataset-2	Dataset-3	Overall (SSIM-based method)	Dual-gradient-based method [19]	Performance improvement of SSIM-based method over dual-gradient-based method
Bias or Difference (D)	Automated (Proposed vs M)	MD (SDD)	μm (μm)	-12.62 (19.38)	-22.79 (20.85)	-14.48 (19.10)	-16.63 (19.79)	2.35 (15.48)	NC (NC)
		Min–Max	μm	-52.98–13.75	-45.17–1.64	-32.06–10.22	-52.98–13.75	–	–
	Manual (M1 vs M2)	MD (SDD)	μm (μm)	-2.18 (15.20)	-6.60 (14.38)	-8.17 (13.97)	-5.65 (14.53)	-1.34 (6.08)	NC (NC)
		Min–Max	μm	-21.36–15.25	-30.67–20.18	-38.71–15.26	-30.67–20.18	–	–
Absolute difference (AD)	Automated (Proposed vs M)	MAD (SDAD)	μm (μm)	19.61 (16.39)	26.45 (18.38)	19.59 (17.46)	21.88 (17.43)	16.27 (11.48)	NC (NC)
		Min–Max	μm	6.15–52.98	5.63–45.17	9.98–32.06	5.63–52.98	–	–
		CVAD	ratio	0.84	0.69	0.89	0.79	0.71	NC
	Manual (M1 vs M2)	MAD (SDAD)	μm (μm)	12.63 (12.62)	14.09 (11.76)	14.50 (10.56)	13.74 (11.67)	8.01 (3.34)	NC (NC)
		Min–Max	μm	5.71–22.4	5.55–30.67	6.20–38.71	5.55–38.71	–	–
		CVAD	ratio	0.99	0.83	0.73	0.85	0.42	NC
	Quotients	QMAD	ratio	1.55	1.87	1.35	1.59	2.03	27.67%
		QCVAD	ratio	0.84	0.83	1.22	0.93	1.69	81.72%
Correlation coefficient (CC)	Automated (Proposed vs M)	MCC (SDCC)	% (%)	99.71 (0.20)	99.56 (0.28)	99.35 (0.42)	99.54 (0.31)	–	–
		Min–Max	(%)	98.84–99.95	98.48–99.95	97.90–99.88	97.90–99.95	–	–
		CVCC	ratio	0.20	0.28	0.42	0.31	–	–
	Manual (M1 vs M2)	MCC (SDCC)	% (%)	99.85 (0.09)	99.81 (0.13)	99.65 (0.24)	99.77 (0.16)	–	–
		Min–Max	%	99.57–99.97	99.20–99.96	98.18–99.92	98.18–99.97	–	–
		CVCC	ratio	0.09	0.13	0.24	0.16	–	–
	Quotients	QMCC	ratio	1.93	2.31	1.85	2.00	–	–
		QCVCC	ratio	2.22	2.15	1.96	1.94	–	–
Dice coefficient (DC)	Automated (Proposed vs M)	MDC (SDDC)	% (%)	95.87 (1.97)	93.94 (1.55)	94.16 (1.47)	94.65 (1.67)	96.7 (2.1)	NC (NC)
		Min–Max	%	88.81–98.73	89.79–98.44	90.42–96.94	88.81–98.73	–	–
		CVDC	ratio	2.05	1.65	1.56	1.76	2.17	NC
	Manual (M1 vs M2)	MDC (SDDC)	% (%)	97.43 (0.82)	96.90 (1.30)	95.87 (1.50)	96.73 (1.24)	–	–
		Min–Max	%	95.00–98.78	93.00–98.75	89.44–98.38	89.44–98.78	–	–
		CVDC	ratio	0.84	1.34	1.56	1.28	–	–
	Quotients	QMDC	ratio	1.60	1.95	1.41	1.63	–	–
		QCVDC	ratio	2.44	1.23	0.99	1.37	–	–

Fig. 9.7 Statistical analysis: Automated versus manual methods. Notation: M1—Manual segmentation-1, M2—Manual segmentation-2, M—Average of M1 and M2, NC—Not comparable

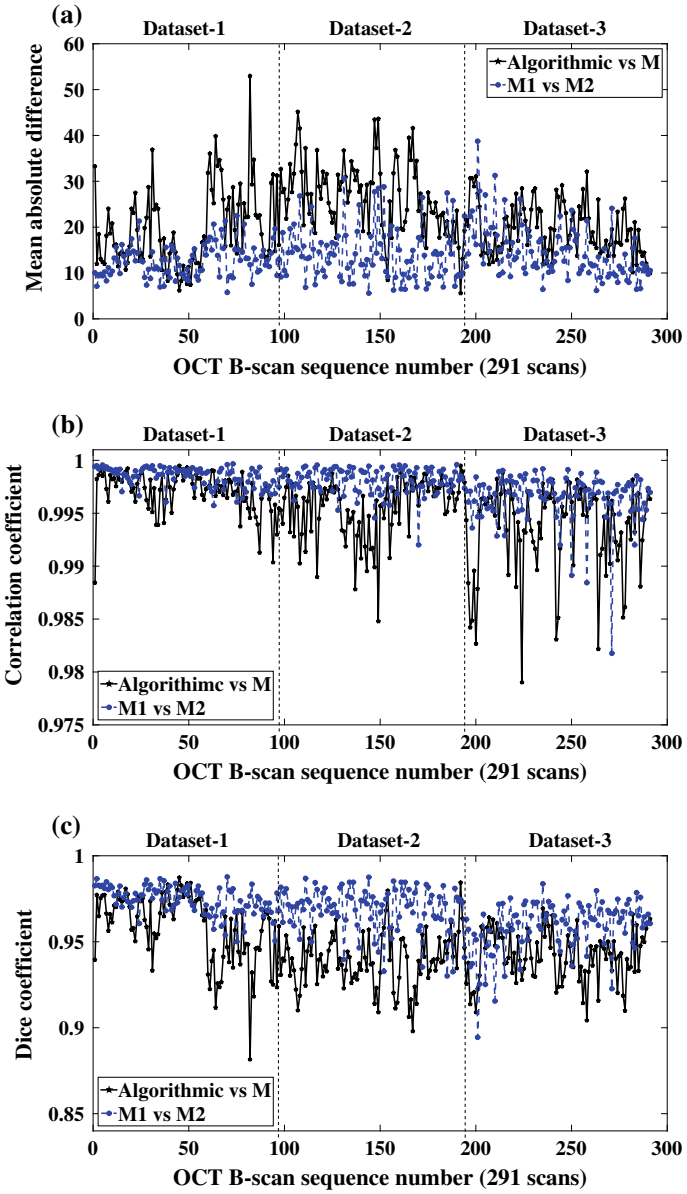

Fig. 9.8 SSIM-based method [26] versus manual: **a** mean absolute difference, **b** correlation coefficient, and **c** Dice's coefficient; notation: M1—Manual segmentation-1, M2—Manual segmentation-2, M—Average of both manual segmentations

B. Correlation coefficient: For two measurements x_i and y_i, $i = 1, \ldots, N$, seen earlier, the correlation coefficient (CC) is defined by [37]

$$CC = \frac{\sum_{i=1}^{N} x_i y_i}{\sqrt{\sum_{i=1}^{N} x_i^2 \sum_{i=1}^{N} y_i^2}}. \tag{9.5}$$

The scan wise CC between the estimated choroid thickness and the reference thickness are now plotted in Fig. 9.8b. In the same figure, the corresponding CC between the thickness values obtained by two manual segmentations, measuring observer repeatability, are also plotted for comparison. The proposed automated algorithm achieves CC between 97.90% and 99.95% with an average (MCC) of 99.54% and standard deviation (SDCC) of 0.31%, across three datasets, while the CC between manual segmentations varies between 98.18% and 99.97% with an MCC of 99.77% and SDCC of 0.16%, thus demonstrating the general reliability of our method.

C. Dice coefficient: Denote the respective sets of pixel indices in the i-th ($i = 1, \ldots, N$) column of two segmentations by C_i^x ($|C_i^x| = x_i$) and C_i^y ($|C_i^y| = y_i$). Then the Dice coefficient (DC) is defined by [38]

$$\mathrm{DC} = \frac{2\sum_{i=1}^{N} |C_i^x \cap C_i^y|}{\sum_{i=1}^{N} |C_i^x| + \sum_{i=1}^{N} |C_i^y|}. \tag{9.6}$$

Now scanwise DC between the estimated choroid thickness and the reference thickness are plotted in Fig. 9.8c, alongside DC between two manual segmentations as a measure of observer repeatability. The proposed algorithm achieves DC between 88.81% and 98.73% with an average (MDC) of 94.65% and SDDC of 1.67%, while DC between two manual segmentations varies between 89.44% and 98.79% with an average (MDC) of 96.73% and SDDC of 1.24%.

9.2.3.1.3 Performance Comparison

A. General comparison: With the above observations, now the performance of SSIM-based [26] algorithm is compared against that of other reported algorithms. However, it remains problematic to clearly establish the advantages of recent methods over earlier work. First, experimental datasets used by various researchers differ in terms of mean wavelengths used in SD-OCT acquisition. Further, some scans have been obtained from healthy subjects, some from diseased subjects [22–24], some from adult, and some from pediatric subjects [19]. Moreover, some scans have been taken only near the foveal cross section [23, 38], rather than at various vertical locations over a wide range. In addition, a variety of evaluation criteria, including correlation coefficient (CC) [22], Dice coefficient (DC) [19, 23, 38], mean border position difference (MBPD) [22, 25], and mean absolute difference (MAD) [19], have been used. The image quality and subjective complexity also appear to vary among various datasets rendering

performance comparison among various algorithms. For fair comparison, ideally, there should be standard datasets, fairly representing possible OCT images, as well as standardized performance measures. Indeed, desired standardization has been achieved in certain fields, such as stereo vision [39] and electrocardiogram (ECG) signal analysis [40]. However, such standardization requires enormous resources. Pending similar standardization in the study of choroid segmentation, to improve contextual comprehension, SSIM-based method compared results generated by the proposed automated algorithm against observer repeatability figures on the same datasets as those figures implicitly reflect image quality. Various aspects of the reported literature including SSIM-based method is presented in Fig. 9.9.

To highlight the issues, consider comparing the SSIM-based algorithm [26] against that reported by dual-gradient-based method by Alonso-Caneiro et al. [19], which is considered as state-of-the-art prior to SSIM-based algorithm. Specifically, we have rival mean difference (MD) values of −16.63 versus 2.35 μm, and rival standard deviation on difference (SDD) 19.79 versus 15.48 μm (see Fig. 9.7). If one considers the above numerical figures alone, one would infer the superiority of the latter algorithm. However, such simplistic comparison inherently ignores the fact that the respective datasets on which the competing algorithms are applied do not necessarily pose similar level of difficulty in choroidal delineation. Indeed, when presented to the human expert, those datasets exhibit respective standard deviation (SDD) values of 14.53 and 6.08 μm on observer repeatability, indicating the relatively higher difficulty level posed by the former (SSIM-based method's) dataset. In other words, SDD for SSIM-based algorithm worsens by 36% compared to manual methods, while such worsening factor is 155% for Alonso-Caneiro et al. Thus, with reference to manual methods, SSIM-based approach exhibits less relative dispersion.

Now similar comparison is made based on other performance criteria. In terms of correlation coefficient (CC), SSIM-based method achieves an overall mean CC (MCC) value of 99.54%, which compares well with the corresponding observer repeatability value of 99.77%. Further, our algorithmic MCC value of 99.54% is much higher than the value 93% reported by Hu et al. [22] (refer to Fig. 9.9). However, as seen in the previous paragraph, the above comparison is not necessarily fair in the absence of the observer repeatability value for the later method. Turning to Dice coefficient (DC), the results reported by Alonso-Caneiro et al. [19], appears to improve on the earlier methods (refer to Fig. 9.9), albeit in an absolute sense, because observer repeatability values are not available. Referring to Fig. 9.7, SSIM-based method obtained an overall mean DC (MDC) of 94.65%, which compares well with the corresponding observer repeatability of 96.73%, but is lower than the algorithmic MDC of 96.7% reported by Alonso-Caneiro et al. Unfortunately, their observer repeatability value, expected to be higher, is unavailable, ruling out fair comparison.

B. Performance quotients: Proceeding further, quotient measures that incorporate observer repeatability are proposed, which not only facilitate performance comparison with reported algorithms, but also to set benchmarks for future research.

Segmentation Method for COB	OCT Mode	Dataset	Evaluation Criterion	Results	Remarks
Gradient based multistage graph search approach [22].	SD-OCT. Wavelength, transverse resolution and axial resolution not specified. Images are averaged 9 times.	37 B-scans per eye, one eye randomly chosen per subject, 20 eyes from 20 healthy and 10 eyes from 10 non-neovascular AMD adult subjects.	Mean border position difference (MBPD), absolute border position difference (ABPD), and correlation coefficient (CC).	MBPD: -3.90μm (SD 15.93μm), ABPD: 21.39μm (SD 10.71μm). Overall CC: 93% (95% CI, 81%–96%). (SD-Standard deviation, CI-Confidence interval).	Observer repeatability and volume comparison not reported.
Gradient based graph search, posed as dynamic programing [38].	SD-OCT (EDI†), 14μm transverse resolution, and 3.9μm axial resolution. Wavelength not specified.	45 B-scans one each from 45 healthy adult subjects.	Dice coefficient (DC).	Mean DC: 90.5% (SD 3%).	Image from each eye that passes through center of fovea is selected. Observer repeatability not reported.Suitability for volume estimation unclear.
Semi-automated gradient based graph search, posed as dynamic programing [23].	SD-OCT (EDI†), 14μm transverse resolution, and 7μm axial resolution. Wavelength not specified. Images are averaged 100 times.	One B-scan per eye, one eye randomly chosen per subject, 30 adult subjects with diabetes.	Dice coefficient (DC).	Mean DC: 92.7% (SD 3.6%).	Images close to the foveal cross section are considered. Observer repeatability not reported. Suitability for volume estimation unclear.
Machine learning using stochastic modeling [24].	1060nm SD-OCT (HP*), 15 to 20μm transverse resolution, and 7μm axial resolution.	871 B-scans from 12 adult eyes (691 diabetes-1 and 180 advanced pathologies).	Fraction of misclassified pixels.	Average error: 13%.	Observer repeatability and volume comparison not reported.
Graph cut segmentation via machine learning using multi-resolution features [25].	870nm SD-OCT (EDI†), 14μm transverse resolution, and 3.9μm axial resolution.	100 B-scans randomly chosen from 10 eyes of 6 healthy adult subjects.	Mean signed and unsigned border position error (MUBPE and MSBPE).	MUBPE: 9.79 pixels (SD 3.29 pixels), MSBPE: 5.77 pixels (SD 2.77 pixels).	Images close to the foveal cross section are considered. Observer repeatability not reported.Suitability for volume estimation unclear.
Graph search, weights obtained using dual gradient probabilistic method, solution using Dijkstra's algorithm [19].	870nm SD-OCT (EDI†), 14μm transverse resolution, and 3.9μm axial resolution. Radial images separated by 30° centered around fovea. Images are averaged 30 times.	1083 pediatric B-scans from 104 healthy subjects and 90 adult B-scans from 15 healthy subjects.	Dice Coefficient (DC), mean absolute difference (MAD).	MAD: 12.6μm (SD 9.00μm) [pediatric]; 16.27μm (SD 11.48μm) [adult]; 8.01μm (SD 3.34μm) [observer repeatability]. Mean DC: 97.3% (SD 1.5%) [pediatric]; 96.7% (SD 2.1%) [adult].	Images passes through fovea center are considered. Suitability for volume estimation unclear. Observer repeatability reported in terms of MAD only for 120 scans.
Structural similarity (SSIM), and adaptive Hessian matrix analysis for segmentation, tensor voting for smoothing [26].	870nm SD-OCT (EDI†), 14μm transverse resolution, and 7μm axial resolution. Images are averaged 25 times.	97 B-scans per eye, one eye randomly chosen per subject, 5 healthy adult subjects.	Mean absolute difference (MAD), Correlation coefficient (CC), Dice coefficient (DC) and absolute volume difference (AVD).	Algorithmic MAD: 19.15μm (SD 15.98μm), mean CC: 99.64% (SD 0.27%), mean DC: 95.47% (SD 1.73%), mean AVD: 0.3046mm^3. Observer repeatability MAD: 11.97μm (SD 10.34μm), mean CC: 99.82% (SD 0.16%), mean DC: 97.28% (SD 1.06%), mean AVD: 0.1240mm^3.	Scans taken at locations even far from fovea. Volumetric analysis performed. Observer repeatability is taken into account for all scans.

Fig. 9.9 Comparative summary of various attempts towards automated choroid layer segmentation. †EDI (enhance depth imaging) SD-OCT: mean wavelength greater than 800 nm (often 870 nm); *HP (high penetration) SD-OCT: mean wavelength greater than 1000 nm (often 1060 nm) [12, 41]

Specifically, two quotients are defined. The quotient of mean, QMz, is defined by the ratio

$$\mathrm{QM}z = \frac{|\mathrm{M}z^{auto} - z^{ideal}|}{|\mathrm{M}z^{ref} - z^{ideal}|}, \tag{9.7}$$

where $\mathrm{M}z^{auto}$ and $\mathrm{M}z^{ref}$, respectively, indicate the mean values obtained by the algorithm and the manual method, and z^{ideal} denotes the ideal value of z. A low QMz value is desirable. Specifically, $\mathrm{QM}z = 1$ would make the algorithmic accuracy indistinguishable from the accuracy of manual methods in terms of mean error. Similarly, quotient of CV, QCVz, is defined by

$$\mathrm{QCV}z = \frac{\mathrm{CV}z^{auto}}{\mathrm{CV}z^{ref}}, \tag{9.8}$$

where $\mathrm{CV}z^{auto}$ and $\mathrm{CV}z^{ref}$, respectively, indicate the CV obtained by the algorithm and that obtained manually. Again, we desire QCVz, measuring relative standard dispersion, to be low, and $\mathrm{QCV}z = 1$ would make the algorithm at par with manual methods. In (9.7) and (9.8), the general quantity z can specifically be either AD, or CC, or DC, as mentioned earlier.

In this backdrop, the respective overall QMAD and overall QCVAD values, obtained by SSIM-based method, are observed to be, 1.59 and 0.93. Interestingly, QCVAD value for SSIM-based algorithm is less than one, indicating that the algorithmic consistency exceeds manual consistency. Further, those quotient values improve upon the respective quotients of 2.03 and 1.69 reported by Alonso-Caneiro et al. [19] by respective factors of 27.67% and 81.72%. Figure 9.7 provides further dataset-wise details. In particular, the SSIM-based method achieves consistent QMAD values of 1.55, 1.87, 1.35 for the three datasets, indicating consistent algorithmic performance across datasets. Such performance consistency is further buttressed by the corresponding consistent QCVAD values of 0.84, 0.83 and 1.22. In addition, the low overall QMCC and QCVCC (resp. QMDC and QCVDC) values of 2 and 1.94 (resp. 1.63 and 1.37), respectively, further corroborate the effectiveness of the SSIM-based algorithm. Figure 9.7 presents further details on dataset-wise performance.

9.2.3.2 Choroidal Volume

Finally, estimation choroidal volume is attempted. As mentioned in Sect. 9.2.2.1, each of the three datasets consists of 97 B-scans taken at a uniform vertical separation of 30 μm. As these datasets were taken from in vivo imaging, all the scans are not spatially aligned, specifically along Z-axis, due to the eye movement. Therefore, choroid layer is not aligned spatially in all the scans and thus volume could not be estimated directly. In view of this, first the scans are geometrically aligned, thereby aligning the choroid layer. In particular, building on eye structure, spherical alignment

is performed which is not only useful for volume estimation but also facilitated life-like visualization of the choroid layer.

9.2.3.2.1 Geometrical Alignment Although eye anatomy is nominally a sphere, all internal layers of the eye are not spherical. For example, the retinal shape deviates considerably from a sphere, especially, near the fovea. Fortunately, the RPE, except in the proximate region of the optic disc, is approximately spherical. In view of this observation, RPE inner boundaries in all the OCT sections are aligned on a nominal sphere. In particular, note that any 3D point (X, Y, Z) lies on the surface of a sphere with center (X_c, Y_c, Z_c) and radius R, if it satisfies

$$(X - X_c)^2 + (Y - Y_c)^2 + (Z - Z_c)^2 = R^2. \tag{9.9}$$

Therefore, the goal is to find (X_c, Y_c, Z_c) and R that best align the boundaries at hand. To this end, the following steps are employed:

A. Scaling: Before proceeding further, it is crucial to notice that X-, Y- and Z-axes are sampled at different intervals. So, in preparation to spherical alignment, all axes are scaled (with the help of OCT metadata) so as to endow each axis with the same unit of length.
B. Optimization: Assuming proper scaling, identify N_i (which should be reasonably large) 3D points $\{(X_{ij}, Y_{ij}, Z_i)\}_{j=1}^{N_i}$ on the retina-RPE boundary on the i-th OCT section, $1 \leq i \leq K$. Here we assume that there are K such sections (in our case, $K = 31$). Now the task is to provide a planar transformation (which possibly varies from slice to slice) to each OCT slice in such a manner that the transformed points deviate the least from a nominal sphere. Since Y-coordinates are already aligned, planar transformations that alters the X-coordinate, but leaves the Y- and Z-coordinates unchanged are considered. Finally, we shall leave the first and the last sections unaltered in order to avoid ambiguity.
   Formally, such planar transformation for the i-th ($1 \leq i \leq K$) section takes the form $T_i : (X_{ij}, Y_{ij}, Z_i) \rightarrow (X'_{ij}, Y'_{ij}, Z'_i)$, where

$$X'_{ij} = \alpha_i X_{ij} + \beta_i Y_{ij} + \gamma_i$$

   for some $(\alpha_i, \beta_i, \gamma_i)$, $Y'_{ij} = Y_{ij}$ and $Z'_i = Z_i$. Further, we fix

$$(\alpha_i, \beta_i, \gamma_i) = (1, 0, 0) = (\alpha_K, \beta_K, \gamma_K),$$

   i.e., $X'_{ij} = X_{ij}$ for each $1 \leq j \leq N_i$ as long as $i = 1$ or $i = K$.
   Thus the task boils down to solving the following optimization problem:

$$(\Phi^*, \Psi^*) = \arg \min_{(\Phi, \Psi)} \sum_{i=1}^{K} \sum_{j=1}^{N_i} ((X'_{ij} - X_c)^2 + (Y_{ij} - Y_c)^2 + (Z_i - Z_c)^2 - R^2)^2. \tag{9.10}$$

where we optimize the center (X_c, Y_c, Z_c) and radius R of the nominal sphere, denoting $\Phi = \{X_c, Y_c, Z_c, R\}$ for convenience, jointly with the free planar transformation parameters $\Psi = (\alpha_i, \beta_i, \gamma_i)_{i=2}^{K-1}$.

C. Optimal planar transformations: The optimal choice of Ψ^* in (9.10) specifies the collection of optimal planar transformations T_i, $2 \leq i \leq K-1$. So, in order to achieve spherical alignment, it is tempting to simply transform the i-th preprocessed section, $2 \leq i \leq K-1$. However, this method generally maps a point on the integer grid to a point that does not lie on the integer grid on the transformed axes. Appropriate interpolation will be performed to obtain image values on the desired integer grid.

In the experiment, a lightfield display (Holovizio 721RC) is used for 3D visualization of volume data. However, here we include several 2D views for easy appreciation by the reader. In Fig. 9.10, the reference unaligned sections, the corresponding spherically aligned sections are depicted. In each row, approximately same perspective is maintained for easy comparison. Notice that the spherically aligned sections stack up to approximate the natural geometry. Indeed those highlight a circular fovea indicating proper alignment.

Further, the choroid layer is visualized in 3D from six different perspectives in Fig. 9.11. Notice the depletion in choroid thickness in the vicinity of the optic disc. In this connection, recall that the presented images are pictures taken of the 3D rendering on a lightfield display. In practice, the depletion stands out more dramatically. In view of this, the current methodology for 3D visualization is believed to come to the aid of ophthalmologists.

For volume computation, one needs choroidal thickness estimates even at intervening vertical locations. To this end, cubic interpolation is performed, while converting B-scan pixels to the physical unit of length (mm). As earlier, ideally, we would like the automated volume measurement to approximate the reference manual

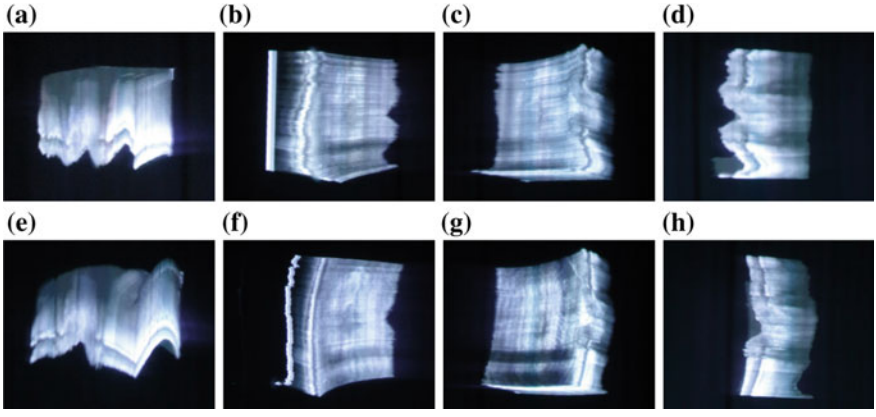

Fig. 9.10 3D visualization using lightfield display: **a**–**d** various perspectives of unaligned OCT sections; **e**–**h** corresponding perspectives after performing spherical alignment

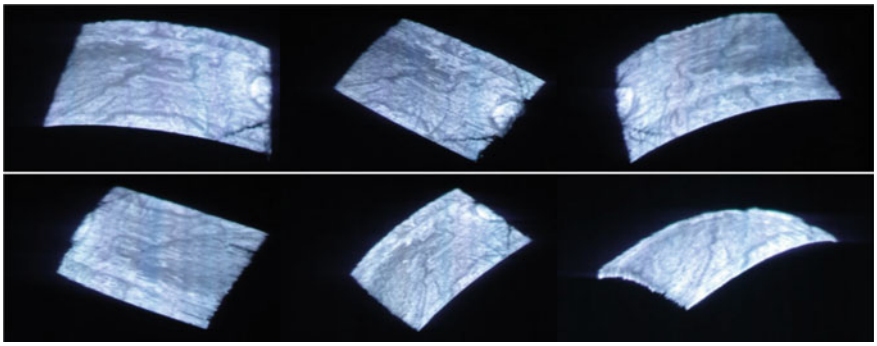

Fig. 9.11 3D visualization of extracted choroid layer from various views using lightfield display

measurement. Accordingly, to quantify the proximity between those volume estimates, next certain statistical measures are introduced systematically.

9.2.3.2.2 General Performance Measures For the three datasets at hand, the respective automated volume estimates by SSIM-based method are obtained as 2.9947, 2.5853, and 8.4426 mm^3 with an average of 4.6775 mm^3. The corresponding estimates found by reference manual segmentation are 3.1532, 2.8755, and 9.1847 mm^3 with an average of 5.0711 mm^3, demonstrating the general accuracy of our method. Now lets turn to more involved performance criteria, beginning with absolute volume difference (AVD). Specifically, the AVD between automated algorithm and manual reference is defined by

$$\mathrm{AVD}^{auto} = |\mathrm{vol}^{auto} - \mathrm{vol}^{ref}|, \tag{9.11}$$

where vol^{auto} denotes the volume estimated by the proposed method, and vol^{ref} denotes that per the manual reference (average of manual segmentations $M1$ and $M2$). Similarly, the AVD between the manual segmentations $M1$ and $M2$ is given by

$$\mathrm{AVD}^{ref} = |\mathrm{vol}^{M1} - \mathrm{vol}^{M2}|, \tag{9.12}$$

which we take as a measure of observer repeatability. As comparing raw AVD values across various eyes could be unfair, we define relative AVD (RAVD) as the ratio of AVD to vol^{ref}:

$$\mathrm{RAVD}^{flag} = \frac{\mathrm{AVD}^{flag}}{\mathrm{vol}^{ref}}, \tag{9.13}$$

where "*flag*" could stand for either "*auto*" (automated) or "*ref*" (manual reference). Further, MAVD^{flag} (resp. MRAVD^{flag}) indicates the mean of AVD^{flag} (resp. RAVD^{flag}) values taken across datasets.

For the three datasets, the SSIM-based method achieves an MRAVD^{auto} of 7.76% vis-à-vis observer repeatability MRAVD^{ref} of 3.59%. Table 9.1 provides further dataset-wise details. In particular, for the datasets under consideration, the respective

Table 9.1 Comparison of choroidal volumes obtained from algorithmic and manual segmentations. Notation: M1—Manual segmentation-1, M2—Manual segmentation-2, M—Average of M1 and M2, AVD—Absolute volume difference, RAVD–AVD relative to reference (M), QAVD—Quotient of AVD, MAVD–Mean AVD, MRAVD–Mean RAVD, QMAVD—Quotient of MAVD

	Unit	Method	Dataset-1	Dataset-2	Dataset-3	Mean
Volume	mm^3	Algorithmic (P)	2.9947	2.5853	8.4426	4.6775
		M1	3.1664	2.9174	9.4024	5.0169
		M2	3.1399	2.8335	8.9669	5.1253
		M	3.1532	2.8755	9.1847	5.0711
AVD (RAVD)	mm^3 (%)					MAVD (MRAVD)
		P and M	0.1580 (5.01)	0.2902 (10.09)	0.7421 (8.08)	0.3936 (7.76)
		M1 and M2	0.0265 (0.84)	0.0839 (2.92)	0.4355 (4.74)	0.1820 (3.59)
QAVD	Ratio					QMAVD
			5.9	3.4	1.7	2.2

RAVD^{auto} values are 5.01, 10.09, and 8.08%. In contrast, the corresponding observer repeatability (RAVD^{ref}) figures are 0.84, 2.92, and 4.74%. Notice that the datasets pose dissimilar challenges to automated and manual methods with regards to volume computation. In particular, dataset-1 is highly amenable to manual approach, but poses significantly more challenge to the automated algorithm. On the other hand, dataset-3 is relatively less amenable to manual approach, but poses only marginally more difficulty to the automated algorithm.

9.2.3.2.3 Performance quotients Now, to quantify the closeness of algorithmic performance with observer repeatability in each dataset, the quotient of absolute volume difference

$$\text{QAVD} = \frac{\text{AVD}^{auto}}{\text{AVD}^{ref}} = \frac{\text{RAVD}^{auto}}{\text{RAVD}^{ref}}, \tag{9.14}$$

is calculated for which a low value is desirable. Similarly, the corresponding quotient QMAVD across all three datasets is defined by

$$\text{QMAVD} = \frac{\text{MAVD}^{auto}}{\text{MAVD}^{ref}} = \frac{\text{MRAVD}^{auto}}{\text{MRAVD}^{ref}}. \tag{9.15}$$

Over the three datasets, a QMAVD value of 2.2 is achieved, i.e., the SSIM-based algorithm incurs just twice the error compared to human expert while computing choroidal volume. However, the dataset-wise QAVD values of 5.9, 3.4 and 1.7 vary significantly.

9.3 Fine-Grain Analysis

In this section, we discuss fine-grain analysis of choroid. In general, such analysis can be performed in multiple ways by considering various fine features of the choroid including choroid vascularity index, variation of choroid vessel diameter, choroid thickness/volume variation within sublayers of choroid. However, in view of recent developments, we restrict our focus to one such parameter namely, choroidal stromal-luminal ratio, employed as a measure of choroidal vascularity index. To this end, we begin by presenting the clinical underpinnings of stromal-luminal analysis. Subsequently, we present present various solution approaches with specific focus on recent methodology.

9.3.1 Problem Setup and Solution Approaches

So far, only two disease determinants namely, choroid thickness distribution and volume are considered for choroidal disease management. Those could even predict the responsiveness of the retina and the choroid to anti-vascular endothelial growth factor [42]. However, those gross indicators provide limited information about the structural changes in the choroid, and ophthalmologists seek additional information for better understanding of diseases. Specifically, quantifying choroidal vascular region is crucial in diagnosing diseases affecting choroid vascularity [15]. Consequently, ophthalmologists visually inspect OCT scans paying attention to the choroid layer, and form an opinion about the relative proportion of the constituent vessel (luminal) and interstitial (stromal) regions (Fig. 9.12). Naturally, they seek to corroborate the qualitative assessment with quantitative evidence.

To reduce physician's burden, it now becomes imperative to algorithmically estimate the ratio of stromal to luminal regions from such images. Here the principal difficulty lies in the absence of ground truth. In certain other clinical studies, such as estimation of choroid thickness distribution, manual demarcation of the inner and outer boundaries of the choroid is taken as the reference, albeit subject to variability in human performance [26]. In contrast, marking choroid vessels at acceptable levels of accuracy is practically infeasible even for experts. To appreciate this, consider the two attempts at manual vessel segmentation, depicted in Fig. 9.13, where most larger and some medium vessels could be marked with reasonable accuracy, but vessels with smaller diameters were largely missed. Here the said infeasibility arises because vessels are sometimes indicated by such extremely fine features that one cannot pinpoint individual features, but can form a gross opinion about the density of such features. Thus it is imperative to leverage technology to identify those features.

In this context, use of the software package, ImageJ, has been widely reported for stromal-luminal analysis [43]. Yet, while this software is versatile, it has not been developed specifically for OCT image analysis, and does not incorporate the idiosyncracies of this imaging modality. So, researchers used ImageJ as an interactive

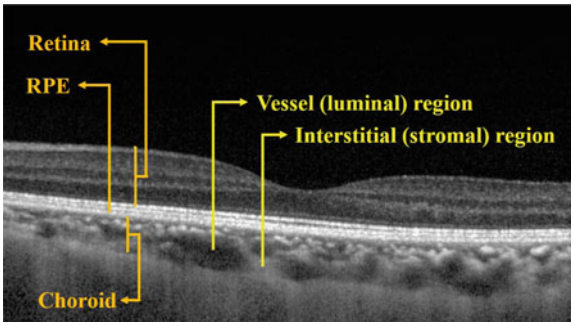

Fig. 9.12 **a** Typical SD-OCT image choroidal vessel (luminal) and interstitial (stromal) regions

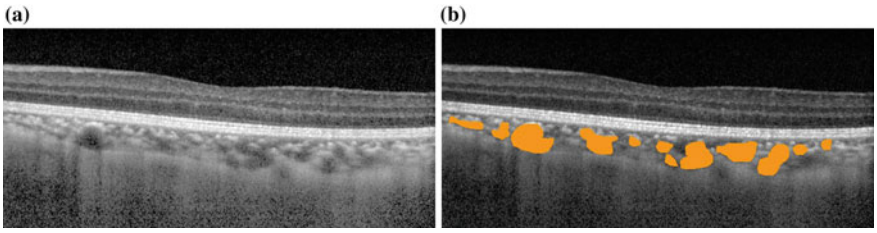

Fig. 9.13 Manual delineation of choroid vasculature: **a** reference image, and **b** manually segmented vessels using ImageJ software

platform, and developed specific protocols for using this platform. Such a protocol generally involves manual selection of a region of interest (ROI), and sample neighborboods that certainly belong to prominent vessels. The software then determines local thresholds according to the Niblack rule involving a combination of local mean and local standard deviation of intensity values. This approach, while an improvement over the qualitative approach, is still cumbersome, and not suitable for high throughput and volume (involving large number of B-scans) analysis. To fill the gap, Vupparaboina et al. proposed a fully automated work flow which produces fast and accurate stromal-luminal analysis for individual B-scans as well as volumes consisting of large number of B-scans [44]. In particular, Vupparaboina et al.'s method considers specific aspects of SD-OCT imaging, including speckle noise, exponential dynamic range compression, and depth-dependent attenuation, and alleviate those using targeted techniques, including median filtering and exponential enhancement. Further, this method builds on earlier reported SSIM-based automated choroid localization method [26] to accurately confine the analysis only to the choroid region. In the subsequent sections, the methodology and experimental results of Vupparaboina et al.'s method, here after referred as exponentiation-based method, are discussed in detail.

9.3.2 Methodology

The exponentiation-based methodology is outlined using a flow chart in Fig. 9.14. Key steps are described below.

9.3.2.1 Preprocessing

OCT B-scan images are generally affected by low-level speckle noise, characteristics of the imaging modality, as seen in Fig. 9.15a [45]. In view of this, median filtering is first employed to mitigate such noise (Fig. 9.15b). At the same time, due to heterogeneity in absorption properties of the eye tissue, the OCT images suffer from regional variation in contrast and brightness levels. Accordingly, the image was divided into 8×8 blocks, and adaptively equalized based on local histograms (Fig. 9.15c).

9.3.2.2 Exponential Enhancement and Thresholding

In SD-OCT imaging, the intensity range is compressed and quantized, while producing the usual B-scans. Noting this, Girard et al. suggested an exponential enhancement method, which is adopted by Vupparaboina et al.'s methodology [46]. To this end, first one needed to undo the associated non-linear mapping (compression), performed before quantization, and transform the OCT B-scan image into raw intensity format (Fig. 9.15d). The said transformation takes the form:

$$J_{raw}(i,j) = \left(\frac{J(i,j)}{255}\right)^4,$$

where $J(i,j)$ is the intensity of the compressed image, and $J_{raw}(i,j)$ is the intensity of the raw image obtained by OCT machine, both at location (i,j).

Subsequently, contrast enhancement is performed by increasing the dynamic range of pixel intensities via exponentiation. In particular, the exponentiated image (Fig. 9.15e) is obtained, where the intensity at location (i,j) was computed as

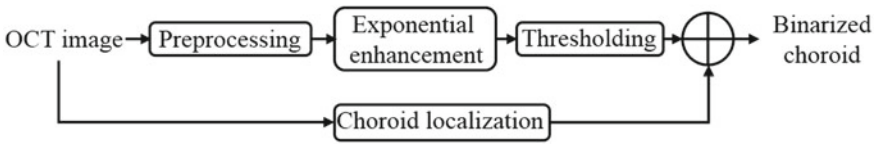

Fig. 9.14 Schematic of choroidal stromal-luminal analysis

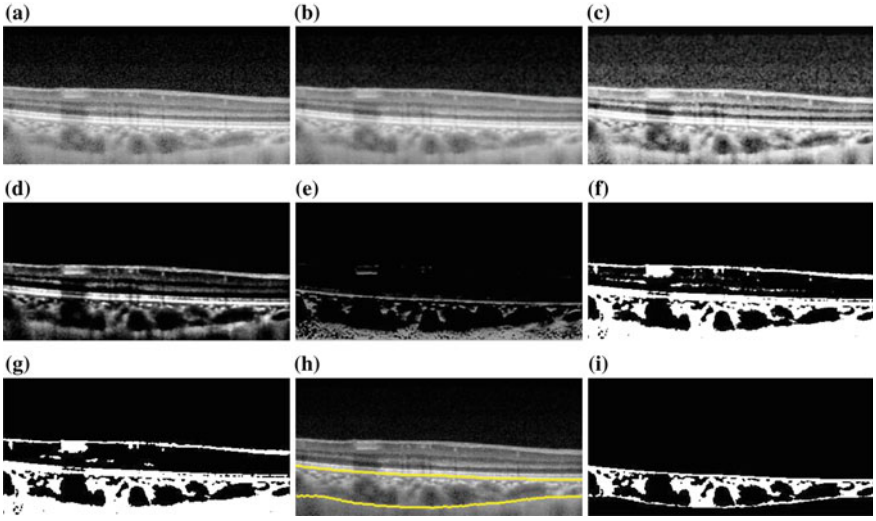

Fig. 9.15 Steps in stromal-luminal analysis: **a** acquired noisy B-scan; **b** median filtering; **c** adaptive histogram equalization; **d** gray scale to raw intensity transformation; **e** exponentiation; **f** multiplication of intensity at each row by square of the row index; **g** intensity transformation to gray scale, median thresholding, and removal of outliers using connected components method; **h** detected choroid inner and outer boundaries; and **i** binarized choroid layer

$$J_{exp}(i,j) = \frac{(J_{raw}(i,j))^n}{2\sum_{k=i}^{p}(J_{raw}(k,j))^n}$$

subject to suitable normalization. Here n denotes the exponentiation factor and the value is empirically fixed as $n = 6$ after trials and errors.

Further, in OCT imaging, a tissue at less depth produces higher intensity, compared to a similar tissue at a greater depth. Noting this, to further enhance the choroidal structures, especially, near sclera, each row of J_{exp} was multiplied by square of its row index to produce the enhanced image J_{enh} (Fig. 9.15f), i.e.,

$$J_{enh}(i,j) = i^2 J_{exp}(i,j)$$

is obtained at each location (i,j). Notice the following. In the original image J, a pixel belonging to a blood vessel generally had a darker shade of gray, and a non-vessel pixel a lighter shade. In the enhanced image J_{enh}, the former took on a much darker shade, and latter a much lighter one, as desired. In view of this, the enhanced image was binarized by setting a threshold at the median intensity. Unwanted outliers were removed via connected components method (Fig. 9.15g).

9.3.2.3 Choroid Localization and Binarized Choroid

At this point, localizing the choroid is left, so that only the choroid layer could be binarized in exclusion of other layers such a retina and sclera. To this end, choroid inner boundary (CIB), and choroid outer boundary (COB) is obtained by employing the SSIM-based methodology described in Sect. 9.2 on raw OCT scans (Fig. 9.15h) [26]. Subsequently, thus obtained boundaries are used to obtain desired choroid region from the previous binarized estimate (Fig. 9.15i).

9.3.3 Stromal-Lumial Analysis: Experimental Results

In this section, performance of Vupparaboina et al.'s methodology is presented vis-à-vis earlier ImageJ-based protocol for different subjects is presented. Subsequently, Vupparaboina et al.'s algorithm is applied for stromal-luminal analysis of OCT volume data.

9.3.3.1 B-Scans

As alluded earlier, the absence of reference (ground truth) procedure does not allow quantitative comparison. So the comparison was made visually, and based on expert opinion. To this end, SD-OCT B-scans acquired from multiple subjects are considered. Those images were analyzed using ImageJ-based protocol reported by Sonoda et al. [16], as well as the Vupparaboina et al.'s method. While Sonoda et al. manually extracted the choroid layer, to ensure fair comparison, the same choroid localization employed by Vupparaboina et al.'s method was also used in conjunction with the ImageJ method. Results for six B-scans from six different subjects (A–F) is depicted in Fig. 9.16. Results obtained by Vupparaboina et al.'s method appear to closely resemble intuitive estimation of vasculature. Indeed, subjective interpretation by multiple clinicians found results of Vupparaboina et al.'s method superior.

9.3.3.2 Volume Analysis

Next volumetric stromal-luminal analysis is performed on each of the eyes of two healthy subjects (subjects A and B). In particular, 97 OCT B-scans with uniform separation of 30 μm were acquired from each eye of the subject and evaluated using the proposed algorithm. Further, bright-dark ratios (ratio between stromal and luminal regions) were estimated for all the B-scans. Figure 9.17 depicts variation in bright-dark ratios with scan index for each eye under consideration. Further, overall bright-dark ratio of each eye is quantified, by first estimating volumes of luminal and stromal regions. Such volume estimates were in turn obtained using cubic interpolation. Table 9.2 presents volume bright-dark ratios for each eye of the two subjects.

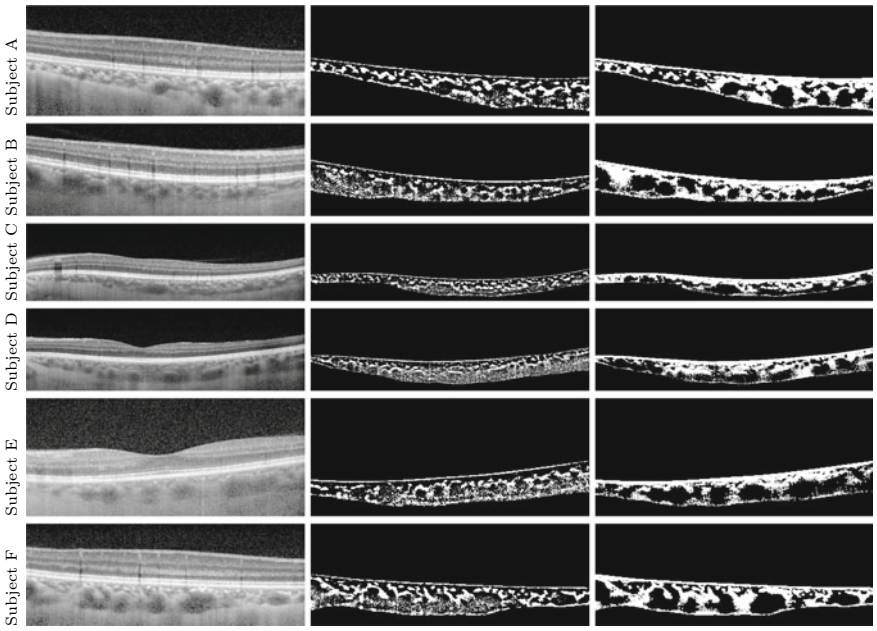

Fig. 9.16 Vupparaboina et al.'s method [44] versus ImageJ-based method [16]: Left—OCT image; middle—ImageJ-based method; right—Vupparaboina et al.'s method

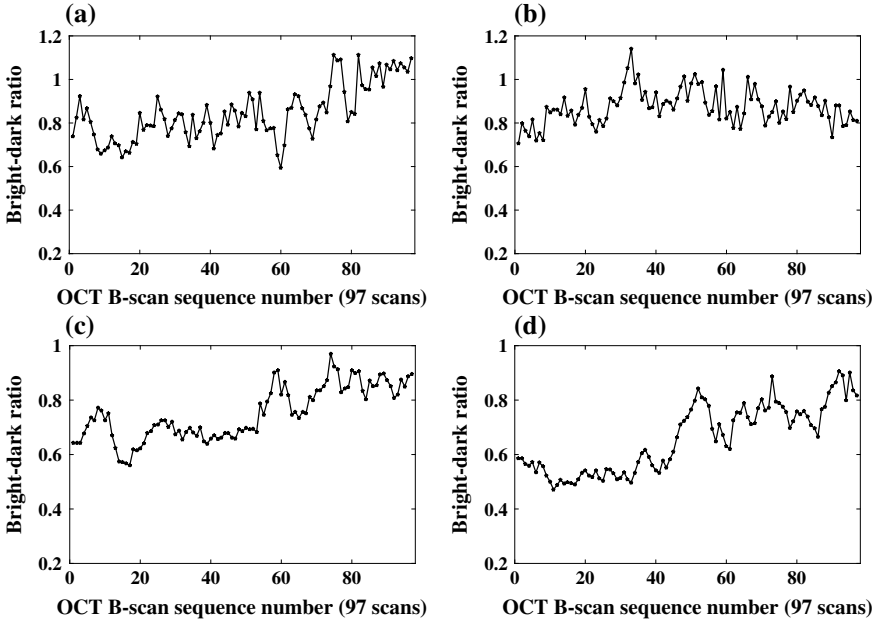

Fig. 9.17 Stromal-luminal ratio obtained across all the B-scans from two healthy subjects: **a** left and **b** right eye of Subject A; **c** left and **d** right eye of Subject B

Table 9.2 Volumetric analysis: Bright-dark ratios between estimated stromal and luminal volumes for each eye of two subjects

Subject	Left eye	Right eye
A	0.828	0.872
B	0.741	0.644

9.4 Summary

In this chapter, automated quantification of choroidal thickness, volume and stromal-luminal ratio is discussed. Firstly, automated quantification of thickness and volume is discussed which mainly involves choroid layer segmentation. To this end, the focus was mainly on recent SSIM-based method which has demonstrated higher accuracy over earlier methods. In particular, this method exploits the structural dissimilarity of the choroid and the sclera layers using structural similarity (SSIM) index. Further, upon smoothening using tensor voting, automated choroid segmentation that exhibits good correlation with manual segmentation is obtained. Subsequently, this method reported automated choroid volume analysis. This method also reported a exhaustive statistical analysis to (i) establish closeness of the automated estimates to the corresponding manual ones, (ii) demonstrate superior performance of our method over known results, and (iii) facilitate future benchmarking.

Secondly, a fully automated exponentiation-based methodology for obtaining binarized choroid based on OCT B-scans for stromal-luminal analysis is discussed. In particular, this method considers specific artefacts of SD-OCT imaging including speckle noise, exponential dynamic range compression, and depth-dependent attenuation, and removed those in a targeted manner via median altering and exponential enhancement. In experts' opinion, this method achieved improved accuracy when compared to earlier ImageJ-based protocol in a representative B-scan dataset. This method also demonstrated volumetric analysis on a subset of subjects. Clinical indicators including choroidal thickness, volume, and stromal-luminal ratio, can be used to develop automated disease detection tool that learns the correlation between various diseases and the indicators [47]. Such tool could assist physicians in making disease diagnosis. Further, such a tool could dramatically enhance the efficacy of early diagnosis and remote eyecare.

As discussed earlier, clinical studies studies are based on only gross indicators such as overall choroidal thickness and volume for disease management. However, choroid consists of sublayers, namely, choriocapillaries, Sattler's and Haller's layers, which are classified according to increasing diameter of blood vessels. In view of this fact, now clinicians envisage to make even more precise diagnosis by investigating choroidal sublayers. For instance, there is active interest in studying the correlation between the Haller's layer (containing vessels with large diameter) thickness and various diseases. Further, there also interest towards understanding the effect of various diseases on vessel diameter in a particular sublayer [48].

References

1. D.L. Nickla, J. Wallman, The multifunctional choroid. Prog. Retinal Eye Res. **29**(2), 144–168 (2010)
2. A. Bill, G. Sperber, K. Ujiie, Physiology of the choroidal vascular bed. Int. Ophthalmol. **6**(2), 101–107 (1983)
3. L.M. Parver, Temperature modulating action of choroidal blood flow. Eye **5**(2), 181–185 (1991)
4. A. Alm, S.F. Nilsson, Uveoscleral outflow-a review. Exp. Eye Res. **88**(4), 760–768 (2009)
5. D. Van Norren, L. Tiemeijer, Spectral reflectance of the human eye. Vis. Res. **26**(2), 313–320 (1986)
6. D.S. Dhoot, S. Huo, A. Yuan, D. Xu, S. Srivistava, J.P. Ehlers et al., Evaluation of choroidal thickness in retinitis pigmentosa using enhanced depth imaging optical coherence tomography. Br. J. Ophthalmol. **97**(1), 66–69 (2013)
7. Y. Imamura, T. Fujiwara, R. Margolis, R.F. Spaide, Enhanced depth imaging optical coherence tomography of the choroid in central serous chorioretinopathy. Retina **29**(10), 1469–1473 (2009)
8. V. Manjunath, J. Goren, J.G. Fujimoto, J.S. Duker, Analysis of choroidal thickness in age-related macular degeneration using spectral-domain optical coherence tomography. Am. J. Ophthalmol. **152**(4), 663–668 (2011)
9. M. Esmaeelpour, B. Považay, B. Hermann, B. Hofer, V. Kajic, S.L. Hale et al., Mapping choroidal and retinal thickness variation in type 2 diabetes using three-dimensional 1060-nm optical coherence tomography. Invest. Ophthalmolo. Vis. Sci. **52**(8), 5311–5316 (2011)
10. D.A. Sim, P.A. Keane, H. Mehta, S. Fung, J. Zarranz-Ventura, M. Fruttiger, et al., Repeatability and reproducibility of choroidal vessel layer measurements in diabetic retinopathy using enhanced depth optical coherence tomography. Invest. Ophthalmol. Vis. Sci. IOVS–12 (2013)
11. R. Margolis, R.F. Spaide, A pilot study of enhanced depth imaging optical coherence tomography of the choroid in normal eyes. Am. J. Ophthalmol. **147**(5), 811–815 (2009)
12. A. Miki, Y. Ikuno, Y. Jo, K. Nishida, Comparison of enhanced depth imaging and high-penetration optical coherence tomography for imaging deep optic nerve head and parapapillary structures. Clin. Ophthalmol. (Auckland, NZ) **7** 1995 (2013)
13. F.H. Adler, P.L. Kaufman, L.A. Levin, A. Alm, *Adler's Physiology of the Eye* (Elsevier, Uppsala, 2011)
14. R.F. Spaide, Enhanced depth imaging optical coherence tomography of retinal pigment epithelial detachment in age-related macular degeneration. Am. J. Ophthalmol. **147**(4), 644–652 (2009)
15. G. Barteselli, J. Chhablani, S. El-Emam, H. Wang, J. Chuang, I. Kozak et al., Choroidal volume variations with age, axial length, and sex in healthy subjects: a three-dimensional analysis. Ophthalmology **119**(12), 2572–2578 (2012)
16. S. Sonoda, T. Sakamoto, T. Yamashita, M. Shirasawa, E. Uchino, H. Terasaki et al., Choroidal structure in normal eyes and after photodynamic therapy determined by binarization of optical coherence tomographic imagesBinarization of OCT on choroid. Invest. Ophthalmol. Vis. Sci. **55**(6), 3893–3899 (2014)
17. J. Chhablani, G. Barteselli, H. Wang, S. El-Emam, I. Kozak, A.L. Doede et al., Repeatability and reproducibility of manual choroidal volume measurements using enhanced depth imaging optical coherence tomography. Invest. Ophthalmol. Vis. Sci. **53**(4), 2274–2280 (2012)
18. L. Zhang, K. Lee, M. Niemeijer, R.F. Mullins, M. Sonka, M.D. Abramoff, Automated segmentation of the choroid from clinical SD-OCT. Invest. Ophthalmol. Vis. Sci. **53**(12), 7510–7519 (2012)
19. D. Alonso-Caneiro, S.A. Read, M.J. Collins, Automatic segmentation of choroidal thickness in optical coherence tomography. Biomed. Opt. Express **4**(12), 2795–2812 (2013)
20. S.J. Chiu, X.T. Li, P. Nicholas, C.A. Toth, J.A. Izatt, S. Farsiu, Automatic segmentation of seven retinal layers in SDOCT images congruent with expert manual segmentation. Opt. Express **18**(18), 19413–19428 (2010)

21. M. Haeker, M. Sonka, R. Kardon, V.A. Shah, X. Wu, M.D. Abràmoff, Automated segmentation of intraretinal layers from macular optical coherence tomography images, in *Proceddings of SPIE*, vol. 6512 (2007), p. 651214
22. Z. Hu, X. Wu, Y. Ouyang, Y. Ouyang, S.R. Sadda, Semiautomated segmentation of the choroid in spectral-domain optical coherence tomography volume scans. Invest. Ophthalmol. Vis. Sci. **54**(3), 1722–1729 (2013)
23. H. Lu, N. Boonarpha, M.T. Kwong, Y. Zheng, Automated segmentation of the choroid in retinal optical coherence tomography images, in *35th Annual International Conference of the Engineering in Medicine and Biology Society (EMBC)* (IEEE, 2013), pp. 5869–5872
24. V. Kajić, M. Esmaeelpour, B. Považay, D. Marshall, P.L. Rosin, W. Drexler, Automated choroidal segmentation of 1060 nm OCT in healthy and pathologic eyes using a statistical model. Biomed. Opt. Express **3**(1), 86–103 (2012)
25. H. Danesh, R. Kafieh, H. Rabbani, F. Hajizadeh, *Segmentation of choroidal boundary in enhanced depth imaging OCTs using a multiresolution texture based modeling in graph cuts* (Comput. Math, Methods Med, 2014)
26. K.K. Vupparaboina, S. Nizampatnam, J. Chhablani, A. Richhariya, S. Jana, Automated estimation of choroidal thickness distribution and volume based on OCT images of posterior visual section. Comput. Med. Imaging Graph. **46**, 315–327 (2015)
27. N. Srinath, A. Patil, V.K. Kumar, S. Jana, J. Chhablani, A. Richhariya, Automated detection of choroid boundary and vessels in optical coherence tomography images, in *36th Annual International Conference of the Engineering in Medicine and Biology Society (EMBC)* (IEEE, 2014), pp. 166–169
28. https://imagej.nih.gov/ij/
29. K. Dabov, A. Foi, V. Katkovnik, K. Egiazarian, Image denoising by sparse 3-D transform-domain collaborative filtering. IEEE Trans. Image Process. **16**(8), 2080–2095 (2007)
30. R.C. Gonzalez, *Digital Image Processing* (Pearson Education India, 2009)
31. Z. Wang, A.C. Bovik, H.R. Sheikh, E.P. Simoncelli, Image quality assessment: from error visibility to structural similarity. IEEE Trans. Image Process. **13**(4), 600–612 (2004)
32. Y. Sato, S. Nakajima, N. Shiraga, H. Atsumi, S. Yoshida, T. Koller et al., Three-dimensional multi-scale line filter for segmentation and visualization of curvilinear structures in medical images. Med. Image Anal. **2**(2), 143–168 (1998)
33. J. Chen, A. Amini et al., Quantifying 3-D vascular structures in MRA images using hybrid PDE and geometric deformable models. IEEE Trans. Med. Imaging **23**(10), 1251–1262 (2004)
34. A.F. Frangi, W.J. Niessen, K.L. Vincken, M.A. Viergever, Multiscale vessel enhancement filtering, in *Medical Image Computing and Computer-Assisted Interventation (MICCAI)* (Springer; 1998), pp. 130–137
35. G. Medioni, C.K. Tang, M.S. Lee. Tensor voting: theory and applications, in *Proceedings of RFIA* (Paris, France. 2000), p. 3
36. G. Medioni, S.B. Kang. *Emerging Topics in Computer Vision* (Prentice Hall PTR, 2004)
37. L. Sörnmo, P. Laguna. *Bioelectrical Signal Processing in Cardiac and Neurological Applications* (Academic Press, 2005)
38. J. Tian, P. Marziliano, M. Baskaran, T.A. Tun, T. Aung, Automatic segmentation of the choroid in enhanced depth imaging optical coherence tomography images. Biomed. Opt. Express **4**(3), 397–411 (2013)
39. http://vision.middlebury.edu/stereo/
40. http://www.physionet.org/physiobank/database/#ecg
41. R.F. Spaide, H. Koizumi, M.C. Pozonni, Enhanced depth imaging spectral-domain optical coherence tomography. Am. J. Ophthalmol. **146**(4), 496–500 (2008)
42. S.W. Kim, J. Oh, S.S. Kwon, J. Yoo, K. Huh, Comparison of choroidal thickness among patients with healthy eyes, early age-related maculopathy, neovascular age-related macular degeneration, central serous chorioretinopathy, and polypoidal choroidal vasculopathy. Retina **31**(9), 1904–1911 (2011)
43. S. Sonoda, T. Sakamoto, T. Yamashita, E. Uchino, H. Kawano, N. Yoshihara et al., Luminal and stromal areas of choroid determined by binarization method of optical coherence tomographic images. Am. J. Ophthalmol. **159**(6), 1123–1131 (2015)

44. K.K. Vupparaboina, A. Richhariya, J. Chhablani, S. Jana, Optical coherence tomography imaging: automated binarization of choroid for stromal-luminal analysis, in *International Conference on Signal and Information Processing (IConSIP)* (IEEE, 2016). pp. 1–5
45. J.M. Schmitt, S. Xiang, K.M. Yung, Speckle in optical coherence tomography. J. Biomed. Opt. **4**(1), 95–105 (1999)
46. M.J. Girard, N.G. Strouthidis, C.R. Ethier, J.M. Mari, Shadow removal and contrast enhancement in optical coherence tomography images of the human optic nerve head. Invest. Ophthalmol. Vis. Sci. **52**(10), 7738–7748 (2011)
47. S. Devarakonda, K. Vupparaboina, A. Richhariya, J. Chhablani, S. Jana. Automated detection of retinal disorders from OCT images using artificial neural network, in *India Conference (INDICON), 2016 IEEE Annual* (IEEE, 2016). pp. 1–6
48. M. Ibrahim, S. Agarwal, K.K. Vupparaboina, J. Chhablani, A. Richhariya, S. Jana. Segmenting and labeling blood vessels in choroidal Haller's layer: a multiple target tracking approach, in *2017 IEEE EMBS International Conference on Biomedical and Health Informatics (BHI)* (IEEE, 2017). pp. 113–116

Chapter 10
Layer Segmentation and Analysis for Retina with Diseases

Fei Shi, Weifang Zhu and Xinjian Chen

Though segmentation of normal retina has been successful, segmentation and analysis of pathological retina are far more important. This chapter first presents an automatic layer segmentation method for retinas with certain deformed layers, and then introduces two layer disruption detection methods based on feature analysis of segmented layers.

10.1 Introduction

It is with the development of optical coherence tomography (OCT) technique, an in vivo and noninvasive scan of the retina that shows its cross-sectional profile, that the layered structure of retina can be extensively studied. Recently introduced spectral domain (SD) OCT produces high resolution real 3-D volumetric scan of the retina that visualize most of the anatomical layers. Automated retinal layer segmentation for normal eyes based on SD-OCT images have been successful [1–14]. However, layer segmentation of retina with diseases is of more value to both pathological study and clinical practice. Some of the methods proposed for normal retinas can also be applied to retinas with certain types of diseases, such as glaucoma [9–11], multiple sclerosis [12], dry age-related macular degeneration (AMD) [13], or other diseases at an early stage, when no dramatic change in the layer structure happens. However, layer segmentation for diseased retina still remains a challenging problem, especially when additional structures exist, such as intraretinal cysts, subretinal or sub-RPE

F. Shi · W. Zhu · X. Chen
School of Electronics and Information Engineering, Soochow University, Suzhou, China

X. Chen (✉)
State Key Laboratory of Radiation Medicine and Protection, Soochow University, Suzhou, China
e-mail: xjchen@suda.edu.cn

X. Chen et al. (eds.), *Retinal Optical Coherence Tomography Image Analysis*,
Biological and Medical Physics, Biomedical Engineering,
https://doi.org/10.1007/978-981-13-1825-2_10

fluid in diabetic macular edema (DME) and wet AMD. In these cases, the large variety of layer morphology and degraded image quality caused by abnormalities greatly affect the segmentation performance. In the first part of this chapter, we focus on segmentation for retinas with serous pigment epithelium detachments (PEDs), which are associated with sub-RPE fluid and RPE deformation. The fully automated, unsupervised 3-D method [15] integrates layer and region segmentation, and can segment the retina into 10 layers.

With the help of retinal layer segmentation, quantitative analysis of the layer morphology can be conducted. This is especially useful for retinal disease detection or progress analysis. Certain retinal diseases affect certain retinal layers. The change of retina layer may occur at an early stage of the disease, and become more evident with the progress of disease. Most existing layer analysis focus on simple indices such as layer thickness [16–20] or intensities [21, 22], but texture analysis can also provide important information. In the second part of this chapter, we describe a method to quantify the disruption of external limiting membrane (ELM) caused by DME from SD-OCT [23]. With the method, each A-scan is classified as disrupted or non-disrupted based on 6 texture features. In the third part of this chapter, we describe an extended method for automatic three-dimensional detection of photoreceptor ellipsoid zone (EZ) disruption caused by trauma [24]. 57 features are extracted, and feature selection and classification is performed to classify each voxel of the EZ as disrupted or non-disrupted. Both methods can effectively differentiate patients with normal ones.

10.2 Segmentation of Retinal Layers with Serous Pigment Epithelial Detachments

10.2.1 Background

Retinal pigment epithelium detachment (PED) is a symptom associated with many chorioretinal diseases, such as AMD, polypoidal choroidal vasculopathy, central serous chorioretinopathy, and uveitis [25, 26]. There are three type of PED, namely serous, fibrovascular, or drusenoid PED. Study shows that the existence of serous PED in AMD patients is related to the development of choroidal neovascularization (CNV), which is a main cause of visual acuity loss [26, 27]. In SD-OCT B-scans, the profile of serous PED is visualized as a dome-shaped elevation of the bright RPE layer (Fig. 10.1). Note that the layers around the PED may appear discontinuous, and thus need to be treated specifically during detection.

Following the definition of Iowa Reference Algorithm [14], we define 11 retinal surfaces (Fig. 10.2), numbered consecutively from top to bottom. The 10 retinal layers thus defined are nerve fiber layer (NFL), ganglion cell layer (GCL), inner plexiform layer (IPL), inner nuclear layer (INL), outer plexiform layer (OPL), outer nuclear layer and inner segment layer (ONL + ISL), connecting cilia (CL), outer

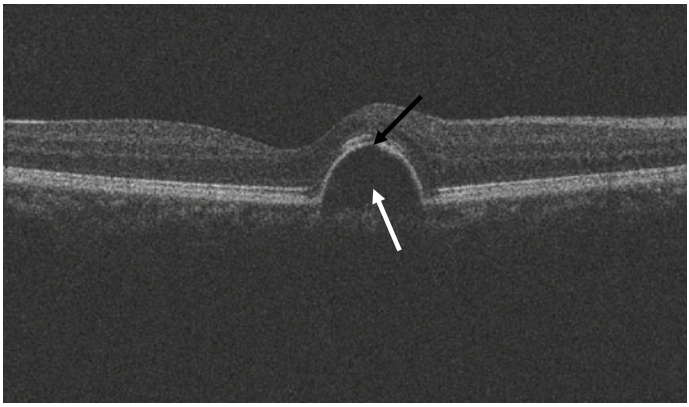

Fig. 10.1 An OCT B-scan visualizing the PED. The black arrow indicates the elevated RPE and the white arrow indicates the detached region

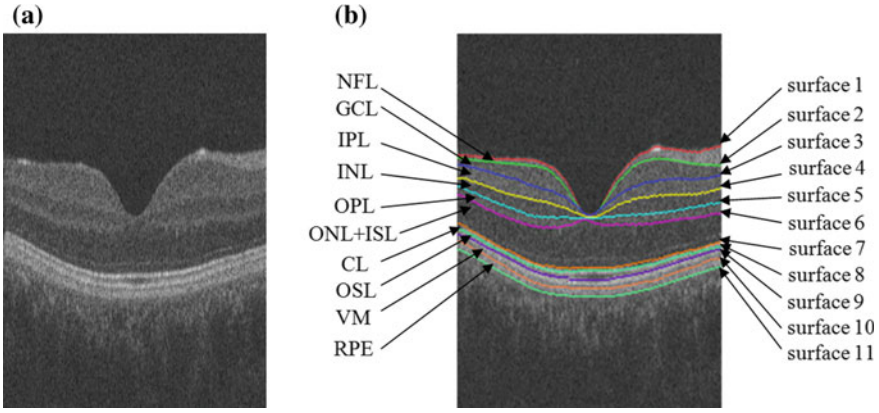

Fig. 10.2 OCT image of a normal eye and the 11 surfaces defining 10 retinal layers, visualized by the software OCT explorer contained in [14]. **a** B-scan image of OCT volume, obtained using Topcon 3D-OCT 1000. **b** 11 surfaces overlaid on the OCT image

segment layer (OSL), Verhoeff's membrane (VM), and retinal pigment epithelium (RPE). As the RPE floor (surface 11) is elevated, the original position of RPE floor is also estimated and defined as surface 12. We describe an automated 3-D method to segment these layers based on multi-resolution graph search algorithm [15]. In this work, layer segmentation and abnormal region segmentation are effectively integrated, where the position of layers and regions serve as constraints for each other.

10.2.2 Method

The automated method consists of pre-processing, layer segmentation and region segmentation. The pre-processing, includes fast bilateral filtering for denoising and B-scan alignment for motion distortion correction. During layer segmentation, Surfaces 1–6, 11, and 12 are detected by multi-resolution graph-search method [2, 28] with various smoothness constraints. Region segmentation is carried out based on the positions of surfaces 11 and 12. Their difference in height (z-coordinate) is used to form a PED footprint map. Finally, the other surfaces are detected in a flattened OCT volume and then corrected using the PED footprints.

In this section, we define the 3-D coordinates as follows. The x-axis is along the width of a B-scan, the y-axis represents the different B-scans, and the z-axis is in the vertical direction. Therefore a B-scan is in the x-z plane.

10.2.2.1 Multi-resolution Graph Search

The 3-D graph search algorithm was proposed by Li et al. [29] for optimal surface segmentation in volumetric images. In the method, the volumetric image is defined as a 3-D matrix $I(x, y, z)$ with size $X \times Y \times Z$, and a feasible surface is defined by a function $S(x, y)$ as the surface height, where $x \in \{0, \ldots, X-1\}$, $y \in \{0, \ldots, Y-1\}$ and $S(x, y) \in \{0, \ldots, Z-1\}$. Two parameters, Δ_x and Δ_y, control the smoothness of feasible surfaces, defined as the maximum height difference between neighboring surface points in x- and y- direction, respectively. A cost function $c(x, y, z)$ is assigned to each voxel, and the optimal surface is found to be the one with minimum overall cost.

To find the optimal surface, the volumetric image is first transformed into a node-weighted directed graph where each node corresponds to one and only one voxel. Arcs are constructed according to the spatial relationship between voxels as well as the smoothness constraints, and node weights are computed from the cost function. Searching for the optimal surface is transformed to seeking a minimum weight closed set in this graph. This graph is then further transformed to an arc-weighted digraph where the optimal solution can be found in polynomial time by computing a minimum s-t cut [30, 31].

In the following we focus on the cost functions, smoothness parameters, and constraints used in our method. From prior knowledge, in each B-scan, surfaces 1, 3, 5, 7, 9 and 10 are edges with dark-to-bright transition, while surfaces 2, 4, 6, 8 and 11 are with bright-to-dark transition. For most surfaces, the edge-based cost functions are used, calculated by 2-D Sobel operator in the z-direction. For different type of transitions, values of the cost function are inversed. An additional region-based cost is used for detection of surface 1, calculated as the summation of intensities of the voxels above but within certain distance to the current voxel. Both surface 1 and 7 are high-contrast dark-to-bright edges, but the region above surface 1 is darker than that above surface 7. Therefore, by adding the region-based cost to the edge-based

cost, surface 1 will have lower costs than surface 7 and can be correctly detected as the optimal surface.

Different smoothness constraints Δ_x and Δ_y are used for detection of different surfaces. Prior knowledge is used in determining the values, namely two facts: the image resolution and the shape of surface. When the resolution is high, small values are used to and ensure the smoothness of the surfaces preventing perturbation caused by noise. On the contrary, when the resolution is low and when quick change in surface height is possible, large values are needed to ensure the desired surface is in the feasible surface set. For example, in the dataset for test, the resolution in y-direction is low, and quick changes may occur in surface 1 around the fovea and in surface 11 above the PED region. Therefore, large Δ_y is set for these two surfaces.

In our method, two approaches are used to improve the performance of surface detection. First, the surfaces with higher contrasts are detected first, and the surfaces detected later are constrained in the subimage defined by previously detected ones. This approach both reduces the interference of different edges and cuts the searching space, resulting in improved accuracy and efficiency. Second, the multi-resolution approach [2] is used to improve the efficiency of surface detection. A three-level image pyramid is constructed by downsampling the image volume by a factor of 2 twice in z-direction. The graph search is first applied in the low resolution image to get a initial result. Then, a rectangular subimage with its height representing the refining range is constructed in the next higher resolution, so that the initial surface position lies in the center. The surface position is then refined using graph search in this subimage. For different surfaces, detection starts from different resolution levels according to prior knowledge of their contrast. Different smoothness parameters are set for different resolutions. The details for the detection orders, constraints, start levels, and smoothness parameters used for the test dataset are given in Table 10.1. Note that, with the aforementioned approaches, the global optimum property of the graph search method is compromised.

10.2.2.2 Pre-processing

(1) Denoising by bilateral filtering

As the dominant quality degrading factor in OCT scans, the presence of speckle noise may affect the accuracy and efficiency of image processing and analysis algorithms. Edge-preserving de-speckling methods are particularly important for segmentation tasks. In this study the bilateral filtering [32] is chosen. The bilateral filter is essentially a weighted average filter, which is an improved version of Gaussian filter. The weights decrease with both the difference in location (distance in the spatial domain S) and the difference in intensity (distance in the range domain R). The filtering result of bilateral filtering is given by

$$I_p^{bf} = \frac{1}{W_p^{bf}} \sum_{q \in S_p} G_{\sigma_s}(\|p - q\|) G_{\sigma_r}(I_p - I_q) I_q, \tag{10.1}$$

Table 10.1 Detailed constraints and parameter selection in surface detection. Note that $\Delta_x = 1$ for all surfaces and all levels

Order in detection	Surface #	Surface above	Surface below	Initial detection level	Δ_y in initial level
1	1	N/A	N/A	1	6
2	7′	1	N/A	1	6
3	2	1	7′	2	3
4	4	2	7′	2	3
5	6	4	7′	2	3
6	3	2	4	3	6
7	5	4	6	3	6
8	11	7′	N/A	1	6
9	12	7′	N/A	1	1
10	10	7	11	3	1
11	8	7	10	3	1
12	9	8	10	3	1

with

$$W_p^{bf} = \sum_{q \in S_p} G_{\sigma_s}(\|p - q\|) G_{\sigma_r}(I_p - I_q), \tag{10.2}$$

where p denotes the pixel being processed, q denotes the pixel in its neighborhood S_p, I_p and I_q represent their original intensities and I_p^{bf} is the intensity of p after filtering. G_{σ_s} and G_{σ_r} are two Gaussian weighting functions with standard deviations σ_s and σ_r, called the space and range parameters, respectively. To improve efficiency, a fast approximation technique reported in [33] is applied in this study. The filtering is applied to each B-scan of the OCT volume, with intensities linearly normalized to [0, 1]. The spatial and range parameters are selected empirically as $\sigma_s = 20$ and $\sigma_r = 0.05$.

(2) Alignment of B-scans

Eye movement during the in vivo OCT imaging is inevitable and causes distortion in the volumetric OCT data. This distortion is most notable as the vertical shift between adjacent B-scans. This misalignment ruins the continuity of the retinal layers in 3-D space, and thus leads to difficulties for 3-D segmentation. This artifact can be visualized in the y-z image, as in Fig. 10.3a, where each column corresponds to a B-scan. Image flattening, which is a common pre-processing step for motion artifact correction in OCT images [1, 2, 5], is not used in this study, because with the deformation of RPE, it is difficult to obtain a reference plane in the early stage.

Instead, we propose a fast B-scan alignment method, which works as follows. First, surface 1 is detected using the multi-resolution surface detection method. As surface 1 is the most prominent among all surfaces, it can be detected quite accurately

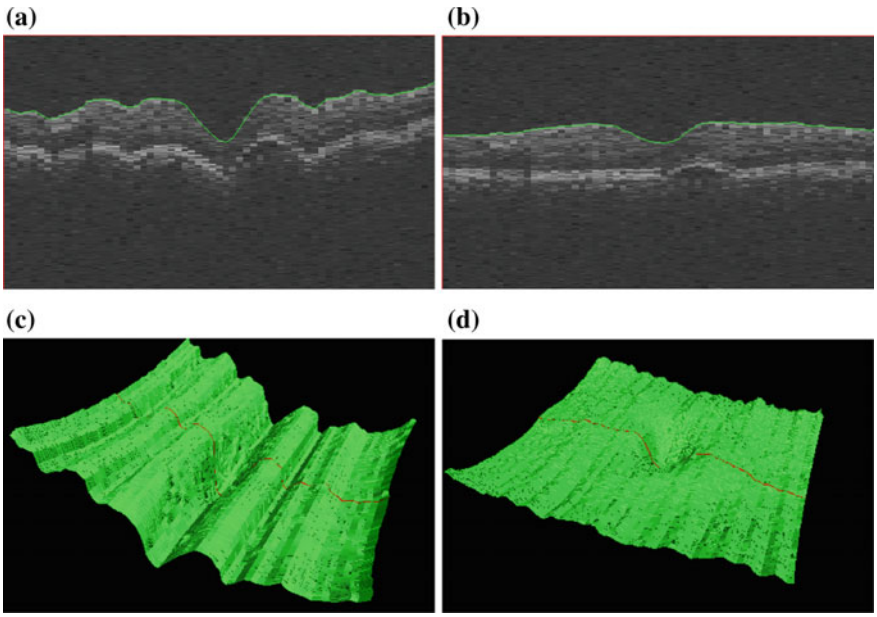

Fig. 10.3 B-scan alignment. **a**, **b** The *y*-*z* image before and after B-scan alignment with surface 1 overlaid. **c**, **d** Surface 1 before and after B-scan alignment. The red curves correspond to surface 1 in the *y*-*z* image as shown in (**a**) and (**b**)

even in the misaligned data. Then the position of the retina in each B-scan is estimated as the average z position of the peripheral surface 1, namely, the left most 20% and the right most 20% of surface 1. The center part is excluded from the averaging because it may include the fovea, which is naturally concave. Each B-scan is then shifted so that the average z positions of peripheral surface 1 become the same for all B-scans.

As shown in Fig. 10.3b, the alignment results in a smoothed appearance of the retina in the *y*-*z* image. Figure 10.3c, d further show the 3-D renderings of surface 1 before and after alignment. After alignment, the smoothness of the surfaces to be detected is improved, so that they can be found by graph search with smaller smoothness constraints, and therefore are less affected by image noise.

10.2.2.3 Detection of Surfaces 1–6

After pre-processing, surfaces 1–6 are detected in the denoised and aligned OCT volume. These surfaces correspond to the inner retina layers, which are not severely affected by PED's. Therefore the detection by multi-resolution graph search is similar to that for normal retinas. To achieve higher accuracy, surface 1 is detected again using the same method as in Sect. 10.2.2.2, but in the aligned data. Then, instead

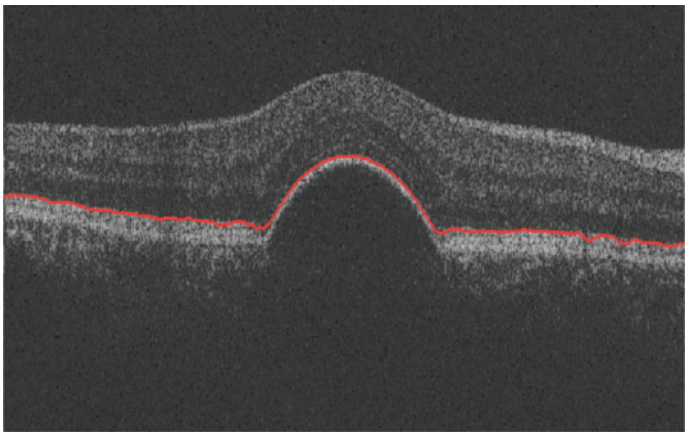

Fig. 10.4 Surface 7′ combining surfaces 7 and 10

of detecting surface 7 to constrain surfaces 2–6 as in normal retina [2], a surface combined by 7 and 10, defined as surface 7′ (see Fig. 10.4) is detected. Here surface 10 replaces surface 7 where it is not visible above the detachment region. The search for this surface is constrained in the subvolume below surface 1. After that, surfaces 2–6 are detected with the order of detection, the starting resolution level, the position and smoothness constraints for each surface shown in Table 10.1. In particular, large Δ_y are set for surfaces 1 and 7′ at resolution level 1 to allow quick position changes in adjacent B-scans caused by the fovea or the PED. To further remove the influence of noise, each surface is smoothed in the x direction using a moving average filter.

10.2.2.4 Detection of the Abnormal Region

In this section we describe the detection of PED regions, whose location is needed to correct the discontinuities in surfaces 7–9 around it. This is done by detecting the elevated RPE floor (surface 11) and estimating the original RPE floor (surface 12), and then finding their differences in height. Size and intensity are also considered to remove false positives.

(1) Detection of the elevated RPE floor and the estimated normal RPE floor

Surfaces 11 and 12 are detected in the subvolume below surface 7′. Surface 11 follows the bottom of the high reflectance and dome-shaped RPE, which changes abruptly in the PED region. Surface 12, as the original pre-disease position of the RPE floor, is a smooth surface by prior knowledge. These two surfaces overlap except where the PED occurs. Therefore, these two surfaces are detected with the same bright-to-dark edge-related cost function, except that surface 11 is detected by employing a large smoothness constraint and surface 12 is detected by employing a small smoothness constraint. Even if surface 12 is invisible under the PED, it is

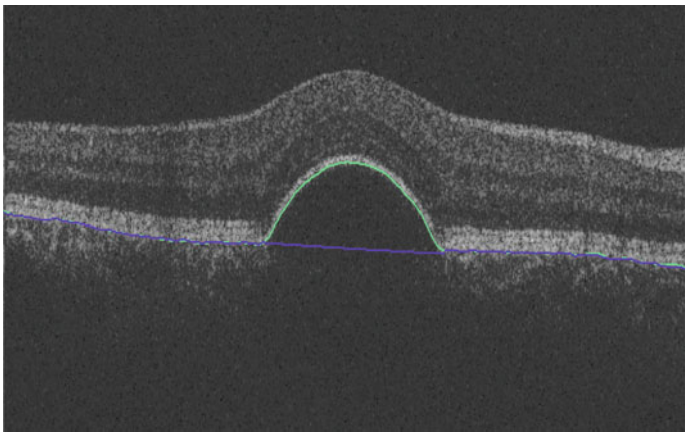

Fig. 10.5 Detected surfaces 11 and 12

forced to follow the smooth bottom of the retina by the small smoothness constraint. However, due to the loose constraint, surface 11 may be distracted by the choroid, leading to inaccurate results outside the PED region. To handle this problem, we correct surface 11 by replacing it with surface 12 wherever it goes below surface 12. Figure 10.5 shows the final detection results of surfaces 11 and 12.

(2) PED footprints detection

In this step, A-scans (image columns) associated with PED's are detected and indicated in the x-y plane as a binary footprint image. This is done by hysteresis thresholding based on the distances between surfaces 11 and 12. Specifically, two thresholds d_1 and $d_2 (d_2 < d_1)$ are applied. First, the set of (x, y) coordinates are obtained and grouped into connected components, where surface 11 is more than d_1 pixels higher than surface 12. For all connected components, those with size less than A are excluded as false positives. Next, to make the boundaries more accurate, these connected components are extended to include connected points where surface 11 is more than d_2 pixels higher than surface 12. Subsequently, the 3-D PED volumes are detected as voxels between surfaces 11 and 12 within each footprint. Finally, the mean intensities of all PED volumes are calculated and those with normalized mean intensity larger than T are rejected as false positives, considering the fact that serous PED's usually appear as dark regions, and the false positives usually include the bright RPE region. The initial and final footprint detection results of one OCT volume are shown in Fig. 10.6a, b, respectively. The details of parameter selection are described in Sect. 10.2.3.1.

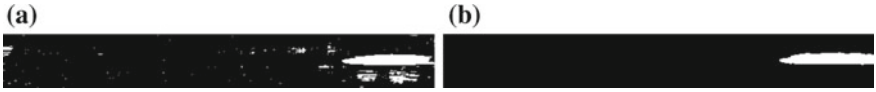

Fig. 10.6 PED footprint detection results. **a** Rough detection result from difference between surface 11 and 12. **b** PED footprint after edge refinement and rejection of false positives

10.2.2.5 Detection of Surfaces 7–10

For normal eyes, surfaces 7–10 usually appears as relatively flat and almost parallel surfaces, but they are often blurred and discontinuous near the PED volume. In this step we try to restore the normal morphology of these surfaces by flattening the OCT volume so that the invisible portions of surfaces 7–9 can be estimated using smoothing constraints.

Using surface 11 detected in Sect. 10.2.2.4 as the reference surface, flattening is done by shifting the A-scans up or down so that surface 11 becomes flat. Then surface 7 is obtained in this image by correcting surface $7'$ (detected in Sect. 10.2.2.3) inside the PED footprint by second-order polynomial curve interpolation. Afterwards, surfaces 8–10 are detected using small smoothness constraints between surfaces 7 and 11. Surfaces 8 and 9, which may appear discontinuous, are also corrected by interpolation within the PED footprint. In the end, surfaces 7–10 are converted back to their positions in the original OCT volume. See Fig. 10.7 for results of image flattening and detection of surfaces 7–10.

10.2.3 Results

10.2.3.1 Experimental Settings and Parameter Selection

The test data includes the PED dataset, and the normal dataset, comprised of macula-centered SD-OCT scans of 20 eyes from 20 subjects diagnosed with serous PED's and 20 eyes from 20 normal subjects (the controls), respectively. All the OCT images were acquired using Topcon 3D-OCT 1000 (Topcon Corporation, Tokyo, Japan). The OCT volumes comprised of $512 \times 64 \times 480$ ($X \times Y \times Z$) voxels with voxel size of $11.72 \times 93.75 \times 3.50$ μm^3, corresponding to a $6 \times 6 \times 1.68$ mm^3 volume. This study was approved by the Intuitional review board of Joint Shantou International Eye Center and adhered to the tenets of the Declaration of Helsinki. Because of its retrospective nature, informed consent was not required from subjects.

The ground truth for evaluating the layer segmentation results comes from the average of two independent manual tracings in the B-scan images by two retinal specialists. For each 3-D OCT volume, 10 out of the 64 B-scans, uniformly distributed in the volumetric data, were selected for manual tracing. Among the 200 manually traced B-scans from the PED dataset, 50 B-scans were manual labeled with

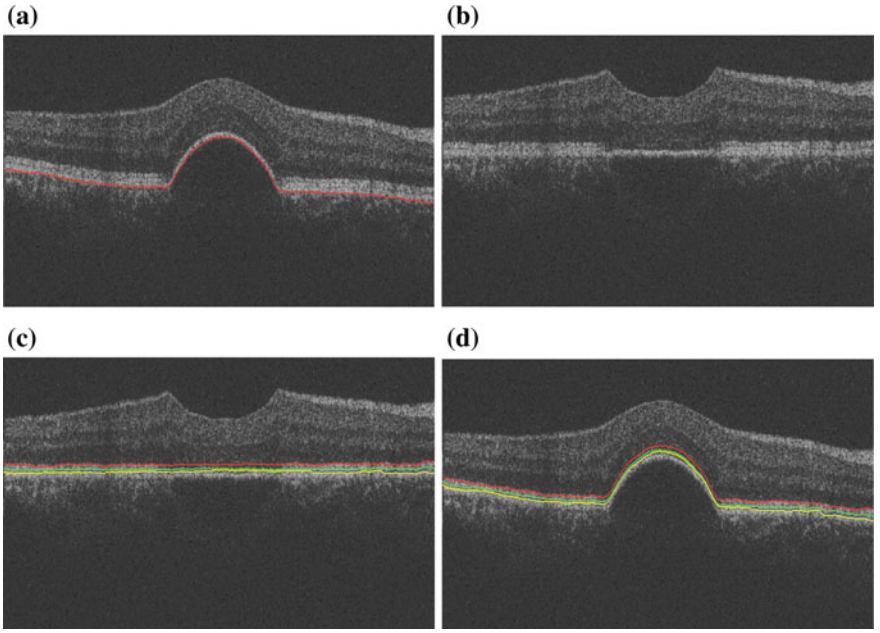

Fig. 10.7 Detection of surfaces 7–10 on a flattened image. **a** Original B-scan with reference surface overlaid, **b** flattened B-scan, **c** surfaces 7–10 overlaid on flattened image, surface 7 is shown in red, surface 8 in green, surface 9 in blue and surface 10 in yellow. Surface 9 may not be visible because it overlaps with surface 10 in many places, **d** surfaces 7–10 mapped back to the original image

PED's. Segmentation of surfaces 3, 8 and 9 were not evaluated because they were not always discernible to human eyes on the test data. Surface 12 was also excluded as it was only a virtual structure defined for auxiliary purpose. The unsigned border positioning error is used as the main performance index, which is defined as the absolute Euclidean distance in the z-axis between automatic segmentation results and the ground truth. The unsigned border positioning errors were compared with the unsigned border positioning differences between the two manual tracings. The results of the proposed method were also compared with those obtained by the general Iowa Reference Algorithm [14] not specifically designed to handle PED's. Paired t-tests were used to compare the segmentation errors and a p-value less than 0.05 was considered statistically significant.

For surface detection, the smoothness constraints were selected according to the rules described in Sect. 10.2.2.1 and are listed in Table 10.1. For the test data, because the resolution was high in the x direction, Δ_x was set to 1 for all surfaces. The resolution in y-direction was 8 times lower, and therefore some layers might have abrupt changes in this direction. In the test we used Δ_y for different surfaces in the initial detection level. As surfaces 1, $7'$ and 11 were the ones affected most by the shape of the fovea or the PED's, large Δ_y was required, which was set as $\Delta_y = 6$ at resolution level 1. As tested, larger values were also acceptable since these surfaces

had strong contrast and thus could endure image noise. Surfaces 2–6 were slightly affected by the fovea or the PED and had weaker contrast. Therefore medium Δ_y was set for these surfaces, with $\Delta_y = 3$ at resolution level 2, and $\Delta_y = 6$ at resolution level 3. Surface 12 and surfaces 8–10 on the flattened image were required to be smooth surfaces. Therefore small Δ_y was needed, set as $\Delta_y = 1$. For the refining step in multi-resolution surface detection, assuming the initial detection was accurate enough, the surface position in higher resolution would be close to the initial one (the center line). Therefore, small smoothness constraints $(\Delta_x = \Delta_y = 1)$ were applied.

For PED footprint detection, the distance thresholds and the area threshold were selected empirically as $d_1 = 3$, $d_2 = 1$, and $A = 30$ in pixels. However, as tested, the region segmentation performance was not sensitive to perturbations of these parameters. Empirically tested, the suggested ranges of parameters were: $d_1 = 3$–7, $d_2 = 1$–2 and $A = 30$–70. Small values were preferred so that PED regions with minor elevation of RPE and small sizes would not be discarded. Most false positives that were not detected by the size criteria could still be ruled out by the intensity criterion that follows. The intensity threshold T was set as the adaptive Otsu threshold [34] considering the fact that the OCT images have a double-peaked histogram.

10.2.3.2 Layer Segmentation Results for PED Dataset

Examples of layer segmentation results are shown in Fig. 10.8 in both 2-D and 3-D. Table 10.2 shows the mean and standard deviation of unsigned border positioning errors for each surface computed on 200 B-scans from the PED dataset, compared with the inter-observer variability and the errors resulting from employing the Iowa Reference Algorithm [14]. The p-values are shown in Table 10.3, with bold fonts indicating that the proposed method has statistically significantly better performance. Compared with the difference between observers, the errors of surfaces 1 and 11 are significantly smaller, the errors of surfaces 4 and 10 are significantly bigger, and the errors of surfaces 2, 5, 6 and 7 are statistically indistinguishable. The overall mean unsigned error is 7.87 ± 3.36 μm, which is statistically indistinguishable from the mean unsigned difference between observers (7.81 ± 2.56 μm). Compared with [14], the errors of surfaces 2 and 11 are statistically significantly smaller, the errors of the other surfaces are statistically indistinguishable, and the overall mean unsigned error is statistically significantly smaller.

The results in Table 10.2 only show minor improvement over the method designed for normal retina in [14] because the PED is a localized structure. Only in a small proportion of B-scans the layers exhibit dramatic morphological changes, and in the remaining B-scans the retina layers appears normal, so that the segmentation method for normal retinas performed well too. To better evaluate the layer segmentation performance near the PED, Table 10.4 shows the mean and standard deviation of unsigned border positioning errors calculated on the 50 B-scans labeled with PED's, compared with both inter-observer variability and the errors resulting from employing the Iowa Reference Algorithm [14]. The p-values are shown in Table 10.5, with bold fonts indicating that the proposed method has statistically significantly bet-

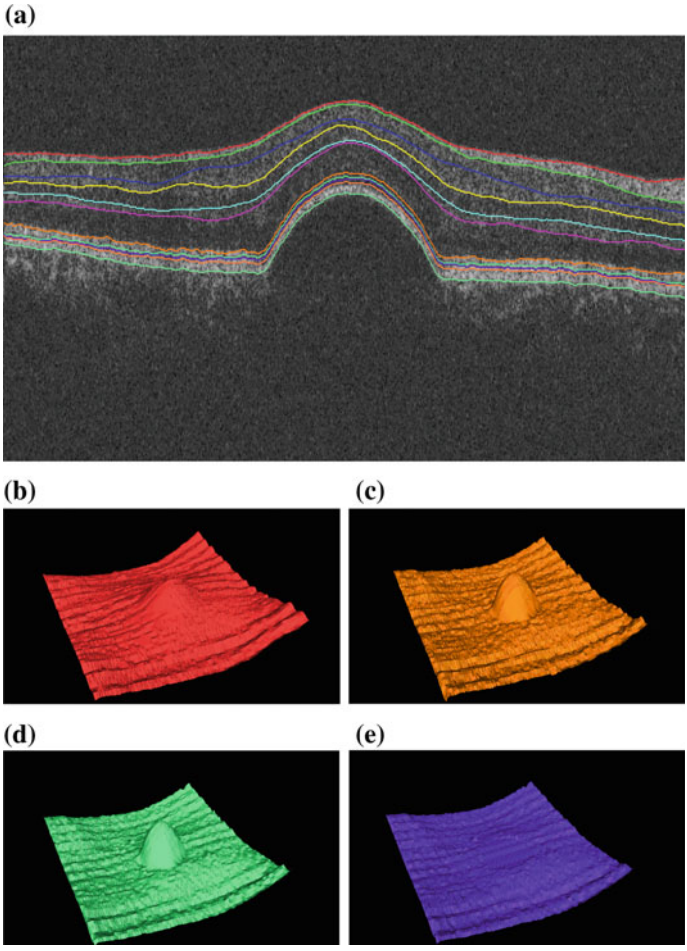

Fig. 10.8 Layer segmentation results. **a** 12 surfaces overlaid on B-scan. **b–e** 3-D visualization of surfaces 1, 7, 11 and 12

ter performance. The error of surface 1 is significantly smaller than the unsigned difference between observers. Errors of the other surfaces and the overall error are statistically indistinguishable from the unsigned difference between observers. Compared with [14], except for surface 1, errors of all the other surfaces are significantly smaller, and the overall mean unsigned error is significantly smaller.

10.2.3.3 Layer Segmentation Results for the Normal Dataset

Though the proposed method is designed for retinas with serous PED's, the method can also be applied for normal retina segmentation. For normal retinas, surfaces 11

Table 10.2 Mean unsigned positioning errors for all labeled B-scans of PED data between our segmentation results and reference standards, compared with mean unsigned positioning differences between manual tracings from two observers and mean unsigned positioning errors of the Iowa reference algorithm [14] (Mean ± SD, in μm, 3.5 μm = 1 pixel)

Surface #	Algo. versus Ref.	Obs. 1 versus Obs. 2	[14] versus Ref.
1	3.91 ± 0.65	5.28 ± 0.79	4.07 ± 0.67
2	7.79 ± 2.47	7.22 ± 1.33	9.82 ± 2.55
4	10.30 ± 2.57	8.09 ± 2.08	12.78 ± 7.36
5	9.14 ± 3.83	9.48 ± 4.59	12.36 ± 8.81
6	9.14 ± 2.87	8.66 ± 1.61	11.42 ± 8.25
7	7.19 ± 3.57	7.18 ± 1.73	8.36 ± 4.26
10	8.99 ± 3.42	7.37 ± 2.39	10.16 ± 5.87
11	6.53 ± 2.28	9.09 ± 1.36	9.49 ± 5.38
Overall	7.87 ± 3.38	7.80 ± 2.54	9.81 ± 6.42

Table 10.3 *p*-values of the proposed algorithm versus reference standards and the Iowa reference algorithm [14] for all labeled B-scans of PED data

Surface #	*p* value Algo. versus Ref.	*p* value Algo. versus [14]
1	**≪0.001**	0.2888
2	0.2951	**≪0.001**
4	0.0009	0.0846
5	0.6493	0.0742
6	0.2914	0.1574
7	0.9896	0.2048
10	0.0398	0.3036
11	**≪0.001**	**0.0030**
Overall	0.7357	**≪0.001**

Here numbers in bold indicate statistically significantly better performance

Table 10.4 Mean unsigned positioning errors for B-scans with PED between our segmentation results and reference standards, compared with mean unsigned positioning differences between manual tracings from two observers and mean unsigned positioning errors of the Iowa reference algorithm [14] (Mean ± SD, in μm, 3.5 μm = 1 pixel)

Surface #	Algo. versus Ref.	Obs. 1 versus Obs. 2	[14] versus Ref
1	4.21 ± 0.89	5.52 ± 1.53	5.17 ± 1.56
2	8.65 ± 3.76	7.07 ± 1.62	10.90 ± 3.36
4	11.48 ± 3.09	8.90 ± 3.02	15.70 ± 6.90
5	11.81 ± 4.30	11.87 ± 6.20	16.08 ± 8.45
6	13.00 ± 4.54	10.25 ± 2.79	16.68 ± 9.55
7	8.70 ± 2.99	10.54 ± 3.66	14.17 ± 5.55
10	9.70 ± 2.95	8.82 ± 3.99	17.99 ± 7.88
11	8.59 ± 6.52	9.41 ± 2.41	18.55 ± 7.60
Overall	9.52 ± 4.61	9.05 ± 3.86	14.41 ± 7.87

Table 10.5 p-values of the proposed algorithm versus reference standards and the Iowa reference algorithm [14] for B-scans with PED

Surface #	p value Algo. versus Ref.	p value Algo.versus [14]
1	**$\ll$0.001**	0.4765
2	0.0733	**$\ll$0.001**
4	0.0062	**$\ll$0.001**
5	0.9503	**0.0430**
6	0.0056	**0.0132**
7	0.0981	**0.0140**
10	0.2834	**$\ll$0.001**
11	0.5595	**$\ll$0.001**
Overall	0.1806	**$\ll$0.001**

Here numbers in bold indicate statistically significantly better performance

and 12 represent the same surface and their detection results will mostly overlap. Obtained with a large smoothness constraint, surface 11 is likely to be less smooth than surface 12 due to the impact of noise, but the regions between surfaces 11 and 12 will be excluded as false positives in PED detection. Then flattening with respect to surface 11 is no more than a step which further removes the eye movement artifacts, as did in [1, 2, 5]. Additionally, correction of surfaces 7–9 is not needed and this step will be automatically skipped when no PED region is detected.

To test the performance in normal data, the method was applied to OCT images from a control group of 20 normal subjects. Table 10.6 shows the mean and standard deviation of unsigned border positioning errors for each surface, compared with inter-observer variability and the errors resulting from employing the Iowa Reference Algorithm [14]. The p-values are shown in Table 10.7, with bold fonts indicating that the proposed method has statistically significantly better performance. The overall mean unsigned error of the proposed algorithm is significantly smaller than the mean unsigned difference between two observers. Compared with [14], the overall error is statistically indistinguishable.

In summary, for the tested PED dataset, the overall layer segmentation errors are comparable to the inter-observer variability, and statistically significantly smaller than those of the Iowa Reference Algorithm [14]. The proposed algorithm outperforms the algorithm in [14] especially in segmenting B-scans with abnormality. The proposed algorithm also works well for normal retinas. For the tested normal dataset, the overall layer segmentation errors are statistically smaller than the inter-observer difference, and statistically indistinguishable from those of the Iowa Reference Algorithm [14]. Although the method is not the most efficient for normal retina segmentation, it allows segmentation of the retinal layers in both normal and diseased retinal images, thus bypassing a need for disease-specific diagnosis prior to automatic processing. The proposed algorithm is an accurate and efficient replacement of manual segmentation, and can be utilized to achieve quantitative analysis of individual reti-

Table 10.6 Mean unsigned positioning errors for normal data between our segmentation results and reference standards, compared with mean unsigned positioning differences between manual tracings from two observers and mean unsigned positioning errors of the Iowa reference algorithm [14] (Mean ± SD, in μm, 3.5 μm = 1 pixel)

Surface #	Algo. versus Ref.	Obs. 1 versus Obs. 2	[14] versus Ref
1	2.92 ± 0.23	4.33 ± 0.38	3.30 ± 0.27
2	7.29 ± 1.04	5.34 ± 0.57	7.43 ± 0.70
4	8.43 ± 1.17	7.78 ± 1.11	9.02 ± 1.09
5	4.62 ± 0.68	7.43 ± 1.32	5.81 ± 0.89
6	6.08 ± 1.25	7.07 ± 0.90	5.67 ± 0.84
7	2.53 ± 0.25	4.06 ± 0.77	3.97 ± 0.42
10	7.21 ± 3.57	7.75 ± 3.60	4.88 ± 1.96
11	5.39 ± 0.89	7.66 ± 1.59	4.79 ± 0.81
Overall	5.56 ± 2.47	9.05 ± 3.86	5.61 ± 2.00

Table 10.7 *p*-values of the proposed algorithm versus reference standards and the Iowa reference algorithm [14] for normal data

Surface #	*p* value Algo. versus Ref.	*p* value Algo. versus [14]
1	**≪0.001**	**≪0.001**
2	≪0.001	0.5354
4	0.0589	**0.0054**
5	**≪0.001**	**≪0.001**
6	**≪0.001**	0.0274
7	**≪0.001**	**≪0.001**
10	0.4430	0.0049
11	**≪0.001**	≪0.001
Overall	**≪0.001**	0.7067

Here numbers in bold indicate statistically significantly better performance

nal layers for both eyes with serous PED's and normal eyes. The method can be extended to other pathological cases where RPE deformation occurs.

10.3 Quantification of External Limiting Membrane Disruption Caused by Diabetic Macular Edema

10.3.1 Background

Diabetic macular edema (DME) is the primary cause of vision impairment in patients suffering from diabetes [35, 36]. Typically, abnormal accumulation of advanced glycation end products leads to the disruption of the blood–retinal barrier, causing inter-

stitial fluid accumulation [37], swelling and thickening of the macular layers, and finally damage to central vision [38, 39]. The external limiting membrane (ELM) is a structure that separates the inner segments from the outer nuclear layer, where the Müller cells are joined to the photoreceptor cells. The ELM serves as a skeleton to keep the photoreceptors aligned [40]. The ELM has been hypothesized to maintain a protein balance between the photoreceptor layer and the outer nuclear layer [41]. Recently, several studies have shown that ELM interruptions visible on spectral-domain optical coherence tomography (SD-OCT) are associated with lower visual acuity outcome in patients with clinically significant diabetic macular edema (CSME) [42–45]. Possibly this is because the integrity of the ELM has a critical role in restoration of the photoreceptor microstructures and alignment [46–48]. Earlier reported approaches [49–51] relied on manual tracing of the corresponding surface or on detecting ELM on 2-D B-scans. However, such studies rely on manual interpretation of the state of the ELM, and high intra- and inter-observer variabilities are likely. Automated 3-D analysis of the ELM is of high interest because of its potential to elucidate structural abnormalities with minimal variability and possibly predict visual outcomes in diabetic macular edema (DME).

In this part we describe a novel and fully automated method to quantify the integrity of the ELM in patients with CSME and in normal subjects based on SD-OCT volumes [23]. This pilot study showing differences between 16 normal controls and 16 CSME patients demonstrates the practical feasibility of the presented methodology and provide preliminary comparisons between these two groups of subjects.

10.3.2 Method

10.3.2.1 ELM Layer Segmentation

The Iowa reference algorithm based on graph search [1, 2, 14, 28, 29] is first applied to segment the OCT volume, yielding 11 surfaces (Fig. 10.9). Then, the subvolume between surfaces 6 and 11 (region between OPL and the ONL), which contains the ELM, was flattened based on the segmented RPE floor (surface 11). Subsequently, the graph search surface-detection method is applied again to segment the ELM layer in this subvolume.

10.3.2.2 ELM Disruption Area Detection

In this section, each A-scan is classified as disrupted or nondisrupted based on the texture and morphology in the vicinity of the ELM surface. The original OCT images are first enhanced by standard normalization. Six texture features are then extracted for classification, including intensity, gradient, local variance, local intensity orientation, local coherence, and retinal thickness. The intensity represents the voxel's gray-level intensity; the gradient represents the intensity difference between the voxel

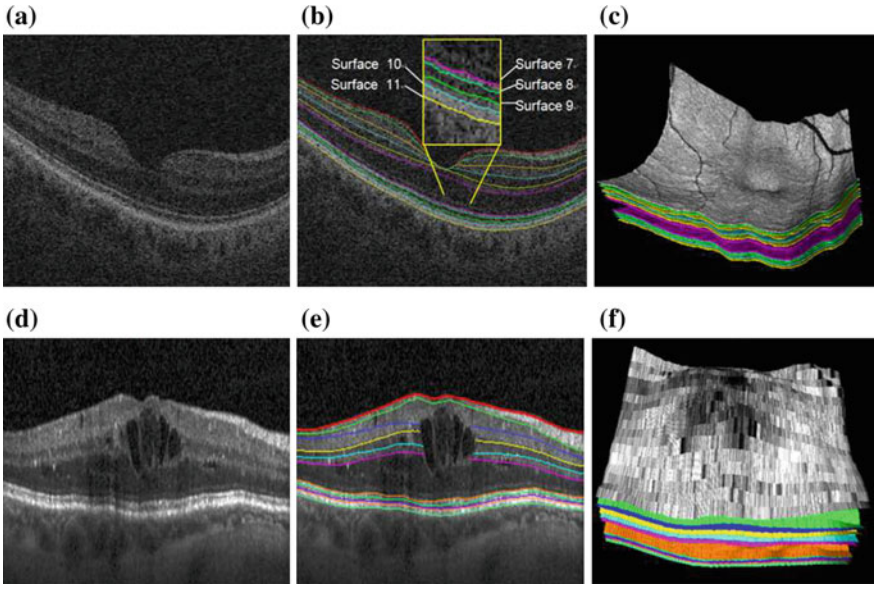

Fig. 10.9 SD-OCT layer segmentation on a normal and a CSME subject. **a** Central slice from the original raw SD-OCT from a normal subject. **b** Eleven-surface segmentation results for (**a**). **c** 3-D rendering of the 11-surface segmentation result for (**b**). **d** Central slice from the original raw SD-OCT from a CSME subject. **e** Eleven-surface segmentation results for (**d**). **f** 3-D rendering of the 11-surface segmentation result for (**e**)

and its neighbor; the local variance is calculated as the variance of the intensity at a 3×3 window centered around the voxel; the local intensity orientation measures the intensity distribution shape at a local line perpendicular to the ELM layer orientation centered around the voxel, with length of 7 voxels, which should be similar to Gaussian shape; the local coherence measures the coherence of the intensity at a 3×3 window centered around the voxel; and the thickness is the distance from the top of RNFL to the bottom of RPE. A disruption probability function based on these six features is defined as follows:

$$\begin{aligned} P(x) = {} & \alpha_1 P_{\text{intensity}}(x) + \alpha_2 P_{\text{gradient}}(x) + \alpha_3 P_{\text{variance}}(x) \\ & + \alpha_4 P_{\text{orientation}}(x) + \alpha_5 P_{\text{coherence}}(x) + \alpha_6 P_{\text{thickness}}(x) \end{aligned} \tag{10.3}$$

$$P_{\text{intensity}}(x) = \exp\left(-\frac{I_x}{\mu_I - \sigma_I}\right) \tag{10.4}$$

$$P_{\text{gradient}}(x) = \exp\left(-\frac{\text{gradient}}{\mu_{\text{gradient}} - \sigma_{\text{gradient}}}\right) \tag{10.5}$$

$$P_{\text{variance}}(x) = \exp\left(-\frac{\text{variance}_x}{\mu_{\text{variance}} - \sigma_{\text{variance}}}\right) \tag{10.6}$$

$$P_{\text{orientation}}(x) = \begin{cases} 1 \text{ if center voxel}'\text{s intensity} > \text{two end voxels}' \text{ intensity} \\ 0 \text{ otherwise} \end{cases} \tag{10.7}$$

$$P_{\text{coherence}}(x) = \frac{\sum_{y \in \text{region}_x} \delta(I_y, \mu_I - \sigma_I)}{N} \quad \text{where} \quad \delta(a,b) = \begin{cases} 1 \text{ if } a < b \\ 0 \text{ otherwise} \end{cases} \tag{10.8}$$

$$P_{\text{thickness}}(x) = \exp\left(-\frac{\text{thickness}_{\max} - \text{thickness}_x}{\sigma_T}\right) \tag{10.9}$$

In the above equations, α_1 through α_6 are the weights, which sum up to 1; μ_I and $\sigma_I$represent the mean and standard deviation of the intensity calculated from all voxels of the ELM layer; μ_{gradient} and σ_{gradient} represent the mean and standard deviation of the gradient calculated from all voxels of the ELM layer; μ_{variance} and σ_{variance} represent the mean and standard deviation of the variance calculated from all voxels of the ELM layer; $region_x$ represents the local neighborhood of x (3×3 window); $\sum_{y \in \text{region}_x} \delta(I_y, \mu_I - \sigma_I)$ computes the number of voxels with intensity below the threshold $\mu_I - \sigma_I$; N is the total number of voxels in the local region ($N = 9$); $thickness_x$ represents the total retinal thickness (from top of RNFL to bottom of RPE) at location x; $thickness_{\max}$ represents the maximum of retinal thickness for the entire retina; and σ_T represents the standard deviation of the retinal thickness at all locations. Then, the disruption is detected as follows:

$$\text{Disruption}(x) = \begin{cases} 0 \text{ if } P(x) < T \\ 1 \text{ otherwise} \end{cases} \tag{10.10}$$

where T is a predefined threshold value.

The vessel silhouettes cause the ELM layer to have low intensity under the vessels (Fig. 10.10), causing voxels in these regions to be initially classified as disrupted. To remove these false detections, a vessel detector [52] is applied to identify the vessel silhouettes in the en face projection image. The resulting vessel segmentation is used as masks to remove false positive detections.

10.3.3 Results

Sixteen subjects diagnosed with CSME underwent macula-centered SD-OCT imaging (Spectralis; $512 \times 19 \times 496$ voxels; Heidelberg Engineering, Vista, CA). Sixteen normal subjects also underwent macula-centered SD-OCT imaging (Cirrus; $200 \times 200 \times 1024$ voxels, Carl Zeiss Meditec, Inc., Dublin, CA). This study were approved by the Institutional Review Board of the University of Iowa and adhered to the tenets of the Declaration of Helsinki; written informed consent was obtained from all participants.

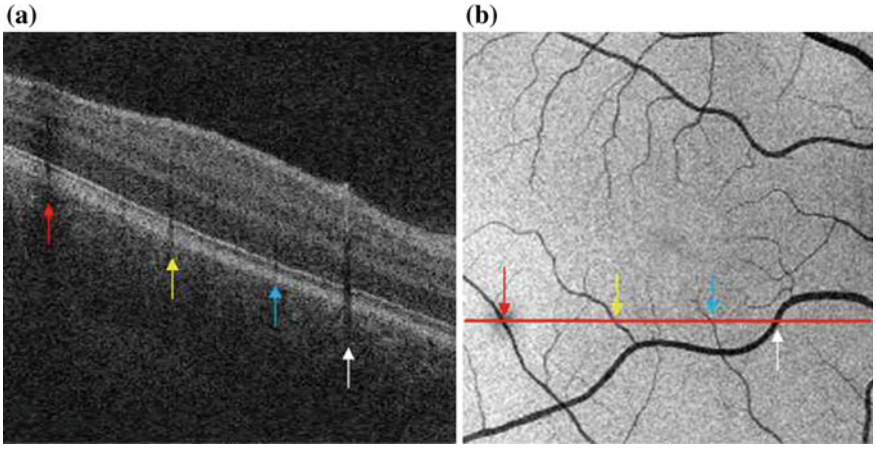

Fig. 10.10 Vessel silhouettes appear as low-intensity regions disrupting the appearance of the ELM layer. **a** The arrows indicate vessel silhouettes formed by the vasculature of the retina. **b** The red line indicates the location of the slice shown in (**a**) on the en face projection image of the retina. Note the correspondence of the locations where vessels cross the slice and the location of the vessel silhouettes in the slice itself depicted by colored arrows

Because the resolution of normal data in the y direction is much higher than the CSME data, a normal down-sampled dataset was obtained by down-sampling the OCT volumes of normal subjects in the y direction (direction of B-scan lines) to produce the same resolution (240 μm) as the CSME data. The detected disruption region volume and the voxel percentage were calculated for the normal, normal down-sampled, and CSME subjects. Paired t-tests were used to compare the ELM disruption region volume between the two groups of subjects. Three different threshold values ($T = 0.4$, 0.5, and 0.6) were applied to compute the detection results, with the aim of showing the robustness of the proposed method.

Figure 10.11 shows the ELM layer segmentation, disruption area detection results, and surface views of the disruption areas on one normal and one CSME subject. Figure 10.12a shows the detected disruption region volume for normal, normal down-sampled, and CSME subjects at three different threshold values, 0.6, 0.5, and 0.4. For $T = 0.5$, the mean and 95% confidence interval of the detected disruption volumes for normal, normal down-sampled, and CSME subjects were $mean_{normal} = 0.00087\ \text{mm}^3$ and $CI_{normal} = (0.00074, 0.00100)$, $mean_{ds} = 0.00076\,\text{mm}^3$, $CI_{ds} = (0.00063, 0.00089)$, $mean_{CSME} = 0.00461\,\text{mm}^3$, and $CI_{ds} = (0.00347, 0.00576)$, respectively. Comparing the CSME group with both full-resolution normal group and down-sampled normal group, the paired t-test resulted both in $p < 0.001$, which demonstrated strong statistical significance of the volume differences between the ELM disruption volumes detected for CSME subjects and normal controls. Figure 10.12b shows the disruption voxel percentages in the ELM layer for normal, normal down-sampled, and CSME subjects at three different threshold values, 0.6, 0.5, and 0.4. Figure 10.13 shows more examples of

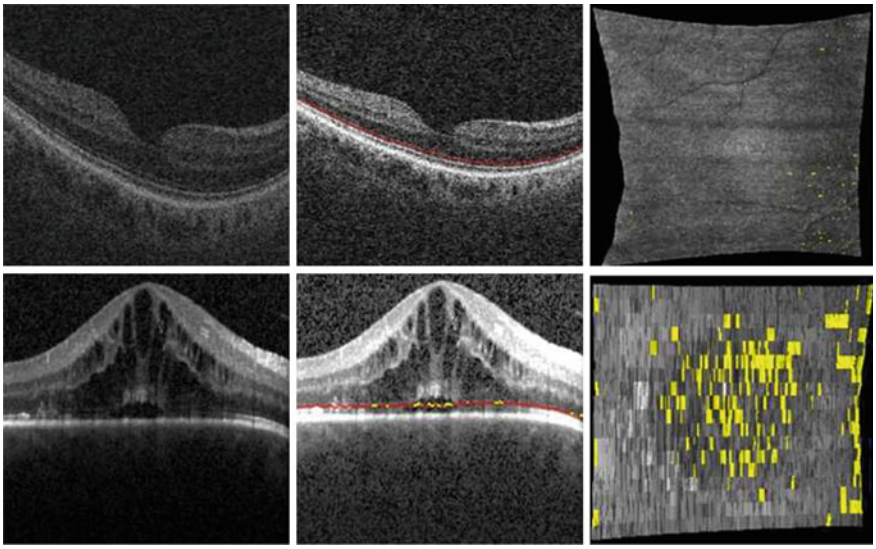

Fig. 10.11 The illustrations for the ELM layer disruption detection. The first column shows the original OCT images; the second column shows the ELM layer segmentation results (indicated by red line) and disruption area detection results (indicated by yellow) on contrast-enhanced OCT images; and the third column shows the surface views of disruption area (indicated by yellow). The top and bottom rows show the results for one normal and one CSME subject, respectively

the ELM disrupted area detection results on the CSME subjects, the normal controls and normal down-sampled images ($T = 0.5$).

In summary, an automated method to quantify the 3-D integrity of the ELM in patients with CSME and in normal subjects and its evaluation were introduced in this section. In this method, texture and morphologic features are used for the classification of the ELM disruption area. Simple thresholding is applied to determine the disrupted voxels. The results of this preliminary study show that in patients with CSME, large areas of disrupted ELM exist, while in normal subjects the ELM is mostly continuous, only with small pinpoint areas detected, which are probably false positives.

Although the detected disruption volume and its percentages over the whole volume are dependent on the threshold value T, as Fig. 10.12 demonstrate, the differences between disruption region sizes obtained from the normal and CSME subjects are very consistent regardless of the value of T. The experimental results also show that the disruption detection results are consistent for the normal and normal down-sampled subjects, regardless of the value of T. Therefore the method is robust for discerning CSME and normal subjects with respect to values of T.

There are several shortcomings in this study. First, the number of subjects was too small to allow determination of the performance of the proposed method. Second, there is no ground truth for the ELM disruption area, so the accuracy analysis cannot be performed. Third, the classification using thresholding is quite crude. Advanced

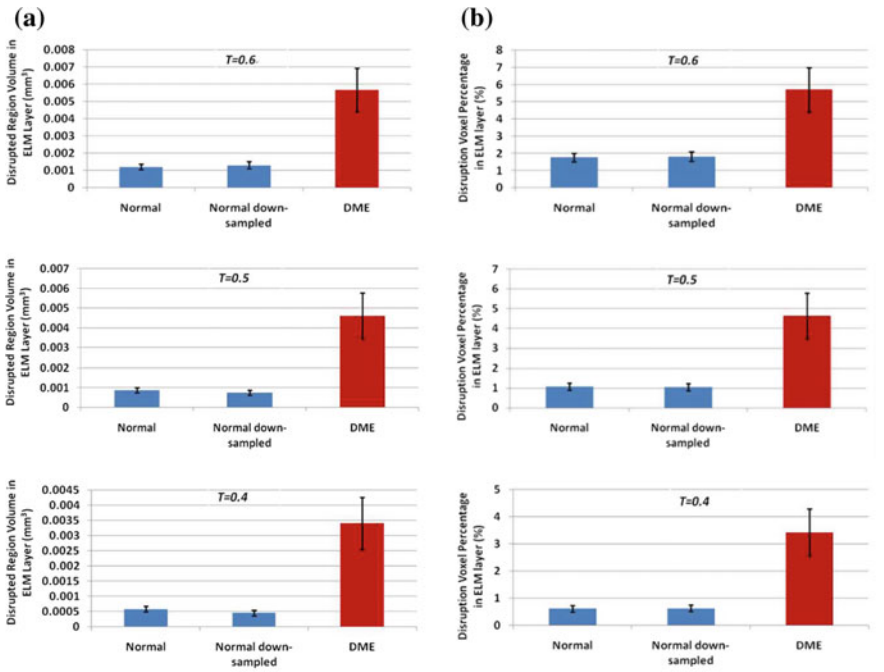

Fig. 10.12 ELM disruption analysis. **a** Detected disruption volume comparison for normal, normal down-sampled, and CSME subjects with $T = 0.6$; $T = 0.5$; $T = 0.4$. **b** Disruption voxel percentage in ELM layer for normal, normal down-sampled, and CSME subjects with $T = 0.6$; $T = 0.5$; $T = 0.4$. The plot shows the average and 95% confidence interval

classifiers exploiting more features can be employed for this purpose. Finally, the study mainly focused on the development of an automatic quantification method, but did not address the clinically more important question whether the ELM quantitative measures developed here correlate with visual acuity and visual outcome.

10.4 Detection of Photoreceptor Ellipsoid Zone Disruption Caused by Trauma

10.4.1 Background

Ocular trauma is a significant cause of visual impairment and blindness [53]. Commotio retinae is characterized by a grey-white discoloration or opacification of the retina after closed globe trauma, when the impact at the level of the ocular surface is transferred to the retina in the posterior segment [54]. Histopathologic studies of human and animal eyes have found that damage of the photoreceptor is a pathogene-

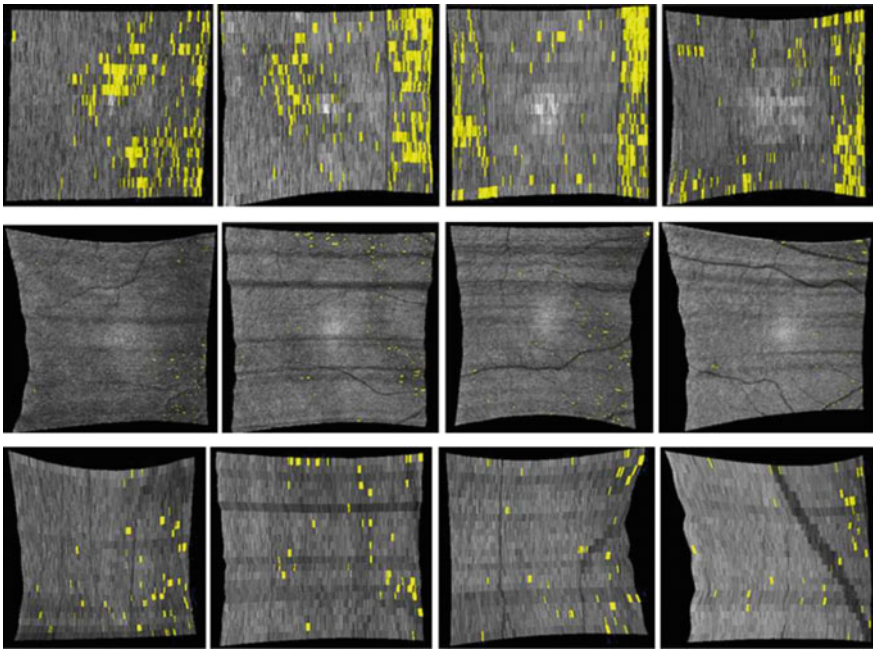

Fig. 10.13 ELM disrupted area detection (in yellow) on 4 CSME subjects (1st row), 4 normal controls and corresponding normal downsampled images ($T = 0.5$)

sis of commotio retinae [55, 56]. Photoreceptors are specialized types of neurons in the retina that are capable of phototransduction. They are critical for vision because they convert light into biological signals. In the SD-OCT image, the ellipsoid zone (EZ) [57], previously called the photoreceptor inner segment/outer segment (IS/OS), is defined as the second hyper-reflective zone of the outer retina and is located just below the external limiting membrane [57]. A disruption of the EZ integrity represents damage to the photoreceptors and is generally linked with poorer vision in commotio retina [58] and other retinal diseases [59–69]. Therefore, it would be very interesting to quantitatively assess photoreceptor damage by quantifying the 3D extent and the volume of EZ disruption.

In this part we describe an automatic 3D framework to detect EZ disruption in macular SD-OCT scans [24]. We apply an adaptive boosting (Adaboost) [70–72] based method to classify the pixels as disrupted or non-disrupted.

10.4.2 Method

10.4.2.1 Method Overview

The proposed method consists of three main parts: pre-processing, classification, and post-processing. In the pre-processing step, the SD-OCT images are first denoised and segmented into 10 intra-retinal layers with 11 surfaces. The retina in the original SD-OCT volume is flattened, where the 11th surface (the bottom of the retinal pigment epithelium) is used as the reference plane. The EZ region between the 7th and 8th surfaces is extracted, which is the volume of interest (VOI) for our analysis. In the classification step, five categories, from a total of 57 features, are extracted for each voxel in the VOIs. Then, principle component analysis (PCA) is adopted for feature selection. Because the disrupted voxels (the minority) in the VOIs are far less numerous than the non-disrupted ones (the majority), it is a typical imbalanced classification problem. To improve the performance of the classification, we apply the following two strategies in the classification training: (1) an Adaboost algorithm is adopted to train some weak classifiers into an integrated strong classifier at the algorithm level; and (2) the majority samples are randomly under-sampled at the data level. In the classifier testing step, every voxel in the VOIs is classified as disrupted or not disrupted. In the post-processing step, the blood vessel silhouettes are identified and excluded by a vessel detector and the isolated points are excluded by morphological operations to avoid false detections. Finally, the volume of the disrupted EZ is calculated.

10.4.2.2 Pre-processing

Speckle noise is the main noise in OCT images, and it affects the performance of image processing and classification. In this paper, we propose applying the bilateral filtering [32] method for denoising because it can remove speckle noise from images effectively while maintaining edge-like features. We have used a fast approximation algorithm [33] to reduce the computation time without significantly impacting the bilateral filtering result. Each B-scan (X-Z image) of the OCT images is smoothed separately by bilateral filtering.

The filtered SD-OCT volume is then automatically segmented into 10 intra-retinal layers using the multi-scale 3D graph-search approach [1, 2, 14, 28, 29], which produces 11 surfaces (see Fig. 10.14). Then, all the surfaces are smoothed using thin plate splines. The retina in the original SD-OCT volume is flattened by adjusting the A-scans up and down in the z-direction, where the 11th surface (the bottom of the retinal pigment epithelium) is used as a reference plane because of its robustness. Then, the EZ regions between the 7th and 8th surfaces are extracted as the volumes of interest (VOIs).

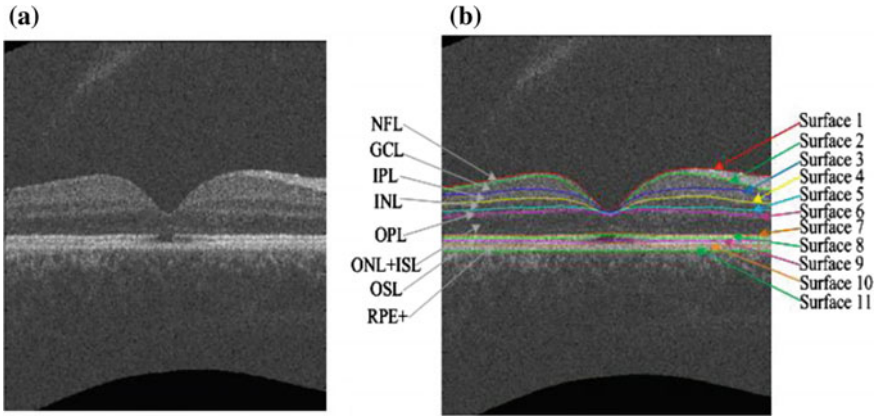

Fig. 10.14 Segmentation results of 11 intra-retinal surfaces (10 layers) on an eye with retinal trauma. **a** B-scan of an eye with retinal trauma. The red arrow indicates ellipsoid zone disruption. **b** Segmentation results of the eye with retinal trauma: nerve fibre layer (NFL), ganglion cell layer (GCL), inner plexiform layer (IPL), inner nuclear layer (INL), outer plexiform layer (OPL), outer unclear layer (ONL) + inner segment layer (ISL), outer segment layer (OSL), and retinal pigment epithelium complex (RPE+)

10.4.2.3 Feature Extraction and Selection

For classification, the following five types of low-level features are extracted: normalized intensity, block mean, block standard deviation, the absolute intensity difference in the 13 directions to be described later (step = 1, 2), and the grey-level co-occurrence matrix (GLCM) based features (contrast, correlation, energy and homogeneity in 13 directions). Therefore, 57 features are extracted, which are listed in Table 10.8.

The normalized intensity represents the voxel's grey level. As shown in Fig. 10.14, the intensity level of the disrupted region of the EZ is lower than the intensity level of the non-disrupted region. Therefore, if a voxel's normalized intensity level is low, it has a higher probability of being classified as a disruption, and vice versa.

The block mean and block standard deviation represent the average intensity level and the variance of the intensity level, respectively, in the local region centred around the voxel (region of $5 \times 5 \times 5$ voxels). The absolute intensity difference in 13 directions represents the variance of the intensity between the centre voxel and its neighbours in 13 directions. Let α_1 stand for the angle between the X-axis and the projection direction on the X-Y plane, and let α_2 stand for the angle between the X-Y projection direction and the Z-axis. The 13 directions can be described as follows: $(\alpha_1, \alpha_2) = (0, 90°)$, $(45°, 90°)$, $(90°, 90°)$, $(135°, 90°)$, $(0, 45°)$, $(180°, 45°)$, $(90°, 45°)$, $(-90°, 45°)$, $(0, 0)$, $(45°, 45°)$, $(135°, 45°)$, and $(-135°, 45°)$. The block mean, block standard deviation and absolute difference in the 13 directions can be used to distinguish the boundary between the disrupted and non-disrupted regions.

The grey-level co-occurrence matrices (GLCMs) for the 3D volumetric data describe the spatial dependence of grey levels across multiple slices [73, 74]. The 3D

Table 10.8 The features extracted in the feature extraction stage

Feature number	Feature name	Details
1	Normalized intensity	$I_{\text{normalized}}(i,j,k) = \frac{I_{\text{bilater\_filtered}}(i,j,k) - I_{\min}}{I_{\max} - I_{\min}}$ (i,j,k) represents the (i,j,k) th voxel in the VOIs.
2	Block mean	$M_{\text{block}}(i,j,k) = \frac{1}{125} \sum_{l=i-2}^{i+2} \sum_{m=j-2}^{j+2} \sum_{n=k-2}^{k+2} I_{\text{normalized}}(l,m,n)$
3	Block standard deviation	$STD_{\text{block}}(i,j,k) = \sqrt{\frac{\sum_{l=i-2}^{i+2} \sum_{m=j-2}^{j+2} \sum_{n=k-2}^{k+2} (I_{\text{normalized}}(l,m,n) - M_{\text{block}}(i,j,k))^2}{124}}$
4, 5	Absolute intensity difference in 13 directions	$AID(i,j,k) = \sum_{\text{13 directions}} \lvert I_{\text{normalized}}(i,j,k) - I_{\text{normalized}}(l,m,n) \rvert$ $l = i, i+step; m = j, j+step; n = k, k+step; step = 1, 2$
6–18	GLCM based contrast (in 13 directions)	$\text{Contrast}_{\text{direction}\,m}(i,j,k) = \sum_{x=1}^{N_g} \sum_{y=1}^{N_g} (x-y)^2 p(x,y)$ $m = 1, 2, \ldots, 13$ $p(x,y)$ represents the (x,y)th entry in the GLCM, N_g represents the number of distinct grey levels in the quantized image. Here, $N_g = 8$.
19–31	GLCM based correlation (in 13 directions)	$\text{Correlation}_{\text{direction}\,m}(i,j,k) = \sum_{x=1}^{N_g} \sum_{y=1}^{N_g} \frac{(x-\mu_x)(y-\mu_y)p(x,y)}{\sigma_x \sigma_y}$ $m = 1, 2, \ldots, 13$ μ_x, μ_y, σ_x and σ_y are the means and standard deviations of the x row and the y column, respectively.
32–44	GLCM based energy (in 13 directions)	$\text{Energy}_{\text{direction}\,m}(i,j,k) = \sum_{x=1}^{N_g} \sum_{y=1}^{N_g} p^2(x,y)$ $m = 1, 2, \ldots, 13$
45-57	GLCM based homogeneity (in 13 directions)	$\text{Homogeneity}_{\text{direction}\,m}(i,j,k) = \sum_{x=1}^{N_g} \sum_{y=1}^{N_g} \frac{p(x,y)}{1+\lvert x-y \rvert}$ $m = 1, 2, \ldots, 13$

method searches for other grey levels in the 13 directions (mentioned above) across multiple planes and constructs 13 GLCMs. Here, the GLCMs in the 13 directions of every $5 \times 5 \times 5$ block are constructed. Then, the following four features are calculated: (1) the contrast, which measures the local contrast of the volumetric image and is expected to be higher when a large grey-level difference occurs more frequently; (2) the correlation, which provides a correlation between the two voxels in a voxel pair and is expected to be higher when the grey levels of a voxel pair are more correlated; (3) the energy, which measures the number of repeated voxel pairs and is expected to be higher if the occurrence of repeated voxel pairs is higher; and (4) the homogeneity, which measures the local homogeneity of a voxel pair and will be larger when the grey levels of each voxel pair are more similar.

Based on above definitions, we have a total of 57 features extracted for each voxel in the VOIs. To reduce the dimensionality of the feature vector and describe the inter-correlated quantitative dependence of the features, a feature selection procedure based on the PCA is performed. In our experiments, the first 10 principle components are selected as the new features; they represent more than 90% of the information in the original features.

10.4.2.4 Adaboost Algorithm and the Under-Sampling Based Integrated Classifier

In this study, the number of non-disrupted samples in the EZ region is far greater than the number of disrupted ones. The disrupted EZ samples and non-disrupted EZ samples belong to the minority and majority classes, respectively. This is a typical imbalanced classification problem, which means the class distribution is highly skewed. Most traditional single classifiers, such as the support vector machine, the k-nearest neighbour classifier, quadratic discriminate analysis, and the decision tree classifier, tend to show a strong bias towards the majority class and do not work well for this type of problem because they aim to maximize the overall accuracy. The Adaboost algorithm based integrated classifier [70–72] is one solution to overcome this problem at the algorithm level; it integrates multiple weak classifiers into a strong classifier and is therefore more sensitive to the minority. Hence, the Adaboost algorithm is adopted in this study.

To further improve the classification performance at the data level, the training datasets are balanced by under-sampling majority samples. In the training step, the Adaboost algorithm-based classifier model is calculated according to leave-one-out cross-validation, using all the disrupted samples and an equivalent number of randomly selected non-disrupted samples. In the testing stage, each voxel in the VOIs is classified as disrupted or non-disrupted using the trained Adaboost model.

10.4.2.5 Post-processing

The vessel silhouettes in the EZ have lower values of intensity, and the voxels in these regions may be falsely classified as disrupted. The vessel silhouettes are identified and detected based on a vessel detector [52]. As in the outer retina (EZ to RPE), the vessel silhouettes offer excellent contrast; only those voxels between the EZ and RPE are selected and each pixel in the 2D projection image is the average in the z-axis direction of the selected voxels at that particular x, y location in the OCT volume. Then, the vessel silhouettes are segmented using a KNN classifier. If the detected EZ disruption regions have the same x and y location as the vessel silhouettes, these regions are regarded as normal and removed as false detections. Due to the physiological connectivity of the EZ disrupted/non-disrupted regions, isolated disrupted/non-disrupted voxels are eliminated through morphological opening operations, where the shape of the structural element is set as ball with a radius of 5 voxels.

10.4.3 Results

In total, 15 eyes in subjects with retinal trauma and 15 eyes in normal subjects were included and underwent a macular-centred (6×6 mm) SD-OCT scan (Topcon 3D OCT-1000, $512 \times 64 \times 480$ voxels, $11.72 \times 93.75 \times 3.50$ μm^3, or $512 \times 128 \times 480$ voxels, $11.72 \times 46.88 \times 3.50$ μm^3). There were 12 males and 3 females in the trauma group, with a mean age of 30.3 ± 11.3 years (range: 8–43 years). There were 9 males and 6 females in the normal group, with a mean age of 33.1 ± 10.8 years (range: 7–46 years). Subjects with other eye diseases were excluded except for those with refractive error <= ± 6 diopter.

The Institutional Review Board of the Joint Shantou International Eye Center approved this study and waived informed consent due to the retrospective nature of this study. Our study also complies with the Declaration of Helsinki. The patient records/information was made anonymous prior to analysis.

To evaluate the performance of the proposed method, all the EZ disruption regions in the 3D SD-OCT images were manually marked by an ophthalmologist slice by slice using the ITK-SNAP software [75] and saved as the ground truth. The leave-one-out method was used to train the Adaboost based integrated classifier models. Because the sample ratio of the majority class (non-disrupted) and the minority class (disrupted) was approximately (110 ± 256):1 on average, non-disrupted samples were randomly selected to match the disrupted ones. The EZ disruption volume was calculated by multiplying the disruption number by the voxel resolution.

The mean and 95% confidence intervals of the segmented EZ disruption region volumes were compared between eyes with retinal trauma and normal eyes. Student's t-test was used to evaluate the statistical significance of the disruption volume differences between the two groups of eyes. Statistical correlation analysis and

Bland-Altman plot analysis were utilized for a performance comparison between the proposed method and the ground truth.

To assess our experiments, several measures based on the segmented volume of the EZ disruption including sensitivity (SEN), specificity (SPE) and balanced accuracy rate (BAR) were adopted. These evaluation indexes are commonly used in imbalanced classification problems and are defined as below:

$$SEN = \frac{TP}{TP + FN} \times 100\% \tag{10.11}$$

$$SPE = \frac{TN}{TN + FP} \times 100\% \tag{10.12}$$

$$BAR = \frac{SEN + SPE}{2} \tag{10.13}$$

where TP, FN, TN and FP represent true positive, false negative, true negative and false negative, respectively.

Figure 10.15 shows one of the detection results using the proposed framework, and the corresponding ground truth for the EZ disruption region. The en face projections of the original VOIs, ground truth, and corresponding detected EZ disruption are also shown. We can see from Fig. 10.15 that while the proposed method detected the EZ disruption well, there were still some false positives and false negatives. The detection results for a normal eye are shown in Fig. 10.16. Most of the negative regions were correctly classified; however, there were still some false positives.

The mean and 95% confidence intervals of the detected disruption volume for the normal eyes were $mean_{normal} = 0.0037\,\text{mm}^3$ and $CI_{normal} = [0.0005, 0.0069]\,\text{mm}^3$, while for the eyes with retinal trauma they were $mean_{trauma} = 0.1035\,\text{mm}^3$ and $CI_{trauma} = [0.0126, 0.1944]\,\text{mm}^3$. The detected EZ disruption volume comparison between the normal eyes and the eyes with retinal trauma is shown in Fig. 10.17. Student's t-test demonstrated a strong statistical significance for the detected EZ disruption volume differences between the two groups of eyes ($p = 9.9112 \times 10^{-8} \ll 0.001$).

For the eyes with retinal trauma, the SEN was $85.69\% \pm 9.59\%$, the SPE was $85.91\% \pm 5.48\%$, and the BAR was $85.80\% \pm 6.16\%$. For the normal eyes, the SPE was $99.03\% \pm 0.73\%$. Because there were no true positives, the values of SEN and BAR were irrelevant.

For the eyes with retinal trauma, the correlation between the segmented EZ disruption volume and the ground truth was $r = 0.8795$ with a significance level $p < 0.0001$. The 95% confidence interval for r was 0.6683–0.9595. Figure 10.18 shows the Bland-Altman plot for the consistency analysis between the automatic segmented EZ disruption volume and the ground truth.

In summary, in this study, we developed and evaluated an automatic method to detect the 3D integrity of the EZ in eyes with retinal trauma. Because the disrupted voxels in the EZ region are much less numerous than the non-disrupted ones, this leads to a typical imbalanced classification problem. To overcome this problem, an Adaboost algorithm (at the algorithm level) and dataset balance strategies (at

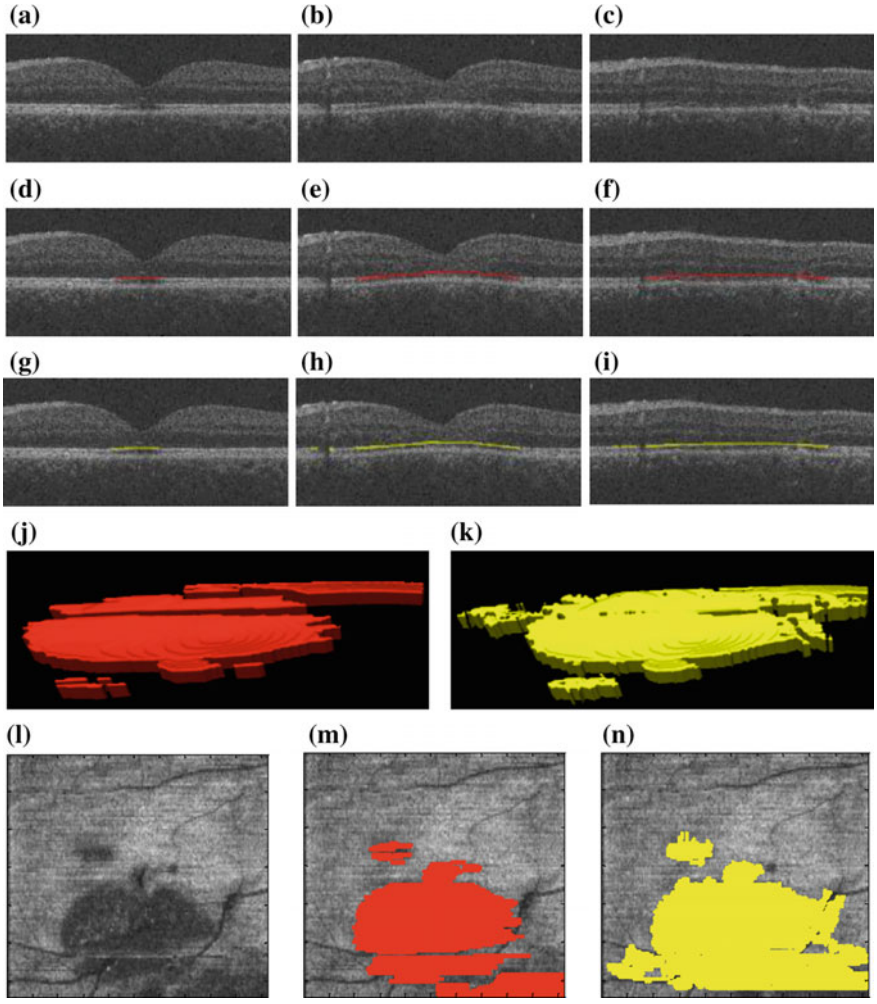

Fig. 10.15 Examples of EZ disruption region detection results and ground truths for a subject with retinal trauma. The red region represents the ground truth, and the yellow region represents the segmented EZ disruption region using the proposed method. **a**–**c** Three original B-scans of an OCT volume. **d**–**f** The corresponding ground truth in the B-scans for (**a**–**c**), respectively. **g**–**i** The corresponding detection results using the proposed method for (**a**–**c**), respectively. **j** The ground truth in a 3D view. **k** The detection results in a 3D view. **l** The en face projection of the VOIs. **m** The en face projection of the ground truth (in red). **n** The en face projection of the detection results (in yellow)

the data level) are utilized. The vessel silhouettes and isolated points are excluded to remove the false detections, using a vessel detector and morphological opening operations, respectively. The average detected EZ disruption volume in the eyes with retinal trauma was statistically much larger than the corresponding volume in

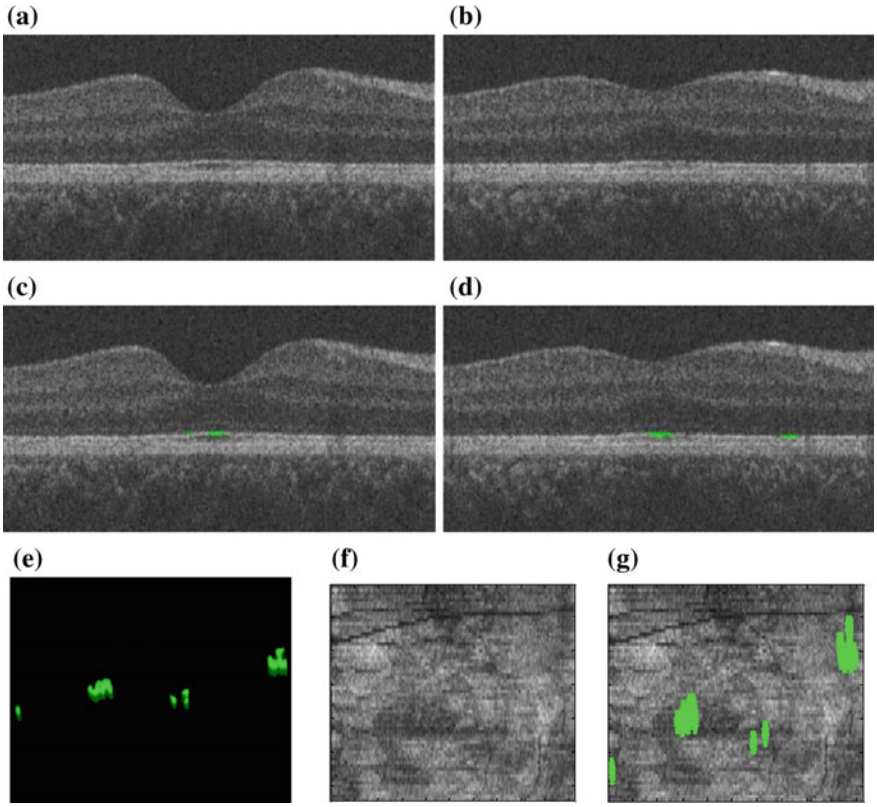

Fig. 10.16 An example of the detection results using the proposed method on a normal subject. **a**, **b** The original B-scans of the OCT volume. **c**, **d** The false positive detection results (in green) using the proposed method. **e** All false positive detection results in a 3D view. **f** The en face projection of the VOIs. **g** The en face of the false positives (in green)

the normal eyes (Student's t-test, $p = 9.9112 \times 10^{-8} < 0.001$). In the eyes with retinal trauma, the SEN, SPE and BAR, using the proposed method, were $85.69\% \pm 9.59\%$, $85.91\% \pm 5.48\%$, and $85.80\% \pm 6.16\%$, respectively. There was a strong correlation between the segmented EZ disruption volume and the ground truth ($r = 0.8795$). In the normal eyes, the SPE was $99.03\% \pm 0.73\%$.

This study has several limitations. (1) Although many studies have shown that the disruption extent of the EZ is an important clinical indicator for the injury degree of the photoreceptors and that EZ disruption may be closely associated with visual acuity in different eye diseases [59–69], there are some controversies [76–79]. Whether the quantitative disruptions of the EZ have quantitative relationships with visual acuity and visual outcome has not yet been addressed. This study focuses on quantitative measurements of the EZ disruption volume; further study will be carried out in the near future to determine the quantitative correlation, if any, of these quantitative

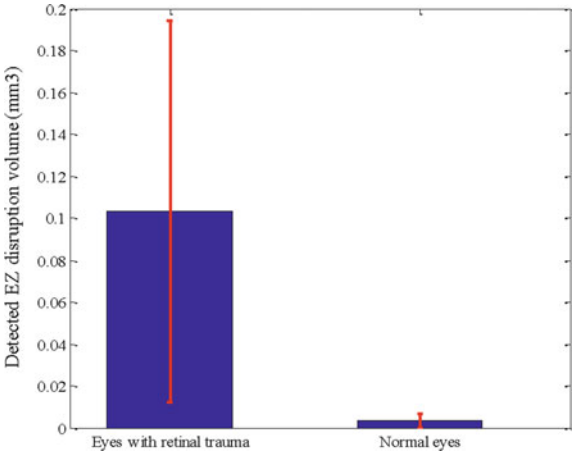

Fig. 10.17 Detected EZ disruption volume comparison. The blue bars show the mean volumes, and the red error bars show the 95% confidence intervals

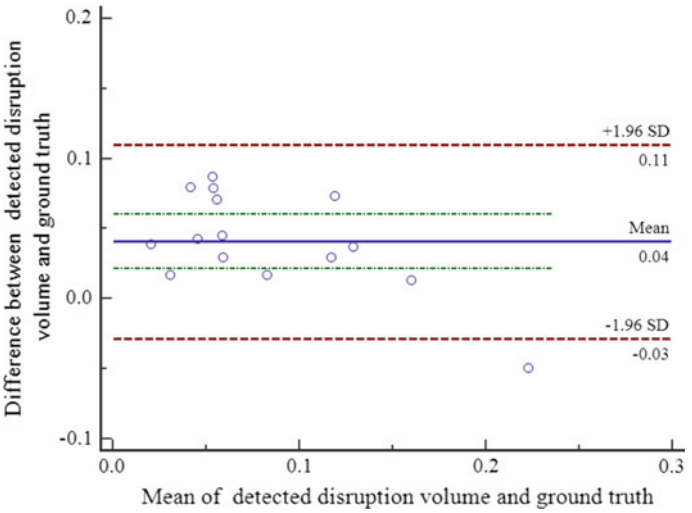

Fig. 10.18 Bland-Altman plot for consistency analysis

measures to visual acuity and to the outcome of eyes with retinal trauma. (2) The sensitivity and specificity of the proposed method could also be further improved. The classification errors could be due to two reasons. (i) The inaccuracy of the surface segmentation results during the image pre-processing stage may cause unreasonable extractions of VOIs. (ii) Because of the poor quality of the SD-OCT images, the ground truths marked by the ophthalmologist are subjective, especially in the transitional region between the disrupted and the non-disrupted regions. (3) Due to the collection difficulties and poor quality of the image data, the proposed method was

tested on a small-sized image dataset (15 eyes with retinal trauma and 15 normal eyes). We are still collecting more data and will validate our method on a larger dataset in the near future.

10.5 Conclusions

In this chapter, several methods for automatic layer segmentation and analysis of diseased retinas are presented. Layer segmentation can serve as a pre-processing step for both abnormal layer analysis and pathological region detection, while layer disruption detection provides quantitative information of the change caused by retinal pathology, which is of great value to diagnosis and progress tracking of the disease. Though these methods achieve good performance, they are tailored for specific type of pathology. More universal method that can deal with various types of diseases is expected, and this remains an open and hot area in OCT image analysis.

References

1. M.K. Garvin, M.D. Abràmoff, X. Wu, S.R. Russell, T.L. Burns, M. Sonka, Automated 3-D intraretinal layer segmentation of macular spectral-domain optical coherence tomography images. IEEE Trans. Med. Imag. **28**(9), 1436–1447 (2009)
2. K. Lee, Segmentations of the intraretinal surfaces, optic disc and retinal blood vessels in 3D-OCT scans. Ph.D. dissertation, University of Iowa, 2009
3. S. Lu, C.Y. Cheung, J. Liu, J.H. Lim, C.K. Leung, T.Y. Wong, Automated layer segmentation of optical coherence tomography images. IEEE Trans. Biomed. Eng. **57**(10), 2605–2608 (2010)
4. A. Yazdanpanah, G. Hamarneh, B.R. Smith, M.V. Sarunic, Segmentation of intra-retinal layers from optical coherence tomography images using an active contour approach. IEEE Trans. Med. Imag. **30**(2), 484–496 (2011)
5. Q. Song, J. Bai, M.K. Garvin, M. Sonka, J.M. Buatti, X. Wu, Optimal multiple surface segmentation with shape and context priors. IEEE Trans. Med. Imag. **32**(2), 376–386 (2013)
6. Q. Yang, C.A. Reisman, Z. Wang, Y. Fukuma, M. Hangai, N. Yoshimura, A. Tomidokoro, M. Araie, A.S. Raza, D.C. Hood, K. Chan, Automated layer segmentation of macular OCT images using dual-scale gradient information. Opt. Express **18**(21), 293–307 (2010)
7. S.J. Chiu, X.T. Li, P. Nicholas, C.A. Toth, J.A. Izatt, S. Farsiu, Automatic segmentation of seven retinal layers in SDOCT images congruent with expert manual segmentation. Opt. Express **18**(18), 19413–19428 (2010)
8. J. Novosel, K.A. Vermeer, G. Thepass, H.G. Lemij, L.J. van Vliet, Loosely coupled level sets for retinal layer segmentation in optical coherence tomography, in *Proceedings of IEEE ISBI* (2013), pp 1010–1013
9. K.A. Vermeer, J. van der Schoot, H.G. Lemij, J.F. de Boer, Automated segmentation by pixel classification of retinal layers in ophthalmic OCT images. Biomed. Opt. Express **2**, 1743–1756 (2011)
10. R. Kafieh, H. Rabbani, M.D. Abramoff, M. Sonka, Intra-retinal layer segmentation of 3D optical coherence tomography using coarse grained diffusion map. Med. Imag. Anal. **17**, 907–928 (2013)

11. B.J. Antony, M.D. Abràmoff, M.M. Harper, J. Woojin, E.H. Sohn, Y.H. Kwon, R. Kardon, M.K. Garvin, A combined machine-learning and graph-based framework for the segmentation of retinal surfaces in sd-oct volumes. Biomed. Opt. Express **4**(12), 2712–2728 (2013)
12. A. Lang, A. Carass, M. Hauser, E.S. Sotirchos, P.A. Calabresi, H.S. Ying, J.L. Prince, Retinal layer segmentation of macular OCT images using boundary classification. Biomed. Opt. Express **4**, 1133–1152 (2013)
13. P.A. Dufour, L. Ceklic, H. Abdillahi, S. Schröder, S. De Dzanet, U. Wolf-Schnurrbusch, J. Kowal, Graph-based multi-surface segmentation of OCT data using trained hard and soft constraints. IEEE Trans. Med. Imag. **32**(3), 531–543 (2013)
14. The Iowa Reference Algorithms (Iowa Institute for Biomedical Imaging, Iowa City, IA.) (Online). http://www.biomed-imaging.uiowa.edu/downloads/
15. F. Shi, X. Chen, H. Zhao, W. Zhu, D. Xiang, E. Gao, M. Sonka, H. Chen, Automated 3-D retinal layer segmentation of macular optical coherence tomography images with serous pigment epithelial detachments. IEEE Trans. Med. Imag. **34**(2), 441–452 (2015)
16. C.E. Al-Haddad, G.M. Mollayess, C.G. Cherfan, D.F. Jaafar, Z.F. Bashshur, Retinal nerve fibre layer and macular thickness in amblyopia as measured by spectral-domain optical coherence tomography. Br. J. Ophthalmol. **95**, 1696–1699 (2011)
17. D. Cabrera G.M. DeBuc, Somfai, Early detection of retinal thickness changes in diabetes using optical coherence tomography. Med. Sci. Monit. **16**, MT15-21 (2010)
18. E.C. Davies, K.M. Galetta, D.J. Sackel, L.S. Talman, E.M. Frohman, P.A. Calabresi, S.L. Galetta, L.J. Balcer, Retinal ganglion cell layer volumetric assessment by spectral-domain optical coherence tomography in multiple sclerosis: application of a high-precision manual estimation technique. J. Neuroophthalmol. **31**, 260–264 (2011)
19. N. Demirkaya, H.W. van Dijk, S.M. van Schuppen, M.D. Abramoff, M.K. Garvin, M. Sonka, R.O. Schlingemann, F.D. Verbraak, Effect of age on individual retinal layer thickness in normal eyes as measured with spectral-domain optical coherence tomography. Invest. Ophthalmol. Vis. Sci. **54**, 4934–4940 (2013)
20. N.R. Kim, S. Hong, J.H. Kim, S.S. Rho, G.J. Seong, C.Y. Kim, Comparison of Macular Ganglion cell complex thickness by Fourier-Domain OCT in normal tension Glaucoma and primary open-angle Glaucoma. J. Glaucoma **22**(2), 133–139 (2013)
21. X. Chen, P. Hou, C. Jin, W. Zhu, X. Luo, F. Shi, M. Sonka, H. Chen, Quantitative analysis of retinal layers' optical intensities on 3D optical coherence tomography. Invest. Ophthalmol. Vis. Sci. **54**(10), 6846–6851 (2013)
22. H. Chen, X. Chen, Z. Qiu, D. Xiang, W. Chen, F. Shi, J. Zheng, W. Zhu, M. Sonka, Quantitative analysis of retinal layers' optical intensities on 3D optical coherence tomography for central retinal artery occlusion. Sci. Rep., **5**, Article number: 9269
23. X. Chen, L. Zhang, E.H. Sohn, K. Lee, M. Niemeijer, J. Chen, M. Sonka, M.D. Abramoff, Quantification of external limiting membrane disruption caused by diabetic macular edema from SD-OCT. Invest. Ophthalmol. Vis. Sci. **53**(13), 8042–8048 (2012)
24. W. Zhu, H. Chen, H. Zhao, B. Tian, L. Wang, F. Shi, D. Xiang, X. Luo, E. Gao, L. Zhang, Y. Yin, X. Chen, Automatic three-dimensional detection of photoreceptor ellipsoid zone disruption caused by trauma in the OCT. Sci. Rep. **6**, 25433 (2016)
25. S. Mrejen, D. Sarraf, S.K. Mukkamala, K.B. Freund, Multimodal imaging of pigment epithelial detachment: a guide to evaluation. Retina **33**(9), 1735–1762 (2013)
26. S. Zayit-Soudry, I. Moroz, A. Loewenstein, Retinal pigment epithelial detachment. Surv. Ophthalmol. **52**(3), 227–243 (2007)
27. P.A. Keane, P.J. Patel, S. Liakopoulos, F.M. Heussen, S.R. Sadda, A. Tufail, Evaluation of age-related macular degeneration with optical coherence tomography. Surv. Ophthalmol. **57**(5), 389–414 (2012)
28. K. Lee, M. Niemeijer, M.K. Garvin, Y.H. Kwon, M. Sonka, M.D. Abràmoff, Segmentation of the optic disc in 3-D OCT scans of the optic nerve head. IEEE Trans. Med. Imag. **29**(1), 159–168 (2010)
29. K. Li, X. Wu, D.Z. Chen, M. Sonka, Optimal surface segmentation in volumetric images—a graph-theoretic approach. IEEE Trans. Pattern Anal. Mach. Intell. **28**(1), 119–134 (2006)

30. D. Hochbaum, A new-old algorithm for minimum-cut and maximum-flow in closure graphs. Networks **37**, 171–193 (2001)
31. J. Picard, Maximal closure of a graph and applications to combinatorial problems. Manage. Sci. **22**, 1268–1272 (1976)
32. C. Tomasi, R. Manduchi, Bilateral filtering for gray and color images, in *Proceedings of IEEE ICCV* (1998), pp. 839–846
33. S. Paris, F. Durand, A fast approximation of the bilateral filter using a signal processing approach. Int. J. Comput. Vis. **81**(1), 24–52 (2009)
34. N. Otsu, A threshold selection method from gray-level histograms. IEEE Trans. Syst. Man Cybern. **9**(1), 62–66 (1979)
35. N. Bhagat, R.A. Grigorian, A. Tutela, M.A. Zarbin, Diabetic macular edema: pathogenesis and treatment. Surv. Ophthalmol. **54**, 1–32 (2009)
36. T.A. Ciulla, A.G. Amador, B. Zinman, Diabetic retinopathy and diabetic macular edema: pathophysiology, screening, and novel therapies. Diab. Care **26**, 2653–2664 (2003)
37. A. Goldin, J.A. Beckman, A.M. Schmidt, M.A. Creager, Advanced glycation end products: sparking the development of diabetic vascular injury. Circulation **114**, 597–605 (2006)
38. M.R. Hee, C.A. Puliafito, J.S. Duker, E. Reichel, J.G. Coker, J.R. Wilkins, J.S. Schuman, E.A. Swanson, J.G. Fujimoto, Topography of diabetic macular edema with optical coherence tomography. Ophthalmology **105**, 360–370 (1998)
39. N. Ahmed, Advanced glycation end products—role in pathology of diabetic complications. Diab. Res. Clin. Pract. **67**, 3–21 (2005)
40. M.D. Abr'amoff, M.K. Garvin, M. Sonka, Retinal imaging and image analysis. IEEE Trans. Med. Imaging **3**, 169–208 (2010)
41. W. Soliman, B. Sander, T.M. Jørgensen, Enhanced optical coherence patterns of diabetic macular oedema and their correlation with the pathophysiology. Acta Ophthalmol. Scand. **85**, 613–617 (2007)
42. T. Wakabayashi, M. Fujiwara, H. Sakaguchi, S. Kusaka, Y. Oshima, Foveal microstructure and visual acuity in surgically closed macular holes: spectral-domain optical coherence tomographic analysis. Ophthalmology **117**, 1815–1824 (2010)
43. A. Sakamoto, K. Nishijima, M. Kita, H. Oh, A. Tsujikawa, N. Yoshimura, Association between foveal photoreceptor status and visual acuity after resolution of diabetic macular edema by pars plana vitrectomy. Graefes Arch. Clin. Exp. Ophthalmol. **247**, 1325–1330 (2009)
44. R.A. Costa, D. Calucci, M. Skaf, J.A. Cardillo, J.C. Castro, L.A. Melo Jr., M.C. Martins, P.K. Kaiser, Optical coherence tomography 3: automatic delineation of the outer neural retinal boundary and its influence on retinal thickness measurements. Invest. Ophthalmol. Vis. Sci. **45**, 2399–2406 (2004)
45. T. Otani, Y. Yamaguchi, S. Kishi, Correlation between visual acuity and foveal microstructural changes in diabetic macular edema. Retina **30**, 774–780 (2010)
46. C.K. Leung, S. Lam, R.N. Weinreb et al., Retinal nerve fiber layer imaging with spectral-domain optical coherence tomography: analysis of the retinal nerve fiber layer map for glaucoma detection. Ophthalmology **117**, 1684–1691 (2010)
47. T. Wakabayashi, Y. Oshima, H. Fujimoto et al., Foveal microstructure and visual acuity after retinal detachment repair: imaging analysis by Fourier-domain optical coherence tomography. Ophthalmology **116**, 519–528 (2009)
48. P.G. Theodossiadis, V.G. Grigoropoulos, G.P. Theodossiadis, The significance of the external limiting membrane in the recovery of photoreceptor layer after successful macular hole closure: a study by spectral domain optical coherence tomography. Ophthalmologica **225**, 176–184 (2011)
49. E.J. Fern´andez, B. Povazay, B. Hermann, et al., Three-dimensional adaptive optics ultrahigh-resolution optical coherence tomography using a liquid crystal spatial light modulator. Vis. Res. **45**, 3432–3444 (2005)
50. S. Schmitz-Valckenberg, M. Fleckenstein, A.P. G¨obel, T.C. Hohman, F.G. Holz, Optical coherence tomography and autofluorescence findings in areas with geographic atrophy due to age related macular degeneration. Invest Ophthalmol. Vis. Sci. **52**, 1–6 (2011)

51. M. Cho, M.T. Witmer, G. Favarone, R.P. Chan, D.J. D'Amico, S. Kiss, Optical coherence tomography predicts visual outcome in macula-involving rhegmatogenous retinal detachment. Clin. Ophthalmol. **6**, 91–96 (2012)
52. M. Niemeijer, M.K. Garvin, B. van Ginneken, M. Sonka, M.D. Abr'amoff, Vessel segmentation in 3D spectral OCT scans of the retina. Proc. SPIE Med. Imaging. **6914**, 69141R (2008). doi:10.1117/12.772680
53. F. Kuhn, V. Mester, A. Berta, R. Morris, Epidemiology of severe eye injuries. United States injury registry (USEIR) and Hungarian eye injury registry (HEIR). Ophthalmologe **95**, 332–343 (1998)
54. R. Berlin, Zur sogenannten commotio retinae. Klin. Monatsbl. Augenh. **11**, 42–78 (1873)
55. J.O. Sipperley, H.A. Quigley, D.M. Gass, Traumatic retinopathy in primates: the explanation of commotio retinae. Arch. Ophthalmol. **96**, 2267–2273 (1978)
56. A.M. Mansour, W.R. Green, C. Hogge, Histopathology of commotio retinae. Retina **12**, 24–28 (1992)
57. G. Staurenghi, S. Sadda, U. Chakravarthy, R.F. Spaid, Proposed lexicon for anatomic landmarks in normal posterior segment spectral-domain optical coherence tomography: the IN•OCT consensus. Ophthalmology **121**, 1572–1578 (2014)
58. H. Chen et al., Prediction of visual prognosis with spectral-domain optical coherence tomography in outer retinal atrophy secondary to closed globe trauma. Retina **33**, 1258–1262 (2013)
59. S. Saxena, K. Srivastav, C.M. Cheung, J.Y.W. Ng, T.Y.Y. Lai, Photoreceptor inner segment ellipsoid band integrity on spectral domain optical coherence tomography. Clin. Ophthalmol. **8**, 2507–2522 (2014)
60. M. Hangai et al., Three-dimension imaging of macular holes with high-speed optical coherence tomography. Ophthalmology **114**, 763–773 (2007)
61. M. Inoue et al., Spectral-domain optical coherence tomography images of inner/outer segment junctions and macular hole surgery outcomes. Graefes Arch. Clin. Exp. Ophthalmol. **247**, 325–330 (2009)
62. O. Jaeryung, E.S. William, W.F.J. Harry, G. Giovanni, L. Brandon, Photoreceptor inner/outer segment defect imaging by spectral domain OCT and visual prognosis after macular hole surgery. Invest. Ophth. Vis. Sci. **51**, 1651–1658 (2010)
63. K. Sayanagi, Y. Ikuno, K. Soga, Y. Tano, Photoreceptor inner and outer segment defects in Myopic Foveoschisis. Am. J. Ophthalmol. **145**, 902–908 (2008)
64. R.F. Spaide, H. Koizumi, K.B. Freund, Photoreceptor outer segment abnormalities as a cause of blind spot enlargement in acute zonal occult outer retinopathy-complex diseases. Am. J. Ophthalmol. **146**, 111–120 (2008)
65. T. Baba et al., Correlation of visual recovery and presence of photoreceptor inner/outer segment junction in optical coherence images after successful macular hole repair. Retina **28**, 453–458 (2008)
66. N. Kitaya, T. Hikichi, H. Kagokawa, A. Takamiya, A. Yoshida, Irregularity of photoreceptor layer after successful maculor hole surgery prevents visual acuity improvement. Am. J. Ophthalmol. **138**, 308–310 (2004)
67. N.L. Gomes et al., Comparison of fundus autofluorescence and retinal structure in patients with stargardt disease. Invest. Ophth. Vis. Sci. **50**, 3953–3959 (2009)
68. H.J. Shin, S.H. Lee, H. Chung, H.C. Kim, Association between photoreceptor integrity and visual outcome in diabetic macular edema. Graefes Arch. Clin. Exp. Ophthalmol. **250**, 61–70 (2012)
69. Y. Itoh, A. Vasanji, J.P. Ehlers, Volumetric ellipsoid zone mapping for enhanced visualisation of outer retinal integrity with optical coherence tomography. Br. J. Ophthalmol. Online First, published on 22 July 2015, https://doi.org/10.1136/bjophthalmol-2015-307105 (2015)
70. Y. Freund, R.E. Schapire, Experiments with a new boosting algorithm, in *Conference Proceedings of 13th International Conference Machine Learning* (1996), pp. 148–156
71. Y. Freund, R.E. Schapire, Game theory, on-line prediction and boosting, in *Conference Proceedings of 9th Annual Conference Computer Learning Theory* (1996), pp. 325–332

72. R.E. Schapire, Y. Singer, Improved boosting algorithms using confidence-rated predictions. Mach. Learn. **37**, 297–336 (1999)
73. Y. Xu, M. Sonka, G. McLennan, J. Guo, E.A. Hoffman, MDCT-based 3-D textural classification of emphyema and early smoking related lung pathologies. IEEE Trans. Med. Imaging **25**, 464–475 (2006)
74. R.M. Haralick, K. Shanmugam, I. Dinstein, Textural features for image classification. IEEE Trans. Syst. Man Cybern. **SMC-3**, 610–621 (1973)
75. P.A. Yushkevich et al., User-guided 3D active contour segmentation of anatomical structures: significantly improved efficiency and reliability. NeuroImage **31**, 1116–1128 (2006)
76. N. Villate, J.E. Lee, A. Venkatraman, W.E. Smiddy, Photoreceptor layer features in eyes with closed macular holes: optical coherence tomography findings and correlation with visual outcomes. Am. J. Ophthalmol. **139**, 280–289 (2005)
77. M.H. Suh, J.M. Seo, K.H. Park, H.G. Yu, Associations between macular findings by optical coherence tomography and visual outcomes after epiretinal membrane removal. Am. J. Ophthalmol. **47**, 473–480 (2009)
78. L.K. Chang, H. Koizumi, R.F. Spaid, Disruption of the photoreceptor inner segment-out segment junction in eyes with macular holes. Retina **28**, 969–975 (2008)
79. A.A. Moshfeghi, H.W. Flynn Jr., S.G. Elner, C.A. Puliafito, J.D.M. Gass, Persistent outer retinal defect after successful macular hole repair. Am. J. Ophthalmol. **139**, 183–184 (2005)

Chapter 11
Segmentation and Visualization of Drusen and Geographic Atrophy in SD-OCT Images

Qiang Chen, Sijie Niu, Luis de Sisternes, Theodore Leng and Daniel L. Rubin

Age-related macular degeneration (AMD) is a major cause of vision loss for elderly people. Drusen and geographic atrophy are two kinds of pathological changes associated with AMD. This chapter presents several methods that achieve abnormal region segmentation for quantitative analysis or enhanced visualization for better qualitative assessment.

11.1 Introduction

Age-related macular degeneration (AMD) is the most common cause of visual impairment among the elderly in developed countries [1]. AMD is a degenerative eye disease that robs a person of their central vision while typically leaving their peripheral vision unaffected (i.e. degenerate the macula). The macula is the central, posterior portion of the retina. It contains the densest concentration of photo-receptors within the retina and is responsible for central high-resolution visual acuity, allowing a person to see fine detail, read, and recognize faces [2]. AMD can be classified into

Q. Chen (✉)
School of Computer Science and Engineering, Nanjing University of Science and Technology, Nanjing, China
e-mail: chen2qiang@njust.edu.cn

S. Niu
School of Information Science and Engineering, University of Jinan, Jinan, China

L. de Sisternes · D. L. Rubin
Department of Radiology, Stanford University, Stanford, USA

T. Leng
Byers Eye Institute at Stanford, Stanford University School of Medicine, Palo Alto, USA

D. L. Rubin
Department of Medicine (Biomedical Informatics), Stanford University, Stanford, USA

X. Chen et al. (eds.), *Retinal Optical Coherence Tomography Image Analysis*,
Biological and Medical Physics, Biomedical Engineering,
https://doi.org/10.1007/978-981-13-1825-2_11

the early and late stages. Generally, the late AMD can be further divided into 'wet' (neovascular) and 'dry' (atrophy) forms. Recent researches indicate that neovascular AMD account for two-thirds of the late cases, while one-third are atrophic. Early AMD, defined by the development of large drusen or pigment changes at the macula may be associated with either no vision loss or early changes in reading central vision. Late AMD includes both neovascular AMD and geographic atrophy, in a ratio of about 2:1. Neovascular ('wet' or exudative) AMD is characterised by the appearance of blurring of the central vision and distortion with straight lines appearing crooked or wavy, with or without a dark or blank patch. Perception of colours is also often affected. Geographic Atrophy ('dry' AMD) reduces capacity for near visual tasks as central vision becomes severely impaired. Note that some people include 'early AMD' within the category of 'dry AMD'. About 1.75 million U.S. residents currently have advanced age-related macular degeneration with associated vision loss, with that number expected to grow to almost 3 million by 2020 [3]. In this chapter, our main focus is on drusen and geographic atrophy of the AMD diseases.

11.1.1 Drusen

With age, one change that occurs within the eye is the focal deposition of acellular, polymorphous debris between the retinal pigment epithelium and Bruch's membrane. These focal deposits, called drusen (Fig. 11.1a), are observed during funduscopic examination as pale, yellowish lesions and may be found in both the macula and peripheral retinal [4]. Drusen are categorized as small (<63 μm in diameter), medium (63–124 μm), or large (>124 μm) on the basis of studies that classified the grade of age-related macular degeneration [5]. Drusen are also categorized as hard or soft on the basis of the appearance of their margins. Hard drusen have discrete margins; conversely, soft drusen generally have indistinct edges, are usually large, and can be confluent [6]. Most patients who develop severe visual loss from AMD have this exudative stage. These fundus changes may predispose the eye to develop the neovascular/exudative stages of AMD. Treatment for AMD has been shown to be effective for only a small proportion of patients who have a well-defined choroidal neovascular membrane (CNVM) more than 200 μ from the foveal center. Even in successfully treated cases, severe visual loss is postponed only for about 18 months because of the high rate of recurrent CNVMs that extend into the fovea. Thus, despite recent breakthroughs in laser treatment for AMD, most patients who develop the exudative form of AMD will develop central visual impairment [7].

11.1.2 Geographic Atrophy

Geographic atrophy is the advanced (late) form of dry AMD (Fig. 11.1b). Here, atrophy refers to the degeneration of the deepest cells of the retina. These are cells

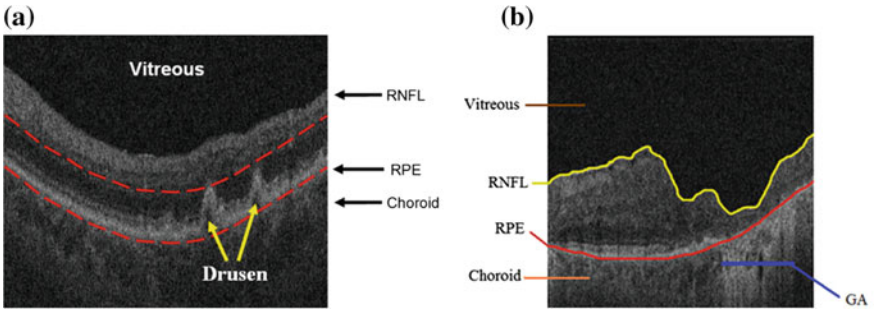

Fig. 11.1 OCT images of drusen and GA. **a** Drusen image, the bottom red curve is the baseline of the normal RPE layer. The top red curve is determined by the largest drusen height in any B-scan, **b** B-scan from SD-OCT volume scans of the retina. The RPE layer and GA region are marked with red and blue lines, respectively. The presence of GA appears as bright pixels in choroid coat (the region underneath the RPE layer) due to the loss of the RPE layer and subsequent increased reflections from the underlying choroid

of the retinal pigment epithelium (RPE). This RPE normally helps maintain the health of the next deepest layer, the photoreceptor cells known as rods and cones. These photoreceptor cells are triggered by light to set off a series of electrical and chemical reactions that result in the brain interpreting what is in the visual field. GA tends to progress slowly. Progression is currently studied using a technique called autofluorescence (AF) imaging to define the areas of GA. A newer technique called high density optical coherence tomography (OCT) allows the doctor to visualize the different layers of the retina, and to determine when cells are becoming thinned or destroyed. Researchers estimates that 3.5% of the United States population age 75 and older has GA, while and its prevalence rises to 22% in people older than 90 [8–10].

11.2 Drusen Segmentation and Visualization

Most of the drusen segmentation methods are proposed for color fundus photographs (CFPs), not OCT images. Duanggate and Uyyanonvara [11] reviewed automatic drusen segmentation from CFPs. Many different approaches to automated segmentation of drusen in CFPs have been developed, which includes histogram-based approaches [12–15], texture-based approaches [16–18], morphological approaches [19], multi-level analysis approach [20] and fuzzy logic approaches [21–23]. A common challenge among these systems is that the margins of the drusen are difficult to discern reliably on CFP since this is a two-dimensional imaging modality.

To achieve drusen segmentation in OCT images, manual segmentation [24, 25] is generally adopted, and few automated methods have been reported. Farsiu et al. [26] and Toth [27] proposed an automatic drusen segmentation algorithm. In the first step,

the location of the retinal nerve fiber layer (RNFL) was estimated and then the RPE layer was localized. By enforcing a local convexity condition and fitting second or fourth order polynomials to the possibly unhealthy (abnormal) RPE curve, the healthy (normal) shape of the RPE layer is estimated. The area between the estimated normal and the segmented RPE outlines was marked as possible drusen. Yi [28] utilized a similar algorithm to automatically segment drusen. The main difference between Farsiu's method and Yi's method was the extraction of RPE layers. While the prior work on automated drusen segmentation is a step in the direction of quantitation, there are unsolved challenges. First, drusen may obscure portions of the image needed for accurate estimation of RPE layers. Second, RPE layer segmentation is difficult even in normal patients because the inner segment/outer segment (IS/OS) retinal layers are often contiguous with the RPE and there is abundant noise in low signal-to-noise ratio (SNR) OCT images. To counteract these potential problems, [26] provided a manual correction using a software interface. According to one study [29], drusen detection in CFP and spectral domain optical coherence tomography (SD-OCT) images has good concordance, and each imaging modality has its own advantages. Our algorithm utilizes the projection image to verify and refine the segmentation results from SD-OCT images, which reduces the influence of RPE estimation error and improves the robustness of drusen segmentation. Gregori [30] and Iwama [31] also segmented drusen based on the distance between the abnormal RPE and the normal RPE floor. Recently, many researchers proposed several other methods [15, 32, 33].

In this section, we tackle the above challenges, and present several novel automated drusen segmentation method in SD-OCT images. Our proposed methods include: (a) Automated Drusen Segmentation and Quantification in SD-OCT Images [34], (b) An improved OCT-Derived Fundus Projection Image for Drusen Visualization [35]. In addition, we also provide a means of generating a high-quality projection image based on RPE layer estimation.

11.2.1 Automated Drusen Segmentation and Quantification in SD-OCT Images

11.2.1.1 Overview of Proposed Method

We briefly introduce the algorithm, for full detail see [34]. A flowchart of our algorithm is shown in Fig. 11.2, which comprises the following operations on the input SD-OCT image:

1. Image denoising: A modified bilateral filtering algorithm is used to reduce noise in order to facilitate the subsequent estimation of the RNFL and RPE retinal layer.
2. RNFL complex removal: The RNFL complex, defined as the region between the inner limiting membrane and the outer plexiform layer (indicated by the

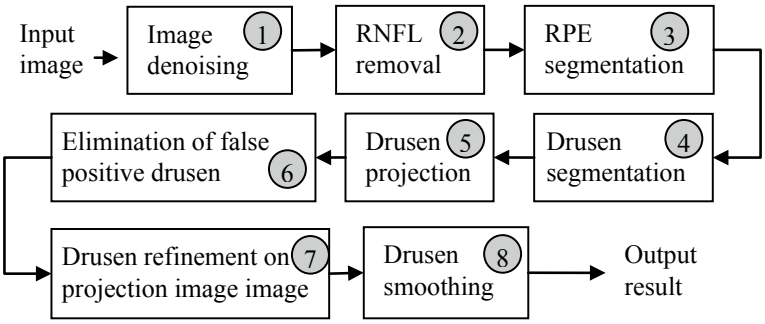

Fig. 11.2 Flowchart of the proposed algorithm

orange dotted outline in Fig. 11.3a, overlies the RPE and is removed to facilitate segmenting the RPE layer of the retina.

3. RPE segmentation: The RPE layer is extracted as a continuous structure through interpolation. In addition, the shape it would have had without drusen is estimated though a fitting procedure to interpolate its shape in areas where it is distorted by drusen.
4. Drusen segmentation: An initial segmentation of drusen is obtained from the RPE segmentation image as the areas located between the interpolated and fitted RPE shapes.
5. Drusen projection: To refine the initial drusen segmentation, an en face drusen projection image is generated on a volume of the SD-OCT image restricted to the sub-volume of the image containing the RPE and drusen segmentation.
6. Elimination of false positive drusen: Consecutive slices are evaluated to eliminate detections that are not drusen.
7. Drusen refinement: The intensity and shape information of drusen on the projection image are utilized to remove false drusen.
8. Drusen smoothing: A smoothing operation is performed in three-dimensional (3D) space to obtain the final segmentation results.

11.2.1.2 Drusen Projection Image Generation

A common method for creating 2D projection from SD-OCT datasets is summed-voxel projection (SVP) Jiao [36], in which all the pixel values in the 3D images are summed along axial lines, producing an image showing the retinal surface en face, similar to the CFP. The SVP cannot effectively reflect the alteration in the RPE layer caused by drusen [37]. To date however, the en face SVP fundus image is not ideal for drusen visualization because most drusen have been found to not be visible when projected using this technique [36]. In order to make drusen appear more clearly in fundus projection images, we present a novel projection method of the RPE layer to generate the fundus image, based on a selective volume projection, analogous

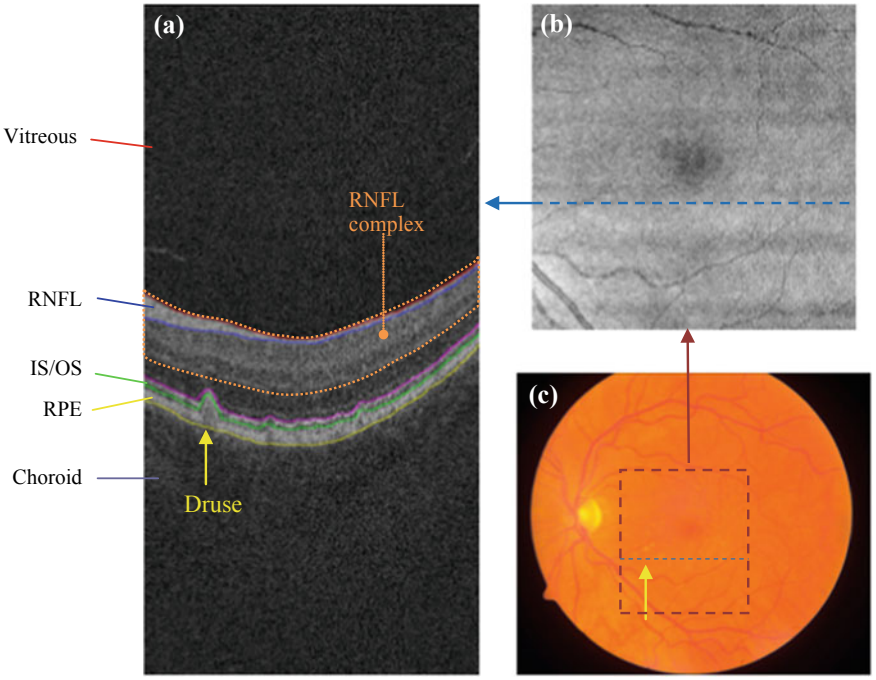

Fig. 11.3 **a** Target retinal layers of a cross-sectional SD-OCT image (B-scan). RNFL: retinal nerve fiber layer; IS/OS: photoreceptor inner/outer segments; RPE: retinal pigment epithelium. The location of a druse is indicated with a yellow arrow. The RNFL complex (defined as the region between the inner limiting membrane and outer plexiform layer) is indicated by the orange dotted region. **b** SVP image of the same eye. The dashed blue line indicates the location of the B-scan presented in **a** within the projection image. **c** Color fundus photograph of the same eye. The maroon dashed square indicates the area in the macula present in the SD-OCT scan. The dashed blue line indicates the location of the B-scan presented in **a** within the fundus photograph. The location of the druse clearly seen in (a) is indicated with a yellow arrow

to that done in Gorczynska [38]. Figure 11.4a shows an example of selection of a sub-volume in a narrow band zone between two parallel curves to isolate the RPE. The bottom red curve is the base of the normal RPE layer, and the top red curve is determined by the tallest drusen in all of B-scans. As a result, the projection region contains only the RPE layer and drusen. To further enhance visualization of drusen, the dark regions beneath the drusen are replaced with the bright pixels in the same column, which enhances visibility of the drusen in the projection. Through this approach, the larger the height of the drusen, the brighter the drusen will appear in the projection image. Figure 11.4b shows an example of drusen projection image, which is rescaled to a square by interpolation. The bright region in the central region of Fig. 11.4b corresponds to the large drusen in Fig. 11.4a, marked with the orange triangle in Fig. 11.4.

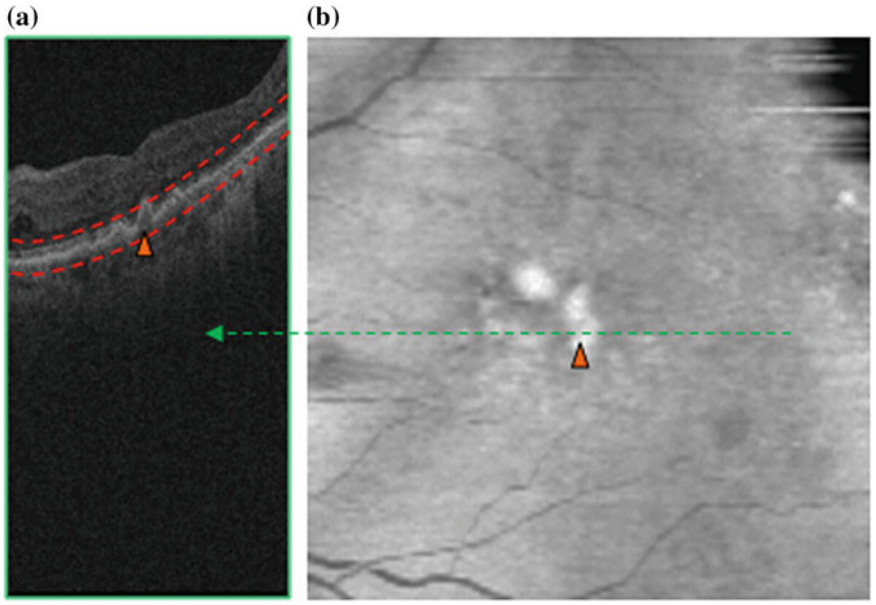

Fig. 11.4 Drusen projection image generation. **a** B-scan image for projection **b** Drusen projection image

11.2.1.3 Post-processing

Drusen are composed of irregularly-shaped globular masses and of distinct spherical entities. Based on the shape characteristics of drusen, the following three step post-processing is adopted to improve drusen segmentation precision: elimination of false positive drusen with consecutive slices, drusen refinement with projection image, and drusen smoothing.

(1) Elimination of false positive drusen. Given the density of the B-scans (128 B-scans per approximately 6 mm.), each drusen should appear in at least two consecutive B-scans with a fixed azimuthal interval (46.9 μm). Here, we assume that the minimum size of drusen in the azimuthal dimension should be larger than such interval. If a drusen was only present in one B-scan, it was removed from the projection image as a likely false positive.
(2) Drusen refinement with projection image. The primary drusen segmentation results were projected on the drusen projection image and the intensity and shape information was utilized to remove false drusen as follows. For each 4 adjacent drusen, if the difference of the average intensity of the inner and outer drusen regions (the outer regions are the background regions near drusen boundaries) is lower than a threshold (4 in this chapter), or the ratio of the width and height of the drusen is larger than a threshold (6 in this chapter), it was considered a false positive drusen and was removed.

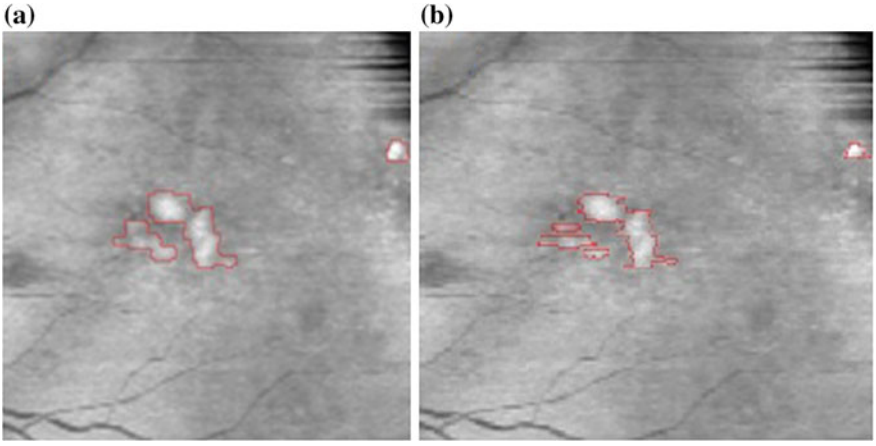

Fig. 11.5 Drusen refinement. **a** Smoothed result of (**b**). **b** Drusen refinement result based on projection image

(3) Drusen smoothing. Since drusen tend to have a smooth nature, Gaussian filtering is used to smooth the drusen segmentation results in 3D space. The drusen thickness map was smoothed with Gaussian filtering by keeping the baseline of drusen, and then the smoothed drusen thickness map was remapped into the original B-scans. Figure 11.5a is the smoothed result of Fig. 11.5b. The drusen boundaries in Fig. 11.5a become smoother, which is consistent with the drusen characteristics.

11.2.1.4 Evaluation of Drusen Quantitation

To show that quantitative features of drusen can be extracted from our automatic segmentations, and to demonstrate the potential utility of using that information as a biomarker of disease status, we performed a pilot analysis of the drusen segmentation results in one patient who had SD-OCT on six different dates. At each time point, we produced a "drusen thickness map" and a "drusen surface map" to summarize the quantitative aspects of the drusen features we extracted. We analyzed two quantitative measurements, drusen area and volume, as biomarkers of disease status, and we plotted them over time. We correlated the temporal evolution in these imaging biomarkers with the evolution of the clinical status of the patient (visual acuity). Once the variance of the manual segmentations was established, we used the same metrics to test the agreement between automated segmentations produced by our proposed method and those drawn by hand. We first compared the automated segmentation with the mean segmentation obtained from the four manual segmentations drawn by the two experts in the dataset of four eyes, taken as the gold standard. Figure 11.6 demonstrates an example of the quantitative evaluation approach by overlapping the

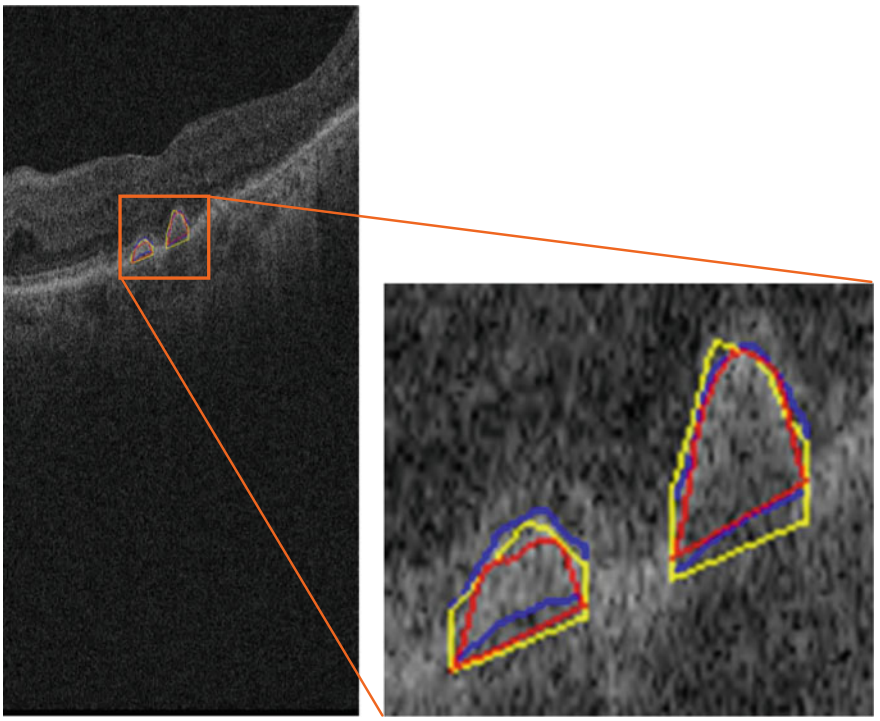

Fig. 11.6 Demonstration of the quantitative evaluation. The blue and yellow lines are the contours of two experts' gold standard, respectively. The red line represents the contour of the automatic segmentation result

manual and automatic segmentation results in a single B-scan. The automatic drusen segmentation results are marked with red line.

11.2.1.5 Drusen Segmentation Accuracy

Table 11.1 shows the segmented drusen area within-expert and between-expert agreement in terms of correlation coefficients, paired Wilcoxon test p-values and absolute drusen area difference (*ADAD*) 340 B-scans coming from 4 different eyes were considered. We noted that the boundaries of the RPE layers were often obscured due to noise and low resolution in OCT images, which produced discrepancies in the manual segmentation made by the two experts. The *ADAD* results are presented both in μm and in percentage values with respect to total segmented drusen area per b-scan. Both within-expert and between-expert evaluations present very high correlation values (between 0.97 and 0.98). The within-expert mean area differences were slightly higher for Expert B and the differences observed between the segmentations done by the two experts were higher in mean absolute value than those observed within-

Table 11.1 Within-expert and between-expert correlation coefficients (cc), paired Wilcoxon test *p*-values and mean absolute drusen area differences

Methods compared	Number of eyes/drusen present B-scans	cc	*p*-value	ADAD [μm] (mean, std)	ADAD [%] (mean, std)
Expert A_1—Expert A_2	4/340	0.97	0.0001	8.33 ± 9.50	12.38 ± 16.55
Expert B_1—Expert B_2	4/340	0.98	0.73	9.64 ± 6.53	14.41 ± 12.24
Expert$A_{1\&2}$—Expert$B_{1\&2}$	4/680	0.97	0.013	9.98 ± 9.49	14.17 ± 14.54

Table 11.2 Overlap ratio evaluation between the manual segmentations

Methods compared	Number of eyes/drusen present B-scans	Overlap ratio [%] (mean, std)
Expert A_1—Expert A_2	4/340	81.08 ± 10.46
Expert B_1—Expert B_2	4/340	80.73 ± 8.73
Expert $A_{1\&2}$—Expert $B_{1\&2}$	4/680	79.24 ± 9.65

experts in the separate sessions. Nevertheless, all of the *ADAD* measurements lay within the standard deviation of each other. The low *p*-values obtained from the paired Wilcoxon test ($p<0.05$) indicate that there were significant differences in segmented drusen area between the two readers and between the two sessions for the first reader (A). Considering the high correlation coefficients of the measurements and low average area differences, these low *p*-values may have been produced by segmentation interpretation differences from the readers, and from the same reader at different times (as we can see for Expert A), such as a reader consistently estimating the drusen areas to be slightly higher than another one.

Table 11.2 shows the within-expert and between-expert agreement in terms of overlap ratio (*OR*). The manual segmentations drawn by expert A were slightly more consistent between the two sessions that those drawn by expert B in average, and the overlapping area was slightly higher for segmentations drawn by the same expert than when comparing areas drawn by different experts. Nevertheless, all measurements lay within the standard deviation of each other.

Table 11.3 shows the agreement between the automated segmentation and the gold standard for the same dataset of 4 eyes employed in the reader agreement measurement and for the complete dataset of 143 eyes. For the smaller dataset, the correlation coefficient between automated segmentations and gold standard (mean segmentation from the 4 manual segmentations) was very high (0.97), and similar to those observed within-experts (0.97 and 0.98) and between-experts (0.97) for the same dataset. The ADAD values were also very similar to those observed for the readers and within their measured standard deviation. The standard deviation values are in the order of the mean values because the segmentation results obtained from different methods resulted very similar, both when comparing two different manual segmentations or manual and automated segmentation results. The logic behind this is that since we are measuring the differences between two segmentation results from the same cases, a minimum requirement for us to say that they are similar is that

Table 11.3 Correlation coefficients (cc), paired Wilcoxon test *p*-values and absolute drusen area differences between the automated segmentation method (Aut. Seg.) and gold standard (GS)

Methods compared	Number of eyes/drusen present B-scans	cc	*p*-value	ADAD [μm] (mean, std)	ADAD [%] (mean, std)
Aut.Seg.—GS	4/340	0.97	0.48	10.29 ± 8.9	15.70 ± 15.50
Aut.Seg.—GS	143/143	0.94	0.006	19.97 ± 14.68	23.77 ± 13.8

the 95% of those differences for the population of tested cases includes the 0 value (which would indicate that the results are exactly the same). There are still differences in the segmentation methods as indicated by the mean values, but those differences are small when compared to the difference ranges, which also include the 0 value. The similar mean and standard deviation values in the inter-reader and intra-reader agreement assessment indicates that we might expect a deviation in the differences of two manual segmentations on the same order as their mean differences, which makes sense since they are drawn in the same set of images. The similar observed ranges of mean and standard deviation differences between automated and manual segmentations indicate that the automated method thus appears to closely represent the segmentation drawn by an average user (our gold standard in this case) in the same ranges as different readers or even the same reader at different sessions would agree on their manual segmentations for the given test. For the larger dataset of 143 eyes, the differences found between the automated segmentation and gold standards (segmentation from a third reader) were higher, but they showed very high correlation and their distribution still lay within the limits described for expert agreement. The correlation between areas of automated and gold standard segmentation was also very high for both datasets, and also in the same ranges when comparing different manual segmentations. The Wilcoxon *p*-values indicate that statistical differences could not be claimed between the distribution of areas of automated segmentations and an average manual segmentation in the first dataset. However, statistical differences ($p < 0.05$) were found in the distribution when compared to manual drawings by a third expert in the second dataset. In the same way as for the inter-reader and intra-reader comparisons, considering the high correlation values, this might be due to the segmenting approach of a reader, as for a reader constantly over-estimating or under-estimating drusen borders.

Table 11.4 shows the overlap ratio (*OR*) between the automated segmentation and gold standard for the two datasets. For the dataset consisting in 4 eyes, the mean *OR* demonstrates that our method can obtain relatively high segmentation accuracy when compared to the gold standard, and its standard deviation was similar to that within and between experts. This suggests that the discrepancies in *OR* between the hand-drawn segmentations are comparable to those observed between the segmentation produced by our algorithm and gold standard. The mean *OR* observed in the dataset consisting in 143 eyes was lower but still showed sufficient overlap in the segmentations, being within the limits established by the smaller dataset.

Table 11.4 Overlap ratio evaluation between the automated segmentation method (Aut. Seg.) and gold standard (GS)

Methods compared	Number of eyes/drusen present B-scans	Overlap ratio [%] (mean, std)
Aut. Seg.—GS	4/340	76.33 ± 11.29
Aut. Seg.—GS	143/143	67.18 ± 9.14

Figure 11.7 shows two segmentation results for drusen with a convex, medium reflectivity and nonhomogeneous pattern. The regions remarked with yellow lines are the segmented drusen. The blue and red lines are the estimated RNFL boundary and RPE layer, respectively. Figure 11.7 indicates that for the most common drusen pattern, the algorithm can effectively segment the drusen. Figure 11.8 shows two segmentation results for drusen with convex, high reflectivity and homogeneous pattern. Since the reflectivity of drusen is similar with that of the RPE layer, it is difficult to segment the RPE layer correctly. Specifically, the posterior RPE border was difficult to estimate. In our algorithm, the middle axes of the RPE layer is used to find drusen. Although the convexity of the posterior RPE border is difficult to estimate, the convexity of the anterior RPE border is easy to estimate. Thus, the

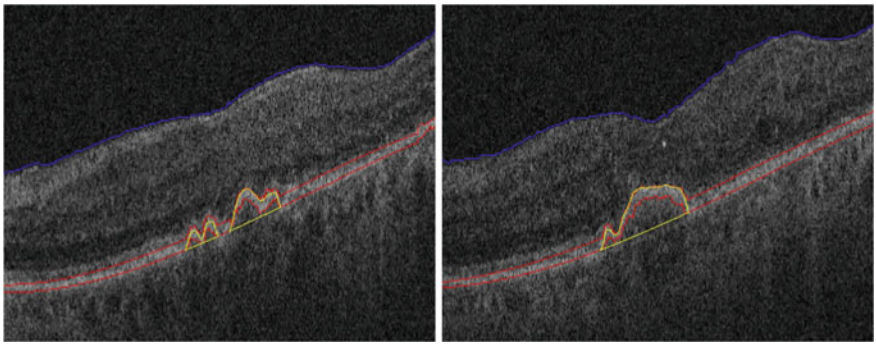

Fig. 11.7 Segmentation results for drusen with convex, medium reflectivity, nonhomogeneous pattern

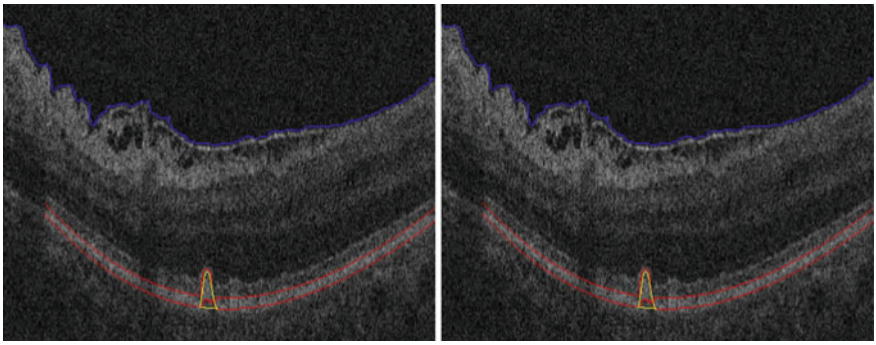

Fig. 11.8 Segmentation results for drusen with convex, high reflectivity, homogeneous pattern

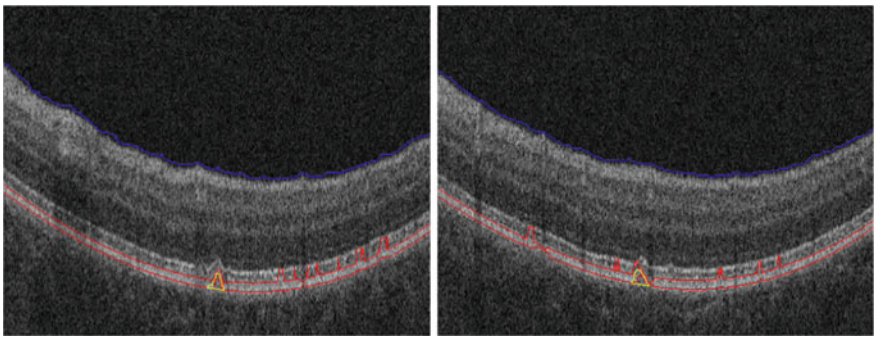

Fig. 11.9 Segmentation results for small drusen with high reflectivity IS/OS layers

middle axes of the RPE layer will be convex for the drusen with high reflectivity and a homogeneous pattern. Figure 11.9 shows two segmentation results for small drusen. For these two images, the IS/OS layers have similar reflectivity with the RPE layers, and the IS/OS layer is spatially close to the RPE layer. From Fig. 11.9, it can be seen that although the RPE layer estimation (the red lines) is not very accurate due to the confounding influence of the IS/OS layers, our algorithm can still obtain good segmentation results. Figure 11.10 shows that even when estimation of the boundary

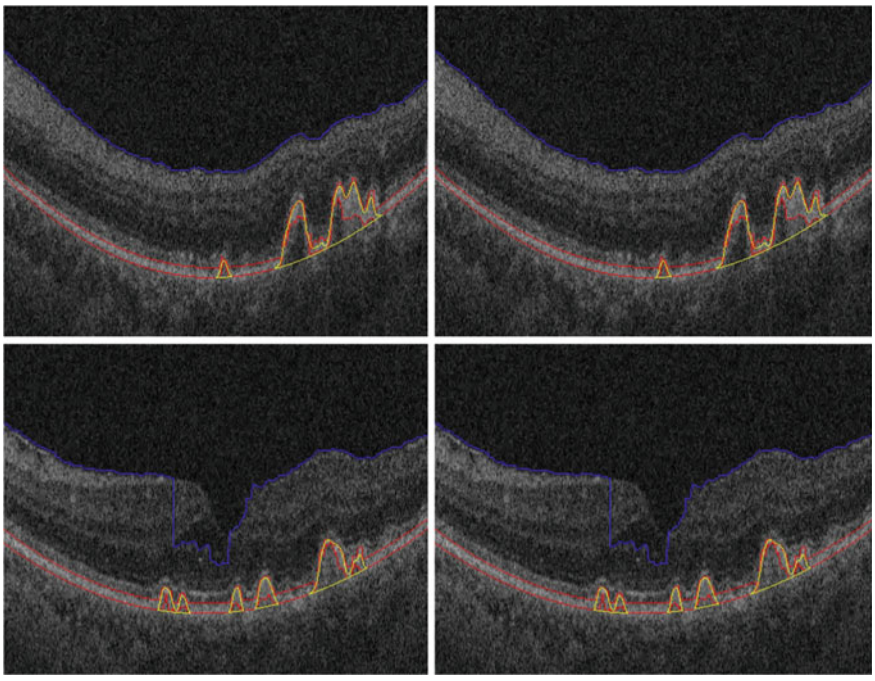

Fig. 11.10 Drusen segmentation results of one patient

of the RNFL is not correct, the algorithm is effective. This is one of the reasons that RNFL removal is part of the image processing pipeline.

11.2.1.6 Conclusions

We have developed a novel automated drusen segmentation algorithm for SD-OCT images, which incorporates the 3D spatial information in retinal structures and information in projection images of drusen. Experimental results demonstrated that the algorithm was able to effectively segment different patterns of drusen. The qualitative features we extract from drusen may be clinically useful for evaluating the progress of these lesions. The algorithm does have limitations in that drusen at the edges of the images and small drusen can be missed. Future refinement and development of this algorithm will be pursued in an attempt to improve detection and segmentation of these drusen.

We have described a method for automatic segmentation of drusen on SD-OCT images, and it addresses the several unsolved challenges emerging from the prior work: (1) obscuration by drusen of portions of the image needed for accurate estimation of RPE layers, (2) noise in low-SNR OCT images which challenges accurate segmentation of the RPE, (3) drusen with reflectivity similar with that of the RPE layer which makes it difficult to segment the RPE layer correctly, and (4) the IS/OS layers have similar reflectivity as RPE.

Our method, which estimates the RPE layer through interpolation and fitting procedures, overcomes these challenges to some degree. By finding the middle axes of the RPE layer, our method is less sensitive to regional areas of obscuration of RPE by drusen. The method includes a bilateral filtering denoising step which addresses the challenge of reliably detecting the RPE. Although bilateral filtering might not be optimal for speckle denoising in SD-OCT, it has a relatively low time complexity and acceptable performance for the needs of our segmentation algorithm. It is also known that a pre-processing noise filtering step can increase SNR and potentially the resulting accuracy of the segmentations, but there is a trade-off in the degrading of the spatial resolution that could also produce the opposite effect. In the future, we plan on investigating the effect of adopting more effective denoising methods to improve the performance of our method. The method can also detect drusen in cases where drusen and RPE have similar reflectivity; in such cases, the IS/OS layer is similar reflectivity to RPE and thus difficult to separate from RPE. Our algorithm can still obtain relatively good segmentation results. The method includes a pre-processing step to remove the RNFL, so even if the boundary of the RNFL is erroneously estimated, the drusen segmentation method can be successful.

A novel aspect of the method is inclusion of analysis of the drusen in an en face projection to eliminate false positive drusen. Not only is this useful to improve the accuracy of the method, it provides a useful visualization to physicians, similar to the CFP view with which they are familiar (Fig. 11.5), and it also provides a means of computing additional imaging biomarkers for drusen evaluation, such as drusen

area. In the future, we could calculate other drusen features from these images, such as shape.

11.2.2 An Improved OCT-Derived Fundus Projection Image for Drusen Visualization

Currently, the gold standard for visualizing and measuring drusen in non-neovascular AMD as well as for visualizing and assessing GA is the evaluation of color fundus photographs (CFPs). While the total drusen area and maximum drusen size are estimated by visual inspection of CFPs, with comparison to a set of standard circles [39]. So, it is a big challenge to reliably locate drusen against the changing background pigments of the macula, RPE, and choroid [40, 41]. Moreover, it is difficult to make reproducible quantitative measurements of drusen in CFPs, and such measurements could be better indicators of disease progression than qualitative visual assessments.

Since SD-OCT images provide 3D data, and the structures visualized in the volume can be projected into 2D, and the current method for creating 2D projections from SD-OCT datasets is the summed-voxel projection (SVP), in which all pixel values in the 3D images are summed along axial lines, producing an image showing the retinal surface en face, similar to the CFP [36]. The SVP fundus image is not good for drusen visualization because most drusen are not visible when projected using this method [36]. Stopa [37] overcame some of these problems by locating pathologic retinal features with color marking in each OCT image before the image volume was collapsed along the depth axis to produce the SVP. Current technique recently introduced into OCT imaging devices is the "slab SVP", is a semi-automated method to restrict the SVP to a sub-volume of the retina in vicinity of the RPE layer (Carl Zeiss Meditch, Inc., unpublished); in this method, user interaction to annotate the image to localize the RPE is required. Using manually annotating pathologic features in a stack of SD-OCT images, for large studies, can be time-consuming and tiring. More so, the SVP image produced by the proposed methods of Stopa et al. only gives location information, but no information about drusen thickness, which is useful for characterizing drusen. Georczynska [38] proposed a better method of generating projection OCT fundus images by selectively summing different retinal depth levels, which enhanced contrast and visualized outer retinal pathology not visible with standard fundus imaging or OCT fundus imaging. In this method, drusen were separated into several projected fundus images summed at different retinal depth levels, and could not be directly visualized.

In this section, we analyze the reasons for poor drusen visualization in SVP fundus images, and present a new, automated projection method combined with image processing of drusen to generate en face fundus images from SD-OCT for enhanced drusen visualization [35].

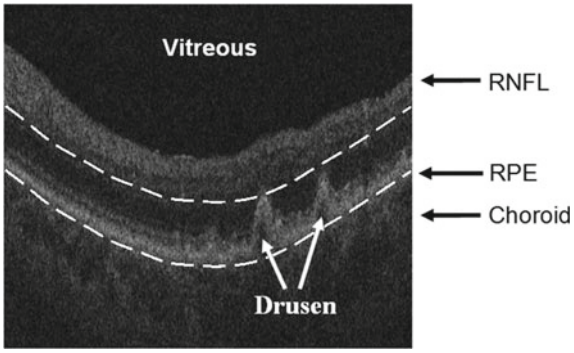

Fig. 11.11 Restricting the OCT image data for generating a fundus projection (the RSVP) to the vicinity of the RPE layer. The bottom white curve is the baseline of the normal RPE layer. The top white curve is determined by the largest drusen height in any B-scan. The RSVP thus excludes extraneous portions of the retina that may contain noise to the projection, such as those caused by the vitreous, retinal nerve fiber layer, and choroid

11.2.2.1 Generation of a Fundus Projection Image Based on RPE Layer

We proposed a novel projection method based on (1) creating a fundus image from image data only in close proximity to the RPE layer, and (2) complementing the projection with image processing methods that enhanced the brightness of drusen and included information related to drusen height. The SVP projection is restricted to a sub-volume of the SD-OCT dataset, which we named restricted SVP (RSVP). We automatically segment the pixels corresponding to this sub-volume from the SD-OCT data.

In Fig. 11.11, we demonstrate the projection of sub-volume, which is the narrow band-like zone between two the white parallel curves. This projection region contains only the RPE layers and drusen. By restricting the volume of retina visualized to only that portion in close proximity to the RPE, the projection includes a minimum of extraneous retinal structure and drusen visualization is maximally enhanced. In addition, we applied image processing to brighten the dark pixels beneath the drusen in each axial column, replacing the original dark pixels with bright pixels. Since the RSVP is based on the sum of the pixel values in each axial column, so the larger the height of the drusen, the brighter the drusen in the RSVP image area.

11.2.2.2 Extraction of RPE Layer

Many OCT automated segmentation methods have been described that use information about normal retinal layers and do not consider the presence of drusen [42–44]. Therefore, they may not be suitable for drusen segmentation with the purpose of generating RSVP images. We present a method to determine the location of RPE, similar to the one presented in [26], but also incorporate the presence of drusen

into account. We first smoothen the OCT images with bilateral filtering [45] and the location of the RNFL was estimated by detecting the margin of the vitreous with a threshold. The initial estimate of the RPE layer was obtained through the highly reflective and locally connected pixels spatially located below the RNFL. We applied a morphological opening operation (erosion followed by dilation) with a kernel consisting of a disk of 2 μm radius was performed on this initial estimate in order to remove small isolated regions from the RPE estimate that are mainly artifacts due to noise present in SD-OCT images, without removing possible drusen larger than this considered size (2 μm). We then adopted a maximum axial thickness constrain of 20 μm for the RPE estimate, so that the influence of bright pixels wrongly detected as part of the RPE but that may be mainly due to other RPE abnormalities such as GA is minimal. Meanwhile, A-scans in the foreground of this estimate that had a larger number of pixels than this threshold were removed from the initial estimation and their RPE location was determined by bilinear interpolation. We estimated two versions of the RPE: (1) the potentially unhealthy (abnormal) RPE in which drusen may be present was obtained by bilinear interpolation of the initial estimate, and (2) a healthy (normal) and drusen-free version of the RPE layer was obtained by fitting the estimated layer with a 3rd polynomial, an operation that would "smooth-out" any drusen. The areas located between the fitted normal and interpolated RPE layers were marked as drusen.

The baseline of the projection region used for the RSVP generation was the fitted lower boundary of the normal RPE layer, while the top boundary of the projection region was determined by displacing the fitted normal RPE layer anteriorly the same distance as the largest drusen peak found in the cube (Fig. 11.11). This selected sub-volume of the OCT excludes structures in the retina that could interrupt with visualization of drusen, especially the RNFL and choroid (Fig. 11.30).

11.2.2.3 Filling in the Dark Regions of Drusen

For each A-scan of the SD-OCT images, we obtained the maximum intensity pixel in the interpolated RPE layer and replaced the values of the pixels underneath it with this maximum intensity value. After the filling process, dark areas of drusen become bright. Some dark regions of the RPE also become brighter, but the change in intensity of RPE was minimal compared to that of drusen, since in the RSVP images we only considered the projection of the pixels between a narrow region using the fitted drusen-absent RPE as baseline (as shown in Fig. 11.11).

11.2.2.4 Algorithm Evaluation

To effectively evaluate the RSVP approach to drusen segmentation, 46 3D SD-OCT retinal images from eight patients were analyzed. Each of the 3D OCT images set was acquired over a 6×6 mm area (corresponding to 512×128 pixels) with a 1024-pixel axial resolution on a commercial SD-OCT device (CirrusOCT; Carl Zeiss Meditec,

Inc., Dublin, CA). We performed both a qualitative and quantitative evaluations on the dataset. To perform the qualitative evaluation, we compared both the conventional SVP and our RSVP images qualitatively for the 46 OCT scans in each of the eight patients. To improve the visualization of conventional SVP images, we also superimposed lesion markings which we derived from applying the techniques in [36] to the images. We also produced SVP projection fundus images using Gorczynska's method [38] and they were compared with RSVP images obtained from the same datasets. Some of the patients also had color fundus photographs (CFP), which served as the gold standard for visualizing the retina in the qualitative assessment. Both drusen and GA were visualized on CFP. To qualitatively assess drusen visualization, we manually outlined the drusen and GA lesions in the CFP, SVP and RSVP of these patients. We are only displaying the qualitative results of four scans from four different patients of the total set of 46 SD-OCT scans evaluated, due to the chapter length limitations. These displayed four scans are a representative example of the results obtained throughout the whole dataset.

To quantitatively assess drusen visualization in SVP and RSVP images, 4 scans from three patients were reviewed by two expert OCT readers independently. Each independent reader marked drusen in the OCT B-scans by hand as previously described [37]. Then, each reader independently marked every image two times in two different sessions to enable assessment of intra-reader variation.

The gold standard for our quantitative evaluation was obtained by collapsing the white bars along the depth axis to produce an *en face* drusen location map (known as a "marking image"). For each of the image scan, the two drusen marking images made per scan by each reader were combined using their intersection to produce a single outline per reader per image:

$$R = R_1 \cap R_2 \tag{11.1}$$

where R_1 and R_2 are the drusen marking images of the same scan, that are made at two different sessions by each reader. The combined reader results were produced by the same interpolation operation between the two reader segmentations for each drusen outline. We also outlined the drusen by hand in the corresponding SVP and RSVP images by each reader, as shown in Fig. 11.14. Then, the outlines produced by SVP and RSVP were then compared quantitatively to the images marked by the readers (the gold standard). In addition, the boundaries of drusen are very blurry in SVP and RSVP images, making the outlines not precise. Therefore, instead of pixel by pixel classification, we used an overlap ratio of the number of visualized drusen as the metric to quantitatively evaluate drusen visualization in each technique:

$$overlap\_ratio = \frac{\#co\_drusen}{\#mark\_drusen} \tag{11.2}$$

where '$\#\ co\_drusen$' denotes the number of drusen outlined both in the gold standard marked image and in the SVP or RSVP images in which outlined areas intersect (depending which technique we were evaluating), and '$\#mark\_drusen$' denotes the

number of drusen in the gold standard-marked image. This metric calculated the accuracy of each technique in identifying drusen present in the cube: if most of the drusen outlined in the gold standard marked images could also be visualized in the *en face* image, the overlap ratio would be closer to 1. However, as more drusen are "missed" in the *en face* images, this overlap ratio approached 0.

11.2.2.5 Results

Figure 11.12shows the SVP fundus image obtained from the same scan with an overlay of **white** markings derived based on other published methods [37].

For every portion of the RPE that is not visualized in an OCT scan, a low pixel intensity was used to fill the incomplete information in the RPE-based fundus image. As a result, these areas appeared dark on the RSVP image. Figure 11.13 shows a comparison of the OCT image projection methods. Figure 11.13a and b are projection results with the conventional SVP and the RSVP method, respectively. Figure 11.13c–f are projection fundus images obtained by processing the OCT data with Gorczynska's method [38], which correspond to four levels at different anatomical layers: outer nuclear layer, photoreceptor outer segment, RPE, and choroid, respectively. Figure 11.13g–i show three B-scans corresponding to the dashed red, blue and yellow lines in the fundus images, respectively. The dark shadow region marked with red triangle (Fig. 11.13g) corresponds to the retinal vessel in the fundus images (Fig. 11.13a–f).

The image contrast of the vessel seen in Fig. 11.13b, was higher than that in Fig. 11.13a. The green and blue triangles show drusen with high and low reflectivity.

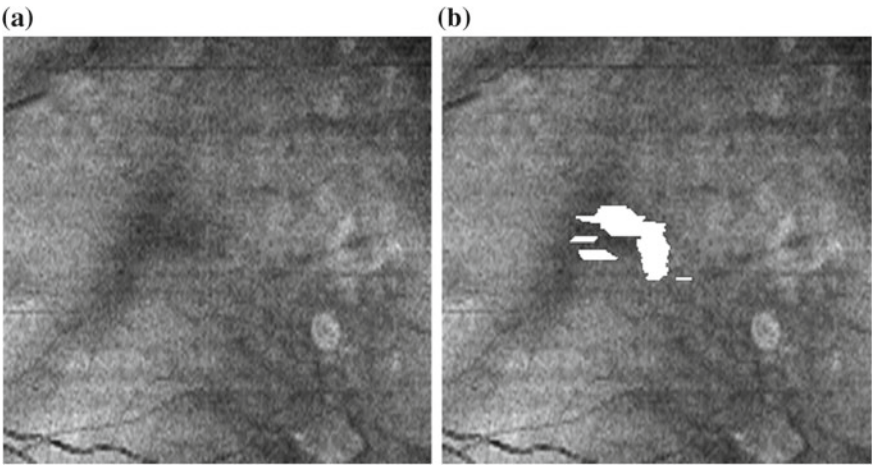

Fig. 11.12 The SVP fundus image (A) with an overlay of white marking drusen (B) obtained from the method suggested by Stopa et al. [62]

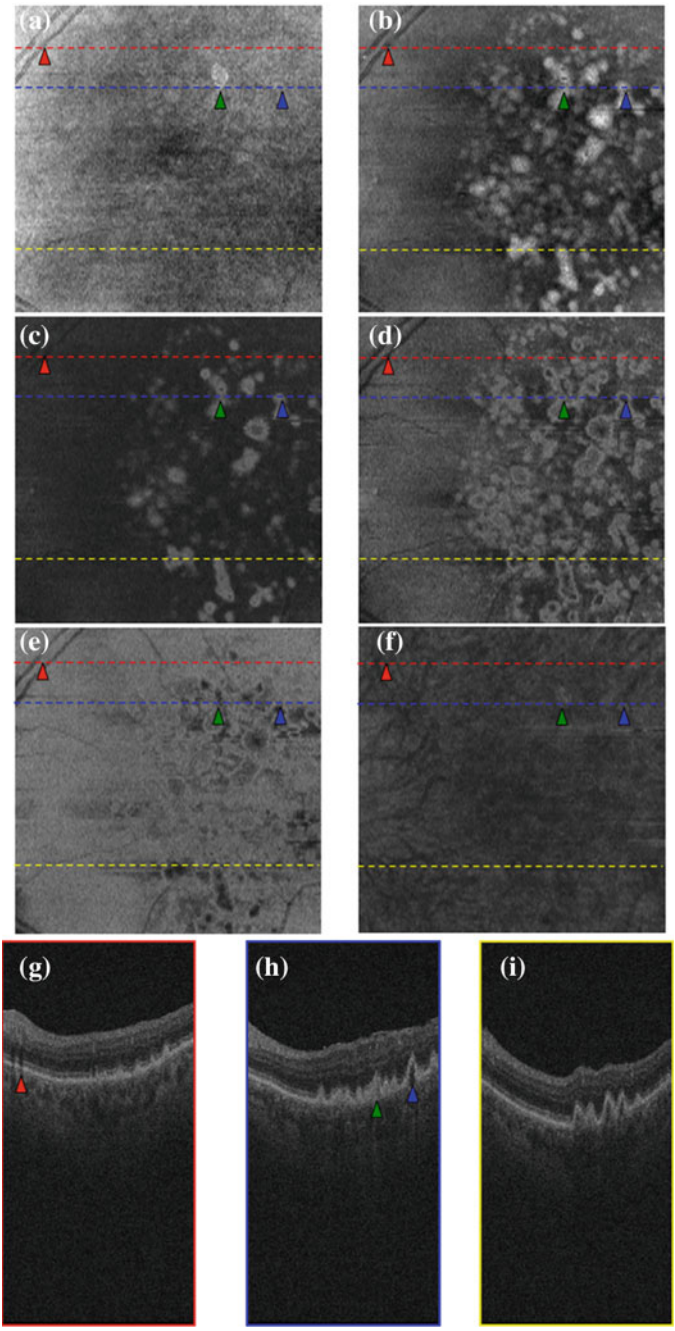
(a)
(b)
(c)
(d)
(e)
(f)
(g)
(h)
(i)

◀**Fig. 11.13** Comparison of OCT retinal image projections. SVP fundus image (**a**). RSVP image (**b**). Projection fundus images (**c**, **d**, **e**, **f**) using Gorczynska's method [38] which are the outer nuclear layer level, photoreceptor outer segment level, RPE level, and choroid level, respectively. **g**, **h**, and **i** are three B-scans corresponding to the red, blue and yellow lines in the projection images (**a**–**f**). The red triangle shows a blood vessel in corresponding images and the green and blue triangles show drusen with high and low reflectivity, respectively

It can be seen that both drusen can be more clearly identified in the RSVP image than in any other individual image.

Figure 11.14 shows drusen boundaries manually outlined by referring to B-scans. Figure 11.14g-i show three B-scans corresponding to the red, blue and yellow lines in Fig. 11.37d–f, respectively. Drusen and GA were easily differentiated in B-scans. The blue and green outlines represent the larger drusen and GA, respectively. Red, blue and yellow triangles delineate corresponding locations of GA in the CFP (14D), SVP (14E), RSVP (14F), and B-scan images (14G-I). GA extent can be identified in the SVP image (14E). However, drusen appear more difficult to visualize with SVP. From Fig. 11.14, it can be observed that nearly all drusen that were outlined on the CFP were also observed in the RSVP image.

For reader 1 and 2, the mean intra-reader overlap ratio measured between two segmentation sessions of the B-scans were 67.04 and 90.88%. While the mean inter-reader overlap ratio measured between the B-scan segmentations of two different readers was 65.14%. Table 11.1 shows the drusen overlap ratio for a method (SVP or RSVP) and the gold standard (B-scan segmentation) in four OCT scans from three different patients. The overlap ratio is evidently higher for RSVP than with SVP. Most of the drusen were not effectively visualized with SVP images; as such, they were completely absent in scans 3 and 4. Most of the drusen were clearly visible in the RSVP images. The "Readers 1 and 2" column corresponds to the evaluation of the combined segmentations of both readers.

11.2.2.6 Discussion

The ability of RSVP images and their quality to visualize retinal drusen were superior to those known conventional SVP images. More so, GA is not visualized with the RSVP method because GA occurs beneath the RPE layers and is not included in the projection images, thereby eliminating a confounding factor for visualizing drusen that is present in conventional SVP images. The RSVP method also gives more accurate characterization of drusen thickness than the color marking method [37] that only defines the location of drusen. The conventional SVP was not able to adequately visualize drusen, but the Gorczynska's method [38] was able to display drusen in fundus images. Hence, drusen were divided up into several fundus images at different anatomic levels. The RSVP method enhanced the visualization of drusen by utilizing a comprehensive single image. In addition, blood vessel visualization was also more effective with the RSVP method because the projected region was

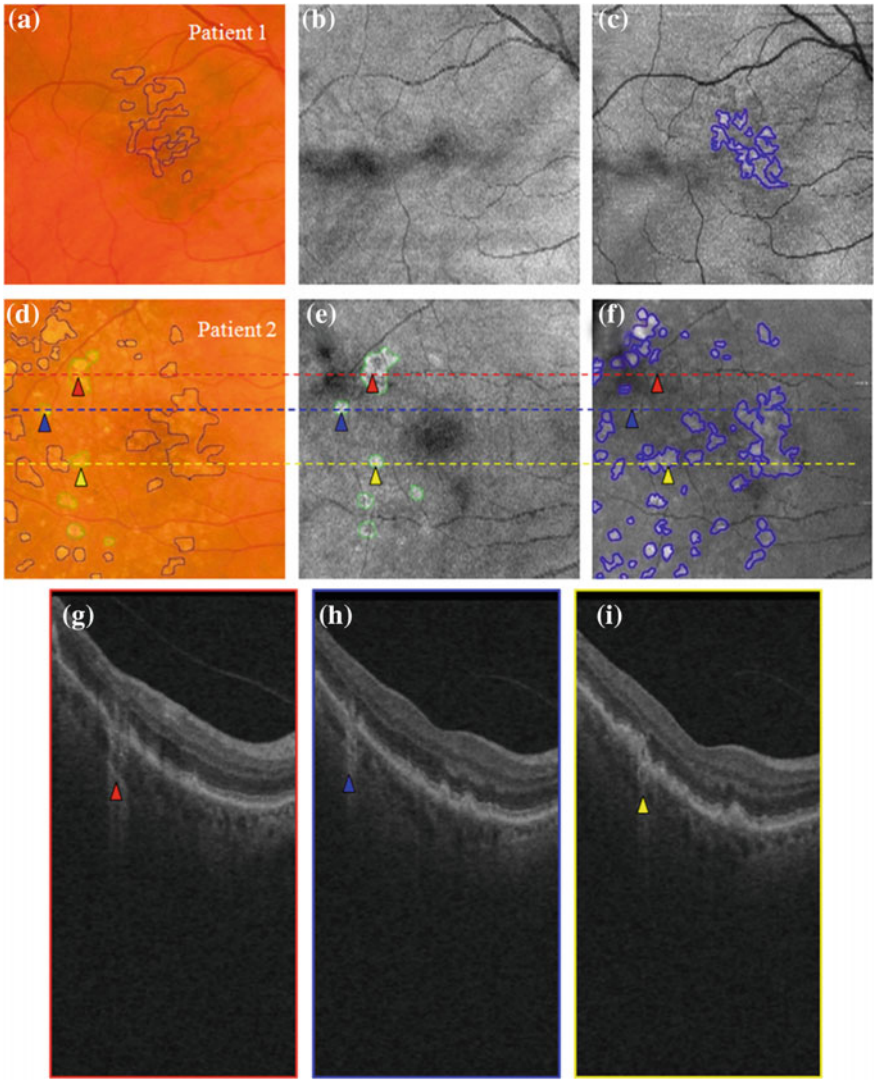

Fig. 11.14 Drusen outlines on CFP (**a**, **d**), SVP (**b**, **e**) and RSVP (**c**, **f**). Blue lines demarcate drusen and green lines outline GA. Three B-scans (**g**–**i**) correspond to the three lines in (**d**–**f**). Red, blue and yellow triangles delineate corresponding locations of GA in the CFP (**d**), SVP (**e**), RSVP (**f**), and B-scan images (**g**–**i**)

restricted to the narrow RPE neighborhood, reducing the effects of noise and the RNFL.

Also the RSVP method was efficient for different types and morphologies of drusen. Due to the pixel filling step in the RSVP method, drusen with low or medium reflectivity (such as the drusen marked with the blue triangle in Fig. 11.13), was able to be visualized. The dark-region filling step had less influence on the visibility on drusen with high reflectivity (such as the drusen marked with the green triangle in Fig. 11.13 in the RSVP images since they were already highly visible by virtue of their inherent pixel brightness and high reflectivity. Alternatively, all of the drusen present were able to be visualized in a single RSVP image, thereby allowing for easier identification of drusen. Some related work has been done in producing a "slab" SVP of the retina to improve visualization of drusen (Cirrus SD-OCT, Carl Zeiss Meditec, Inc, Software version 6.0.1) which is similar with the Georczynska's method [43]. To our knowledge there have been no articles on this method published in the peer-reviewed literature; however, based on our understanding of the method in the Cirrus system, the RSVP method is different, new and novel in that (1) it is fully automated (the Cirrus software requires input from the operator to specify the "slab" to be processed), (2) the "slab" method includes the retina from the RNFL to the RPE, whereas the RSVP method includes a highly restricted volume of the OCT scan in proximity to the RPE where drusen reside; thus, one expects that drusen visualization in the RSVP approach will be degraded less than with the "slab" method, and (3) the RSVP method incorporates image processing to enhance the conspicuity of drusen by filling in the dark regions within drusen with bright pixels. With respect to the qualitative and quantitative analysis above, the RSVP method is more effective for drusen visualization than the SVP method, and more convenient than the manual marking method [37] and the selective depth level method [38] which can be important for ophthalmologists to directly and rapidly assess the macula of patients with non-exudative age-related macular degeneration. Our future work will be to undertake a comparison of the RSVP method to the manual "slab" method.

Some of the limitations of the present study will be discuss below. Because the filling of the dark region beneath drusen and extraction of the RPE layer and are based on automatic algorithms, errors may occur in the RPE-based fundus image. For instance, the red circled regions in Fig. 11.36 show areas which are not actual drusen, but rather areas caused by the incorrect extraction of the RPE layer. Till now, these errors are minimized or constitute to no affect on drusen visualization. Another limitation is that filling the region under drusen with bright pixels may inadvertently fill (and therefore obscure) small, focal pigment epithelial detachments (PEDs), incorrectly characterizing them as drusen. Although this did not occur during this research, the automated algorithm used will be modified in future work to recognize the relatively dark areas under PEDs (as opposed to brighter areas contained in drusen) and exclude such regions from the filling-in process, thereby avoiding this potential problem. The last limitation was that the overlap ratio with the gold standard was imperfect, being derived from two readers. An accurate gold standard would be based on histological slides, which would be very difficult to obtain. More so, the quantity of scans and readers we included in our quantitative evaluation was relatively small. Since each reader needed to review many individual B-scans for drusen in each case, it would have been too labor intensive and time consuming to manually segment many cases.

As such, with the high differences in overlap radio were so great between SVP and RSVP (as opposed to the inter-reader difference), the RSVP method was concluded to be superior when compared to conventional SVP.

In conclusion, we developed a new method to improve visualization of drusen on an RPE-based projection of 3D OCT retinal images. This method uses automated RPE segmentation, drusen segmentation, and image post-processing to enhance the conspicuity of drusen on the projection image and to minimize the amount of extraneous retinal tissue contributing to the projection. Using quantitative evaluation analysis, by comparing RSVP and conventional SVP images against a gold standard, the RSVP method was evidently more effective for drusen visualization, which may be useful to ophthalmologists in directly and rapidly assessing the macula of patients who have non-exudative age-related macular degeneration.

11.3 Geographic Atrophy Segmentation and Visualization

Several semi-automatic and automatic GA segmentation methods [45, 46] have been proposed for FAF images. A region-growing method was proposed by Deckert [47], where separate GA regions needed to be manually seeded to be included in the segmentation. Lee [48] adopted a level set model, and proposed a hybrid approach by identifying hypo-fluorescence GA regions from other interfering vessel structures in the FAF images [49] and an interactive segmentation approach by using the watershed transform algorithm [50]. Sayegh [51] evaluated SD-OCT for grading GA compared with FAF images, and concluded that SD-OCT is an appropriate imaging modality for evaluating the extent of GA lesions. Chiu [52] used graph theory and dynamic programming to segment retina layers in eyes with GA and drusen. Schütze [53] suggests that the current available automated segmentation methods are limited in their ability to accurately assess retinal layer thickness and are thus not accurate in detecting GA. At present, if quantitative assessment of GA in SD-OCT images is desired, it needs to be performed by an expert who manually circumscribes the GA lesions in the B-scan images (the primary output from an SD-OCT device, comprising 2D contiguous slices through a volumetric cube of the retina), and subsequently projecting the segmentations onto an en face image to show the extent of GA across the retinal surface—a similar view to that seen in FAF images. Each SD-OCT volumetric image dataset generally contains 128 or 200 B-scan images (for CirrusOCT (Carl Zeiss Meditec, Inc., Dublin, CA)). Since this manual circumscription of GA lesions in the B-scans is very time-consuming, it is not routinely performed in clinical practice. Other methods are also proposed recently by researchers [54–56].

This section presents two novel GA segmentation and two visualization algorithms for SD-OCT images, namely; (a) Semi-automatic geographic atrophy segmentation for SD-OCT images [57], (b) Automated GA segmentation for SD-OCT images using CVLSF model [58], (c) Restricted summed-area projection for geographic atrophy visualization in SD-OCT images [59] and (d) A false color fusion strategy for drusen and GA visualization in OCT images [60].

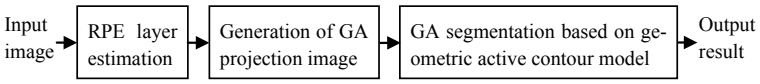

Fig. 11.15 Flowchart of the proposed algorithm

11.3.1 Semi-automatic Geographic Atrophy Segmentation for SD-OCT Images

Our semi-automatic approach starts with the computation of a sub-volume of the retina from the three-dimensional (3D) SD-OCT dataset which enhances detection of GA (rather than simply segmenting and evaluating just the RPE). In addition, we generate a two-dimensional (2D) en face projection of the retina from that sub-volume, similar in appearance to FAF images, in order to visualize the extent of GA. Finally, we segment the en face projection to quantify the extent of GA.

11.3.1.1 Overview of the Method

The flowchart of the semi-automatic algorithm is presented in Fig. 11.15, which comprises of three steps: (1) For each B-scan, the RPE layer is segmented automatically, and from this, a sub-volume of the retina in the SD-OCT cube is extracted which facilitates generating a projection image with minimal noise where possible GA lesions reside. This sub-volume is restricted to a region beneath the RPE layer containing the choroid, which is the site where abnormal high reflections due to the presence of GA and RPE thinning can be observed in OCT images. (2) An en face GA projection image is generated from the SD-OCT image sub-volume. (3) A geometric active contour model is adopted to segment GA detected in this projection image, and this contour is used to calculate the area (extent) of GA lesions. We propose an active contour model as a GA segmentation tool on en face projection images with enhanced GA visualization, which are generated from the three dimensional SD-OCT sub-volume data. These planar images are constructed by projecting those voxels contained in a restricted volume within the choroid region in the axial direction along each A-scan.

11.3.1.2 RPE Layer Segmentation

Numerous researchers have presented several automatic retinal layers segmentation methods in SD-OCT [42–44]. These methods are based on normal retinal layers, and do not consider the possible presence of GA. Thus, they are not ideal for the segmentation of the RPE layers containing GA and tend to fail when GA in present. We adopted a simplified RPE segmentation method [34] that takes into account the possible presence of GA. As a first step, the SD-OCT retinal images are smoothed

with bilateral filtering [61]. The location of the retinal nerve fiber layer (RNFL) is estimated by detecting the upper vitreous region. The purpose of detecting the RNFL layer is to facilitate segmenting the RPE layer. The reflectivity of the vitreous region is usually similar throughout the B-scans in an OCT cube, and thus a constant threshold can be used to extract this background region, which helps identify the contour of the surface of the RNFL. The bottom boundary of the vitreous region is taken as the location of the inner limiting membrane and inner boundary of the RNFL layer.

RPE layer can be identified in SD-OCT retinal images by its bright pixel values, as shown in Fig. 11.16. Thus, intensity-based methods can be useful to extract it. In addition, the healthy RPE has an approximately constant thickness (20 μm). Based on this information and the histogram statistics of the image pixels underneath the segmented RNFL (outside vitreous region), a threshold can be determined, which separates the bright RPE region from the darker background to produce a binary image forming an initial RPE estimation. A narrow band with a radius 20 μm (determined by approximate mean RPE thickness) is generated and the regions in the initial estimation not connected with this band are later removed. The RPE layer segmentation is then further refined by removing small selected regions (regions containing less than 150 pixels). To ensure that the RPE is a continuous linear structure, missing pixels between selected regions are also interpolated. Finally, the middle axis of the resulting RPE segmentation is computed for each A-scan (i.e., the individual axial lines forming a B-scan) which produces the final RPE segmentation. Further details are explained in [57].

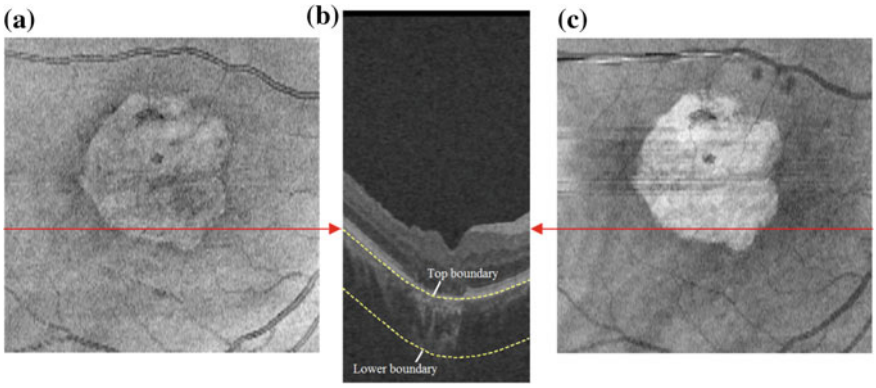

Fig. 11.16 **a** and **c**: SVP and RSVP projection for visualizing GA lesions. The red lines correspond to the cross section of retina visualized in the B-scan shown (**b**). The top boundary and the lower boundary of the projection sub-volume are marked with two parallel yellow dash lines in (**b**)

11.3.1.3 Generation of GA Projection Image

A common method for creating a 2D projection from SD-OCT volumetric datasets is the summed-voxel projection (SVP) [36], in which all the voxel values in the 3D data are summed along the axial A-scan lines in the B-scans, producing an image showing the retinal surface en face, similar to color fundus photographs (CFPs) and FAF images. However, the en face SVP fundus image is not ideal for GA visualization due to the confounding influence of highly reflective retinal layers above and below GA lesions in the retina (in particular the RNFL and RPE layers) which obscure GA lesions. The commercial software on the Cirrus HD-OCT (version 6.0) provides a sub-RPE slab function [62]. The sub-RPE slab is formed by axially projecting only the OCT image data from a region below the contour of the RPE fit. Our projection method, which is also derived by restricting the sum of the voxel values to the sub-volume beneath the segmented RPE layer, where the choroid resides and where the high reflections indicating GA will be seen, improves the traditional SVP image in terms of GA visualization. The lower boundary of the sub-volume is parallel to the top boundary (RPE layer), where the parallel distance is equal to the minimum distance between the end of the cube and the segmented RPE layer. The average intensity of the sub-volume in the axial direction is taken as the intensity value of the GA projection image. We call this the restricted summed-voxel projection (RSVP).

Figure 11.16 shows an example, comparing the traditional SVP projection [36] and the RSVP projection in a patient with GA. Figure 11.3 shows that the contrast of GA in the RSVP image is higher than in the SVP image, which can improve the performance of a computerized GA segmentation method. On the other hand, this process can introduce aberrant bright signals (e.g., the bright spots near the upper blood vessels in Fig. 11.16), caused by an inaccurate RPE layer segmentation. In practice, this did not negatively impact our results (see the evaluation of our GA segmentation method below).

11.3.1.4 GA Segmentation Based on Geometric Active Contour Model

For derivation of the shape and size of GA lesions, we used geometric active contour model for the segmentation of the GA lesions on the RSVP images. These images were denoised using bilateral filtering [45] as a preliminary step to reduce the influence of noise on the segmentations. Geometric active contour (GAC) models were simultaneously proposed by Caselles [63] and by Malladi [64], introduced as an alternative to parametric deformable models and as a way to overcome their limitations. GAC models are based on the theory of curve evolution and geometric flows, and implemented using the level-sets based numerical algorithm. The basic idea of these models is to transform a planar curve movement track into a three-dimensional curved surface movement track, which has the advantage of being able to handle the change of topological structure easily. During the evolution of traditional level set methods, re-initialization is necessary to keep the evolving level set function close to a signed distance function. In order to eliminate the need of the costly re-initialization

procedure, Li [65] presented a new formulation that forces the level set function to be close to a signed distance function. The formulation proposed is:

$$E(\phi) = \mu P(\phi) + E_m(\phi), \tag{11.3}$$

where

$$P(\phi) = \frac{1}{2}\int_{\Omega} (|\nabla\phi| - 1)^2 dxdy. \tag{11.4}$$

For full detail of our approach see [58].

11.3.1.5 Qualitative Evaluation

The first dataset consisted of 55 longitudinal SD-OCT cube scans from twelve eyes in eight patients with GA (acquired with the CirrusOCT device, Carl Zeiss Meditec, Inc., Dublin, CA.). Each cube consisted of $512 \times 128 \times 1024$ voxels corresponding to a $6 \times 6 \times 2$ mm^3 volume centered at the macular region of the retina in the lateral, azimuthal and axial directions, respectively). The second dataset consisted in 56 SD-OCT cube scans from 56 eyes in 56 patients with GA (acquired with the CirrusOCT device). Each cube consisted of $200 \times 200 \times 1024$ voxels corresponding to a $6 \times 6 \times 2$ mm^3 volume centered at the macular region of the retina in the lateral, azimuthal and axial directions, respectively). Figures 11.17 and 11.18 show the GA segmentation results for two different patients with GA from the first dataset who had multiple SD-OCT studies over the course of their disease.

11.3.1.6 Quantitative Evaluation: Our Method Versus Expert Graders

We evaluated the variability observed in the GA segmentations by different graders (inter-observer agreement) and by the same grader at different sessions (intra-observer agreement) in the SD-OCT RSVP images using the first scan dataset. Figure 11.16 indicates that the contrast for the visualization of GA in RSVP images is better than that in SVP images. The results from this evaluation are summarized in Table 11.5, where A_1 represents the segmentations of the first grader in the first session, A_2 is first grader in the second session, B_1 is the second grader in the first session and B_2 is the second grader in the second session.

11.3.1.7 Conclusions

This section presents a semi-automated segmentation algorithm for GA in SD-OCT images. A projection image constructed from a sub-volume of the retina beneath the RPE which shows the GA abnormalities most clearly appears to improve the visu-

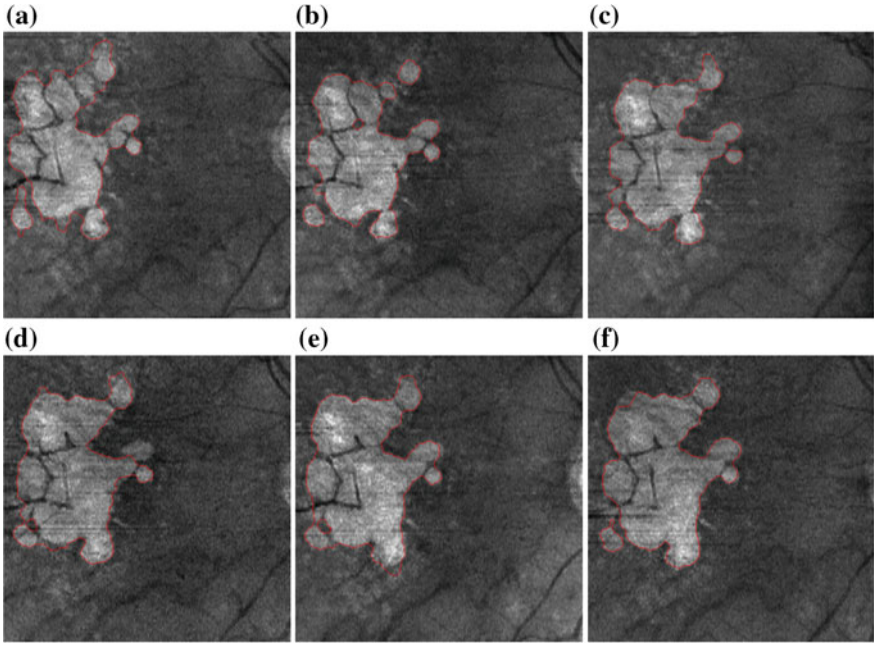

Fig. 11.17 GA segmentation results on RSVP images for the right eye of an 88 year old female patient. The imaging dates of **a–f** are 3/14/2008, 9/26/2008, 4/3/2009, 2/17/2010, 6/16/2010, 12/8/2010, respectively

Table 11.5 Within-expert and between-expert correlation coefficients (cc), paired U-test p-values, absolute GA area differences and overlap ratio evaluation between the manual segmentations

Methods compared	Number of eyes/cubes	cc	p-value (U-test)	AAD [mm^2] (mean, std)	AAD [%] (mean, std)	OR[%] (mean, std)
Expert A_1—Expert A_2	8/55	0.998	0.658	0.239 ± 0.210	3.70 ± 2.97	93.29 ± 3.02
Expert B_1—Expert B_2	8/55	0.996	0.756	0.243 ± 0.412	3.34 ± 5.37	93.06 ± 5.79
Expert$A_{1\&2}$ —Expert$B_{1\&2}$	8/110	0.995	0.522	0.314 ± 0.466	4.68 ± 5.70	91.28 ± 6.04

alization of GA lesions. A study of the variability in segmentations between experts and within the same expert at different sessions suggests that these projection images provide a robust visualization of GA. An edge-based geometric active contour model was adopted to segment GA on the resulting RSVP projection images. Qualitative and quantitative experimental results indicate that the algorithm shows promising results when compared to expert segmentations in the patient datasets studied and

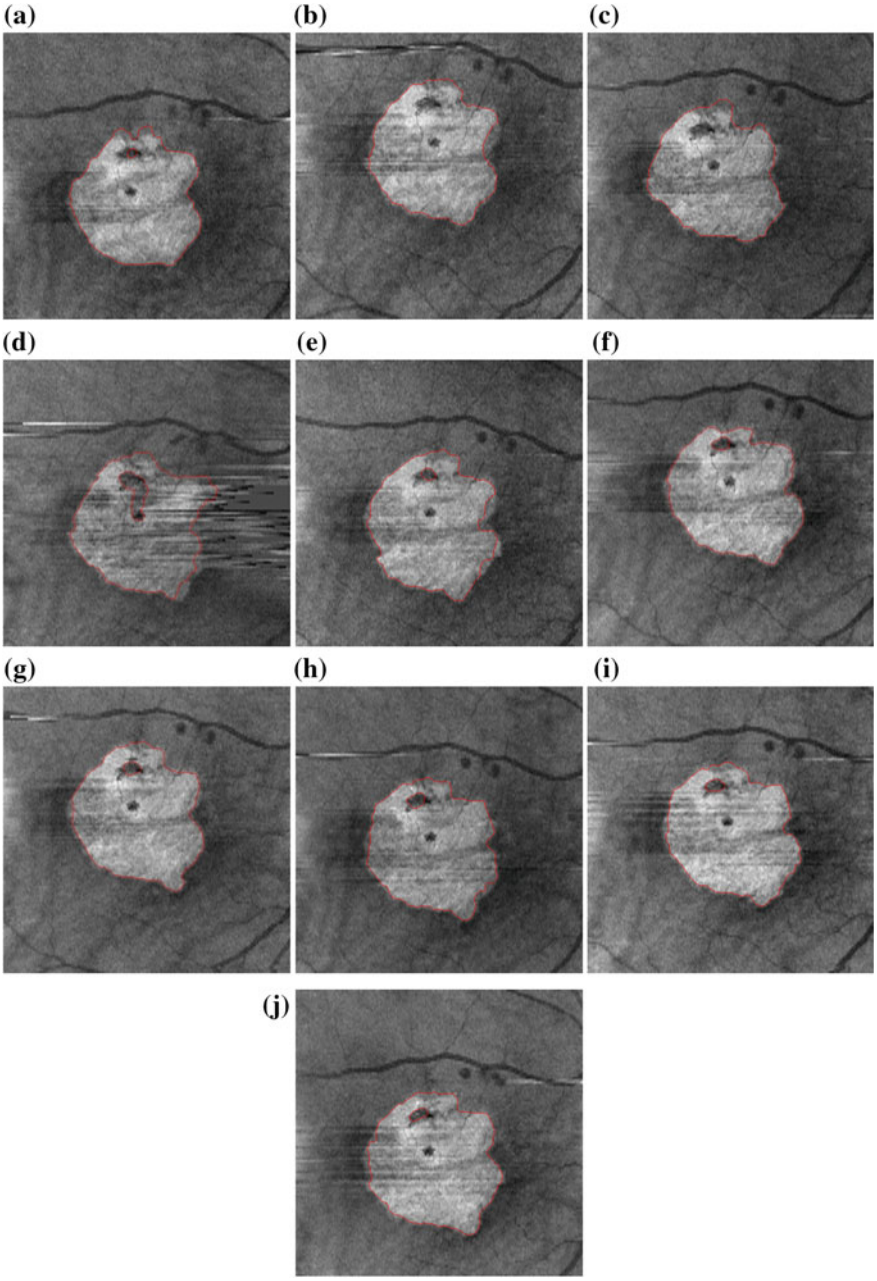

Fig. 11.18 GA segmentation results on RSVP images for the right eye of a 76 year old female patient. The imaging dates of **a**–**j** are 8/21/2008, 1/6/2010, 4/7/2010, 7/13/2010, 8/17/2010, 9/14/2010, 10/12/2010, 11/15/2010, 12/20/2010, 1/24/2011, respectively

that the method may be effective for the GA segmentation in SD-OCT images. This segmentation algorithm can also be used to extract and assess GA quantitative features in longitudinal OCT studies, such as the area and extent of GA. A performance comparison of our algorithm with a commercially-available GA segmentation software program suggests that our algorithm provides more accurate GA segmentations than the commercial software.

11.3.2 Automated Geographic Atrophy Segmentation for SD-OCT Images Using Region-Based C-V Model via Local Similarity Factor

11.3.2.1 Methods

We have developed a fully automated pipeline for GA segmentation, as shown in Fig. 11.19. The data input comprises the series of SD-OCT scan data. The axial location of the layered structure in the SD-OCT scans is estimated using an intra-retinal segmentation algorithm [66], the results of which are used to generate topographic GA projection images [57]. We segment the coarse GA regions using an iterative segmentation method and then fill the missing regions with a set of GA candidate regions, extracted from an intensity profile set recorded at each horizontal location in each B-scan image. These results are then taken as the initialization for a modified region-based Chan-Vese (C-V) [67] method with local similarity factor (CVLSF), built to further identify and refine GA regions.

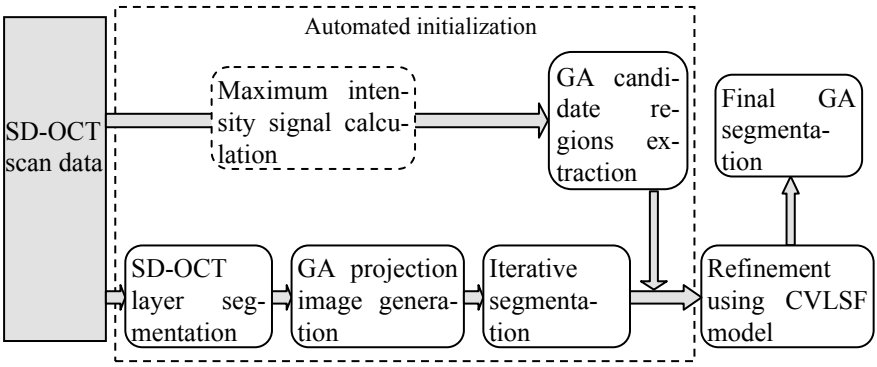

Fig. 11.19 The pipeline of the proposed automatic GA segmentation method

11.3.2.2 Iterative GA Segmentation

Considering the intensity inhomogeneity and high noise level typically present in GA projection images (shown in Fig. 11.20a and b), conventional thresholding techniques [68, 69] would produce masks that are too coarse to be considered as an adequate initialization for the subsequent CVLSF model, because they frequently exclude large portions of GA regions that cause convergence into local minima during the refinement step. An alternative iterative threshold method based on global image information is proposed here to coarsely segment GA regions from the projection image. This iterative threshold is computed considering a restricted region within the image that gets updated during subsequent iterations, and is set to decrease and converge to a certain value (see later experimental results and analysis section).

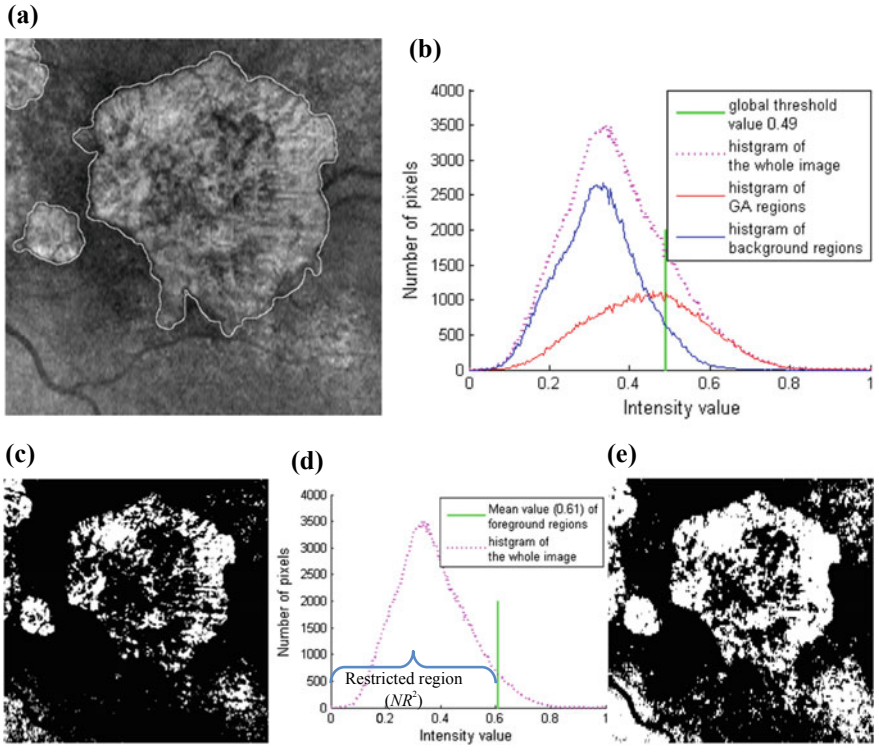

Fig. 11.20 **a** GA projection image with GA contour generated by manual segmentation. **b** Histogram of GA region and background and the threshold using OTSU method over the whole projection image. **c** Segmentation result obtained by OSTU method in the first iteration. **d** Histogram of the whole image where the mean value of the foreground region resulting from the first iteration and the values corresponding to the restricted region for the second iteration are indicated. **e** Final result for the coarse GA segmentation

11.3.2.3 GA Candidate Region Extraction

The coarsely segmented GA regions obtained in the previous iterative step, are still insufficient to be considered as an initialization outline for the CVLSF method. Isolated low-intensity false negative regions within correctly detected GA regions and extensive false positive regions (as can be observed in Fig. 11.20e) tend to cause "leakage" (segmentation expansion to neighboring structures) in Chan Vese methods, yielding sub-optimal results. A GA candidate region extraction refinement is considered here with the goal of further including isolated background regions and excluding false positive locations in the CVLSF model initialization outline.

11.3.2.4 Segmentation of GA Regions Based in an Improved C-V Model via Local Similarity Factor

The results obtained after the coarse segmentation refinement are taken as an initialization for an improved region-based C-V model [67] with a local similarity factor (CVLSF), which is introduced here to suppress noise influence, while guaranteeing detail preservation in the segmentation results. The objective function for partitioning an image $I(x, y) \in \Omega$ into two regions (GA region and background) is defined as:

$$E(c_1, c_2, C) = \lambda_1 \iint\limits_{in(C)} \Big(|I(x, y) - c_1|^2 + LSF_1(x, y)\Big)dxdy + \lambda_2 \iint\limits_{out(C)} \Big(|I(x, y) - c_2|^2 + LSF_2(x, y)\Big)dxdy + \mu Length(C) \tag{11.5}$$

where $\mu \geq 0$ is fixed constant parameter, and $\lambda_1 > 0, \lambda_2 > 0$ control the contributions of the internal energy and external energy terms, respectively, where object regions taken as internal term are the inside of the contour C ($in(C)$) and background regions considered as external term are the outside of C ($out(C)$). Using the level set definition [70] to represent C, that is, C is the zero level set of a level set function $\Phi(x, y)$, we can rewrite this objective function as:

$$\begin{aligned} E(c_1, c_2, \Phi(x, y)) = \lambda_1 \iint\limits_{\Omega} \big(|I(x, y) - c_1|^2 H(\Phi(x, y)) \\ + LSF_1(x, y) H(\Phi(x, y)))dxdy \\ + \lambda_2 \iint\limits_{\Omega} \big(|I(x, y) - c_2|^2 (1 - H(\Phi(x, y))) \\ + LSF_2(x, y)(1 - H(\Phi(x, y))))dxdy \\ + \mu \iint\limits_{\Omega} \delta(\Phi(x, y))|\nabla \Phi(x, y)|dxdy \end{aligned} \tag{11.6}$$

where $H(\Phi(x, y))$ and $\delta(\Phi(x, y))$ are Heaviside function and Dirac function, respectively, which are generally defined as:

$$H_\varepsilon(z) = \frac{1}{2}\left(1 + \frac{2}{\pi}\arctan\frac{z}{\varepsilon}\right) \text{ and } \delta_\varepsilon(z) = \frac{1}{\pi}\frac{\varepsilon}{\varepsilon^2 + z^2}, \quad z \in R. \tag{11.7}$$

If we keep $\Phi(x, y)$ fixed and minimize the energy function (11.6) with respect to the constants c_1 and c_2

$$\begin{cases} c_1(\Phi(x, y)) = \frac{\iint_\Omega I(x,y)H(\Phi(x,y))dxdy}{\iint_\Omega H(\Phi(x,y))dxdy} \\ c_2(\Phi(x, y)) = \frac{\iint_\Omega I(x,y)(1-H(\Phi(x,y)))dxdy}{\iint_\Omega (1-H(\Phi(x,y)))dxdy} \end{cases} \tag{11.8}$$

The local similarity factor is then defined as:

$$\begin{cases} LSF_1(x, y) = \sum\limits_{(i,j)\in N_{(x,y)}} \frac{|I(i,j)-c_1|^2}{d_{(x,y),(i,j)}} \\ LSF_2(x, y) = \sum\limits_{(i,j)\in N_{(x,y)}} \frac{|I(i,j)-c_2|^2}{d_{(x,y),(i,j)}} \end{cases} \tag{11.9}$$

where $N_{(x,y)}$ represents a neighborhood defined around the central pixel (x, y) (in our experiments defined as a 5×5 pixel window) and $d_{(x,y),(i,j)}$ is the Euclidean distance between pixels located at (x, y) and (i, j).

Minimizing the energy function (11.4) with respect to $\Phi(x, y)$, we obtain the corresponding variational level set formulation as follows:

$$\frac{\partial\Phi(x, y)}{\partial t} = \delta(\Phi(x, y))\left(\begin{array}{l} \lambda_2|I(x, y) - c_2|^2 - \lambda_1|I(x, y) - c_1|^2 \\ \quad + \lambda_2 LSF_2(x, y) - \lambda_1 LSF_1(x, y) + \mu\nabla\left(\frac{\nabla\Phi(x, y)}{\|\nabla\Phi(x, y)\|_2}\right) \end{array}\right). \tag{11.10}$$

The data term in the CVLSF model (Eq. 11.10) is similar to the traditional C-V model [67], differing by the introduction of the local similarity factor LSF. For full detail, see [58].

11.3.2.5 Evaluation of GA Segmentation

Figure 11.21 displays several examples with GA regions of different size in the testing dataset, where red outlines indicate the segmentation results for the CVLSF model. These examples show cases with different intensity in-homogeneity and complexity, in which accurate GA segmentation is a difficult challenge. We can observe that the outlines produced by the method presented here were relatively precise, given the difficulty of the task.

Figure 11.22, displays example collected manual outlines in examples from the first test dataset (as indicted in Sect. 2.5) with outlines made by the two readers at the two repeated sessions indicated with different colors. The intra-observer and inter-observer differences can be visualized. The quantitative results in inter-observer and intra-observer agreement evaluation for this first dataset are summarized in Table 11.6, where A_i ($i = 1, 2$) represents the segmentations of the first grader in the i-th session, and B_i ($i = 1, 2$) represents the segmentations of the second grader in the i-th session. Inter-observer differences were computed by considering the union of both sessions for each grader: $A_{1\&2}$ and $B_{1\&2}$ represent the first and second grader, respectively. The intra-observer and inter-observer comparison showed very high correlations coefficients (cc) and U-test p-values, indicating very high linear correlation and no statistical differences both between different readers and for the same reader at different sessions. The overlap ratios (all > 90%) and the absolute GA area differences (all < 5%) indicate very high inter-observer and intra-observer agreement, highlighting that the measurement and quantification of GA regions in the generated projection images seem effective and feasible.

We evaluated the performance of the proposed segmentation algorithm in the first dataset by comparing its results to the manual segmentation gold standard and to the previously published QC's method. The results obtained for four example cases are shown in Fig. 11.23. We can observe that for these cases, the GA outlines obtained by QC's method slightly deviate from the gold standard boundary (expert average), whereas the segmentation results obtained by our method seem closer to such gold

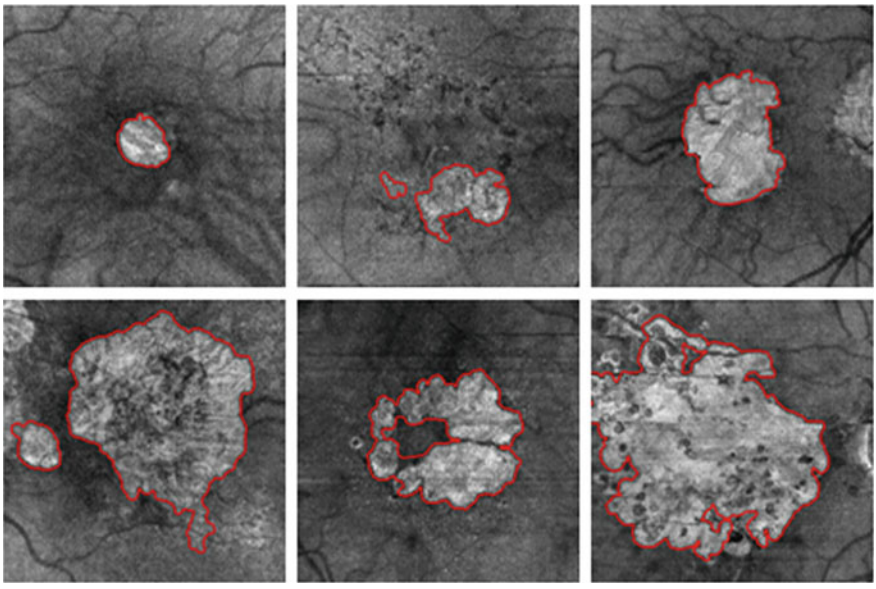

Fig. 11.21 Examples displaying the automatically segmented GA regions in SD-OCT projection images

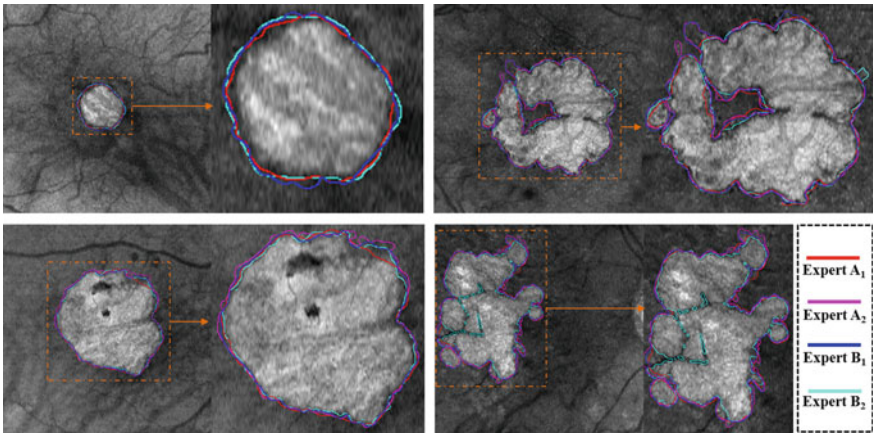

Fig. 11.22 Manual segmentation examples by two different experts and at two different sessions outlined in RSVP projection images. The region of interest outlined in orange in each RSVP projection image is also shown zoomed in for larger detail. The color label for each observer and session outline is indicated in the legend in the bottom right

Table 11.6 Intra-observer and inter-observer correlation coefficients (*cc*), paired *U*-test *p*-values, absolute GA area differences (AAD) and overlap ratio (OR) evaluation

Methods compared	Patients /cubes	cc	*p*-value (*U*-test)	AAD [mm^2] (mean, std)	AAD [%] (mean, std)	OR[%] (mean, std)
Expert A_1—Expert A_2	8/55	0.998	0.658	0.239 ± 0.210	3.70 ± 2.97	93.29 ± 3.02
Expert B_1—Expert B_2	8/55	0.996	0.756	0.243 ± 0.412	3.34 ± 5.37	93.06 ± 5.79
Expert$A_{1\&2}$—Expert$B_{1\&2}$	8/55	0.995	0.522	0.314 ± 0.466	4.68 ± 5.70	91.28 ± 6.04

standard. Table 11.7 summarizes the results of the quantitative comparison between our algorithm proposed here and manual gold standard (average expert segmentation) and between the previous QC's method and gold standard. The values obtained by our algorithm are displayed in the table in bold face and between parentheses. We also compared the differences of each method to each of the manual readers and sessions independently. Overall, our method presented higher similitudes to the manual gold standard than QC's method, presenting higher correlation coefficients (0.979 vs. 0.97), lower absolute area differences (12.95 vs. 27.17%), and higher overlap ratio (81.86 vs. 72.6%). Lower area differences indicate the area estimated by our method seems closer to the values measured by hand by an average reader than when estimated by the previous method, which would translate into a more accurate GA characterization. The differences observed between our method and the

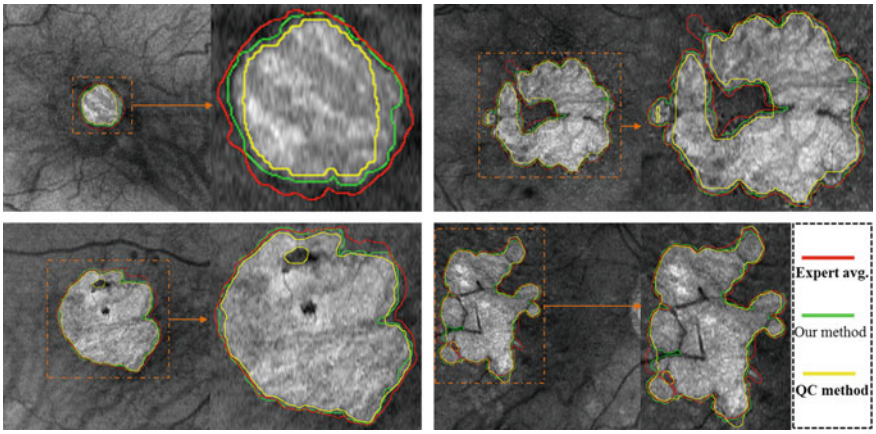

Fig. 11.23 Segmentation results using the proposed method, QC's method and average expert segmentation (considered as manual gold standard). The cases shown are the same as in Fig. 11.22 for direct comparison. The region of interest outlined in orange in each RSVP projection image is also shown zoomed in for larger detail. The color label for each segmentation method is indicated in the legend in the bottom right

manual gold standard was also very similar to those between our method and each of the independent readers. These differences were higher than the inter-observer and intra-observer differences shown in Table 11.6, but they were within the same ranges. In fact, the paired U-test in measured GA area differences between automated method and each of the manual segmentations was not significant (all with p-value > 0.05), while it was significant for differences between QC's method and manual segmentations (all with p-value < 0.05). This indicates the results produced by our method seem more similar to manual outlines than QC's method. In conclusion, our algorithm showed better segmentation performance than QC's method when compared to the manual segmentation.

A set of example results in the second dataset evaluated is shown in Fig. 11.24, where the outlines generated by manual segmentation, commercial software, QC's method, and our method are displayed. We can observe that our method produced results that were similar to the manual outlines, correcting limitations observed in prior methods. Table 11.8 summarizes the quantitative evaluation in this second dataset, comparing each segmentation method (our method presented here, QC's method, and the commercial software) to the manual outlines drawn in FAF images. The correlation coefficients between areas measured using different methods were very high, and all U-test p-values testing for differences in area measurements showed no statistical significance (p-value > 0.05). The overlap ratio was the highest (70%) between our method and the manual segmentation in FAF images, while it was lower than in the previous data set (Table 11.7), most probably due to the intrinsic differences between SD-OCT and FAF images and possible bias introduced by the registration process. Surprisingly, the differences in AAD between our algorithm

Table 11.7 Quantitative comparison of our algorithm segmentation results (shown in boldface and between parenthesis) and QC's method results to manual gold standard (Avg. Expert) and individual reader segmentation

	QC's (**OurSeg.**) versus Avg. Expert	QC's (**OurSeg.**) versus Expert A_1	QC's (**OurSeg.**) versus Expert A_2	QC's (**OurSeg.**) versus Expert B_1	QC's (**OurSeg.**) versus Expert B_2
Patients/cubes	8/55	8/55	8/55	8/55	8/55
cc	0.970 (**0.979**)	0.967 (**0.975**)	0.964 (**0.976**)	0.968 (**0.976**)	0.977 (**0.975**)
p-value (*U*-test)	0.026 (**0.221**)	0.047 (**0.389**)	0.024 (**0.201**)	0.017 (**0.138**)	0.022 (**0.191**)
AAD [mm^2]	1.438 ± 1.26	1.308 ± 1.28	1.404 ± 1.31	1.597 ± 1.33	1.465 ± 1.14
	(**0.811 ± 0.94**)	(**0.758 ± 0.99**)	(**0.853 ± 1.04**)	(**0.984 ± 1.08**)	(**0.897 ± 1.05**)
AAD [%]	27.17 ± 22.06	25.23 ± 22.71	26.14 ± 21.48	29.21 ± 22.17	27.62 ± 20.57
	(**12.95 ± 11.83**)	(**12.62 ± 12.86**)	(**13.32 ± 12.74**)	(**14.91 ± 12.65**)	(**14.07 ± 11.78**)
OR [%]	72.60 ± 15.35	73.26 ± 15.61	73.12 ± 15.15	71.16 ± 15.42	72.09 ± 14.82
	(**81.86 ± 12.01**)	(**81.42 ± 12.12**)	(**81.61 ± 12.29**)	(**80.05 ± 13.05**)	(**80.65 ± 12.51**)

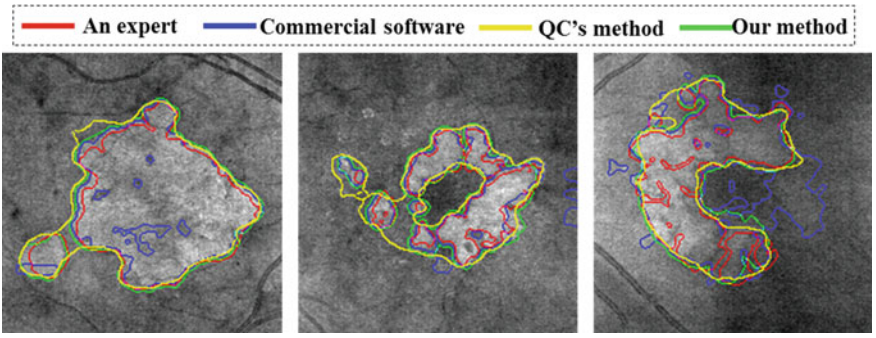

Fig. 11.24 Comparison of outlines generated by manual segmentation, commercial software, QC's method and our method presented here in three GA patients form the second dataset. The color employed for each outline is indicated in the legend on top of the images

and manual segmentations (1.215 ± 1.58 mm^2) are slightly higher than between QC's method and manual segmentation (0.951 ± 1.28mm^2), but both were in the same ranges. The higher overlap ratio with the manual markings observed for our method, but also slightly higher AAD as compared to QC's method, may be due to QC's method producing slight regions or both over- and under-estimation of GA regions, while the method presented here had overall higher similitudes to the manual outlines.

Table 11.8 Correlation coefficients (cc), paired p-values U-test, absolute differences and overlap ratio in areas of GA between our segmentation method (Our Seg.), QC's method, commercial software segmentation (Com. Sw. Seg.), and expert segmentations manually outlined in FAF images (FAF)

Methods compared	Patients /cubes	cc	p-value (U-test)	AAD [mm^2] (mean, std)	AAD [%] (mean, std)	OR [%] (mean, std)
QC's Seg.—FAF	56/56	0.955	0.524	0.951 ± 1.28	19.68 ± 22.75	65.88 ± 18.38
Our Seg.—FAF	56/56	0.937	0.261	1.215 ± 1.58	22.96 ± 21.74	70.00 ± 15.63
Com.Sw. Seg.—FAF	56/56	0.807	0.140	1.796 ± 2.51	34.13 ± 38.62	62.40 ± 21.16

11.3.2.6 Discussion

We have presented a novel automated GA region segmentation method in SD-OCT images. As summarized in Table 11.7, our method demonstrated very high accuracy when compared to a manual gold standard generated by two different readers and repeated at two separated sessions (mean OR $= 81.86\% \pm 12.01\%$; AAD $=$ 0.811 ± 0.94 mm2; cc $= 0.979$; U-test p-value $= 0.221$), and also higher than another known semi-automated technique [57]. Our method also showed good agreement with manual segmentations drawn in FAF images and later registered to the OCT image domain, presenting higher overlap than for particular commercial software and the prior semi-automated technique (Table 11.8). The example images shown in Figs. 11.23 and 11.24 corroborate these findings, highlighting the similitudes between our proposed segmentation method and manually drawn outlines. We anticipate that the robust results produced by our method may aid the automated characterization of GA area, extent, and location, providing a quantitative, objective and reliable approach to measure and track GA expansion and progression of advanced non-exudative age-related macular degeneration (AMD).

The main difficulties in automated GA segmentation in SD-OCT images is the high noise level and variability, as image quality and noise characteristics vary throughout images acquired using machines from the same vendor and even more so across different vendors. A key aspect of our work to overcome this difficulty is the design of an improved Chan-Vese method considering a local similarity factor (CVLSF). The level-set nature of the method allows the algorithm to handle change of topological structure and irregular shapes easily. The introduced local similarity factor (LSF), balancing similarities observed by the spatial distance and gray level differences within a local window, presents properties that allows the results to be less sensitive to noise of higher intensity and of different characteristics.

11.3.2.7 Conclusions

This section presents a novel algorithm for automated GA segmentation in SD-OCT images to enable robust, accurate, and objective quantitative measurements of GA extent and location automatically. The proposed method combines a region-based C-V model with a local similarity factor in projection images of a choroid sub-volume. This technique seems more robust to presence of noise, while preserving image detail. Quantitative experimental results demonstrate that the algorithm shows good agreement when compared to manual segmentation by different experts at different sessions and to a consensus manual gold standard, resulting in higher agreement than with a previously known semi-automated method and a commercially-available software package. The proposed algorithm may be clinically useful in providing relatively reliable GA quantitative data that may improve tracking of GA extent, location and expansion in patients diagnosed with advanced non-exudative AMD.

11.3.3 Restricted Summed-Area Projection for Geographic Atrophy Visualization in SD-OCT Images

The main principle of the existing fundus projection GA visualization techniques generated from SD-OCT images lies in the identification of the typical choroidal brightening that appears in the regions affected by GA. However, the many blood vessels in the choroid, which normally manifest in low reflection values, decrease the contrast and distinction of macular regions affected by GA. As an example, Fig. 11.25 shows the choroidal vasculature influence on GA visualization, where Fig. 11.25a and b are the SVP and Sub-RPE Slab projection images generated from one 3D SD-OCT scan acquired with a Cirrus OCT (Carl Zeiss Meditec) system, respectively.

The RPE boundaries were delineated by hand. Figure 11.25c displays the B-scan corresponding to the yellow dashed line in Fig. 11.25a, and several structures that can be observed in this image are manually labeled.

11.3.3.1 GA Visualization Based on RSAP

The main strategy of the RSAP technique lies in utilizing the intensity distribution beneath the RPE layer as observed in SD-OCT images to fill the low intensity regions produced by the presence of choroidal vessels. Vessel presence is identified by analyzing intensity profiles. An example of intensity distribution beneath the RPE in a typical SD-OCT scan, namely the region between the two dashed green curves in Fig. 11.25c, where GA is present is displayed in Fig. 11.26. We can observe that the intensity distribution decreases towards the x direction (depth), and the rate of this decrease in the GA region is typically slower than that in the normal region.

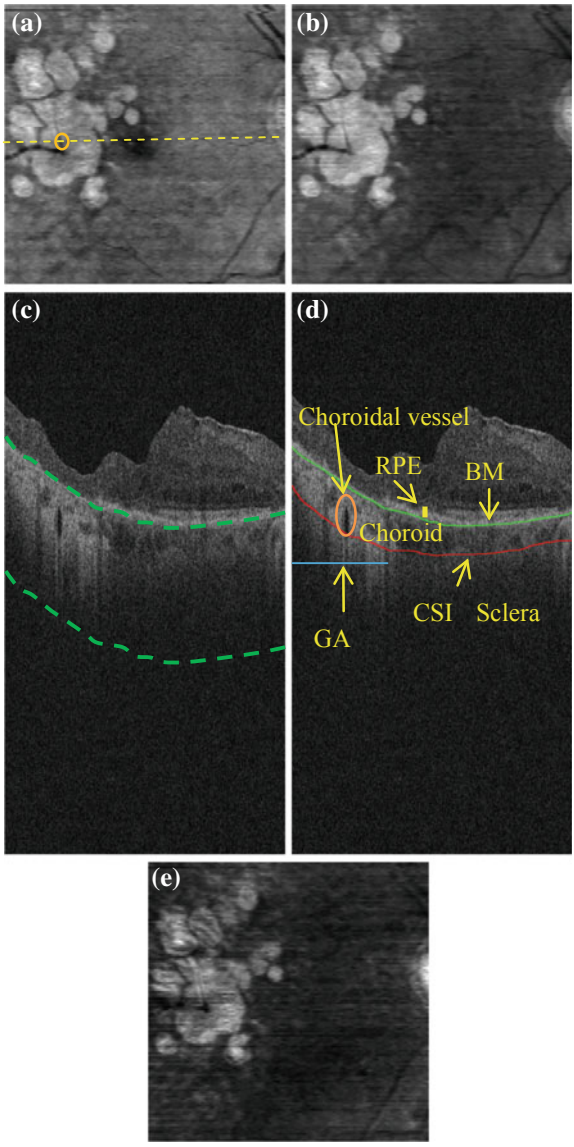

Fig. 11.25 Choroidal vasculature influence on GA visualization. (**a**) SVP projection image. **b** Sub-RPE slab projection image. **c** Example B-scan. **d** Example B-scan with structure labels. **e** Sub-CSI slab projection image

Figure 11.28a and b show two intensity profiles (marked with the red curve) of the sub-RPE region (Fig. 11.26a) in the GA and the normal regions, respectively. This principle constitutes the basic idea of the proposed RSAP technique. The flowchart of our technique is shown in Fig. 11.27, which comprises the following operations, for full detail see [41]:

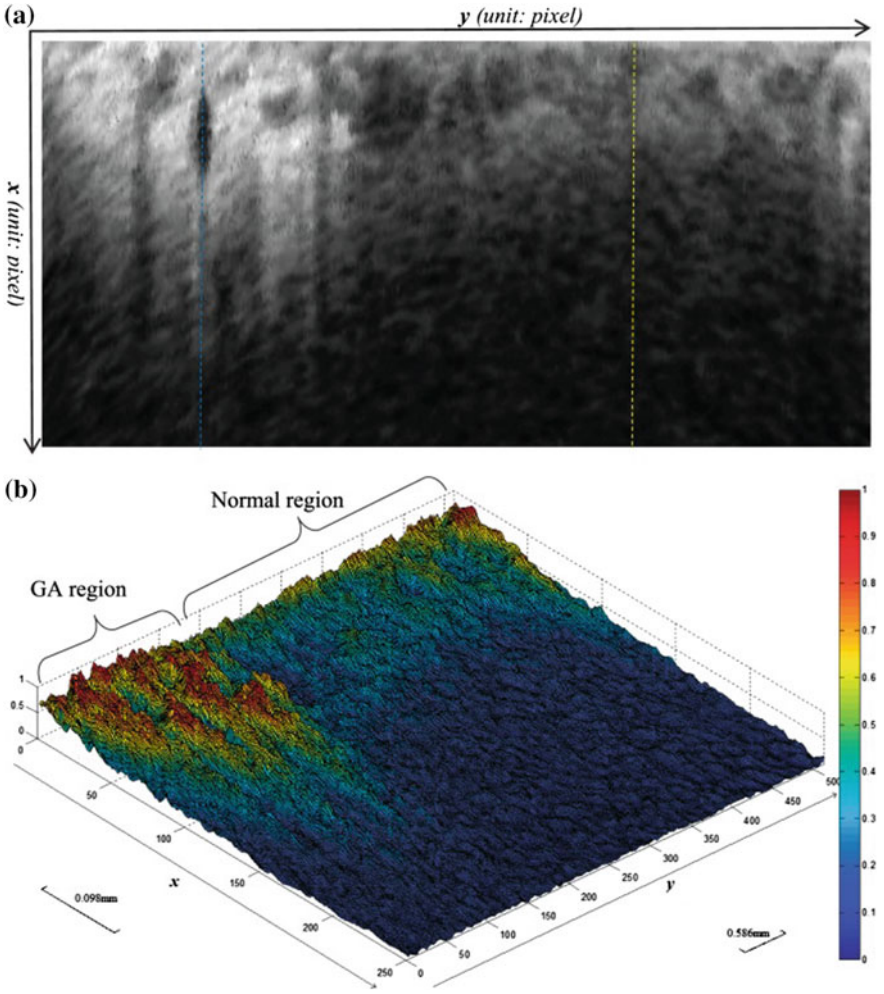

Fig. 11.26 Intensity distribution analysis. **a** Flattened sub-RPE region. **b** Intensity surface of (**a**)

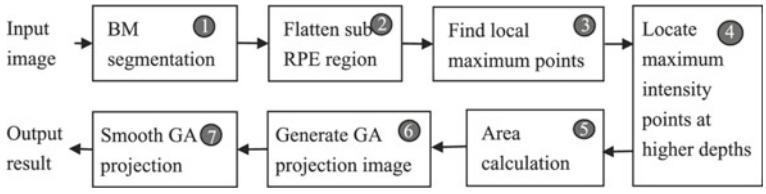

Fig. 11.27 Flowchart of the proposed technique

(1) **Segmentation of BM boundary**: The BM boundaries were segmented with the automatic 3-D graph search method [44].

(2) **Flattening of sub-RPE region**: An image is composed by taking the recorded intensity values beneath the segmented BM boundary up to a maximum depth where GA can be detected, constituting a flattened sub-RPE image. This maximum depth is set up as an independent parameter in this work (depth of sub-RPE, as explained in the later parameter evaluation). The flattened sub-RPE region is shown in Fig. 11.26a.
(3) **Finding local maximum intensity points**. For each column in the flattened sub-RPE region (A-scan location), the points with local maximum intensity value (namely the intensity value of the point is larger than those of its two connected points) are found, as marked with the blue circle in Fig. 11.28.
(4) **Locating maximum intensity points at higher depths**. The maximum intensity points whose value follows a constantly decreasing function with depth (x axis) are selected, as marked with the magenta stars in Fig. 11.28. The purpose of this step is to ensure a constantly descendent intensity profile beneath RPE.
(5) **Calculating the area below the surface constructed with the maximum intensity points at higher depths**. We interpolate the intensity profile in the axial locations between the selected maximum intensity points at higher depths using linear interpolation (magenta lines in Fig. 11.28), and calculate the area of the polygon formed by this interpolation and a baseline of zero intensity (area below the magenta lines marked in Fig. 11.28).
(6) **Taking the calculated area above as the primary GA projection value at each projection location**.
(7) **Using a median filter to smooth the generated GA projection image**: To alleviate the noise influence and make the final GA projection image smoother, a simple median filter with a 3×3 neighborhood was used.

Figure 11.29a shows the GA projection image with the proposed RSAP technique, and Fig. 11.29b shows a detail comparison of three GA projection techniques in regions of interest corresponding to the red dashed rectangles in Fig. 11.30a. Compared with the SVP and Sub-RPE Slab projection images (Fig. 11.25a and b), the RSAP projection image displays a higher contrast and also overcomes the influence of the choroidal vasculature on GA visualization, as shown in Fig. 11.29b.

11.3.3.2 Results

The proposed RSAP technique was tested and compared with the SVP and Sub-RPE Slab techniques qualitatively and quantitatively. The influence of the parameter controlling the maximum considered depth for the sub-RPE region, mentioned earlier, was first evaluated and later fixed for all 99 test images. Figure 11.30 shows the GA separability for different depths of sub-RPE regions in one SD-OCT image, where the depth was varied from 100 to 300 pixels (approximately 0.2–0.6 mm in the collected images) with an interval of 10 pixels. Figure 11.30 demonstrates that the GA separability increases when the depth increases from 100 to 240 pixels, and then remains stable with further depth increases. Figure 11.31 shows the relation-

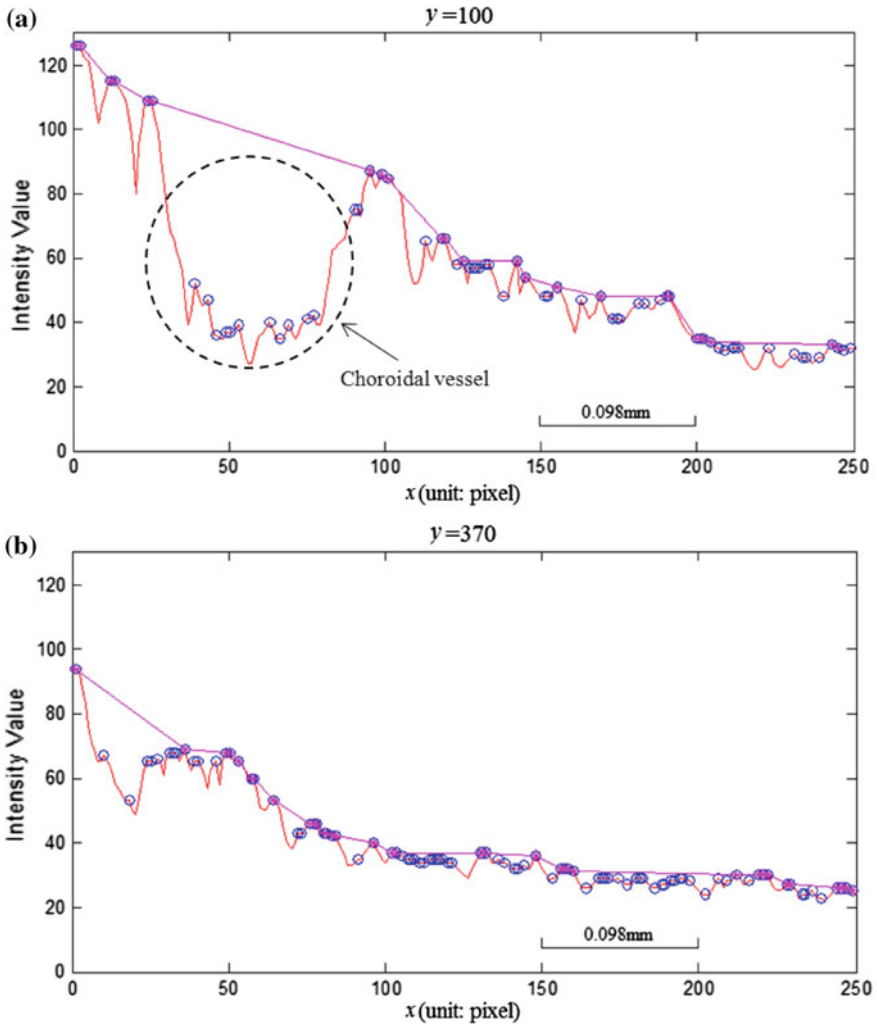

Fig. 11.28 Intensity profiles of columns #100 (**a**) and #370 (**b**), marked with the dashed blue and yellow lines in Fig. 11.26a, respectively. Red curve: intensity values of two columns. Blue circle: local maximum intensity point. Magenta star: maximum intensity point at higher depths (in the x direction). **a** Intensity distribution in GA region. **b** Intensity distribution in normal region

ship between the mean and standard deviation of the GA separability and the depth of sub-RPE region for all 99 SD-OCT images, which indicates an optimal depth range from 190 to 210 pixels (approximately 0.37–0.41 mm). When the depth of sub-RPE region is much smaller than the axial region where GA can be observed in the SD-OCT images, the GA separability is low because only a limited region of the high-intensity values associated with GA near the BM are used. When this depth

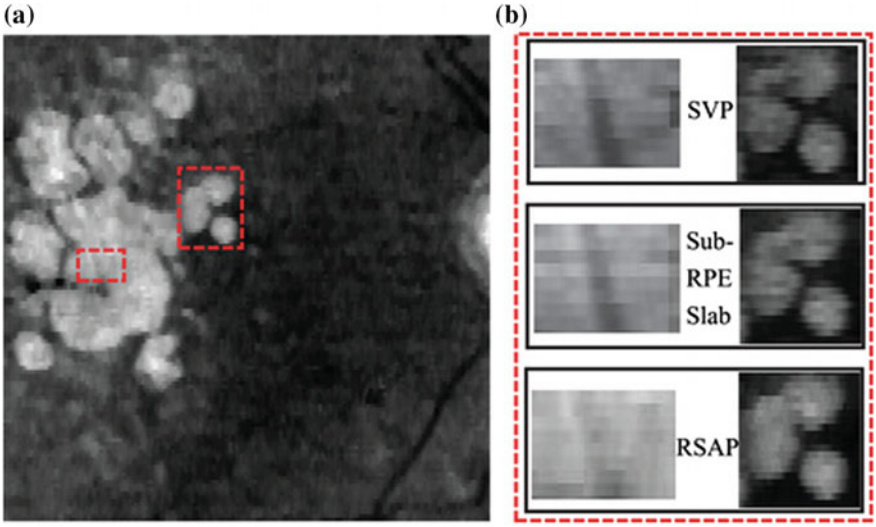

Fig. 11.29 GA projection image with RSAP. **a** RSAP projection image. **b** Results by the three discussed techniques in regions of interest as indicated in (**a**)

Table 11.9 Average mean difference (MD) and GA separability (SGA) of the SVP, Sub-RPE Slab and RSAP projection images

Methods compared	Number of eyes/cubes	MD	SGA
SVP	27/99	0.129	0.880
Sub-RPE Slab	27/99	0.238	0.919
RSAP	27/99	0.276	0.938

is increased to values that are larger than optimal, the GA separability decreases because more background intensity in sclera is included. In this chapter, the depth of sub-RPE region was set to be 200 pixels (approximately 0.39 mm) for all test images.

Table 11.9 shows the average performance of the three tested techniques, where all of 99 cubes (3D SD-OCT images) from 27 eyes in 21 patients are used. Figure 11.32 shows the mean difference and separability values for each case included in our analysis. Figure 11.33a–c show the GA projection images generated from the SD-OCT scan of a patient's left eye using the three techniques tested, SVP, Sub-RPE Slab and RSAP, respectively. Figure 11.33d shows a one-line profile of the rows of Fig. 11.33a–c marked with a dashed line. The region marked with the dashed oval in Fig. 11.33d corresponds to the bright regions in the GA projection images (Fig. 11.33a–c).

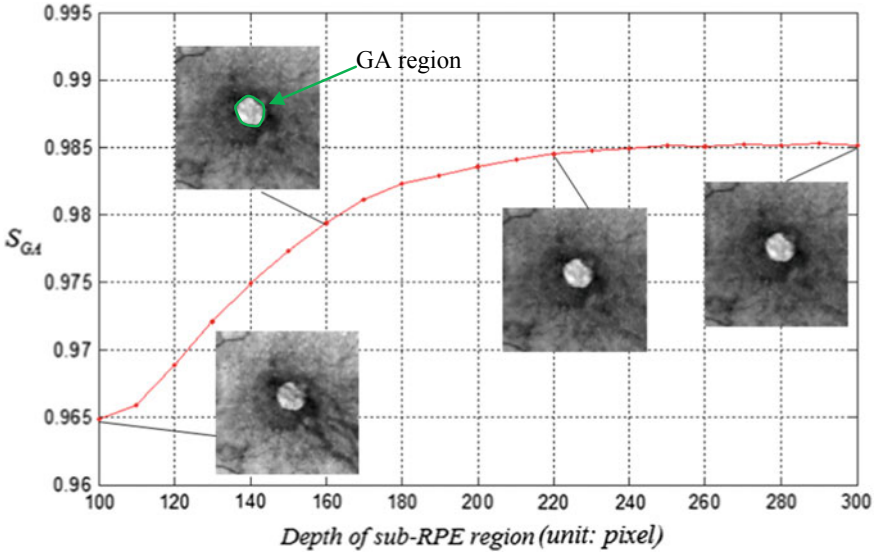

Fig. 11.30 Depth of sub-RPE region for GA separability for one SD-OCT scan. Four GA projection images corresponding to four red points are inset

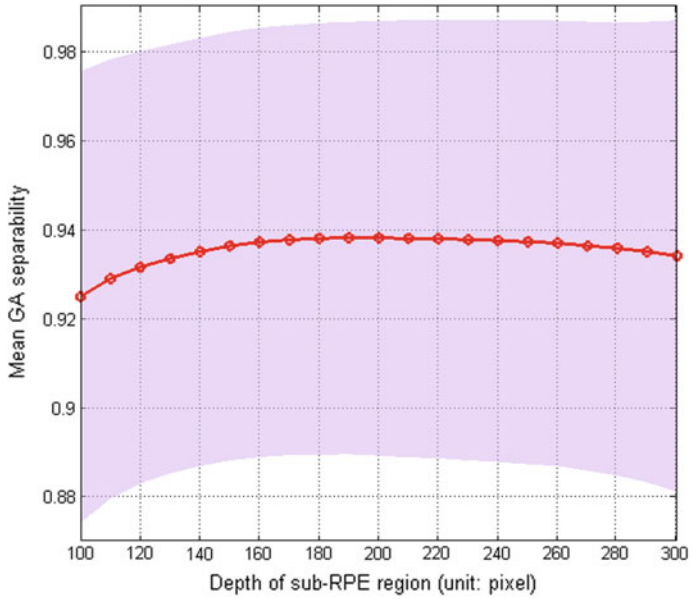

Fig. 11.31 Mean (redline) and standard deviation (pale pink shading) of the GA separability across the 99 SD-OCT images in this study, considering different values of depth of sub-RPE region

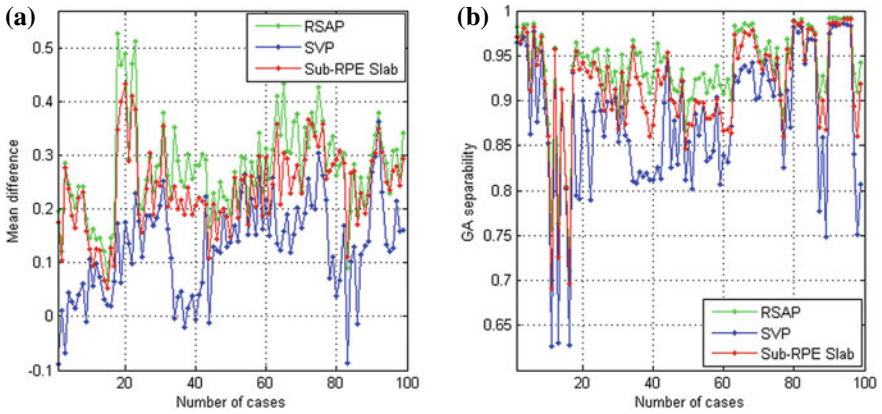

Fig. 11.32 Comparison of the three tested GA projection techniques. **a** Mean difference. **b** GA separability

11.3.3.3 Discussion

We have presented a novel technique, the RSAP, to increase the contrast and distinction of GA in a fundus projection image. In addition, we compared the images produced to the ones produced by two known methods, the SVP and Sub-RPE Slab techniques. Identifying and quantifying GA area is becoming more important in the diagnosis and management of advanced dry AMD [71]. With the development of pharmacologic and cell-based therapies for GA, accurately identifying and monitoring GA over time will be important in order to clinically determine the efficacy or failures of these novel treatment modalities [72, 73]. Although SD-OCT has the potential to become the preferable technique for imaging the retina, direct visualization of GA in SD-OCT has been limited by low contrast and overlapping of retinal pathologies and structures when generating a fundus image. The RSAP method presented here improves direct visualization of GA by considering a restricted projection and the contribution of the choroidal vasculature.

In conclusion, we present a projection technique from 3D SD-OCT images based on intensity distribution in sub-RPE regions for the visualization of GA, which we called the RSAP technique. The RSAP technique improves on the previous methods by considering and utilizing the intensity distribution characteristics in sub-RPE regions. Quantitative comparison in 99 3D SD-OCT scans from 21 patients demonstrated that the RSAP is more effective for GA visualization than the SVP and Sub-RPE Slab due to increased GA contrast and distinction.

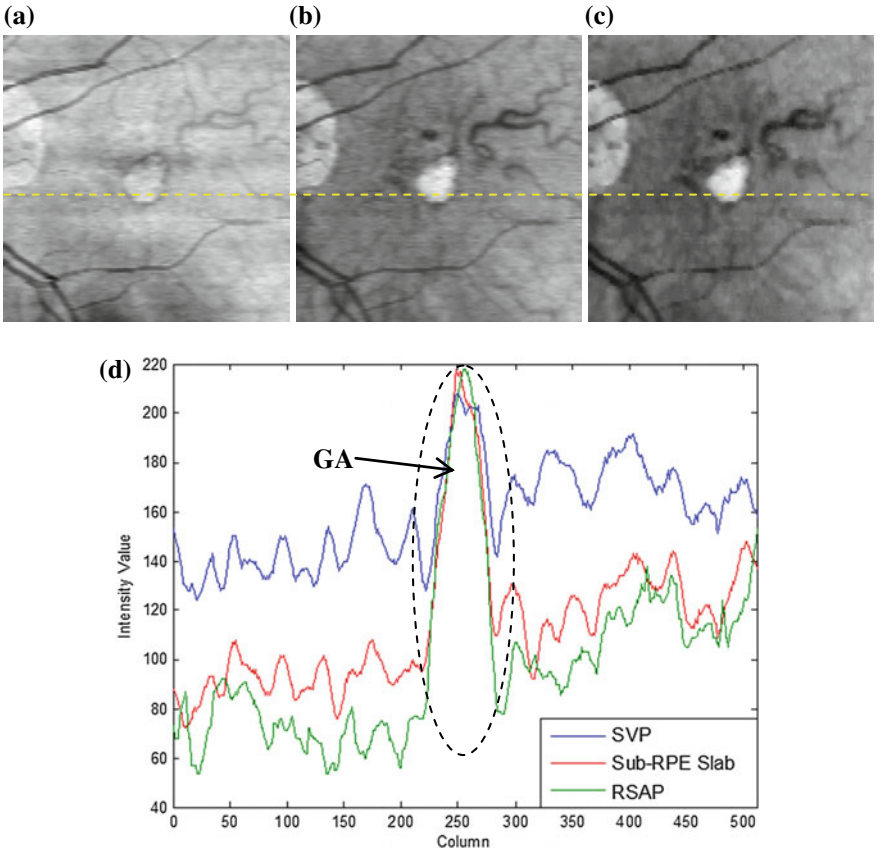

Fig. 11.33 Comparison of three GA projection techniques in the left eye of one patient. **a** SVP. **b** Sub-RPE Slab. **c** RSAP. **d** One-line profile

11.3.4 A False Color Fusion Strategy for Drusen and GA Visualization in OCT Images

The inability to visualize drusen completely, which is the major limitation of SVP fundus image technique in drusen visualization [36], is due to the collapsing of the image volume during the projection. However, these small anomalies are always indistinct when the image volume is collapsed when making these projection. Stopa [37] presented a solution to this limitation by utilizing the pathological retinal features to produce the SVP. The delineation of pathological features in SVP visualizations was preserved by this method. A recent technique introduced into OCT imaging devices is the "slab SVP", which is a semi-automated method to limit the SVP to a sub-volume of the retina in the neighborhood of the RPE layer (Carl Zeiss Meditch, Inc., unpublished data); more so, the user needs to annotate the image

to localize the RPE. Using manually annotating pathologic features in a full SD-OCT stack images is time-consuming and costly in a clinical setting, which required quick and precise results. However, the methods by Stopa [29] lacks information about drusen thickness, which is needed for characterizing drusen. Georczynska [38] presented a more robust approach using each single OCT cube by selectively summing different retinal depth levels to generate a series of projection OCT fundus images, which enhanced contrast and visualized outer retinal pathology that are not visible with standard fundus imaging or OCT fundus imaging techniques. This technique separated drusen into several-projected fundus images summed at different retinal depth levels, hence this cannot be directly visualized in a single image. The evolution of the GA that causes a deformation in the main retinal layer is still not very clear; either the RPE, choriocapillaris, or photoreceptors (PR) layers that can resulted in layer deformities in patients with GA [74, 75]. Recently, new histopathological findings suggest that the first place in which the GA appearance can be confirm is the RPE cell loss, then with ensuing PR cell death and choriocapillaris atrophy [76–79]. Bearelly [75] researched on the PR-RPE interface in GA using SD-OCT in an effort to test in vivo whether SD-OCT provides enough resolution for reproducible measurement of the PR layer at the margins of GA, and if the relationship between PR layer and RPE at those margins could be delineated successfully. The research work emphasized the direct association between GA and cell loss or "thinning" of PR and RPE as seen in SD-OCT images. These GA can also be viewed in en face SVP fundus images as a bright and more uniform delimited region, due to the mentioned cell loss and consequent increased penetration of light into the choroid coat, combine with the constant high reflection of light from the choroid coat [72]. In addition, there are some specific cases in which the highly reflective retinal layers, above the RPE complex complicate and obscure GA visualization, making the use of the SVP fundus imaging technique for GA inspection suboptimal.

In this section, we present a new combined method for drusen and GA visualization that enhances the conspicuity of GA lesion by utilizing RPE loss and increase of reflections from the choroid coat. Mores so, a false color fusion technique by combining drusen and GA projection images is presented to accurately and effectively display drusen and GA in a single fundus image.

11.3.4.1 Drusen Visualization

Recently we presented the RSVP method [35], which is a fully automated technique with no user input such as indicating a seed point. This approach restricted the projected volume to the sub-volume in the vicinity of the RPE layer of a 3D SD-OCT to create an en face voxel projection image. Figure 11.1a shows an example of the vicinity region which is projected in the RSVP method.

The presence of drusen was taken into account in order to determine the location of the RPE layers. A bilateral filter [61] was first applied to smoothen the SD-OCT retinal images. After which, a thresholding method was applied to detect the margin of the vitreous, which is used in estimating the location of the RNFL. The highly

reflective and locally connected pixels that are spatially located below the RNFL are taken as the initial estimate of the RPE layer. The morphological opening and thickness constraint (RPE is approximately constant thickness) are adopted to smooth and refine the RPE estimation. Lastly, the unhealthy (abnormal) and healthy (normal) RPE layers are obtained by interpolation and fitting. The fitted lower boundary of the normal RPE layer is taken as the baseline of the projection region used for the RSVP generation, while the top boundary of the projection region is determined by displacing the fitted normal RPE layer upwards the same distance as the largest drusen peak found in the cube (Fig. 11.1a).

More so, to effectively improve the drusen visualization, this method (RSVP) method also incorporates the brightening of the drusen substance region. We find the maximum intensity pixel in the interpolated RPE layer and replace the values of the pixels underneath it with this maximum intensity value, for each axial column of the SD-OCT scans.

11.3.4.2 GA Visualization

There are two primary characteristics of GA which can be observed in SD-OCT images: choroid brightening and RPE thinning. The choroid in GA regions is always brighter than in healthy regions, due to RPE cell loss, increase of light penetration in the retina, and subsequent increased reflections from the choroid coat. In the GA regions, the RPE thickness is always thinner than in other regions. Thus, we designed a GA visualization algorithm that is based on the detection regions with increased brightness in the choroid region, and the RPE thinning characteristics is also used to enhance the GA visualization.

11.3.4.3 Choroid Region Summing

We restricted the SVP projection to a sub-volume beneath the RPE layer where the choroid resides and where the high reflections (or bright choroid) indicate where GA is present, in order to improve the traditional SVP image for GA visualization. Figure 11.34 shows a GA visualization example with the traditional SVP projection (Left) and the RSVP projection (Right). The contrast of GA in the RSVP image is higher than in the SVP image, which could potentially improve the performance of a computerized GA segmentation method. The RSVP projection appears more blurred than the SVP projection; this is due to smoothing with bilateral filtering for SD-OCT retinal images.

11.3.4.4 RPE Thickness

As observed for healthy retina without GA, the RPE thickness is approximately constant (20 μm). Therefore, we employed the segmented RPE layer vicinity described

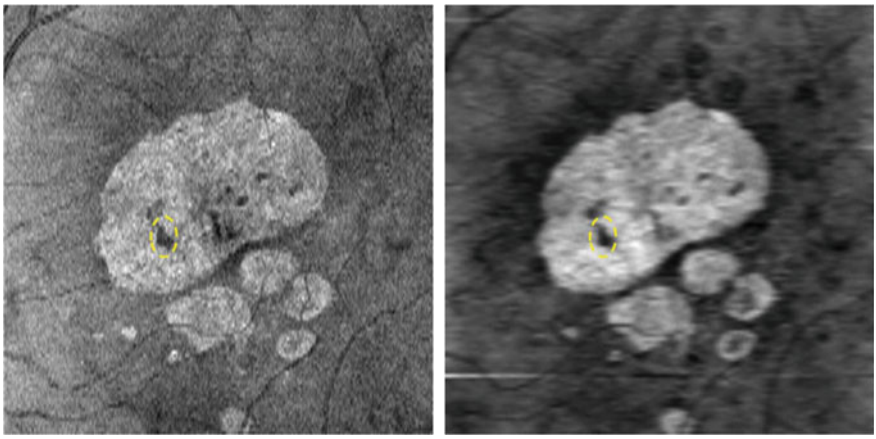

Fig. 11.34 SVP (**a**) and RSVP (**b**) projection for visualizing GA lesions. **b** The dashed yellow oval represents a drusen within the big GA region

above (drusen projection region delimited with the red lines in Fig. 11.1a to obtain an en-face mapping related to RPE thickness at each A-scan position. By selecting the maximum of the values resulting from using a sliding window to average pixel intensity in the segmented RPE layer vicinity, we computed the values of this mapping A-scan by A-scan. A 20 μm sliding window size was chosen, which corresponded to normal RPE thickness. The mapping done because the RPE is the brightest region within the selected vicinity and has approximately constant brightness within the cube, a larger number of bright pixels within the window indicates a thicker region of the RPE, and in the same way, a lower number of bright pixels indicates RPE thinning. Where there is RPE thinning, although this mapping does not produce actual RPE thickness values, but it produces a good representation of areas.

11.3.4.5 Combination of Two Characteristics

We take P1 and P2 to be matrices representing the normalized RSVP projection image and RPE thickness map, respectively. The resultant GA projection image can be obtained as:

$$P_{GA} = P_1 \circ (1 - P_2)^a \tag{11.11}$$

where the constant a belongs to (0, 1) and its purpose is to control the impart of the RPE thickness on the GA projection image. Here we considered a = 0.5, which was determined by observation of the results produced in a number of different cases. The operator '○' represents the element-wise multiplication, namely the multiplications of the corresponding elements of P_1 and $(1 - P_2)^a$.

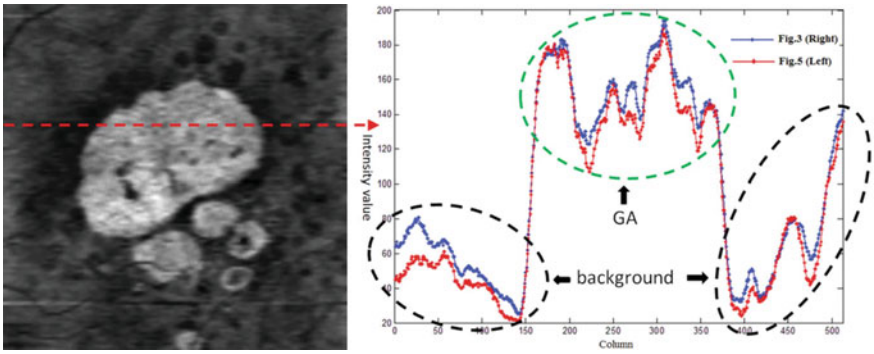

Fig. 11.35 GA projection image by combining two GA characteristics. Final GA projection image (Left). One line profile (Right)

Figure 11.35 (Left) shows the final GA projection image obtained with the Eq. (11.1), which combines the two GA characteristics: bright choroid and thin RPE. Figure 11.35 (Right) shows one line profile of the 170th rows of Figs. 11.34 (Right) and 11.35 (Left), marked with the dashed line in Fig. 11.35 (Left). The RPE thickness map can enhance the GA display by suppressing the background, as marked with the dashed black circles in Fig. 11.35 (Right). The edge slope between the GA (marked with the dashed gray circle in the middle) and background regions indicates that the final projection image (Fig. 11.35 (Left)) has a better contrast for the GA visualization than the RSVP projection image (Fig. 11.34 (Right)). Since the background intensity near the GA boundary is suppressed by the RPE thickness map, the intensity gradient of the GA boundary is higher in the final GA projection image than that in the RSVP projection image. This is helpful for enabling automated GA segmentation. While within the GA region, the intensity values have some decrease in the final GA projection image.

11.3.4.6 False Color Fusion

The proposed drusen and GA projection techniques described above are specific to display one pathological feature (either drusen or GA). To display drusen and GA simultaneously in one image, we adopted a false color fusion strategy. The three components (R, G, B) of the false color image consist of the SVP projection image, the drusen image, and the GA projection image, respectively. Figure 11.36 shows the false color fusion result (Bottom Right) by combining the SVP projection image (Top Left), drusen (Top Right) and GA projection (Bottom Left) images. It could be observed that GA appears in the R and B components, and drusen appears in the G component. We also noticed that drusen are darker in the GA projection image because they reduce the choroidal brightness. However, it is noticeable that in the false color image, the drusen is greenish and the GA is purple hue. The false color

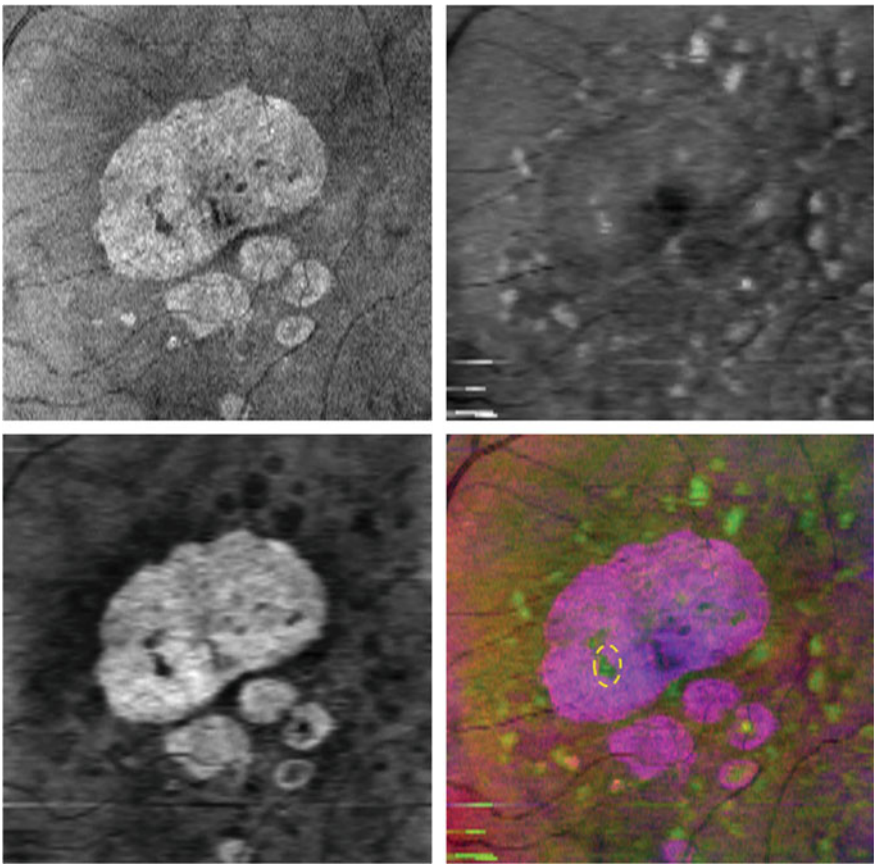

Fig. 11.36 False color fusion for drusen and GA visualization. Top Left: SVP projection image (R component). Top Right: Drusen projection image (G component). Bottom Left: GA projection image (B component). Bottom Right: False color image, where the dashed yellow oval represents a drusen within the big GA region

image (Bottom Right) can display drusen and GA with different colors in one image, and allow for analysis of the location of drusen with respect to GA. In a case shown below, the location of drusen marked with the dashed yellow oval can be observed within the GA region (Bottom Right).

11.3.4.7 Result

We carried out both a qualitative and quantitative evaluation of the cases analyzed. In this work, some of the patients also had color fundus photographs (CFPs) of their retinas, where both drusen and GA can be visualized. Manually outlining of the

drusen and GA lesions in the CFPs, SVP and false color image of these patients was done to qualitatively assess the drusen and GA visualization in each technique. Only two different cases from two patients are qualitatively discussed, due to the length limitation of this chapter.

A good assessment of drusen and GA can be done by looking at each B-scan in an SD-OCT cube. To quantitatively evaluate drusen and GA visualization in false color images, three SD-OCT cubes from three patients were reviewed independently, B-scan by B-scan (128 B-scans per cube), by two readers (NSJ and SJJ) in order to create a gold standard. Both readers had expertise in reviewing OCT retinal studies. Manually marking all 128 B-scans each cube was a very tedious task and time consuming, so only three of the 82 available SD-OCT cubes were reviewed in this quantitative study. We randomly selected three cases from the set of 82. Each of the readers independently marked drusen in the OCT B-scans by hand, in a similar manner as in [62]. To enable the assessment of intra-reader variation, each of the reader marked each image twice in two different sessions. The marked bars were then collapsed along the depth axis to produce an en face drusen/GA location maps (called "marking images"), which we used as the gold standard for our quantitative evaluation. We combined the two segmentations of the drusen (or GA) made by each reader in the two separate reading sessions using their intersection to produce a single outline per reader per image. More so, we applied the same intersection operation between the two segmentations made by different readers for each drusen (or GA) outline, producing a combined reader result.

We also outlined the drusen and GA by hand in the corresponding CFPs, SVP and false color images. The outlines images were then compared quantitatively to the images manually marked by the readers (the gold standard). The outlines are not precise, due to the blurred boundaries of drusen and GA in CFPs, SVP and false color images. As such, we used an overlap ratio of the number of visualized lesions as the metric to quantitatively evaluate drusen and GA visualization in each technique, instead of pixel by pixel classification:

$$overlap\_ratio = \frac{\#co\_lesion}{\#mark\_lesion} \tag{11.12}$$

where '$\#co\_lesion$' denotes the number of drusen (or GA) outlined both in the gold standard image and in the false color images, and ' ' denotes the number of drusen (or GA) in the gold standard image. Additionally, this metric represented the accuracy of the proposed method to detect drusen and GA present in the cube: if most of the drusen (or GA) outlined in the gold standard images could also be visualized in the en face image, the overlap ratio would be closer to 1. Meanwhile, if most of the drusen (or GA) are "missed" in the en face images, this overlap ratio would approach zero. The boundaries of lesions in CFPs, SVP and false color images are too obscure to be accurately outlined, therefore we used an overlap ratio of the number of total lesions found in each image, and not of outlined pixels. To reflect false positives, an over-estimated ratio is also

Table 11.10 Overlap ratio evaluation (unit: %) in inter-reader and intra-reader segmentations

Image		Patient 1	Patient 2	Patient 3	**Mean**
Reader 1_1—Reader 1_2	Drusen	81.8	94.9	29.4	**68.7**
	GA	88.9	100.0	100.0	**96.3**
Reader 2_1—Reader 2_2	Drusen	73.2	84.4	66.7	**74.8**
	GA	100.0	100.0	100.0	**100.0**
Reader 1-Reader 2	Drusen	90.3	81.5	66.7	**79.5**
	GA	66.7	66.7	100.0	**77.8**

$$overestimated\_ratio = \frac{\#false\_lesion}{\#mark\_lesion} \tag{11.13}$$

where '$\#false\_lesion$' denotes the number of drusen (or GA) outlined in the false color images, but not identified in the gold standard images.

11.3.4.8 Qualitative Evaluation

Figure 11.37 shows the comparison of the false color image and the CFP in one patient. The corresponding SVP projection image is shown in Fig. 11.36 (Top Left). Compared with the CFP (Fig. 11.37 (Top Right)), the false color image (Fig. 11.37 (Top Left)) is qualitatively better for displaying and differentiating the drusen and GA, due to the high contrast of the false color images, while also the color difference between drusen and GA is more obvious in the false color image. The remains of artifacts can be seen in the false color image, due to an inaccurate RPE extraction in some problematic areas. As shown below, the circled region in Fig. 11.37 (Top Left) shows areas which are not actual drusen, where these artifacts only minimally affect the drusen visualization.

11.3.4.9 Quantitative Evaluation

Table 11.10 presents the inter-reader and intra-reader agreement in terms of overlap ratio, where "Reader ki" denotes the segmentation outlined by reader k in the i-th session. We observed that the overlap ratio was higher for GA segmentations than for drusen segmentations, while the manual segmentations outlined by reader 2 were slightly more consistent between the two sessions that those outlined by reader 1 in average.

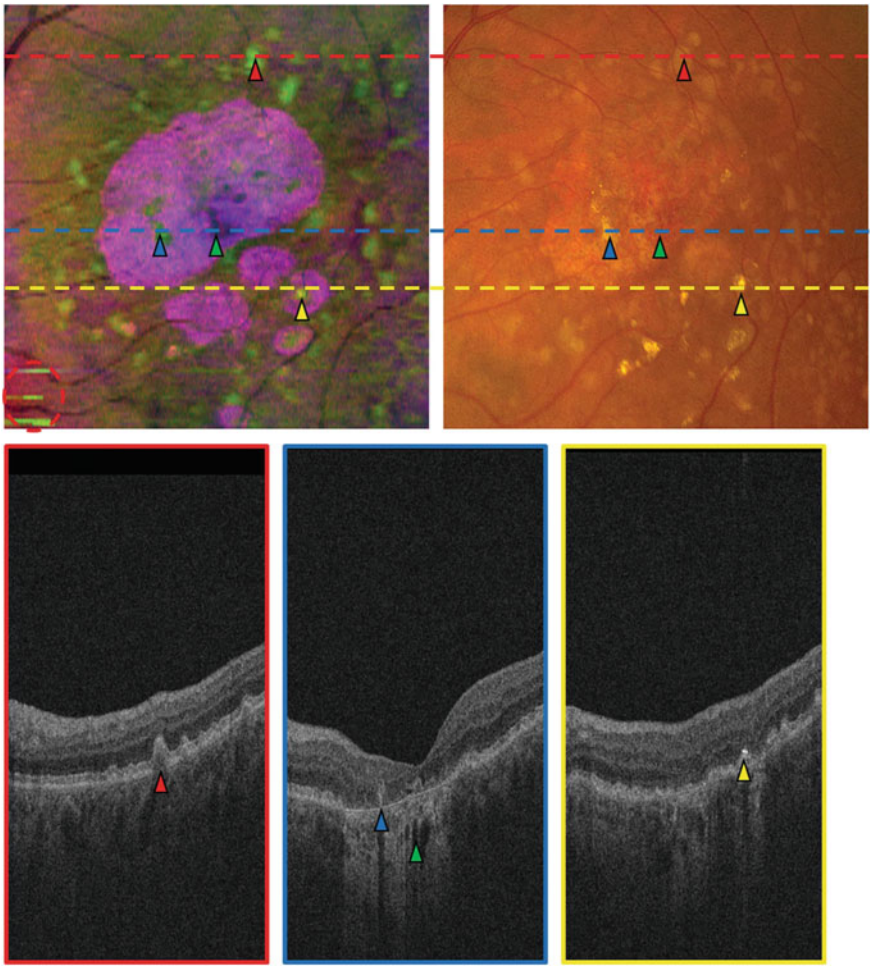

Fig. 11.37 Comparison of false color image (Top Left) and CFP (Top Right) in the left eye of a patient. Three B-scans (Bottom row) correspond to the three lines in (Top row). A red triangle indicates a druse in the fundus images (Top row) and the B-scan (Bottom Left); blue and yellow triangles mark two drusen within GA regions; a green triangle indicates a dark hole within the bright choroid; a yellow triangle marks a very bright region in the B-scan (Bottom Right), and a corresponding bright region in the fundus images (Top row). The red circled region in (Top Left) indicates artifacts in the false color image, produced by an inaccurate estimation of the RPE in a problematic area

Table 11.11 shows the comparison between the SVP, CFP and the proposed method for drusen and GA overlap ratio in three OCT scans from three different patients. Table 11.12 shows the comparison of drusen and GA over-estimated ratio, and Table 11.13 shows the number of drusen and GA in gold standard, SVP, CFP and false color images. The rows labeled as "Readers 1 & 2" correspond to the results

Table 11.11 Drusen and GA overlap ratio (unit: %) in SVP, CFP, and the proposed method ("Ours") compared with the gold standard. The maximum overlap ratios for each method are shown in bold

Image		Reader 1		Reader 2		Reader 1 & 2	
		Drusen	GA	Drusen	GA	Drusen	GA
Patient 1	SVP	4.9	**100.0**	3.2	**66.7**	3.9	**100.0**
	CFP	43.9	25.0	41.9	33.3	50.0	25.0
	Ours	**63.4**	**100.0**	**80.7**	**66.7**	**88.5**	**100.0**
Patient 2	SVP	11.8	**100.0**	11.0	**100.0**	15.4	**100.0**
	CFP	**85.3**	75.0	**88.9**	66.7	**92.3**	75.0
	Ours	64.7	**100.0**	70.4	**100.0**	80.8	**100.0**
Patient 3	SVP	0.0	**100.0**	0.0	**100.0**	0.0	**100.0**
	CFP	44.0	**100.0**	**66.7**	**100.0**	50.0	**100.0**
	Ours	**77.8**	**100.0**	**66.7**	**100.0**	**87.5**	**100.0**
Mean	SVP	5.6	**100.0**	4.7	**88.9**	6.4	**100.0**
	CFP	57.7	66.7	65.8	66.7	64.1	66.7
	Ours	**68.6**	**100.0**	**72.6**	**88.9**	**85.6**	**100.0**

Table 11.12 Drusen and GA over-estimated ratio (unit: %) in SVP, CFP, and the proposed method ("Ours") compared with the gold standard. The maximum over-estimated ratios for each method are shown in bold

Image		Reader 1		Reader 2		Reader 1 & 2	
		Drusen	GA	Drusen	GA	Drusen	GA
Patient 1	SVP	0.0	0.0	3.23	0.0	3.85	0.0
	CFP	**39.0**	0.0	**71.0**	0.0	**88.5**	0.0
	Ours	29.3	0.0	41.9	0.0	61.5	0.0
Patient 2	SVP	0.0	100.0	0.0	100.0	0.0	100.0
	CFP	**52.9**	100.0	**51.9**	100.0	**84.6**	100.0
	Ours	26.5	100.0	11.1	100.0	42.3	100.0
Patient 3	SVP	0.0	0.0	0.0	0.0	0.0	0.0
	CFP	**200.0**	0.0	**266.7**	0.0	**225.0**	0.0
	Ours	11.1	0.0	16.7	0.0	12.5	0.0
Mean	SVP	0.0	33.3	1.08	33.3	1.28	33.3
	CFP	**97.3**	33.3	**129.9**	33.3	**132.7**	33.3
	Ours	22.3	33.3	23.2	33.3	38.8	33.3

drawn by the two different readers and represent the evaluation for an average reader from overlapping the manual outlines.

From Tables 11.11, 11.12, 11.13, we observed that the false color images are preferably more effective for the visualization of drusen and GA than SVP and CFP. It can be seen that the SVP images allow the visualization of GA with the same performance as our method, yet drusen are almost invisible, therefore the overlap ratio and the over-estimated ratio with the gold standard are both very small. Meanwhile,

Table 11.13 Number of drusen and GA in gold standard, SVP, CFP and false color images

Image		Reader 1	Reader 2	Readers 1 & 2	SVP	CFP	Ours
Drusen	Patient 1	41	31	26	2	35	38
	Patient 2	34	27	26	3	45	29
	Patient 3	9	6	8	0	22	7
GA	Patient 1	8	3	8	6	2	6
	Patient 2	4	3	4	6	6	6
	Patient 3	2	1	1	1	1	1

the CFP images present a more acceptable performance in displaying drusen but worse GA visualization, making it difficult to distinguish between the two diseases. Because in CFPs the contrast of GA is low (as shown in Fig. 11.37, Top Right), so it is difficult to distinguish drusen and GA, the GA overlap ratio of CFP is evidently lower than those of SVP and false color images, and the drusen over-estimated ratio of CFP is higher than those of SVP and false color images. For the drusen visualization of patient 2, CFP is better than the proposed method, likely because the proposed method missed some small drusen due to some artifacts produced by an inaccurate segmentation of RPE layers. However, the proposed method was better on average. The GA overlap ratio is visibly higher than the drusen overlap ratio because GA lesions are usually larger and more easily identifiable than the drusen. As a matter of fact, all GA regions were correctly identified in the proposed method in the segmentations by Reader 1, and nearly all by Reader 2. When combining the outlines drawn by the two readers, it could be observed that drusen were identified better by Reader 2 and the overlap was very high (85.6%). It is also interesting to note that the proposed method produced an overlap ratio both for drusen and GA (Table 11.11) that resulted similar to the differences observed between the readers when inspecting the cubes B-scan by B-scan (Table 11.10). The differences observed between the segmentations drawn by a reader in the images produced by the proposed method and the ones drawn by the same reader when inspecting B-scan by B-scan were comparable to the ones observed when inspecting the B-scans in two separate sessions. In the same way, the differences found between the proposed method and the gold standard (B-scan inspection) for an average reader segmentation were similar to those observed between two different readers inspecting the B-scans.

11.3.4.10 Discussion

This section presents a novel visualization technique in which drusen and GA areas can be clearly assessed in the same image. In the state-of-art techniques, drusen and GA are usually identified in CFPs. In most cases, drusen can sometimes be very hard to distinguish in CFPs and can also be masked by the presence of GA due to the limitation of CFPs to resolve structures in the depth axis. The most efficient and

reliable way to identify and distinguish areas of drusen and GA is by inspecting SD-OCT cubes B-scan by B-scan.

More so, the traditional SVP projection usually masks drusen and does not take advantage of the ability of SD-OCT to resolve structures in the depth-axis. The proposed method takes advantage of this ability and allows the visualization of both drusen and GA present in the macula in a single image, while clearly distinguishing between them using a false color mapping. The examples of this improved visualization technique is presented in Fig. 11.37. Since we analyzed visually the results from 82 different cases, we only showed the results from two of the cases given the chapter length limitations. We also obtained satisfactory result by visual inspection for the rest of the cases. We analyzed the results produced by three of the cubes quantitatively, by comparing with SVP and CFP. Overall, the proposed method is better for the drusen and GA visualization than SVP and CFP. A combination of two readers was able to clearly identify all GA areas in our proposed method, while also identifying the majority of drusen.

The aim of this section is to simultaneously display drusen and GA in a single projection image from 3D SD-OCT images, not to segment drusen and GA. Using the difference between the actual RPE segmentation and the RPE floor (or Bruch's membrane), drusen can be segmented from OCT images.

In conclusion, we present a new visualization method for drusen and GA. It enhances GA visualization by utilizing the bright choroid and thin RPE characteristics of GA in the visualization method. To efficiently and effectively display drusen and GA in a single image, we present a false color fusion strategy to combine the drusen and GA projection images. Our experimental results show that the false color image is more effective for the drusen and GA visualization than the SVP image and CFP. Most of the drusen are not visible in SVP images, and the contrast of GA in SVP images is lower than that in the GA projection image. Even though, drusen and GA are visible in CFPs, they are difficult to distinguish because of low contrast. In false color images, the color difference between drusen and GA is more obvious. The proposed method may be used in improving the ability of ophthalmologist to visualize and evaluate drusen and GA.

11.4 Conclusion

This chapter presents several novel algorithm for semi-automated, automated GA and drusen segmentation and visualization in SD-OCT images to enable robust, accurate, and objective quantitative measurements of both drusen and GA extent and location automatically. The proposed method combines different novel algorithms and utilizes well known techniques in the implementation of our algorithms. Our technique seems more robust, through quantitative and qualitative experimental results which demonstrate that our algorithms show good agreement when compared to segmentation performed by other researcher's algorithm. The proposed algorithms may be clinically useful in providing relatively reliable GA and drusen qualitative and quan-

titative data that may improve tracking of GA extent, location and expansion in patients diagnosed with advanced non-exudative AMD.

References

1. H.R. Coleman, C.C. Chan, F.L. Ferris, E.Y. Chew, Age-related macular degeneration. Lancet **372**(9652), 1835–1845 (2008)
2. R.D. Jager, W.F. Mieler, J.W. Miller, Age-related macular degeneration. N. Engl. J. Med. **358**(24), 2606–2617 (2008)
3. R. Klein, T. Peto, A. Bird, M.R. Vannewkirk, The epidemiology of age-related macular degeneration. Am. J. Ophthalmol. **137**(3), 486–495 (2004)
4. D.V. Alfaro, P.E. Liggett, W.F. Mieler, H. Quiroz-Mercado, R.D. Jager, Y. Tano (eds.), *Age-related macular degeneration: a comprehensive textbook* (Lippincott Williams & Wilkins, Philadelphia, 2006)
5. A.C. Bird, N.M. Bressler, S.B. Bressler, I.H. Chisholm, G. Coscas, M.D. Davis, P.T. De Jong, C.C. Klaver, B.E. Klein, R. Klein et al., An international classification and grading system for age-related maculopathy and age-related macular degeneration: the International ARM Epidemiological Study Group. Surv. Ophthalmology **39**(5), 367–374 (1995)
6. R. Klein, B.E. Klein, K.L. Linton, Prevalence of age-related maculopathy: the Beaver Dam Eye Study. Ophthalmology **99**(6), 933–943 (1992)
7. Neil M. Bressler, Susan B. Bressler, Stuart L. Fine, Age-related macular degeneration. Surv. Ophthalmol. **32**(6), 375–413 (1988)
8. R. Klein, B.E. Klein, T. Franke, The relationship of cardiovascular disease and its risk factors to age-related maculopathy: the Beaver Dam Eye Study. Ophthalmology **100**(3), 406–414 (1993)
9. J.R. Vingerling, I. Dielemans, A. Hofman, D.E. Grobbee, M. Hijmering, C.F. Kramer, P.T. De Jong, The prevalence of age-related maculopathy in the Rotterdam Study. Ophthalmology **102**(2), 205–210 (1995)
10. H. Hirvela, H. Luukinen, E. Laara, L. Laatikainen, Risk factors of age-related maculopathy in a population 70 years of age or older. Ophthalmology **103**(6), 871–877 (1996)
11. C. Duanggate, B. Uyyanonvara, A review of automatic drusen detection and segmentation from retinal images, in the 3rd International Symposium on Biomedical Engineering, 222–225 2008
12. K. Rapantzikos, M. Zervakis, Nonlinear enhancement and segmentation algorithm for the detection of age-related macular degeneration (AMD) in human eye's retina, in Proceedings International Conference on Image Processing, vol. 3, pp. 1055– 1058 2001
13. K. Rapantzikos, M. Zervakis, K. Balas, Detection and segmentation of drusen deposits on human retina; potential in the diagnosis of age-related macular degeneration. Med. Image Anal. **7**(1), 95–108 (2003)
14. P. Checco, F. Corinto, CNN-based algorithm for drusen identification, in Proceedings IEEE International Symposium on Circuits and Systems, 2181–2184 2006
15. R.T. Smith, J.K. Chan, T. Nagasaki, U.F. Ahmad, I. Barbazetto, J. Sparrow, M. Figueroa, J. Merriam, Automated detection of macular drusen using geometric background leveling and threshold selection. Arch. Ophthalmol. **123**(2), 200–206 (2005)
16. S.S. Parvathi, N. Devi, Automatic drusen detection from colour retinal images. in International Conference on Computational Intelligence and Multimedia Applications, vol. 2, pp. 377–381 2007
17. N. Lee, A.F. Laine, T.R. Smith, Learning non-homogeneous textures and the unlearning problem with application to drusen detection in retinal images, In 5th IEEE International Symposium on Biomedical Imaging, 1215–1218 2008
18. D.E. Freund, N. Bressler, P. Burlina, Automated detection of drusen in the macula, in 6th IEEE International Symposium on Biomedical Imaging, 61–64 2009

19. Z.B. Sbeh, L.D. Cohen, G. Mimoun, G. Coscas, G. Soubrane, An adaptive contrast method for segmentation of drusen. in International Conference on Image Processing, vol. 1, pp. 255–258 1997
20. Brandon, L., Hoover, A. Drusen detection in a retinal image using multi-level analysis, in Proceedings. International Conference on Medical Image Computing and Computer-Assisted Intervention, vol. 2878, pp. 618–625 2003
21. A. Thaibaoui, A. Raji, A.Bunel, A fuzzy logic approach to drusen detection in retinal angiographic images, in 15th International Conference on Pattern Recognition, vol. 4, pp. 748–751 2000
22. Z. Liang, D.W.K. Wong, J. Liu, K.L. Chan, T.Y. Wong, Towards automatic detection of age-related macular degeneration in retinal fundus images, in 32nd Annual International Conference of the IEEE Engineering in Medicine and Biology Society, vol. 1, pp. 4100–4103 2010
23. G. Quellec, S.R. Russell, M.D. Abramoff, Optimal filter framework for automated, instantaneous detection of lesions in retinal images. IEEE Trans. Med. Imaging **30**(2), 523–533 (2011)
24. S.R. Freeman, I. Kozak, L. Cheng, D.U. Bartsch, F. Mojana, N. Nigam, M. Brar, R. Yuson, W.R. Freeman, Optical coherence tomography-raster scanning and manual segmentation in determining drusen volume in age-related macular degeneration. Retina **30**(3), 431–435 (2010)
25. B.A. Bower, S.J. Chiu, E. Davies, A.M. Davis, R.J. Zawadzki, A.R. Fuller, D.F. Wiley, J.A. Izatt, C.A. Toth, Development of quantitative diagnostic observables for age-related macular degeneration using Spectral Domain OCT. Proc. SPIE. **6426**, 64260W (2007)
26. S. Farsiu, S.J. Chiu, J.A. Izatt, C.A. Toth, Fast detection and segmentation of drusen in retinal optical coherence tomography images, in Ophthalmic Technologies XVIII, Proceedings of SPIE, vol. 6844, pp. 68440D.1–68440D (2008)
27. C.A. Toth, S. Farsiu, S.J. Chiu, A.A. Khanifar, J.A. Izatt, Automatic drusen segmentation and characterization in spectral domain optical coherence tomography (SDOCT) images of AMD eyes. Association for Research in Vision and Ophthalmology (ARVO) Annual Meeting, E-Abstract, vol. 5394 2008
28. K. Yi, M. Mujat, B.H. Park, W. Sun, J.W. Miller, J.M. Seddon, L.H. Young, J.F. de Boer, T.C. Chen, Spectral domain optical coherence tomography for quantitative evaluation of drusen and associated structural changes in non-neovascular age-related macular degeneration. Br. J. Ophthalmol. **93**(2), 176–181 (2009)
29. N. Jain, S. Farsiu, A.A. Khanifar, S. Bearelly, R.T. Smith, J.A. Izatt, C.A. Toth, Quantitative comparison of drusen segmented on SD-OCT versus drusen delineated on color fundus photographs. Invest. Ophthalmol. Vis. Sci. **51**(10), 4875–4883 (2010)
30. G. Gregori, F. Wang, P.J. Rosenfeld, Z. Yehoshua, N.Z. Gregori, B.J. Lujan, C.A. Puliafito, W.J. Feuer, Spectral domain optical coherence tomography imaging of drusen in non-exudative age-related macular degeneration. Ophthalmology **118**(7), 1373–1379 (2011)
31. D. Iwama, M. Hangai, S. Ooto, A. Sakamoto, H. Nakanishi, T. Fujimura, A. Domalpally, R.P. Danis, N. Yoshimura, Automated assessment of drusen using three-dimensional spectral-domain optical coherence tomography. Invest. Ophthalmol. Vis. Sci. **53**(3), 1576–1583 (2012)
32. A.D. Mora, P.M. Vieira, A. Manivannan, J.M. Fonseca, Automated drusen detection in retinal images using analytical modelling algorithms. BioMed. Eng. Online **10**, 59 (2011)
33. Akram, M.U., Mujtaba S., Tariq A. Automated drusen segmentation in fundus images for diagnosing age related macular degeneration, in Electronics, Computer and Computation (ICECCO) in International Conference on, Ankara, pp. 17–20 2013
34. Q. Chen, T. Leng, L. Zheng, L. Kutzscher, J. Ma, L. de Sisternes, D.L. Rubin, Automated drusen segmentation and quantification in SD-OCT images. Med. Image Anal. **17**(8), 1058–1072 (2013)
35. Q. Chen, T. Leng, L.L. Zheng, L. Kutzscher, L. de Sisternes, D.L. Rubin, An improved OCT-derived fundus projection image for drusen visualization. Retina **0**(0), 1–13 (2014)
36. S. Jiao, R. Knighton, X. Huang, G. Gregori, C. Puliafito, Simultaneous acquisition of sectional and fundus ophthalmic images with spectral-domain optical coherence tomography. Opt. Express **13**(2), 444–452 (2005)

37. M. Stopa, B.A. Bower, E. Davies, J.A. Izatt, C.A. Toth, Correlation of pathologic features in spectral domain optical coherence tomography with conventional retinal studies. Retina **28**(2), 298–308 (2008)
38. I. Gorczynska, V.J. Srinivasan, L.N. Vuong, R.W.S. Chen, J.J. Liu, E. Reichel, M. Wojtkowski, J.S. Schuman, J.S. Duker, J.G. Fujimoto, Projection OCT fundus imaging for visualizing outer retinal pathology in non-exudative age-related macular degeneration. Br. J. Ophthalmol. **93**(5), 603–609 (2009)
39. R. Klein, M.D. Davis, Y.L. Magli, P. Segal et al., The Wisconsin age-related maculopathy grading system. Ophthalmology **98**, 1128–1134 (1991)
40. R.T. Smith, J.K. Chan, T. Nagasaki et al., A method of drusen measurement based on reconstruction of fundus background reflectance. Br. J. Ophthalmol. **89**, 87–91 (2005)
41. D.S. Shin, N.B. Javornik, J.W. Berger, Computer-assisted, interactive fundus image processing for macular drusen quantitation. Ophthalmology **106**, 1119–1125 (1999)
42. S.J. Chiu, X.T. Li, P. Nicholas, C.A. Toth, J.A. Izatt, S. Farsiu, Automatic segmentation of seven retinal layers in SDOCT images congruent with expert manual segmentation. Opt. Express **18**(18), 19413–19428 (2010)
43. S. Lu, C.Y.L. Cheung, J. Liu, J.H. Lim, C.K.S. Leung, T.Y. Wong, Automated layer segmentation of optical coherence tomography images. IEEE Trans. Biomed. Eng. **57**(10), 2605–2608 (2010)
44. M.K. Garvin, M.D. Abramoff, X. Wu, S.R. Russell, T.L. Burns, M. Sonka, Automated 3-D intraretinal layer segmentation of macular spectral-domain optical coherence tomography images. IEEE Trans. Med. Imaging **28**(9), 1436–1447 (2009)
45. A. Bindewald, A.C. Bird, S.S. Dandekar, J. Dolar-Szczasny, J. Dreyhaupt, F.W. Fitzke, W. Einbock, F.G. Holz, J.J. Jorzik, C. Keilhauer, N. Lois, J. Mlynski, D. Pauleikhoff, G. Staurenghi, S. Wolf, Classification of fundus auto-fuorescence patterns in early age-related macular disease. Invest. Ophthalmol. Vis. Sci. **46**(9), 3309–3314 (2005)
46. S. Schmitz-Valckenberg, C.K. Brinkmann, F. Alten, P. Herrmann, N.K. Stratmann, A.P. Gobel, M. Fleckenstein, M. Diller, G.J. Jaffe, F.G. Holz, Semiautomated image processing method for identification and quantification of geographic atrophy in age-related macular degeneration. Invest. Ophthalmol. Vis. Sci. **52**(10), 7640–7646 (2011)
47. A. Deckert, S. Schmitz-Valckenberg, J. Jorzik, A. Bindewald, F.G. Holz, U. Mansmann, Automated analysis of digital fundus autofluorescence images of geographic atrophy in advanced age-related macular degeneration using confocal scanning laser ophthalmoscopy (cSLO). BMC Ophthalmol. **5**, 1–8 (2005)
48. N. Lee, A.F. Laine, I. Barbazetto, M. Busuoic, R. Smith, Level set segmentation of geographic atrophy in macular autofluorescence images. Invest. Ophthalmol. Vis. Sci. **47**(10) (2006)
49. N. Lee, A.F.Laine, R.T. Smith, A hybrid segmentation approach for geographic atrophy in fundus auto-fluorescence images for diagnosis of age-related macular degeneration, in Proceeding of the 29th Annual International Conference of the IEEE Engineering in Medicine and Biology Society, 4965–4968 2007
50. N. Lee, A.F. Laine, R.T. Smith, Interactive segmentation for geographic atrophy in retinal fundus images, in the 42nd Asilomar Conference on Signals, Systems and Computers, vol. 42, pp. 655–658 2008
51. R.G. Sayegh, C. Simader, U. Schechy, A. Montuoro, C. Kiss, S. Sacu, D.P. Kreil, C. Prunte, U. Schmidt-Erfurth, A systematic comparison of spectral-domain optical coherence tomography and fundus autofluorescence in patients with geographic atrophy. Ophthalmology **118**(9), 1844–1851 (2011)
52. S.J. Chiu, J.A. Izatt, R.V. O'Connell, K.P. Winter, C.A. Toth, S. Farsiu, Validated automatic segmentation of AMD pathology including drusen and geographic atrophy in SDOCT images. Invest. Ophthalmol. Vis. Sci. **53**(1), 53–61 (2012)
53. C. Schütze, C. Ahlers, S. Sacu, G. Mylonas, R. Sayegh, I. Golbaz, G. Matt, G. Stock, U. Schmidt-Erfurth, Performance of OCT segmentation procedures to assess morphology and extension in geographic atrophy. Acta. Ophthalmol. **89**(3), 235–240 (2011)

54. Albert K. Feeny, Mongkol Tadaratic, David E. Freund, Neil M. Bressler, Philippe Burlina, Automated segmentation of geographic atrophy of the retinal epithelium via random forests in AREDS color fundus images. Comput. Biol. Med. **65**(1), 124–136 (2015)
55. Hu Zhihong, Gerard G. Medioni, Matthias Hernandez, Amirhossein Hariri, Wu Xiaodong, SriniVas R. Sadda, Segmentation of the geographic atrophy in spectral-domain optical coherence tomography and fundus autofluorescence images. Invest. Ophthalmol. Vis. Sci. **54**(13), 8375–8383 (2013)
56. Muneeswar Gupta Nittala, Amirhossein Hariri, Erin Henry, Eric C. Strauss, Phillip Lai, Srinivas R. Sadda, Correlation between fundus autofluorescence and spectral domain optical coherence tomography measurements in geographic atrophy. Invest. Ophthalmol. Vis. Sci. **55**(13), 5896 (2014)
57. Qiang Chen, Luis de Sisternes, Theodore Leng, Luoluo Zheng, Lauren Kutzscher, Daniel L. Rubin, Semi-automatic geographic atrophy segmentation for SD-OCT images. Biomedical Optics Express **4**(12), 2729–2750 (2013)
58. Sijie Niu, Luis de Sisternes, Qiang Chen, Theodore Leng, Daniel L. Rubin, Automated geographic atrophy segmentation for SD-OCT images using region-based C-V model via local similarity factor. Biomed. Opt. Express **7**(2), 581–600 (2016)
59. Q. Chen, S. Niu, H. Shen, T.N. Leng, L. De Sisternes, D.L. Rubin, Restricted summed-area projection for geographic atrophy visualization in SD-OCT images. Translational Vision Sci. Technol. **4**(5), 2 (2015)
60. Q. Chen, T. Leng, S. Niu, J. Shi, L. De Sistermes, D.L. Rubin, A false color fusion strategy for drusen and GA visualization OCT images. Retina (Philadelphia, Pa.) **34**(12), 2346–2358 (2014)
61. C. Tomasi, R. Manduchi, Bilateral filtering for gray and color images, in Proceedings of the International Conference on Computer Vision (ICCV) pp. 839–846 1998
62. Z. Yehoshua, C.A.A. Garcia Filho, F.M. Penha, G. Gregori, P.F. Stetson, W.J. Feuer, P.J. Rosenfeld, Comparison of geographic atrophy measurements from the OCT fundus image and the sub-RPE slab image. Ophthalmic Surg. Lasers Imaging Retina. **44**(2), 127–132 (2013)
63. V. Caselles, F. Catte, T. Coll, F. Dibos, A geometric model for active contours in image processing. Numer. Math. **66**, 1–31 (1993)
64. R. Malladi, J.A. Sethian, B.C. Vemuri, Shape modeling with front propagation: a level set approach. IEEE Trans. Pattern Anal. Mach. Intell. **17**(2), 158–175 (1995)
65. C. Li, C. Xu, C. Gui, M.D. Fox, Level set evolution without re-initialization: a new variational formulation, in Proceedings of the IEEE Computer Society Conference on Computer Vision and Pattern Recognition, vol. 1, pp. 430–436 2005
66. L. De Sisternes, J. Hu, D.L. Rubin, M.F. Marmor, Localization of damage in progressive hydroxychloroquine retinopathy on and off the drug: inner versus outer retina, parafovea versus peripheral fovea. Invest. Ophthalmol. Vis. Sci. **56**(5), 3415–3426 (2015)
67. T.F. Chan, L.A. Vese, Active contours without edges. IEEE Trans. Image Process. **10**(2), 266–277 (2001)
68. N. Otsu, A threshold selection method from gray-level histograms. IEEE Trans. Syst. Man Cybem **9**(1), 62–66 (1995)
69. R. Gonzales, R. Woods, Digital Image Processing. (Prentice Hall, 1992) Chapter 6
70. S. Osher, J.A. Sethian, Fronts propagating with curvature-dependent speed: algorithms based on Hamilton-Jacobi formulation. J. Comput. Phys. **79**(1), 12–49 (1988)
71. Z. Yehoshua, P.J. Rosenfeld, G. Grgori et al., Progression of geographic atrophy in age related macular degeneration imaged with spectral domain optical coherence tomography. Ophthalmology **118**(4), 679–686 (2011)
72. C. Volz, D. Pauly, Antibody therapies and their challenges in the treatment of age-related macular degeneration. Eur. J. Pharm. Biopharm. pii: S0939–6411 (15) 00102–2 2015
73. K. Zhang, J.J. Hopkins, J.S. Heier, D. Birch G., L.S. Halperin, T.A. Albini, D.M. Brown, G.J. Jaffe, W. Tao, G.A. Williams, Ciliary neurotrophic factor delivere0d by encapsulated cell intraocular implants for treatment of geographic atrophy in age-related macular degeneration, in Proceedings of the National Academy of Sciences of the United States of America, 108(15), 6241–6245

74. Z. Yehoshua, P.J. Rosenfeld, T.A. Albini, Current clinical trials in dry AMD and the definition of appropriate clinical outcome measures. Seminars Ophthalmology **26**(3), 167–180 (2011)
75. S. Bearelly, F.Y. Chau, A. Koreishi et al., Spectral domain optical coherence tomography imaging of geographic atrophy margins. Ophthalmology **116**(9), 1762–1769 (2009)
76. J.L. Dunaief, T. Dentchev, G.S. Ying, A.H. Milam, The role of apoptosis in age-related macular degeneration. Arch. Ophthalmol. **120**(11), 1435–1442 (2002)
77. G.S. Hageman, P.J. Luthert, Chong N.H. Victor et al., An integrated hypothesis that considers drusen as biomarkers of immune-mediated processes at the RPE-Bruch's membrane interface in aging and age-related macular degeneration. Prog. Retin. Eye Res. **20**(6), 705–732 (2001)
78. G. Lutty, J. Grunwald, A.B. Majji, M. Uyama, S. Yoneya, Changes in choriocapillaris and retinal pigment epithelium in age-related macular degeneration. Mol. Vis. **5**, 35 (1999)
79. D.S. McLeod, M. Taomoto, T. Otsuji et al., Quantifying changes in RPE and choroidal vasculature in eyes with age-related macular degeneration. Invest. Ophthalmol. Vis. Sci. **43**(6), 1986–1993 (1993)

Chapter 12
Segmentation of Symptomatic Exudate-Associated Derangements in 3D OCT Images

Lingjiao Pan and Xinjian Chen

Exudative AMD is an advanced form of AMD which can cause severe vision loss. Quantitative analysis of the exudates is essential for the treatment and follow-up. This chapter presents an automatic method for segmentation of the exudate regions in 3D SD-OCT images using on a graph-based model.

12.1 Introduction

The primary cause of vision loss and blindness among the adults (>50 years old) is Age-related macular degeneration (AMD) [1]. Exudative AMD or neovascular AMD is an advanced form of AMD, due to the growth of abnormal blood vessels from the choroidal vasculature, leading to sub- and intra-retinal leakage of vascular fluid. Recently, anti-vascular endothelial growth factor agents (including Ranibizumab and bevacizumab) [2–4] through intra-vitreal injection, as a treatment of exudative AMD has become available. It leads to a regression of the neovascularization and resulting resorption of fluid. The frequency of the injections is primarily guided by the amount of intra-retinal fluid. The amount of intra-retinal fluid can be clinically estimated subjectively from a limited number of spectral domain optical coherence tomography (SD-OCT) slices [5–8]. The intra- and inter-observer variability is high potentially leading to substantial inconsistency in treatment, and automated fluid segmentation has the potential to improve this [9, 10]. In this chapter, we use the term symptomatic exudate-associated derangement (SEAD) for the main retinal manifestations of AMD, including subretinal fluid, intraretinal fluid, and pigment epithelial

L. Pan · X. Chen (✉)
School of Electronics and Information Engineering, Soochow University, Suzhou, China
e-mail: xjchen@suda.edu.cn

X. Chen
State Key Laboratory of Radiation Medicine and Protection, Soochow University, Suzhou, China

X. Chen et al. (eds.), *Retinal Optical Coherence Tomography Image Analysis*,
Biological and Medical Physics, Biomedical Engineering,
https://doi.org/10.1007/978-981-13-1825-2_12

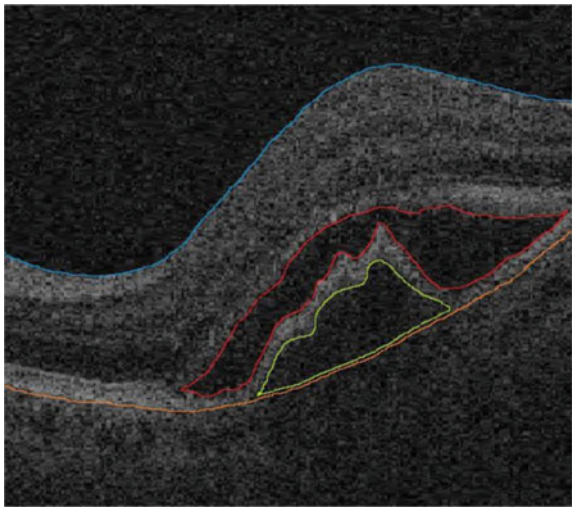

Fig. 12.1 Examples of SEADs. The red curve is a manual segmentation of the SEAD consisting by the intraretinal fluid and the green curve outlines a SEAD resulting from a pigment epithelial detachment

detachment (as shown in Fig. 12.1). The segmentation of SEADs is a challenging task since the signal-to-noise ratio (SNR) is relatively low and the SEADs have considerable shape variability in SD-OCT scans. Full segmentation of the 3-D SEAD volumes is more challenging.

Graph search (GS) methods can be successfully applied to surface segmentation [11, 12], and graph cut (GC) methods are widely used to the segmentation of region object [13–15]. Synergistically combine the graph search and graph cuts methods could be applied to solve more complex and challenging medical image segmentation problems including segmentation of the SEADs and layers simultaneously.

In this chapter we introduce a fully 3-D and fully automated method for SEAD segmentation, which effectively combines the GS and GC methods [16]. The top and bottom retinal surfaces serve as the constraints for SEAD segmentation. An automatic voxel classification based on the layer-specific texture features are used for initialization. The new GC–GS method significantly outperformed both the traditional graph cut and traditional graph search approaches and has the potential to improve clinical management of patients with choroidal neovascularization due to exudative age-related macular degeneration.

12.2 Related Methods

12.2.1 Conventional Graph-Cut Algorithm

GC methods have been widely used for image segmentation in recent years [13, 15, 17–23]. A conventional graph-cut framework [13, 15] was thought to be feasible to

solve SEAD segmentation in 3-D OCT [24]. By introducing both a boundary term and a regional term into the energy function, the method computed a minimum cost s/t cut on an appropriately constructed graph [17, 18]. For multiple object-region segmentation, an interaction term can be introduced to the energy function as a hard geometric constraint [11]. The overall problem can also be solved by computing an s/t cut with a maximum-flow algorithm. The conventional graph-cut framework can be applied to objects with different topological shapes, but it cannot avoid segmentation leaks in lower resolution images.

12.2.2 Optimal Surface Approach—Graph-Search Approach

Optimal surface approach (GS methods) [12, 25–27] is another graph based method which is important for the analysis of multiple intra-retinal layers in 3-D OCT images [28, 29]. Take SEAD cases as example, most of the subretinal fluid, lesions intra-retinal fluid and the pigment epithelial detachments are all associated with surrounding retinal layers. The GS methods modeled the boundaries between layers as terrain-like surfaces and suggested representing the terrain-like surface as a related closed set. GS methods segment the terrain-like surface by finding an optimal closed set. For the multiple-surface case, the optimal surface approach constructed a corresponding subgraph for each terrain-like surface [25], and added weighted inter-graph arcs, which enforced geometry constraints between subgraphs. The multiple optimal surfaces segmentation could be solved simultaneously as a single s/t cut problem by using a maximum-flow algorithm. The method worked well in finding stable results of globally optimal terrain-like surfaces. However, it was limited by the prior shape requirement. For the multiple-SEAD in a single OCT image, it can be modeled as a problem with multiple regions interacting with multiple surfaces. A surface-region graph-based method was proposed to segment multiple regions and multiple surfaces simultaneously [30].

12.3 Probability-Constrained Graph Search-Graph Cut

The graph search-graph cut method consists of two main steps: initialization and segmentation (Fig. 12.2). In the initialization step, preprocessing steps are applied first to the input OCT image. The preprocessing steps include: segmenting the layers, fitting a surface to the bottom [retinal pigment epithelium (RPE)] layer, determining SEAD footprints [31], ignoring points within the SEAD footprints, and flattening the scan images; a texture classification based method is employed producing the initialization results. Following initialization step, probability normalization refines the initialization results. In the segmentation step, the GS-GC method synergistically integrates the results from the initialization.

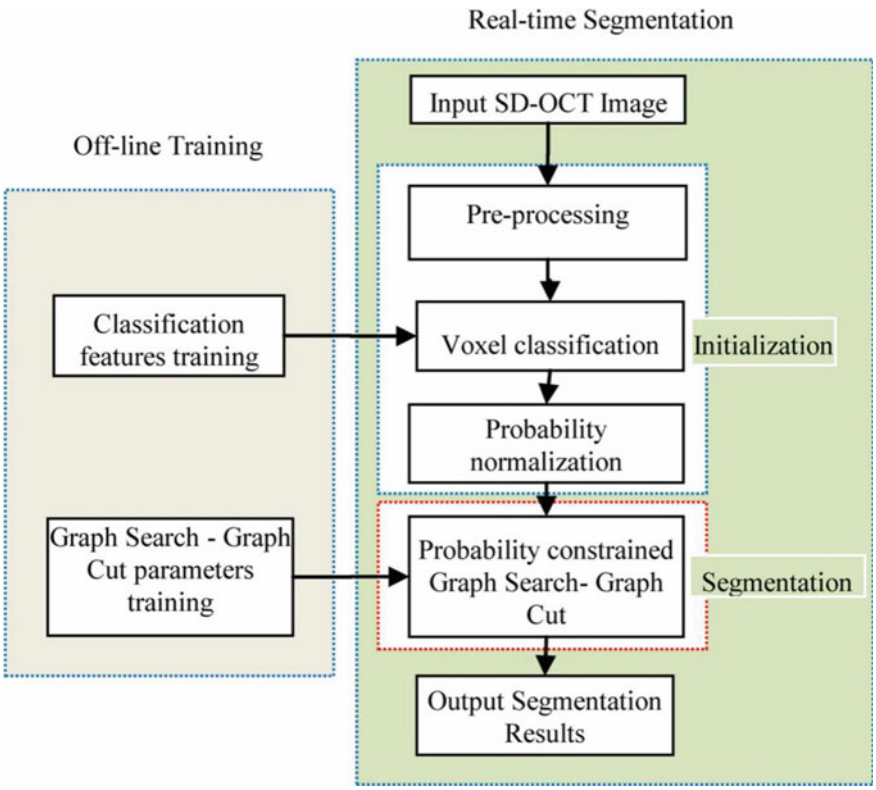

Fig. 12.2 Flowchart of the proposed system

12.3.1 Initialization

An initial segmentation of the SEAD regions is required to initialize the graph-based SEAD segmentation algorithm. A statistical voxel classification approach is applied directly to the preprocessed input image to find voxels that are likely inside of a SEAD region. The classifier assigns a likelihood to each voxel that it belongs to a SEAD. This likelihood map serves as constraints for the graph-based segmentation algorithm.

12.3.1.1 Preprocessing

First, the output of our 11-surface segmentation [29] is used to determine the upper and lower surface of the retina in the scan. For these 11 surfaces, the top retinal surface corresponds to the inner limiting membrane and bottom layer corresponds to the RPE. Although, the top retinal surface is usually segmented successfully even in OCT scans

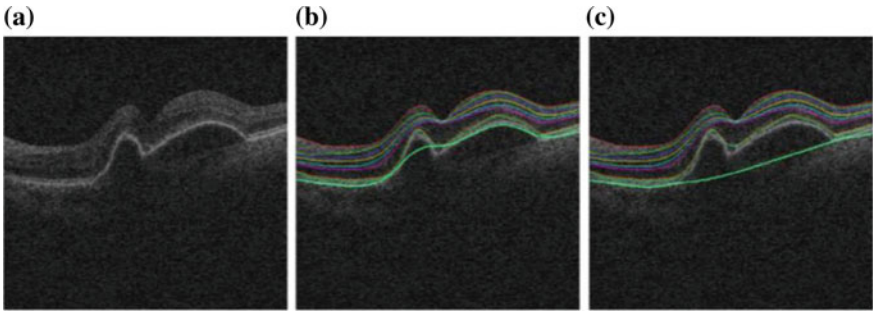

Fig. 12.3 Illustration of retinal layer correction. **a** One slice from the original OCT image. **b** Segmentation of all surfaces, with surface 11 at the bottom (cyan). **c** Surface 11 after thin-plate spline fitting

with SEADs, the bottom surface segmentation can be problematic, especially with SEADs located under the retinal pigment epithelium (RPE, see Fig. 12.3). In these cases, the layer segmentation may follow the top of the SEAD instead of identifying the bottom of the retina.

A method for detection of SEAD locations in the XY-plane by analyzing the thickness and textural properties of individual layers in groups of A-scans was previously presented [31]. The likelihood that an A-scan belongs to a SEAD footprint is calculated from the number of standard deviations from the normal atlas value. The binary SEAD footprint is generated by thresholding the likelihood map and the binary SEAD footprint is used to enhance the bottom surface segmentation result so that it is approximately located at the position in the scan where the bottom of the retina would have been located had the SEAD not been present. This is accomplished by fitting a thin plate spline to a set of 1000 randomly sampled points from the bottom surface 11, located outside of the 2-D SEAD footprint map. Figure 12.3 shows a representative example of the bottom surface before and after thin plate spline fitting. The retinal images are subsequently flattened according to the identified thin-plate spline surface.

12.3.1.2 Voxel Classification

A supervised voxel classification approach trained on the voxels between the previously segmented top and bottom surface of the retina is applied to generate an initial segmentation of the fluid-filled SEAD areas. The training images are first subsampled by a factor of 2 in the X and Y directions and a factor of 4 in depth to speed up feature extraction and subsequent voxel classification. (1) Features: For each voxel, many of the structural, textural and positional features are calculated (see Table 12.1). Textural features (16–45) describe local texture while structural features (1–15) describe the local image structure. The location (height) of the voxel in the retina is encoded in three location features (46–48), the L2 distance in voxels from previously segmented

Table 12.1 Used classification features

Feature nr.	Feature description
1–5	First eigenvalues of the Hessian matrices at scales $\sigma = 1, 3, 6, 9$ and 14
6–10	Second eigenvalues of the Hessian matrices at scales $\sigma = 1, 3, 6, 9$ and 14
11–15	Third eigenvalues of the Hessian matrices at scales $\sigma = 1, 3, 6, 9$ and 14
16–45	Output of a Gaussian filter bank up to and including second order derivatives at scales $\sigma = 2, 4, 8$
46–48	Voxel distances from surfaces 1, 7 and 11
49–52	Layer texture features as described in [31]: mean intensity, co-occurrence matrix entropy and inertia, wavelet analysis standard deviation (level 1)

surfaces 1, 7, and 11. Finally, four features (49–52) are included that were determined in our previous work [31] as relevant to SEAD detection and description. (2) Training Phase: In the training phase, the preprocessed training images are randomly sampled to collect voxels that are either inside or outside of the SEADs. Due to differences in the number of SEAD voxels in individual OCT images both the normal and the SEAD voxels in a scan are sampled separately to ensure that a sufficient number of positive training samples are obtained in each scan. For each training image, 10,000 positive samples and 50,000 negative samples (i.e., two classes) were randomly collected. All available positive voxels were included in the training set if there were less than 10,000 positive voxels in any training image, [32]. Since the SEADs in our data are fluid filled, voxels inside the SEADs correspond to fluid while voxels outside of the SEADs do not, two-class classification was used. Based on the performance in comparative preliminary experiments on a small, independent set of images, a k-nearest neighbor classifier was chosen. The employed k-NN implementation [33] allows approximate nearest neighbor classification and the maximum error parameter epsilon was set to two for this algorithm. Training time for this classifier is low, taking less than 20 s. The training phase only needs to be run for once, after this, the trained classifier can be used to classify unseen voxels [34]. (3) Testing Phase: Test images by using the previously described trained classifier. After preprocessing and feature extraction, each voxel between the top and the bottom surfaces was assigned a likelihood between 0 and 1 that the voxel is inside of a SEAD region.

12.3.1.3 Initialization Postprocessing by Probability Normalization

The previously described initialization is not always successful (see second and third rows of Fig. 12.7). A postprocessing method was proposed to cope with the high

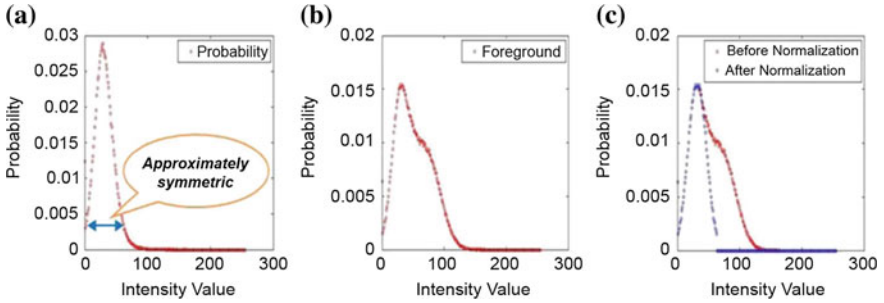

Fig. 12.4 Initialization post-processing: Probability normalization. **a** Intensity distribution of SEAD regions in the reference standard. **b** Intensity distribution in a specific initialization result. **c** Probability normalization resulting from the flip-duplicate step (see text)

image noise in these cases. It was revealed that in the low intensity range, the intensity distribution of the SEAD regions closely follows the Gaussian distribution. This knowledge was used to postprocess the initialization results, as shown in Fig. 12.4. (1) Find the largest intensity value on the original curve. (2) Using this value, flip-duplicate the left part of the curve. (3) Set the probability of those intensity values outside the symmetric part to zero. After the postprocessing, the subsequent graph-based segmentation is constrained by the resulting likelihood map.

12.3.2 Graph Search-Graph Cut SEAD Segmentation

The GS and GC methods were synergistically combined to segment the SEADs. Two layers (one layer above the SEAD region and another below the SEAD region) are included as the auxiliary target objects to constraint the SEAD segmentation.

12.3.2.1 Cost Function Design

The segmentation problem usually formulated as an energy minimization problem. The goal is to find a solution that minimizes the energy function $E_n(\mathrm{f})$. Our cost function is designed as follows:

$$En(\mathrm{f}) = E(Surface) + E(Regions) + E(Interactions) \tag{12.1}$$

where $E(\mathrm{Surface})$ represents the cost associated with the segmentation of all surfaces, $E(\mathrm{Regions})$ represents the cost associated with the segmented regions, and $E(\mathrm{Interactions})$ represents the cost of constraints between the regions and surfaces.

(1) Surface cost function: For the terrain-like multiple-surface segmentation, the graph search method [12] is utilized. Similar to [12], the cost function is designed as

$$E(S) = \sum_{V \in S} C_v + \sum_{(p,q) \in N} h_{p,q}(S(p) - S(q)) \tag{12.2}$$

where S is the desired surface, C_v is an edge-based cost which is inversely related to the likelihood that S contains the voxel v. (p, q) is a pair of neighboring columns N. $h_{p,q}$ is a convex function penalizing the surface S shape change on p and q.

(2) Region cost function: The graph cut method [13] has been successfully applied to regional segmentation. The typical graph cut energy function is defined as,

$$E(f) = \sum_{p \in P} R_p(\mathrm{f_p}) + \sum_{p \in P, q \in Np} B_{p,q}(f_p, f_q) \tag{12.3}$$

where N_p is the set of pixels in the neighborhood of p. $R_p(f_p)$ is the cost of assigning label $f_p \in \mathrm{L}$ to p which is usually defined based on the image intensity and can be considered as a log likelihood of the image intensity for the target object, and $B_{p,q}(f_p, f_q)$ is the cost of assigning labels $f_p,\ f_q \in \mathrm{L}$ to p and q that could be based on the gradient of the image intensity.

Importantly, the whole framework integrated the results of the initialization step: (1) Source seeds were the high likelihood voxels (over 0.8, followed by morphologic erosion). Sink seeds were voxels with low probability (here 0). (2) The proposed probability-constrained energy function was defined as follows:

$$E = \sum_{p \in P} (\alpha \cdot D_p(f_p) + \beta \cdot C_p(f_p)) + \sum_{p \in P, q \in N_p} \gamma \cdot B_{p,q}(f_p + f_q) \tag{12.4}$$

where α, β, γ are the weights for the data term, probability constrained term, and boundary term, respectively, satisfying $\alpha + \beta + \gamma = 1$. These components are defined as follows:

$$D_p(f_p) = \begin{cases} -\ln P(I_p|O), & if\ \ f_p = object\ label \\ -\ln(P(I_p|B)), & if\ \ f_p = background\ label \end{cases} \tag{12.5}$$

$$B_{p,q}(f_p, f_q) = \exp\left(-\frac{(I_p - I_q)^2}{2\sigma^2}\right) \cdot \frac{1}{d(p,q)} \delta(f_p, f_q) \tag{12.6}$$

and

$$\delta(f_p, f_q) = \begin{cases} 1, & if\ \ f_p \neq f_q \\ 0, & otherwise \end{cases}$$

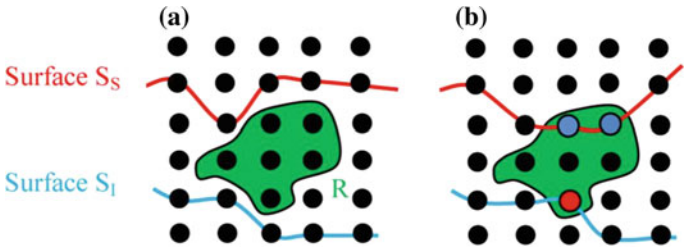

Fig. 12.5 Illustration of surface-region interactions on a 2D example. **a** The two terrain-like surfaces: S_S and S_I, and the region R in green. **b** Incorporation of the constraints between the region and surfaces. If the voxel in the region is superior to surface S_S, then a penalty is given (as illustrated in blue). And if the voxel in the region is inferior than surface S_I, then a penalty is given (as illustrated in red)

where I_p is the intensity of pixel p, object label is the label of the object (foreground). $P(I_p|O)$ and $P(I_p|B)$ are the probabilities of intensity of pixel p belonging to object and background, respectively, which are estimated from object and background intensity histograms during the separate training phase (details given below). $d(p, q)$ is the Euclidian distance between pixels p and q, and σ is the standard deviation of the intensity differences of neighboring voxels along the boundary,

$$C_p(\mathrm{f_p}) = 1 - \exp(-\lambda \cdot Init\,P(p)) \tag{12.7}$$

where $Init\ P(p)$ is the probability of p which is the initialization result, λ is a constant (here $\lambda = 1$).

In the training stage, the intensity histogram of each object is estimated from the training images. $P(I_p|O)$ and $P(I_p|B)$ can be computed based on this. As for the parameters α, β and γ in Eq. (12.4), since $\alpha + \beta + \gamma = 1$, only α and β are estimate by optimizing the accuracy as a function of α and β and set $\gamma = 1 - \alpha - \beta$. The gradient descent method [35] is used for the optimization.

(3) Interaction between the surfaces and regions: The E(Interactions) represents the interactions between the regions and surfaces. We included two surfaces: S_I and S_S to constrain the regions, as shown in Fig. 12.5. If the voxel in the region is located lower than surface S_I, then a penalty is given. Similarly if the voxel in the region is located higher than surface S_S, then a penalty is given. The proposed interaction term is defined as follows,

$$E(Interactions) = \sum_{\substack{v \in p \\ z(v) - Ss(p) > d}} w_v f_v + \sum_{\substack{v \in p \\ S_I(p) - z(v) > d}} w_v f_v \tag{12.8}$$

where $z(v)$ represents the z coordinate of voxel v, p is a column which contains v, $S_s(p)$ and $S_I(p)$ are the z values for the surfaces S_s and S_I on the column p,

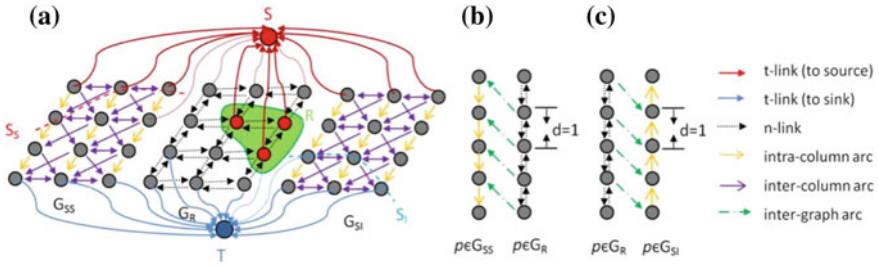

Fig. 12.6 Illustration of graph construction on a 2D example. **a** Final constructed graph G which consists of three sub-graphs G_{SS}, G_R and G_{SI}. **b** Geometric constraints between surfaces G_{SS} and G_R. **c** Geometric constraints between surfaces G_R and G_{SI}

respectively, d is a pre-defined distance threshold (here, $d = 1$), w_v is a penalty weight for v and $f_v = 1$ if $v \in$ region R.

12.3.2.2 Graph Construction

Three sub-graphs are constructed for superior surface S_s, inferior surface S_I and region R. These three sub-graphs are merged together to form as a single s-t graph G which can be solved by a min-cut/max-flow technique [13].

For the surface S_s, a sub-graph $G_{SS}(V_{SS}, A_{SS})$ is constructed by following the method in [12]. Each node in V_{SS} corresponds to exactly one voxel in the image. Two types of arcs are added to the graph: (1) The inter-column arcs incorporating the penalties $h_{p,q}$ between the neighboring columns p and q; and (2) The intra-column arcs with $+\infty$ weight, which enforces the monotonicity of the target surface. A weight w_n is assigned to each node such that the total weight of a closed set in the graph G_{SS} equals to the edge-cost term of E(Surface). Following the method in [36], each node is connected to either the sink T with the weight w_n if $w_n > 0$ or the source S with the weight $-w_n$ if $w_n < 0$.

For the surface S_I, the same graph construction method is applied creating another sub-graph $G_{SI}(V_{SI}, A_{SI})$.

For the region term cost function, the graph cut method in [13] is used to construct the third sub-graph $G_R(V_R, A_R)$. Here, each node in V_R is also corresponding to exactly one voxel in the image. The two terminal nodes: sink T and source S are the same nodes already used in G_{SS} and G_{SI}. Each node has t-links to the sink and source, which encode the data term. N-link connect each pair of neighboring nodes, which encodes the boundary term. Figure 12.6 shows the graph construction. The nodes in V_R, V_{SS} and V_{SI} are all corresponding, so these three sub-graphs can be merged into a single graph G.

Additional inter-graph arcs are added between G_{SS} and G_R, as well as between G_R and G_{SI} to incorporate geometric interaction constraints. For G_{SS} and G_R, if a node (x, y, z) in the sub-graph G_R is labeled as "source" and the node (x, y, z+d) in

the sub-graph G_{SS} is labeled as "sink", i.e. z-S_{SS}(x, y) > d, then a directed arc with a penalty weight from each node G_R(x, y, z) to G_{SS} (x, y, z + d) will be added, as shown in Fig. 12.6b. For G_R and $G_{SI,}$ the same approach is employed.

12.4 Performance Evaluation

12.4.1 Experimental Methods

For the initialization, we compared the performance before and after probability normalization to show the efficacy of the probability normalization.

For the segmentation, we compared the traditional GC in [13], the traditional GS method in [29] and the proposed probability constraints GS-GC. A multivariate analysis of variance (MANOVA) test [37] was based on the three performance measures: true positive volume fraction (TPVF) which indicates the fraction of the total amount of fluid in the reference standard delineation, false positive volume fraction (FPVF) [33] which denotes the amount of fluid falsely identified and relative volume difference ratio (RVDR) which measures the volume difference ratio comparing to the reference standard volume to show the statistical significance of performance differences. They are defined as follows,

$$TPVF = \frac{|C_{TP}|}{|C_{\mathrm{td}}|} \tag{12.9}$$

$$FPVF = \frac{|C_{FP}|}{|U_{\mathrm{d}} - C_{td}|} \tag{12.10}$$

$$RVDR = \frac{||V_M| - |V_R||}{|V_R|} \tag{12.11}$$

where, U_d is assumed to be a binary scene with all voxels in the scene domain set to have a value 1, and C_{td} is the set of voxels in the true delineation, $|\cdot|$ denotes volume. $|V_M|$ is the segmented volume by method M, and $|V_R|$ is the volume of the reference standard. More details can be seen in [38].

For statistical correlation analysis, we used linear regression analysis [39] and Bland-Altman plots [40] to evaluate the agreement and relationship between the automatic and manual segmentations.

For the reproducibility analysis, the retinal specialist was invited to manually segment the intra- and sub-retinal fluid at the onset of the project and again after more than 3 months. The manual segmenting of all the slices for one eye required more than 2 h of expert tracing, so the re-tracing was performed on 5 randomly selected eyes from the entire data set.

Macula-centered 3D OCT volumes ($200 \times 200 \times 1024$ voxels, $6 \times 6 \times 2$ mm^3, voxel size $30 \times 30 \times 1.95$ μm^3) were obtained from 15 eyes of 15 patients with exudative AMD. For the reference standard, a retinal specialist (MDA) manually

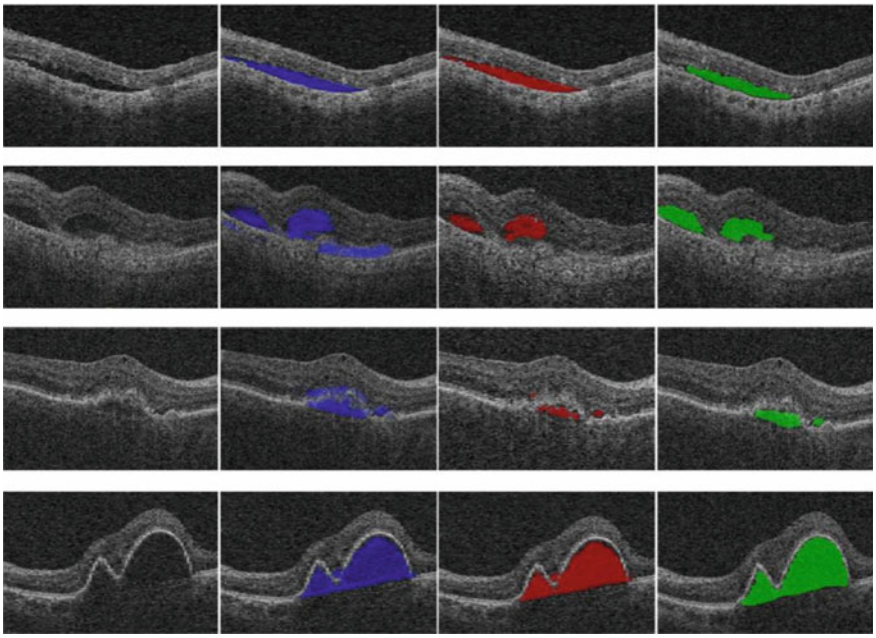

Fig. 12.7 Experimental results for four examples of SEAD initialization. The 1st column shows the original image, the 2nd column shows the initialization results, the 3rd column shows the final initialization results after probability normalization, and the last column shows the ground truth. Note the improvements obtained by probability normalization in columns 3 and 4

segmented the intra- and sub-retinal fluid in each slice of each eye using Truthmarker software [41] on iPad.

12.4.2 Assessment of Initialization Performance

Four examples of initialization and its post-processing by probability normalization are shown in Fig. 12.7. We can see that for the 3rd and 4th images, reflective of probability normalization, the numbers of falsely detected voxels have decreased substantially. The initialization performance of TPVF, FPVF and RVD before and after probability normalization are shown in the 1st and 2nd rows of Table 12.2. We can see that after the probability normalization, the FPVF decreased noticeably (from 5.2 to 3.0%).

Table 12.2 Mean ± standard deviation (median) of TPVF, FPVF and RVDR for initialization, initialization after probability normalization, traditional GC in [13], traditional GS [29] and the proposed probability constrained GS-GC

	TPVF (%)	FPVF (%)	RVDR (%)
Initialization	72.3 ± 17.6 (77.5)	4.5 ± 3.7 (3.6)	21.1 ± 41.2 (16.4)
Initialization after probability normalization	72.5 ± 17.5 (77.5)	3.0 ± 3.2 (2.5)	20.8 ± 40.5 (16.2)
Traditional GC [13]	77.9 ± 23.9 (81.4)	3.6 ± 3.3 (3.2)	20.2 ± 37.6 (6.5)
Traditional GS [29]	82.8 ± 10.5 (86.0)	3.2 ± 4.5 (2.6)	22.8 ± 45.6 (12.5)
The proposed probability constrained GS-GC	86.5 ± 9.5 (90.2)	1.7 ± 2.3 (0.5)	12.8 ± 32.1 (4.5)

12.4.3 Assessment of Segmentation Performance

Three examples of the obtained segmentation results are shown in Fig. 12.8. Table 12.2 summarizes the quantitative assessment of the segmentation performance achieved by the proposed method expressed in TPVF, FPVF and RVDR. The proposed probability constrained GS-GC method achieved a better performance compared to the traditional GC [13] and GS [29]. The p-value of the MANOVA test for the proposed method versus the traditional GC [13] and the proposed method versus the traditional GS [29] is $p < 0.01$ and $p < 0.04$, respectively, i.e., both of the performance improvements are statistically significant. The average TPVF, FPVF and RVDR for the proposed method are about 86.5, 1.7 and 12.8%, respectively. A 3D visualization of the typical SEAD segmentation results are shown in Fig. 12.9.

The proposed method was tested on an HP Z400 workstation with 3.33 GHz CPU, 24 GB of RAM. The computation times for the initialization and segmentation were 15 and 10 min, respectively.

12.4.4 Statistical Correlation Analysis and Reproducibility Analysis

The linear regression analysis comparing SEAD volumes and Bland-Altman plots for the fully automated probability constrained GS-GC method versus Manual 1 is shown in Fig. 12.10. The reproducibility assessment of manual tracing Manual 1 versus Manual 2 is illustrated in Fig. 12.11. The figures demonstrate that: (1) the intra-observer reproducibility has the highest correlation with $r = 0.991$. In comparison, the automated analysis achieves a high correlation with the Manual 1 segmentation ($r = 0.945$). (2) Analyzing the Bland-Altman plots reveals that the 95% limits of agreement were $[-0.34, 0.45]$ and $[-0.24, 1.16]$ for the Automated method ver-

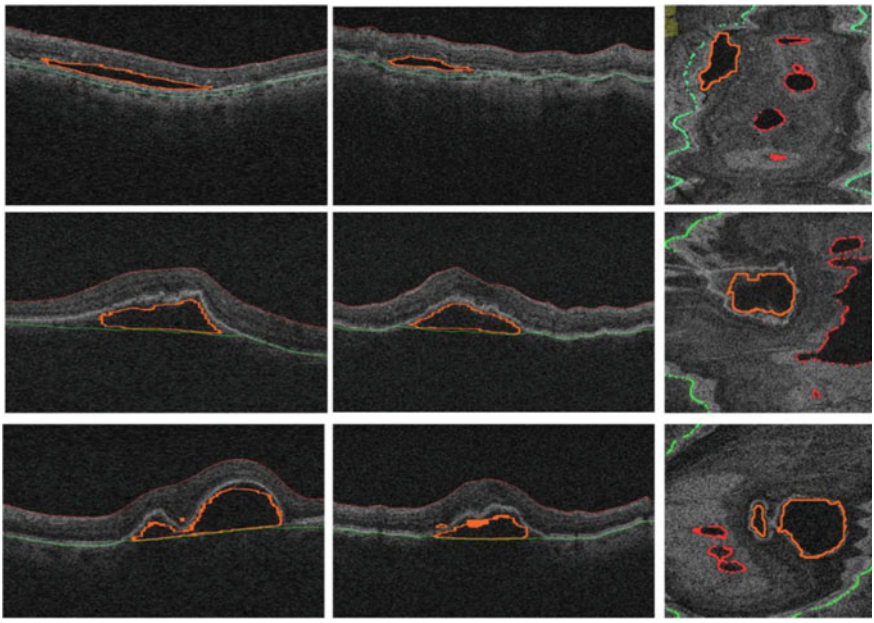

Fig. 12.8 Experimental results for three examples of SEAD segmentation. The 1st, 2nd and 3rd columns correspond to the axial, sagittal and coronal views, respectively. Red color represents the upper retinal surface, green color represents the lower retinal surface, and yellow color depicts the surface of the segmented SEAD

sus Manual 1, and Manual 1 versus Manual 2, respectively. The Automated versus Manual 1 showed a much lower bias compared to the Manual 1 versus Manual 2.

12.5 Conclusion

The results show that the probability constrained graph cut—graph search method significantly outperforms both the traditional graph cut and traditional graph search approaches, and its performance to segment intra- and subretinal fluid in SD-OCT images of patients with exudative AMD is comparable to that of a clinician expert.

12.5.1 Importance of SEAD Segmentation

As mentioned in the Introduction, current treatment is entirely based on subjective evaluation of intra- and subretinal fluid amounts from SD-OCT by the treating clinician. Though never confirmed in studies, anecdotal evidence and experience in other

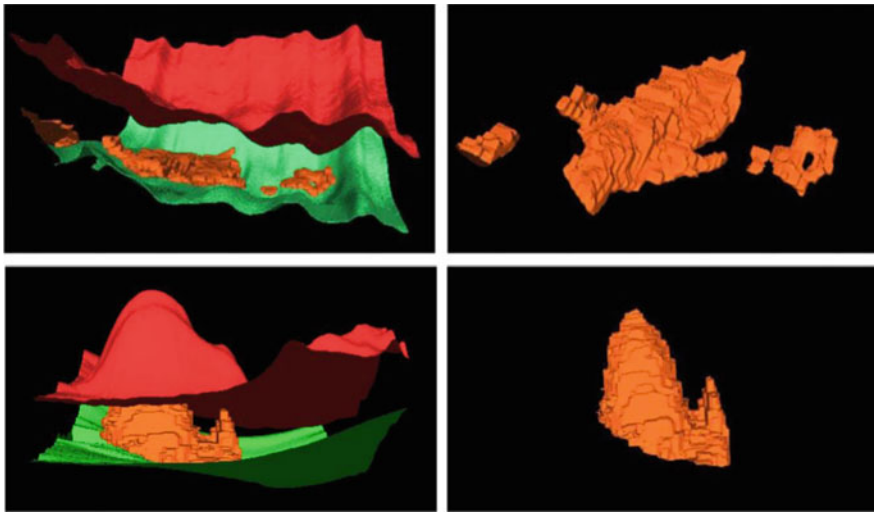

Fig. 12.9 3D visualization of SEAD segmentation on two examples (the 1st and 3rd cases in Fig. 12.8). Red color represents the upper retinal surface, green color the lower retinal surface, and orange color depicts the surface of the segmented SEAD

fields show that the resulting intra- and interobserver variability will lead to considerable variation in treatment and therefore, under- and overtreatment. Though each treatment, based on regular and frequent intravitreal injections of anti-VEGF, has less than a 1:2000 risk of potentially devastating endophthalmitis and visual loss, because of the high number of lifetime treatments, the cumulative risk is still considerable. In addition, the cost of each injection is high millions of patients are being treated every month so that the total burden on health care systems is in billions of US$ (year 2012). The potential of our approach to avoid overtreatment is therefore double attractive, because both lowering of the risk to patients and cost-savings can be achieved. However, before our approach can be translated to the clinic, validation in larger studies are required.

12.5.2 Advantages of the Probability Constrained Graph Cut—Graph Search Method

A graph-theoretic based method for SEAD segmentation is reported here. The multi-object strategy was employed for segmenting the SEADs, during which two retinal surfaces (one above the SEAD region and another below the SEAD region) were included as auxiliary target objects for helping the SEAD segmentation. Natural constraints for the SEAD segmentation is provided by the two auxiliary surfaces and they also make the search space become substantially smaller, thus yielding a

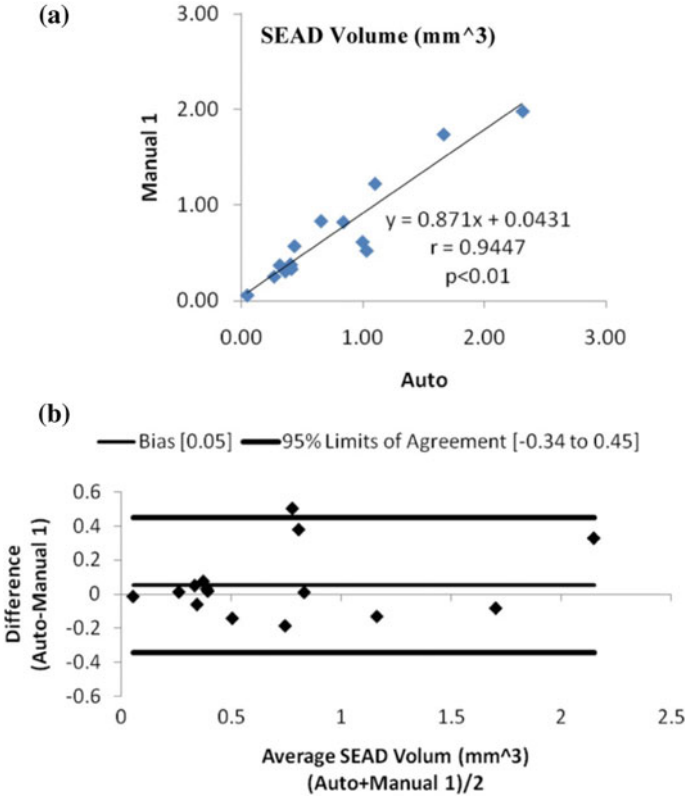

Fig. 12.10 Statistical correlation analysis between the Automated method GS-GC and manual tracings Manual 1. **a** Linear regression analysis results comparing SEAD volumes. **b** Bland-Altman plots

more accurate segmentation result. The similar idea has also been proved in [42]. The proposed graph-theoretic based method effectively combined the GS and GC methods for segmenting the layers and SEADs simultaneously. An automatic voxel classification-based method was used for initialization which was based on the layer-specific texture features following the success of our previous work [14, 31]. The later GS- GC method effectively integrate the probability constraints from the initialization which further improved the segmentation accuracy.

12.5.3 Limitations of the Reported Method

This graph-theoretic based method approach has some limitations. The first limitation is that it largely relies on the initialization results. If the probability constraints from

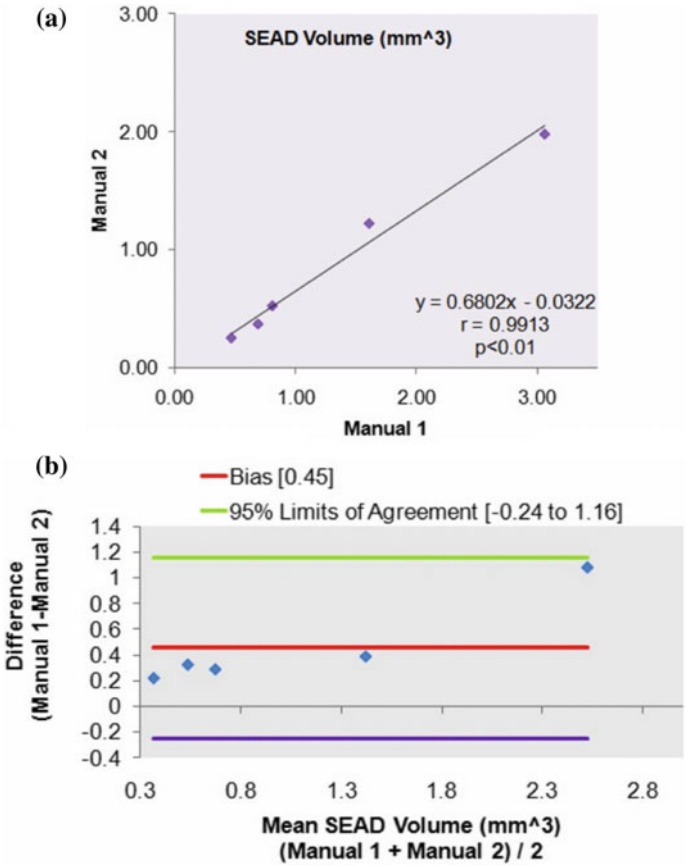

Fig. 12.11 Statistical correlation analysis of reproducibility comparing manual tracings Manual 1 and Manual 2. **a** Linear regression analysis results comparing SEAD volumes. **b** Bland-Altman plots

the initialization step are incorrect, the final segmentation results may fail. One example that mis-detects the SEAD due to the inaccurate initialization is shown in Fig. 12.12.

The probability constrained graph cut—graph search method shows high correlation with manual segmentation and if validated in a larger study, may be applicable to clinical use. It can be seen from Figs. 12.10 and 12.11 that the Automated versus Manual 1 showed a much lower bias compared to the Manual 1 versus Manual 2, which may be caused by the Manual 2 analysis being available for a subset of only 5OCT images—because of the laboriousness of expert tracing, even when accelerated with Truth marker.

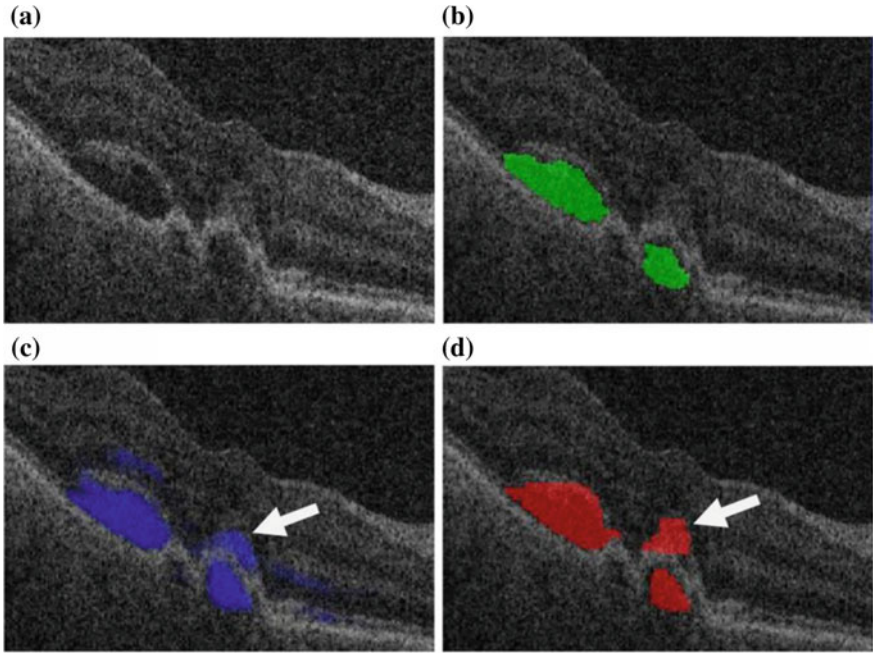

Fig. 12.12 One example of erroneous segmentation of a SEAD due to inaccurate initialization. **a** Original OCT slice. **b** Ground truth. **c** Initialization. **d** SEAD segmentation result. Arrow points to the mis-initialized and therefore mis-segmented SEAD

12.5.4 Segmentation of Abnormal Retinal Layers

Several methods were proposed for the retinal surface and layer segmentation [11, 28, 29, 43–45]. However, all these methods have been evaluated on datasets from non-AMD subjects, where the retinal layers and other structures are intact. When the retinal layers are disrupted, and additional structures are present that transgress layer boundaries, as in exudative AMD or Diabetic Macular Edema, segmentation becomes exponentially more challenging. This chapter provided an idea for the abnormal layer segmentation. The main task, the SEAD segmentation, has been tackled by combining two auxiliary surfaces. In this process, the normal (surface) provides constraints for the abnormal (SEAD) segmentation, and as a return, the abnormal help refine the segmentation of normal. As shown by the experiment results (see Fig. 12.8), whenever a successful SEAD segmentation is achieved, the segmentation of bottom surface is also correct. This idea may also be applied to segment other targets in abnormal data set, such as liver tumor segmentation in liver CT scans.

References

1. R.D. Jager, W.F. Mieler, J.W. Miller, Age-related macular degeneration. N. Engl. J. Med. **358**, 2606–2617 (2008)
2. P.J. Rosenfeld, D.M. Brown, J.S. Heier, D.S. Boyer, P.K. Kaiser, C.Y. Chung, R.Y. Kim, Ranibizumab for neovascular age-related macular degeneration. N. Engl. J. Med. **355**, 1419–1431 (2006)
3. N. Ferrara, K.J. Hilan, H. Gerber, W. Novetny, Discovery and development of bevacizumab, an anti-VEGF antibody for treating cancer. Nat. Rev. Drug Discovery **3**, 391–400 (2004)
4. P.V. Algvere, B. Steén, S. Seregard, A. Kvanta, A prospective study on intravitrealbevacizumab (Avastin®) for neovascular age-related macular degeneration of different durations. Acta Ophthalmol. **86**, 482–489 (2008)
5. C. Cukras, Y.D. Wang, C.B. Meyerle, F. Forooghian, E.Y. Chew, W.T. Wong, Optical coherence tomography-based decision making in exudative age-related macular degeneration: comparison of time- versus spectral-domain devices. Eye **24**, 775–783 (2010)
6. G.A. Lalwani, P.J. Rosenfeld, A.E. Fung, S.R. Dubovy, S. Michels, W. Feuer, J.L. Davis, H.W. Flynn Jr., M. Esquiabro, A variable-dosing regimen with intravitrealranibizumab for neovascular age-related macular degeneration: year 2 of the PrONTO study. Am. J. Ophthalmol. **148**, 43–58 (2009)
7. F. Coscas, G. Coscas, E. Souied, S. Tick, G. Soubrane, Optical coherence tomography identification of occult choroidal neovascularization in age-related macular degeneration. Am. J. Ophthalmol. **144**, 592–599 (2007)
8. A.H. Kashani, P.A. Keane, L. Dustin, A.C. Walsh, S.R. Sadda, Quantitative subanalysis of cystoid spaces and outer nuclear layer using optical coherence tomography in age-related macular degeneration. Invest. Ophthalmol. Vis. Sci. **50**, 3366–3373 (2009)
9. A.E. Fung, G.A. Lalwani, P.J. Rosenfeld, S.R. Dubovy, S. Michels, W.J. Feuer, C.A. Puliafito, J.L. Davis, H.W. Flynn Jr., M. Esquiabro, An optical coherence tomography-guided, variable dosing regimen with intravitrealranibizumab (Lucentis) for neovascular age-related macular degeneration. Am. J. Ophthalmol. **143**, 566–583 (2007)
10. H. Dadgostar, A.A. Ventura, J.Y. Chung, S. Sharma, P.K. Kaiser, Evaluation of injection frequency and visual acuity outcomes for ranibizumabmonotherapy in exudative age-related macular degeneration. Am. J. Ophthalmol. **116**, 1740–1747 (2009)
11. A. Delong, Y. Boykov. Globally optimal segmentation of multi-region objects, in *IEEE International Conference on Computer Vision (ICCV)* (2009)
12. K. Li, X. Wu, D.Z. Chen, M. Sonka, Efficient optimal surface detection: theory, implementation and experimental validation. in *Proceedings of SPIE International Symposium Medical Imaging: Image Processing*, vol. 5370 (May 2004), pp. 620–627
13. Y. Boykov, G. Funka-Lea, Graph cuts and efficient N-D image segmentation. Int. J. Comput. Vis. (IJCV) **70**, 109–131 (2006)
14. M. Niemeijer, K. Lee, X. Chen, L. Zhang, M. Sonka, M.D Abràmoff, Automated estimation of fluid volume in 3D OCT scans of patients with CNV due to AMD, in *ARVO Annual Meeting* (2012)
15. Y. Boykov, V. Kolmogorov, An experimental comparison of min-cut/max-flow algorithms for energy minimization in vision. IEEE Trans. Pattern Anal. Mach. Intell. **26**, 1124–1137 (2004)
16. X. Chen, M. Niemeijer, L. Zhang, K. Lee, M.D. Abràmoff, M. Sonka, 3D segmentation of fluid-associated abnormalities in retinal OCT: probability constrained graph-search–graph-cut. IEEE Trans. Med. Imaging **31**(8), 1521–1531 (2012)
17. Y. Boykov, M.P. Jolly, Interactive graph cuts for optimal boundary and region segmentation of objects in ND images, in *IEEE International Conference on Computer Vision (ICCV)*, vol. I (2001), pp. 105–112
18. V. Kolmogorov, R. Zabih, What energy function can be minimized via graph cuts? IEEE Trans. Pattern Anal. Mach. Intell. **26**, 147–159 (2004)
19. O. Veksler, Star shape prior for graph-cut image segmentation, in *10th European Conference on Computer Vision (ECCV)*, vol. 5304 (2008), pp. 454–467

20. D. Freedman, T. Zhang, Interactive graph cut based segmentation with shape priors, in *IEEE Conference on Computer Vision and Pattern Recognition (CVPR)* (2005) pp. 755–762
21. J. Malcolm, Y. Rathi, A. Tannenbaum, Graph cut segmentation with nonlinear shape priors, in *IEEE International Conference on Image Processing* (2007), pp. 365–368
22. N. Vu, B.S. Manjunath, Shape prior segmentation of multiple objects with graph cuts, in *IEEE Conference on Computer Vision and Pattern Recognition (CVPR)* (2008), pp. 1–8
23. X. Chen, U. Bagci, 3D automatic anatomy segmentation based on iterative graph-cut-ASM. Med. Phys. **38**(8), 4610–4622 (2011)
24. M. Dolejší, M.D. Abràmoff, M. Sonka, J. Kybic, Semi-automated segmentation of symptomatic exudate-associated derangements (SEADs) in 3D OCT using layer segmentation. Biosignal (2010)
25. K. Li, X. Wu, D.Z. Chen, M. Sonka, Optimal surface segmentation in volumetric images—A graph-theoretic approach. IEEE Trans. Pattern Anal. Mach. Intell. **28**, 119–134 (2006)
26. Y. Yin, X. Zhang, R. Williams, X. Wu, D.D. Anderson, M. Sonka, LOGISMOS—Layered optimal graph image segmentation of multiple objects and surfaces: cartilage segmentation in the knee joint. IEEE Trans. Med. Imaging **29**(12), 2023–2037 (2010)
27. B. Appleton, H. Talbot, Globally minimal surfaces by continuous maximal flows. IEEE Trans. Pattern Anal. Pattern Recogn. (PAMI) **28**(1), 106–118 (2006)
28. M.K. Garvin, M.D. Abramoff, R. Kardon, S.R. Russell, X. Wu, M. Sonka, Intraretinal layer segmentation of macular optical coherence tomography images using optimal 3-D graph search. IEEE Trans. Med. Imaging **27**, 1495–1505 (2008)
29. M.K. Garvin, M.D. Abramoff, X. Wu, S.R. Russell, T.L. Burns, M. Sonka, Automated 3-D intraretinal layer segmentation of macular spectral-domain optical coherence tomography images. IEEE Trans. Med. Imaging **28**, 1436–1447 (2009)
30. Q. Song, M. Chen, J. Bai, M. Sonka, X. Wu, Surface-region context in optimal multi-object graph-based segmentation: robust delineation of pulmonary tumors, in *Proceedings of the 22nd Biennial International Conference on Information Processing in Medical Imaging (IPMI)* (2011)
31. G. Quellec, K. Lee, M. Dolejsi, M.K. Garvin, M.D. Abramoff, M. Sonka, Three-dimensional analysis of retinal layer texture: identification of fluid-filled regions in SD-OCT of the macula. IEEE Trans. Med. Imaging **29**, 1321–1330 (2010)
32. M.D. Abramoff, W.L.M. Alward, E.C. Greenlee, L. Shuba, C.Y. Kim, J.H. Fingert, Y.H. Kwon, Automated segmentation of the optic disc from stereo color photographs using physiologically plausible features. Invest. Ophthalmol. Vis. Sci. **48**(4), 1665–1673 (2007)
33. S. Arya, D.M. Mount, N.S. Netanyahu, R. Silverman, A.Y. Wu, An optimal algorithm for approximate nearest neighbor searching. J. ACM **45**, 891–923 (1998)
34. M. Niemeijer, B. v Ginneken, J. Staal, M.S.A. Suttorp-Schulten, M.D. Abràmoff, Automatic detection of red lesions in digital color fundus photographs. IEEE Trans. Med. Imaging **24**(5), 584–592 (2005)
35. J.A. Snyman, *Practical Mathematical Optimization: An Introduction to Basic Optimization Theory and Classical and New Gradient-Based Algorithms* (Springer, 2005). ISBN0-387-24348-8
36. X. Wu, D.Z. Chen, Optimal net surface problems with applications. ICALP 1029–1042 (2002)
37. W.J. Krzanowski, *Principles of Multivariate Analysis* (Oxford University Press, New York, 1988)
38. J.K. Udupa, V.R. Leblanc, Y. Zhuge, C. Imielinska, H. Schmidt, L.M. Currie, B.E. Hirsch, J. Woodburn, A framework for evaluating image segmentation algorithms. Comput. Med. Imaging Graph. **30**(2), 75–87 (2006). [PubMed: 16584976]
39. D.R. Cox, D.V. Hinkley, *Theoretical Statistics* (Chapman & Hall (Appendix 3), 1974). ISBN 0412124203
40. J.M. Bland, D.G. Altman, Statistical methods for assessing agreement between two methods of clinical measurement. Lancet **1**, 307–310 (1986). [PubMed: 2868172]
41. M. Christopher, D.C. Moga, S.R. Russell, J.C. Folk, T. Scheetz, M.D. Abràmoff, Validation of tablet-based evaluation of color fundus images. Retina (2012) (in press)

42. X. Chen, J.K. Udupa, A. Alavi, D.A. Torigian, Automatic anatomy recognition via multiobject oriented active shape models. Med. Phys. **37**(12), 6390–6401 (2010)
43. D.C. Fernandez, H.M. Salinas, C.A. Puliafito, Automated detection of retinal layer structures on optical coherence tomography images. Opt. Express **13**(25), 10200–10216 (2005). [PubMed: 19503235]
44. M. Markus, H. Joachim, Y.M. Christian, P.R. Tornow, Retinal nerve fiber layer segmentation on FD-OCT scans of normal subjects and glaucoma patients biomedical. Opt. Express **1**(5), 1358–1383 (2010)
45. S.J. Chiu, X.T. Li, P. Nicholas, C.A. Toth, J.A. Izatt, S. Farsiu, Automatic segmentation of seven retinal layers in SDOCT images congruent with expert manual segmentation. Opt. Express **18**(18), 19413–19428 (2010)

Chapter 13
Modeling and Prediction of Choroidal Neovascularization Growth Based on Longitudinal OCT Scans

Fei Shi, Shuxia Zhu and Xinjian Chen

Choroidal neovascularization (CNV) is common in many chorioretinal diseases and is a cause of severe visual impairment. This chapter presents a reaction-diffusion CNV growth model based on longitudinal OCT images. It can be used to predict the future CNV region and thus can provide guidance for the treatment planning.

13.1 Introduction

Choroidal neovascularization (CNV) refers to the growth of new but abnormal blood vessels from the choroid and into the retina. It occurs in many chorioretinal diseases such as age-related macular degeneration (AMD), pathological myopia macular degeneration and histoplasmosis. Due to the recurrent neovascular leakage and rupture, the patients' macula are seriously damaged, causing permanent visual impairment.

According to pathological studies, the occurrence of CNV is highly associated with the high concentration of vascular endothelial growth factors (VEGF) [1]. Currently intravitreal injection of anti-VEGF medicine is the most effective medical treatment for CNV. It can both inhibit the growth of CNV and reduce the amount of retinal fluid. However, multiple injections are usually needed, which adds to the risk of serious ocular adverse events that can result in impairment of sight or complete loss of vision. Moreover, this treatment is expensive and the patient-specific response is

F. Shi · S. Zhu · X. Chen (✉)
School of Electronics and Information Engineering, Soochow University, Suzhou, China
e-mail: xjchen@suda.edu.cn

X. Chen
State Key Laboratory of Radiation Medicine and Protection, Soochow University, Suzhou, China

X. Chen et al. (eds.), *Retinal Optical Coherence Tomography Image Analysis*,
Biological and Medical Physics, Biomedical Engineering,
https://doi.org/10.1007/978-981-13-1825-2_13

quite different [2]. Ideally, a patient-specific treatment plan with minimally necessary number of anti-VEGF injections is required.

First proposed in 1991 by Huang et al. [3], optical coherence tomography (OCT) is a non-invasive imaging technique which provides 3D cross-sectional images of biological tissues with a high resolution. Based on the retinal OCT images, the size, position and shape of lesion area, including cystoid edema, intraretinal and subretinal fluid, and CNV, can be quantified, and tracking can be achieved from longitudinal OCT scans [4–6]. Therefore OCT has become the most effective tool for monitoring the condition of CNV. In PrONTO trial [7], also known as prospective optical coherence tomography imaging of patients with neovascular AMD treated with intra-ocular ranibizumab, OCT was used to help design the treatment plans for CNV. All patients were given three intravitreal injections at 4 weeks interval during an induction phase. After that, a variable dosing regimen was used, where patients received injections when specific criteria were met. These criteria included intraretinal or subretinal fluid viewed in OCT images and central retinal thickness measured based on OCT. Figure 13.1 shows an example of retinal OCT image with CNV.

Several previous studies focused on OCT based prediction of retinal diseases. Bogunovic et al. [8] predicted the outcome of the anti-VEGF treatment for exudative AMD based on a classifier using features extracted from longitudinal OCT images. However they can only predict responder or non-responder at the end of the induction phase instead of the future status of disease regions. In [9], Wolf-Dieter et al. proposed two data-driven machine learning approaches to predicted the macular edema recurrence caused by retinal vein occlusion (RVO). Only simple features including the retinal thickness and the image gradient magnitude were used for quantitative analysis.

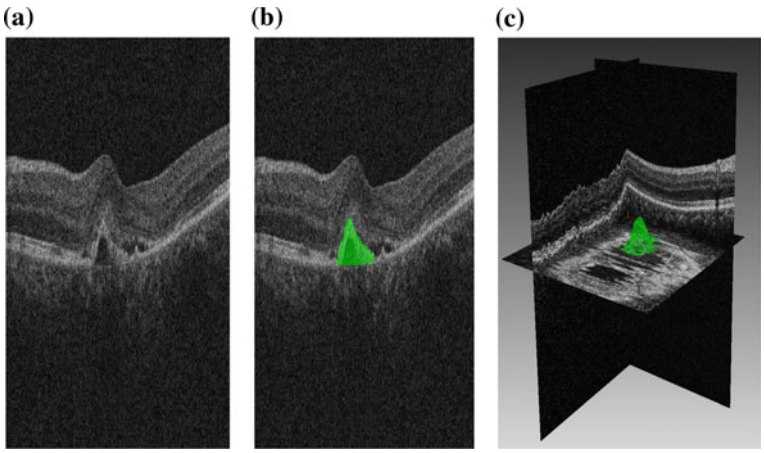

Fig. 13.1 An example of retinal OCT image with CNV in green color. **a** A Bscan of the original retinal OCT image, **b** CNV ground truth shown in green, **c** 3D visualization

In this chapter, we introduce a CNV growth model for longitudinal OCT images based on the reaction diffusion model [10]. Finite element method (FEM) is used to solve the model equation. Optimal growth parameters are obtained by minimizing an objective function measuring prediction accuracy. The method was tested on a dataset with 7 patients, each with 12 monthly-scanned OCT images. The experimental results showed the accuracy of the proposed method.

13.2 Method

13.2.1 Method Overview

Figure 13.2 shows the framework of our method. Suppose there are N longitudinal images for each subject in the study. The first $N - 1$ images are used for training, from which the growth parameters are obtained to predict the Nth image. First, image preprocessing, including registration and segmentation, are conducted on all OCT images. Secondly, tetrahedral meshes are constructed for the segmented CNV volumes and the related retinal regions. Thirdly, the CNV growth model is applied on the first $N - 1$ images to get their growth parameters are learned by optimization. Then, the growth parameter for the Nth image is estimated from the previous ones by curve fitting, and is used in the model to obtain the predicted Nth image. The prediction result is validated by comparing the synthesized image with the ground truth of the Nth image.

13.2.2 Data Acquisition

Seven eyes from seven subjects diagnosed with CNV associated with AMD were scanned once a month during a one year period. 3D OCT images with $512 \times 128 \times 1024$ voxels (each with size of $11.72 \times 46.88 \times 1.95\ \mu m^3$), covering the volume of $6 \times 6 \times 2\ mm^3$ were obtained by Zeiss Cirrus OCT scanner (Carl Zeiss Meditec, Inc., Dublin, CA). The subjects were enrolled in a trial of anti-VEGF medicine. In this trial, patients were randomly divided into the treatment group or the reference group. The treatment plan included two phases: the core treatment and the extended treatment. The core treatment involved 3 monthly intravitreal anti-VEGF injections (conbercept, 0.5 mg), and the extended treatment meant injections in three-month intervals. The difference between the two groups was that: the reference group started the real treatment 3 months later than the treatment group, and was given condolences agent in the first 3 month. Figure 13.3 shows the detailed treatment plans of treatment group and reference group, respectively. Among the 7 subjects studied in this experiment, 4 subjects were in the treatment group and the rest 3 were in the reference group.

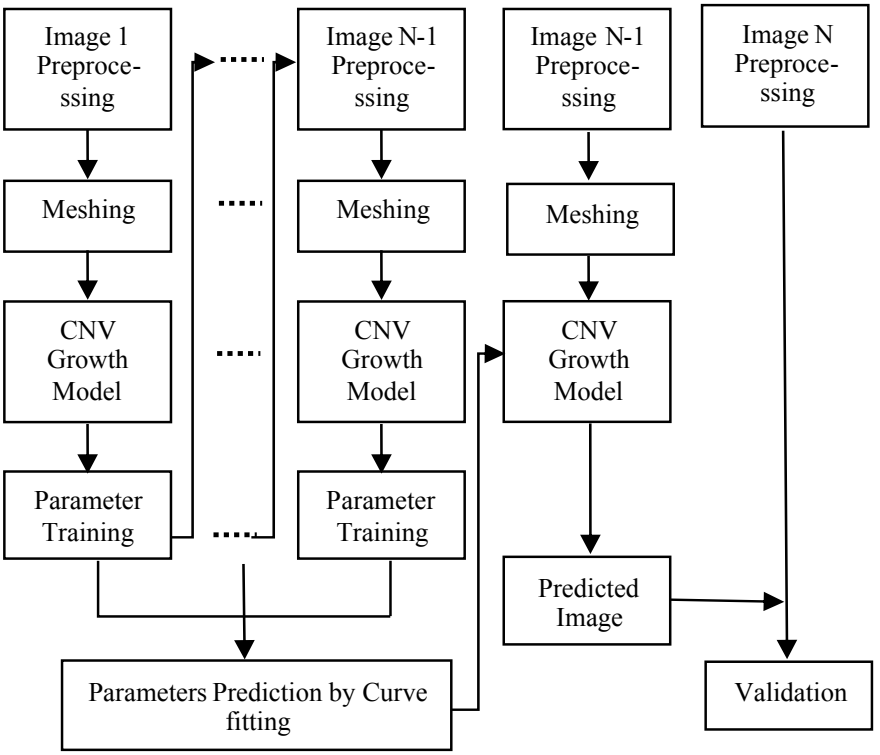

Fig. 13.2 Framework of the proposed method

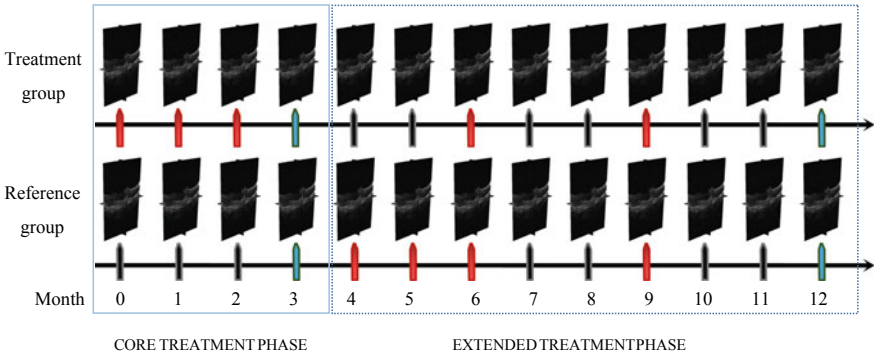

Fig. 13.3 Illustration of the injection on treatment group and reference group. The red arrows represent treatment of intravitreal injections, the black arrows represent the injection of condolences agent and the blue arrows represent the assessment time

13.2.3 Preprocessing

In this longitudinal study, the images are collected one month each, and thus displacement of the retina in OCT images caused by different eye position during scanning is inevitable. Therefore, to guarantee of prediction accuracy, it is important to registrate images so that the change of lesion area at the same positions can be measured. The first image is set as the reference image and the other images are registered to it using rigid transform based on manually inputted landmarks [11]. Figure 13.4 shows one example of the registration results.

After registration, segmentation is performed to get the regions of interest, including the CNV region and the surrounding tissues. A 3-D graph-search based method [12, 13] is applied to segment several retinal surfaces. As shown in Fig. 13.5, surfaces 1–4 are first segmented, which corresponds to the upper boundary of nerve fiber layer (NFL), the boundary between outer plexiform layer (OPL) and outer nuclear layer (ONL), the boundary between Verhoeff's membrane (VM) and retinal pigment epithelium (RPE) and the Bruch membrane, respectively. Some inaccurate segmentation results were manually corrected under the guidance of an experienced ophthalmologist. Surface 5, defined as the lower boundary of choroid, is approximated by a surface with a fixed distance to surface 4. The CNV volume is defined as including the voxels between surface 3 and 4. As shown in Fig. 13.5, the segmentation gives the CNV volume as well as three layers: the inner retina, the outer retina and the choroid.

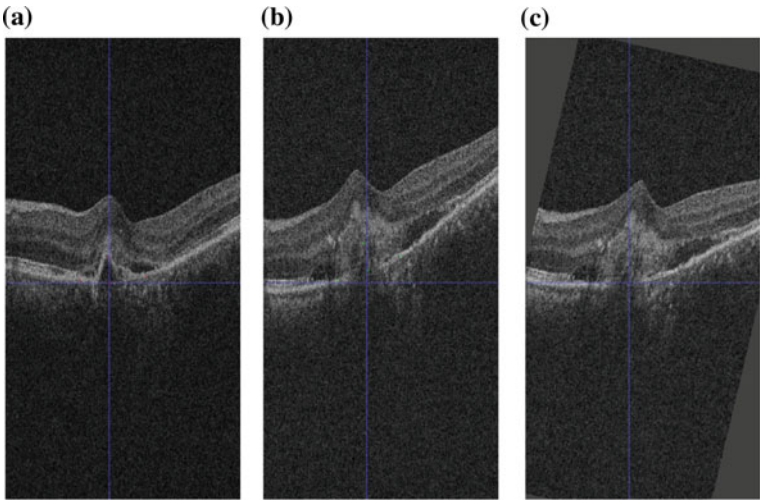

Fig. 13.4 Example of registration. **a** Fixed image; **b** moving image; **c** registration result

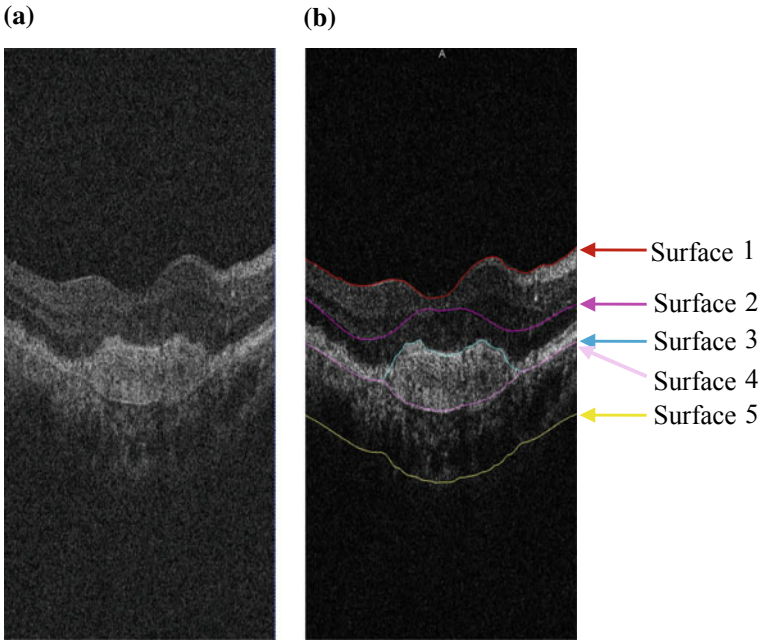

Fig. 13.5 Example of layer segmentation. **a** Original OCT image; **b** surface segmentation result with local modification

13.2.4 Meshing

The ISO2Mesh method [14] is used for conducting tetrahedral meshing on the segmented CNV volumes and the three retinal layers. It is a 3-D surface and volumetric mesh generator that can produce high quality 3-D tetrahedral mesh or triangular surfaces directly from segmented, binary or grayscale medical images [15].

Meshing procedure includes the following two steps: (1) Generating triangular iso-surfaces with the specified density. (2) Filling the sub-volumes bounded by iso-surfaces with tetrahedral elements. In the second step different labels can be supplied so that the resulting FEM mesh carries sub-domains that correspond to CNV volumes or the retinal layers. Figure 13.6 shows the result of retinal volumetric mesh generation.

13.2.5 CNV Growth Model

The reaction-diffusion model [16], which is widely used in geology, biology and physics, is used here to characterize the growth of CNV. The model describes the spatial distribution and temporal development of certain substance. In [17–19], it

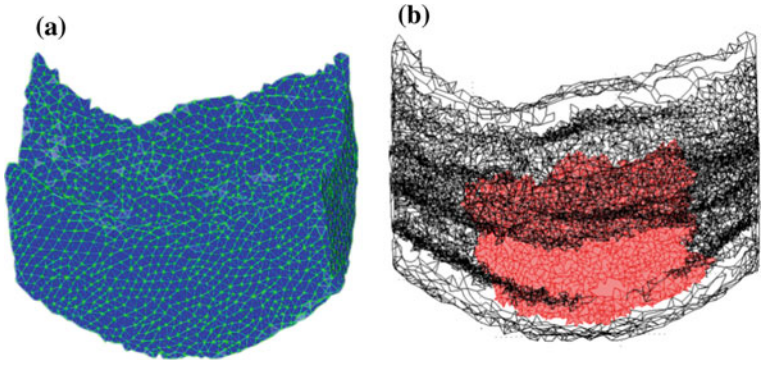

Fig. 13.6 Retinal volumetric mesh generation. **a** The meshing surface; **b** the meshing CNV region in red

was used to model the tumor growth. Compared with these existing ones, the model used in this section can simulate not only the invasion of CNV, but also the shrinkage of CNV under treatment. Specifically, we design the treatment term to represent the effect of medicine. The model is defined as:

$$\frac{\partial u}{\partial t} = f(u,t) + \nabla \cdot (c\nabla u) - a \cdot u \tag{13.1}$$

where u represents the concentration of CNV, initialized as 4000, c stands for the diffusion coefficient representing the growing of CNV towards surrounding tissues, and $a \cdot u$ is the treatment term, where a is set to a constant.

The source function f is formulated following the Logistic model [20], a popular technique for prediction of numeric values. It is defined as:

$$f(u,t) = \rho \cdot u(1-u) \tag{13.2}$$

where ρ is the growth rate of CNV. Substituting (13.1) into (13.2), we can get

$$\frac{\partial u}{\partial t} = \rho \cdot u(1-u) + \nabla \cdot (c\nabla u) - a \cdot u \tag{13.3}$$

The boundary condition is enforced by

$$c\nabla u \cdot \vec{n}_{\partial\Omega} = 0 \tag{13.4}$$

which is the Neumann boundary condition on the retinal domain Ω. Then, the FEM [21, 22] is applied to solve the partial differential equations. Based on the Galerkin method [23], the continuous problem can discretized in a subvectorial space of finite dimension.

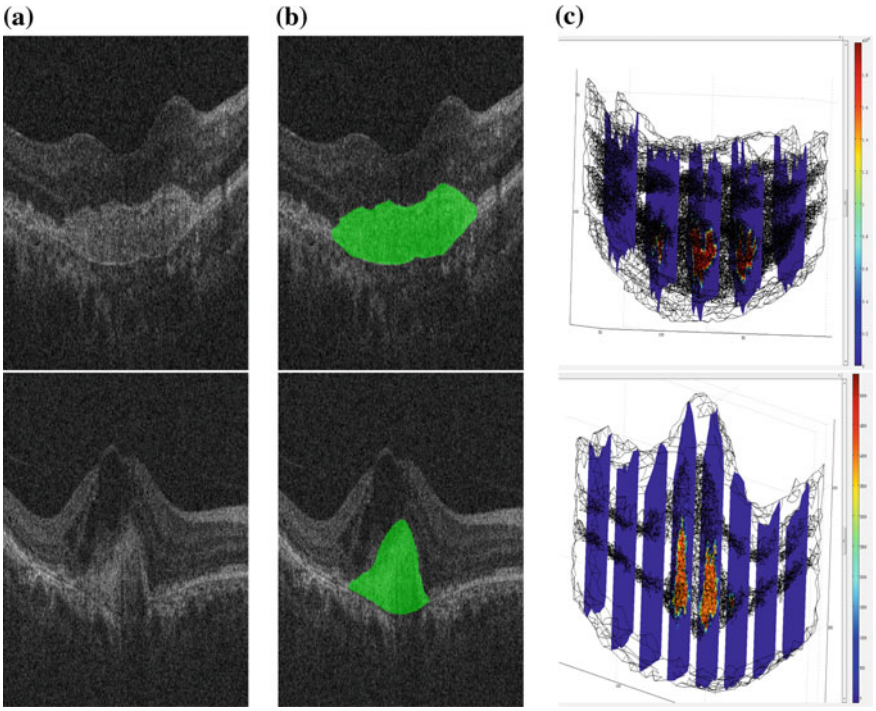

Fig. 13.7 Two examples of the modeling result. **a**, **b** and **c** represent original image, CNV area with green color and simulated CNV density, respectively

Figure 13.7 shows two examples of the resulting estimated CNV concentration. The concentration map is segmented using the threshold value of 4000 to get the simulated CNV binary image.

13.2.6 Estimation of Growth Parameters

In our CNV growth model, The parameters ρ and c need to be estimated for each particular subject. We assume that c is a constant over time, while the value of ρ varies with time. We define the set of parameters as $\theta = \{\rho_1, \rho_2 \ldots \rho_{N-2}; c\}$, whose values are estimated from the longitudinal OCT images.

To get θ^*, the optimal value of θ, we minimize the objective function $E(\theta)$ representing overlap accuracy for the 2nd to N − 1th training data [24].

$$\theta^* = \arg\min_{\theta} E(\theta) \tag{13.5}$$

where

$$E(\theta) = \sum_{i=1}^{N-2} w \cdot (1 - TPVF(\widehat{I}_{i+1}(\theta), I_{i+1})) + (1 - w) \cdot FPVF(\widehat{I}_{i+1}(\theta), I_{i+1}). \tag{13.6}$$

and

$$TPVF = \frac{|\widehat{I}_{i+1} \cap I_{i+1}|}{|I_{i+1}|} \tag{13.7}$$

$$FPVF = \frac{|I_{i+1}| - |\widehat{I}_{i+1} \cap I_{i+1}|}{|I_{\Omega}|} \tag{13.8}$$

In (13.6)–(13.8), |*| represents the volume of *, $\widehat{I}_{i+1}$ is the model-simulated CNV region achieved from the true ith image and I_{i+1} is the ground truth CNV region in the $i+1$th image. The true positive volume fraction (TPVF) represents the proportion of correctly identified CNV volume to the ground truth CNV volume, and the false positive volume fraction (FPVF) represents the proportion of falsely predicted CNV volume to the total background volume. In the experiment the weight w is set to 0.5 to enforce equal importance of true positive and false positive.

The optimization is achieved by genetic algorithm [25]. Using random initialization, the algorithm is run several times. With outliers excluded, the average value of the output is taken as the optimal parameter.

The growth parameter ρ_{N-1} for the last time point, is then estimated by curve fitting based on the optimal value of $\rho_1, \rho_2 \ldots \rho_{N-2}$.

13.3 Experimental Results

In the experiment, there are 7 subjects, each scanned at 12 time points, i.e., $N = 12$. This means the reaction-diffusion model is applied to the first 11 images to compute the prediction result for the 12th image. Then the result is validated by comparing it with the real 12th image. The ground truth of CNV volumes are obtained by manual segmentation in each B-scan by two experts independently. Figure 13.8a shows the high correlation (r = 0.978) of CNV volumes between ground truth I and II.

Figure 13.8b, c show the correlation of CNV volumes between the prediction results and ground truth I, or ground truth II. From the figure, we can see that the predicted results are highly positively correlated with both of the ground truth. The correlation coefficient are 0.988 and 0.993 respectively. Therefore in the following we choose ground truth I for comparison.

Figure 13.9 shows the curve fitting results of the CNV growth parameters for the 7 patients, in the treatment group and reference group, respectively. The last point in

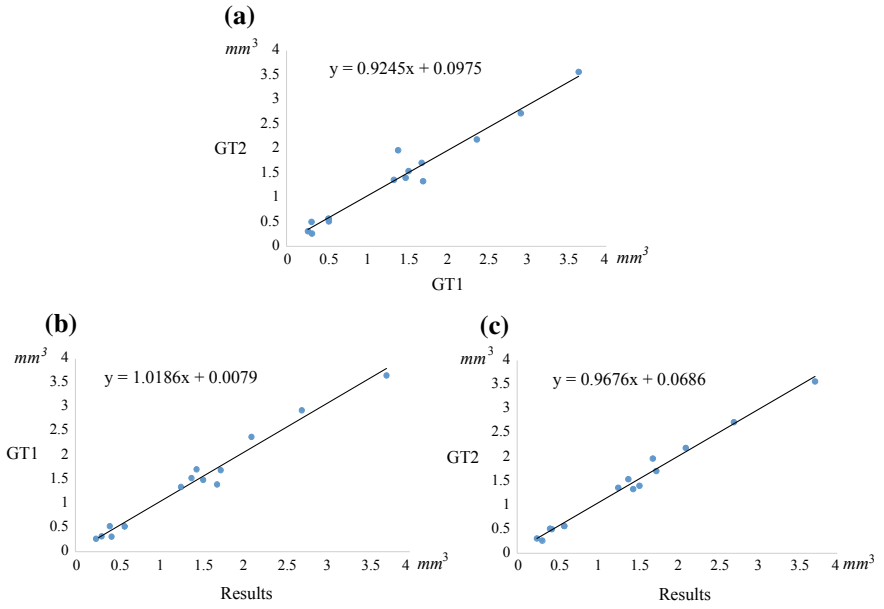

Fig. 13.8 **a**, **b** and **c** represent the correlation of ground truth I with ground truth II, the correlation of ground truth I with the predicted results and the correlation of ground truth II with the predicted results, respectively

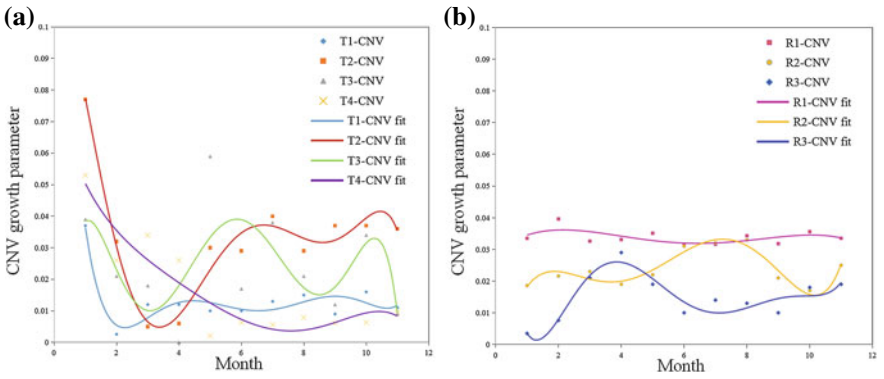

Fig. 13.9 **a** and **b** represent CNV growth parameters curve of treatment group and reference group

each curve represents the estimated parameter for the last time point. Figure 13.10 shows two examples of results of CNV growth prediction, compared with the ground truth. The TPVF, FPVF and Dice coefficients (DC) for each subject are listed in Table 13.1. The mean values of TPVF, FPVF and DC are 78.41, 2.44 and 79.22%, respectively, which shows the efficacy of the proposed method to predict the future status of CNV.

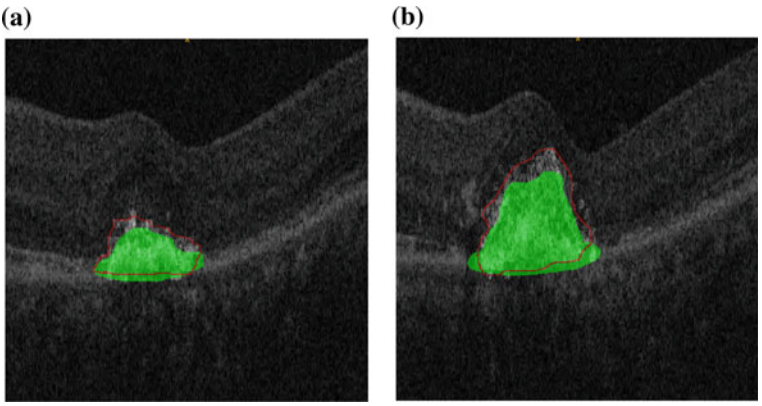

Fig. 13.10 Two examples of CNV growth prediction results. Green regions represent ground truth I. Red curves represent the boundary of predicted CNV regions

Table 13.1 TPVF, FPVF and DC by comparing the prediction results with ground truth I

	TPVF (%)	FPVF (%)	DC(%)
Patient T1	83.54	3.52	76.72
Patient T2	75.56	3.72	72.02
Patient T3	74.67	3.56	80.85
Patient T4	87.58	1.89	84.91
Patient R1	79.51	2.89	80.24
Patient R2	82.40	1.41	83.56
Patient R3	65.63	0.12	76.24
Mean	78.41	2.44	79.22

13.4 Conclusions

In this chapter, we present a method to predict the CNV status in the future time under treatment from longitudinal OCT scans. This is a pioneer study for predicting both the size and location of CNV in 3-D data. The proposed method is tested on a dataset with 84 longitudinal OCT images collected from 7 patients under two treatment plans. The average prediction accuracy, measured by the Dice coefficient, is 79.22%. The linear regression analysis of the predicted results and the manually segmented ground truth also show that they have strong correlations. Therefore the method achieves promising results for prediction the future status of CNV. Moreover, from the estimated CNV growth parameters for each time point (Fig. 13.9), the patient-specific response to anti-VEGF injections can be analyzed. We can see the drop in CNV growth rate corresponding to treatment for patients T1, T2, T3, T4, and R3, while R1 and R2 respond little to the treatment. In summary, the information provided by the method can be useful in clinical practice for guidance of treatment planning.

The method still has two limitations. First, it needs to be tested in a bigger dataset to further prove its prediction accuracy. Secondly, to enhance its performance, the image preprocessing methods, including registration and segmentation, needs improvement.

References

1. N. Kwak, N. Okamoto, J.M. Wood, P.A. Campochiaro, VEGF is major stimulator in model of choroidal neovascularization. Invest. Ophthalmol. Vis. Sci. **41**(10), 3158–3164 (2000)
2. A. Kubicka-Trząska, J. Wilańska, B. Romanowska-Dixon, M. Sanak, Circulating antiretinal antibodies predict the outcome of anti-VEGF therapy in patients with exudative age-related macular degeneration. Acta Ophthalmol. **90**(1), 21–24 (2012)
3. D. Huang, E.A. Swanson, C.P. Lin, J.S. Schuman, W.G. Stinson, W. Chang, M.R. Hee, T. Flotte, K. Gregory, C.A. Puliafito, J.G. Fujimoto, Optical coherence tomography. Science **254**, 1178–1181 (1991)
4. W. Drexler, J.G. Fujimoto, State-of-the-art retinal optical coherence tomography. Prog. Retinal Eye Res. **27**(1), 45–88 (2008)
5. G.J. Jaffe, J. Caprioli, Optical coherence tomography to detect and manage retinal disease and glaucoma. Am. J. Ophthalmol. **137**(1), 156–169 (2004)
6. M.R. Hee, C.R. Baumal, C.A. Puliafito, J.S. Duker, E. Reichel, J.R. Wilkins, J.G. Coker, J.S. Schuman, E.A. Swanson, J.G. Fujimoto, Optical coherence tomography of age-related macular degeneration and choroidal neovascularization. Ophthalmology **103**(8), 1260–1270 (1996)
7. P.J. Rosenfeld, A.E. Fung, G.A. Lalwani, Visual acuity outcomes following a variable-dosing regimen for ranibizumab (LucentisTM) in neovascular AMD: the PrONTO study. Invest. Ophthalmol. Vis. Sci. **47**(13), 2958 (2006)
8. H. Bogunovic, M.D. Abràmoff, L. Zhang, M. Sonka, Prediction of treatment response from retinal OCT in patients with exudative age-related macular degeneration, in *Medical Imaging and Computer-Assisted Interventions Workshop* (2014)
9. W.D. Vogl, S.M. Waldstein, B.S. Gerendas, U. Schmidterfurth, G. Langs, Predicting macular edema recurrence from spatio-temporal signatures in optical coherence tomography images. IEEE Trans. Med. Imaging **36**(9), 1773–1783 (2017)
10. S. Zhu, F. Shi, D. Xiang, W. Zhu, H. Chen, X. Chen, Choroid neovascularization growth prediction with treatment based on reaction-diffusion model in 3-D OCT images. IEEE J. Biomed. Health Inform. **21**(6), 1667–1674 (2017)
11. X. Guo, Three-dimensional moment invariants under rigid transformation. Lect. Notes Comput. Sci. **719**, 518–522 (1993)
12. F. Shi, X. Chen, H. Zhao, W. Zhu, D. Xiang, E. Gao, M. Sonka, H. Chen, Automated 3-D retinal layer segmentation of macular optical coherence tomography images with serous pigment epithelial detachments. IEEE Trans. Med. Imaging **34**(2), 441–452 (2015)
13. X. Chen, M. Niemeijer, L. Zhang, K. Lee, M.D. Abràmoff, M. Sonka, Three-dimensional segmentation of fluid-associated abnormalities in retinal OCT: probability constrained graph-search-graph-cut. IEEE Trans. Med. Imaging **31**(8), 1521–1531 (2012)
14. Q. Fang, ISO2Mesh: a 3D surface and volumetric mesh generator for MATLAB/octave [Online]. Available: http://iso2mesh.sourceforge.net/cgi-bin/index.cgi?Home (2010)
15. Q. Fang, D.A. Boas, Tetrahedral mesh generation from volumetric binary and grayscale images, in *Proceedings of the Sixth IEEE international conference on Symposium on Biomedical Imaging: From Nano to Macro* (IEEE Press, 2009), pp. 1142–1145
16. A.E. Islam, N. Goel, S. Mahapatra, M.A. Alam, Reaction-diffusion model. Springer Series Adv. Microelectron. **139**, 181–207 (2016)
17. X. Chen, R.M. Summers, J. Yao, Kidney tumor growth prediction by coupling reaction-diffusion and biomechanical model. IEEE Trans. Biomed. Eng. **60**(1), 169–173 (2013)

18. K.C.L. Wong, R.M. Summers, E. Kebebew, J. Yao, Pancreatic tumor growth prediction with multiplicative growth and image-derived motion. Inf. Process. Med. Imaging 501–513 (2015)
19. M. Lê, H. Delingette, J. Kalpathy-Cramer, E.R. Gerstner, T. Batchelor, J. Unkelbach, N. Ayache, *Medical Image Computing and Computer-Assisted Intervention* (Springer International Publishing, 2015), pp. 424–432
20. J. Friedman, T. Hastie, R. Tibshirani, Additive logistic regression: a statistical view of boosting. Ann. Stat. **28**(1), 2000 (1998)
21. K.-J. Bathe, *Finite Element Method* (Butterworth-Heinemann, 2000), pp. 394–409
22. A. Mohamed, C. Davatzikos, Finite element modeling of brain tumor mass-effect from 3D medical images. Med. Image Comput. Comput. Assist. Interv. **8**(Pt1), 400–408 (2005)
23. A. Hanhart, M.K. Gobbert, L.T. Izu, A memory-efficient finite element method for systems of reaction-diffusion equations with nonsmooth forcing. J. Comput. Appl. Math. **169**(2), 431–458 (2010)
24. C. Hoge, C. Davatzikos, G. Biros, An image-driven parameter estimation problem for a reaction-diffusion glioma growth model with mass effects. J. Math. Biol. **56**(6), 793–825 (2008)
25. S. Austin, An introduction to genetic algorithms. Quart. Rev. Biol. **24**(4/5), 325–336 (1996)

Index

X. Chen et al. (eds.), *Retinal Optical Coherence Tomography Image Analysis*,
Biological and Medical Physics, Biomedical Engineering,
https://doi.org/10.1007/978-981-13-1825-2